SLAM SIMULATIONS : AN APPLICATION OF COMPUTATIONAL FLUID DYNAMICS

by

PAUL GALLAGHER BSc

This Thesis is submitted for the degree of Doctor of Philosophy to the Department of Naval Architecture and Ocean Engineering, University of Glasgow

May 1985

ProQuest LLC.
789 East Eisenhower Parkway
P.O. Box 1346
Ann Arbor, MI 48106 – 1346

DECLARATION

Except where reference is made to the work of others, this thesis is believed to be original.

TO

Julie and Stuart

ACKNOWLEDGEMENTS

I wish to thank Professor D Faulkner, Head of the Department of Naval Architecture and Ocean Engineering, who made it possible to carry out this work.

I am also grateful to Dr R C McGregor, my supervisor, for his support and encouragement throughout this work.

I am indebted to Edwin and Patricia Peters whose combined talents resulted in the highly efficient typing of this thesis.

I would like to thank the Education Department of the States of Jersey for their financial assistance over the first two years of study.

Last, but not least, I am deeply grateful to my wife for her constant support, especially during the production of this thesis.

CONTENTS

SUMMARY

The ability of ships and other marine vehicles to maintain forward speed in heavy weather is often limited by the phenomenon of slamming. The hydrodynamics of this impact problem are poorly understood in a quantative sense, though previous research has identified various physical mechanisms important to ship slamming. This thesis describes the development of a number of numerical tools designed to study the non-linear free surface flow problems caused by slamming.

The research focused on two major areas of study. Firstly, a generalised simulation method for the solution of the mass and momentum conservation equations over a fluid domain bounded by a free surface and containing dynamic boundaries was developed. This technique was used to study the hydrodynamic impact of an arbitrary shaped body. A finite difference time marching solution to the continuity coupled Navier Stokes equations was employed as the basis of the simulation technique. A novel application of the well known source distribution method was used to model moving solid boundaries of arbitrary shape within the confines of the regular finite difference mesh. This particular aspect of the research allowed a marriage of traditional hydrodynamic theory and the more recent developments in computational fluid dynamics.

The second area of study examined the behaviour of the compressible air layer formed between the free surface and an approaching bluff body. Again, the techniques of computational fluid dynamics were employed to solve the equations of mass and momentum

conservation in the air layer and the associated free surface motions caused by the build up of pressure beneath the falling body.

The thesis presents a number of computational examples in order to illustrate the development and final levels of accuracy achieved by the two classes of numerical algorithm mentioned above. Simulations of steady viscous free surface flow, wavemaker modelling, vehicle motions and added mass computations are employed to test the numerical algorithms. Results from hydrodynamic impact simulations are presented and compared with existing numerical and experimental data, for a range of hull shapes. The effects of air entrapment on impact geometry is discussed via a comparison of results obtained by the present method and data from both computations and experiment reported in the open literature.

Conclusions concerning the quantitative importance of the various physical parameters involved in slamming on the ship scale are presented at the end of the thesis.

GENERAL

A	Submerged sectional area
B	Bulk modulus of water
C_a	Speed of sound in air
C_p	Specific heat at constant pressure
C_v	Specific heat at constant volume
C_s	Slam coefficient
C	Speed of sound in water
C_x	Phase speed
D	Diameter of cylinder
E_s	Energy per unit volume (air)
E_ε	Strain energy
F	Fluid fractional volume
F_B	Body fractional volume
F_r	Froude number
G	Amplification factor
$K(x,t)$	Kernel of integral relationship for free surface height
L_u, L_v	Matrix operators for implicit numerical methods
M	Mass
M_a	Added mass
M_b	Body mass
$P(\phi)$	Probability distribution function
Q_{ij}	Discrete source strength
R	Radius of a cylinder
R_ρ, R	Ratios of fractional adjustment rates
R_e	Reynolds number
R_{ec}	Cell Reynolds number

R	Gas constant
S	Right hand side of Poisson steady pressure equation
T	Temperature
U_p, V_p	Marker particle velocities
U_b, V_b	Body velocity components
V_i	Impact velocity
V_t	Threshold velocity
WD	Work done
Xg, Yg	Components of body force
x	Fractional adjustment rate
a_0, a_1, a_2 b_0, b_1, b_2	Polynomial coefficients
b	Wetted beam of a hull section
e	Internal energy per unit volume
g	Acceleration due to gravity = 9.81m/s
i,j	Nodal indices
n	Integer numbe of time steps
p	Fluid pressure
t	Time
u,v	x and y velocity component for fluid
x,y	cartesian co-ordinate system
z	Immersion of section below mean free surface
Δ	Discrete step (eg Δt)
θ	Half angle, bisecting submerged arc of cylinder
ϕ	Fluid velocity potential
ψ	Fluid stream function
η	Free surface elevation
μ	Molecular viscosity
ν	Kinematic viscosity
ρ_a	Density of air

ρ	Density of water
$\delta_x \delta_y$	General finite difference operators
σ_s	Slam whipping stress
∇	Divergence of
∇^2	Laplacien or diffusion operator

SPECIFIC NOMENCLATURE

Chapter 2

N_s	Number of slams per unit time
R_σ	Variance of slamming stress
T_s	Duration of slam pressure pulse
T_p	Natural period of steel plate
h	Ship draught at slamming station
n	Number of observations (slams)
C	Damping coefficient
ω	Circular frequency

Chapters 3, 7, 10

C_a	Sound speed in air
R	Gas constant
h	Thickness of trapped air layer
u_a	Velocity in trapped air layer
p_a	Pressure in air layer
n,s	outward normal and tangential vectors
n_x, n_y	x and y components of outward normal vector
γ	Ratio of specific heats
ρ_a	Density in air layer
β	Deadrise angle

Chapters 4, 9

A	Amplitude operators
G	Amplification factor
[L]	Influence matrix for SOR calculation
[N]	Finite element shape functions
[U]	Nodal finite element velocity vector
Z	Error amplitudes
h	Depth of water
R, δR	Fluid domain and boundary
δ	Small variation in
δ_x, δ_y	General finite difference operators
β	Mesh size ratio
ω	Relaxation factor

Chapter 6

α, γ, β	Weighting values for variational method
λ	Lagrange multiplier

CHAPTER 1

INTRODUCTION

CHAPTER 1

INTRODUCTION

Whilst making a passage in heavy weather, a ship will be subjected to severe motions which may cause hydrodynamic impact loadings to occur on certain forward areas of the hull. Heaving and pitching allow the relative velocity between the bow sections and the oncoming seas to contain a considerable vertical component. Slamming may then arise from two sources:-

a. bow flare loadings.

b. bottom impacts.

In the first case, various factors such as 'swell up' and heavy sectional flare may add to the contribution from a high relative vertical velocity between bow and waves to produce impulsive hydrodynamic loads. These loads are the result of a high time rate of change of added virtual mass. The outcome is a rapid deceleration in vertical motion at the bow, accompanied by a 'shudder' or whipping vibration felt throughout the hull.

In the latter case slamming is the result of much more violent motions. Sections of the keel forward clear the water completely. Upon re-entry, excessive pressures are generated local to the point of impact. Damage, such as permanent set in hull plating, may occur. The overall response of the hull is much the same as for bow flare slamming.

Research has concentrated upon both statistical and deterministic representations of slamming phenomena. The former attempts to quantify slam frequencies, whipping stress exceedence, etc. The latter area examines local loadings and overall response.

This study addresses itself to a deterministic examination of the local hydrodynamic loading problem. The objective is to gain a quantitative representation of the physics behind the general impact phenomenon.

The thesis consists of three main sections. First, a literature survey of previous slamming research defines the limits of present knowledge in a number of subjects associated with impacts upon structures at sea. Conclusions are drawn as to the areas of study most worthy of attention.

The second section describes the techniques developed by this author and subsequently used to study the fluid mechanics of the impact problem. Chapters 2 to 7 are devoted to the discipline of computational fluid dynamics as applied to the three physical regimes thought to be of importance in slamming. These three domains of fluid behaviour are:-

a. Viscous/inviscid, incompressible flow as described by the continuity coupled Navier Stokes equations applied to a domain bounded by a free surface and containing moving solid boundaries.

b. A 'slightly' compressible flow, needed to model the sharp pressure peaks associated with some types of slamming problem.

c. The aerodynamics associated with the development of a cushioning air layer beneath a bluff body prior to impact with the free surface.

The rest of the thesis is concerned with the results and conclusions derived from the application of computational fluid dynamics to flow simulation.

Chapter 8 describes two computer programs, FLOW88 and NWAV90, used to evaluate the accuracy and convergence characteristicss of a general algorithm for free surface flow.

Chapter 9 develops the theme of dynamic simulation to model the hydrodynamic water entry problem and includes an application of the slightly compressible flow algorithm. A study of the role of air entrapment and cushioning effects in slamming is made in chapter 10.

Finally, chapter 11 combines the various aspects of flow modelling used in the previous chapters and details the lessons learned concerning the quantitative physics of the slamming problem.

CHAPTER 2

A REVIEW OF AVAILABLE LITERATURE

CHAPTER 2

A REVIEW OF AVAILABLE LITERATURE

1. INTRODUCTION

Research into slamming on marine vehicles has concentrated in two main areas:-

a. Seakeeping.

b. Local hydrodynamics.

Within the area of seakeeping, the main aims have been to predict slamming frequency and overall response. Consideration of the hydrodynamic problem at the point of impact seeks to quantify the local slam loading distribution.

The following review examines both the experimental and computational efforts to remove uncertainty over the effects of slamming, made by various authors over the past thirty years.

2. FULL SCALE SEAKEEPING TRIALS

Whilst many incidents of slamming and slamming damage had been reported during the first half of the century, particularly during the second world war, deliberate measurements of such loadings at sea did not begin until the mid 1950's. In 1956 Greenspon et al measured pressures on a coastguard cutter during rough weather. Peak values at the keel reached 1.84 N/mm^2 ($270lbs/in^2$) with most pressures recorded being between 0.34 - 0.68 N/mm^2 (50 - $100lbs/in^2$). The pressure pulses were triangular in shape and were between 0.05s and 0.2s in duration.

Later (1958), Jasper and Birmingham (2) investigated the magnitude of whipping stresses on the USS Essex during storms near Cape Horn. Peak to peak values of 120 N/mm^2 (20Kpsi) at a frequency of 5.44 rad/s^{-1}(0.866 Hz) were recorded for whipping stresses alone, in quartering seas of characteristic wave height 6.06 m (20 ft) and at a ship speed of 17 knots. The maximum stresses occurred in sag, and were sufficient to cause some buckling damage to the upper deck structure. In later trials on the USS Ranger (3), no storms were encountered but long swells caused bow flare slamming which resulted in whipping stresses of up to 43 N/mm^2(7.2Kpsi).

In a number of papers on seakeeping trials performed between 1963 and 1972, Aertssen (4-8) reviewed the effects of slamming on four merchant ships. No bottom pressure measurements were taken and information on sea-state was restricted to subjective observation by the officer on watch. However, some general points were noted:-

a. All bottom slamming occurred in ballast condition.

b. Whipping stresses started in sag and produced a sag/hog ratio greater than unity. This is illustrated by figure 2-1, showing a record of whipping stress in the upper deck of the container ship "Dart Europe".

c. The choice of criterion by which to decide whether a slam had occurred was difficult, but could be based on a threshold midships whipping stress or a value of bow decceleration. These values were dependent upon ship size.

d. The ship's master's subjective judgement of slamming severity varied greatly.

e. The application of Tick's formula (76) for the prediction of the number of slams per second,

$$N_s = \frac{1}{2\pi} \frac{R_v}{R_h} \exp\left(-\frac{1}{2}\left(\frac{h^2}{R_h} + \frac{V_t^2}{R_v}\right)\right) \qquad \text{--- 2.1/1}$$

where N_s = number of slams per second,

h = ship draught at the bow,

V_t = slamming threshold velocity,

R_h = variance of relative bow motion,

R_v = variance of relative bow velocity.

proved to be inaccurate.

The largest whipping vibration stresses encountered were measured on the container ship "Dart Europe" (6). The sag component alone reached 150 N/mm^2. Figure 2-1 (taken from reference 6) shows a total stress range of 270 N/mm^2 for a particularly heavy slamming event.

During the late 1960's, the merchant ship SS Wolverine State was fitted with instrumentation to measure bottom pressures, whipping

Figure 2-1 Midship Bending Stress Record
From Reference 6

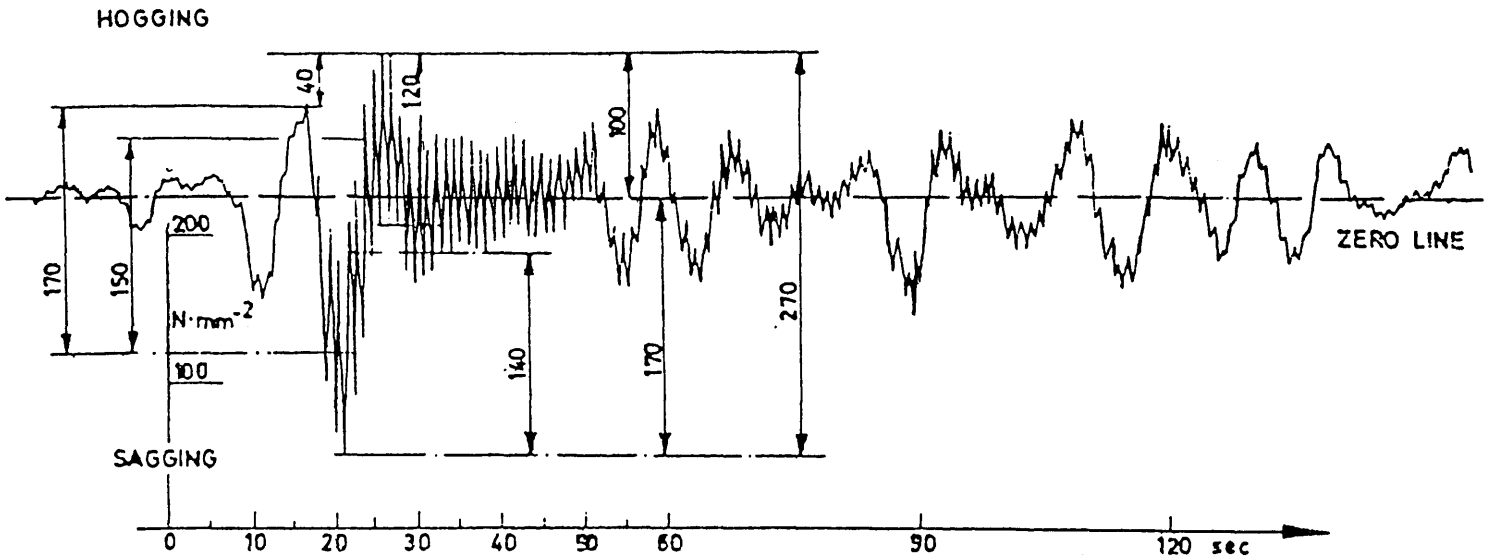

stress magnitudes and motions during long ocean voyages. Only three storms severe enough to cause significant slamming were encountered. However, Wheaton et al (9) found fairly modest peak whipping stresses of 32 N/mm^2 with bottom pressures reaching 0.47 N/mm^2 (69lbs/in^2). The pulse duration varied with longitudinal position, being greater at the forward sections where the section rise of floor was more pronounced. The maximum pulse duration recorded was 0.2 seconds at the forward pressure transducer. The shortest pulses were recorded at a position one tenth of the LBP from the forward perpendicular and lasted 0.5 seconds. This was also the position of the highest recorded pressures, though there was no correlation between magnitude and duration. The peak pressure loading was seen to move forward and/or aft, with speeds of up to 70m/s.

No attempt was made to measure relative impact velocities and, hence, no relationship between ship motions and peak pressures could be ascertained. For the particular records used, the number of slams per unit time seemed to fit a Rayleigh type probability distribution. Maclean and Lewis (10) also analysed this data and found the slamming statistics to be insensitive to the sea conditions when the ship's master's actions were taken into account.

A later examination of the Wolverine State data by Wheaton (11) threw doubt on the conclusions concerning the statistics of slamming occurrence. It was noted that some ten per cent of the slams occurred within intervals less than the natural pitching period of the vessel. It was not clear in some cases whether the whipping vibrations had been caused by bottom impacts or bow flare slams. On some occasions bottom emergence was recorded without a subsequent slam.

High speed trials on two frigates in severe head seas were reported independently by Andrews and Lloyd (12) in 1981, and Clarke (13) in 1982. The increase in slam occurences in any given sea state with speed was very marked. However, the slamming stresses did not increase as rapidly showing asymptotic behaviour, though the magnitude of the limit could not be defined. The sag/hog ratio for whipping stresses was again seen to be greater than unity. The statistics of the midships bending stress induced by slamming, seemed to follow a Rayleigh distribution, ie

$$P(\sigma_s) = \frac{\pi}{2}\left(\frac{\sigma_s}{R_\sigma}\right) \exp\left(\frac{\pi}{4}\left(\frac{\sigma_s}{R_\sigma}\right)\right)$$

— — — 2.1/2

where σ_s : slam stress

R_σ : variance of slam stress.

A threshold level of 2.0N/mm^2 for the midships bending stress in the two node mode was suggested, in order to distinguish between whipping and springing (13). This may be compared with a figure of 1.0N/mm^2 chosen by Aertssen for a ship of similar length. The choice of the threshold whipping stress is of great importance to the statistics of slamming and, of the two values quoted, neither seems to guarantee the separation of whipping and springing data. A great deal more data is required before such a choice can be made for any particular ship.

3. SEAKEEPING MODEL EXPERIMENTS

The first attempt to examine the behaviour of a ship model subject to slamming was reported by Akita and Ochi (16). The model was six metres long, 'U' shaped in section and symmetrical fore and aft. Various experiments were carried out to examine the effect of ship speed, wave height, wave length, draught and trim on the slamming characteristics of the model. Heavy slamming was noted at encounter frequencies close to resonance, also coinciding with a ninety degree phase difference between pitch and heave. Peak impact pressures increased linearly with ship speed and reached a maximum value of $2.3 \times 10^{-3} N/mm^2$ on the model scale, with a wave height to draught ratio of 0.169.

This may be expressed using an approximate pressure coefficient for the equation:-

$$P_m = \frac{1}{2} C_s \rho_w V_i^2 \qquad \text{---} \quad 2.3/1$$

of 4.60 . As with the full scale measurements cited in section 2.2, sag/hog ratios were greater than unity.

Later, Ochi (17) compared the effects of bow form on ship slamming using two models, one with 'U' shaped sections, the other being 'V' shaped. A number of general points emerged. Maximum bottom slamming pressures were confirmed to be approximately proportional to the square of the relative impact velocity. A definite threshold impact velocity was found to be 3.45 m/s (11.5 ft/sec), for a full scale ship (157m). Whipping stresses were found to be proportional to the square of the difference betwen the wave height and a threshold wave height, below which no slams occurred despite bow emergence, ie:-

$$\sigma_s \propto (h_w - h_t)^2$$

--- 2.3/2

where h_w : wave height

h_t : threshold height

σ_s : whipping stress.

This result must be considered suspect in the light of evidence from measurements at sea that the maximum bending moments in both hog and sag show asymptotic behaviour with increasing wave height (13). The highest bottom pressures always occurred at the keel at the instant of contact with the water surface. For any given time after initial contact the highest pressures occurred at the outer edge of the wetted beam. The V form hull was considered superior in slamming performance to the U form. Unfortunately, data on pressure pulse duration was not reported.

Further model experiments by Ochi (18) found bulbous bows to have little overall effect on the slamming phenomenon. Tests performed by Bledsoe and Schwartz (19), and backed up with earlier computations by Todd (20), qualitatively confirmed Ochi's measurements of pressure distribution but revealed the sensitivity of the pressure magnitudes to the type of experiment performed. Whereas Ochi's tests were performed in waves, Bledsoe and Schwartz carried out rotational drop tests on a series 60 ship model (C_B = 0.80) on a calm water surface. The peak pressures thus measured were one, sometimes two, orders of magnitude greater than those found by Ochi. The expression for peak pressure put forward by Todd was:-

$$p_m = \frac{1}{2}\rho_w V_i^2 (1 + 1/\theta)$$

--- 2.3/3

where θ is the effective slope of the section.

These experiments were performed at almost zero draught, making it possible for to become extremely small, thus predicting very large pressures. Of the two experimental practices, that of Ochi must be considered more reliable in measuring the peak pressures. Whilst there is a finite probability of very small relative impact angles between sea surface and ship hull to exist, the complete physical picture is somewhat different to that modelled by Bledsoe and Schwartz.

In 1962, Ochi repeated his experiments on U and V shaped hull forms (21) with similar results. The position of maximum pressure was seen to move aft with increasing ship speed, the effect being more pronounced with the V form hull. More detailed tests at various heading angles were reported (22), again by Ochi, in 1964. The prediction of slamming occurrence by use of a Rayleigh distribution (equation 2.1/2) was found reasonably accurate. The probability distribution function for slamming pressure was assumed to follow a truncated exponential distribution given by:-

$$f(p_m) = \left(\frac{1}{2C_s \rho_w R_v}\right) \exp\left(-\left(\frac{1}{2C_s \rho_w R_v}\right)(p_m - p_o)\right), \qquad p_m > p_o \qquad \text{--- 2.3/4}$$

where p_m : peak slamming pressure,

p_o : threshold slamming pressure,

R_v : twice the variance of the relative velocity between wave and ship bow.

Figure 2-2 illustrates the accuracy of this expression in fitting one particular set of experimental data (from Reference 22). Ochi was able to present a simple method to predict permanent set in bottom plating using this probability law. Pressure pulse duration was noted to be between 0.08 and 0.12 seconds at the keel, a much narrower range than reported from tests on the Wolverine State (9,11) and

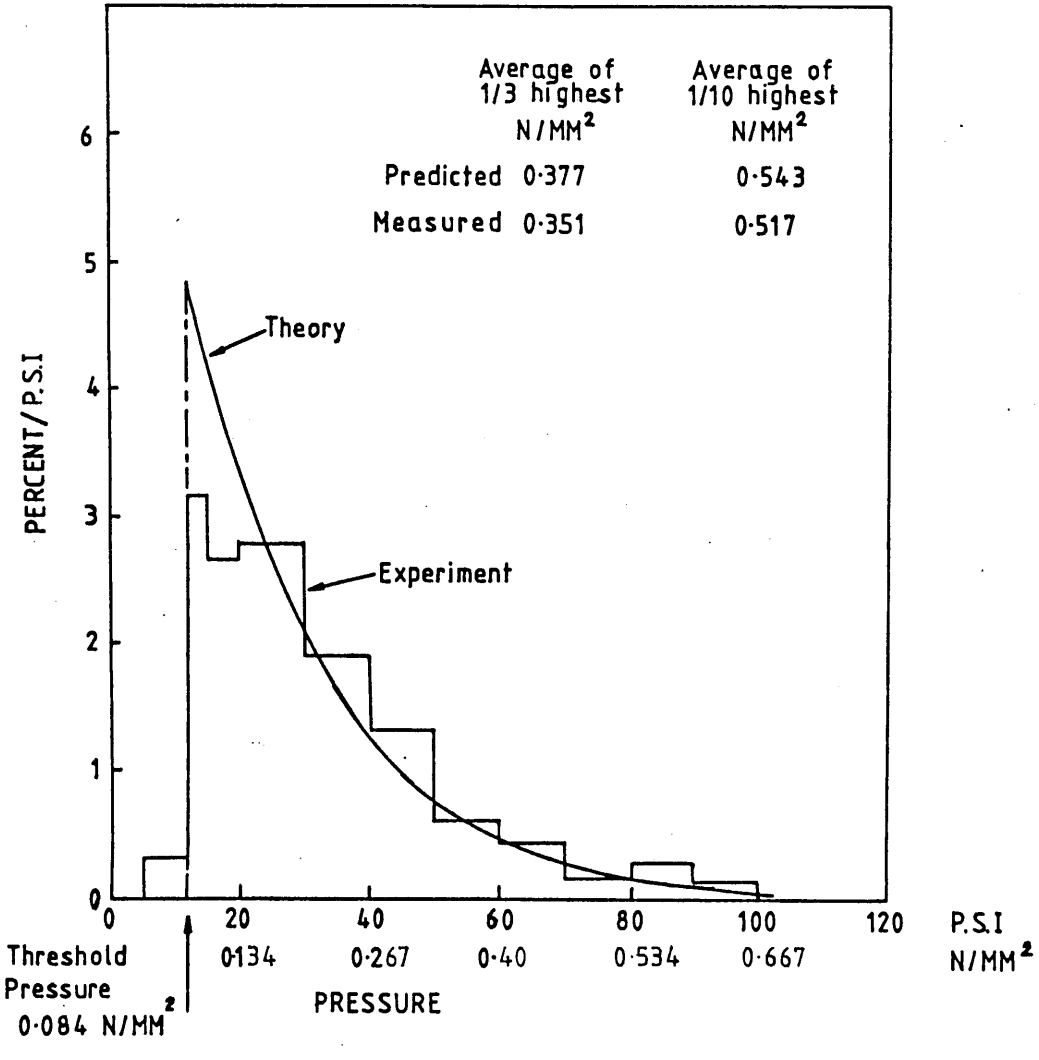

Figure 2-2 Distribution Of Slam Pressure Exceedence (Reference 22)

seemingly not subject to any scaling laws. Perhaps the most dramatic consequence of these tests was to show how pitching motions and the resulting slam occurrence could be reduced by a change in heading angle. Further experiments in bi-directional seas showed an increase in slamming frequency but recorded lower average stresses.

In 1969, Lewison (23) made use of the air entrapment phenomenon observed during drop tests (section 2.4) during a series of experiments with a ship model in waves. Peak bottom pressures were dramatically reduced by attaching vertical plates either side of the keel in the region of the forefoot, enabling a cushion of air to be formed beneath the hull. Lewison also experimented with a technique of blowing compressed air into recesses built into the keel area. This also reduced peak slamming pressures. Doubts were expressed concerning the use of both techniques on the full scale during subsequent discussion of the paper. It was thought that protection against damage could be ensured more economically by the addition of extra stiffening to bottom plating elements.

The impact of a ship secion onto a fluid free surface may be idealised by the classic water entry problem. The resulting view of slamming has been exploited in two ways. Firstly, this simplified situation may be reproduced by experiment. Secondly, assumptions concerning the physical behaviour of the fluid may be made for the purposes of computation. In some cases results from drop test experiments have motivated the development of new computational techniques in order to quantify the underlying physics behind the general impact phenomenon.

The first attempt to calculate the loads on a wedge shaped section whilst plunging through the free surface was made by Von Karman (25). The mathematical model used was that of an expanding flat plate, see figure 2-3. The total force was derived via Newton's third law, ie:-

$$F = \frac{d}{dt}(M V_b) = \dot{M} V_b + M \dot{V}_b \qquad \text{---} \quad 2.4/1$$

which, upon consideration of the instantaneous added mass of the section, and of the use of the relationship:-

$$\frac{d}{dt} = \frac{d}{dz}\frac{dz}{dt} = V_b \frac{d}{dz}$$

yields,

$$F = \frac{d}{dt}(M V_b) = (M_b + M_a(z))\dot{V}_b + \frac{d(M_a)}{dz} V_b^2 \qquad \text{---} \quad 2.4/2$$

where M_b : mass of body.

M_a : Added mass of body (a function of immersion Z)

$M_b + M_a$: total instantaneous mass.

V_b : Body velocity.

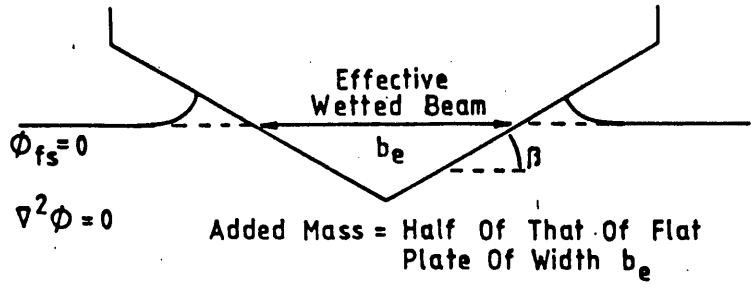

Figure 2-3 Von-Karman Expanding Flat Plate Model.

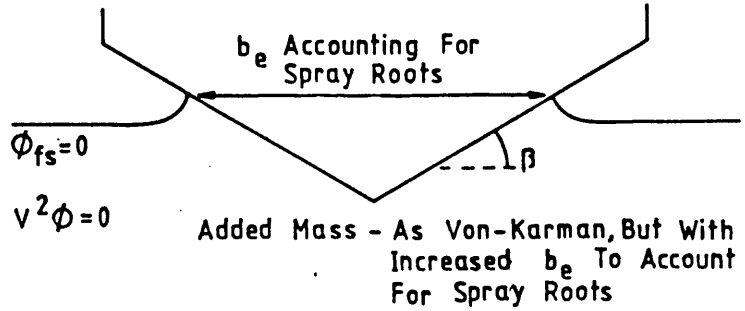

Figure 2-4 Wagner's Expanding Flat Plate Model

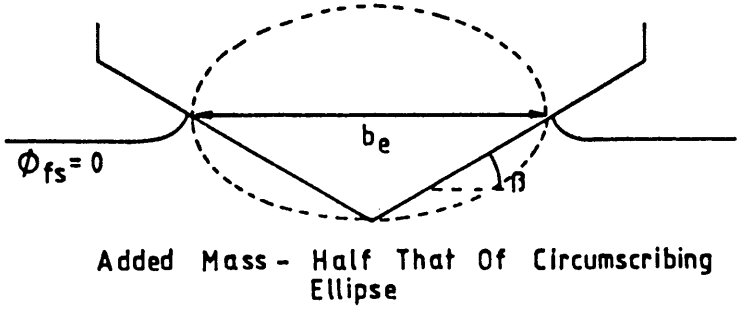

Figure 2-5 Fabula's Ellipse Fitting Model Of Wedge Impact

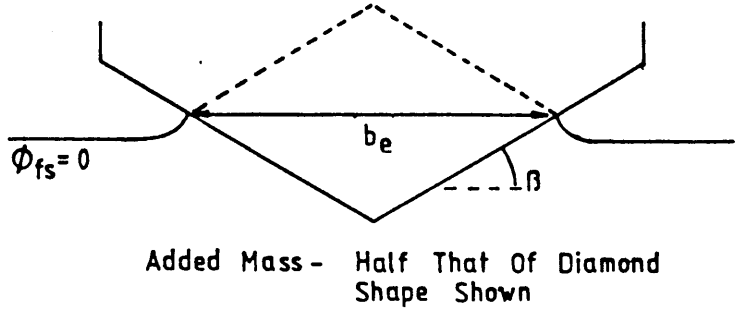

Figure 2-6 Bisplinghoff And Doherty's Diamond Reflection Model

The quantity $$F_s = \frac{d(M_a)}{dz} V_b^2 \quad --- \quad 2.4/3$$

is taken to be the total slamming force which for a constant impact velocity gives the total load on the section as:-

$$F_T = F_s + F_B$$

where F_B : total buoyancy force.

Half the added mass of a flat plate per unit length is:-

$$M_a = 0.5 \pi \rho_w (b(t))^2 \quad --- \quad 2.4/4$$

where b(t) : beam of the section.

The rate of change of added mass is then simply given by:-

$$\frac{dM_a}{dt} = \pi \rho_w (b(t))' \frac{d(b(t))'}{dt} \quad --- \quad 2.4/5$$

where the suffices indicate instantaneous values.

Von Karman used the rate of change of beam at the still water free surface level in equation 2.4/5. In using the expanding flat plate model, no account of the underwater shape of the section was allowed.

Wagner (26) later formulated the problem to take account of the piled up water at the spray root. As can be seen in figure 2-4, the effect is to increase the rate of change of wetted beam. Wagner assumed the free surface to be a zero potential line and then expressed the free surface height in terms of an integral equation based on the relationship betweem the body velocity and free surface velocity, ie:-

$$\eta(x) = \int_0^b K(x,b)\left(\frac{dz}{db}\right)db = \int_0^x \frac{\dot{\eta}(x,b)}{V_b} V_b dt \qquad \text{---} \quad 2.4/6$$

where $\eta(x)$: free surface height

$$K(x,b) = 1/\left(1-(b/x)^2\right)^{1/2} \qquad \text{---} \quad 2.4/7$$

$$z = \int_0^b \left(\frac{dz}{dc}\right) dc \qquad \text{---} \quad 2.4/8$$

Wagner solved these integral equations using a power series expansion method, wherein equation 2.4/6 is replaced by:-

$$\eta(x) = \int_0^b K(x,b)\left(\frac{dz}{dt} / \frac{db}{dt}\right)db = \int_0^b K(x,b)\, u(b)\, db \qquad \text{---} \quad 2.4/9$$

where u(b) is the ratio of the body velocity to the rate of change of beam and is given by:-

$$u(b) = a_0 + a_1 b + a_2 b^2 + \text{.....} a_n b^n \qquad \text{---} \quad 2.4/10$$

The free surface height at the edge of the plate, $\eta(b)$ (see figure 2-4), may also be expressed in terms of a power series function of beam:-

$$\eta(b) = c_0 + c_1 b + c_2 b^2 + \text{.....} c_n b^n \qquad \text{---} \quad 2.4/11$$

Thus, substitution of 2.4/10 into 2.4/9 allows the integration to be performed on each term from the power series. Equating coefficients in b^n from equation 2.4/11 and the resulting integral and assuming small deadrise angles such that,

$$\eta(b) = b.\beta \qquad \text{---} \quad 2.4/12$$

where β = the deadrise angle allows for the solution of the coefficients a_n. Consideration of the potential flow resulting from

the expansion of the flat plate in a steady flow, yields an expression for the pressure on the body via Bernoulli's equation, ie:-

$$P(x) = \frac{1}{2}\rho_w V_b^2 \left(\frac{\pi}{\beta(1-(x/b)^2)} - \frac{(x/b)^2}{(1\ (x/b)^2)} \right) \qquad --- \ 2.4/13$$

This gives a maximum pressure of:-

$$P(x) = \frac{1}{2}\rho_w V_b^2 \left(1 + \left(\frac{\pi}{2\beta}\right)^2\right) \qquad --- \ 2.4/14$$

at $$x = b\left(1-\left(\frac{2\beta}{\pi}\right)^2\right)^{1/2} \qquad --- \ 2.4/15$$

In 1952, Szebehely (27), reviewed the above techniques and suggested their use in solving the ship slamming problem. Fabula (28) extended the technique replacing the flat plate added mass by half the added mass of an ellipsoid of equal beam and draught to the section being studied, see figure 2-5. In this case, the kernel of the integral relationship 2.4/6 is given by:-

$$K(x,b) = \frac{1}{\left(1-\left(\frac{\eta(b)}{b}\right)\right)}\left[\left(1-\left(\frac{b}{x}\right)^2\left(1-\left(\frac{\eta(b)}{b}\right)^2\right)\right)^{1/2} - \frac{\eta(b)}{b}\right] \qquad --- \ 2.4/16$$

with a power series expansion in u(b) again being applied in the form:-

$$\lim_{b\to 0} u(b) = \lim_{b\to 0} \sum_{n=1}^{\infty} \frac{\eta^n(x=0)}{N!} . b^{n-1} \frac{2\Gamma\left(\frac{n+1}{2}\right)}{\Gamma\left(\frac{1}{2}\right)\Gamma\left(\frac{n}{2}\right)} \qquad --- \ 2.4/17$$

This technique no longer allows for simple evaluation and a computer must be used in order to arrive at a solution with a reasonable degree of accuracy.

The above methods are known as fitting techniques since they attempt to put a best fit to a given section using known geometrical

shapes. A further class of solution exists, known as the body reflection technique, in which the instantaneous added mass of a simple section (for example a wedge) is taken as half that due to the shape reflected about the free surface. In the case of a wedge such a shape is supplied by a diamond, see fig. 2-6. This latter geometry was exploited by Bisplinghoff and Doherty (29). The instantaneous wetted beam is again derived using Wagner's method and, therefore, the technique is restricted to 'small' deadrise angles. The body reflection method was also exploited by Kaplan (52), as reviewed later in this chapter, in work on wave slam on horizontal cylinders.

Lack of agreement between theory and experiment lead Ogilvie (31) to formulate the wedge entry problem using a compressible potential flow. The fluid potential was expressed in two parts:-

$$\phi_f = \phi_i + \phi_c \qquad \text{--- 2.4/18}$$

where ϕ_i : potential of incompressible flow

ϕ_c : potential of compressible flow

The solution for each component was found from the equations:-

$$\nabla^2 \phi_i = 0 \qquad \text{--- 2.4/19}$$

$$\nabla^2 \phi_c = \frac{1}{c_w^2} \frac{\partial^2 \phi_c}{\partial t^2} \qquad \text{--- 2.4/20}$$

where c_w : speed of sound in water.

The results were disappointing, predicting slam pressures up to the acoustic limit given by:-

$$P_m = \rho_w c_w V_b \qquad 2.4/21$$

These values were far too high and have never been measured in practice.

In 1966, Ferdinande (32), made use of the Schwartz-Christoffel transformation to map the domain contained between the boundary of a wedge reflected about the free surface and infinity on to the upper half plane. The resulting method requires the use of a computer to evaluate the pressure distribution for various deadrise angles but is not restricted to any assumptions concerning the size of β.

Another attempt to produce better agreement between theory and experiment was reported by Chuang (33). A series of drop tests with small, light, flat bottomed bodies were performed, with instrumentation capable of measuring the acoustic pressures predicted by Ogilvie. Examination of high speed film of the impacts revealed the formation of a cushioning air layer prior to contact between the body and the free surface. Maximum pressures were approximately one tenth of the acoustic value (equation 2.4/21), very much lower than had been predicted. A curve fit to measured pressure time histories (see figure 2-7), gave the expression:-

$$p(t) = 2 p_m \exp(-1.4 t/T) \sin(\pi t/T) \qquad \text{--- 2.4/22}$$

where T : characteristic time given by:-

$$T = 4b/C_a \qquad \text{--- 2.4/23}$$

The value of p_m was found by assuming the total impulse to be the same whether air had been trapped or not. This yielded a relationship for p_m given by:-

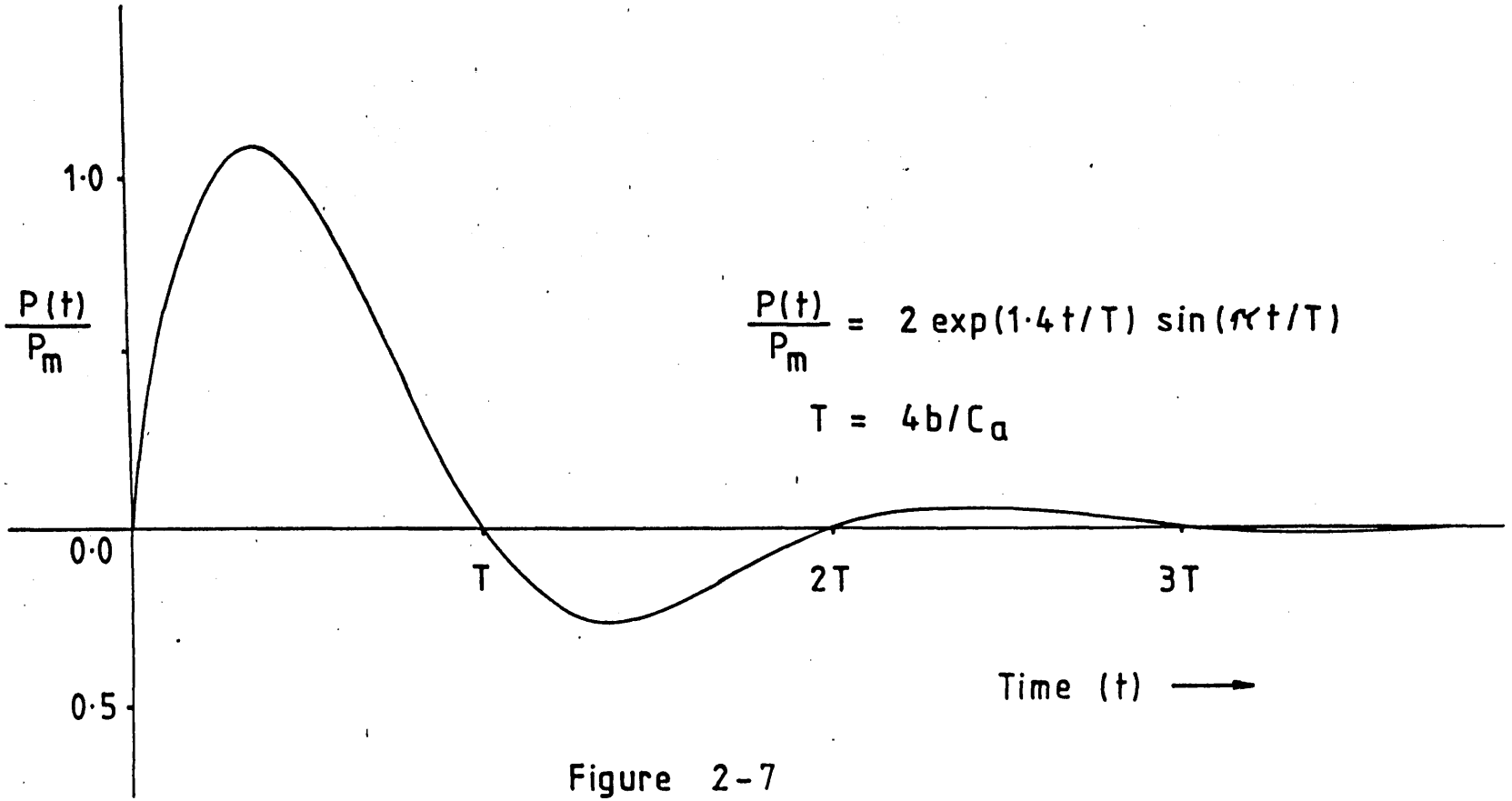

Figure 2-7

Best Fit To Slam Time History, From Ref. 33

$$p_m = 45 V_b \qquad \text{--- 2.4/24a}$$

where p_m is in psi

V_b is in ft/sec

In metric units:-

$$p_m = 0{\cdot}1 V_b \qquad \text{--- 2.4/24b}$$

where p_m is in N/mm^2

V_b is in m/s

This curve fit seems inappropriate for a number of reasons. Firstly, figure 2-7 shows that it is possible for $p(t)/p_m$ to be greater than unity for the function given by 2.4/22. Secondly, the initial pressure gradient and curvature with respect to time do not exhibit the required features. The pressure gradient should vary with mass loading. Chuang's experiments were performed with a single model weighing 255lbs, equivalent to a mass loading per unit area of $340Kg/m^2$. This is still within the range where dynamic effects on the model will affect the shape of the pressure curve. More serious is the way in which equation 2.4/22 ignores the 'slow' pressure build up typical of this type of drop test. Therefore, the second derivative of pressure with respect to time should be positive whereas Chuang's expression gives a negative value.

However, the finding that p_m was linearly proportional to V_b for flat bottomed bodies was significant. In a later publication (34) Chuang examined the effect of deadrise angle. It was found that the air entrapment phenomenon was of importance between angles of zero and three degrees. The following table, taken from ref (34) reveals the effects of deadrise angle on the power to which V_b is raised.

Thus, for $p_m \propto V^n$

β	n
0°	1.0
1.0°	1.4
3.0°	1.6
6.0°	2.0

Table 2.a

Verhagen (35) attempted to model the escaping air flow beneath the falling body by solving the one dimensional equations of mass and momentum conservation in the air layer (see chapter 3, section 8) using the method of characteristics. The free surface motions were calculated using a potential flow solution given by Wehausen and Laitone. This closed form solution was based on the linearised free surface boundary condition and its use prohibited a simulation of full penetration of the free surface by the body. Figure 2-8, taken from ref (34) summarises Verhagen's results for the variation of peak pressure with drop height and mass loading per unit area for a flat plate.

Lewison and Maclean (36) experimented with heavily loaded flat bottomed models and tried to correlate their results with calculations of pressure in the air layer. Figure 2-9 taken from ref (36) shows a typical pressure and acceleration record for one of these tests. Two different techniques of solution were attempted. That which proved most successful used the one dimensional mass and momentum equations (see chapter 3, section 8) and included thermodynamic effects. However, it is not clear from the text whether the subsequent variation in local sound speed was allowed for in the

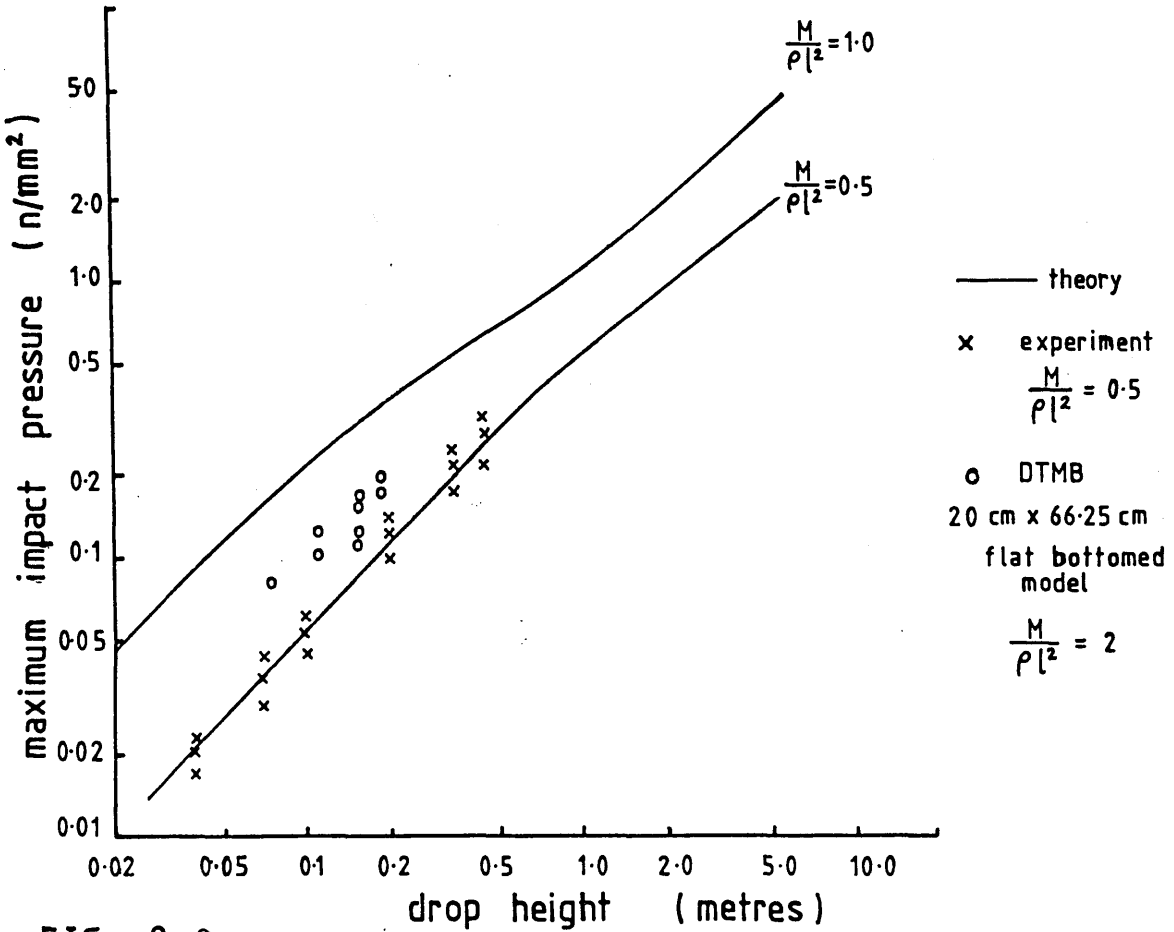

FIG 2-8
From Reference 48

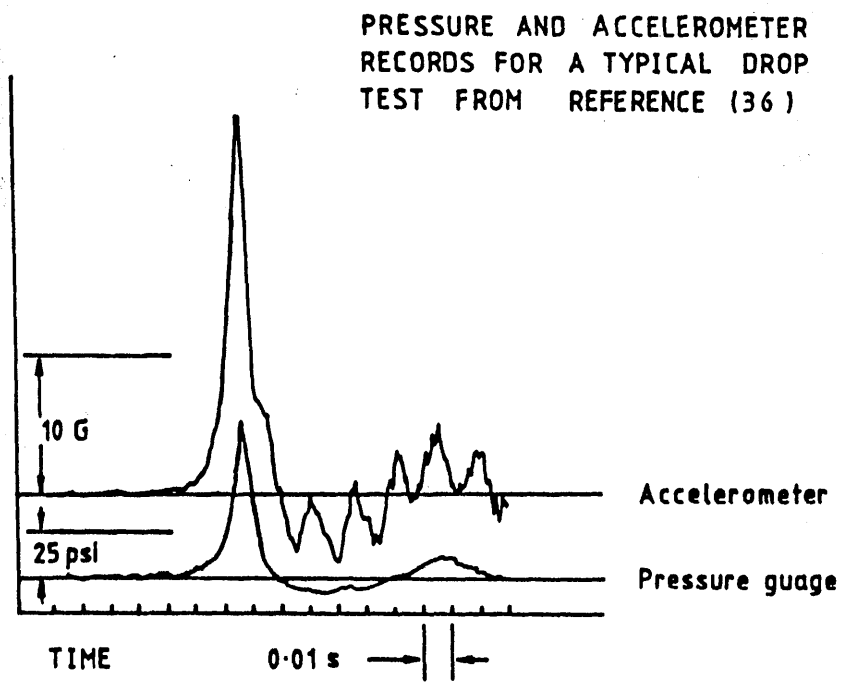
PRESSURE AND ACCELEROMETER
RECORDS FOR A TYPICAL DROP
TEST FROM REFERENCE (36)
10 G
25 psi
Accelerometer
Pressure guage
TIME
0·01 s

Figure 2-9

solution. Calculated pressure-time histories agreed well with experiment. In two papers (37,38) Johnson simulated the pressure rise beneath the body by solving the two dimensional equations of mass and momentum conservation using the method of near characteristics. Unfortunately, the work was limited by the choice of solution technique, since it was impossible to model shocks. This latter failing was accentuated by the use of a rigid flat plate to model the free surface. Theoretically, infinite velocities may be reached in the air layer due to this choice of model, a phenomenon never borne out in practice.

In order to examine three dimensional effects in the water entry problem, Chuang (39) solved the potential flow problem about a cone, modifying Wagner's expanding flat plate model to an expanding disc in a cylindrical co-ordinate system. The kernel of the integral relationship 2.4/6 thus became:-

$$K(r,b) = \left[\frac{2}{\pi} \frac{1}{(1-(b/r)^2)} + (1 - \frac{2}{\pi}) \right] \qquad \text{---} 2.4/25$$

Wagner's power series expansion method was again applied in order to relate the rate of change of wetted beam to the impact velocity. The resulting expression for pressure distribution over the surface of the cone was given as:-

$$P(r) = \frac{1}{2} \rho_w V_b^2 \left(\frac{2}{\pi}\right)^2 \left[\frac{2(\pi-1)}{\beta (1-(r/b)^2)^{1/2}} - \frac{(r/b)^2}{1-(r/b)^2} \right] + \frac{1}{2} \rho_w V_b^2$$

$$\text{---} 2.4/26$$

for a constant velocity impact. This has a similar form to the distribution over a wedge and, likewise, may be differentiated, with respect to r, in order to find the position of maximum pressure, which is:-

$$p_m = \frac{1}{2}\rho_w V_b^2 \left(\frac{2}{\pi}\right)^2 \left[1 + \frac{(\pi - 1)^2}{\beta^2}\right] + \frac{1}{2}\rho_w V_b^2 \qquad \text{--- 2.4/27}$$

at

$$r = b\left[1 - \left(\frac{\beta}{\pi - 1}\right)^2\right]^{1/2} \qquad \text{--- 2.4/28}$$

Since this method was an extension of that used by Wagner, it too was limited to 'small' angles of deadrise. Later experiments by Chuang and Milne (40) were intended to discover the range over which the above expressions were valid. It was found that cone shaped bodies trapped air over a lower range of deadrise angles than the two dimensional wedge. In fact, the peak pressure for a cone with one degree of deadrise was greater than that for a one degree wedge, since it was able to expel relatively more air before impact. However, in general, peak pressures were some thirty per cent lower as a result of the three dimensional nature of the air flow. Comparison of results for peak pressures with calculated values, from formulae 2.4/26, 2.4/27 and 2.4/28 was complicated by the pressure not being proportional to the square of the impact velocity, as the following table shows:-

For $p_m \propto V^n$

β	n
0°	1.9-1.96
1.0°	1.60
3.0°	1.83
6.0°	1.84
10.0°	1.91
15.0°	1.70

Table 2.b

When the results for pressure were plotted against the square of the velocity and a least squares straight line fit applied, the theoretical formulae were seen to be reasonably valid for deadrise angles between 3 and 12 degrees.

Further investigation of three dimensional effects were made by Chuang (41) in 1969, in which a model of a high speed craft was dropped, at various angles of trim, at various forward speeds, onto still water and waves. The formulae for pressures derived from 'cone theory' were found to give the best correlation with experimental results.

Jones and Allen (42) used relationships between pressure and velocity derived from two dimensional theory to produce a semi-emperical computer program to predict three dimensional slamming loads. Ochi and Motter (43) assumed two dimensional strip theory to be sufficient to predict the local load distribution due to a slam. These authors suggested that the pressure coefficient could be found from the following non-dimensional formula:-

$$C_s = \exp(1{\cdot}377 + 2{\cdot}419\,a_1 - 0{\cdot}8739\,a_3 - 9{\cdot}62\,a_5) \qquad \text{---} 2.4/29$$

where a_1, a_3, a_5 are the Lewis form, three parameter mapping coefficients. The constants in the above expression were found by regression analysis of data from a number of seakeeping tests and, therefore, may compensate for the lack of attention to the three dimensional nature of the flow by the use of strip theory.

Chuang (44) continued research into the three dimensional nature of slamming with experiments on ship models in waves. Again,

the best agreement between computation and experiment was found using cone theory. This technique was also applied by Chuang et al (45) in an examination of slamming on a catamaran cross structure in waves.

By applying dimensional analysis, Whitman and Pacione (46) revealed a number of simple relationships useful in the study of the physics behind the slam impulse. In particular, the mass loading per unit surface area of the body was seen to be directly proportional to the initial rate of change of pressure. This was also noted in (47), upon examination of pressure time histories for a series of independently reported experimental results. In retrospect, such studies are of little value to the ship slamming problem, where the rigid body motions of the vessel are unlikely to be affected by the magnitude of the slamming impulse.

A practical calculation technique for wedge type impact problems was suggested by Stavovy and Chuang (48). The curve of peak slamming pressures versus deadrise angle, see figure 2-10, derived from experiment, was divided into a number of subregions. Each subregion was then subjected to a curve fitting process. A careful calculation of deadrise angle based on hull lines and wave slope is required. The effective pressure coefficient is then given by:-

$$K = K_1 / \cos^4 \beta \qquad \text{---} 2.4/30$$

where $K_1 = 0.37\beta/2.2 + 0.5$

for $0 < \beta < 2.2$ degrees

$$K_1 = 2.1820894 - 0.9451815\beta + 0.2037541\beta^2 - 0.0233896\beta^3 + 0.0013578\beta^4 - 0.00003132\beta^5$$

for $2.2 < \beta < 11$ degrees

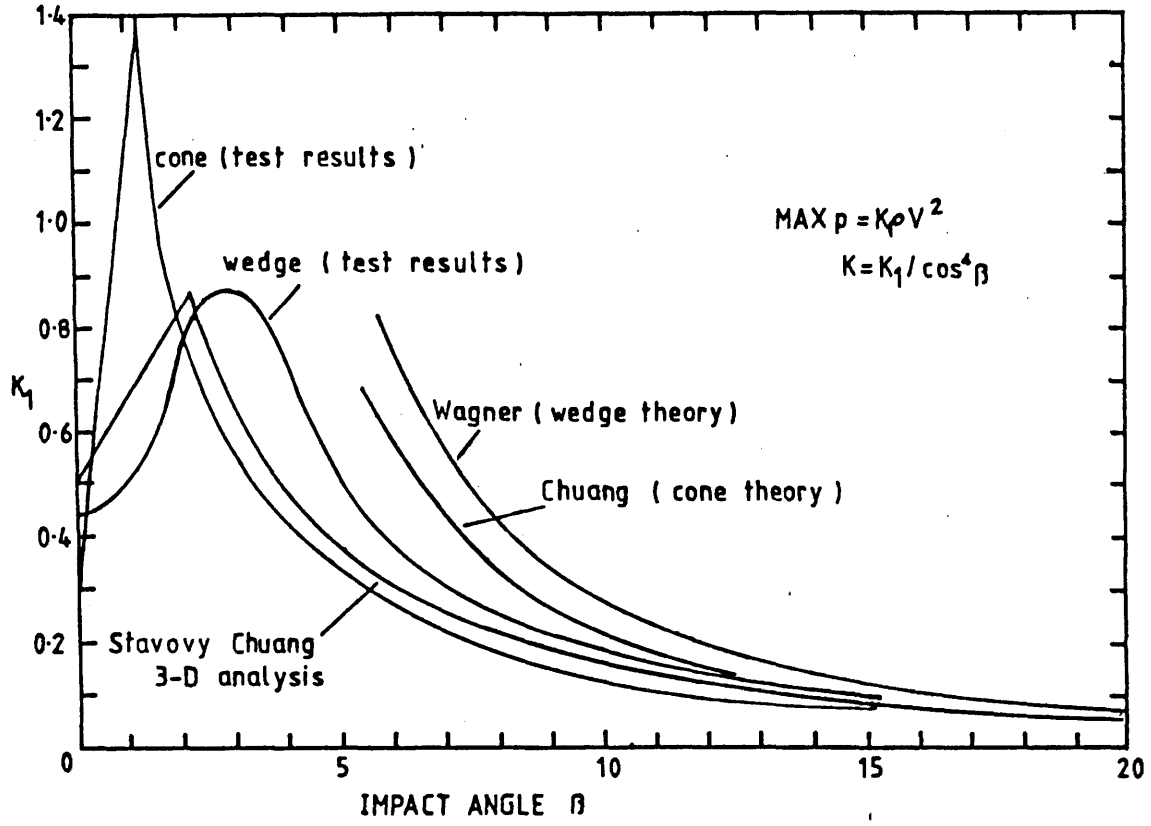

Figure 2-10 Pressure Coefficient $K_1/144$ From Reference 48

$$K_1 = 4.748742 - 1.3450284\beta + 0.1576516\beta^2$$

$$- 0.0092976\beta^3 + 0.0002735\beta^4 - 0.00000319\beta^5$$

for $11 < \beta < 20$ degrees

$$K_1 = (1 + 2.4674/\tan^2\beta) \times 0.76856471$$

for $\beta > 20^\circ$

Unfortunately, no recommendations concerning pulse duration was included in this formulation.

A further contribution to the air entrapment problem came from Koehler and Kettleborough (49), in 1977. The one dimensional mass and momentum conservation equations for the air layer were solved using a time marching finite difference scheme. Thermodynamic effects were not included. The behaviour of the fluid region and associated free surface was modelled using the two dimensional incompressible Navier Stokes equations, again discretised using finite differences. Viscous effects at the air/water interface were included. However, owing to the nature of the non-dimensional form of the equations used, the authors were unable to follow the simulation beyond the instant of first contact.

An application of the boundary element method by Geers (50) introduced a computational technique designed to include the structural response directly. The boundary element method was only capable of solving the ideal flow problem, however, and ignored phenomena such as air entrapment. A linear free surface boundary condition further limited the applicability of this technique.

5. LOCAL RESPONSE

Few authors have investigated the dynamic response of local plate elements during a slam. The duration of the pressure pulse, T_s, and its relationship to the first mode natural period of the plate T_p, is an important factor in any such analysis. In particular, if T_s is greater than $T_p/2$, deflections may be analysed via a static analysis. If T_s is less than $T_p/2$, dynamic factors require consideration.

Greenspon (51) analysed stresses and deflections in plate elements using a dynamic membrane theory, based on a modal analysis approach. Various response characteristics were noted depending upon the time history of the slam loading. Later, an examination of measured values of permanent set in bottom plating elements of various craft, and in particular the USCGC Unimak (1), was made by Nagai (52,53). The analysis sought to calculate the types of load time history and distribution responsible for the recorded values of damage.

Application of modal analysis was again applied by Leibowitz and Greenspon (54) to examine local plate and overall grillage response to a range of slamming load time histories. However, the analysis was completely within the elastic range of material behaviour and sought only to define a series of dynamic load factors for design. It has been found that in practice, some degree of permanent set in bottom plating due to slamming is quite permissible. The inference from the recommendations made by Leibowitz and Greenspon was that the plating elements should be designed with an elastic yield criterion as an upper limit. This could well lead to 'over-design' of ship bottom structure.

Experimental work by Chuang (55) on flat bottomed slamming, using a highly flexible model, showed that structural deflections tended to reduce maximum bottom pressures. This phenomenon was undoubtedly due to the enhanced level of air entrapment made possible by local deformations. Reasonable agreement between computation and experiment was obtained by use of a modal analysis for structural deflections with the dynamic response calculated by use of a convolution integral approach. An extension of these results and the work of ref (41) lead to suggestions for design criteria for hydrofoil hull bottom plating by Chuang (56).

Sellars (57,58) attempted to resolve the disagreement between measured slamming pressures at sea and those found during drop tests by the use of dimensional analysis. Again, the mass loading per unit area was found to be of importance, as were the elastic properties of the structure. However, it is thought that such disagreement is more likely to be due to differences in behaviour of the trapped air layer for the two and three dimensional cases, as reported earlier by Chuang (44).

In ref (58), Jones identified the local plate's lowest natural period to be the deciding factor in whether a static or dynamic analysis should be used. In most cases, it was concluded that the former is more appropriate. Curves of the degree of permanent set versus a plate stiffness paramater, for a triangular pressure pulse were given, see figure 2-11. Good agreement was found between these values and measured permanent deflections (eg from ref (1)).

Yuhara (60) reported the results of a series of tests to

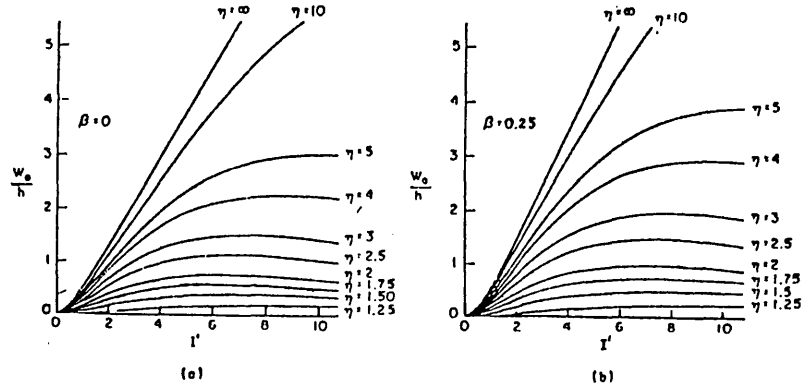

Maximum permanent lateral deflections of fully clamped rectangular plates subjected to a triangular pressure pulse (a) $\beta = 0$ (beam), (b) $\beta = 0.25$

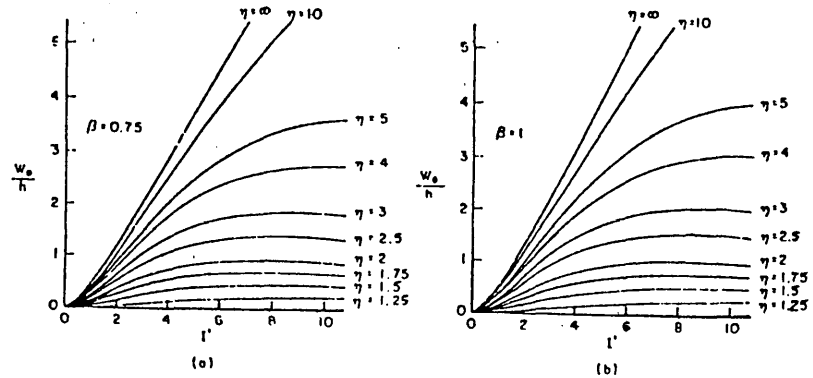

Maximum permanent lateral deflections of fully clamped rectangular plates subjected to a triangular pressure pulse (a) $\beta = 0.75$, (b) $\beta = 1$ (square plate)

Figure 2-11 (from reference 59)

simulate bow damage due to slamming. Figure 2-12 taken from ref (60) shows the effect of repeated impacts on permanent set in a panel and on permanent deformations of the overall structure. The degree of set is shown to behave asymptotically. However, the behaviour of the overall structure is less encouraging, showing a trend of increasing damage with repeated impacts.

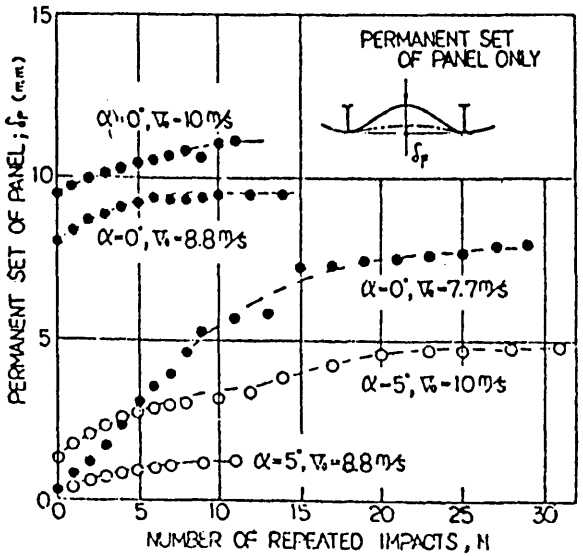

Fig. 2 Net Permanent Deformation of Panel ① under Repeated Impacts (AS-0° and AS-5° model)

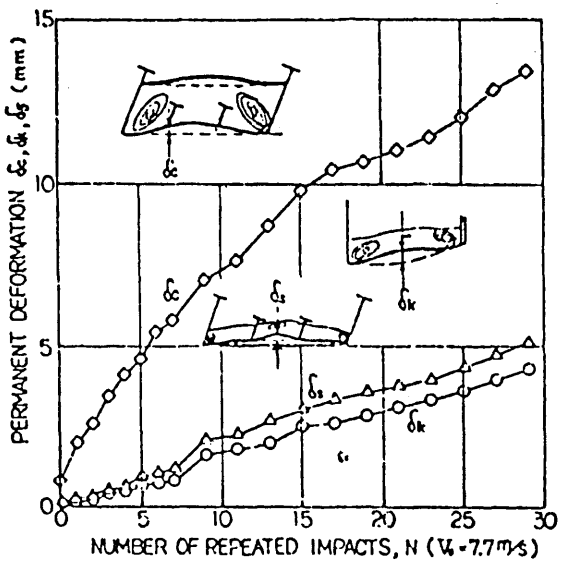

Fig. 3 Permanent Deformations of Center Section ©, Horizontal Girder Ⓕ, and Vertical Stiffener Ⓑ of AS-0° Model under Repeated Drops of 3 m (V_0=7.7 m/s)

Figure 2-12 (From Reference 60)

6. OVERALL STRUCTURAL RESPONSE

Slamming is known to excite vibrational responses in the ship hull girder. Generally denoted as whipping, this response is mainly concentrated in the two, three and four nodes of vibration. Figure 2-13 taken from ref (68) shows a typical whipping response for a large tanker in the ballast condition (calculated).

Borg (61) idealised the ship hull girder by use of a simple free-free beam model and examined the passage of a stress wave due to an impact at one end of the hull. A critical factor in this type of model was the total value of hull structural damping. An elaborate method based on conservation of energy was applied in order to calculate hull deflections. Unfortunately, such close attention to the physics of the problem did not result in a practical computational technique.

In two reports for the David Taylor Model Basin (62,63), Leibowitz calculated the response of a Dutch destroyer by means of a finite difference representation of the hull girder equilibrium equations. A time marching solution method was applied. The slamming force was calculated via a rate of change of added mass approach, based on equation 2.4/2. A strip theory representation of the hull girder was used in association with a database of added mass coefficients for various draughts.

Thus, calculation of the slam coefficient:-

$$C_s = 2\frac{\partial M_a}{\partial Z}/\rho_w$$

was easily carried out numerically. Whilst this approach is suitable

Figure 2-13

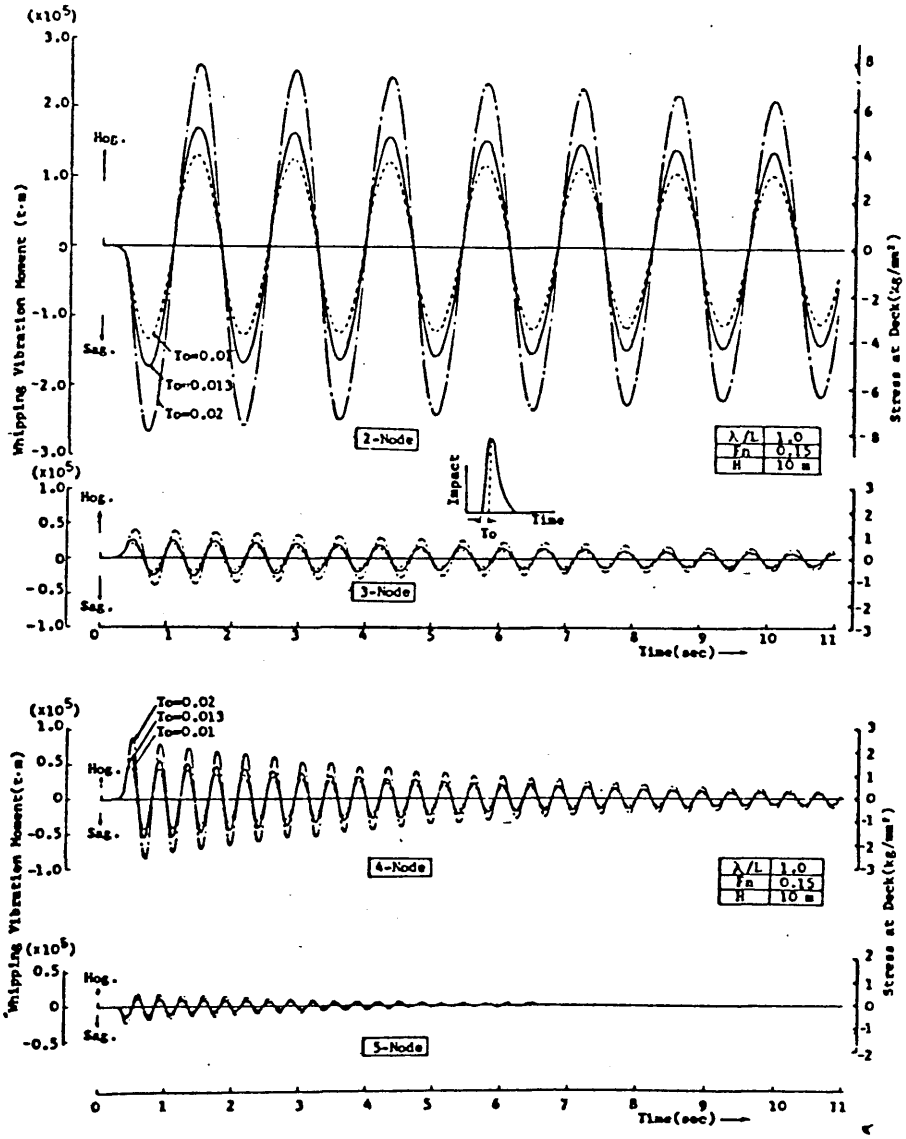

Whipping Response Modes

(From Reference 68)

for bow flare type impacts and the re-entry of 'fine' forward sections, it is insufficient for the general slamming problem. Despite this, the numerical model was capable of reproducing responses similar to those measured at sea.

In work undertaken for the International Ship Structures Committee, Kaplan and Sargent (64) used a modal analysis to examine hull whipping vibrations due to bottom and bow flare slamming. A convolution integral method was used to represent the dynamic response of each mode of vibration due to the slam impulses. The response functions thus generated were used to drive an analogue computer simulation.

In common with Leibowitz, the slamming impulses were calculated via the rate of change of added mass approach. In general, predicted stresses were too high, since the time steps chosen were large in comparison with a typical slamming pulse duration. Unfortunately, a lack of computing power prohibited any attempts to cure this failing.

Mansour and d'Oliveira (65) examined hull response due to bottom slamming in regular waves, again using a modal analysis plus convolution integral approach. Results for a Mariner Class vessel were good, predicting response in two, three and four node modes effectively. The authors noted that owing to the limitation of the whipping vibration to the first three modes, the extra accuracy available through the use of a detailed finite element analysis was unnecessary.

Calculations performed by Gran et al (66), examined the

effect of bow flare slamming on a fast cargo ship. A normal mode plus convolution integral analysis for response to a sinusoidal slamming force of duration 1.25 seconds was used. Maximum hull stresses were experienced at a position one-sixth of the overall length of the hull away from the bow.

In a review of the available literature, Nagai and Chuang (67) noted that bow flare slamming tended to excite the two node mode of vibration only, whereas the effect of bottom slamming was less discriminatory. The ability of bottom hull plating to absorb slamming impulses once permanent set had occurred was noted.

In a study of a large full ship, Kawakami et al (68) calculated the overall response of the hull, again using a modal analysis plus convolution integral approach.

Computations were performed for both model and full-scale and compared with experiment for both cases. Agreement at full-scale was more easily reached. In general, lack of data on hull damping factors was seen as a major cause of error. The onset of slamming was predicted using Tick's formula, equation 2.1/1. As a result of assuming Rayleigh type probability density functions for slam pressure prediction, a method to predict the whipping vibration stresses was proposed. The highest significant whipping stress was found to be up to 95% of the normal wave bending stress in sag, for a significant wave height of 13-16 metres.

Yamamoto et al (69) examined the response of a trawler and a container ship to head seas, both by computation and model experiment. A modal analysis which included rigid body motions was used, the

resulting modal equation being integrated using the Newmark-Beta method. Good agreement between theory and experiment was obtained with the three-node mode response being significant in the bow region of the container ship.

In two papers, Bishop, Price et al (70,71) applied previous work in ship hull dynamics (72-74) to the slamming response problem. The accepted modal response approach was used along with an input force history which was allowed to vary spacially over the bottom of the hull. Agreement with full-scale measurements made on two frigates in a severe weather trial was reasonable.

A subsequent publication (75) revealed the sensitivity of the results to the theory used to calculate the slam loading. The 'Leibowitz' approach (rate of change of added mass with immersion) was considered inadequate by these authors, the greatest success being achieved with the Stavovy-Chuang method (48). Ochi's method (43) of calculating hull pressures was found to be grossly inaccurate.

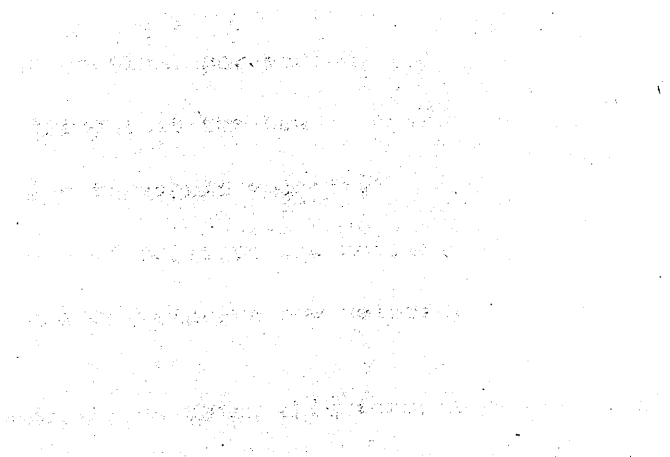

7. STOCHASTIC THEORIES FOR SLAMMING

The earliest attempt to apply order statistics to the slamming problem was made by Tick (76). It was assumed that slamming occurrence would obey statistical laws associated with a stationary, Gaussian random process. Three conditions were put forward as being necessary for a bottom slam to occur:-

a. Bow emergence.

b. The relative velocity between the keel and the free-surface should exceed a 'threshold' value.

c. The angle between the keel and the free surface should be small.

The joint probability distribution for these three conditions proved complex in form, hence the last of these conditions was relaxed. The resulting formula for the number of slams per unit time is given by equation 2.4/1 but is repeated below for clarity:-

$$N_s = \frac{1}{2\pi}\left(\frac{R_v}{R_h}\right)^{1/2} \exp\left(-\frac{1}{2}\left(\frac{h^2}{R_h} + \frac{V_t^2}{R_v}\right)\right)$$

---2.7/1

N_s : number of slams per second

h : ship draught at the bow

V_t : slamming threshold velocity

R_v : variance of relative bow motion

R_h : variance of relative bow velocity.

Initial computations using this formula proved promising.

Ferdinande (77) later re-arranged Tick's formula, replacing

the joint bow emergence and relative impact velocity exceedence criteria, with a single, equivalent bow emergence condition. This single criterion may be written as:-

$$h' = (h^2 + (V_t/\omega_o)^2)^{1/2} \qquad \text{---} 2.7/2$$

which leads to the following formula for the expected number of slams per second:-

$$N_s = \frac{\omega_o}{2\pi} \exp\left(-\frac{1}{2}\left(\frac{h'^2}{R_h}\right)\right) \qquad \text{---} 2.7/3$$

In attempting to validate this statistical formulation by examination of data from a series of model tests in head seas, Ferdinandė found that the value of the threshold velocity varied with ship speed, slam severity (as measured by bow deceleration) and the longitudinal position of the slam.

Despite this evidence, Ochi and Motter (78) used Tick's formulation to produce a probability distribution for slamming pressure. The function was based on a truncated exponential distribution using a 'threshold' pressure derived from the square of the threshold impact velocity (see fig. 2-2 and equation 2.3/4). It was possible to produce two statistical measures considered to be useful to the designer:-

a. The most probable value of the extreme pressure during n observations (slams) over a given period:-

$$p_n = p_0 + \frac{1}{R_v} \ln(n) \qquad \text{---} 2.7/4$$

where p_n : most probable value of extreme pressure

p_0 : threshold pressure = $\frac{1}{2} K \rho_w V_t^2$

R_v : twice the variance of relative bow velocity

b. The chance of exceeding a given value of pressure during n observations (slams):-

$$P(p > \bar{p}) = 1 - (1 - \exp(-R_v(\bar{p} - p_0)))^n \qquad \text{---2.7/4}$$

where $\bar{p}$ is a value for bottom pressure set by design considerations.

Two examples were presented to confirm the accuracy of the method.

A later paper from Ochi and Motter (79) summarised previous work and suggested a procedure for design against slamming damage. However, reservations were expressed in subsequent discussion of the paper since many of the basic assumptions concerning the statistics and physics of the problem were as yet unproven. In particular, the calculation of the number of slams in a given period (n) for a known sea state and heading angle using a Rayleigh probability distribution was considered imprecise. Further, the choice of threshold velocity (V_t) and slam coefficient (C_s) was considered difficult.

The uncertainty over the use of the Rayleigh distribution to calculate the number of slams over a given period was, to some extent, resolved by Psaraftis (80). By assuming the slamming expectance to vary with time, better agreement was obtained between computations of the distribution of slamming intervals and data from the voyages of the SS Wolverine State. Figure 2-14, taken from Reference (78) illustrates the effect these assumptions have on the computation of the distribution of slamming intervals. It would seem, from this data,

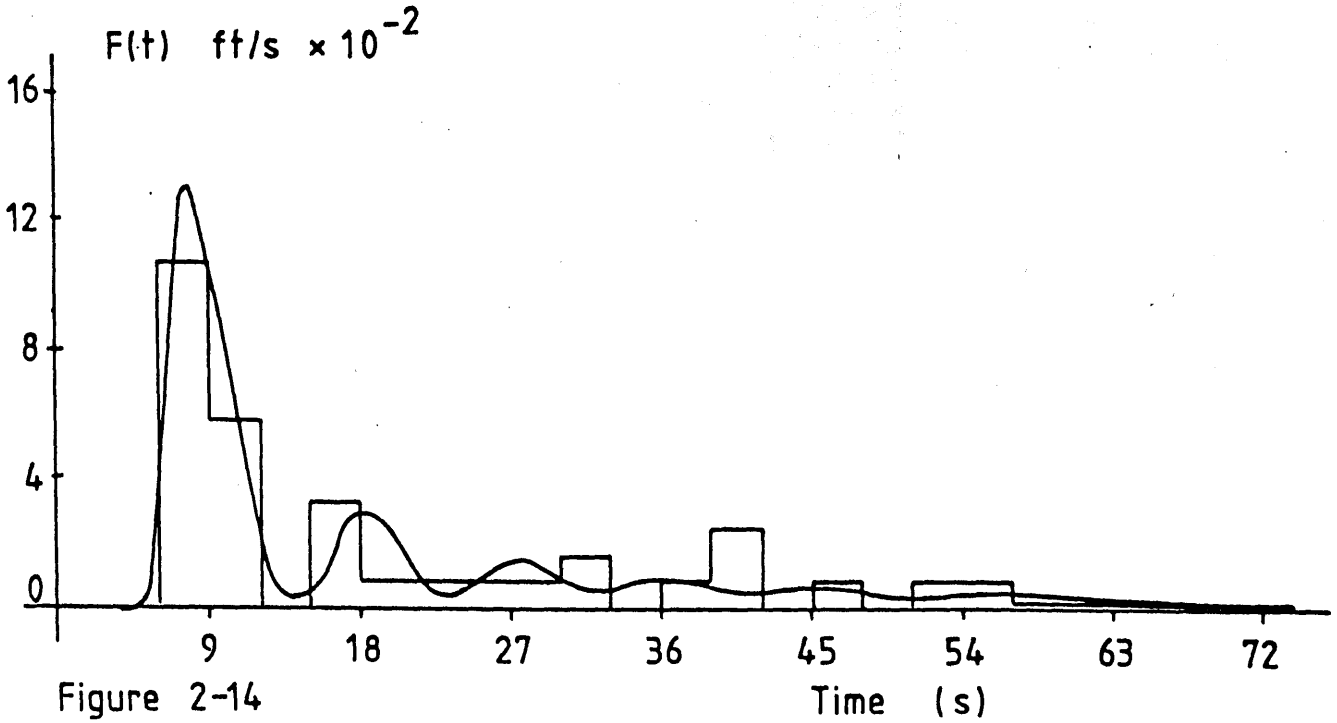

Figure 2-14

Comparison Between Psaraftis's Time Dependent P.D.F And Data For The Distribution Of Slamming Intervals From Voyage 288 Of The S.S Wolverine State

that slamming is a Markov or memory dependent statistical process. Thus, slamming events are not independent of each other when violent pitching is taking place.

Ochi (81) later showed wave grouping phenomena to be important in the statistical representation of extreme ship motions. This may be viewed as another cause of non-stationary behaviour in the statistics of slamming. However, the extent to which non-linearities in the description of vehicle dynamics and wave grouping, acting either separately or in combination, affect the statistical representation of extreme ship motions is still unclear.

Working from Psaraftis's assumptions, Chen (82) formulated the response to slamming using the non-stationary Markov process. The probability distribution, as a function of time, associated with the single degree of freedom model used for the relative vertical displacement of the bow, was obtained by solution of the Fokker-Plank equation:-

$$\frac{\partial p_r}{\partial t} = -\dot{y}\frac{\partial p_r}{\partial y} + \frac{\partial}{\partial \dot{y}}\left[\left(2C\omega\dot{y} + \omega^2 y\right)p_r\right] + I(t)\frac{\partial p_r}{\partial \dot{y}^2} \qquad \text{--- 2.7/6}$$

where p_r : probability distribution function

$y, \dot{y}$: state variables of relative displacement and velocity

C : damping coefficient

ω : frequency

I : intensity function of a random impulse

This technique was applied to two examples, though one in particular was of relevance to slamming. Unfortunately, the computations were not verified by experiment or measurements at sea. Further, strip theory was used to calculate added mass and damping

coefficients which would have eliminated one source of non-linear behaviour.

In 1982, Mansour and Lozow (83) published calculations on the statistics of marine vehicle response to impulsive loadings. In this case extreme value statistics used were based on the work of Rice (84) and assumed a variable band width. The large influence of speed on the statistical values of slam induced wave bending moment was very apparent.

Ferro (85) has recently examined the relationship between slamming statistics and a first order reliability method. Some confusion is evident concerning the differences between whipping and springing. The work is continuing.

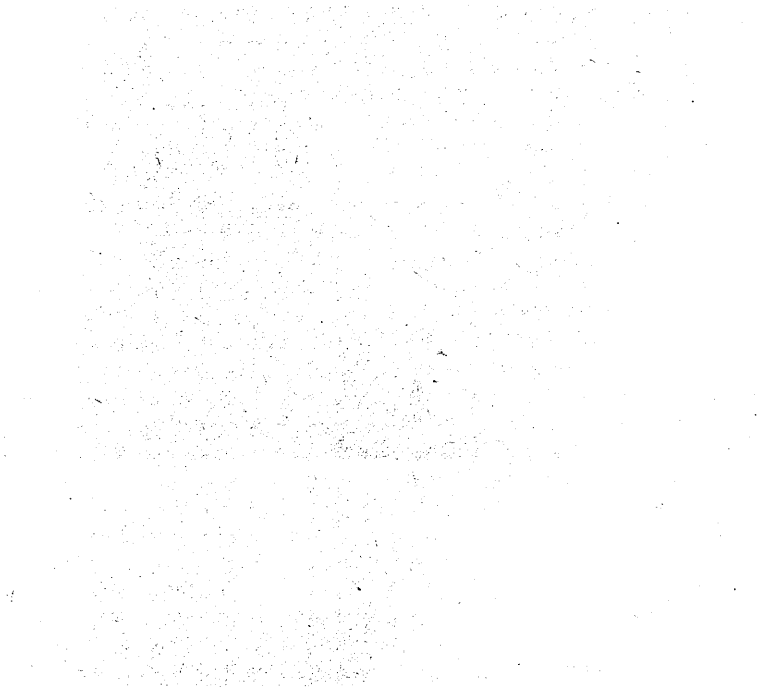

By use of the classic 'rate of change of added mass with immersion' formulation, Kaplan and Silbert (86) calculated slamming loads on horizontal circular cylinders in the splash zone. The instantaneous value of added mass was taken as half that due to an immersed arc reflected about the free surface. The following expression for the added mass, derived by J Lockwood-Taylor (87) was used:-

$$M_a = \frac{\rho_w R^2}{2}\left[\frac{2\pi^3}{3}\frac{(1-\cos\theta)^2}{(2\pi-\theta)^3} + \frac{\pi}{3}(1-\cos\theta) + \sin\theta - \theta\right] \qquad ---2.8/1$$

where θ : half the angle subtended by the wetted beam.

No account of 'piled up water' was made. Hence, the expression for the rate of change of added mass with draught (z) could be found by simple geometrical considerations alone, giving:-

$$\frac{\partial M_a}{\partial Z} = \frac{\rho_w R}{\sin\theta/2}\left[\frac{2\pi^3}{3}\left(\frac{\sin\theta}{(2\pi-\theta)^2} + \frac{2(1-\cos\theta)}{(2\pi-\theta)^2}\right) + \right.$$

$$\left. + \frac{\pi}{3}\sin\theta + \cos\theta - 1\right] \qquad ---2.8/2$$

Equations 2.8/1 and 2.8/2 were then used in the following formula which summates the effects of buoyancy, inertia and slam loads to give:-

$$F_t = \rho_w g A + (M_a + \rho_w A)\ddot{\eta} + \frac{M_a}{Z}(\dot{\eta})^2 \qquad --- 2.8/3$$

where F_t : is the total force per unit length

A : is the submerged sectional area

$\dot{\eta}, \ddot{\eta}$: are the velocity and acceleration at the free surface, respectively.

The loads thus calculated were found to give dynamic reponses which were higher than those measured by experiment. In a paper presented during the same Offshore Technology Conference, Dalton and Nash (88) showed the flow about circular cylinders being passed by waves to be highly complex. Load rise times were long by comparison with ship slamming such that it was considered doubtful whether slamming had, in fact, occurred. Measured 'slam' coefficients varied greatly with Keulegan-Carpenter number, Reynolds number and position below the free surface.

Miller (89) also found that wave impacts upon circular cylinders produced highly complex flow fields during experiments at the National Maritime Institute. The form of the load time history included fluid acoustic effects, hydrodynamic slamming, buoyancy, lift, drag and inertia forces. Qualitative agreement between theory and experiment was reached but quantitative correlation was poor. A slam coefficient C of 3.6 + 1.0 was recommended for use in design. However, some doubt was cast upon this figure in subsequent discussion. It compares well with a Von-Karman type analysis, in which half the added mass of an expanding flat plate at the still water level was used to derive a slam coefficient of .

Fabula (28) also attempted this problem but took account of the piled up water effect, following the method of Wagner (26). This gives a theoretical value for C_s of 2π, a figure backed during discussion of Reference (89) by Wellicome, whose own work at Southampton University is discussed below. It is well worth noting that the fluid compressibility was considered of importance for the slam load rise time.

Whereas Chuang (33) had shown that the air entrapment/cushioning phenomenon ruled out such considerations for flat plates and wedges of low deadrise angle, Miller's work seems to show that free surface distortion prior to impact may enhance the possibility of compressible fluid behaviour.

As previously mentioned, forced impact tests on circular cylinders carried out by Campbell, Weynberg and Welicome (90-92) produced a higher slam coefficient at 5.15 for a smooth cylinder. A curve fit to measured force time histories gave an expression for the slam coefficient of:-

$$C_s = 5{\cdot}15/(1 + 19V_b t/D) + 0{\cdot}55V_b t/D \qquad \text{---} 2.8/4$$

where V_b : impact velocity

t : elapsed time

D : cylinder diameter

Interestingly, fouled cylinders were also tested and gave lower peak impact pressures. The force/time history for the slam coefficient was:-

$$C_s = 4{\cdot}1/(1 + 8{\cdot}3V_b t/D) + 0{\cdot}45V_b t/D \qquad \text{---} 2.8/5$$

Ochi and Tasai (93) recently measured slam forces on vertical circular cylinders due to broken and breaking waves. By assuming the peak pressure to vary with the square of the wave speed, slam coefficients of:-

$C_s = 1.34$ for broken waves

$C_s = 1.38$ for breaking waves

were given. By considering the statistics behind the occurrence of these types of waves, probability distribution functions for slam pressure exceedence in any given sea-state were presented.

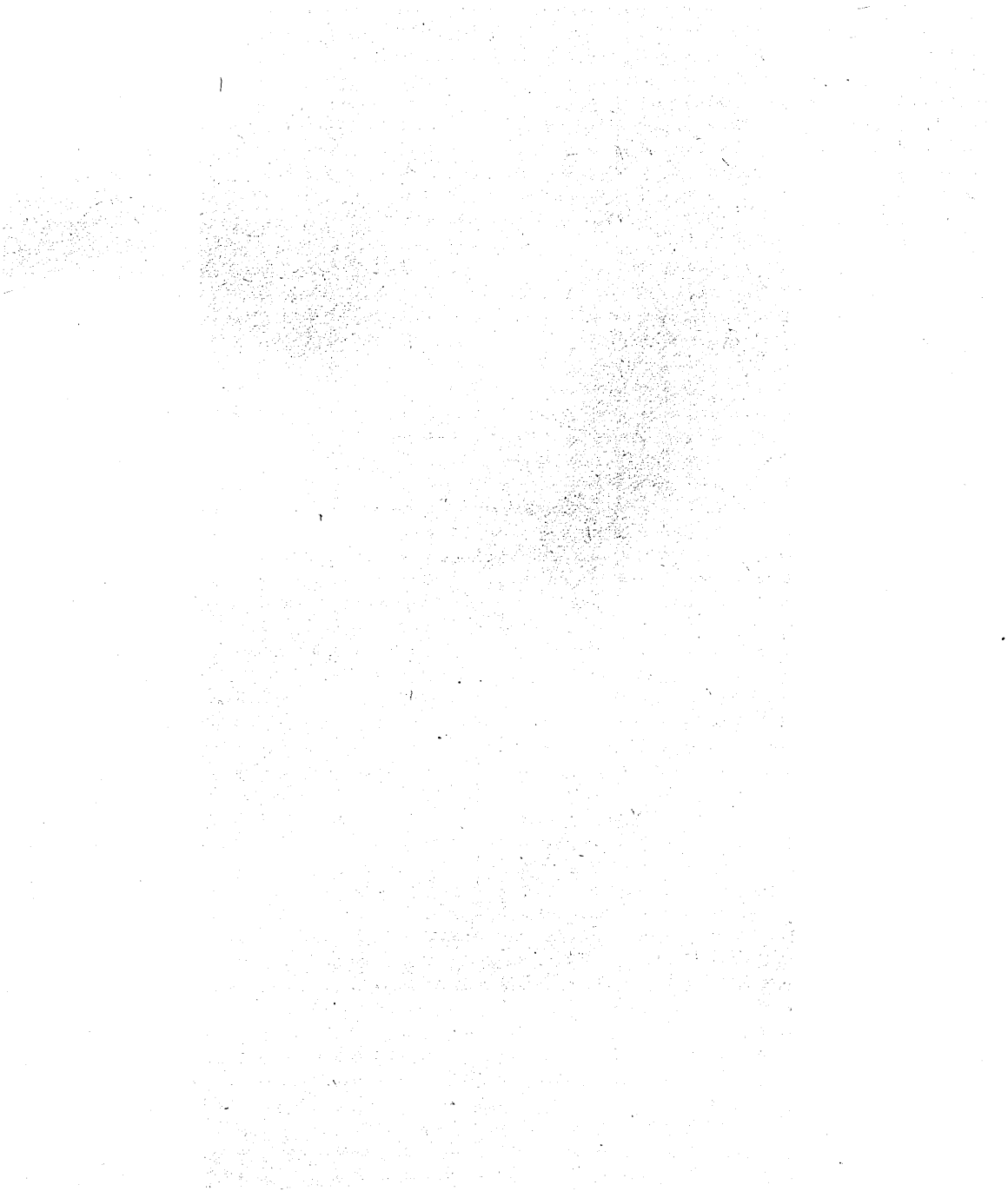

9. CONCLUSIONS

From consideration of the literature, a number of areas of uncertainty still exist. In regard to the success of previous research, one should consider to what extent it is now possible to use such work directly in the design process. To this end, the ISSC have examined the possibility of such considerations.

Lewis et al (94), in a 'state of the art' review of ship design load criteria, made a number of recommendations concerning the effects of whipping. As previously mentioned, Ochi and Motter (78,79) suggested a basis for a probabilistic design process, which was later reviewed by the 1976 ISSC committee on slamming and dynamic loads (95).

Despite such efforts, the amount of information available to the ship designer is still very small. A concensus of opinion over methods of computation is lacking.

For example, techniques to accurately compute hull pressure distributions for a given impact velocity, in anything but 'ideal' conditions are still unavailable for the full scale. Correlations between measured slam pressure distributions and time histories from drop test experiments, model seakeeping tests and full scale sea trials are poor. In general, Froude scaling for threshold velocities, slam pressure coefficients and time histories has been applied but without any formal basis in the physics of the problem.

This lack of information concerning the mechanisms behind the impact phenomenon has led to gross assumptions being made when dealing

with the problem of response.

As far as local plating elements are concerned, knowledge of extreme pressure pulse magnitude and duration is required before a decision can be made as to whether to treat the problem statistically or dynamically. This type of information is still unavailable for any given situation.

The effect of bottom slamming on grillages will be almost certain to produce a local vibratory response. This area has attracted very little study, such that information concerning the transmission of local loading to overall whipping response is completely unavailable. The question of how much energy goes into each mode of response from a particular slam has never found a satisfactory answer.

Transient whipping vibrations have received much attention, due mainly to the ease with which good qualitative results for stress/time histories may be achieved. Many of the techniques have used very simple models of the slamming impact load.

No attempts have been made to study differences betwen the effects of the different types of slam loading on the whipping response other thansa small number of computations made by Kawakami et al (68). It was seen that the magnitude of peak whipping moment tended to increase with increasing slam pressure rise time. This type of variation cannot in general, be true, however, since measurements at sea show maximum wave bending stress to behave asymptotically with increasing severity of sea state. One further aspect of the response problem which has received little attention is the effect of whipping vibrations on fatigue.

Lewis et al (95) suggested that a figure of 10^6 stress reversals be added to that due to wave bending during a ship's lifetime. However, this can be considered, at best, an educated guess. More research is required in this area.

The prediction of slamming occurrence has been examined using either stationary or non-stationary processes, with the latter techniques proving of benefit in explaining the available data more thoroughly. In general however, very little information exists with which to decide the method to be employed. It should also be considered that the non-stationary or Markov processes are much more difficult to use in a practical sense.

The statistics of the slam pressure magnitude are better known. When the probability distribution of peak pressure is based on the number of slams encountered, a stationary random process may be assumed. Again, more data is required.

It was considered by this author that the greatest area of uncertainty was in the quantification of the physics behind the hydrodynamics of impact on the full scale. Given a full description of the pressure distribution and time history over the bottom of the hull for the 'general' impact case at sea, many of the uncertainties involved in describing slamming to the ship designer could be overcome.

The seemed as though there were three regimes of fluid behaviour each one of which could, given the correct body/free surface geometry, provide the dominant mechanism for slam loading. A general

program, to describe the fluid flow around a ship section plunging through a free surface, was needed. This requirement dominated subsequent research, since no acceptable solution procedure existed when the work was begun.

Physical reasoning indicated that finite rise times for load time histories showed that there had to be some compressible behaviour within the fluid domain at the instant of contact. The entry of a 'sharp nosed' body into water would, using an incompressible model of fluid flow, require an infinite rate of change of added mass at the instant of contact. Clearly, this was an unreasonable assumption and, hence, a 'slightly' compressible model of fluid behaviour was to be developed. A further refinement was to be the addition of the effects of air entrapment to the slamming model.

It was hoped that many of the problems encountered by previous workers in slamming research could be quantitatively investigated following the development of a good physical model of the impact problem.

CHAPTER 3

FLUID EQUATIONS TO BE MODELLED

CHAPTER 3

FLUID EQUATIONS TO BE MODELLED

1. GENERAL WATER ENTRY PROBLEM

A time history of the pressure distribution over the surface on an arbitrary shaped body as it crosses the interface between air and water is to be calculated. The body need not be moving in a direction normal to the free surface and its velocity need not be constant. The free surface may be considered initially flat and quiescent or be given some initial shape and motion characteristics.

There are two possible models of fluid behaviour. In general, the fluid was to be considered viscous and incompressible, governed by the continuity coupled Navier Stokes equations as defined in section 3.3. For the case of 'heavy' impacts, described in the previous chapter, a model of slightly compressible fluid behaviour was developed and is detailed in section 3.7. When required, the compressible air layer between body and free surface was modelled by the equations of mass and momentum conservation for a perfect gas.

The problem was to combine solution algorithms for the fluid dynamic equations of motion with boundary conditions defined by the kinematics of the body, to produce an interactive time simulation of a slam. The aim of the routine was to provide the position, resultant velocity and acceleration of the body, as well as fluid pressures, velocities and position of the free surface at any instant during the impact.

The solution routine needed to fulfil a number of requirements such that it suited the engineering approach to the problem. The form of the algorithm had to be insensitive to the shape of the fluid domain. The accuracy of the method had likewise to be invariant with the type of problem to be solved, and to be readily quantifiable.

The physical parameters of the fluid such as viscosity, were to be open to variation without affecting the method of solution or accuracy. Since the form of the solution was that of a dynamic simulation, mass conservation at each time step was of paramount importance. In many steady flow solution algorithms based on iterative methods, this criterion may be relaxed to aid the process of convergence. This was not admissible in the case of the dynamic simulation.

The total energy of the modelled system had to remain bounded by its initial value, the total work done (eg by gravity in the case of a freely falling body) and by radiation. It will be seen later that careful consideraton of energy conservation greatly aided the stability of the algorithm.

The effect of the size of the time-step used on the error in the solution had to be easily assessed. In the limit, as the size of the time step is reduced, this error should decrease in magnitude. Alternatively, the size of the time step may be linked to the physics of the problem. In such a case, the choice of mesh size and fluid properties, such as compressibility, were critical.

Though developed as a two dimensional flow problem, the

algorithm was to be easily applied to three dimensional flow simulations.

2. FLUID DOMAIN TO BE MODELLED

Figure (3-1) illustrates a two dimensional model fluid domain. The equations of fluid mass and momentum conservation, to be detailed in section 3.3, were to be solved over this region, subject to boundary conditions imposed in areas near:-

a. solid walls

b. moving solid boundaries

c. inlet boundaries (upstream)

d. radiation boundaries (downstream)

e. bed or bottom boundaries

f. free surfaces.

The co-ordinate axes were stationary with respect to the fluid and any moving bodies within the flow. The origin was placed at the free surface, still water level. The computational domain was restricted in size by the numerical algorithms chosen to solve the continium equations of fluid motion and, ultimately by the computing power available.

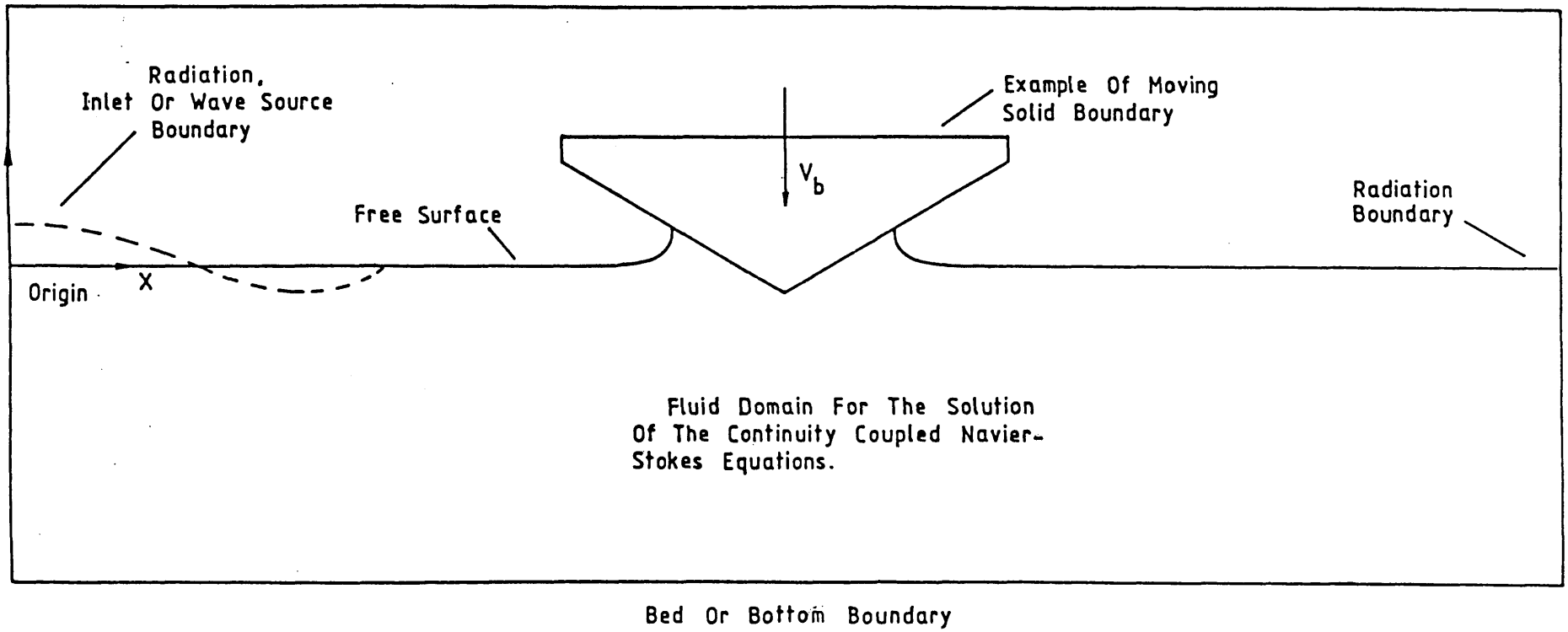

Figure 3-1 General Two Dimensional Fluid Domain.

3. EQUATIONS OF FLUID MASS AND MOMENTUM CONSERVATION FOR AN INCOMPRESSIBLE FLUID

The equations stated in this section are for two dimensional flow of a viscous incompressible fluid. Their derivation may be found in many standard texts on fluid dynamics (96,97,98). Cartesian (x,y) co-ordinates are used throughout, along with the standard convention of representing the x and y components of the velocity vector by u and v respectively and pressure by the letter p.

3.1. Mass Conservation

Considering the control volume in two dimensions shown in figure 3-2), the conservation of fluid mass may be represented by the well known continuity equation for an incompressible fluid.

$$\frac{\partial u}{\partial x} + \frac{\partial v}{\partial y} = \nabla \bar{u} = 0 \qquad \text{---3.3/1}$$

3.2. Momentum Conservation

The equations for momentum conservation in a viscous flow may be stated for each co-ordinate direction as:-

$$\frac{\partial \rho u}{\partial t} + \frac{\partial \rho u^2}{\partial x} + \frac{\partial \rho uv}{\partial y} = X_g - \frac{\partial p}{\partial x} - \mu \left(\frac{\partial^2 u}{\partial x^2} - \frac{\partial^2 u}{\partial y^2} \right)$$

$$\frac{\partial \rho v}{\partial t} + \frac{\partial \rho v^2}{\partial y} + \frac{\partial \rho uv}{\partial x} = Y_g - \frac{\partial p}{\partial y} - \mu \left(\frac{\partial^2 v}{\partial x^2} - \frac{\partial^2 v}{\partial y^2} \right)$$

---3.3/2

This is the 'conservation' form of the equations such that, for constant fluid density and assuming equation 3.3/1 to be satisfied, the above relationships are identical to the Navier Stokes equations for a viscous incompressible fluid.

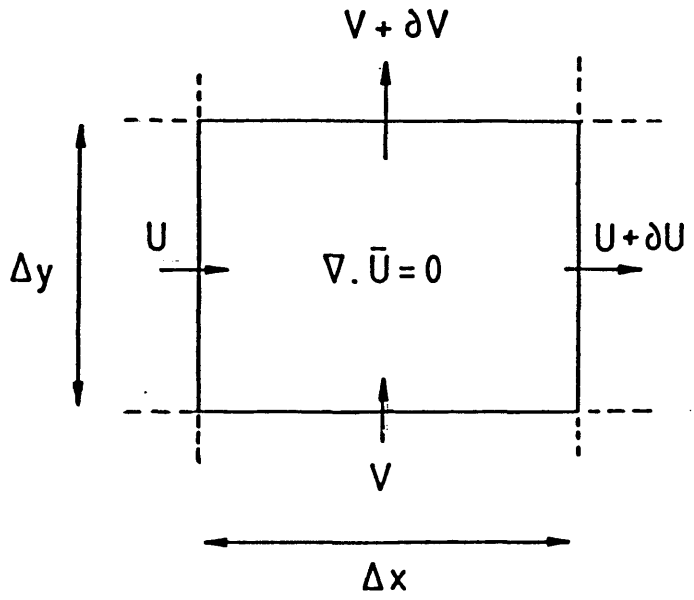

Figure 3-2 Simple Control Volume For Mass Conservation (Incompressible Flow)

$$\frac{\partial u}{\partial t} + u\frac{\partial u}{\partial x} + v\frac{\partial u}{\partial y} = X_g' - \frac{\partial p'}{\partial x} + \nu\left(\frac{\partial^2 u}{\partial x^2} + \frac{\partial^2 u}{\partial y^2}\right)$$

$$\frac{\partial v}{\partial t} + v\frac{\partial v}{\partial y} + u\frac{\partial v}{\partial x} = Y_g' - \frac{\partial p'}{\partial y} + \nu\left(\frac{\partial^2 v}{\partial x^2} + \frac{\partial^2 v}{\partial y^2}\right)$$

--- 3.3/3

The values X_g', Y_g' represent the components of the body forces (eg gravity) per unit volume, ν is the viscosity of the fluid. X_g, Y_g are components of the body force per unit mass and p' is the fluid pressure divided by the density. The latter form of these equations was used in the computer programs described in this thesis.

The non-linear quantities on the left hand side of equations 3.3/3 ie:-

$$u\frac{\partial u}{\partial x} \quad , \quad v\frac{\partial u}{\partial y} \quad , \quad v\frac{\partial v}{\partial y} \quad , \quad u\frac{\partial v}{\partial x}$$

are commonly known as the convection or advection terms. The Laplaciens in u and v on the right hand side represent the accelerations due to the viscous shear forces and are often referred to as the diffusion terms.

If the terms representing gravity and pressure gradients are neglected, the Navier Stokes relationships can be reduced to a coupled set of non-linear parabolic equations. Later in this thesis, it will be seen that many aspects of the behaviour of the numerical models may be derived by assuming such approximations to be valid.

4. FORMULATIONS OF THE NAVIER STOKES EQUATIONS FOR AN INCOMPRESSIBLE FLUID

4.1. Introduction

Some advantage may be derived from manipulating the equations given in the previous section. In particular, a method of solving for the pressure field is required. Two routes may be taken in order to achieve this. Both methods yield formulations based on solving separately, transport equations and elliptic equations for scalar quantities. For clarity, the Navier Stokes relationships are re-stated below. It may be assumed that the cartesian co-ordinate system is orientated such that the y direction is vertically up. In this case, the X_g body force may be ignored, the Y_g body acceleration taking the value $9.81 m/s^2$. Further, the main variables are non-dimensionised with respect to some standard flow velocity V , and some standard length paramater, L , dependent upon the geometry of the problem.

$$\frac{\partial u'}{\partial t} \quad u'\frac{\partial u'}{\partial x} + v'\frac{\partial u'}{\partial y} = -\frac{\partial p''}{\partial x'} + \frac{1}{R_e}\left(\frac{\partial^2 u'}{\partial x'^2} + \frac{\partial^2 u'}{\partial y'^2}\right) \qquad \text{--- 3.4/1}$$

$$\frac{\partial v'}{\partial t} + v'\frac{\partial v'}{\partial y} + u'\frac{\partial v'}{\partial x} = \frac{Y_g'}{F_r^2} - \frac{\partial p''}{\partial y'} + \frac{1}{R_e}\left(\frac{\partial^2 v'}{\partial x'^2} + \frac{\partial^2 v'}{\partial y'^2}\right) \qquad \text{--- 3.4/2}$$

where $u' = u/V$ $\quad v' = v/V$

$x' = x/L$ $\quad y' = y/L$

R_e = Reynolds number, F_r = Froude number

Finally, the above equations are stated without superscripts for further clarity and with the Laplacien operator in the diffusion terms.

$$\frac{\partial u}{\partial t} + u\frac{\partial u}{\partial x} + v\frac{\partial u}{\partial y} = -\frac{\partial p}{\partial x} + \frac{1}{R_e}\nabla^2 u \qquad \text{---3.4/3}$$

$$\frac{\partial v}{\partial t} + v\frac{\partial v}{\partial y} + u\frac{\partial v}{\partial x} = -\frac{\partial p}{\partial y} + \frac{1}{R_e}\nabla^2 v + \frac{Y_g}{F_r^2} \qquad \text{---3.4/4}$$

4.2. Stream-Function-Vorticity Approach

This formulation is by far the most popular historically. Much of the early work in computational fluid dynamics was based on this approach (99). Equation 3.4/3 is differentiated with respect to y and equation 3.4/4 with respect to x.

$$\frac{\partial}{\partial t}\frac{\partial u}{\partial y} + \frac{\partial}{\partial y}u\frac{\partial u}{\partial x} + \frac{\partial}{\partial y}v\frac{\partial u}{\partial y} = -\frac{\partial p}{\partial x\partial y} + \frac{1}{R_e}\nabla^2\frac{\partial u}{\partial y} \qquad \text{---3.4/5}$$

$$\frac{\partial}{\partial t}\frac{\partial v}{\partial x} + \frac{\partial}{\partial x}v\frac{\partial v}{\partial y} + \frac{\partial}{\partial x}u\frac{\partial v}{\partial x} = -\frac{\partial p}{\partial x\partial y} + \frac{1}{R_e}\nabla^2\frac{\partial v}{\partial x} \qquad \text{--3.4/6}$$

if the vorticity is defined in two dimensions as

$$\omega = \frac{\partial u}{\partial y} - \frac{\partial v}{\partial x} \qquad \text{--- 3.4/7}$$

then subtracting equation 3.4/6 from 3.4/5, the non-linear parabolic vorticity transport equation is obtained.

$$\frac{\partial \omega}{\partial t} + u\frac{\partial \omega}{\partial x} + v\frac{\partial \omega}{\partial y} = \nu\nabla^2\omega \qquad \text{---3.4/8}$$

This equation may be solved for vorticity at any instant in time. The stream function is defined by the relationships

$$\frac{\partial \psi}{\partial y} = u \qquad \frac{\partial \psi}{\partial x} = -v \qquad \text{---3.4/9}$$

Thus manipulating equation 3.4/7 gives:-

$$\nabla^2\psi = -\omega \qquad \text{---3.4/10}$$

which may be solved for the stream function . The pressure field is then found by solving the following Poisson equation:-

$$\nabla^2 p = 2\left(\left(\frac{\partial \psi}{\partial x^2}\right)\left(\frac{\partial \psi}{\partial y^2}\right) - \frac{\partial^2 \psi}{\partial x \partial y}\right) \qquad ---3.4/11$$

4.3. The Method of Primitive Variables

For this formulation, the 'primitive' variables (u,v,) are solved for directly. The premise is that the solution for the pressure field is linked to the solution of the continuity equation such that a coupling of mass conservation and the Navier Stokes relationships yields three equations in three unknowns.

This type of solution process again requires the formulation of an equation for the pressure field. However, on this occasion equation 3.4/3 is differentiated with respect to x and equation 3.4/4 with respect to y, yielding:-

$$\frac{\partial}{\partial t}\frac{\partial u}{\partial x} + \frac{\partial}{\partial x}u\frac{\partial u}{\partial x} + \frac{\partial}{\partial x}v\frac{\partial u}{\partial y} = -\frac{\partial^2 p}{\partial x^2} + \frac{1}{R_e}\nabla^2\frac{\partial u}{\partial x} \qquad ---3.4/12$$

$$\frac{\partial}{\partial t}\frac{\partial v}{\partial y} + \frac{\partial}{\partial y}v\frac{\partial v}{\partial y} + \frac{\partial}{\partial y}u\frac{\partial v}{\partial x} = -\frac{\partial p}{\partial y^2} + \frac{1}{R_e}\nabla^2\frac{\partial v}{\partial y} \qquad ---3.4/13$$

By assuming that, during the solution process, the error in the velocity field is represented by the divergence, $\nabla.\bar{u}$, and by using the rate of change of divergence;

$$\frac{\partial}{\partial t}\nabla.\bar{u} = \frac{\partial}{\partial t}\left(\frac{\partial u}{\partial x} + \frac{\partial v}{\partial y}\right) \qquad ---3.4/14$$

as a measure of convergence rate, the pressure equation for the method of primitive variables may be obtained. Equations 3.4/12 and 3.4/13

are added together. The identity 3.4/14 is used in the resulting equation to yield

$$-\nabla^2 p = \left(\frac{\partial u}{\partial x}\right)^2 + 2\frac{\partial u}{\partial y}\frac{\partial v}{\partial x} + \left(\frac{\partial v}{\partial y}\right)^2 + \frac{\partial}{\partial t}\nabla \bar{u} - \frac{1}{R_e}\nabla^2(\nabla.\bar{u})$$

---3.4/15

This can be shown to be a modified form of the steady pressure equation 3.4/11. The ability to compute the fluid pressure field using equation 3.4/15 greatly simplifies the development of the numerical schemes to solve the Navier Stokes equations.

4.4. Note Concerning the Poisson Pressure Equations

Both the method of primitive variables and the stream function-vorticity approach require the solution of a linear elliptic equation in the scalar pressure. This equation, along with its boundary conditions (see section 3.5), is subject to the property of superposition of solutions (100). For example, equation 3.4/15 could be solved separately for various terms from its right hand side. The final answer being the summation of all such results. More importantly, boundary conditions may be individually imposed, yielding greater insight into the physics of the flow problem.

5. BOUNDARY CONDITIONS

5.1. The Stream Function Vorticity Approach

In most steady flow problems, providing values for the stream function (ψ) at solid boundaries, parallel or normal to the flow direction is relatively trivial. The resulting Dirichelet boundary conditions have allowed the development of numerical procedures for the solution of the stream function equation (3.4/10) to a high degree of computational efficiency (101). If a body is moving within the flow with a known resultant velocity, conditions on the normal and tangential gradients of the stream function at the body surface may be applied. In particular, an inviscid model of the flow will result in the need for a free slip condition at the surface of the body, such that:-

$$\frac{\partial \psi}{\partial n} = V_n \qquad \text{---} 3.5/1$$

where n represents the outward normal vector to the body surface and

V_n is the normal component of body velocity

For a viscous flow, the zero slip condition leads to the requirement:-

$$\frac{\partial \psi}{\partial S} = 0 \qquad \text{---} 3.5/2$$

where S represents the tangent vector to the body surface.

The application of boundary conditions on vorticity is a much more complicated problem. The boundary/mesh arrangement may be designed in a manner so as to be convenient for the evaluation of wall vorticity, thus providing Dirichelet boundary conditions where

required. It is much more difficult to provide conditions on vorticity gradient at boundaries, as may be required for the solution of the vorticity transport equation. This problem is compounded when the mesh and boundary do not coincide conveniently. The choice of solution algorithm and whether to favour the stream function vorticity approach over the method of primitive variables, is dominated by the problem of how best to apply boundary conditions, as will be seen in section 3.6.

5.2. Method of Primitive Variables

5.2.1. Conditions on Flow Velocity

a. Solid walls: When considering flow past a solid wall, conditions on normal and tangential velocity components are required. The assumption for the former case is that there is no fluid flux allowed to pass through the wall hence:-

$$\bar{u}.\bar{n} = 0 \qquad \text{---} \ 3.5/3$$

$\bar{u}$: (u.v) vector,

$\bar{n}$: unit normal vector.

Two situations exist for the tangential velocity component. For flows in which the study of viscosity is of primary importance, the tangential velocity component is set to zero:

$$\bar{u}.\bar{s} = 0 \qquad \text{---} \ 3.5/4$$

This will be referred to as the no-slip boundary condition. When viscous effects may be considered small in comparison with other features of the flow, or when an inviscid flow is being modelled deliberately, a free-slip

condition should be applied. This is achieved by setting the normal gradient of the tangential velocity component equal to a constant:-

$$\frac{\partial}{\partial n}(\bar{u}.\bar{s}) = K \qquad \text{--- 3.5/5}$$

The equivalent condition;

$$\frac{\partial^2}{\partial n^2}(\bar{u}.\bar{s}) = 0 \qquad \text{--- 3.5/6}$$

on the second derivative of the tangential velocity component normal to the wall, often proves more convenient to use in practice.

b. Moving Solid Boundaries: This type of boundary typifies the conditions required for a body moving without the flow. The situation is very much the same as for stationary solid walls in as much as the normal component of fluid velocity is set equal to the normal component of body velocity. The no-slip condition requires the tangential components of fluid and body velocity to be equal. However, the free-slip condition for moving boundaries is identical to 3.5/3 and 3.5/4.

c. Inlet Boundaries: Some problems in hydrodynamics may require the study of the dynamics of a structure when placed in a uniform flow. In such a situation it is usual to assume that the flow velocity is fixed at some point upstream. This condition is satisfied by the inlet boundary condition, on which the horizontal velocity component (u), is fixed at a constant value. The vertical component (v) may be assumed to be zero.

d. Downstream or Radiation Boundaries: There are three ways of dealing with the downstream boundary. The first is to apply known solutions from much simpler models of the flow (eg potential flow solutions). It is assumed that the effect of the 'real' fluid parameters such as viscosity and vorticity are concentrated in some small area of interest sufficiently far 'upstream' such that the accuracy of the model is unimpared.

One alternative is to formulate a boundary condition which allows the convection of variables out of the domain without affecting the flow upstream. Historically this type of condition is the most difficult to resolve. The general form of the equation to be modelled is, from reference (102)

$$\frac{\partial \phi}{\partial t} + C_x \frac{\partial \phi}{\partial x} = 0 \qquad \text{---3.5/7}$$

where may be any variable. Equation 3.5/5 is known as the Sommerfeld radiation condition.

The third technique is to apply high viscous damping to the variables on the boundary, (see Reference (103)). An analogy is to assume the presence of a 'sponge' at the downstream end of the domain. This may be represented by the transport equation:-

$$\frac{\partial \phi}{\partial t} - K \nabla^2 \phi = 0 \qquad \text{---3.5/8}$$

where k is a negative damping coefficient to be found by numerical experiment.

Further to these three techniques, the numerical methods employed for solution of the continium equations within the fluid domain, may be modified in the region of the downstream boundary in order to smooth out local solutions.

e. Bed or Bottom Boundaries: This type of boundary is dealt with in the same manner as a solid wall in most problems. It is possible to apply a downward facing radiation condition if necessary, though no records of such formulations are available at the present time.

f. Free-Surfaces: In essence, no velocity boundary conditions can be applied directly on the contour of the free-surface, since these are local variables to be solved for. In some linearised formulations, a mean boundary is assumed (104,105), usually along the still water level, and conditions applied along this line. A preferable technique is to model the free surface such that no asumptions concerning its shape or motion characteristics are required. This is especially true of the slamming simulations to be addressed in this thesis.

However, two physical conditions which must be applied are those of continuity and zero tangential stress along the contour for a viscous flow.

The former simply implies that no 'spurious' fluid flux is allowed to pass through the free surface. The latter condition is more complex and can be stated as (106)

$$\nu\left[n_x n_y \frac{\partial u}{\partial x} - \frac{1}{2}(n_y n_y - n_x n_x)\left(\frac{\partial u}{\partial y} + \frac{\partial v}{\partial x}\right) - n_y n_y \frac{\partial v}{\partial y} \right] = 0$$

---3.5/9

where n_x. n_y are the x and y components of the unit outward normal vector given by

$$n_x = \frac{\partial \eta}{\partial x}\left(1 + \left(\frac{\partial \eta}{\partial x}\right)^2\right)^{-1/2}$$

$$n_y = \left(1 + \left(\frac{\partial \eta}{\partial x}\right)^2\right)^{-1/2}$$

η = free surface elevation.

5.2.2. Conditions on Fluid Pressure

The pressure boundary conditions stated below are applied to the solution of the Poisson equation 3.4/15 only. It will be shown later that, as far as numerical evaluation of the Navier Stokes equations are concerned, no pressure boundary conditions need be applied owing to the geometry of the staggered mesh used. The only exception to this is where a curved boundary (free surface or moving body contour) crosses the mesh. These particular problems will be dealt with separately in section 4.7.

a. Solid Walls: In general, the pressure acting on some stationary solid boundary within a flow is unknown. For an inviscid flow, this dictates that the normal pressure gradient should be zero

$$\frac{\partial p}{\partial n} = 0 \qquad \text{---3.5/10}$$

as can be seen by examining the Navier Stokes equations with ν set to zero (Euler equations). For a viscous flow,

it can be shown that the normal pressure gradient is given by (99).

$$\frac{\partial p}{\partial n} = -\frac{1}{R_e}\frac{\partial \omega}{\partial s} \qquad \text{---3.5/11}$$

b. Moving Solid Boundaries: In this case one may require knowledge of the method of solution for the full pressure field. Since the absolute value of the pressure on the body is an unknown, one is restricted to applying normal pressure gradient boundary conditions. Examination of the Navier Stokes equations reveals that for the inviscid case the normal pressure gradient is equal to the force per unit volume applied by the body in the fluid. Thus in steady flow, equation 3.5/6 is applied. If the body is accelerating the following Neumann boundary condition is applied.

$$\frac{\partial p}{\partial n} = -\frac{\partial}{\partial t}(\bar{u}.\bar{n}) \qquad \text{---3.5/12}$$

For a viscous flow one must also consider the extra constraint of equation 3.5/7. Thus an accelerating body in a viscous flow requires:-

$$\frac{\partial p}{\partial n} = -\frac{\partial}{\partial t}(\bar{u}.\bar{n}) - \frac{1}{R_e}\frac{\partial \omega}{\partial s} \qquad \text{---3.5/13}$$

c. Inlet Boundaries: The upstream value of fluid pressure may be fixed at some constant value p_0. In many cases a zero 'base' pressure condition ($p_0 = 0$) is applied.

d. Radiation Boundaries: If the method of using a known solution from, for example potential flow, is to be used downstream for velocities, then the fluid pressure is

fixed at the boundary by the Bernoulli equation. When the Sommerfeld radiation condition is being applied, pure convection is assumed, hence the pressure gradient normal to the boundary is set to zero. Similar reasoning may be applied when the highly damped model of the boundary condition given by equation 3.5/7 is used.

e. Bed or Bottom Boundary: These boundaries are dealt with in the same way as solid walls (eqns 3.5/6, 3.5/7). However, it should be noted that hydrostatic pressures should be applied in free surface flow problems in addition to those given above. Mixing gradient (Neumann) and known value (Dirichelet) boundary conditions, can prove problematical, hence separate application of these conditions in a solution by the method of superposition sometimes proves necessary

f. Free-Surfaces: At the free-surface, the pressure may be set to the atmosphere value, or for convenience, zero, along the contour of the fluid. If a 'mean free-surface' approach has been used for the velocity boundary conditions, an equivalent Dirichelet condition:

$$P_b = g\eta \qquad \text{---3.5/14}$$

η = local free surface height.

is often applied. Since this technique is common to potential flow solutions, 3.5/12 may be regarded as equal to the more familiar linearised free-surface condition;

$$\frac{\partial^2 \phi}{\partial t^2} = -g \frac{\partial \phi}{\partial y} \qquad \text{---3.5/15}$$

ϕ = fluid potential.

With $$\frac{\partial \eta}{\partial t} = V_f = \frac{\partial \phi}{\partial y}$$

V_f = vertical component of fluid velocity at the free surface.

For viscous flow a further condition needs to be applied. It is necessary to have a zero normal stress condition, which produces the following relationship (106,107)

$$p - 2\nu\left[n_x n_x \frac{\partial u}{\partial x} + n_x n_y\left(\frac{\partial u}{\partial y} + \frac{\partial v}{\partial x}\right) + n_y n_y \frac{\partial v}{\partial y}\right) = 0$$

---3.5/16

where n_x, n_y are again the x and y components of the outward normal vector. If the curvature is small, 3.5/14 may be approximated by

$$p - 2\nu\left(\frac{\partial(\bar{u}.\bar{n})}{\partial n}\right) = 0 \qquad \text{---3.5/17}$$

where $\bar{u}$ = (u,v)

6. CHOICE OF FORMULATION

At an early stage in the work, the decision was made to concentrate on the formulation of the Navier Stokes equations based on the primitive variables (u,v,). Primarily, the restriction of the stream function vorticity approach to two dimensional flows for ease of computation was considered a great disadvantage. Difficulty with boundary conditions was foreseen at an early stage and later, the inability of the method to directly examine dynamic pressure fields was realised. Further, the overall computational time was predicted to be longer as a result of the need to solve two elliptic equations in stream function and pressure at each step, as opposed to the one Poisson equation in pressure for the chosen method.

As research progressed, reference to the stream function vorticity method was made on a number of occasions. However, it was noted that in practice many more problems existed than were initially envisaged. The boundary conditions were to prove to be particularly intractable. Further, no direct formulation to deal with accelerating boundaries was possible. Whilot suitable for steady flows, it is considered that in retrospect, the stream function vorticity method is unsuitable for resolving fully dynamic fluid structure interaction problems.

7. 'SLIGHTLY' COMPRESSIBLE FLUID MODEL

A tentative explanation of the physics behind 'heavy' impacts was given in section 2.9. Finite rise times in pressure histories for impacts without air entrapment and the unreasonable prediction of infinite hydrodynamic pressures at the first instant of contact, indicated that a carefully designed compressible fluid model was required.

A very high percentage of the effort in developing computational fluid dynamics has been spent on its use as a tool in resolving transonic and supersonic flows about aerofoils and blunt or sharp nosed bodies. Such models require a fully compressible form of the equations of mass and momentum conservation, resulting in the ability to study the formation of standing shock waves around bodies in high speed flows. Many standard texts cover the subject fully (99,108). However, this type of model of compressible behaviour is of little use in the direct water entry problem wherein:-

a. the body is not stationary with respect to the shock wave,

b. the fluid is initially stationary,

c. the shock wave moves with respect to the axes,

d. the presence of the free surface restricts the area over which the compressible model may be used.

The last of these four problems is also a deciding factor on whether or not the fluid behaves compressibly at all. If the rate of increase of wetted beam of the section as it plunges through the free surface exceeds the speed of the shock wave, the fluid under the body will be compressed. Once the wetted beam reaches its maximum limit,

the shock wave will 'catch up'. The effect of the free surface boundary then comes into play, inducing hydrodynamic flow. However, the effective angle of deadrise must be very small for these conditions to prevail. Despite the added complication of air entrapment, it may well be possible that fluid compressibility has some role to play on the local level, as a prerequisite to impulsive hydrodynamic response.

It was with this in mind that a model of a 'slightly' compressible fluid was evolved. The mass conservation equation becomes:-

$$\frac{\partial \rho}{\partial t} + \frac{\partial(\rho u)}{\partial x} + \frac{\partial(\rho v)}{\partial y} = 0 \qquad \text{---3.7/1}$$

where ρ is the fluid density.

For the slighly compressible model, density convection effects are considered small, hence 3.7/1 may be manipulated to yield

$$\frac{\partial \rho}{\partial t} + \rho \nabla.\bar{u} = 0$$

$$\frac{\partial \rho}{\partial t} = \rho\left(\frac{\partial u}{\partial x} + \frac{\partial v}{\partial y}\right) \qquad \text{---3.7/2}$$

An acoustic pressure component results from the variation in fluid density. For water, the fluid pressure is very sensitive to changes in density. The resulting equation of state is dependent upon the fluid bulk modulus B, and is given by

$$\frac{\partial p_a}{\partial \rho} = c_w^2 \,, \qquad c_w^2 = \frac{B}{\rho} \qquad \text{---3.7/3}$$

where c_w is the speed of sound in water and may be taken as 1,410m/s . p_a is the acoustic pressure component.

In consideration of momentum conservation, as given by equations 3.3/2, it must be understood that the acoustic pressure gradient will be the dominant term. The fluid is initially stationary, and hence convection will be of no significance. Viscosity, it is proposed, will likewise have negligible effect. Therefore, it was considered that the following equations were perfectly adequate to describe the initial evolution of the flow field over the extremely short time scale of the pressure rise:-

$$\frac{\partial u}{\partial t} = -\frac{1}{\rho}\frac{\partial p_a}{\partial x} \qquad \text{---} 3.7/4$$

$$\frac{\partial v}{\partial t} = -\frac{1}{\rho}\frac{\partial p_a}{\partial y} \qquad \text{---} 3.7/5$$

8. EQUATIONS FOR TRAPPED AIR LAYER

8.1. Introduction and Initial Formulation

As reviewed in chapter 2, an extra problem exists in resolving the flow when an impact occurs on a section which is nearly parallel with the fluid free surface. Pressures develop in the air layer beneath the body such that the free surface is depressed in the middle and rises at the edges. A cushioning effect results, in which some air may remain trapped after impact. Thus the general water entry problem is complicated by the need to compute the evolution of the pressure field between the body and the free surface, prior to impact.

The assumptions made in previous examinations of this phenomenon (35,36,49) were the initial subject of study. The air was assumed to be a perfect or near perfect gas and the flow conditions were assumed adiabatic. Owing to the high Reynolds number for the escaping air, the flow was assumed turbulent such that the horizontal velocity (u_a) had a constant vertical distribution, ie:-

$$\frac{\partial u_a}{\partial y} = 0 \qquad \text{---3.8/1}$$

Therefore, for the two dimensional model of an impact, a one dimensional inviscid flow was assumed for the air-layer, see figure (3-3). This assumption also eased the practicalities of the computation. Any numerical model of the flow employing the two dimensional equations of motion would require discretisation to be applied in both the horizontal and vertical directions. The resulting mesh would have been distorted as the body approached the free surface. Further, the vertical mesh spacing Δy would tend to zero, resulting in a badly conditioned numerical model. Control volumes for

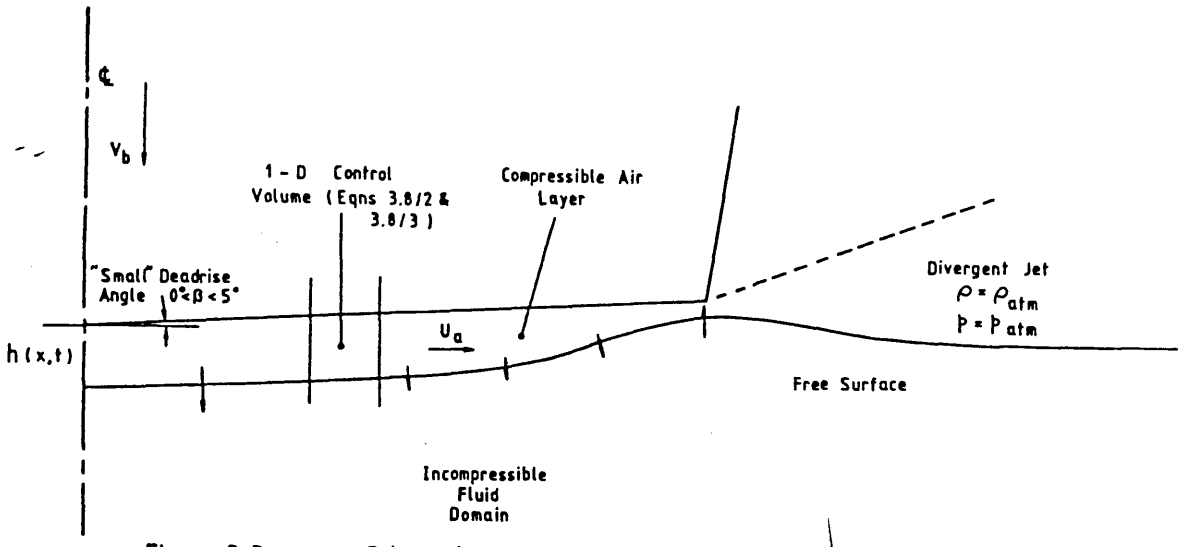

Figure 3-3 Schematic View Of Escaping Air Layer.

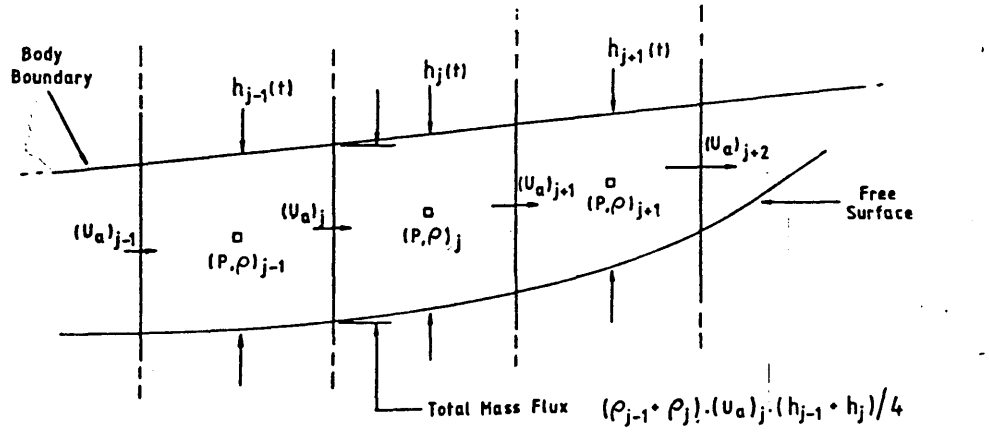

Figure 3-4 One Dimensional Control Volume And Principal Variables For Air Layer.

the one dimensional model are shown in figure (3-4). Assuming the size of the air gap h to be a function of time, it can be shown that the expression for mass conservation is:-

$$\frac{\partial(\rho_a h)}{\partial t} + \frac{\partial}{\partial x}(\rho_a u_a h) = 0 \qquad \text{---} 3.8/2$$

One dimensional conservation of momentum is given by:-

$$\frac{\partial u_a}{\partial t} + u_a \frac{\partial u_a}{\partial x} = -\frac{1}{\rho_a}\frac{\partial p_a}{\partial x} \qquad \text{---} 3.8/3$$

At any instant one may equate the sum of the vertical component of body velocity and the downward velocity of the free surface to the rate of change of h such that:-

$$\frac{\partial h}{\partial t} = V_b - \frac{\partial \eta}{\partial t} \qquad \text{---} 3.8/4$$

Equations 3.8/2,3,4 provide the means to solve the four unknowns u_a, h, ρ_a and p_a if a convenient relationship between p_a and ρ_a can be found. In practice, the equation:-

$$\frac{\partial p_a}{\partial \rho_a} = C_a^2 \qquad \text{---} 3.8/5$$

where C_a = speed of sound in air, is used. The alternative form:-

$$\frac{p_1}{p_2} = \left(\frac{\rho_1}{\rho_2}\right)^{\gamma} \qquad \text{---} 3.8/6$$

where ($\gamma = 1.4$) is the ratio of specific heats, proves most useful for the numerical procedures used in this thesis.

8.2. Air Entrapment Simulation Using Additional Conservation of Energy With Air Layer

The behaviour of the air layer as described by equations

3.8/2 to 3.8/5 assumes a constant relationship between pressure and density, ie that the acoustic speed for the medium does not vary.

In order to test this premise, it was decided to perform the full air entrapment computation using the equations of conservation of mass momentum and energy for an inviscid compressible fluid. A one dimensional flow model was again assumed, which allowed the mass conservation equation to remain unchanged. However, this was not the case for the momentum equation which was re-cast as:-

$$\frac{\partial}{\partial t}(\rho_a u_a) + \frac{\partial}{\partial x}(\rho_a u_a^2 + p_a) = 0 \qquad \text{---3.8/7}$$

The additional state variables e, the internal energy per unit volume and T, the gas temperature, are required in order to formulate a relationship between the pressure and density. The internal energy e is given by:-

$$e = C_V T \qquad \text{---3.8/8}$$

where C_V is the specific heat at constant volume. The pressure is derived from:-

$$p_a = \rho_a R T \qquad \text{---3.8/9}$$

where R is the gas constant given by:-

$$R = C_p - C_V \qquad \text{---3.8/10}$$

(C_p = specific heat at constant pressure).

A rearrangement of the above relationships leads to an equation for pressure suitable for inclusion in a numerical scheme:-

$$p_a = (\gamma - 1)\rho_a e \qquad \text{---3.8/11}$$

where γ is the ratio of specific heats as used in equation 3.8/6.

The variable e, is found via the energy conservation equation. However, the primary variable in this last transport equation is the total energy per unit volume E_s, given for the non-dimensional flow model by:-

$$E_s = e + \frac{1}{2} u_a^2 \qquad \text{---3.8/12}$$

The total energy is subject to the transport equation:-

$$\frac{\partial(\rho_a E_s)}{\partial t} + \frac{\partial}{\partial x}((\rho_a E_s + p_a)u_a) = 0 \qquad \text{---3.8/13}$$

This represents the balance between energy convection, given by the term:-

$$\frac{\partial}{\partial x}(\rho_a E_s u_a) = u_a \frac{\partial}{\partial x}(\rho_a E_s) + \rho \frac{\partial}{\partial x}(u_a E_s) + E_s \frac{\partial}{\partial x}(\rho_a u_a)$$

and work done per unit volume given by:-

$$\frac{\partial}{\partial x}(p_a u_a) = p_a \frac{\partial u_a}{\partial x} + u_a \frac{\partial p_a}{\partial x}$$

The full set of equations used for this non-isothermal model of a perfect gas were 3.8/2, 3.8/4, 3.8/7 and 3.8/13. The numerical scheme devised is described in a later chapter.

8.3. Three Dimensional Impact Simulation With Air Entrapment

It has been noted that, for a two dimensional fluid computational domain, a one dimensional model of the air layer promises the best numerical algorithm. Since it was possible to make

these savings in computational effort, it was decided to study a three dimensional impact simulation with air entrapment. The two dimensional gas flow model which results was considered to be within the reach of the computing power available. Further, as stated in chapter two, many discrepancies exist between pressure time histories calculated for two dimensional impact problems and measurements made at sea. It was hoped that some light could be shed upon the cause of some of these differences.

The continium equations used for the two dimensional trapped air layer were very much the same as those for the one dimensional isothermal case. Figure 3-5 shows the three dimensional domain and two dimensional control volumes used. The equation of mass conservation for the case becomes:-

$$\frac{\partial}{\partial t}(\rho_a h) + \frac{\partial}{\partial x}(\rho_a u_a h) + \frac{\partial}{\partial y}(\rho_a v_a h) = 0 \qquad \text{---3.8/14}$$

where h is now a function of the x and y co-ordinates but may still be found by local application of equation 3.8/4.

Two transport equations are required to satisfy momentum conservation and, as with the one dimensional isothermal case, are cast in a simplified format similar to that of the original Navier Stokes equations, ie:-

$$\frac{\partial u_a}{\partial t} - u_a\frac{\partial u_a}{\partial x} \quad v_a\frac{\partial u_a}{\partial y} = -\frac{1}{\rho_a}\frac{\partial p_a}{\partial x} \qquad \text{---3.8/15}$$

$$\frac{\partial v_a}{\partial t} - v_a\frac{\partial v_a}{\partial x} \quad u_a\frac{\partial v_a}{\partial y} = -\frac{1}{\rho_a}\frac{\partial p_a}{\partial y} \qquad \text{---3.8/16}$$

The pressure field may again be found using the simplified relationship given by equation 3.8/6.

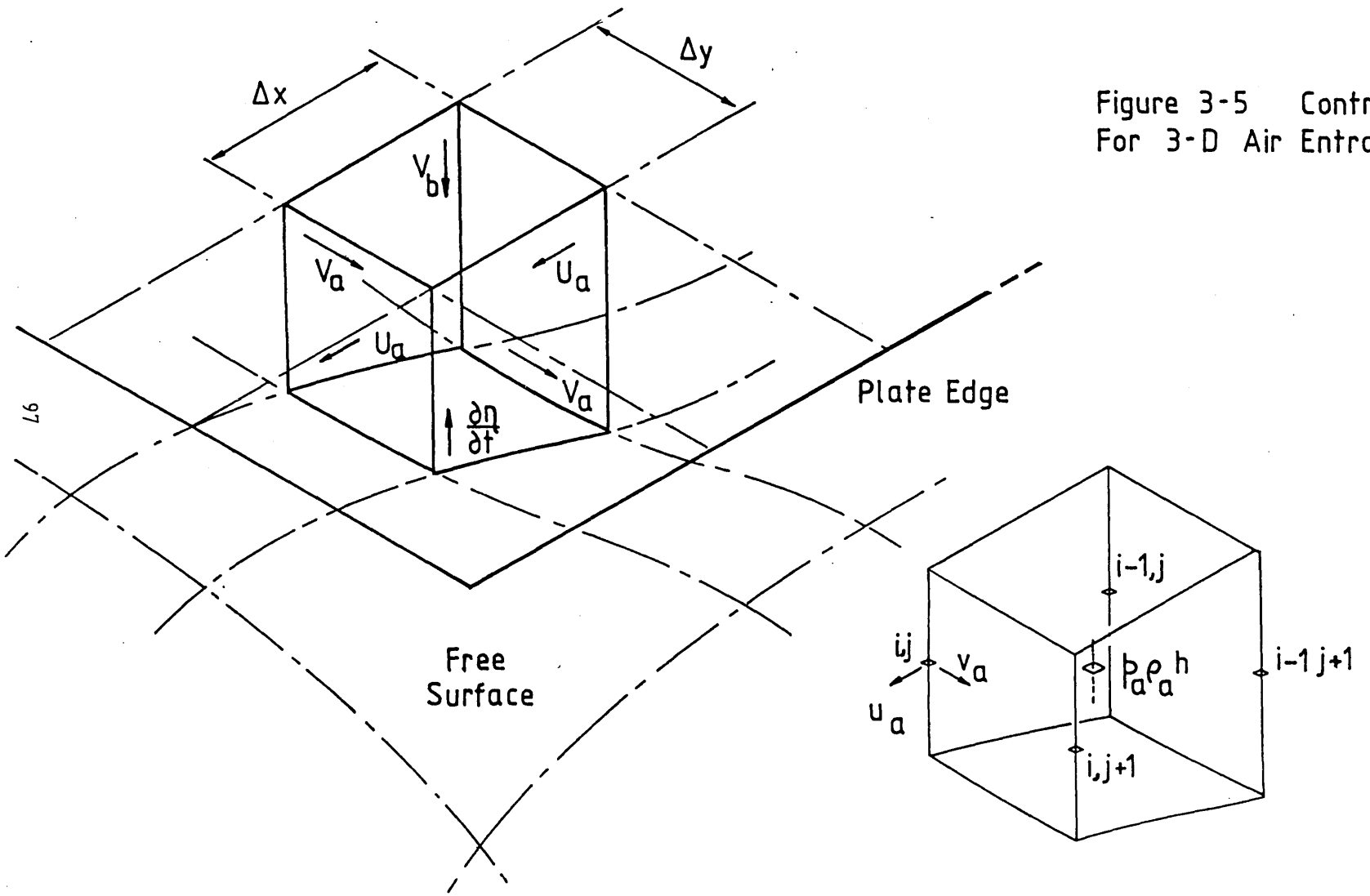

Figure 3-5 Control Volume
For 3-D Air Entrapment Problem

9. TREATMENT OF BODY DYNAMICS

At any instant during the simulation, the fluid reactions acting on the body may be found by integrating the pressures around its contour. The resultant force components depend upon the type of situation being modelled.

For a falling body, the instantaneous acceleration components are found from:-

$$\dot{V}_b = (M_b g + F_y) / M_b$$

$$\dot{U}_b = (F_x / M_b)$$

---3.9/1

where M_b = mass of body

F_x, F_y = x and y components of fluid reactions

g = acceleration due to gravity.

The case of 'forced' motion might also be investigated, in which a known initial acceleration (other than due to gravity) is applied. Similarly, the downward velocity of the body may be assumed constant. In either case the fluid reactions are ignored with respect to the kinematics of the body.

If a full interaction simulation is required, the kinetics of the body are assumed to follow the well known relationships given below:-

$$V_b^{n+1} = V_b^n + \dot{V}_b \Delta t$$

$$U_b^{n+1} = U_b^n + \dot{U}_b \Delta t$$

$$Y_b^{n+1} = Y_b^n + V_b^n \Delta t + \frac{1}{2} \dot{V}_b \Delta t^2$$

$$X_b^n = X_b^n + U_b^n \Delta t + \frac{1}{2} \dot{U}_b \Delta t^2$$

---3.9/2

Since the simulation follows a time stepping routine, the above equations can be seen to assume constant accelerations over these small values of t. The superscripts n, n+1 refer to the present time level and the future time level respectively.

CHAPTER 4

NUMERICAL METHODS

CHAPTER 4

NUMERICAL METHODS

1. TYPES OF MODEL AVAILABLE

1.1 Introduction

As inferred by the title of this chapter, no analytical mathematical techniques exist for the solution of the form of the Navier Stokes equations cited in the previous section. Some special cases have been formulated, such as purely viscous one dimensional or Stokes flow, the boundary layer equations (97), etc. Such formulations may be susceptible to solutions via polynomial expansion or separation of variables but are in general too simple for use in the types of problem encountered herein. Further, the complicated domain geometry over which the equations had to be solved, would cause difficulty for even the simplest of flow models (eg, a potential flow), when it came to applying boundary conditions.

With the advent of the digital computer it has become possible to perform large scale analyses of mathematical problems using purely numerical methods. As far as the solution of problems in continium mechanics is concerned, the capability of inverting large matrices and/or tirelessly performing iterative computations, has resulted in the development of discretised models of the relevant partial differential equations.

The rest of this chapter is devoted to the development of a discretised model of fluid behaviour during a slam. Models are

developed for both the incompressible (sections 4.2-4.9) and the 'slightly' compressible (section 4.11) flows. A full computational cycle is detailed in section 4.10. The modelling of the equations for the trapped air layer is dealt with separately in chapter 7.

The two most promising candidates for modelling the equations detailed in chapter 3, with their boundary conditions, were the finite difference and finite element methods.

Both were considered candidates for simulations of the water entry problem.

2. NUMERICAL METHODS AVAILABLE

2.1. Finite Difference Discretisation

In this technique the fluid domain is replaced by a finite difference mesh, enclosing control volumes over which the derivatives in the equations of section 3.2 are approximated. The fluid variables (u,v,p) are assumed to be concentrated at discrete points (nodes) throughout the mesh. Partial derivatives are replaced by finite difference approximations, derived via the use of Taylor expansions about the node with reference to the value of the variable on the surrounding mesh, (see figure 4-1).

Each level of approximation yields a formula for the derivative which will be accurate up to some order of polynomial 'fit' for the variable. These expressions are only precise when stated for a particular position on the mesh, ie they are only pointwise accurate.

The method of solution depends upon the partial differential equations being modelled. In general, it usually consists of formulating a discretised version of the equation to be solved at each node. When boundary conditions are applied, a set of N simultaneous equations in N unknown nodal values are generated which may be solved by a variety of computational techniques.

2.2. Finite Element Discretisation

Again the fluid domain is divided up into a mesh, or a series of finite elements. It is assumed that each variable may be approximated by a polynomial expression, eg:-

Figure 4-1 Simple Finite Difference "Star" On A Rectangular Mesh.

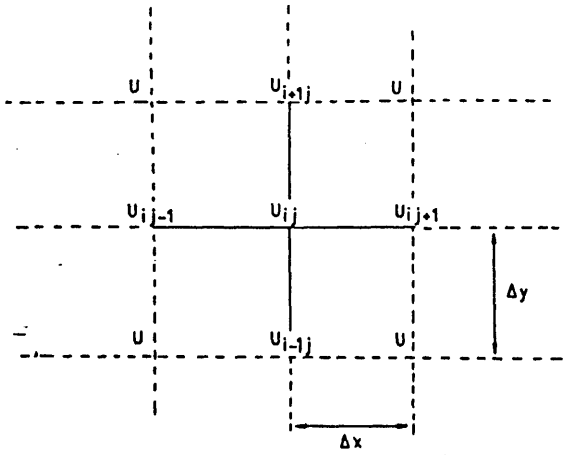

By Taylor Expansion :

$$U_{ij+1} = U_{ij} + \Delta x \frac{\partial U}{\partial X} + \frac{\Delta x^2}{2} \frac{\partial^2 U}{\partial X^2} + \text{-----}$$

$$U_{ij-1} = U_{ij} - \Delta x \frac{\partial U}{\partial X} + \frac{\Delta x^2}{2} \frac{\partial^2 U}{\partial X^2} + \text{-----}$$

$$U_{i+1j} = U_{ij} + \Delta y \frac{\partial U}{\partial Y} + \frac{\Delta y^2}{2} \frac{\partial^2 U}{\partial Y^2} + \text{-----}$$

$$U_{i-1j} = U_{ij} - \Delta y \frac{\partial U}{\partial Y} + \frac{\Delta y^2}{2} \frac{\partial^2 U}{\partial Y^2} + \text{-----}$$

Figure 4-2 Typical Isoparametric Finite Element

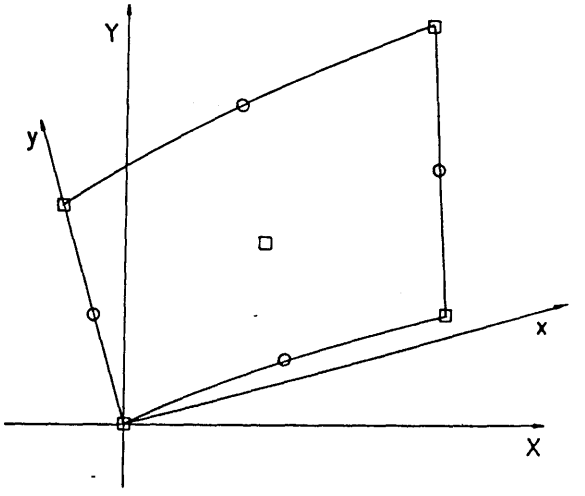

○ (u,v) Nodes

□ Combined (p,u,v) Nodes

9 (u,v) Nodes Per Element - Parabolic Velocity Distribution

5 (p) Nodes Per Element - Linear Pressure Distribution

$$U(xy) = a_0 + a_1 x + a_2 y + a_3 xy \qquad \text{---4.2/1}$$

over any one element.

The values $a_0\ a_1\ a_2\ a_3$ may be derived by writing equation 4.2/1 for each of the nodal points shown in figure (4-2) to produce the matrix expression:-

$$\begin{bmatrix} U_1 \\ U_2 \\ U_3 \\ U_4 \end{bmatrix} = \begin{bmatrix} 1, x_1, y_1, x_1y_1 \\ 1, x_2, y_2, x_2y_2 \\ 1, x_3, y_3, x_3y_3 \\ 1, x_4, y_4, x_4y_4 \end{bmatrix} \cdot \begin{bmatrix} a_0 \\ a_1 \\ a_2 \\ a_3 \end{bmatrix}$$

or

$$[U]=[C][A]$$

hence

$$[A]=[C]^{-1}[U] \qquad \text{---4.2/2}$$

It can be seen from 4.2/1 that:-

$$[U] = [1, x, y, xy][A] = [H][A] \qquad \text{---4.2/3}$$

hence the variable U(x,y) may be expressed in terms of its nodal values by:-

$$U(x,y) = [H][C]^{-1}[U] = [N][U] \qquad \text{---4.2/4}$$

where [N] is the shape function. [N] may be differentiated as its elements are functions of the x and y co-ordinates alone, hence derivatives of U may be simply stated, eg:-

$$\frac{\partial U}{\partial x} = \frac{\partial [N]}{\partial x}[U] \qquad \text{---4.2/5}$$

These approximations may be substituted directly back into the original partial differential equations. The solution of the equations is found by direct integration. In particular, the Navier

Stokes equations require a formulation known as the weighted residual method. Suffice it to say that by writing down this formulation for each element and by choice of a suitable numerical integration scheme, sufficient equations are generated to produce a solution for all the unknown variables. Many texts are now available on the subject (109,110)

2.3. Choice of Numerical Method

The choice of numerical approach proved very difficult. When surveying the literature prior to this decision, care was taken not to make a judgement based on the claimed advantages of one technique over the other, unless it was possible to relate such a gain to the particular problem to be solved.

For the general class of fluid dynamic problems met in engineering, the finite element method holds definite advantages. Many computer based mesh generation routines now exist for complicated shapes of computational domain. A great deal of effort has gone into producing matrix assembly and inversion algorithms in the field of structural mechanics (111,112) and much of this has been of use to the computational fluid dynamicist. From the mathematical standpoint, the finite element method is preferable owing to its rigorous adherence to the principles of variational calculus and its ability to produce piecewise continuous expressions for a function over an element, as opposed to the pointwise approximation given by the finite differences.

However, despite such advantages, the finite element method has had less success in solving real engineering problems than might

have been hoped for. Initially developed very successfully for the solution of elliptic equations, which are easily subjected to variational formulations, it has proved more difficult to apply to the parabolic convection/diffusion problem. Further, it suffers from the same types of numerical instability and inaccuracy as the finite difference method. Indeed, approximations for derivatives such as given by equation 4.2/5 can be shown to be exactly equivalent to finite difference formulae in common use.

The finite difference method has a number of advantages with respect to understanding the physics of a particular situation. Experience has shown that the direct modelling of derivatives via these techniques has definite gains when conceptual research is being attempted. Many more algorithms or 'schemes' exist for the solution of finite difference models, illustrating that the method has an overall greater level of versatility. Furthermore, a greater number of reports exist illustrating the modelling of free-surface flows using the finite difference method (113,114), than the finite element method (115).

Finally, it is difficult to model fully dynamic problems in fluid flow using finite elements. Many specialised techniques exist for time marching solutions but these usually rely on the flow problem reaching some quasi-steady state situation (eg, vortex shedding). Only recently have any such attempts been made (116), for the case of a fluid/structure interaction problem.

Consequently, the choice was made to concentrate on producing a finite difference model of the fluid flow problem caused by a slam. The most important factor in this decision was the overall simplicity

involved in relating the numerical model to the complicated fluid dynamics of the problem.

3. THE FINITE DIFFERENCE METHOD

A number of excellent tests on the use of the finite difference method in solving partial differential equations exist. In particular, Richtmyer (117), Ames (118) and Mitchell (119) have covered general numerical methods for P.D.E's. Roache (99) and Mitchell and Griffiths (120), have produced texts of particular interest to computational fluid dynamicists. Further, there are many international journals in applied physics, mathematics and engineering which regularly publish work on both the mathematics and applications of the finite difference method.

Many different methods of finite difference discretisation exist. Finite difference approximations are usually derived via the use of a Taylor expansion about a point, as will be briefly detailed in the next section. It is not proposed that a full exposition of the finite difference method will appear in this thesis. Instead, specific schemes will be put forward. A great deal of effort went into experimenting with various finite difference operators and overall algorithims. Only those which proved successful or those which help explain particular characteristics of numerical schemes, will be mentioned.

The theme of flow simulation is common to the algorithms in this work. The typical fluid domains illustrated in fig. (4-3,4-4,4-5) were split up into finite difference meshes which extended above the free surface. Therefore, the discretised domain consisted of full, partially full and empty finite difference cells. Continuity was applied only to full cells. The partially full cells constituted the free surface model and were subject to a particular form of the free

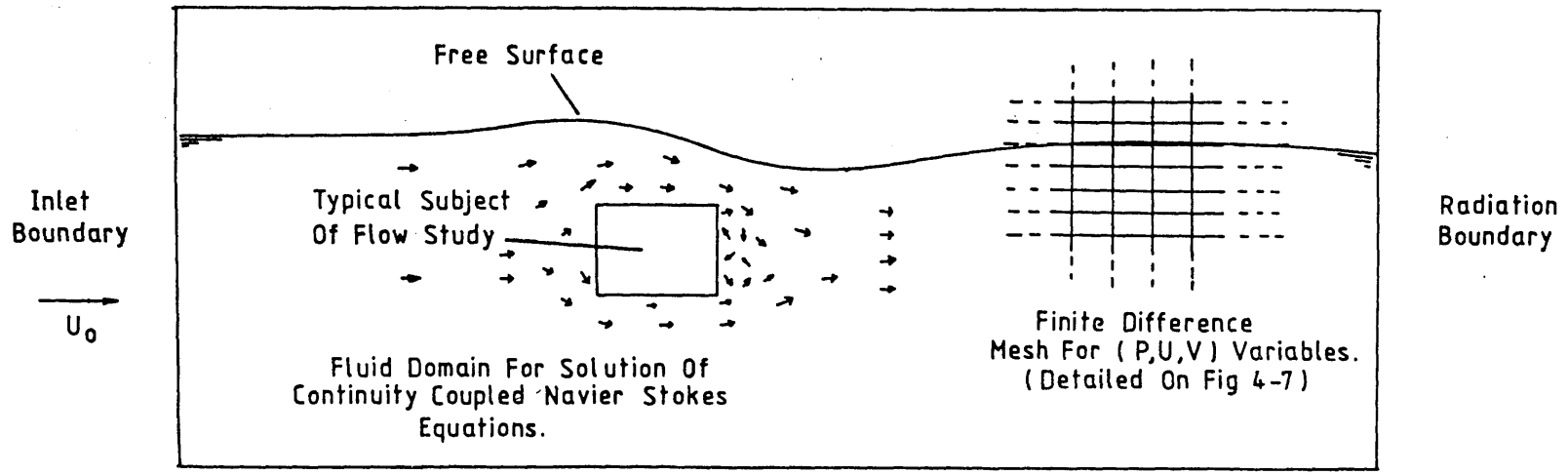

Figure 4-3

Enlarged View Of Flow Domain About Area Of Study

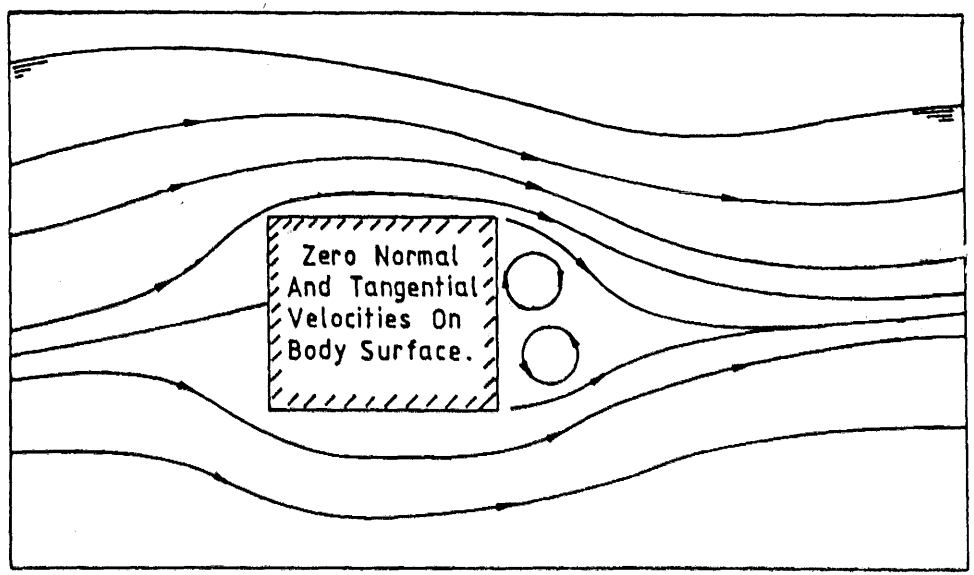

Figure 4-4 Schematic View Of Flow Domain For Wave Tank Simulation.

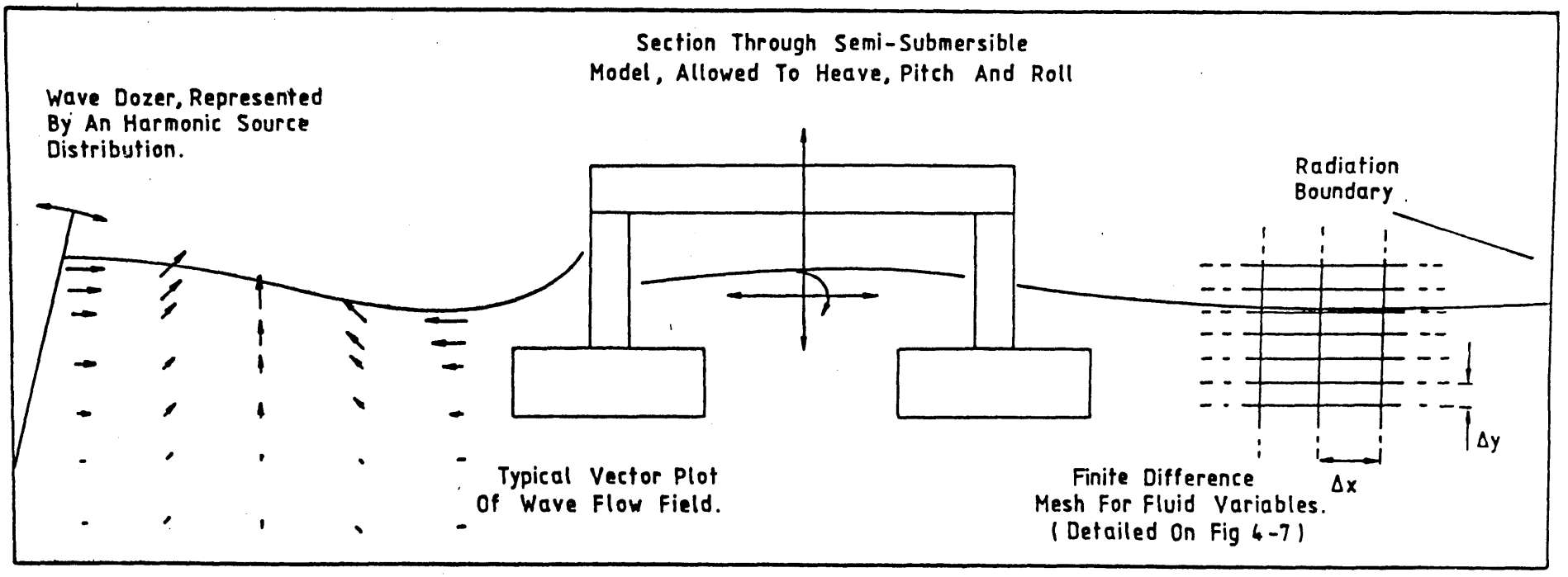

Figure 4-5

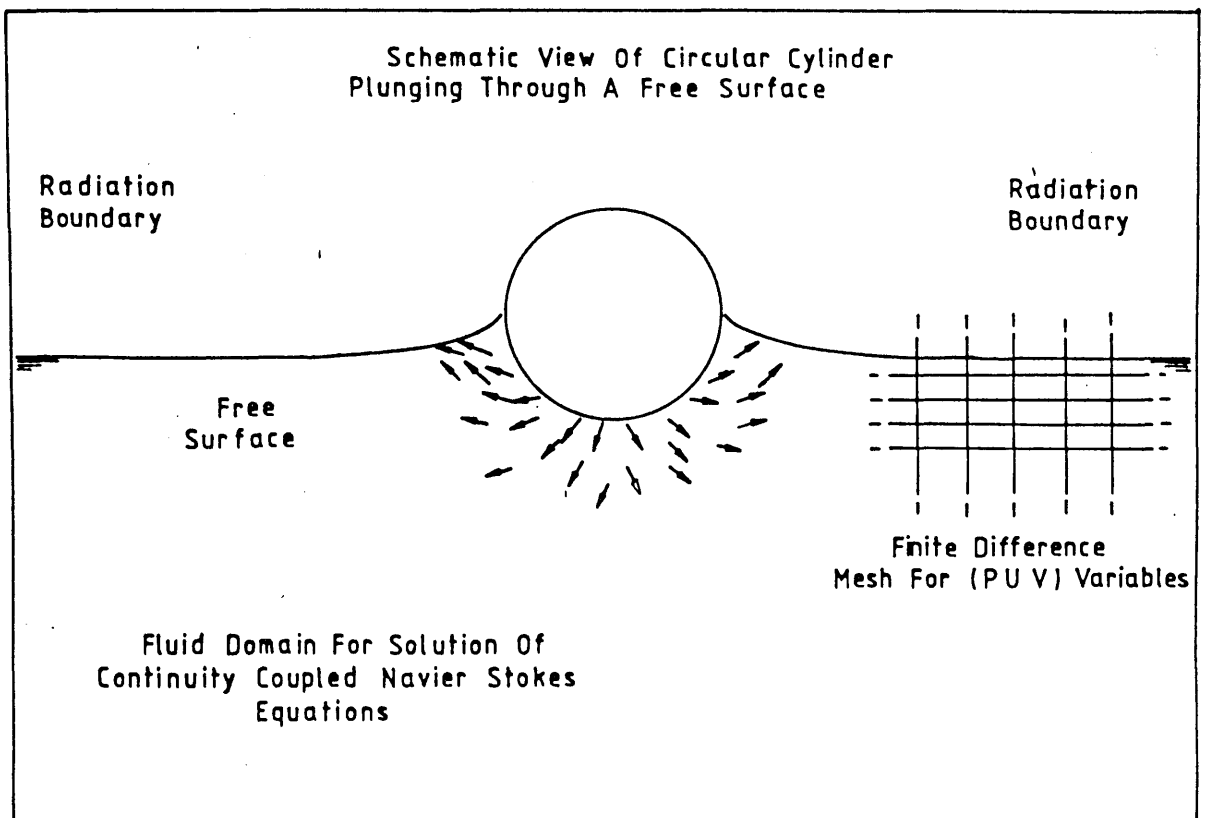
Schematic View Of Circular Cylinder
Plunging Through A Free Surface
Radiation
Boundary
Radiation
Boundary
Free
Surface
Finite Difference
Mesh For (P U V) Variables
Fluid Domain For Solution Of
Continuity Coupled Navier Stokes
Equations
Bottom Boundary V = 0

surface kinematic boundary condition which will be described in 5.1. The discretised version of the Navier Stokes equations was applied at all (u,v) nodes within the fluid domain. In the techniques described herein, moving bodies were represented by closed contours, which in general, did not coincide with the mesh. Special consideration of the boundary conditions thus imposed was found to be necessary.

It will be shown that, within the fluid domain, equations 3.3/3 and 3.3/4 provide a method of calculating the velocity components (u,v) at any node, for any instant $t = (n+1)\Delta t$, given knowledge of their state at previous times $n\Delta t, (n-1)\Delta t$. This ability to predict changes in the character of the flow field in a step by step manner constituted the basis of the simulation procedure. Figure (4-6) shows a flow chart of the general solution method.

Having updated the velocity field, the solution of the continuity equation was required to remove the effect of finite difference truncation errors inherent in the discretisation process. Next, the pressure field was calculated subject to its own boundary conditions. At this stage a certain amount of book keeping was required, changing the domain shape by moving the free surface and any dynamic boundaries within the flow. The simulation then continued with the next (u,v) updating step on the newly defined computational domain.

In many steady state flow problems, this technique has long been used to provide convergence to the solution of the Navier Stokes equations. In the dynamic flow problems set up by the slamming phenomenon, the Navier Stokes equations are simply used to provide 'dynamic equilibrium' during the simulation process. Any 'solving' of

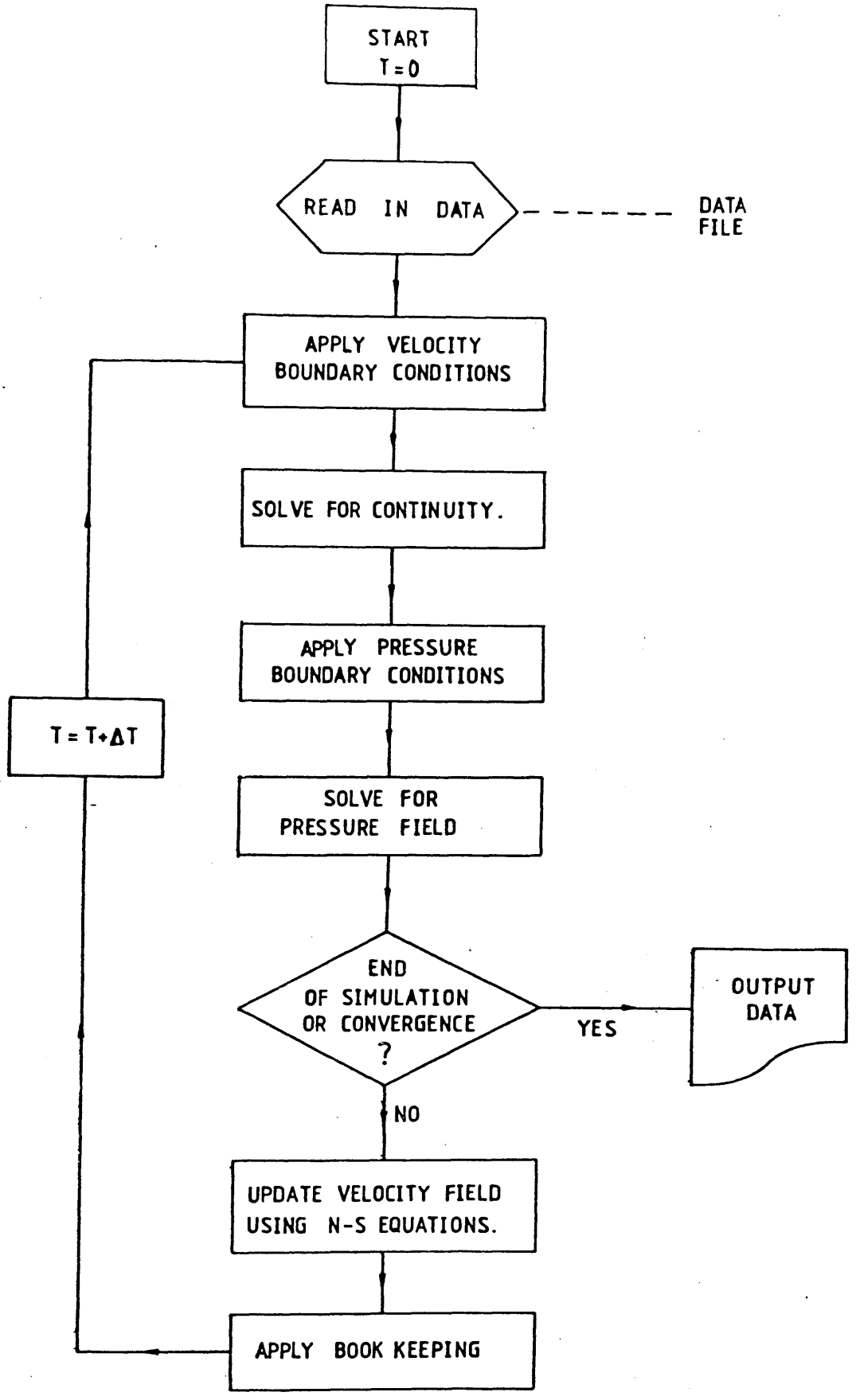

Figure 4-6 Flow Chart Of Basic Computational Procedure

partial differential equations is restricted to the continuity and pressure field boundary value problems.

4. FINITE DIFFERENCE OPERATORS

4.1. Formulations for Specific Derivatives

Consider figure (4-7). The type of mesh arrangement illustrated is known as the T3 grid as it was used by the T3 research group at the University of California's Los Alamos Laboratories whilst developing the Marker and Cell Method (113). The positioning of the nodes for velocity components and pressure is particularly convenient when continuity is of importance. The finite difference operators needed to replace the partial differential terms in equations 3.2/1, 3.3/3 and 3.3/4 will be specified for this mesh arrangement.

The replacement of a partial derivative by its finite difference equivalent is achieved by use of a Taylor expansion about a single node. For example, in discrete notation and with reference to figure 4-1:-

$$U_{ij+1} = U_{ij} + \Delta x \frac{\partial U}{\partial x} + \frac{(\Delta x)^2}{2!} \frac{\partial^2 U}{\partial x^2} + \text{-----} O(\Delta x)^3 \qquad \text{---4.4/1}$$

$$U_{ij-1} = U_{ij} - \Delta x \frac{\partial U}{\partial x} + \frac{(\Delta x)^2}{2!} \frac{\partial^2 U}{\partial x^2} - \text{-----} O(\Delta x)^3 \qquad \text{---4.4/2}$$

Subtracting equation 4.4/2 from 4.4/1 gives:-

$$U_{ij+1} - U_{ij-1} = 2\Delta x \frac{\partial U}{\partial x} + \frac{(\Delta x)^3}{3} \frac{\partial^3 U}{\partial x^3} + \text{----} O(\Delta x)^4$$

yielding:-

$$\frac{\partial U}{\partial x} = \frac{U_{ij+1} - U_{ij-1}}{2\Delta x} - \frac{(\Delta x)^2}{6} \frac{\partial^3 U}{\partial x^3} + \text{----} O(\Delta x)^4 \qquad \text{---4.4/3}$$

This, as an example, is known as a central difference

Figure 4-7 "T 3" Computational Mesh And Primary Variables (p,U,V).

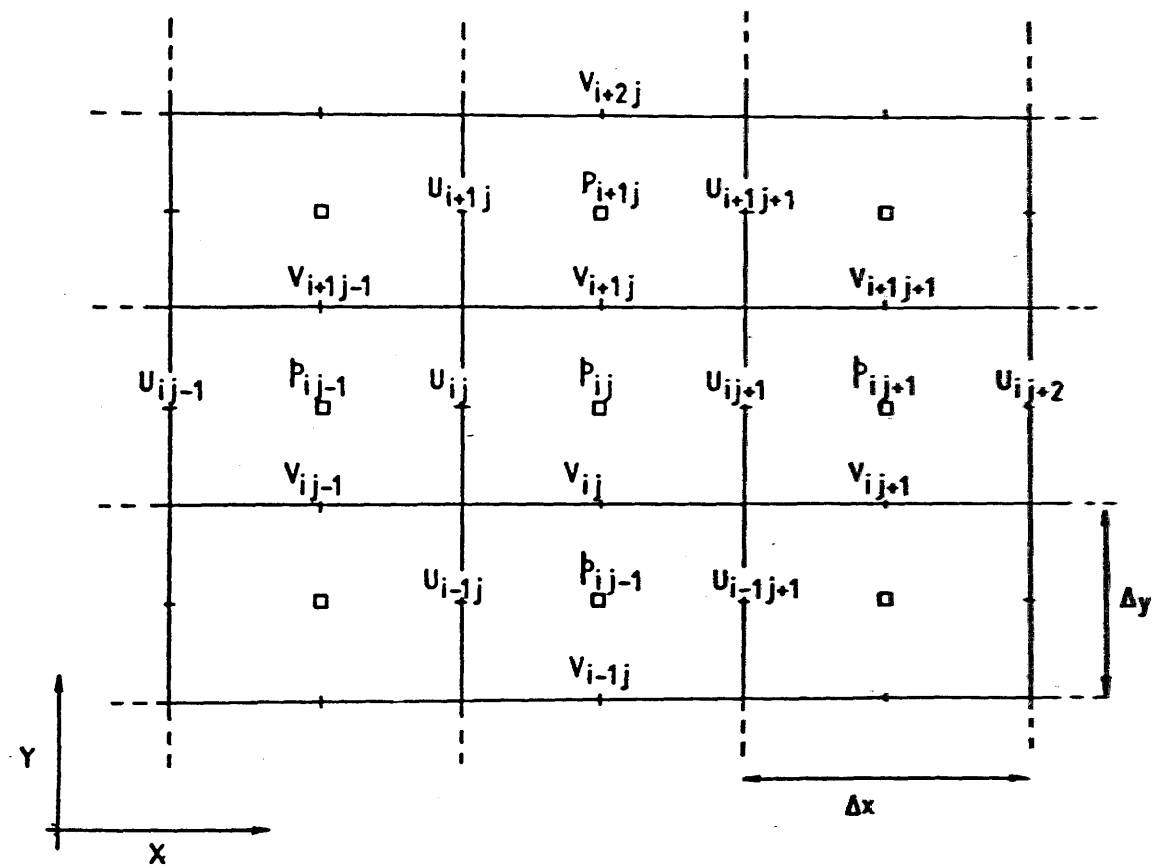

N.B. $(i,j) \not\equiv (x,y)$

approximation for the first derivative of u. The term:-

$$\frac{(\Delta x)^2}{6}\frac{\partial^3 u}{\partial x^3}$$

is known as the truncation error. The approximation is accurate to within this value for polynomials up to second order.

By adding equations 4.4/1 and 4.4/2, the central difference approximation to the second derivative of u is obtained as:-

$$\frac{\partial^2 u}{\partial x^2} = \frac{u_{ij+1} + u_{ij-1} - 2u_{ij}}{(\Delta x)^2} + \frac{(\Delta x)^3}{12}\frac{\partial^4 u}{\partial x^4} \quad ---- O(\Delta x)^5$$

---4.4/4

In this case, the finite difference operator is accurate to the level of its truncation error for polynomials of up to third order.

Many more examples may be derived from the Taylor expansions. A full study is beyond the scope of this thesis, the reader is referred to the texts previously mentioned for such information. Particular formulations for the equations describing an incompressible flow field will now be detailed.

4.2. Continuity Equation

Referring to equation 3.2/1, a central differencing scheme is used for the two first derivatives in u and v with respect to x and y. For the T3 grid shown, the finite difference operators specify the gradient for the mid point of the cell hence the effective mesh spacing is half that used in the derivation of equation 4.4/3. The discrete approximation to the continuity equation is therefore:-

$$\nabla.\bar{u} \approx \frac{u_{ij+1} - u_{ij}}{\Delta x} + \frac{v_{i+1j} - v_{ij}}{\Delta y} \qquad \text{---4.4/5}$$

The truncation error is given by:-

$$\frac{(\Delta x)^2}{12}\frac{\partial^3 u}{\partial x^3} + \frac{(\Delta y)^2}{12}\frac{\partial^3 v}{\partial x^3}$$

4.3. Navier Stokes Equations for Incompressible Flow

The finite difference operators for the Navier Stokes equations are evaluated at the (u,v) nodes. The type of numerical solution algorithm or scheme is highly dependent upon the operators used. The types of scheme available will be detailed in the next section. Some of the operators in common use are detailed below.

4.3.1 Time Derivatives

By use of the Taylor expansion along the time axis, the following simple formulae may be derived:-

a. Forward time step

$$\frac{\partial u}{\partial t} = \frac{u_{ij}^{n+1} - u_{ij}^{n}}{\Delta t} - \frac{\Delta t}{2}\frac{\partial^2 u}{\partial t^2} + \text{----} O(\Delta t)^2 \qquad \text{---4.4/6}$$

b. Backward time step

$$\frac{\partial u}{\partial t} = \frac{u_{ij}^{n} - u_{ij}^{n-1}}{\Delta t} + \frac{\Delta t}{2}\frac{\partial^2 u}{\partial t^2} + \text{-----} O(\Delta t)^2 \qquad \text{---4.4/7}$$

c. Central time step

$$\frac{\partial u}{\partial t} = \frac{u_{ij}^{n+1} - u_{ij}^{n-1}}{2\Delta t} - \frac{(\Delta t)^2}{6}\frac{\partial^3 u}{\partial t^3} + \text{-----} O(\Delta t)^4 \qquad \text{---4.4/8}$$

4.3.2. Convection Operators

The type of convection operator applied has the greatest effect upon the numerical stability in practice. A vast amount of effort has been expended by many authors (for reviews see references (99,121,122)), in order to suppress the well known instability phenomenon of 'wiggles'. More detail concerning this problem will be given later.

Detailed below are a few of the FD operators in common use:-

a. Central Difference Approximation: The simple expression, given by equation 4.4/3 is modified to fit the convection term thus:-

$$U\frac{\partial U}{\partial x} = U_{ij}\frac{U_{ij+1}-U_{ij-1}}{2\Delta x} - \frac{U_{ij}(\Delta x)^2}{6}\frac{\partial^3 U}{\partial x^3} + \text{----}\,O(\Delta x)^4 \qquad \text{---}\,4.4/9$$

b. Upwind/Downwind Operators: Used specifically to remove 'wiggles', these operators are given by:-

$$U\frac{\partial U}{\partial x} = U_{ij}\frac{U_{ij}-U_{ij-1}}{\Delta x} - \frac{U_{ij}\Delta x}{2}\frac{\partial^2 U}{\partial x^2} + \text{-----}\,O(\Delta x)^2 \qquad U_{ij} > 0 \qquad \text{---}\,4.4/10$$

$$U\frac{\partial U}{\partial x} = U_{ij}\frac{U_{ij+1}-U_{ij}}{\Delta x} + \frac{U_{ij}\Delta x}{2}\frac{\partial^2 U}{\partial x^2} - \text{-----}\,O(\Delta x)^2 \qquad U_{ij} < 0 \qquad \text{---}\,4.4/11$$

c. High Order Central Difference Operators

$$U\frac{\partial U}{\partial x} = U_{ij}\left[\frac{U_{ij+1}-U_{ij-1}}{2\Delta x} - \frac{U_{ij+2}-2(U_{ij+1}-U_{ij-1})-U_{ij-2}}{12\Delta x}\right] - \frac{(\Delta x)^4}{4}\frac{\partial^5 U}{\partial x^5} + \text{----}\,O(\Delta x)^6 \qquad \text{---}\,4.4/12$$

d. High Order Upwind/Downwind Operators: These schemes are derived by biasing the Taylor expansion method in one particular direction, depending on the flow characteristics. For example, the 'third order accurate' Quadratic Upstream Interpolation for Convective Kinematics (QUICK) operators given by Leonard (123).

$$U\frac{\partial U}{\partial x} = U_{ij}\left[\frac{U_{ij+1}-U_{ij-1}}{2\Delta x} - \frac{U_{ij+1}-3(U_{ij}-U_{ij-1})-U_{ij-2}}{6\Delta x}\right]$$

$$-\frac{(\Delta x)^3}{12}\frac{\partial^4 U}{\partial x^4} - \cdots\cdots O(\Delta x)^5$$

$$U_{ij} > 0 \qquad \text{---} \; 4.4/13$$

$$U\frac{\partial U}{\partial x} = U_{ij}\left[\frac{U_{ij+1}-U_{ij-1}}{2\Delta x} + \frac{U_{ij+2}-3(U_{ij+1}-U_{ij})-U_{ij-1}}{6\Delta x}\right]$$

$$+\frac{(\Delta x)^3}{12}\frac{\partial^4 U}{\partial x^4} + \cdots\cdots O(\Delta x)^5$$

$$U_{ij} < 0 \qquad \text{---} \; 4.4\,14$$

4.3.3 Pressure Gradient Operators

Owing to the nature of the staggered mesh, a central difference approximation using an effective spacing equal to x/2 may be used to estimate the pressure gradient in the Navier Stokes equations, ie:-

$$\frac{\partial p}{\partial x} = \frac{p_{ij}-p_{ij-1}}{\Delta x} - \frac{(\Delta x)^2}{12}\frac{\partial^3 p}{\partial x^3} + \cdots\cdots O(\Delta x)^4$$

$$\text{---} 4.4/15$$

It is also necessary to specify an approximation to the second derivatives during the solution of the Poisson equation given by 3.3/15. Again, the central difference scheme is perfectly adequate, for example:-

$$\frac{\partial^2 p}{\partial x^2} = \frac{p_{ij+1} + p_{ij+1} - 2p_{ij}}{(\Delta x)^2} + \frac{(\Delta x)^3}{12}\frac{\partial^4 p}{\partial x^4} + \text{------} O(\Delta x)^4$$

--- 4.4/16

4.3.4. Diffusion Operators (∇^2)

The spacial derivatives which constitute the Laplacien operator may be modelled using the third order accurate central difference expression to produce an approximation for the diffusion terms as

$$\nabla^2 U = \frac{U_{ij+1} + U_{ij-1} - 2U_{ij}}{(\Delta x)^2} + \frac{U_{i+1j} + U_{i-1j} - 2U_{ij}}{(\Delta y)^2} + \frac{(\Delta x)^3}{12}\frac{\partial^4 U}{\partial x^4} + \frac{(\Delta y)^3}{12}\frac{\partial^4 V}{\partial y^4} + \text{----} O[(\Delta x)^5 (\Delta y)^5]$$

--- 4.4/17

4.3.5. Other Methods of Formulation

The use of the Taylor exapansion to approximate the derivatives is not the only technique available. In particular, simple control volume analysis (99) is capable of producing finite difference schemes in both convection and diffusion problems. Such an approach has the advantage of ensuring that the finite difference approximations which result, share the conservation properties of the original equations. Another popular technique is the Donor/Acceptor cell methods of Gentry, Martin and Daly (124). Various methods of averaging the flux into and out of a fluid control volume are applied. In many cases, equivalent finite difference schemes result. The technique was used in the free surface height convection algorithms detailed in section 5.1.

5. SOME FINITE DIFFERENCE TIME MARCHING SCHEMES

By combining the operators given in the previous section, various formulations or 'schemes' may be derived for the prediction of the velocity components from one time step to the next. Many of the schemes thus developed are used as recursive relationships for steady flow problems. It is worth reiterating that in dynamic simulations, such schemes are used to guess the actual velocity field at the next time step.

In either case, there are three categories of algorithm produced by these formulations:-

a. Fully Explicit Schemes

b. Explicit/Implicit Schemes

c. Fully Implicit Schemes

5.1. Explicit Schemes

These are perhaps the simplest techniques and in many cases the most effective. Their major feature is that values for velocity components at nodes are updated for the next time-step using information from previous time levels only.

As an example, consider the forward time, centred difference scheme shown below. This is a combination of operators 4.4/6, 4.4/9, 4.4/15 and 4.4/17.

$$\frac{U_{ij}^{n+1} - U_{ij}^{n}}{\Delta t} + U_{ij}^{n}\frac{U_{ij+1}^{n} - U_{ij-1}^{n}}{2\Delta x} + V_{m}^{n}\frac{U_{i+1j}^{n} - U_{i-1j}^{n}}{2\Delta y} =$$

$$-\frac{P_{ij}^{n} - P_{ij-1}^{n}}{\Delta x} + \frac{1}{R_e}\frac{U_{ij+1} + U_{ij-1} - 2U_{ij}}{(\Delta x)^2} + \frac{1}{R_e}\frac{U_{i+1j} + U_{i-1j} - 2U_{ij}}{(\Delta y)^2}$$

--- 4.5/1

$$\frac{V_{ij}^{n} - V_{ij}^{n}}{\Delta t} + V_{ij}^{n}\frac{V_{i+1j}^{n} - V_{i-1j}^{n}}{2\Delta y} + U_{m}^{n}\frac{V_{ij+1}^{n} - V_{ij-1}^{n}}{2\Delta x} =$$

$$-\frac{P_{ij}^{n} - P_{i-1j}^{n}}{\Delta y} + \frac{1}{R_e}\frac{V_{ij+1}^{n} + V_{ij-1}^{n} - 2V_{ij}^{n}}{(\Delta x)^2} + \frac{1}{R_e}\frac{V_{i+1j}^{n} + V_{i-1j}^{n} - 2V_{ij}^{n}}{(\Delta y)^2}$$

$$+ \frac{Y_g}{F_r^2}$$

--- 4.5/2

where, considering the staggered T3 grid shown in figure (4-7):-

$$U_{m}^{n} = [\, U_{i-1j}^{n} + U_{i-1j-1}^{n} + U_{ij+1}^{n} + U_{ij}^{n} \,] / 4$$

$$V_{m}^{n} = [\, V_{ij}^{n} + V_{i+1j}^{n} + V_{i+1j-1}^{n} + V_{ij-1}^{n} \,] / 4$$

A recursive or time marching relationship for U_{ij} , V_{ij} may thus be written down as:-

$$U_{ij}^{n+1} = U_{ij}^{n} - \frac{U_{ij}^{n}\Delta t}{2\Delta x}(U_{ij+1}^{n} - U_{ij-1}^{n}) - \frac{V_{m}^{n}\Delta t}{2\Delta y}(U_{i+1j}^{n} - U_{i-1j}^{n})$$

$$- \frac{\Delta t}{\Delta x}(P_{ij} - P_{ij-1}) + \frac{\Delta t}{(\Delta x)^2 R_e}(U_{ij+1} + U_{ij-1} - 2U_{ij})$$

$$+ \frac{\Delta t}{(\Delta y)^2 R_e}(U_{i+1j} + U_{i-1j} - 2U_{ij})$$

--- 4.5/3

$$V_{ij}^{n+1} = V_{ij}^{n} - \frac{V_{ij}^{n}\Delta t}{2\Delta y}(V_{i+1j}^{n} - V_{i-1j}^{n}) - \frac{U_{m}^{n}\Delta t}{2\Delta x}(V_{ij+1}^{n} - V_{ij-1}^{n})$$

$$- \frac{\Delta t}{\Delta y}(P_{ij} - P_{ij-1}) + \frac{\Delta t}{(\Delta x)^2 R_e}(V_{ij+1}^{n} + V_{ij-1}^{n} - 2V_{ij}^{n})$$

$$+ \frac{\Delta t}{(\Delta y)^2 R_e}(V_{i+1j}^{n} + V_{i-1j}^{n} - 2V_{ij}^{n}) - \frac{Y_g}{F_r^2}$$

--- 4.5/4

Equations 4.5/3 and 4.5/4 are termed explicit since all the terms on the right hand side are from the same time level. In fact these equations represent a simple 'linear acceleration' iterative techniqDe when used to produce a steady state solution. Given limits on the values of Δt, Δx and Δy dictated by numerical stability (section 4.6) and other criteria relating to the flow Reynolds number (section 4.6), the above relationships are suitable for both steady state and dynamic simulation problems. Most alternative formulations consider changes to the time differencing and convection terms only. In particular, the approximations 4.4/10-11 and 4.4/13-14 are of interest in their ability to suppress 'wiggles' or 'non-linear instability' phenomenon (section 4.6), when used to replace the centred difference convection terms.

One technique which proved useful in aspects of the dynamic problems encountered herein was the replacement of the forward time difference by the centred scheme given by equation 4.4/8. As an example, equation 4.5/1 is re-arranged to give:-

$$\frac{U_{ij}^{n} - U_{ij}^{n}}{2\Delta t} = U_{ij}^{n}\frac{U_{ij+1}^{n} - U_{ij-1}^{n}}{2\Delta x} + V_{m}^{n}\frac{U_{i+1j}^{n} - U_{i-1j}^{n}}{2\Delta y} - \frac{P_{ij}^{n} - P_{ij-1}^{n}}{\Delta x} + \frac{1}{R_e}\frac{U_{ij+1}^{n} + U_{ij-1}^{n} - 2U_{ij}^{n}}{(\Delta x)^2} + \frac{1}{R_e}\frac{U_{i+1j}^{n} + U_{i-1j}^{n} - 2U_{ij}^{n}}{(\Delta y)^2} \quad \text{---} \; 4.5/5$$

The above method illustrates a 'leapfrog' scheme which can be shown to have good stability charateristics for inviscid flow problems (120). Introduction of the diffusion terms at the time level (n) produces a weak instability into the problem (99). However, this can be 'cured' by use of the (n-1) time level for the diffusion terms.

The method given is still fully explicit and has the advantage of truncation errors for all derivatives of order (Δt) , (Δx) ,(Δy) .

5.2. Implicit/Explicit Schemes

This type of scheme attempts to improve accuracy and convergence rate by introducing data from the (n+1) time step into the right hand side of equations 4.5/3 and 4.5/4. However, regard for the form of the computational routine is required. With reference to figure (4-7), it can be seen that the process of evaluation the updated components U_{ij}^{n+1} ,V_{ij}^{n+1} via nested DO loops in fortran coding, is equivalent to 'sweeping' through the mesh points one by one. For any given node, denoted N(ij), calculations will already have been performed on nodes N(i-1,j) and N(ij-1). Thus data from the (n+1) time step effectively exists for these points. This may be incorporated in the equations cited above, to produce quasi-implicit or implicit/explicit forms as shown below.

$$U_{ij}^{n+1} = U_{ij}^{n} - \frac{U_{ij}^{n}\Delta t}{2\Delta x}\left(U_{ij+1}^{n} - U_{ij-1}^{n+1}\right) - \frac{V_{m}^{n}\Delta t}{2\Delta y}\left(U_{i+1j}^{n} - U_{i-1j}^{n+1}\right)$$
$$- \frac{\Delta t}{\Delta x}\left(P_{ij}^{n} - P_{ij-1}^{n}\right) - \frac{\Delta t}{(\Delta x)^2 R_e}\left(U_{ij+1}^{n} + U_{ij-1}^{n+1} - 2U_{ij}^{n}\right)$$
$$- \frac{\Delta t}{(\Delta y)^2 R_e}\left(U_{i+1j}^{n} + U_{i-1j}^{n+1} - 2U_{ij}^{n}\right)$$

---4.5/6

$$V_{ij}^{n+1} = V_{ij}^{n} - \frac{V_{ij}^{n}\Delta t}{2\Delta y}\left(V_{i+1j}^{n} - V_{i-1j}^{n+1}\right) - \frac{U_{m}^{n}\Delta t}{2\Delta x}\left(V_{ij+1}^{n} - V_{ij-1}^{n+1}\right)$$
$$- \frac{\Delta t}{\Delta y}\left(P_{ij}^{n} - P_{i-1j}^{n}\right) - \frac{\Delta t}{(\Delta x)^2 R_e}\left(V_{ij+1}^{n} + V_{ij-1}^{n+1} - 2V_{ij}^{n}\right)$$
$$- \frac{\Delta t}{(\Delta y)^2 R_e}\left(V_{i+1j}^{n} + V_{i-1j}^{n+1} - 2V_{ij}^{n}\right)$$

---4.5/7

This concept may also be applied to the convection terms of the 'leapfrog' scheme of equation 4.5/5. A special application to the diffusion terms leads to the well-known Dufort-Frankel method (120). The centre node, Nij, value is replaced by its average at times (n+1)Δt and (n-1)Δt thus, (re-arranging equation 4.5/5).

$$U_{ij}^{n+1} = U_{ij}^{n-1} - \frac{U_{ij}^{n}\Delta t}{\Delta x}(U_{ij+1}^{n} - U_{ij-1}^{n+1}) - \frac{V_m^{n}\Delta t}{\Delta y}(U_{i+1j}^{n} - U_{i-1j}^{n+1})$$

$$- \frac{2\Delta t}{\Delta x}(P_{ij}^{n} - P_{ij-1}^{n}) + \frac{2\Delta t}{(\Delta x)^2 R_e}(U_{ij+1}^{n} \; U_{ij-1}^{n+1} - U_{ij}^{n+1} - U_{ij}^{n-1})$$

$$+ \frac{2\Delta t}{(\Delta y)^2 R_e}(U_{i+1j}^{n} + U_{i-1j}^{n+1} - U_{ij}^{n+1} - U_{ij}^{n-1})$$

--- 4.5/8

which on further re-arrangement yields:-

$$U_{ij}^{n+1} = [U_{ij}^{n-1} - \frac{U_{ij}^{n}\Delta t}{\Delta x}(U_{ij+1}^{n} \; U_{ij-1}^{n+1}) - \frac{V_m\Delta t}{\Delta y}(U_{i+1j}^{n} \; U_{i-1j}^{n+1})$$

$$- \frac{2\Delta t}{\Delta x}(P_{ij}^{n} - P_{ij-1}^{n}) - \frac{2\Delta t}{(\Delta x)^2 R_e}(U_{ij+1}^{n} \; U_{ij-1}^{n+1} \; U_{ij}^{n-1})$$

$$- \frac{2\Delta t}{(\Delta y)^2 R_e}(U_{i+1j}^{n} \; U_{i-1j}^{n+1} \; U_{ij}^{n-1})] \Big/ [1 \; \frac{2\Delta t}{R_e}(\frac{1}{(\Delta x)^2} + \frac{1}{(\Delta y)^2})]$$

--- 4.5/9

Such a scheme promises a greater level of numerical accuracy as reviewed in section 4.6. However, these methods have been developed for steady flow simulation problems in which a 'solving' process is undertaken. It is necessary to be careful when using such methods for the purpose of dynamic simulations, especially when defining quantities such as 'convergence rate' and 'stability' criteria.

5.3. Fully Implicit Methods

As with the explicit/implicit methods, improvements in accuracy and stability are sought by introducing data from the (n+1)

time step into the right hand side of equations 4.5/3 and 4.5/4. The particular methods worth attention in this case are the Alternating Direction Implicit techniques of Peaceman and Rachford (125). These were originally developed for the stream function vorticity formulation and therefore, apply mainly to problems in pure convection and diffusion. A particular scheme was therefore separately deduced for the Navier Stokes equations in their primitive variable form. The pressure gradient terms were regarded separately in the time marching process and the u and v coefficients in the convection terms were treated as 'constants' by setting them to their values at the n. t time level.

The derivation will be briefly stated below since, unlike the previous schemes, it is non-trivial. Consider the form of the Navier Stokes equations as:-

$$\frac{\partial u}{\partial x} = L_u u - p_x \qquad \text{---} 4.5/10$$

$$\frac{\partial v}{\partial x} \qquad L_v u - p_y \qquad \text{---} 4.5/11$$

where

$$L_u = \left(-u\frac{\partial}{\partial x} - v\frac{\partial}{\partial y} + \frac{1}{R_e}\nabla^2\right) = -u\delta_x - v\delta_y + \frac{1}{R_e}\left(\delta_x^2 + \delta_y^2\right) \qquad \text{---} 4.5/12$$

$$L_v = \left(-v\frac{\partial}{\partial y} - u\frac{\partial}{\partial x} + \frac{1}{R_e}\nabla^2\right) = -v\delta_y - u\delta_x + \frac{1}{R_e}\left(\delta_x^2 + \delta_y^2\right) \qquad \text{---} 4.5/13$$

Following the practice of Mitchell and Griffiths (120), equation 4.5/10 may be re-written in explicit form (dropping pressure gradient terms):-

$$u^{n+1} = \exp\left(\Delta t . L_u\right) u^n$$

The implicit form of this is given by:-

$$\exp\left(-\frac{1}{2}\Delta t\, L_u\right) u^n = \exp\left(\frac{1}{2}\Delta t\, L_u\right) u^n$$

--- 4.5/14

replacing L_u by 4.5/12 and re-arranging yields;

$$\exp\left(\frac{U\Delta t}{2}\delta_x - \frac{\Delta t}{2R_e}\delta_x^2\right) \exp\left(\frac{V\Delta t}{2}\delta_y - \frac{\Delta t}{2R_e}\delta_y^2\right) u^{n+1} =$$

$$\exp\left(-\frac{U\Delta t}{2}\delta_x + \frac{\Delta t}{2R_e}\delta_x^2\right) \exp\left(-\frac{V\Delta t}{2}\delta_y + \frac{\Delta t}{2R_e}\delta_y^2\right) u^n$$

---4.5/15

δx, δy are general finite difference operators for first derivatives in x and y respectively. δ_x^2 , δ_y^2 are general finite difference operators for second derivatives in x and y respectively.

Expanding the exponential terms in a power series, and by taking the first two terms only gives:-

$$\left(1 + \frac{U\Delta t}{2\Delta x}\delta_x - \frac{\Delta t}{2(\Delta x)^2 R_e}\delta_x^2\right)\left(1 + \frac{V\Delta t}{2\Delta y}\delta_y - \frac{\Delta t}{2(\Delta y)^2 R_e}\delta_y^2\right) u^{n+1} =$$

$$\left(1 - \frac{U\Delta t}{2\Delta x}\delta_x + \frac{\Delta t}{2(\Delta x)^2 R_e}\delta_x^2\right)\left(1 - \frac{V\Delta t}{2\Delta y}\delta_y + \frac{\Delta t}{2(\Delta y)^2 R_e}\delta_y^2\right) u^n$$

--- 4.5/16

The above relationship is then 'time-split' in order to produce a method of solution, ie:-

$$\left(1 + \frac{U\,\Delta t}{2\,\Delta x}\delta_x - \frac{\Delta t}{2(\Delta x)^2 R_e}\delta_x^2\right)U^{n+1/2} = \left(1 - \frac{V\,\Delta t}{2\,\Delta y}\delta_y + \frac{\Delta t}{2(\Delta y)^2 R_e}\delta_y^2\right)U^{n}$$

$$\left(1 + \frac{V\,\Delta t}{2\Delta y}\delta_y - \frac{\Delta t}{2(\Delta y)^2 R_e}\delta_y^2\right)U^{n+1} = \left(1 - \frac{U\,\Delta t}{2(\Delta x}\delta_x + \frac{\Delta t}{2(\Delta x)^2 R_e}\delta_x^2\right)U^{n+1/2}$$

--- 4.5/17

The equations 4.5/17 represent two systems of simultaneous equations to which matrix solution techniques need to be applied. When written in vector form for one node, using central difference approximations for both first and second derivatives, the equations take the following form:-

$$\left[\frac{\Delta t}{2\Delta x}\left(U_{ij}^n - \frac{1}{\Delta x R_e}\right), \left(1 + \frac{\Delta t}{(\Delta x)^2 R_e}\right), \frac{-\Delta t}{2\Delta x}\left(U_{ij}^n + \frac{1}{\Delta x R_e}\right)\right] \begin{bmatrix} U_{ij+1} \\ U_{ij} \\ U_{ij-1} \end{bmatrix} =$$

$$\left[\frac{-\Delta t}{2\Delta y}\left(V_{ij}^n + \frac{1}{\Delta y R_e}\right), \left(1 - \frac{\Delta t}{(\Delta y)^2 R_e}\right), \frac{\Delta t}{2\Delta y}\left(V_{ij}^n - \frac{1}{\Delta y R_e}\right)\right] \begin{bmatrix} U_{i+1j} \\ U_{ij} \\ U_{i-1j} \end{bmatrix}$$

--- 4.5/18

$$\left[\frac{\Delta t}{2\Delta y}\left(V_m^n - \frac{1}{\Delta y R_e}\right), \left(1 + \frac{\Delta t}{(\Delta y)^2 R_e}\right), \frac{-\Delta t}{2\Delta y}\left(V_m^n + \frac{1}{\Delta y R_e}\right)\right] \begin{bmatrix} U_{i+1j} \\ U_{ij} \\ U_{i-1j} \end{bmatrix} =$$

$$\left[\frac{-\Delta t}{2\Delta x}\left(U_{ij}^n + \frac{1}{\Delta x R_e}\right), \left(1 - \frac{\Delta t}{(\Delta x)^2 R_e}\right), \frac{\Delta t}{2\Delta x}\left(U_{ij}^n - \frac{1}{\Delta x R_e}\right)\right] \begin{bmatrix} U_{ij+1} \\ U_{ij} \\ U_{ij-1} \end{bmatrix}$$

--- 4.5/19

Equations 4.5/18 and 4.5/19 may be used in a matrix assembly routine, not dissimilar from those common to the finite element method, to yield the tri-diagonal matrix systems:-

$$[P_u][U]^{n+1/2} = [Q_v][U]^n - [p_x]^n$$

$$[P_v][U]^{n+1} = [Q_u][U]^{n+1/2}$$

whose solutions may be stated as:

$$[U]^{n+1/2} = [P_u]^{-1}[Q_v][U]^n - [P_u]^{-1}[p_x]^n$$

$$[U]^{n+1} = [P_v]^{-1}[Q_u][U]^{n+1/2}$$

It is obvious that P_u and P_v are tri-diagonal matrices whose inversion may be carried out fairly simply on a computer. The advantage of such a formulation is that it can be shown to be unconditionally stable, (Section 4.6). The disadvantages are the large amounts of computer storage required, as compared with the explicit methods.

The choice of which of the three general approaches was most suitable depended to a great extent upon the computing facilities available. Numerical experiments, to be detailed later, were undertaken, to ascertain how important aspects of stability and accuracy in the time marching process were, in comparison with the more physical constraints of mass conservation. In the next section, theoretical aspects of stability and convergence will be examined for the schemes discussed.

6. NUMERICAL STABILITY

The rigorous study of the numerical stability of the Navier Stokes equations is restricted to very simple examinations of the linearised one dimensional, Burger's equation:-

$$\frac{\partial u}{\partial t} + c_x \frac{\partial u}{\partial x} = \nu \frac{\partial^2 u}{\partial x^2} \qquad \text{---} 4.6/1$$

where c_x is a constant phase speed.

In particular, the examination of the numerical schemes given in the previous section is required. Many texts on computational fluid dynamics provide methods of simple analysis (99,120). The Von-Neuman stability analysis and the heuristric stability analysis of Hirt (126) are used herein. The latter technique allows a less meticulous examination of particular problems of instability in the full Navier Stokes equations.

6.1. Von-Neuman Analysis

This technique analyses particular finite difference schemes by applying a Fourrier analysis to the discretised equations. Thus for the explicit forward time, centred difference scheme for equation 4.6/1, given by:-

$$\frac{u_j^{n+1} - u_j^n}{(\Delta x)} + c_x \frac{u_{j+1}^n - u_{j-1}^n}{(\Delta x)} = \nu \frac{u_{j+1}^n \quad u_{j-1}^n - 2u_j^n}{(\Delta x)^2} \qquad \text{---} 4.6/2$$

the terms u_j^n are replaced by:-

$$u_j^n = A^n e^{iK(j\Delta x)} = A^n e^{i(j\theta)} \qquad \text{---} 4.6/3$$

where k is a wave number component, $i = \sqrt{-1}$, $\theta = K\Delta x$.

Substitution of equation 4.6/3 into 4.6/2 yields:

$$(A^{n+1} - A^n)e^{i(j\theta)} \quad \frac{C_x \Delta t}{2\Delta x} A^n (e^{i(j+1)\theta} - e^{i(j-1)\theta}) =$$

$$A^n \frac{\nu \Delta t}{(\Delta x)^2} (e^{i(j+1)\theta} + e^{i(j+1)\theta} - 2e^{i(j\theta)})$$

---4.6/4

cancelling common terms in $e^{i(j\theta)}$ leads to an amplification factor G given by:-

$$G = \frac{A^{n+1}}{A^n} = \left(1 - \frac{i C_x \Delta t}{\Delta x} \text{SIN}\,\theta - \frac{2\nu\Delta t}{(\Delta x)^2}(1 - \text{COS}\,\theta)\right)$$

---4.6/5

The stability requirement is that the modulus of the amplification factor is less than unity, which in the above case results in the need for the ellipse given by equation 4.6/5 to be bounded by the unit circle in the complex plane (see figure 4-8). Two restrictions result from this analysis:-

a. The Courant-Friedrichs-Lewy criterion (127):

$$\frac{C_x \Delta}{\Delta x} \leq 1$$

---4.6/6

which for the non-linear case restricts the local flow speed.

b. The diffusion criterion:

$$\Delta t \leq \frac{(\Delta x)^2}{\nu}$$

---4.6/7

which for (ideally modelled) low viscosity flows, such as

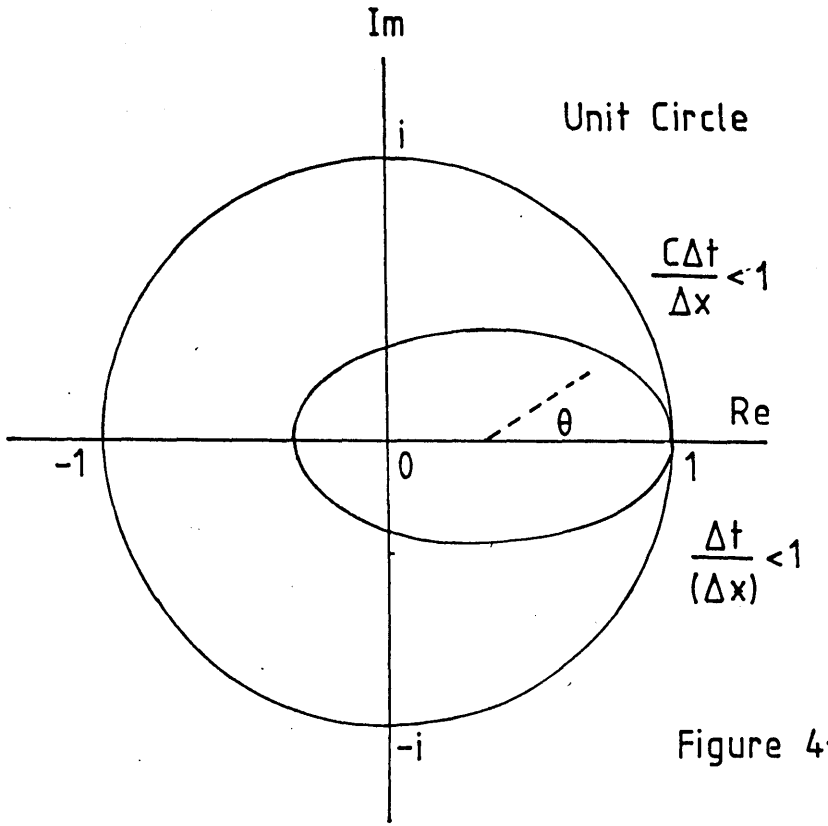

Stable
Schemes

Figure 4-8

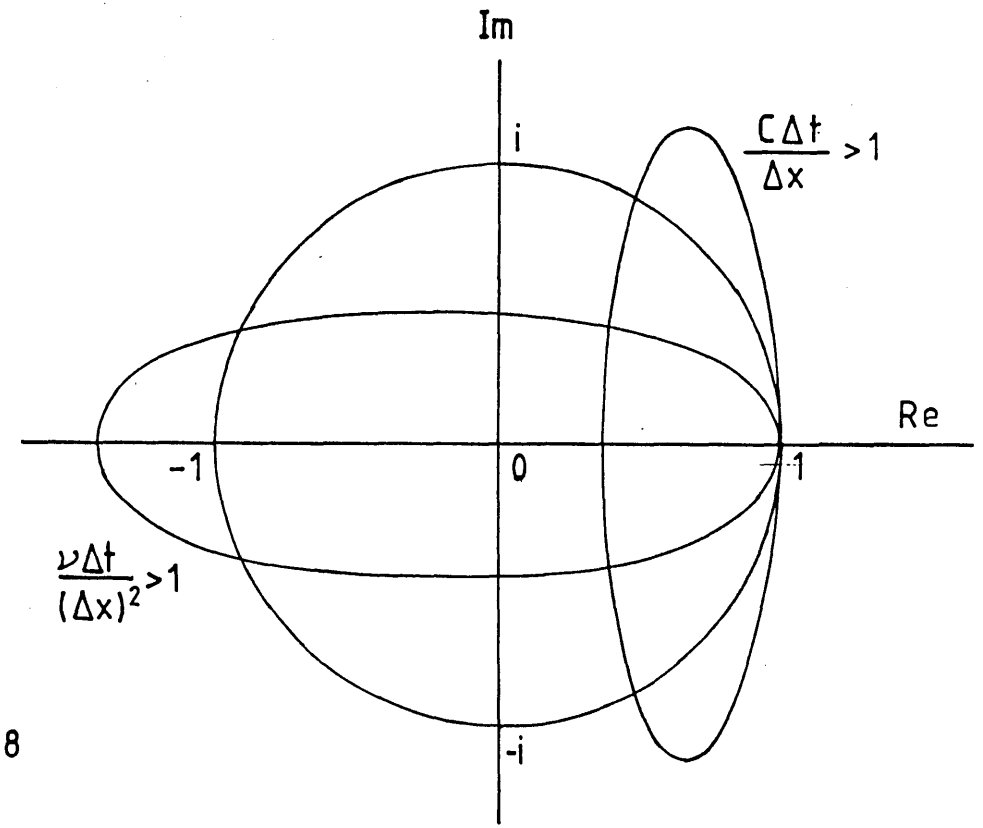

Unstable
Schemes

those found in hydrodynamics, may virtually be ignored.

This type of analysis is common practice in computational fluid dynamics. However, in many cases of the modelling of real flows, such considerations are inadequate. For the fully non-linear convection terms, the amplification factor is found to be dependent upon the local solution. In such cases, stability criteria are best determined by numerical experiment.

Much can be learned from the linear approach, however, since it is obvious that 4.6/6 may still be relevant in a local sense. The main complications arise from applying the Von-Neuman analysis to two-dimensional flow problems.

Application of Von-Neuman's analysis to the centred time difference schemes leads to an amplification factor which varies with time. The expression for this new factor is:-

$$G^{n+1} = \frac{1}{G^n} - \frac{2i\Delta t}{\Delta x}\,\mathrm{SIN}\,\theta - \frac{4\nu\Delta t}{(\Delta x)^2}(1-\mathrm{COS}\,\theta) \qquad \text{---} \; 4.6/8$$

which is similar is form to 4.6/5. As long as the amplification factor at the previous time step is less than unity, the stability of this technique is ensured, given the usual C.F.L and diffusion criteria. However, the accuracy is improved due to the smaller truncation error for the time marching scheme.

The Von-Neuman method has been shown to produce some useful results for simple discretisations of the model equation given by 4.6/1. For analysis of formulations with mixed time levels (ie implicit/explicit methods), the algebra becomes difficult. A less

mathematically rigorous, but equally useful method was shown by Hirt (126) to be applicable to more general systems of equations.

6.2. Hirt's Analysis

In this technique, the source of instability is defined as being the result of the truncation errors from the temporal finite difference operators. If each term in equation 4.6/2 is expanded in a Taylor series, the original partial differential equation may be recovered by truncating the series expansions at a common order of derivative giving:-

$$\frac{\partial U}{\partial t} + \frac{\Delta t}{2}\frac{\partial^2 U}{\partial t^2} = -C_x\frac{\partial U}{\partial x} + \nu\frac{\partial^2 U}{\partial x^2} \qquad \text{---4.6/9}$$

It will be noted that, owing to the use of the forward time step operator, an extra second order time derivative has appeared, converting the previously parabolic Burger's equation to an hyperbolic form. This interpretation does indeed hold good for the behaviour of this particular discretisation. In fact, application of the method of characteristics for hyperbolic equations yields the two stability criteria 4.6/6 and 4.6/7. Further manipulation reveals more interesting results. By differentiating the original model equation 4.6/1 with respect to time and replacing the $\partial^2 u/\partial t^2$ term with the resulting expansion yields:-

$$\frac{\partial U}{\partial t} = -C_x\frac{\partial U}{\partial x} + \left(\nu - \frac{C_x^2\Delta t}{2}\right)\frac{\partial^2 U}{\partial x^2} + C_x\nu\Delta t\frac{\partial^3 U}{\partial x^3} - \frac{\nu^2\Delta t}{2}\frac{\partial^4 U}{\partial x^4} \qquad \text{---4.6/10}$$

Ignoring third order terms and above, it can be seen that this interpretation has introduced an 'effective viscosity' of:-

$$\nu_e = \nu - \frac{c_x^2 \Delta t}{2}$$

---4.6/11

Thus the difusion stability criterion 4.6/7 now becomes more important. In particular, if ν_e is negative, the numerical method will be unstable. This provides a heavy stability penalty on schemes using central differencing for convection terms and forward time marching. Further, it explains the enhanced success of the leapfrog schemes, whose leading time marching truncation error is of the order $\partial^3/\partial t^3$, and therefore, does not reduce to equation 4.6/8 when Hirt's analysis is applied.

One great advantage of Hirt's analysis is the property that it may be applied to the full Navier Stokes equations. Upon examination of the discretised form of the two dimensional Navier Stokes equations used in the M.A.C method (113), Hirt showed that the effective viscosity ν_e for this forward time step, centred difference scheme, modified the difference equations such that they represented:-

$$\frac{\partial u}{\partial t} + u\frac{\partial u}{\partial x} + v\frac{\partial u}{\partial y} = -\frac{\partial p}{\partial x} + \left(\nu - \frac{\Delta t}{2}u^2 - \frac{\Delta x^2}{2}\frac{\partial u}{\partial x}\right)\frac{\partial^2 u}{\partial x^2} + \left(\nu - \frac{\Delta t}{2}v^2 - \frac{\Delta y^2}{4}\frac{\partial v}{\partial y}\right)\frac{\partial^2 u}{\partial y^2}$$

---4.6/12

$$\frac{\partial v}{\partial t} + v\frac{\partial v}{\partial y} + u\frac{\partial v}{\partial x} = -\frac{\partial p}{\partial y} + \left(\nu - \frac{\Delta t}{2}u^2 - \frac{\Delta x^2}{4}\frac{\partial u}{\partial x}\right)\frac{\partial^2 v}{\partial x^2} + \left(\nu - \frac{\Delta t}{2}v^2 - \frac{\Delta y^2}{2}\frac{\partial v}{\partial y}\right)\frac{\partial^2 v}{\partial y^2}$$

---4.6/13

Thus retaining a positive, effective viscosity can be seen to be very difficult for these schemes.

6.3. 'Wiggles'

The well reported phenomenon of 'wiggles' or 'non-linear instability' of centrally differentiated convection schemes (99), may well have its roots in the above analysis. However, Leonard (128) suggested that the source of this form of instability lies in the inconsistent order if accuracy applied when using central difference approximations for both convection and diffusion terms. Further, Leonard maintains that "central differencing (of any order) has no inherent numerical stability when applied to derivatives of odd order."

The usual time 'cure' for such problems has often been to use the 'upwind' differencing formulas given by 4.4/10 and 4.4/11. Examination of the truncation errors shows that one effective diffusion coefficient:-

$$\nu_e = \frac{U \Delta x}{2} \qquad \text{---} \; 4.6/14$$

results from this approach. Stability is therefore achieved at the expense of lowering the effective Reynolds number. Examination of the cell Reynolds number,

$$R_{ec} = \frac{U \Delta x}{\nu_e} \qquad \text{---} \; 4.6/15$$

shows that for a fully upwinded scheme, R_{ec} is fixed at a value of 2. In practical engineering flows, R_{ec} needs to be of the order 100 - 1000. Therefore, upwinding must be considered a very suspect method of producing numerical stability.

6.4. Stability of Implicit/Explicit Schemes

Of the implicit/explicit schemes generally applied in computational fluid dynamics, most have been used for modelling compressible flow. In many cases, the discretised equations are time-split or are subject to changes in sweep direction. One particularly useful and well tried technique is the MacCormack scheme (129) which unfortunately is not susceptable to analytical study of its stability criteria. However, numerical studies have defined a bound for the time step which is given by:-

$$\Delta t \leqslant \frac{(\Delta x)^2}{C_x \Delta x + 2\nu} \qquad \text{---4.6/16}$$

when the method is applied to Burger's equation.

The algorithms used in this thesis are exclusively one step schemes for which analytical study of stability criteria are somewhat simpler. Again, however, a full analysis of the amplification factors for the two dimensional Navier Stokes equations is out of the question. However, Peyret and Viviand (130) have gone some of the way by analysis of the following, Gauss-Siedel inspired, scheme for Burger's equation.

$$\frac{U_j^{n+1} - U_j^n}{\Delta t} = \frac{-C_x}{2\Delta x}\left(U_{j+1}^n - U_{j-1}^{n+1}\right) + \frac{\nu}{(\Delta x)^2}\left(U_{j+1}^n + U_{j-1}^{n+1} - 2U_j^n\right) \qquad \text{---4.6/17}$$

which can be seen to be similar in formulation to the implicit/explicit, on step, method for the Navier Stokes equations given by 4.5/6 and 4.5/7.

The resulting time step restriction given in reference (130), may be stated as:-

$$\Delta t \leq \frac{2(\Delta x)^2}{C_x \Delta x + 2\nu}$$

---4.6/18

Numerical experiment is required in order to test the claimed greater speed of convergence for these explicit/implicit schemes. It should also be noted that the slamming or water entry problem demands a dynamic simulation for which the definition of convergence used in the above anlyses may be misleading

6.5. Stability of Fully Implicit Schemes

Formulations of the type given by equation 4.5/16 are difficult to analyse by Von-Neuman's method, though some general conclusions may be drawn. Again, following the method given by Mitchell and Griffiths (120), equation 4.5/16 may be re-written for the error in U_{ij} or V_{ij} as follows:-

$$\left(1 + \frac{U\Delta t}{2\Delta x}\delta_x - \frac{\Delta t}{2(\Delta x)^2 R_e}\delta_x^2\right)\left(1 + \frac{V\Delta t}{2\Delta y}\delta_y - \frac{\Delta t}{2(\Delta y)^2 R_e}\delta_y^2\right) Z_{ij}^{n+1}$$

$$\left(1 - \frac{U\Delta t}{2\Delta x}\delta_x + \frac{\Delta t}{2(\Delta x)^2 R_e}\delta_x^2\right)\left(1 + \frac{V\Delta t}{2\Delta y}\delta_y - \frac{\Delta t}{2(\Delta y)^2 R_e}\delta_y^2\right) Z_{ij}^{n}$$

---4.6/19

where $$Z_{ij}^{n+1} = U_{ij}^{n+1} - U_{ij}^{n}$$

A similar expression may be written for the error in .

By Von-Neuman's analysis:-

$$Z_{ij}^{n} \quad Z_0 e^{in\theta} e^{im\phi}$$

---4.6/20

substitution of 4.6/20 into 4.6/19 allows the formulation of an expression for the amplification factor Z_a which must satisfy:-

$$|Z_a| < 1 \qquad \text{---4.6/21}$$

thus 4.6/18 leads to:-

$$Z_a = \frac{\left(1 - \frac{U\Delta t}{2\Delta x}\text{SIN}\theta + \frac{\Delta t}{2(\Delta x)^2 R_e}\text{SIN}^2(\theta/2)\right)\left(1 - \frac{V\Delta t}{2\Delta y}\text{SIN}\phi + \frac{\Delta t}{2(\Delta y)^2 R_e}\text{SIN}^2(\phi/2)\right)}{\left(1 + \frac{U\Delta t}{2\Delta x}\text{SIN}\theta + \frac{\Delta t}{2(\Delta x)^2 R_e}\text{SIN}^2(\theta/2)\right)\left(1 + \frac{V\Delta t}{2\Delta y}\text{SIN}\phi + \frac{\Delta t}{2(\Delta y)^2 R_e}\text{SIN}^2(\phi/2)\right)}$$

---4.6/22

where $\theta = n\Delta x$

$\phi = m\Delta y$

It can be shown that the above expression does satisfy 4.6/21, though the algebra is very complex and similar analyses may be found elsewhere (99,120). Furthermore, it is often more profitable to examine the eigenvalues of the influence matrices given in 4.5/20. This may be easily carried out by the use of standard computer software libraries, such as NAG routines. In either case, the fully implicit scheme was found to exhibit a high level of numerical stability and thus was considered suitable for further investigation.

6.6. Conclusions on Numerical Stability

It has been seen that an analytical study of the numerical stability of the Navier Stokes equations is, at the very least difficult and, in most cases, impossible to perform satisfactorily. The one dimensional convection/diffusion model equation, (Burger's relationship) has proved useful in defining the minimum criteria, given by equations 4.6/6 and 4.6/7, for the explicit and explicit/implicit algorithms.

When attempting to solve problems in real flow situations, further difficulties may be encountered for a number of reasons. The choice of the value of C_x in equation 4.6/6 becomes critical. It may be replaced by the magnitude of the resultant flow velocity locally, or by the largest resultant flow velocity on a global scale, in order to ensure that the C.F.L condition is satisfied everywhere. The value of C_x may be set by other physical constraints, in particular, it will be seen in section 4.9 how the need to pursue the analogy between the dynamic pressure equation and the wave equation may not only fix the value of C_x, but also define the time step for the computational algorithm.

Boundary conditions also have a great influence on stability and convergence. Firstly, the method used to apply the boundary conditions will alter the form of the discretised conservation equations locally. It may prove necessary to check that these approximations do not upset any stability criteria used in the simulation, as local instabilities will certainly lead to a global failure of the algorithm. Secondly, time step criteria may be set by the need to accurately predict the shape of moving boundaries. One good example of this is the kinematic condition applied to the free surface. Even an unconditionally stable time marching scheme for the overall solution process will ultimately be bound by time step criteria set for the solution of the free-surface kinematic condition or tracking method.

It is also important to examine whether the size of the time step has any effect on the accuracy of the solution, even if all stability criteria are met and the computer simulation seems to run smoothly. One consequence of Hirt's analysis and the resulting form of

the Navier Stokes equations, is that the effective Reynolds number may be time step dependent. Thus even when it seems that a particular computer program for the solution of the Navier Stokes equations is performing satisfactorily, numerical experiments involving the major modelling parameters of mesh size and time step must be undertaken.

7. DISCRETISATION OF BOUNDARY CONDITIONS

7.1. Conditions on Flow Velocity

With regard to figure (4-9), solid walls and bottom boundaries are set to coincide with the finite difference mesh as shown. This allows the normal velocity component, whether it be u or v, to be set equal to zero without complication.

The zero-slip boundary condition is required when evaluating the viscous terms and possibly convection terms (if central differencing is applied), at nodes at one half mesh spacings away from the boundary. To this end, an imaginary or 'dummy' node is positioned one half mesh spacing outside the domain, and given a value such that zero tangential velocity is implied at the boundary. For example, the diffusion term for the u node positioned as shown in figure (4-9), is given by setting $U_d = -U_{1,j}$ such that:-

$$\left.\frac{\partial^2 U}{\partial y^2}\right|_{1j} \approx \frac{U_{2j} + U_d - 2U_{1j}}{(\Delta y)^2} = \frac{U_{2j} - 3U_{1j}}{(\Delta y)^2} \qquad \text{---} \; 4.7/1$$

Higher order approximations are possible. The formula given by 4.7/1 assumes a linear distribution of tangential velocity component between the first fluid node inside the domain and the boundary. Polynomial curve fits may be made using more information from nodes within the flow and the value of velocity at the 'dummy' node found by extrapolation. The result of such a process can usually be manipulated to form simple expressions similar in form to 4.7/1. For example, a quadratic vertical distribution of u in figure (4-10) given by:-

$$u(y) = a_0 + a_1 y + a_2 y^2 \qquad \text{---} \; 4.7/2$$

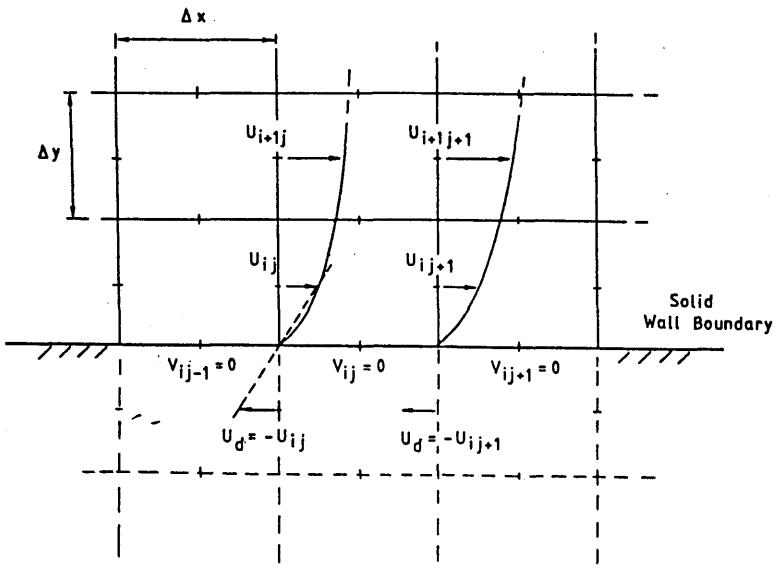

Figure 4-9 Use Of "Dummy Nodes" To Apply Zero-Slip Boundary Conditions.

Figure 4-10 Use Of Dummy Nodes To Apply Zero-Slip Boundary Conditions (Parabolic Extrapolation)

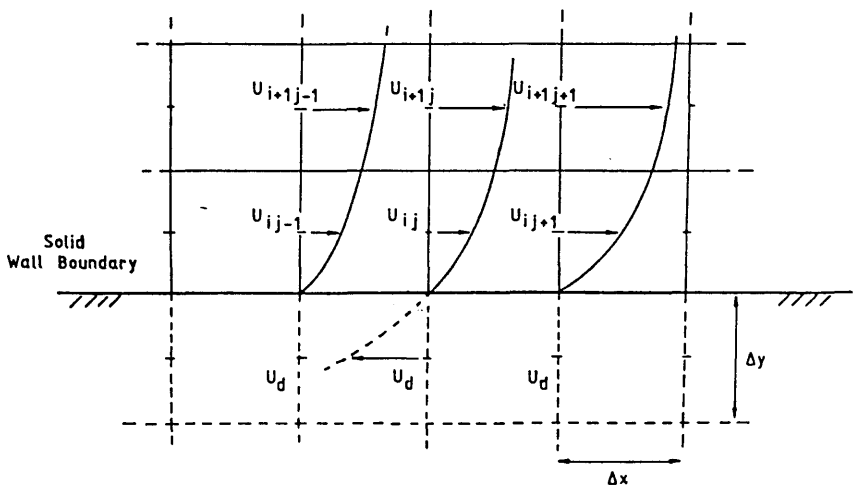

Equation 4.7/3 $U_d=-2.U_{ij}+U_{i+1j}/3$

may be used. If a_0, a_1, a_2 are evaluated by applying zero velocity at the boundary and by using data from the first two fluid nodes, N(1,J) and N(2,J), it can be shown that,

$$U_d = -2U_{1j} + U_{2j}/3 \qquad \text{---4.7/3}$$

leading to a formula for $\partial^2 u/\partial^2 y$ as:-

$$\frac{\partial^2 U}{\partial y^2} \approx \frac{4(U_{2j} - 3U_{1j})}{3(\Delta y)^2} \qquad \text{---4.7/4}$$

The free-slip boundary condition may be invoked simply by equating the second normal derivative of the tangential velocity component to zero, which for the case under examination by figure (4-11) results in:-

$$U_d = 2U_{1,j} - U_{2,j} \qquad \text{---4.7/5}$$

A particular problem exists at the boundary of a moving body. The position of the body surface will be unlikely to coincide with a convenient node. The conventional solution to this problem for both normal and tangential velocity boundary conditions is to use 'dummy' nodes within the body, in a technique similar to that used for solid walls. As can be seen from figure 4-12, the free slip boundary condition (case 1) requires no information concerning the position of the body contour relative to the computational nodes. This can be of considerable advantage when writing the relevant computer coding. The zero slip boundary condition (case 2) uses a parabolic extrapolation technique to derive the dummy node value. This method may be problematical when y, becomes small.

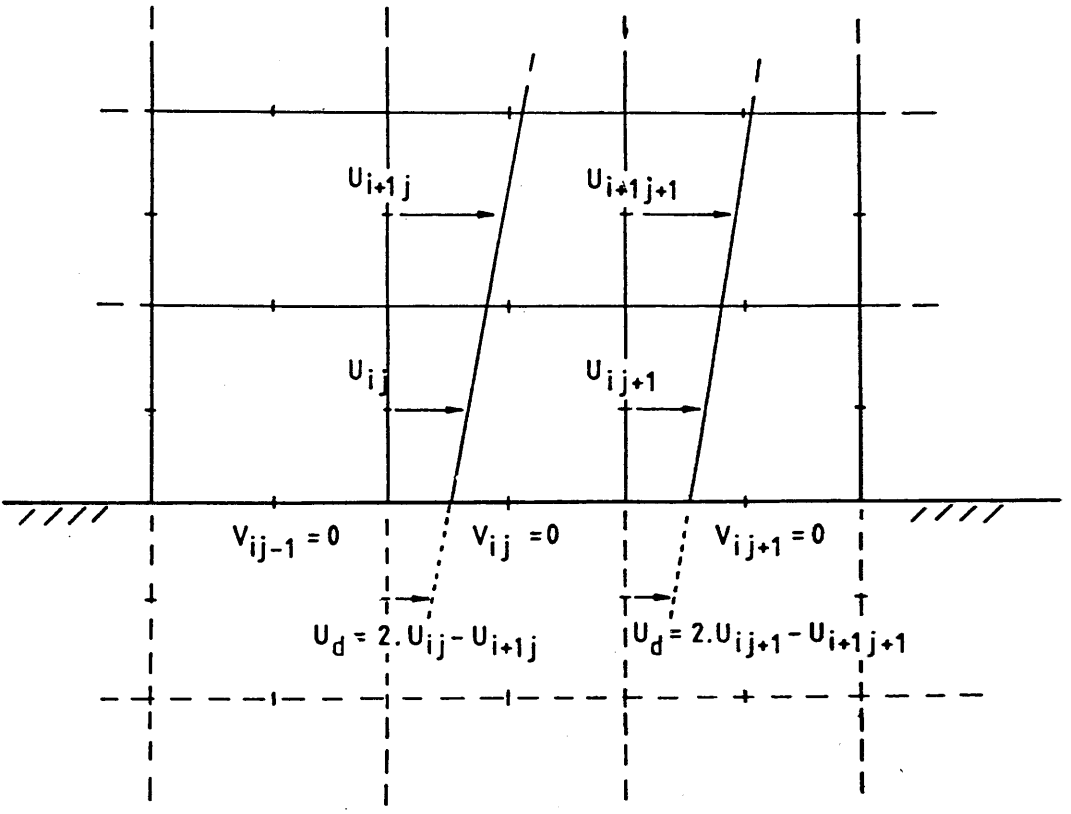

Figure 4-11 Use Of "Dummy Nodes" To Apply Free-Slip Boundary Conditions.

Figure 4-12 Use Of Dummy Nodes Inside A Moving Boundary.

Case 1 : Free-Slip Condition

Case 2 : Zero-Slip Condition (Parabolic Extrapolation Using U_{ij}, U_{i-1j}, U_b)

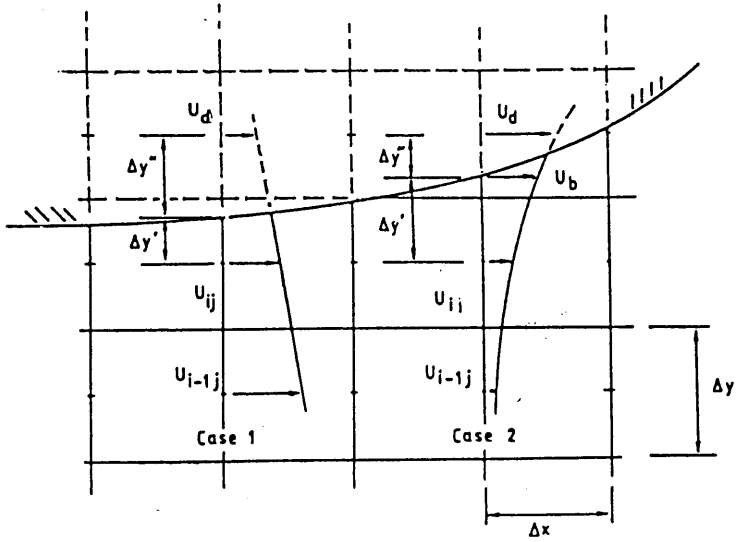

Figure 4-13 "Irregular" Star Formulation For Second Partial Derivatives.

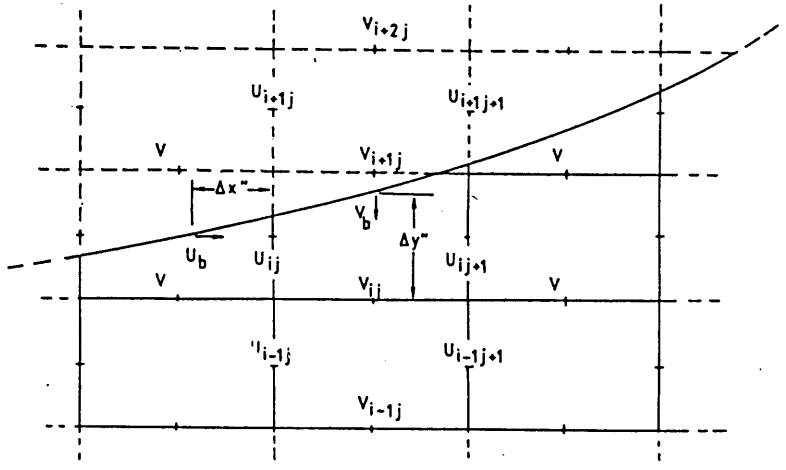

$$\frac{\partial^2 U}{\partial x^2} = \frac{2}{(1+\beta).\Delta x.\Delta x''}\left(U_{ij+1} + \beta.U_{ij-1} - (1+\beta).U_{ij} \right)$$

$$\frac{\partial V}{\partial Y} = \frac{2}{(1+\beta).\Delta y.\Delta y''}\left(V_{i-1j} + \beta.V_{i+1j} - (1+\beta).V_{ij} \right)$$

In many cases the method of 'irregular stars', as illustrated in figure (4-13) is also adequate though again, care must be taken when the body surface is close to a node. For this method, specialised formulae for derivatives local to the body are determined as if for a completely irregular mesh of mesh size ratio .

For the downstream boundary conditions listed, the Sommerfeld radiation condition was found most useful. For the geometry shown in figure (4-14), it can be seen that an upwinded differencing scheme for convection is necessary. A forward time step may be used when calculating the value of u at the boundary node giving:-

$$\frac{U_{ijx}^{n+1} - U_{ijx}^{n}}{\Delta t} = - \frac{C_x}{\Delta x} (U_{ijx}^{n} - U_{ijx-1}^{n}) \qquad \text{---4.7/6}$$

This exhibits heavy damping due to the use of the upwinded convection operator. Further, the forward time step scheme is not as accurate as a central time step, as discussed in the case of the full Navier Stokes discretisation. Orlanski (102) suggested the following leapfrog formula:-

$$\frac{U_{ijx}^{n+1} - U_{ijx}^{n-1}}{2\Delta t} = - \frac{C_x}{\Delta x} \left(\frac{U_{ijx}^{n+1} + U_{ijx}^{n-1}}{2} - U_{ijx-1}^{n} \right) \qquad \text{---4.7/7}$$

which for a C.F.L condition of unity, ie

$$C_x = \frac{\Delta x}{\Delta t} \qquad \text{---4.7/8}$$

gives

$$U_{ijx}^{n+1} = U_{ijx-1}^{n} \qquad \text{---4.7/9}$$

which follows from the method of characteristics for hyperbolic equations.

Figure 4-14

Downstream Radiation Boundary

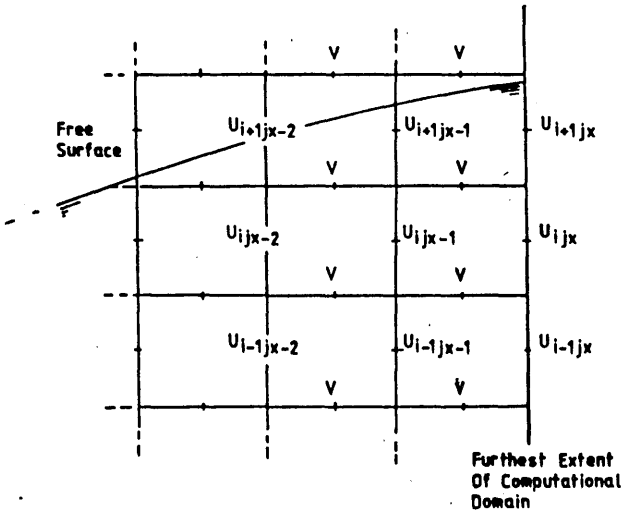

V Components —Updated Using Discretised Navier Stokes Equations.

$U_{i\pm n,jx}$ Components —Found Using Upwinded Form Of Sommerfield Radiation Condition.

Figure 4-15

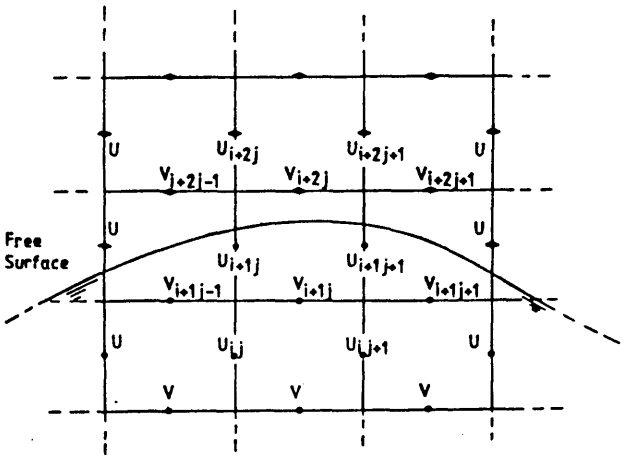

• Nodes Within Computational Fluid Domain.

• "Dummy" Nodes Outside Computational Fluid Domain.

The value of C_x, the phase speed, may be set by the physics of the problem. For example, a shallow water wave may require the phase speed to be given by:-

$$C_x = \sqrt{gh}$$

where h = depth of water. g = 9.81 m/s^2

For the general open boundary condition, C_x may be calculated by re-arranging equation 4.7/7, one step back in time and one grid point back from the boundary, giving:-

$$C_x = \frac{\left(U^{n}_{ijx-1} - U^{n-2}_{ijx-1} \right)}{\left(U^{n}_{ijx-1} + U^{n-2}_{ijx-1} \right) - 2\,U^{n}_{ijx-2}} \frac{\Delta x}{\Delta t} \qquad \text{---} \; 4.7/10$$

Use of this technique results in a simple weighting formula for U^{n+1}_{ijx} based on the value U^{n}_{ijx} and U^{n}_{ijx-1}. It is possible that C_x will be negative in some circumstances, resulting in spurious oscillations propagating upstream from the boundary. In such a case, the phase speed is set to zero resulting in:-

$$U^{n+1}_{ijx} = U^{n}_{ijx} \qquad \text{---} \; 4\;7/11$$

It has been noted in section 3.5.1 that no boundary conditions on velocity can be applied on the contour of the free surface. Figure (4-15) shows a typical free-surface orientation which might occur during the simulation. It can be seen that, in order to evaluate the convection and diffusion terms in the Navier Stokes equations some knowledge is required of the velocities at 'dummy' nodes outside the flow field.

This information may be acquired by assuming continuity applies over the whole area of a free surface cell, instead of just

over the area occupied by the fluid. Three situations may therefore be possible, where, for any individual free surface cells, one, two or three of its nodes may be outside the fluid domain.

7.1.1. One Node Only Exposed

The continuity equation may be directly applied. For the situation shown in figure (4-16I) therefore, v_{i+1j}, will be given by:-

$$V_{i+1j} = V_{ij} - \frac{\Delta y}{\Delta x}\left(U_{ij+1} - U_{ij} \right) \qquad \text{---4.7/12}$$

7.1.2. Two Nodes Exposed

Common sense restricts the number of geometries which cause this situation to those where adjacent u, v nodes are exposed, ie where the free-surface has a slope of approximately 45 degrees. In this situation, the two velocity gradients are separately equated to zero, ie:-

$$\frac{\partial u}{\partial x} = 0 \quad , \quad \frac{\partial v}{\partial y} = 0$$

hence for the situation shown in figure (4-16II),

$$U_{ij+1} = U_{ij} \quad , \quad V_{i+1j} = V_{ij} \qquad \text{---4.7/13}$$

7.1.3. Three Nodes Exposed

For the case shown in figure (4-16III), it is assumed that:-

$$\frac{\partial v}{\partial y} = 0 \quad , \quad V_{i+1j} = V_{ij} \qquad \text{---4.7/14}$$

However, it can be seen that no information exists for the u or u nodes. For the case of continuity only being applied, it is assumed that:-

Figure 4-16 I

One Node Exposed

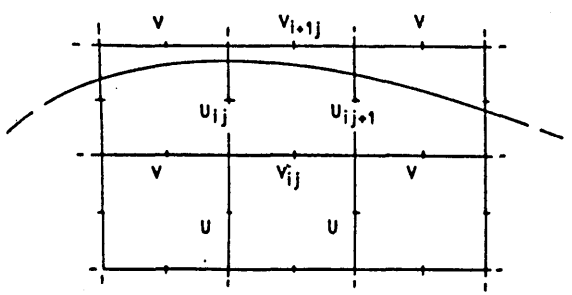

$$V_{i+1j} = V_{ij} - \Delta y.(U_{ij+1} - U_{ij})/\Delta x$$

Figure 4-16 II

Two Nodes Exposed

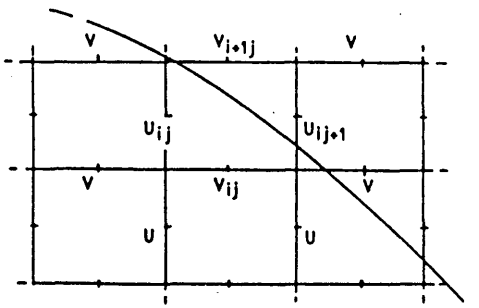

$$U_{ij+1} = U_{ij} \qquad V_{i+1j} = V_{ij}$$

Figure 4-16 III

Three Nodes Exposed

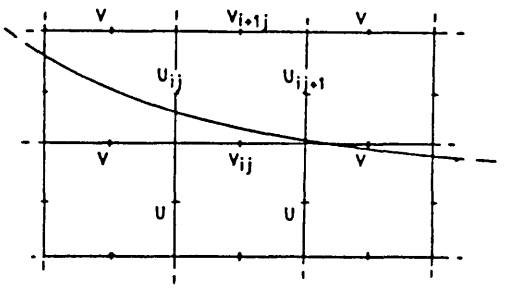

$$V_{i+1j} = V_{ij}$$

$$U_{ij} = U_{i-1j} \qquad U_{ij+1} = U_{i-1j+1}$$

$$\frac{\partial u}{\partial y} = 0$$

hence:-

$$u_{ij} = u_{i-1j} \quad , \quad u_{ij+1} = u_{i-1j+1} \qquad \text{---4.7/15}$$

The zero tangential stress condition may be used to provide more information. When the curvature of the free surface is small, equation 3.5/6 may be approximated by, (107):-

$$\nu \left(\frac{\partial(\bar{u}.\bar{n})}{\partial s} + \frac{\partial(\bar{u}.\bar{s})}{\partial n} \right) = 0 \qquad \text{---4.7/16}$$

Further, if the free surface is nearly vertical or horizontal, the tangential stress condition may be reduced to:-

$$\frac{\partial v}{\partial x} + \frac{\partial u}{\partial y} = 0 \qquad \text{---4.7/17}$$

If the free surface slope is approximately equal to 45 degrees from the horizontal, the tangential stress condition may be stated as:-

$$\frac{\partial u}{\partial x} - \frac{\partial v}{\partial y} \qquad \text{---4.7/18}$$

The use of these relationships to supply values to velocity nodes outside the fluid domain, follows a pattern similar to that used to apply continuity. Consider figure (4-17). In this case, the continuity condition may be used to supply values for $v_{i+1\ j-1}$ and v_{i+1j} following the re-arrangement of equation 4.7/11. The value of u_{i+1j} may then be found by applying equation 4.7/16 in discrete form, ie:-

$$u_{i+1j} = u_{ij} - \frac{\Delta y}{\Delta x}\left(v_{i+1j} - v_{i+1j-1} \right) \qquad \text{---4.7/19}$$

Figure 4-17

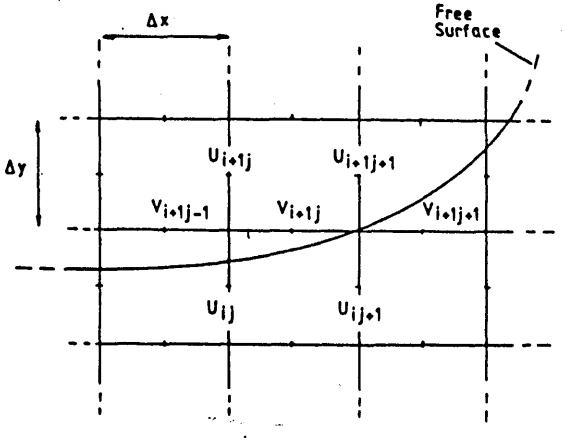

V_{i+1j-1} And V_{i+1j} Found By Applying Continuity.

U_{i+1j} Found Using Equation 4.7/18.

Figure 4-18

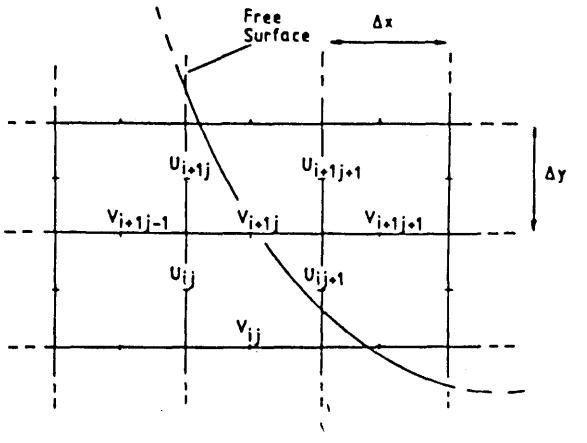

U_{ij+1} May Be Found By Applying Either Continuity Or Zero Tangential Stress Condition.

As another example, consider figure(4-18) in which the free surface has a slope of about 45 degrees. In this case, either continuity or equation 4.7/18, in discrete form, may be applied. In the latter case, for the geometry shown, it can be seen that:-

$$U_{ij+1} = U_{ij} + \frac{\Delta x}{\Delta y} (V_{i+1j} - V_{ij}) \qquad ---4.7/20$$

However, this is incompatible with the continuity condition and therefore in making a choice between the two, continuity would always be preferred. Equation 4.7/18 does however, confirm the assumptions made for the case of two nodes exposed, (equation 4.7/13), since equating both velocity gradients to zero will identically satisfy both continuity and the zero tangential stress condition. Figure (4-19) also shows a situation where 4.7/18 may be of use. This three nodes exposed geometry may use equation 4.7/17 to supply values for v_{i+1j} and v_{ij}. If required, continuity may then be applied in order to compute a value for u_{ij+1}.

It is obvious that programming the application of these conditions such that they may apply to any shape of free surface is a difficult task. A vast amount of 'decision making' needs to be coded concerning free surface slope, which nodes are eligible for such treatment etc. In practice, continuity is considered of primary importance and is applied to the single exposed node case first. This is followed by a check on free surface slope and subsequent application of condition 4.7/17 where required. Finally, where the modulus of the free surface gradient is close to unity, the individual velocity gradients $\partial u/\partial x$, $\partial v/\partial y$, are set to zero across the boundary for the two nodes exposed case.

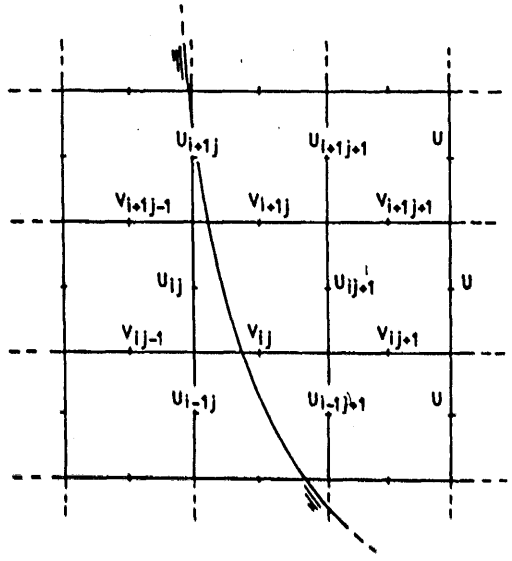

V_{i+1j} And V_{ij} Found By Applying Zero Tangential Stress Condition.

U_{ij+1} Found By Applying Continuity

Figure 4-19

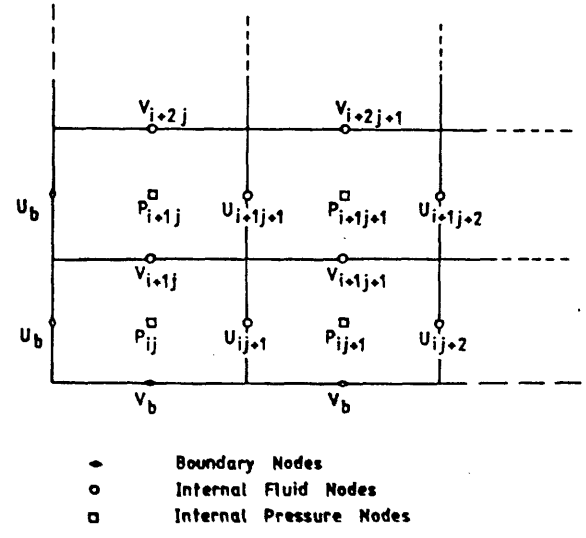

Figure 4-20 Corner Of Fluid Domain.

Note: No Requirement For Pressure Boundary Conditions In Updating Internal Fluid Nodes.

An alternative method was suggested by Chan and Street (114) in which all 'dummy' values outside the fluid are found by extrapolation. Initially, this technique looks easier to code. In practice, however, it is restricted to fairly simple free surface geometries. Further, like many 'irregular star' formulations, inaccuracies may arise where the free surface contour passes close to a node.

7.2. Conditions on Fluid Pressure

As stated in section 3.5, the geometry of the staggered mesh used for the numerical computations in this thesis, removed the need to apply pressure boundary conditions when evaluating the Navier Stokes equations, except in two special cases.

It can be seen from figure (4-20) that since only the velocity field within the flow domain is subject to updating, none of the pressure nodes required for this process are on or outside the fluid domain if the T3 grid is used. This is of considerable advantage to most fluid dynamics problems.

The two exceptional cases occur at the moving body boundary and the free surface. In the case of the moving body, a number of formulations exist. A polynomial curve fit may be made for p in the required direction, ie for figure 4-21.:-

$$p(y) = B_0 + B_1 y + B_2 y^2 \text{ ----} \qquad \text{---4.7/21}$$

The coefficients B_0, B_1, B_2 may be found by applying the constraints given by the value of at nodes N(I-1,J), N(I-2,J) and N(I-3,J). Pressure gradients at the body contour may also be used as

Figure 4-21

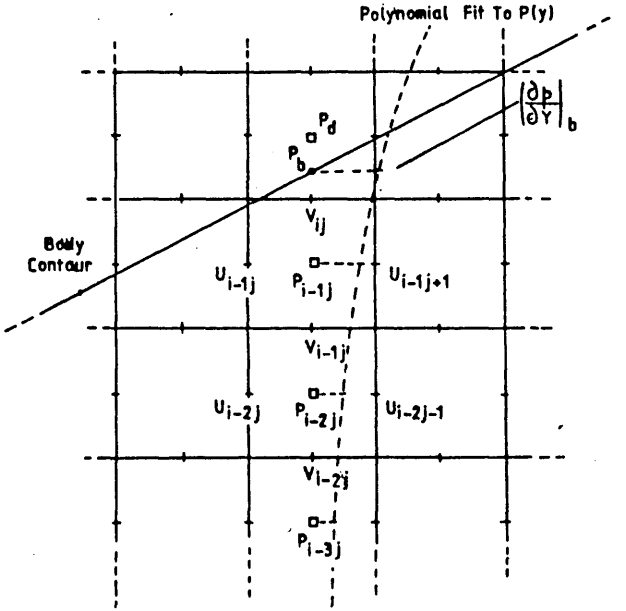

Polynomial $P(y) = B_0 + B_1 y + B_2 y^2 + \ldots$

Coefficients Found From Constraints At Fluid Nodes And Body Contour.

Figure 4-22

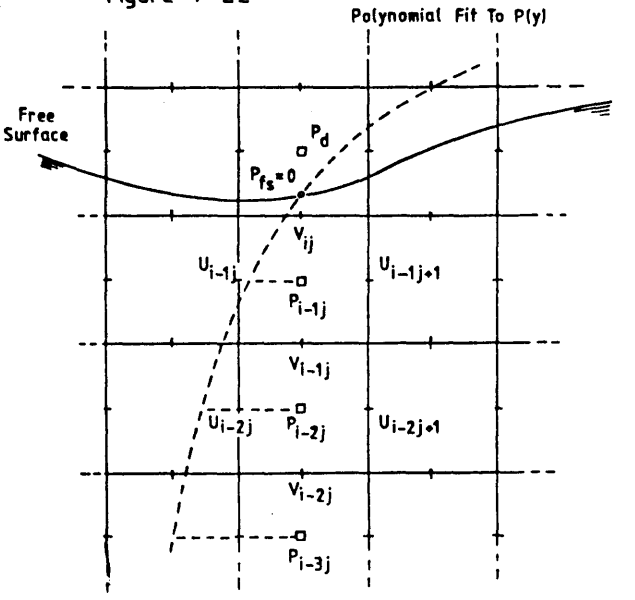

Polynomial $P(y) = B_0 + B_1 y + B_2 y^2 + \ldots$

Coefficients Found From Constraints At Fluid Nodes And Free Surface Contour.

data in evaluating the coefficients in equation 4.7/21. By differentiating 4.7/21 one obtains:-

$$\frac{\partial p}{\partial y} = B_0 + 2B_2 y \quad \text{-----} \qquad \text{---4.7/22}$$

which may be evaluated at the co-ordinates of the v node under examination.

Alternatively, 4.7/21 may be used to calculate the pressure at a dummy node within the body. The pressure gradient is then found by numerical differentiation. The advantage of the latter technique is that dummy node pressures may be found in a separate routine making it possible to evaluate the Navier Stokes equations without recourse to checking whether or not boundary conditions need be applied.

The same extrapolation technique may be used at the free surface, as shown in figure (4-22). Since the pressure field has been found by solving equation 3.4/15 with its attendant boundary conditions, there is no need to explicitly apply these conditions during evaluation of the pressure gradient terms in the Navier Stokes equations. Therefore, it is useful to check that the polynomial curve fits used in this part of the algorithm are accurate enough to satisfy the boundary conditions set for the problem.

7.3. Application of Boundary Conditions Using A 'Least Squares' Surface Fit Algorithm

The methods of applying boundary conditions outlined so far in this section, are standard techniques, which allowed the computer programs used throughout this work to produce reliable simulations. However, the need for a finite mesh size tended to produce non-smooth

or stepped pressure distributions upon the immersed body surface. This tended to make the overall load calculations somewhat inaccurate for the first few time steps. A solution was arrived at by which a least-squares surface fit to the fluid pressure field was used to define a global function, which could be integrated along the contour of the immersed body section.

Not only did this idea prove highly successful in its primary aim of smoothing out the surface pressure distribution, but it also provided a means of applying boundary conditions to particular computational routines. The surface fit method was applied in two main areas:-

a. the computation of 'dummy node' values for pressure, horizontal velocity component (u), and vertical velocity component (v), within the contour of the moving body during the Navier Stokes updating routine.

b. the computation of 'dummy node' values for velocity components, again within the contour of the moving body, in order to allow the evaluation of the right hand side of equation 3.3/15 in its finite difference form. (Section 4.8 details the finite difference approximations used).

The least-squares formulation was as follows. The pressure and/or velocity field distribution was assumed to be of the form:-

$$f(x,y) = \sum_{-nx}^{nx} A_n R^n + \sum_{-nx}^{nx} B_n x R^n + \sum_{-nx}^{nx} C_n y R^n \qquad \text{---} 4.7/23$$

where A_n , B_n , C_n are a series of constants forming a vector of unknown coefficients K_m, m = 3n.

where R is the distance of a field point from the body co-ordinate axes and is given by:-

$$R_{ij} = [(x_{ij} - X_g)^2 + (y_{ij} - Y_g)^2]^{1/2} \qquad ---4.7/24$$

This form was believed to be particularly convenient as a generalised solution for the pressure or velocity components about regular smooth cylinders in inviscid flow.

The least squares formulation may be written as the following minimisation problem:-

$$Q = \sum_{1}^{ix} \sum_{1}^{jx} (F_{ij} - f(x_{ij}, y_{ij}))^2$$

$$\frac{\partial Q}{\partial K_m} = -2 \sum \sum (F_{ij} - f(x_{ij}, y_{ij})) \frac{\partial f(x_{ij}, y_{ij})}{\partial K_m} = 0 \qquad ---4.7/25$$

where F_{ij} are the discrete values at nodes i,j.

Therefore for each value of m:-

$$\sum_{1}^{ix} \sum_{1}^{jx} f(x_{ij}\ y_{ij}) \frac{\partial f(x_{ij}\ y_{ij})}{\partial K_m} = \sum_{1}^{ix} \sum_{1}^{jx} F_{ij} \frac{\partial f(x_{ij}\ y_{ij})}{\partial K_m} \qquad ---4.7/26$$

Equation 4.7/26 provides 3n simultaneous equations in the 3n unknown coefficients. The resultant matrix problem was solved using a standard computer library 'NAG' routine. Computing dummy node values for the variable in question then consisted of evaluating equation 4.7/23 within the contour of the body. When solving for a surface fit to the velocity field in inviscid flow, the body velocity could be included in the assembly of the data points F_{ij} with, for example:-

$$x_{ij} = a \cos \theta$$

$$y_{ij} = a \sin \theta$$

$$R_{ij} = a$$

for a circular cylinder of radius a.

Having computed the coefficients A_n, B_n, C_n, equation 4.7/23 could be used to compute either pressure distributions upon the cylinder contour, or 'dummy' node values for the discrete variables within the body contour.

For ease of reference, equation 3.3/15 is re-stated below as:-

$$-\nabla^2 p = S + E \qquad \text{---} 4.8/1$$

where

$$S = \left(\frac{\partial u}{\partial x}\right)^2 + 2\frac{\partial u}{\partial y}\frac{\partial v}{\partial x} + \left(\frac{\partial v}{\partial y}\right)^2 \qquad \text{---} 4.8/2$$

$$E = -\frac{\partial}{\partial t}(\nabla \bar{u}) + \frac{1}{R_e}\nabla^2(\nabla.\bar{u}) \qquad \text{---} 4.8/3$$

It should be noted that the right hand side term S is derived from the convection terms in the Navier Stokes equations and represents the effect of the steady or stagnation pressure. The term E represents the error in the pressure caused by the lack of continuity in the velocity field. For dynamic simulations this term must be zero (or very small). A method to solve the continuity equation at each time step such that E may be set to zero will be detailed in a later section.

As was noted in section 3.4, the principle of superposition was used in the solution of the pressure equation. The pressure field was assumed to consist of four 'components'. These were:-

a. stagnation pressure field p_s ,

b. dynamic pressure field p_d ,

c. viscous pressure field p_v ,

d. hydrostatic pressure field p_h .

The solution for each of these components may be found by:-

a. for stagnation pressures

solve

$$-\nabla^2 p_s = S$$

on fluid domain R, stagnation pressure boundary conditions on δR.

b. for dynamic pressure field,

solve

$$-\nabla^2 p_d = 0$$

on fluid domain R with dynamic pressure boundary conditions given by equation 3.5/9, ie:-

$$\frac{\partial p_d}{\partial n} = \frac{\partial}{\partial t}(\bar{u}.\bar{n})$$

c. for viscous pressure field,

solve

$$-\nabla^2 p_v = 0$$

on fluid domain R with viscous pressure boundary conditions given by equation 3.5/8, ie

$$\frac{\partial p_v}{\partial n} = -\frac{1}{R_e}\frac{\partial \omega}{\partial s}$$

d. for hydrostatic pressures,

solve

$$-\nabla^2 p_h = 0$$

on fluid domain R with hydrostatic pressure boundary conditions on δR.

In spite of problems usually encountered when mixing boundary conditions (120), it was found to be acceptable to solve for stagnation, viscous and hydrostatic pressures at the same time. It will be shown later how a sensible choice of boundary conditions made this possible. However, first, the discretisation and solution procedure for equation 4.8/1 will be discussed.

Central difference approximations to the second order derivatives of the Laplacien operator on pressure were used, as given by 4.4/16. This resulted in the following formula for the Poisson equation 4.8/1, given the mesh shown in figure (4-23):-

$$\frac{p_{ij+1} + p_{ij-1} - 2p_{ij}}{(\Delta x)^2} + \frac{p_{i+1j} + p_{i-1j} - 2p_{ij}}{(\Delta y)^2} = -S_{ij} \qquad \text{---4.8/4}$$

The right hand side value, -S, is a scalar quantity which may be evaluated for each pressure node as:-

$$-S_{ij} = \left(\frac{\partial u}{\partial x}\right)^2_{ij} + 2\left(\frac{\partial u}{\partial y}\frac{\partial v}{\partial x}\right)_{ij} + \left(\frac{\partial v}{\partial y}\right)^2_{ij}$$

where

$$\left(\frac{\partial u}{\partial x}\right)_{ij} = \frac{(u_{ij+1} - u_{ij})^2}{(\Delta x)^2} \qquad \text{---4.8/5}$$

$$\left(\frac{\partial v}{\partial y}\right)_{ij} = \frac{(v_{i+1j} - v_{ij})^2}{(\Delta y)^2} \qquad \text{---4.8/6}$$

$$\left(\frac{\partial u}{\partial y}\right)_{ij} = \left(\frac{(u_{i+1j} - u_{i-1j})}{2\Delta y} + \frac{(u_{i+1j+1} - u_{i+1j-1})}{2\Delta y}\right)/2 \qquad \text{---4.8/7}$$

$$\left(\frac{\partial v}{\partial x}\right)_{ij} = \left(\frac{(v_{i+1j+1} - v_{i+1j-1})}{2\Delta x} + \frac{(v_{ij+1} - v_{ij-1})}{2\Delta x}\right)/2 \qquad \text{---4.8/8}$$

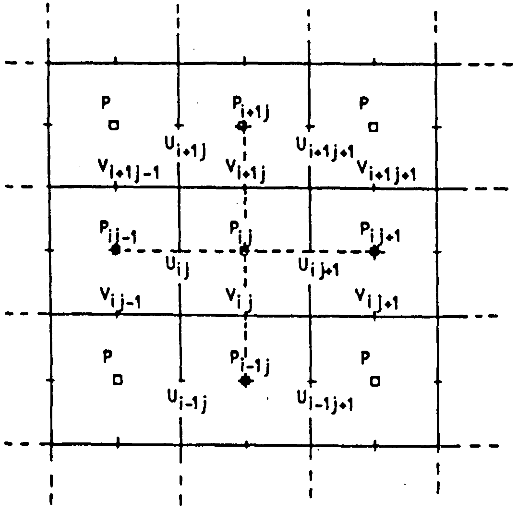

Figure 4-23 Local Arrangement Of Variables (P,U,V) For Poisson Solver.

(Equations 4.8/4/5/6/7/8)

Figure 4-24

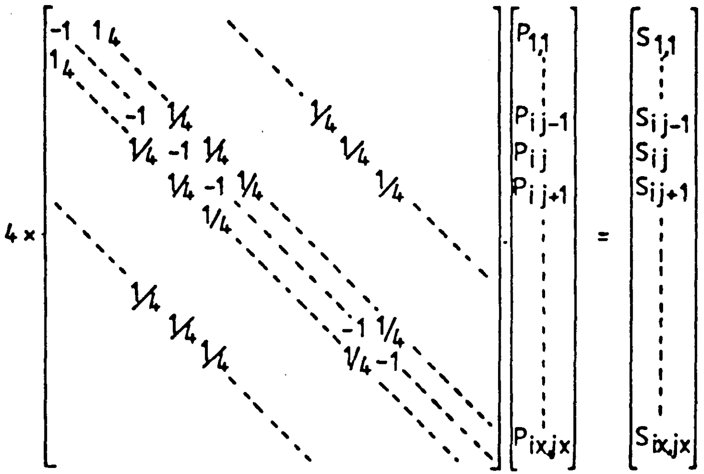

Matrix Formulation Of Poisson Pressure Solver Prior To Application Of Boundary Conditions

When written down for each node, equation 4.8/4 represents a set of simultaneous equations which may be expressed in matrix form as shown in figure (4-24). The matrix system:-

$$[L][p] = [S] \qquad \text{---4.8/9}$$

has a diagonally dominant influence matrix L , whose eigenvalues are well bounded (99). Therefore, during iterative solution, convergence is assumed and can be shown to have a rate given by (131):-

$$CR = \cos^2 \frac{\pi h}{2} \approx 1 - \frac{\pi^2 h^2}{4} + O(h)^4 \qquad \text{---4.8/10}$$

(assuming $\Delta x = \Delta y = h$)

However, the solution procedure used was not a matrix inversion method as such. For the large systems of equations envisaged, relaxation methods (99,112) offered the most efficient solution schemes. The original techniques of Southwell have been superceded with the advent of electronic computers, by various over-relaxation methods which offer better rates of convergence (99). Frankel (132) and Young (133) developed the technique which has since become known as the successive over-relaxation, or SOR method.

Equation 4.8/4 may be re-written as:-

$$2(1+\beta^2)p_{ij} = p_{ij+1} + p_{ij-1} + \beta^2(p_{i+1j} + p_{i-1j}) + (\Delta x)^2 S_{ij} \qquad \text{--- 4.8/11}$$

where $\beta = \Delta x/\Delta y$

This equation may be used in a recursive solution technique. For example, if K represents the iteration level, then

$$p_{ij}^{k+1} = \frac{1}{2(1+\beta^2)}\left(p_{ij+1}^{k} + p_{ij-1}^{k} + \beta\left(p_{i+1j}^{k} + p_{i-1j}^{k}\right) + (\Delta x)^2 S_{ij}\right)$$

___4.8/12

gives the Jacobi method. Advantage may be made of the computational procedure of sweeping through the mesh, such that all k+1, updated, values are used on the right hand side of 4.8/12 when available yielding:-

$$p_{ij}^{k+1} = \frac{1}{2(1+\beta^2)}\left(p_{ij+1}^{k} + p_{ij-1}^{k+1} + \beta\left(p_{i+1j}^{k} + p_{i-1j}^{k+1}\right) + (\Delta x)^2 S_{ij}\right)$$

___4.8/13

The above formula illustrates the Gauss-Seidel method, which exhibits faster convergence than 4.8/12 (99). Further improvement in convergence rate is achieved through the use of over-relaxation (133). Briefly, the new value of ij is weighted between the old value p^k and p^{k+1} given in 4.8/13, ie:-

$$p_{ij}^{k+1\,*} = (1-\omega)p_{ij}^{k} + \omega p_{ij}^{k+1}$$

which (dropping the * symbol), produces the recursive relationship:-

$$p_{ij}^{k+1} = (1-\omega)p_{ij}^{k} + \frac{\omega}{2(1+\beta^2)}\left(p_{ij+1}^{k} + p_{ij-1}^{k+1} + \beta\left(p_{i+1j}^{k} + p_{i-1j}^{k+1}\right) + (\Delta x)^2 S_{ij}\right)$$

___4.8/14

where $1 < \omega < 2$ is the relaxation factor

An optimum relaxation factor ω_o, may be theoretically given by, (99)

$$\omega_o = 2\left(\frac{1-\sqrt{1-\mathcal{E}}}{\mathcal{E}}\right) \qquad ___4.8/15$$

$$\mathcal{E} = \left[\frac{\cos\frac{\pi}{(JX-1)} + \beta^2\cos\frac{\pi}{(IX-1)}}{1+\beta^2}\right]^2 \qquad ___4.8/16$$

where JX, IX are the maximum number of nodes in the x and y directions respectively. Numerical experiments were also performed to determine the value of ω_o for comparison with 4.8/15. (See Appendix).

Boundary conditions on pressure may be applied by modifying 4.8/14 locally, in a way dependent upon the flow being modelled. In strady flow problems such as illustrated in figure (4-4), the inlet base pressure p_0 , may be set to zero. On the T3 grid used, this amounts to using a dummy node pressure given by:-

$$p_d = p_{ij-1} = -p_{ij}$$

which results in equation 4.8/14 being re-arranged as:-

$$p_{ij}^{k+1} = \frac{(1-\omega)}{(1-\omega/2(1+\beta^2))} p_{ij}^{k} + \frac{\omega}{2(1+\beta^2)(1-\omega/2(1+\beta^2))} (p_{ij+1}^{k} + \beta^2 (p_{i+1j}^{k} - p_{i-1j}^{k+1}) + (\Delta x)^2 S_{ij}) \quad \text{---} \ 4.8/17$$

and applied to the pressure nodes at one half mesh spacing in from the inlet boundary.

A general case may be written for the situation wherein a Neuman condition is to be applied on a boundary co-incident with the mesh. Dummy node values may be expressed as:-

$$p_d = p_{ij} + h \frac{\partial p}{\partial n} \quad \text{---} \ 4.8/18$$

where h is either Δx or Δy.

The pressure gradient may be deduced from equations 3.5/7, 3.5/8, 3.5/9 or 3.5/10 as appropriate.

The resulting recursive relationship for the nodes, one half mesh space in from the downstream boundary where 3.5/7 applies would therefore be:-

$$p_{ij}^{k+1} = \frac{1-\omega}{(1-\omega/2(1+\beta^2))} p_{ij}^{k} + \frac{\omega}{2(1+\beta^2)(1-\omega/2(1+\beta^2))} (p_{ij-1}^{k+1} + \Delta x \frac{\partial p}{\partial x} + \beta^2 (p_{i+1j}^{k} + p_{i-1j}^{k+1}) + (\Delta x)^2 S_{ij})$$

--- 4.8/19

Another example may be cited for the bed or bottom boundary condition in a viscous flow. Condition 3.5/8 is re-arranged to give:-

$$\frac{\partial p}{\partial n} = \frac{-1}{R_e} \frac{\partial \omega}{\partial S} = \frac{-1}{R_e} \frac{\partial}{\partial x} \frac{\partial u}{\partial y}$$

for the geometry given in figure (4-25). When discretised this becomes:-

$$\frac{\partial p}{\partial n} \approx \frac{-1}{R_e} \frac{2}{\Delta x \Delta y} (u_{1j-1} - u_{1j})$$

--- 4.8/20

since the dummy u nodes outside the flow are set to:-

$$u_d = -u_{1j}$$

Thus 4.8/18 may be written as:-

$$p_d = p_{1j} - 2 (u_{1j+1} - u_{1j}) / \Delta x R_e$$

yielding a recursive pressure equation for the nodes one half mesh spacing in from the bed boundary as:-

$$p_{ij}^{k+1} = \frac{1-\omega}{(1-\omega\beta^2/2(1+\beta^2))} p_{ij}^{k} + \frac{\omega}{2(1+\beta^2)(1-\omega\beta^2/2(1+\beta^2))} (p_{ij+1}^{k} + p_{ij-1}^{k+1} + \beta^2 (p_{i+1j}^{k} - 2 (u_{1j+1} - u_{1j}) / \Delta x R_e) + (\Delta x)^2 S_{ij})$$

--- 4.8/21

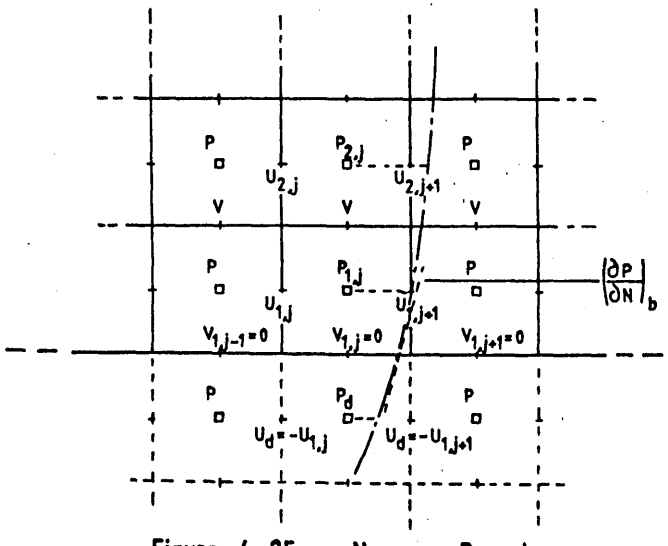

Figure 4-25 Neuman Boundary Condition On Pressure As Given By Eqn. 4.8/21

Figure 4-26

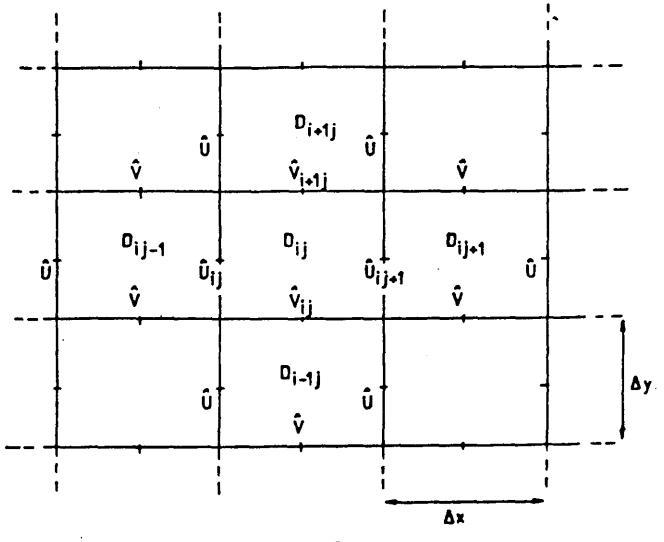

$$\frac{\hat{U}_{ij+1} - \hat{U}_{ij}}{\Delta x} + \frac{\hat{V}_{i+1j} - \hat{V}_{ij}}{\Delta y} = D_{ij} \qquad \text{Eqn. 4.9/2}$$

Where the boundary coincides with the mesh, it is fairly easy to code the various forms of the modified SOR pressure equation. The two exceptions again, are on curved boundaries at free surfaces or moving bodies.

An early approximation to free-surface boundary conditions, used in the Marker and Cell method (113), was to set the pressure in surface or empty cells to zero. It was soon realised that this was not accurate enough for some problems. Chan and Street (114) suggested setting the pressure on the contour of the free surface to zero. All the pressure nodes within the fluid took part in the computation, whilst those outside had their values found by extrapolation (at each iterative step). This was further modified by Hirt and Shannon, who found the pressures of the free surface from 3.5/14. The latter approach was used for flows at very low Reynolds numbers however, and was considered inappropriate for the near inviscid fluid behaviour being modelled in this thesis. Thus the technique of Chan and Street was adopted herein.

As far as the moving body boundary was concerned, the process of extrapolation was again applied. Since only the steady flow components were being solved for, pressure gradients given by 3.5/9 could be disregarded. Thus the polynomials used for extrapolation of pressures to dummy nodes within the body, were constrained by outside pressure values and pressure gradients on the surface given by 3.5/7 and 3.5/8. It should be noted that the internal pressure nodes had to be updated by this process after each iterative sweep. In later computations, this was found to slow convergence considerably.

In conclusion, at each time step of the simulation process, a

Poisson equation for the steady pressure components was solved by successive over-relaxation. This could only be done after continuity had been satisfied. (It will be shown in the next section how dynamic pressures could be found whilst solving the continuity equation). The steady pressures were then added to the known dynamic pressure field in order to continue the time marching of the Navier Stokes equations.

During the initial development of the computer programs for this thesis, the Marker and Cell (131) solution algorithms were heavily relied upon (134). The pressure solver in these schemes retained the terms:- (eqn 4.8/3).

$$E = -\frac{\partial}{\partial t}(\nabla \bar{u}) - \frac{1}{R_e}\nabla^2(\nabla \bar{u}) \qquad \text{---4.9/1}$$

By assuming the error in the velocity field at the next time step to be zero, the first term on the right hand side of 4.9/1 was discretised as:-

$$\frac{\partial}{\partial t}(\nabla.\bar{u}) \quad \text{—} \left((\nabla.\bar{u})^{n+1} - (\nabla.\bar{u})^{n} \right) = -\frac{(\nabla.\bar{u})^{n}}{\Delta t}$$

This type of approach is suitable for steady state or near steady state problems only. However, it was found (134) that at the initial point of impact for the slamming problem, $\nabla.\bar{u}$ local to the body was unreasonably high and could not be reconciled with the physics of the problem without recourse to a fully compressible fluid model. There was an obvious need for a continuity solver.

Consider the control volume shown in figure(4-26). After updating the velocity field via the discretised Navier Stokes equations, the approximate solution $(\hat{u}, \hat{v})$ will induce some divergence in the finite difference cell, ie:-

$$\frac{\hat{u}_{ij+1} - \hat{u}_{ij}}{\Delta x} + \frac{\hat{v}_{i+1j} - \hat{v}_{ij}}{\Delta y} = D_{ij} \qquad \text{---4.9/2}$$

by substituting

$$\hat{U}_{ij} = U_{ij} + \Delta U_{ij}$$
$$\hat{V}_{ij} = V_{ij} + \Delta V_{ij}$$

where (U,V) is the velocity field which satisfies the discretised continuity equation, the error equation:-

$$\frac{\Delta U_{ij+1} - \Delta U_{ij}}{\Delta x} + \frac{\Delta V_{i+1j} - \Delta V_{ij}}{\Delta y} = D_{ij} \qquad ---4.9/3$$

where $\Delta U, \Delta V$ is the error velocity field

is produced. By assuming that:-

$$\Delta U_{ij+1} = -\Delta U_{ij} \qquad \Delta V_{i+1j} = -\Delta V_{ij}$$

and re-arranging 4.9/3, the relationship:-

$$\Delta y\, \Delta U_{ij} + \Delta x\, \Delta V_{ij} = \Delta x\, \Delta y\, D_{ij}/2 \qquad ---4.9/4$$

is obtained which simply relates the total error in fluid flux to the cell divergence. It may be assumed that the truncation error in the updated u field is of the same order as that of the v field, hence:-

$$\Delta y\, \Delta U_{ij} = \Delta x\, \Delta V_{ij}$$

$$\Delta U_{ij} = -\Delta x\, D_{ij}/4 \quad , \quad \Delta U_{ij} = \Delta x\, D_{ij}/4$$

$$\Delta V_{jj} = -\Delta y\, D_{ij}/4 \quad , \quad \Delta V_{ij} = \Delta y\, D_{ij}/4 \qquad ---4.9/5$$

An iterative routine was programmed such that for any flow problem, the divergence in each cell could be calculated and the velocity components updated using 4.9/5. The technique was applied to full cells only since free surface cells were, by definition, divergent. This method was used for some time as a modification to the

algorithms used in SPLASH (135). Eventually however, the author made use of the SOLA code (136) which can be shown to perform the above continuity solving process identically and yet is also applied to calculating dynamic pressures. The basis of the SOLA code is derived from the Marker and Cell pressure equation:-

$$-\nabla^2 p_{ij}^n = \frac{\nabla . \bar{U}_{ij}^n}{\Delta t} = \frac{D_{ij}^n}{\Delta t} \qquad \text{---4.9/6}$$

The dynamic pressure equation:-

$$-\nabla^2 p_d = 0 \qquad \text{---4.9/7}$$

may be used to form the residual relationship:-

$$\nabla^2 (p_d + \delta p_d)_{ij} = \frac{-D_{ij}^n}{\Delta t}$$

which on application of 4.9/7 yields:-

$$\nabla^2 \delta p_{d\,ij} = \frac{-D_{ij}}{\Delta t} \qquad \text{---4.9/8}$$

This equation may be solved iteratively by Newton's method, ie by using the relationship:-

$$\delta p_{ij}^n = -D_{ij}^n / (\frac{\partial D}{\partial p}) \qquad \text{---4.9/9}$$

It can be shown from the finite difference form of 4.9/8, for a regular mesh, that:-

$$\frac{\partial D}{\partial p} = \frac{1}{2\Delta t (1/(\Delta x)^2 + 1/(\Delta y)^2)} \qquad \text{---4.9/10}$$

The form of the resulting solution is a series of 'sweeps' through the mesh, updating the velocity field in an implicit/explicit manner. For any finite difference cell encountered during this sweep,

the divergence D_{ij} is calculated and hence the residual pressure δp_{ij} is found from 4.9/9. The velocities at the cell sides may then be updated using:-

$$U_{ij}^{k+1} = U_{ij}^{k} - \frac{\Delta t}{\Delta x}\delta p_{ij}^{k}$$

$$U_{ij+1}^{k+1} = U_{ij+1}^{k} + \frac{\Delta t}{\Delta x}\delta p_{ij}^{k}$$

$$V_{ij}^{k+1} = V_{ij}^{k} - \frac{\Delta t}{\Delta y}\delta p_{ij}^{k}$$

$$V_{i+1j}^{k+1} = V_{i+1j}^{k} + \frac{\Delta t}{\Delta y}\delta p_{ij}^{k} \qquad \text{---} 4.9/11$$

This process is equivalent to applying an implicit/explicit discretisation of:-

$$\frac{\partial u}{\partial t} = \frac{\partial(\delta p)}{\partial x} \quad , \quad \frac{\partial v}{\partial t} = \frac{\partial(\delta p)}{\partial x}$$

ie

$$U_{ij}^{k+} = U_{ij}^{k} - \frac{\Delta t}{\Delta x}(\delta p_{ij}^{k} - \delta p_{ij-1}^{k+1}) \quad , \quad V_{ij}^{k} = V_{ij}^{k} - \frac{\Delta t}{\Delta x}(\delta p_{ij}^{k} - \delta p_{i-1j}^{k+1})$$

$$\text{---} 4.9/12$$

where k is the iteration level.

At the end of each sweep, the dynamic pressures are updated using:-

$$p_{ij}^{k+1} = p_{ij}^{k} + \delta p_{ij}^{k}$$

$$\text{---} 4.9/13$$

It can be shown that this process is equivalent to solving the dynamic pressure equation via a relaxation technique. In fact if a relaxation factor ω is introduced into equation 4.9/9, giving:-

$$\delta p = -\omega D/\left(\frac{\partial D}{\partial p}\right)$$

$$\text{---} 4.9/14$$

the technique is equivalent to successive over relaxation.

In steady flow problems this 'dynamic' pressure field is a function of the total error in the solution of the continuity-coupled Navier Stokes equations and reduces to zero on convergence. In unsteady flows, this pressure field consists both of errors from the Navier Stokes updating process and physical dynamic pressures found by solving 4.9/7 with the relationships 3.5/9 defined on accelerating boundaries. A two stage solution is required therefore, first to remove truncation errors from the velocity field, then to solve for physical dynamic pressures. The latter computation could be performed by solving 4.9/7 with its attendant boundary conditions using successive over-relaxation. However, this was not a very attractive idea. After some initial trials, it was noted that the 'irregular star' or extrapolation methods of applying pressure boundary conditions were unwieldy and inaccurate (99,134).

The following modifications to the SOLA code were made in an attempt to rectify this problem. Consider figure (4-27a) showing a section of body contour moving through a finite difference cell. The presence of this moving boundary is equivalent to a volume flux of fluid into the cell, causing a rate of change of volumetric strain or divergence. This may be modelled by the presence of a fluid source within the cell, and modifies the discretised continuity equation locally to:-

$$\frac{U_{ij+1} - U_{ij}}{\Delta x} + \frac{V_{i+1j} - V_{ij}}{\Delta y} - \frac{Q_{ij}}{\Delta x \Delta y} = 0 \qquad \text{---4.9/15}$$

where Q_{ij} is the source strength (dimensions L^2/T for two dimensional flow).

For steady state flow past a stationary body (whose contour

is represented by a source/sink distribution), the identity 4.9/15 is easily complied with. If the body is considered to be moving through the mesh, and is viewed from a stationary co-ordinate system, then 4.9/15 will be more difficult to satisfy. For the steady motion case, the (u,v) components will be influenced by convection close to the body, requiring the value of Q to increase or decrease accordingly. For the case of an accelerating body, the increases in (u,v) due to convection will be augmented by the dynamic pressure field close to the body. The variation in the source strength as a result of the accelerated motion of the body, may be directly related to this dynamic pressure field by use of the modified SOLA algorithm.

Consider again the situation wherein a body is moving at constant velocity through the finite difference mesh. Equation 4.9/15 is considered to be satisfied at each time instant. The source strength is calculated as the rate of change of cell volume (area) per unit time. When the body is moving at constant velocity, the source strength depends only upon the geometry of figure (4-27a). The SOLA code may then be applied by setting the divergence in relationship 4.9/9 equal to that given by 4.9/15. The strength of the source is calculated as the area A,B,C,D from figure (4-27a), swept out per unit time.

The change in source strength due to the acceleration of the body is calculated as the difference between the time rates of change of area swept out at constant velocity A_c, and the area actually swept out during the updating process A_s. The two stage computation therefore applies SOLA, first with:-

$$Q_{ij}^{n+1} = A_c / \Delta t \qquad \text{---4.9/16}$$

FIGURE 4-27A

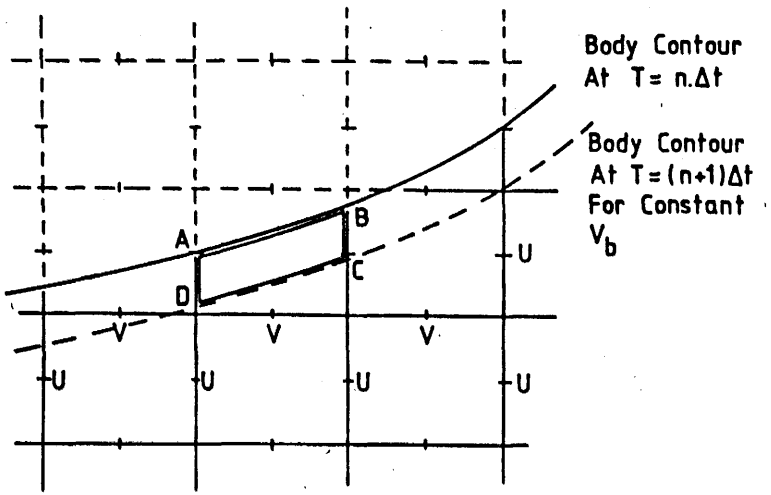

Area ABCD Swept Out At Constant Velocity = A_c

FIGURE 4-27 A

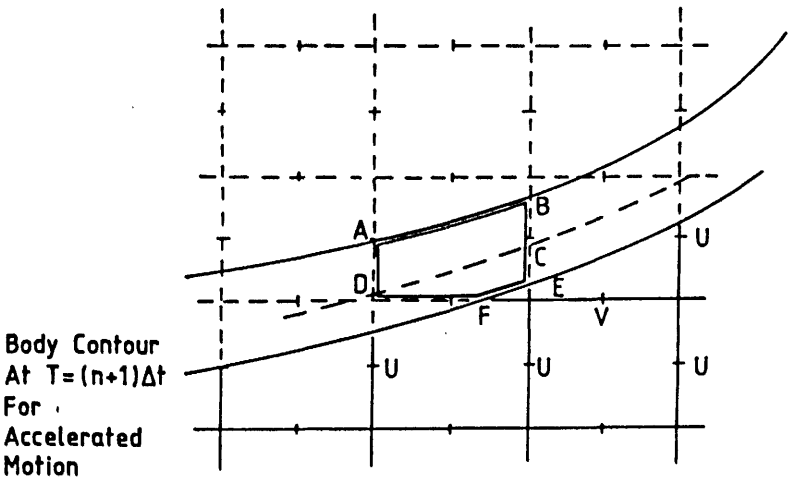

Area ABEF Swept Out Under Accelerated Motion = A_s

without updating the dynamic pressure field, then with:-

$$Q^{n+1} = A_s / \Delta t \qquad \text{---4.9/17}$$

with dynamic pressures fully updated.

The first stage is performed simply to remove truncation error from the velocity field, and therefore no updating of dynamic pressures is required. The change in the source term introduced at the second stage may be stated:-

$$\delta Q_{ij}^{n+1} = (A_s - A_c)/\Delta t \qquad \text{---4.9/18}$$

The divergence at this second stage is wholly attributable to this change in source strength and is a function of the body acceleration changes on dynamic pressure may be equated to the changes in the source term as:-

$$D = -\delta Q / \Delta x \Delta y$$

from 4.9/9 therefore

$$\delta p = (\delta Q/\Delta x\Delta y)/\left(\frac{\delta D}{\delta p}\right) \qquad \text{---4.9/19}$$

dividing by δt, a discrete time step, gives:-

$$\frac{\delta p}{\delta t} \quad \frac{\delta Q}{\delta t} / \Delta x \Delta y \frac{\partial D}{\partial p} \qquad \text{---4.9/20}$$

from 4.9/10 with $\delta t = \Delta t$

$$\frac{1}{\delta t}\frac{\partial D}{\partial p} = \frac{1}{2\Delta t^2 (1/(\Delta x)^2 + 1/(\Delta y)^2)}$$

which for $\Delta x = \Delta y = h$ gives:-

$$\frac{1}{\delta t}\frac{\partial D}{\partial p} = \frac{h^2}{4(\Delta t)^2} = \frac{c^2}{4} = \left(\frac{c}{2}\right)^2$$

where C is the constant wave speed, thus:-

$$\frac{\delta p}{\delta t} = \left(\frac{c}{2}\right)^2 \frac{\delta Q}{\Delta x \Delta y} = c_p^2 \frac{\delta Q}{\Delta x \Delta y}$$

or

$$\frac{\delta p_{ij}}{\delta t} = - c_p^2 D_{ij}$$

From 4.8/3 however:-

$$- \nabla^2 p_{d\,ij} = \frac{\partial}{\partial t} D_{ij}$$

hence

$$\nabla^2 p_{d\,ij} = \frac{1}{c_p^2} \frac{\partial^2 p}{\partial t^2} \qquad ---4.9/21$$

which is familiar as the wave equation for dynamic pressure, with a phase speed based on the Courant number for the discretised domain.

This relationship was later used to set the time step for the simulation of the free suirface wave problem (chapter 8), in which a source distribution was used to represent a wave making device.

10. COMPUTATIONAL CYCLE FOR TIME MARCHING ALGORITHM

The simulation procedure described in section 4.3 will now be alaborated upon for a typical example of incompressible flow. Figure (4-28) illustrates the initial conditions for the two dimensional water entry problem applied to a 30 degree wedge, including the book keeping variables. At t = 0, the apex of the wedge is just touching the undisturbed free surface and is moving at velocity V_b, accelerating under the influence of gravity. All fluid variables are set to zero.

Figure (4-29) shows a detailed flow chart for the subsequent computational cycle. It begins by applying the book keeping processes to move the wedge a distance:-

$$\Delta S = V_b \Delta t + \frac{1}{2} g (\Delta t)^2$$

into the fluid. The resulting source strengths for the finite difference cells containing portions of the body are calculated. Dynamic pressures and continuity are solved for directly without first removing errors due to time marching of the Navier Stokes equations, since no such errors can yet exist. Having achieved the correct velocity and dynamic pressure field at t = Δt, the 'steady' pressure components are solved for using successive over relaxation as shown in section 4.8. Given this pressure field, the load on the body may be found, and its resultant acceleration calculated.

An examination of the velocity field is then made to find the largest velocity component which is used in the application of the C.F.L condition (4.6/6) to calculate the size of the next time step.

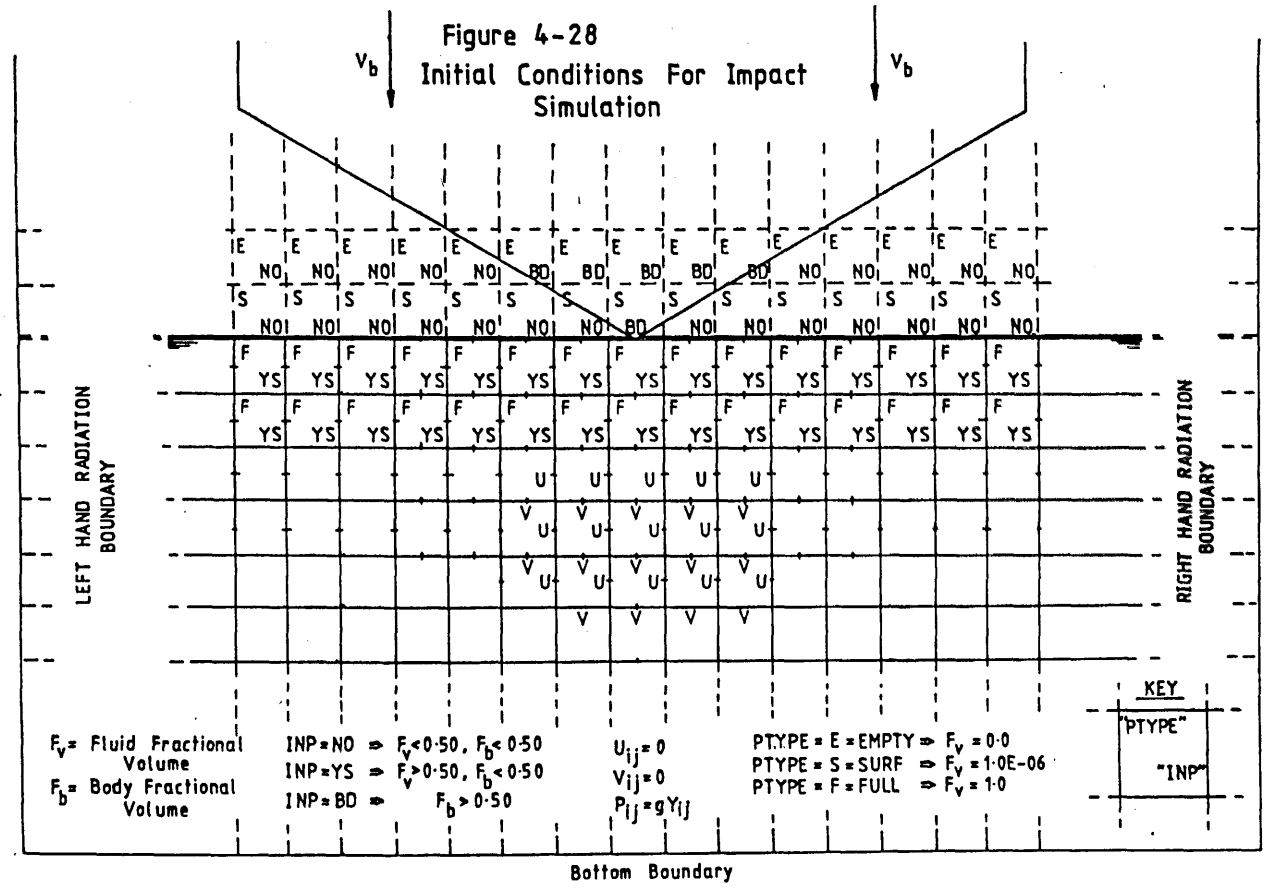

Figure 4-28
Initial Conditions For Impact Simulation

Figure 4-29

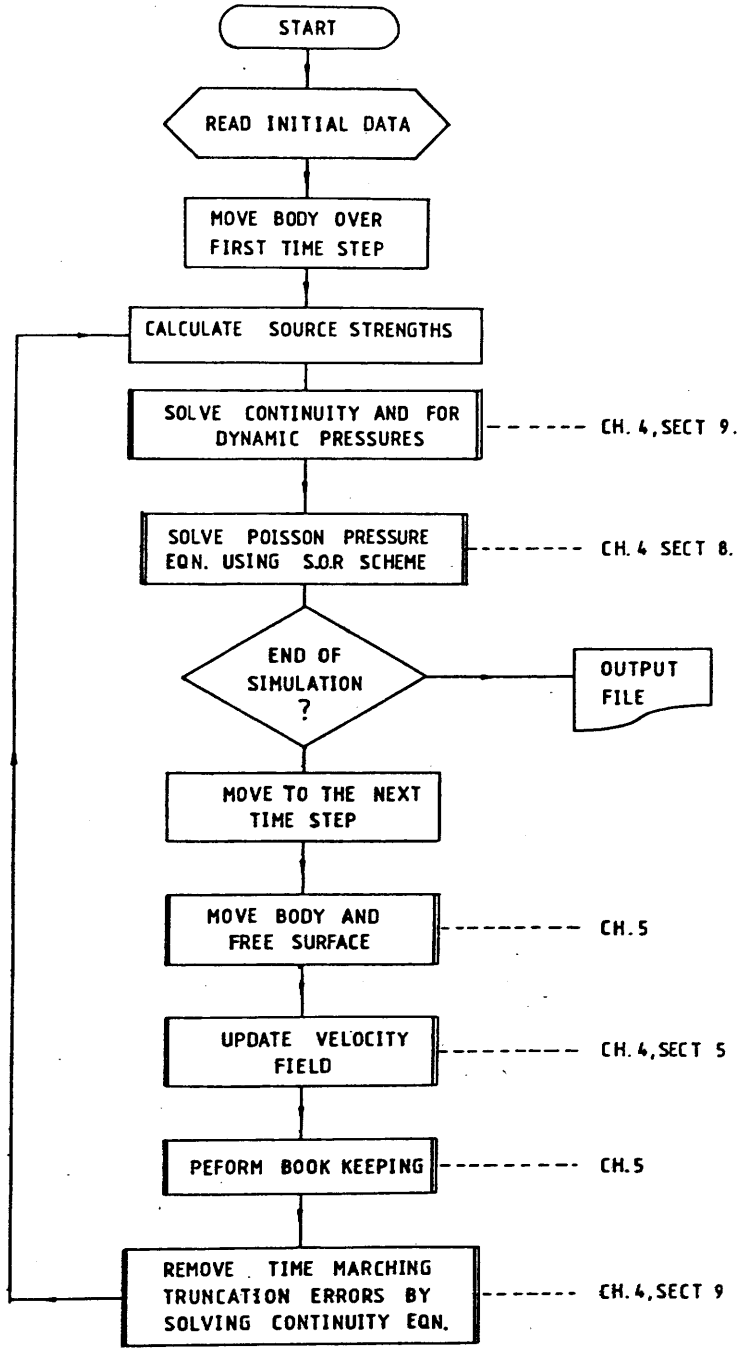
START
READ INITIAL DATA
MOVE BODY OVER FIRST TIME STEP
CALCULATE SOURCE STRENGTHS
SOLVE CONTINUITY AND FOR DYNAMIC PRESSURES
CH. 4, SECT 9.
SOLVE POISSON PRESSURE EQN. USING S.O.R SCHEME
CH. 4 SECT 8.
END OF SIMULATION ?
OUTPUT FILE
MOVE TO THE NEXT TIME STEP
MOVE BODY AND FREE SURFACE
CH. 5
UPDATE VELOCITY FIELD
CH. 4, SECT 5
PEFORM BOOK KEEPING
CH. 5
REMOVE TIME MARCHING TRUNCATION ERRORS BY SOLVING CONTINUITY EQN.
CH. 4, SECT 9

The updating process continues by moving the body and calculating its new velocity via the relationships:-

$$\Delta S = V_b^n \Delta t + \frac{1}{2} \dot{V}_b^n (\Delta t)^2$$

$$V_b^{n+1} = V_b^n + \dot{V}_b^n \Delta t$$

The new free surface shape is then found using the volume fluxing techniques of section 5.1. The new velocity field may also be updated using any of the methods of section 4.5.

A book-keeping process is then applied in order to decide:-

a. which velocity nodes are within the fluid.

b. which pressure nodes are within the fluid.

c. which finite difference cells are either full, free surface or empty cells.

d. which velocity or pressure nodes lie within the contour of the body.

e. which finite difference cells are within, on the borders of, or outwith the body contour.

Only finite difference cells which are fully within the fluid (though they may contain some portion of the body boundary), are subject to the next part of the routine, which is to eliminate divergence caused by truncation error from the velocity field via the continuity solver.

The modified SOLA code is then applied to calculate dynamic pressures, followed by the calculation of steady pressures using the SOR method of section 4.8. The simulation then continues within the

looping process illustrated by figure (4-29).

The routine may continue indefinitely, as long as numerical stability is maintained. The C.F.L time step constraint is often sufficient to ensure this, through the method is very sensitive to the degree to which continuity is enforced. With finite limits on computational time, some choice as to the tolerence level for the continuity solver had to be set. Like all relaxation processes, convergence for the boundary value problem showed an exponential character, slowing rapidly as the error was reduced. Thus the total computational time was not linearly proportional to the degree of accuracy. On the introduction of the variational energy checking method, described in the next chapter, these problems of compromising accuracy to speed were, to a great extent, overcome.

With regard to the modelling of the moving body contour using a 'source in cell' method, the compressible behaviour at the fluid/boundary interface may be examined using a 'piston' type analogy. In finite difference cells containing non-zero source terms, equation 3.7/2 may be re-written as:-

$$\frac{\delta \rho}{\delta t} + \rho \left(\frac{\delta u}{\delta x} + \frac{\delta v}{\delta y} - \frac{Q}{\delta x \delta y} \right) = \qquad \text{---4.11/1}$$

For any particular finite difference cell this may be approximated using a central difference scheme, with the density node placed at the cell center. This leads to a formula for the change in density as:-

$$\Delta \rho_{ij} = -\rho_{ij} \Delta \left(\frac{U_{ij+1} - U_{ij}}{\Delta x} + \frac{V_{i+1j} - V_{ij}}{\Delta y} - \frac{Q}{\Delta x \Delta y} \right) \qquad \text{---4.11/2}$$

The change in density is used as the main variable, as it is required in this form for the variational energy method described in chapter 6. Further, it is more accurate than carrying the density, which is a number of order 10^3, whereas $\Delta\rho$ is of order 10^{-3} . The effect of rounding error in the computer would therefore, endanger the accuracy of the method if densities were stored in their updated form.

The change in fluid pressure is computed as:-

$$\Delta p_{a\,ij} = c_w^2 \, \Delta \rho_{ij} \; . \qquad \text{---4.11/3}$$

which due to the size of C_w is very sensitive to inaccuracies.

The time marching of the velocity field was achieved using discretised forms of equations 3.7/4 and 3.7/5. A forward time

stepping, central differencing scheme was used leading to the formula:-

$$U_{ij} = U_{ij} - \frac{\Delta t}{\rho_{ij}\Delta x}\left(p_{aij} - p_{aij-1}\right) \qquad ---4.11/4$$

$$V_{ij} = V_{ij} - \frac{\Delta t}{\rho_{ij}\Delta y}\left(p_{aij} - p_{ai-1j}\right) \qquad ---4.11/5$$

It should be noted that ρ_{ij} in these formulae represents the density at the velocity nodes and should be taken as the mean of the densities from cell centres adjacent to the cell sides.

The size of the time step is set by the acoustic courant number, ie:-

$$\Delta t = MIN(\Delta x, \Delta y)/C_w$$

In terms of a practical calculation involving slight compressibility, the method requires a special formulation. It has been noted that only the fluid beneath the body will be compressed and even then, only if the rate of increase in beam is greater than the acoustic wave speed C_w. The value of Δt is chosen such that the pressure front does not move more than one mesh spacing per time step. For the slamming model used in these simulations, the increase in wetted beam is approximated by the sequential 'switching on' of sources in free surface cells. The minimum requirement for sustained compressible behaviour beneath the body in this model is to have one extra source switched on at each time step. If this condition cannot be met, owing to the shape and impact speed of the body, the flow reverts to being purely incompressible in nature. This results in the continuity solver being applied rigorously throughout the fluid domain.

If the flow is to be considered compressible, then cells with non-zero source strengths, plus those directly beneath, are used in the computation of changes in density via 4.11/2. All other cells are subject to the continuity condition. Since an explicit time marching procedure is being used, the domain over which the velocity field is allowed to evolve expands at the same rate as the acoustic pressure field.

At the instant the acoustic shock wave finally 'catches up' with the edge of the body and the free surface, the flow field beneath the body needs to revert to being hydrodynamic in nature. It is at this point that the significance of the analogy between the modified SOLA routine for solving dynamic pressures, and the pressure wave equation (section 4.9) becomes apparent. The total change in density in each cell up to this point may be equated to the equivalent cell divergence. Thus the acoustic pressure field may directly be converted to an hydrodynamic pressure field. This process is accompanied by a shrinking of the compressed region beneath the body, and the loss of stored strain energy to fluid kinetic energy.

It should be noted that this type of fluid behaviour is restricted to the case of heavy impacts, ie those in which substantial portions of the body contact the free surface simultaneously. In practice this rarely happens. Thus, this part of the programming routine should really be regarded as a special case.

CHAPTER 5

BOOK KEEPING ROUTINES

CHAPTER 5

BOOK KEEPING ROUTINES

1. MODELLING OF FREE SURFACE

1.1. Methods Available

At any instant during the simulation, the shape and extent of the fluid domain may be considerably different to that at t = 0. However, this variation in shape cannot be predicted beforehand. A technique was required in which the form of the free surface boundary was allowed to evolve as part of the overall time marching algorithm. There were four possible candidates for this free boundary model:-

a. Time marching discretisation of the kinematic free surface condition.

b. Lagrangian free-surface particle motions.

c. The 'Marker and Cell' method (113).

d. The 'Volume of Fluid' technique (136)

The first of these methods requires the discretisation of the equation:-

$$\frac{\partial \eta}{\partial t} = V_f - U_f \frac{\partial \eta}{\partial x} \qquad \text{---} \; 5.1/1$$

where η = free surface height, measured along y axis

U_f, V_f = components of local free surface velocity.

With reference to figure(5-1), it can be seen that one possible method is given by the following fully explicit forward-time, centred difference formula:-

$$\frac{\eta_j^{n+1} \; \eta_j^n}{\Delta t} = V_f - U_f \frac{\eta_{j+1}^n \; \eta_{j-1}^n}{2\Delta x} \qquad \text{---} \; 5.1/2$$

A number of problems existed in the application of this method. Primarily, is single valued and will not allow breaking waves to be modelled. Further, the technique becomes inaccurate for free surface slopes with magnitudes greater than unity. It can also be seen that U_f, V_f are difficult to quantify on the mesh used, requiring either extrapolation from within the flow domain, or interpolation from boundary conditions applied as in 4.7. A further difficulty exists in the definition of the free surface height at the spray root, where solid and free surface boundaries coincide.

The second technique represents the free surface by a series of marker particles spread along the boundary, see figure 5-2. At any instant the velocity of the particles may be found by interpolation from the surrounding nodes. The particles are moved at each time step according to the well known kinematic relationships:-

$$DS_x = U_p \Delta t + \frac{1}{2} U_p (\Delta t)^2$$

$$DS_y = V_p \Delta t + \frac{1}{2} V_p (\Delta t)^2 \qquad \text{---} \; 5.1/3$$

where DS_x, DS_y are the particle displacements

U_p, V_p are the interpolated particle velocities

Inaccuracies may again arise from the interpolation scheme used. Computational problems may be encountered if 'cross over' between particles occurs. Since the particles are numbered in a

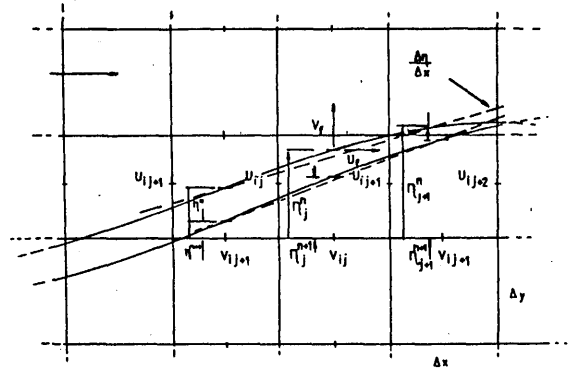

Figure 5-1 Discrete Geometry For Free Surface Kinematic Boundary Condition.

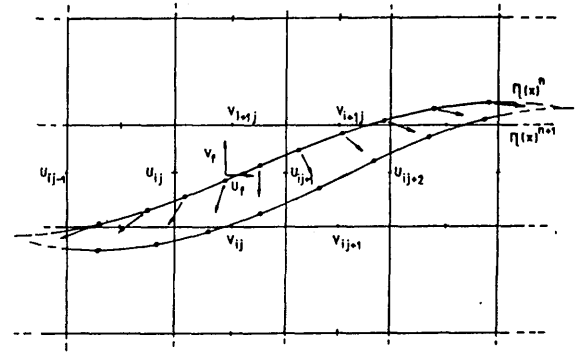

Figure 5-2 Free Surface Marker Particle Model

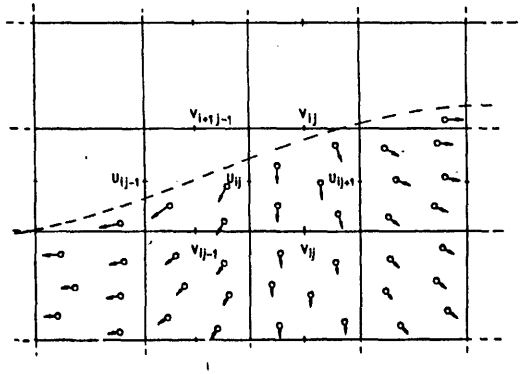

Figure 5-3 "Marker And Cell" Model

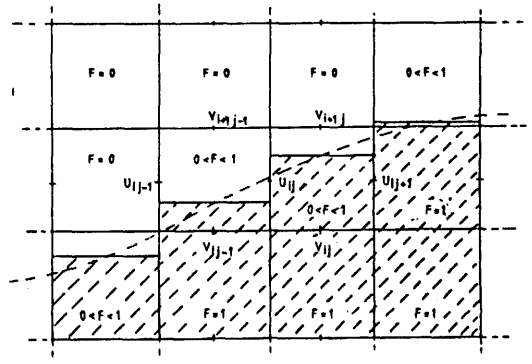

Figure 5-4 "Volume Of Fluid" Method

specific order, this cross-over can cause confusion when defining the position of the free surface. In practice, the technique is best restricted to simple free surface shapes as an analogue to 5.1/1.

In the Marker and Cell method, figure 5-3, the marker particles extend throughout the fluid. Again their trajectories are calculated using velocities and accelerations interpolated from nearby nodes. A specific number of particles are assigned to each finite difference cell at the beginning of the computation. Whilst exchange of 'markers' between cells occurs continuously throughout the simulation, the number of particles in each control volume must remain constant as a check on continuity. Full fluid cells are denoted by those with the original number of particles in them. Free surface cells have less than the number whilst empty cells contain no fluid markers. The free surface shape is delineated fairly roughly by this method, though it is possible to estimate the shape of the boundary by using the proportion of particles to represent the fractional height of the free surface within the cell. The main drawback of this technique is the large computing time and storage space required.

The method using free-surface marker particles was originally investigated for use in SPLASH (134). However, this was soon superceded by the Volume Of Fluid technique. In this method, the amount of fluid within a finite control volume is represented by a fractional volume F such that, (figure 5-4):-

F = 1.0 - 'full' cell

$0 < F = 1.0$ - 'surface' cell

F = 0 - 'empty' cell

The value of F may be represented by a scalar function in

space, whose evolution in time is represented by the pure convection equation:-

$$\frac{\partial F}{\partial t} + U\frac{\partial F}{\partial x} + V\frac{\partial F}{\partial y} = 0 \qquad \text{---5.1/4}$$

This may be approximated by the use of finite differences to provide formulae to calculate F at each time step. However, ideally, F varies as a unit step function in space. Hence, common finite difference operators tend to be inaccurate, 'smearing' out the true position of the free-surface. The Volume Of Fluid method (136) proposes to cure this problem by use of the upwind or donor/acceptor cell method as illustrated in sections 4.4 and 4.6. In short, some numerical damping is applied to the discretised form of equation 5.1/4.

In this thesis, the analogy between equation 5.1/4 and the free surface kinematic boundary condition, 5.1/1 was used to develop the free boundary model.

For the control volumes shown in figure (5-4), 5.1/4 may be re-written as:-

$$\frac{\partial F}{\partial t} + \frac{\partial FU}{\partial x} + \frac{\partial FV}{\partial y} - F\nabla.\bar{u} = 0 \qquad \text{---5.1/5}$$

For 'full' cells, $\nabla\bar{u} = 0$, and F is equal to unity, so 5.1/5 is simply a statement of mass conservation. A free surface cell will be divergent however, and F may be used as a measure of the mean height of the free surface in the middle of the cell. By reference to the value of F in adjacent cells, 'fluxing heights', ($F_W\Delta y, F_N\Delta x, F_E\Delta y, F_S\Delta x$) at the cell sides may be derived such that a simple volume fluxing analogue of 5.1/5 may be obtained.

The effect of the first convection term may be modelled, for a near horizontal free surface as (see figure 5-5):-

$$\frac{\partial FU}{\partial x} = \frac{(F_W U_W - F_E U_E)\Delta y}{\Delta x \Delta y} \qquad ---5.1/6$$

where F_W, F_E are the fractional cell side fluxing heights, found from weighted averages of the fractional volumes in adjacent cells. The increase in fractional volume owing to the vertical velocity component is then added to give:-

$$\Delta F = \Delta t \left(\frac{V_S \Delta x}{\Delta x \Delta y} + \frac{(F_W U_W - F_E U_E)\Delta y}{\Delta x \Delta y} \right) \qquad ---5.1/7$$

which can be seen to give an analogue to equation 5.1/1, if ($\Delta F.\Delta y$) taken as a measure of the change in mean free surface height. In order to complete the analogy, the term:-

$$F \nabla.\bar{U} = F_{ij} \left(\frac{U_E - U_W}{\Delta x} + \frac{V_N - V_S}{\Delta y} \right) \qquad ---5.1/8$$

must be taken into account. It will be shown later that for certain methods of averaging fractional volumes to obtain cell side fractional heights, 5.1/8 makes no change to the simple volume fluxing analogue. In some cases however, 5.1/8 is required to ensure compatability between the control volume approach and the convection equation 5.1/4.

The contour tracking algorithm simply sums up the net influx into a free-surface cell given the fluxing heights $F\Delta y$, $F\Delta x$ and the fluid velocity components u, v. However, some controlling factors require consideration. For example, a surface cell cannot lose more liquid than it contains. Consider figure (5-6). The volume of fluid to be fluxed from cell (I,J-1) into cell (I,J), may be greater than its own capacity, ie:-

$$U_{ij} \Delta t F_W \Delta y > F_{ij-1} \Delta x \Delta y \qquad ---5.1/9$$

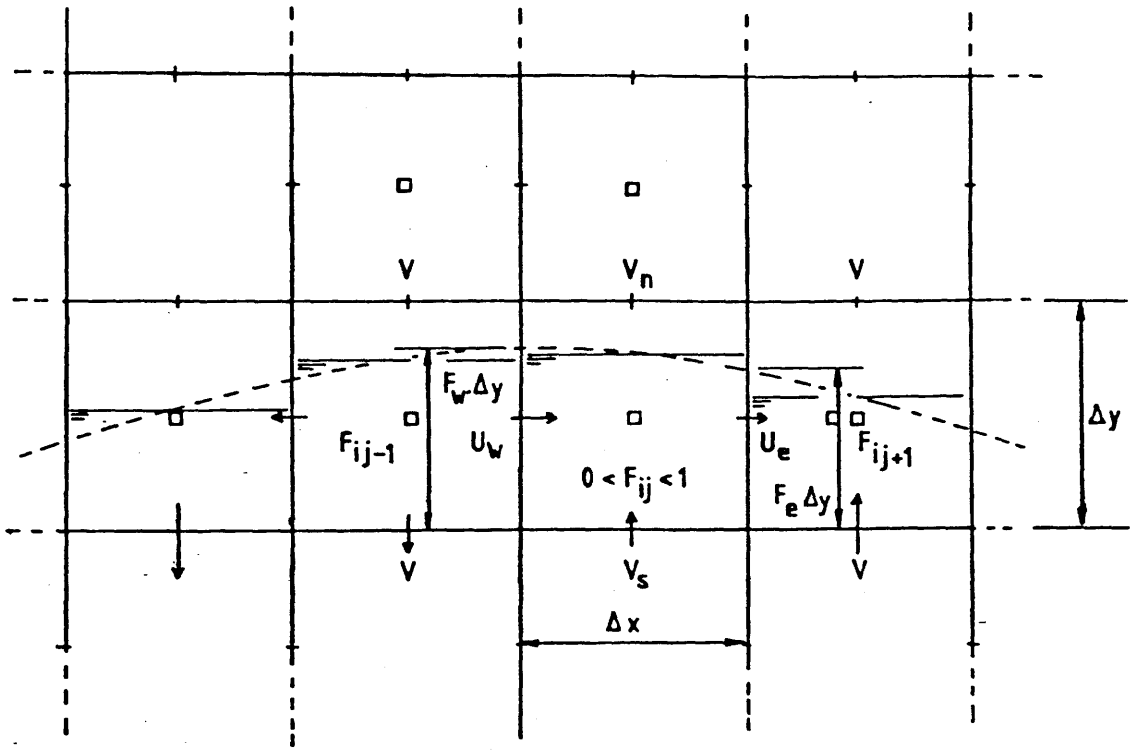

Figure 5-5 Horozontal Convection Of Fractional Volume (Equation 5.1/6)

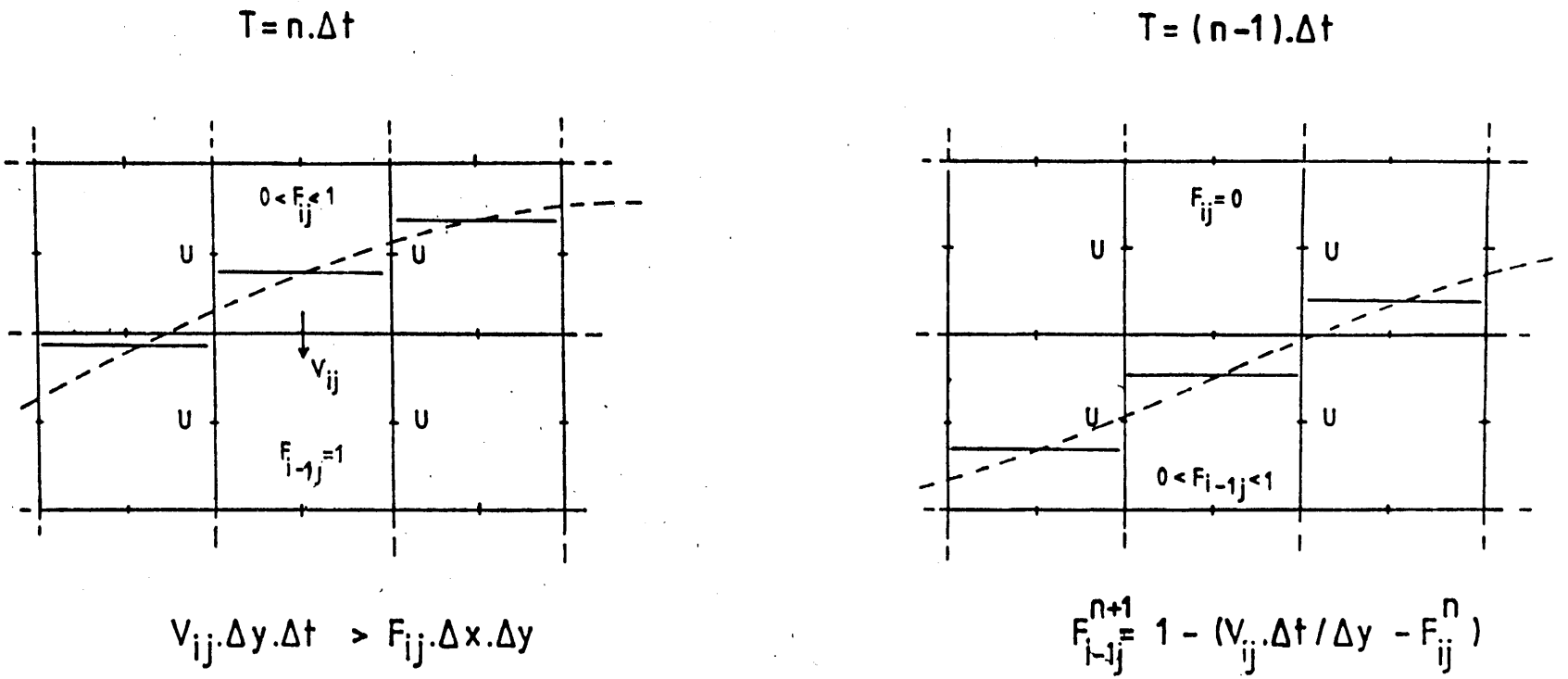

Figure 5.6 The Emptying Of Cell (I,J)

In such a case the new fractional volumes may be expressed as:-

$$F_{ij} = F_{ij} + MIN \left(U_{ij} \Delta t F_W / \Delta x , F_{ij-1} \right)$$

$$F_{ij-1} = F_{ij-1} - MIN \left(U_{ij} \Delta t F / \Delta x \quad F_{ij-1} \right) \qquad \text{---5.1/10}$$

In this way, cell (I,J-1) may empty, and cell (I,J) may become a free surface cell.

A further rule, put forward in (136) is that there must be no fluid fluxing between 'surface' and 'empty' cells. This is to ensure that at least one of the cells involved in the exchange of fluid satisfies the continuity condition.

It can also be seen that numerical inaccuracies may result in a cell gaining more fluid than it can contain. The only 'cure' for this problem is to ensure continuity as completely as possible (given a finite computing time), and to restrict the time step.

Having completed the updating of fluid fractional volumes, the free surface height may be found as the sum of fractional heights, ie:-

$$\eta_j = \sum_{i=1}^{ix} F_{ij} \Delta y \qquad \text{---5.1/11}$$

1.1.2. Computation of Cell Side Fluxing Heights

As previously noted, the values of F_W, F_E of 5.1/6 and figure (5-5), are found by averaging fractional volumes amongst local cells. With regard to equation 5.1/6, equivalent finite difference formula may be obtained for a mean velocity $u_w = u_E = u_m$ or:-

$$U_m = \frac{U_W - U_E}{2}$$

leading to the following representation of the convection term:-

$$\frac{\partial FU}{\partial x} \qquad \frac{U_m(F_W - F_E)\Delta y}{\Delta x \Delta y} \qquad \text{---} 5.1/12$$

A few simple cases are cited below:-

a. Simple Averaging: Using the fractional volumes of the cells immediately adjacent to each other, see figure 5-7(a).:-

$$F_W = (F_{ij} + F_{ij-1})/2 \quad , \quad F_E = (F_{ij} + F_{ij+1})/2 \qquad \text{---} 5.1/13$$

leading to the central difference expression when substituted in 5.1 /12:-

$$\frac{\partial F}{\partial x} = \frac{F_{ij+1} - F_{ij-1}}{2\Delta x} \qquad \text{---} 5.1/14$$

b. A 'Simpson's second rule' Average (figure 5-7(b)):-

$$F_W = (F_{ij-2} + 3F_{ij-1} + 3F_{ij} + F_{ij+1})/8$$

$$F_E = (F_{ij-1} + 3F_{ij} + 3F_{ij+1} + F_{ij+2})/8 \qquad \text{---} 5.1/15$$

leading to the 'fourth order' central difference expression:-

$$\frac{\partial F}{\partial x} = \frac{2}{3}\frac{F_{ij+2} - F_{ij-2}}{4\Delta x} + \frac{1}{3}\frac{F_{ij+1} - F_{ij-1}}{2\Delta x} \qquad \text{---} 5.1/16$$

c. 'Donor/Acceptor' cell method (136) (Figure 5-7(c)):-

$$F_W = F_{ij-1} \qquad U_{ij} > 0$$

$$F_W = F_{ij} \qquad U_{ij} < 0$$

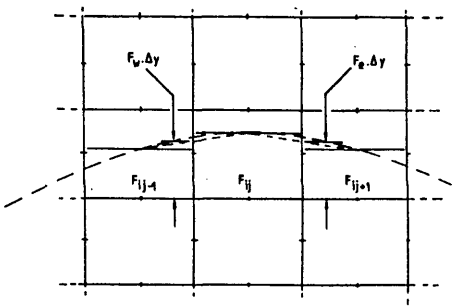

Figure 5-7 a Simple Averaging Scheme.
Equations 5.1/13 & 14

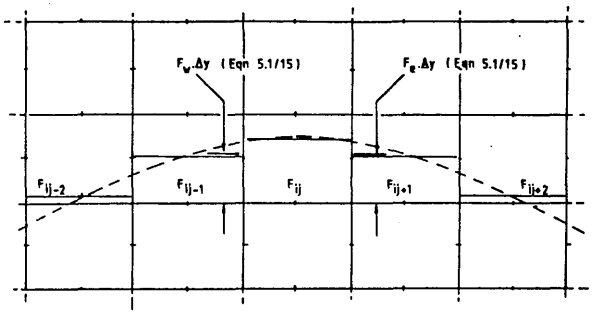

Figure 5-7 b "Simpson's Second Rule" Averaging Scheme.
Equations 5.1/15 & 16

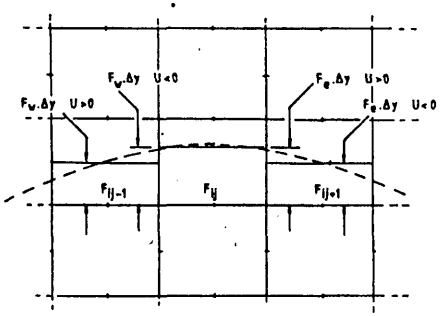

Figure 5-7 c Donor/Acceptor Cell Scheme.
Equations 5.1/17 & 18

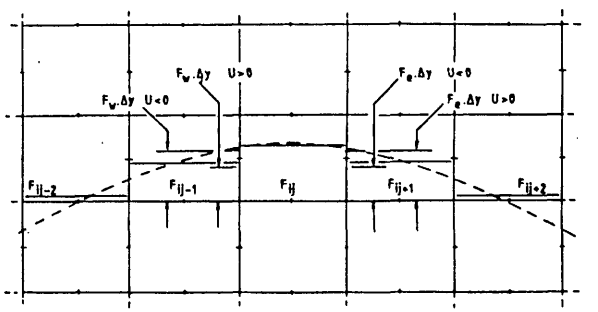

Figure 5-7 d "Simpson's First Rule" Averaging Scheme.
Equations 5.1/19 & 20

$$F_E = F_{ij} \qquad U_{ij+1} > 0$$

$$F_E = F_{ij+1} \qquad U_{ij+1} < 0$$

---5.1/17

which leads to the fully upwind scheme:-

$$\frac{\partial F}{\partial x} \quad \frac{F_{ij} - F_{ij-1}}{\Delta x} \qquad U_{ij}, U_{ij+1} > 0$$

$$\frac{\partial F}{\partial x} \quad \frac{F_{ij+1} - F_{ij}}{\Delta x} \qquad U_{ij}\, U_{ij+1} > 0$$

--- 5.1/18

d. Simpson's 'First Rule' Averaging (figure 5-7(d)):-

$$F_W = (F_{ij-2} + 4F_{ij-1} + F_{ij})/6 \qquad U_{ij} > 0$$

$$F_W = (F_{ij-1} + 4F_{ij} + F_{ij+1})/6 \qquad U_{ij} < 0$$

$$F_E = (F_{ij-1} + 4F_{ij} + F_{ij+1})/6 \qquad U_{ij} > 0$$

$$F_E = (F_{ij} + 4F_{ij+1} + F_{ij+2})/6 \qquad U_{ij} < 0$$

---5.1/19

giving the following formula for $\partial F/\partial x$ as a sum of weighted, central and upwind schemes:-

$$\frac{\partial F}{\partial x} = \frac{1}{3}\frac{F_{ij} - F_{ij-2}}{2\Delta x} + \frac{1}{3}\frac{F_{ij+1} - F_{ij-1}}{2\Delta x} + \frac{1}{3}\frac{F_{ij} - F_{ij-1}}{\Delta x}$$

$$U_{ij}, U_{ij+1} > 0$$

$$\frac{\partial F}{\partial x} = \frac{1}{3}\frac{F_{ij+1} - F_{ij-1}}{2\Delta x} + \frac{1}{3}\frac{F_{ij+2} - F_{ij}}{2\Delta x} + \frac{1}{3}\frac{F_{ij+1} - F_{ij}}{\Delta x}$$

$$U_{ij}, U_{ij+1} > 0$$

---5.1/20

The ability to form equivalent finite difference rules from the various averaging schemes leads to a reverse formulation from which, known high order finite difference formula (eg QUICK schemes (123)), may be set up in terms of the simple volume fluxing process used herein for free-surface tracking. One of the test examples reviewed in chapter 8 and reported in (137) gave the

opportunity to study the evolution of the free surface shape as a pure convection problem.

It was found that the correction term 5.1/8 had no effect on the centrally differenced schemes, which remained in their original form on its addition. However, upwind schemes did require these extra terms in order to maintain the analogy between the non-conservative and fully conservative forms of 5.1/4.

The above brief analysis has shown how a simple method of updating fluid cell volumes via a sum of fractional increments may be used to model equation 5.1/4. The model is not restricted to near horizontal free surfaces since the relationship:-

$$\frac{\partial \xi}{\partial t} = U_f - V_f \frac{\partial \xi}{\partial x} \qquad \text{---5.1/21}$$

where ξ is the horizontal co-ordinate of the free surface

may be used where the free surface is near vertical and is modelled by the equation (see figure 5-8):-

$$\Delta F = \Delta t \left(\frac{U_W}{\Delta x} - \frac{F_N V_N - F_S V_S}{\Delta y} \right) \qquad \text{---5.1/22}$$

where the magnitude of the free surface slope is approximately unity the model equation:-

$$\Delta F = \Delta t \left(\frac{F_W U_W \quad F_E U_E}{\Delta x} + \frac{F_N V_N \quad F_S V_S}{\Delta y} \right) \qquad \text{---5.1/23}$$

may be applied.

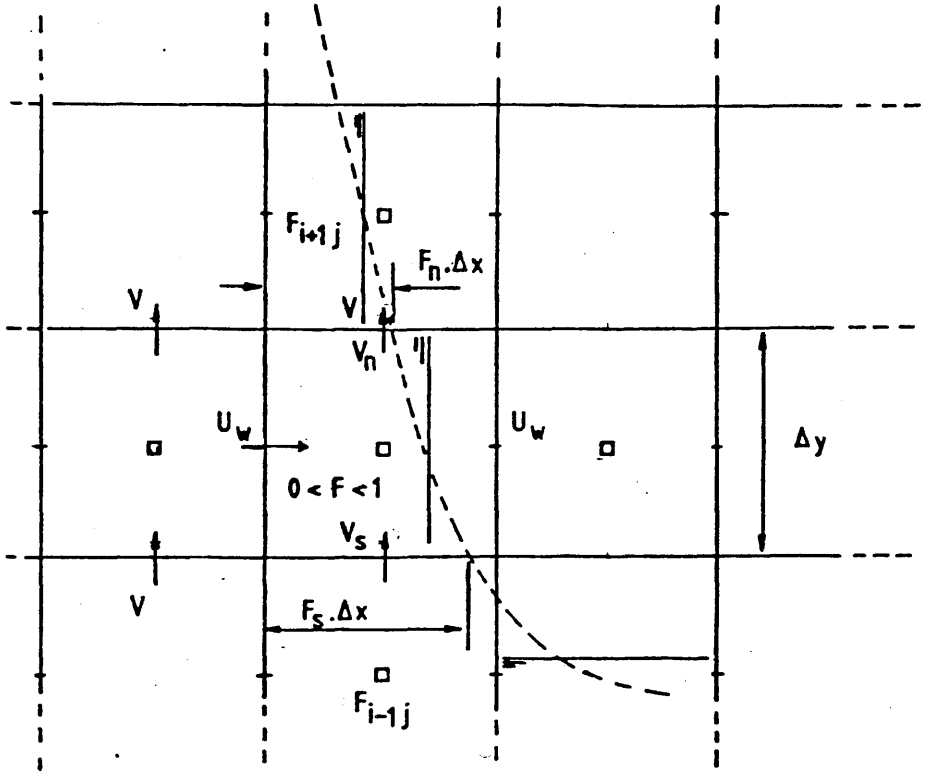

Figure 5-8 Convection Of Fractional Volume For A Steep Free Surface

2. ANCILLARY BOOK KEEPING VARIABLES

The purpose of the book keeping routines were twofold:-

a. To define the main computational domain.

b. To define the areas where boundary conditions were to be applied.

A number of variable types had to be established, principally the fluid fractional volume was used to define the computational domain. It was also found useful to assign an equivalent body fractional volume, to denote the areas of the mesh enclosed by the body contour.

Four more type variables were specified on the basis of the numerical analysis of the fluid and body fractional volumes. Fortran 77 character variables were employed, primarily for their ease of interpretation during program development. These variables are defined in table (5-A).

TABLE OF VARIABLES

Fortran Name	String Length	Responses	Comments
PTYPE	4	'FULL'	F = 1
		'SURF'	0 < F < 1
		'EMTY'	F = 0
BODYP	2	'PS'	FB = 1
		'YS'	0 < FB < 1
		'NO'	FB = 0
INP (INU,INV)	2	'YS'	Node within Fluid
		'NO'	Node outside Fluid
		'BD'	Node within body contour
NEWU/NEWV (NEWP)	2 2	'YS' 'NO'	Checks whether nodes have been updated or need to be updated

Table (5-A)

The PTYPE variable was used for clarity in defining full, free surface and empty cells. It is more consistent to rely on character variables, owing to the finite errors inherent in the use of real numbers on a computer.

The BODYP variable was used to define which nodes are outside ('NO') or within ('PS') the body, and those cells which contain a proportion of the body contour ('YS'). It is the cells for which BODYP = 'YS' which have non-zero source terms in the continuity and SOLA routines.

The INP character variable denotes whether a cell centre pressure node is within the fluid ('YS'), outside the free surface ('NO') or within the body contour ('BD'). Only nodes with INP = 'YS' take part in the SOLA, or SOR routines for pressures. A similar variable exists for each of the velocity component nodes. Thus only when INU = 'YS' or INV = 'YS' do these nodes get updated during the Navier Stokes marching steps.

The NEWU/NEWV character variables, in combination with the INU/INV variables, check on which nodes have been updated, or those which need updating. For example, after moving the free surface, a u node may become covered, ie INU = 'YS'. The NEWU variable will still be set to 'NO' from the previous time step, signifying that the normal updating process cannot be applied to this variable. A new value will be given to this node by interpolation from surrounding u values prior to the next Navier Stokes updating step.

Another example is where a node becomes uncovered, ie INU = 'NO'. The variable NEWU will be changed from 'YS' to 'NO' signifying that this node requires a value to be applied using the boundary conditions detailed in 4.7. As these boundary conditions are computed, the NEWU value is set to 'YS', in order that the sequential process described in 4.7 may be applied without duplication occurring.

Further combinations may be made when applying boundary conditions at the moving body. Any node passed by the body contour during one time step, will have its INP variable changed from 'YS' to 'BD' and NEWP from 'YS' to 'NO'. All nodes with INP = 'BD' and NEWP = 'NO' may then be used as dummy variables with values set by extrapolation from within the flow field as required.

One interesting combination is that of PTYPE = 'SURF' and BODYP = 'YS', which denotes the cells representing the fluid spray root. Primarily these are surface cells within which the dynamic pressure is set to zero. The BODYP = 'YS' condition indicates that the free surface fluxing routine must take account of the reduced cell volume, (owing to the encroachment of the body) and the net increase of flux caused by the source representing the body motion.

Table (5-B) illustrates all of the possible states and combinations of book-keeping variables that may arise during a simulation and their subsequent effect on the computation.

3. METHODS TO DEFINE BODY SHAPE

A tehnique was required to define the contour of the body section. The method had to be compatible with the mesh co-ordinate system and provide an easy description of the body motions. The routine had to allow the rapid computation of source strengths and the assignment of values to the book-keeping variables detailed in the previous section.

It proved necessary to establish the body fractional volume FB, analogues to the fluid fractional volume, to model the body shape on the finite difference mesh. It has already been shown in tables (5A) and (5B), how the body fractional volume was used in association with the book keeping character variables. It is also easily seen that the source strengths may be calculated from the rase of change of body fractional volume, ie:-

$$Q_{ij} = \Delta x \Delta y \left(\frac{\partial FB}{\partial t} \right)_{ij} \qquad \text{---} 5.3/1$$

There were three choices for the method to describe the body shape. The first was applied to simple contours, such as flat bodies and wedges. The extent of the body could be defined as lying within straight lines given by the expression:-

$$y = M (x - X_g) + (Y_g - C) \qquad \text{---} 5.3/2$$

where M is the deadrise gradient and (Xg, Yg) are the co-ordinates of the centre of gravity. (See figure 5-9).

The second technique was to 'discretise' the above method for

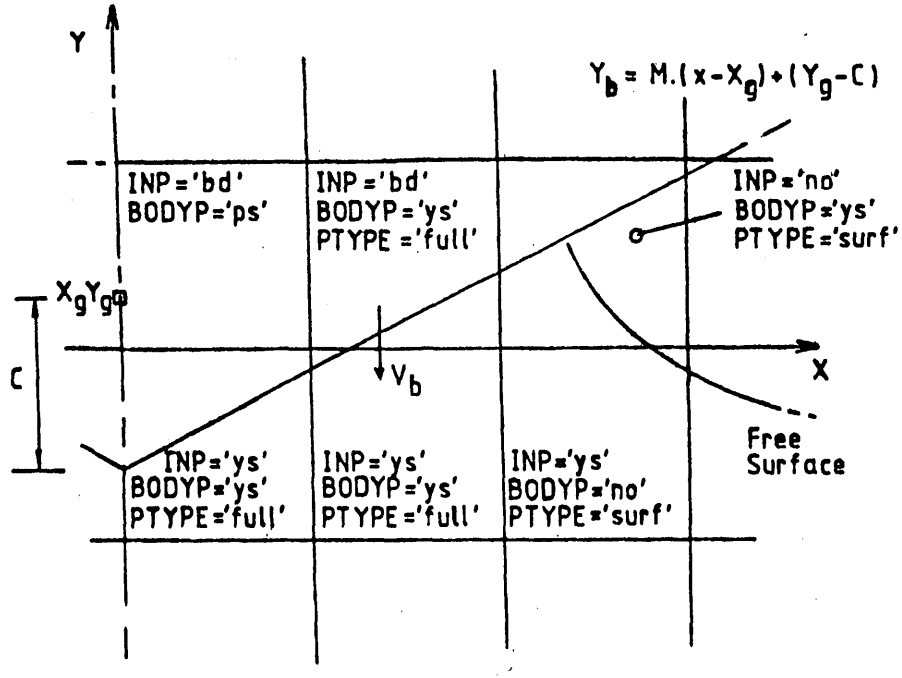

Figure 5.9 Wedge Geometry On F.D Mesh

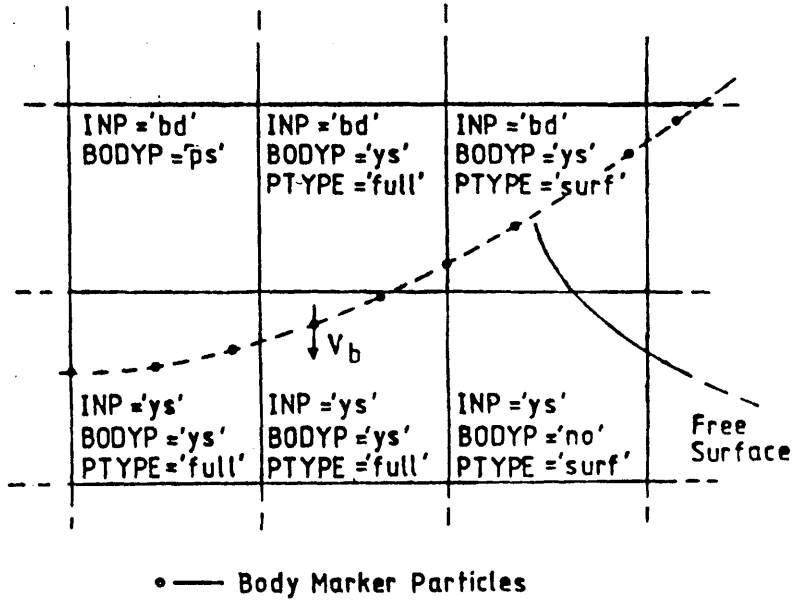

Figure 5.10 Definition Of Body Shape By Marker Particles

more complicated shapes. The contour was represented by a series of marker particles, joined by straight lines. An elaborate computational procedure was required to calculate the body fractional volume of each cell whose sides were cut by lines joining the particles, see figure (5-10).

The third method was to find a mathematical expression for the body fractional volume based on the contour shape. The function would need to be truncated at zero and unity, and be differentiable in the x and y co-ordinate directions.

With the first technique, the body fractional volumes were found by geometrical considerations as shown in figure (5-9). The source strengths were given by the finite difference formula:-

$$Q_{ij}^{n} = \Delta x \, \Delta y \, (FB_{ij}^{n+1} - FB_{ij}^{n}) / \Delta t \qquad \text{---} 5.3/3$$

With the second method, an increase in FB owing to the area of the arc segment for a forward section had to be taken into account. The calculation of the source strength in the cell could be made in two ways. The first method was to apply equation 5.3/2 as before, and relied upon an accurate computation of body fractional volume. An alternative was to consider each marker particle to represent a single source, such that:-

$$Q_p = (U_b \text{SIN}\,\theta - V_b \text{COS}\,\theta)\, h \qquad 5.3/4$$

where Q_p particle source strength

h length of arc segment associated with the marker particle

θ contour gradient.

The total source strength in each cell was then given by the summation of source values Q in each cell. In this way, the body fractional volume could also be computed on a time simulation basis.

The third method used the convection equation:-

$$\frac{\partial FB}{\partial t} \quad U_b \frac{\partial FB}{\partial x} + V_b \frac{\partial FB}{\partial y} = 0 \qquad \text{---53/5}$$

to calculate the rate of change of body fractional volume for use in equation 5.3/1. If a vertical co-ordinate represents the value of FB, it can be shown that, for a circular contour (radius R), the function may be given by a truncated cone, of gradient 1/h, ($\Delta x = \Delta y = h$). The required function is therefore:-

$$f(x,y) = (R - r)/h \qquad r^2 = (x - X_g)^2 + (y - Y_g)^2$$

with limits

$$f(x,y) < 0 \quad , \quad FB = 0$$

$$0 < f(x,y) < 1 \quad , \quad FB = f(x,y)$$

$$f(x,y) > 1 \quad , \quad FB = 1$$

Thus for cells where BODYP = 'YS', the gradients $\partial(FB)/\partial x$ may be evaluated easily and substituted into 5.3/3.

In practice, it was difficult to find such functions for other shapes of section, and to extend the method for use on rectangular meshes. For the case of a circle, however, it did provide an elegant procedure for the evaluation of source strengths.

The first two techniques were most heavily used despite the more cumbersome computer coding required. There was little effect on the overall computing time, as this was mainly governed by the

equation solving routines for continuity and pressure.

Pure source/sink distributions were, for some time, considered as candidates in the representation of the body contour. Some of the computational experiments shown in chapter 8 illustrate an attempt to model free-slip boundaries usng an arrangement of sources and sinks in a uniform flow. Whilst this was successful in itself, the difficulty of finding the correct source strengths and distributions eliminated this technique from consideration for the slamming problem.

The assigning of the value 'BD' to the book-keeping variables INP, INU, INV was achieved by consideration of the geometry of the section. Checks were confined to those nodes within the range of beam and total height about the centre of the body. For the case of a circular contour, INU equalled 'BD' if the distance from the node to the circle centre was less than its radius. Similar algorithms for other shapes of body were easily formulated.

There are two possible approaches to assigning values to the book-keeping variables subject to the degree of distortion in the free surface shape. If it is envisaged that, during the simulation the magnitude of the free surface slope will not exceed the mesh aspect ratio (ie unity for a uniform mesh), then a single height function , may be used. Otherwise, it is possible to use fluid fractional volumes only to perform the decision making processes required.

The free surface height values η were found as the vertical sum of fractional heights as given by equation 5.1/11. If any pressure node was found to be below the free surface, for example:-

$$YP_{ij} < \eta_j$$

where YP_{ij} is the vertical co-ordinate of pressure node (I,J).

Then the value of INP was set to 'YS'. Any pressure nodes above the surface had INP set to 'NO'. The same process was applied to u,v nodes using INU and INV variables. Calculation of the free surface gradient was performed using the finite difference approximation:-

$$\frac{\partial \eta}{\partial x} = \frac{\eta_{j+1} - \eta_{j-1}}{2\Delta x} \qquad ---5.4/1$$

This quantity was continually checked to ensure that the use of the free surface height values was valid. A central difference was selected based on the experience that one sided finite difference operators were too sensitive and could reflect transient instabilities in the free surface shape.

For the general flow modelling problem set by the slamming

simulation the above assumptions were not relied upon. It has already been shown how the PTYPE variable was assigned according to the fluid fractional volume of the cell. By assuming the free surface to be locally represented by a straight line from one cell side to the next, it can be seen that, for any geometry, the following conditions may be applied

$$0 \leqslant F_{ij} < 0{\cdot}5 \qquad \text{INP} = \text{'NO'}$$

$$0{\cdot}5 \leqslant F_{ij} \leqslant 1{\cdot}0 \qquad \text{INP} = \text{'YS'}$$

This method of deciding whether a point is outside or within the fluid domain may also be applied to the u and v nodes by averaging the fractional volumes across a cell side, ie:-

$$0 \leqslant \frac{F_{ij} + F_{ij-1}}{2} < 0{\cdot}5 \qquad \text{INU} = \text{'NO'}$$

$$0{\cdot}5 \leqslant \frac{F_{ij} + F_{ij-1}}{2} \leqslant 1{\cdot}0 \qquad \text{INU} = \text{'YS'}$$

$$0 \leqslant \frac{F_{ij} + F_{i-1j}}{2} < 0{\cdot}5 \qquad \text{INV} = \text{'NO'}$$

$$0{\cdot}5 \leqslant \frac{F_{ij} + F_{i-1j}}{2} \leqslant 1{\cdot}0 \qquad \text{INV} = \text{'YS'}$$

In this way any free surface geometry may be modelled.

CHAPTER 6

THE VARIATIONAL ENERGY METHOD

CHAPTER 6

THE VARIATIONAL ENERGY METHOD

1. INTRODUCTION

The following chapter is devoted to a variational method used to restrict the total energy in the discretised model to the limits imposed by the physics of the problem. This technique was particularly useful when applied to the slightly compressible fluid model. From a practical computational standpoint, limiting the energy of the system removed many of the problems associated with numerical stability. In this way, fewer iterations were required for the continuity solver and it was found that the reputedly unstable central differencing schemes for convection operators could be retained. Since the usual 'cure' for this latter problem was to impose an unphysical, numerical viscosity by virtue of upwinded convection operators, the variational energy algorithm was of considerable use.

The technique used herein was inspired by the work of Sasaki (138) on the shallow water equations. Details of this author's approach may also be found in (139), a paper presented at the third international conference on Numerical Methods in Laminar and Turbulent Flow, Seattle, 1983. The basis of the method is to restrict the difference between the 'correct' discrete solution and the approximate solution, to the difference in the energy between the approximate solution and the real physical system. The main source of the errors is assumed to be caused by truncation of finite difference operators.

A simple, illustrative example will be given below, before the more complex techniques are described.

2. VARIATIONAL METHOD APPLIED TO KINETIC ENERGY ALONE

Consider the discrete solution for velocity components in a fluid problem to be given by (u, v), with an approximate solution given by $(\hat{u}, \hat{v})$. No work is done on the system, the flow is incompressible and there is no free surface. The following variational statement may be made:-

$$J = \sum [\alpha(u - \hat{u})^2 + \alpha(v - \hat{v})^2]\Delta x\,\Delta y + \lambda\left(\sum \left[\frac{1}{2}\rho(u^2 + v^2)\right]\Delta x\,\Delta y - KI\right) \quad \text{---6.2/1}$$

where α represents an unknown weighting function

λ Lagrange multiplier

KI initial kinetic energy of the fluid

$\sum$ summation over all fluid nodes.

Differentiating 6.2/1 leads to the expression:-

$$\delta J = \sum [2\alpha(u-\hat{u})\delta u \; 2\alpha(v-\hat{v})\delta v]\Delta x\Delta y + \delta\lambda\left(\sum\left[\frac{1}{2}\rho(u^2 + v^2)\right]\Delta x\Delta y - KI\right) + \lambda\left(\sum\rho[u\,\delta u + v\delta v]\right)\Delta x\Delta y \quad \text{---6.2/2}$$

re-arranging 6.2/2 yields:-

$$\delta J = \sum [2\alpha u - 2\alpha\hat{u} + \lambda\rho u]\delta u\,\Delta x\Delta y + \sum [2\alpha v - 2\alpha\hat{v} + \lambda\rho v]\delta v\,\Delta x\Delta y + \left(\sum\left[\frac{1}{2}\rho(u^2+v^2)\right]\Delta x\Delta y - KI\right)\delta\lambda \quad \text{---6.2/3}$$

Equating δJ to zero requires each bracketed term to be individually set to zero, yielding the following Euler Lagrange equations:-

$$U = \frac{2\alpha \hat{U}}{2\alpha + \rho\lambda} = X\hat{U} \qquad \text{---6.2/4}$$

$$V = \frac{2\alpha \hat{V}}{2\alpha + \rho\lambda} = X\hat{V} \qquad \text{---6.2/5}$$

$$\sum \rho \frac{U^2 + V^2}{2} \Delta x \Delta y = KI \qquad \text{---6.2/6}$$

Where X is the fractional adjustment rate, equating the ideal discrete solution to the approximate value. X is taken to be identical for both (u) and (v) components as their truncation errors are of the same order for a square mesh. Substitution of 6.2/4 and 6.2/5 into 6.2/6. yields an expression for the fractional adjustment rate as:-

$$X^2 = \frac{KI}{\sum \frac{1}{2}\rho(\hat{U}^2 + \hat{V}^2)\Delta x \Delta y} \qquad \text{---6.2/7}$$

Several effects on the solution and its stability may be noted. Firstly, if the numerical scheme is tending towards instability, the value of the denominator will become greater than KI, hence X will be less than unity. Not only will this reduce the velocity field, but it will also reduce the fluid divergence, ie:-

$$\nabla . X\bar{U} = X\nabla . \bar{U} < \nabla . \bar{U} \quad \text{For} \quad X < 1 \qquad \text{---6.2/8}$$

It has been previously stated that the convergence characteristics for the continuity solver and SOLA code are exponential in nature. If the error in the velocity field is

considered to be composed of a number of Fourrier components, it can be shown that (131) the convergence rate is dependent upon the error wavelength to mesh size ratio. Error components with wavelengths close to the mesh spacing will be rapidly smoothed. Those errors with wavelengths close to the global size of the domain will be difficult to eliminate. This logic is the basis of the Multilevel Adaptive Techniques of Brandt (140), Hackbush (141) etc. in which a series of meshes of different size are used to remove the various error components. However, the Multilevel techniques become difficult to code on the complex and time dependent domain shapes encountered during the computer simulations described in this thesis.

The energy method described above, also provides an efficient way of removing global error components. The combination of relaxation and variational techniques provides fast, simple and numerically stable solution algorithms without recourse to the Multilevel techniques mentioned above.

3. APPLICATION TO SLAMMING PROBLEM

In application of this technique to the simulation of a hydrodynamic impact, consideration of a number of extra sources of energy had to be made. Primarily, the fluid potential energy, as calculated from free surface heights had to be considered. Since this quantity is linearly proportional to the height of the free surface, it could not be directly included into the variational scheme.

The free surface height was considered to be given accurately by the fluxing technique. The result was that the value of KI had to be adjusted at each application of the variational method. For the simplest case, equation 6.2/7 became:-

$$X^2 \quad \frac{KI - \sum \rho . g . \eta \Delta x}{\sum \frac{1}{2} \rho (\hat{U}^2 + \hat{V}^2) \Delta x \Delta y} \qquad \text{---} 6.3/1$$

derived from equation 5.1/11.

In the general slamming problem, KI represents the change in kinetic energy of the body, and varies throughout the simulation to take account of the work done on the system, thus:-

$$KI^n = KI^0 + \int_0^{n\Delta t} F_b(t) . V_b(t) \, dt \qquad \text{---} 6.3/2$$

where $F_b(t)$: Force time history on body.

$V_b(t)$: Velocity time history of body

There were two cases to be examined, the forced motion problem and the free fall problem.

The first of these two situations is perhaps the most realistic in terms of examining ship slamming. The body is assumed to have a known velocity time history, for example, many analytical methods of examining water entry use constant velocity. The work done by the body on the flow is calculated from the fluid loading time history acting on the section.

The free fall simulation requires a fully interactive model of the impact. The kinetic energy of the body is reduced by the loading on it caused by the fluid and increased by its change of gravitational potential energy during descent. In either of these two cases, the change in kinetic energy of the body at each time step may be computed. For an incompressible fluid, the aim of such a computation is to find the amount of energy to be assigned to fluid kinetics only.

For the case of the nearly incompressible flow used for heavy impact simulations, a certain amount of potential energy is stored by local fluid compression. Here, however, it is possible to include this quantity in the variational procedure. The strain energy stored in the fluid may be expressed as:-

$$E_s = \int_R \frac{1}{2} B \left(\frac{\Delta\rho}{\rho}\right)^2 dR \qquad \text{---6.3/3}$$

where B is the fluid bulk modulus.

This quantity can now be included in equation 6.2/1. The change in density may be computed as illustrated in section 4.11. In this procedure, it is important to note that the of equation

6.3/3 is the total change in fluid density, whereas the time marching method computes only the variation from one time step to the next. Thus, having completed the energy balance for one instant, the total fluid strain energy must be assigned to the 'catch-all' term KI , since the variational procedure works only with discrete changes in fluid density.

Equation 6.2/1 may therefore be re-written as:-

$$J = \sum[\alpha(u-\hat{u})^2 + \alpha(v-\hat{v})^2 + \beta(\Delta\rho - \Delta\hat{\rho})^2]\Delta x\Delta y + \lambda(\sum[\frac{1}{2}\rho(u^2+v^2) + \frac{1}{2}B(\frac{\Delta\rho}{\rho})^2]\Delta x\Delta y - KI) \quad \text{---6.3/4}$$

which, after manipulation similar to that applied to equation 6.2/1 yields:-

$$U = \frac{2\alpha\hat{u}}{2\alpha+\rho\lambda} \qquad V = \frac{2\alpha\hat{v}}{2\alpha+\rho\lambda} \quad \text{---6.3/5}$$

$$\Delta\rho = \frac{2\beta\Delta\hat{\rho}}{2\beta+\lambda B/\rho^2} \quad \text{---6.3/6}$$

$$\sum[\frac{1}{2}\rho(u^2+v^2) + \frac{1}{2}B(\frac{\Delta\rho}{\rho})]\Delta x\Delta y = KI \quad \text{---6.3/7}$$

where KI has to be updated to take account of:-

a. Work done on the fluid by the body or loss of potential energy by the body in free fall,

b. Changes in fluid potential energy,

c. Accumulated changes in fluid strain energy.

The use of the variational energy method had definite

attractions in the modelling of heavy impacts involving fluid compressibility. In particular, the constraints of pure hydrodynamic theory, wherein for the initial instant of contact infinite fluid pressures are generated, are removed. Further, a link is provided between two distinct models of fluid behaviour. It can be seen that equations 6.3/5 and 6.3/6 may again be expressed as simple relationships:-

$$U = X_u \hat{U} \qquad V = X_u \hat{V} \qquad \Delta\rho = X_\rho \Delta\hat{\rho} \qquad \text{---6.3/8}$$

The association between X_u and X_ρ depends upon the ratio of truncation errors used in updating the velocity and density fields, and is expressed by the relationship between the weights α, β .

For $X_u = X_\rho$, ie truncation errors assumed to be of equal order, then:-

$$\frac{\alpha}{\beta} = \frac{B}{\rho^3} \qquad \text{---6.3/9}$$

which for water of bulk modulus 1.99×10^9 N/m^2 gives:-

$$\alpha \approx 2\beta \qquad \text{---6.3/10}$$

Numerical experiments were conducted wherein the ratio $X_u : X_\rho$ was varied according to the truncation errors. If for example, $X_u : X_\rho$ is taken as 2:1, then substitution of 6.3/8 into 6.3/7 yields:-

$$X_\rho^2 = \frac{KI}{\sum 2\rho(\hat{U}^2 + \hat{V}^2)\,\Delta x \Delta y + \sum \frac{1}{2}(B/\rho^2)\,\Delta\hat{\rho}^2\,\Delta x \Delta y} \qquad \text{---6.3/11}$$

Since manipulating the ratio $X_u:X_\rho$ does not usually lead to the convenient relationship given by 6.3/9, numerical experiment is the best way to evaluate the effect of relationships such as given by 6.3/11.

It will be noted that the density ρ appears as a constant throughout the above analysis despite being a variable in the main part of the time marching routine. As implied by the form of Navier Stokes equations used (section 3.7), the changes in fluid density are very small. It was assumed that the exclusion of as a variable in the variational energy method would have little effect upon the overall algorithm.

As a precaution however, equation 6.3/4 was re-arranged such that the spatial variation in density could be included. The result of this formulation is a polynomial expression for the fractional adjustment rate X, ($X_u = X_\rho = X$), given by (139).

$$PX^3 + QX^2 + RX - KI = 0 \qquad \text{---6.3/12}$$

where P is the perturbed kinetic energy of the fluid caused by change in density.

Q Fluid kinetic plus strain energy

R Perturbed potential energy of the fluid caused by the change in density.

The roots of the equation were found by Mueller's method.

The final stage in the development of the variational model was to include the kinetic energy of the body itself. This was done

for both the incompressible and partially compressible fluid models. However, the inclusion of the body kinetic energy could only be made for the drop test type of simulation as the body velocity was not considered as a variable in the forced impact case. The major advantage was perceived to be the elimination of the error involved in integrating the pressures over the body in order to calculate the loading, and hence work done on the fluid by the falling body. Equation 6.2/1 becomes:-

$$J = \sum\left(\left[\alpha(u - \hat{u})^2 + \alpha(v - \hat{v})^2 \right] \Delta x \Delta y + \gamma(V_b - \hat{V}_b) \right)$$

$$+ \lambda\left(\sum\left[\frac{1}{2} \rho(u^2 + v^2) \right] \Delta x \Delta y + \frac{1}{2} M_b V_b^2 - KI \right)$$

---6.3/13

leading to the Euler Lagrange equations:-

$$U = \frac{2\alpha \hat{U}}{2\alpha + \lambda\rho} \qquad V = \frac{2\alpha \hat{V}}{2\alpha + \lambda\rho} \qquad ---6.3/14$$

$$V_b = \frac{2\gamma \hat{V}_b}{2\gamma + \lambda M_b} = X_b \qquad ---6.3/15$$

$$\sum\left[\frac{1}{2} \rho(u^2 + v^2) \right] \Delta x \Delta y + \frac{1}{2} M_b V_b^2 = KI \qquad ---6.3/16$$

A relationship between α and γ, the weights for errors in (u), (v) and body velocity respectively cannot be easily seen. They should both be of the same order however, though recourse to numerical experiment was required in order to fully understand the relative magnitudes of error involved. The value of KI for this version of the algorithm was nearly constant as it consisted of the sum of the initial kinetic energy and the, slightly varying, fluid potential energy.

The assumption again had to be made that the ratio $X_b : X_u$ was equal to some constant R_b, such that X_u could be derived from:-

$$X_u^2 = \frac{KI}{\sum \frac{1}{2}(\hat{U}^2 + \hat{V}^2)\rho \Delta x \Delta y + R_b^2(\frac{1}{2}M_b V_b^2)} \qquad \text{---} \ 6.3/17$$

and hence X_u could be easily found.

This technique may be further extended to deal with the slightly compressible flow model by adjusting equation 6.3/4 to give:-

$$J = \sum[\alpha(U-\hat{U})^2 + \alpha(V-\hat{V})^2 + \beta(\Delta\rho - \Delta\hat{\rho})^2]\Delta x \Delta y + \delta(V_b - \hat{V}_b)^2$$

$$+ \lambda(\sum[\frac{1}{2}\rho(U^2+V^2) + \frac{1}{2}B(\frac{\Delta\rho}{\rho})^2]\Delta x \Delta y + \frac{1}{2}M_b V_b^2 - KI)$$

$$\text{---} \ 6.3/18$$

which upon application of the variational method yields equations 6.3/5, 6.3/6 and 6.3/15, with an additional energy balance given by:-

$$\sum[\frac{1}{2}\rho(U^2+V^2) + \frac{1}{2}B(\frac{\Delta\rho}{\rho})^2]\Delta x \Delta y + \frac{1}{2}M_b V_b^2 = KI$$

$$\text{---} \ 6.3/19$$

by assuming the respective fractional adjustment rates to be in the ratios:-

$$X_\rho : X_u = R_\rho \qquad X_b : X_u = R_b$$

the formula for X_u:

$$X_u^2 \quad \frac{KI}{\sum[\frac{1}{2}\rho(\hat{U}^2+\hat{V}^2) + \frac{1}{2}R_\rho^2 B(\frac{\Delta\rho}{\rho})^2] + \frac{1}{2}M_b(R_b V_b)^2} \qquad \text{---} \ 6.3/20$$

is obtained. Again, the relative sizes of $R\rho$, R_b are best found by numerical experiment. Most computations began by using $R\rho = R_b = 1$ as a first guess. However, no matter what values were chosen, the

computational schemes always satisfied energy conservation and thus were numerically stable.

4. APPLICATION TO COMPUTER CODING

The variational energy balance algorithm fitted into the general simulation coding as a subroutine, applied after continuity had been solved, but before dynamic pressures were calculated. If the method had been utilised after the modified SOLA calculation, this would have implied a global error in the dynamic pressure field. In any case, the technique was used only to correct for errors in the time marching process and it was found unnecessary to apply the method at every time step, unless the body velocity was included as a major variable.

CHAPTER 7

AIR ENTRAPMENT MODELS

CHAPTER 7

AIR ENTRAPMENT MODELS

1. TWO DIMENSIONAL SIMULATION

The one dimensional finite difference 'grid' used in this calculation is shown in figure 7-1. The main computational domain ends at the corners (chines) of the body. The two end points provide the boundary values for the computation. The size of the domain was restricted in this way for the sake of computational efficiency. Both Verhagen (35), Lewison and MacLean (36) and, Koehler and Kettleborough (49) used this idea successfully. However, Johnson (37,38) included the area around the body in his model which resulted in a noticeably less efficient routine.

The discretisation of the equations for the trapped air layer given in section 3.8, was performed using the usual finite difference operators as detailed in section 4.4. The computational cycle proceeded as follows. The rate of change of distance (h) between body and free surface was computed first using equation 3.8/4, ie:-

$$\frac{\delta h}{\delta t} = V_b - \frac{\eta^n - \eta^{n-1}}{\Delta t} \qquad \text{---7.7/1}$$

The next step was to update the velocity u_a, using a backward time step formula applied to equation 3.8/3. The convection term could be discretised using either a central or upwinded operator. The mesh arrangement was such that the pressure gradient could be represented most easily by a central difference formula. Thus a fully central scheme could be derived giving:-

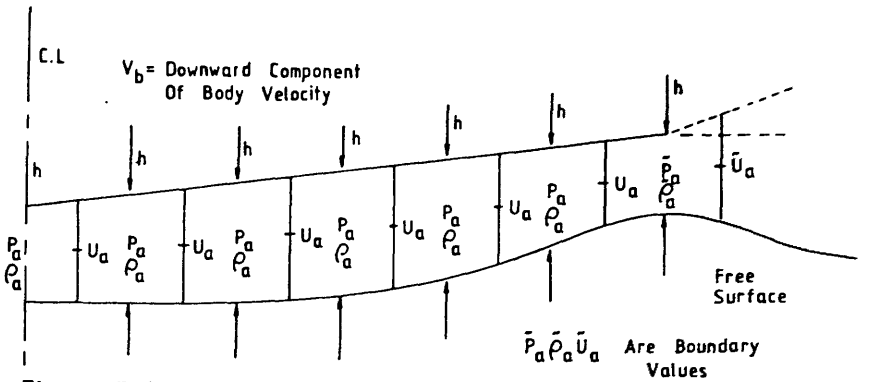

Figure 7-1

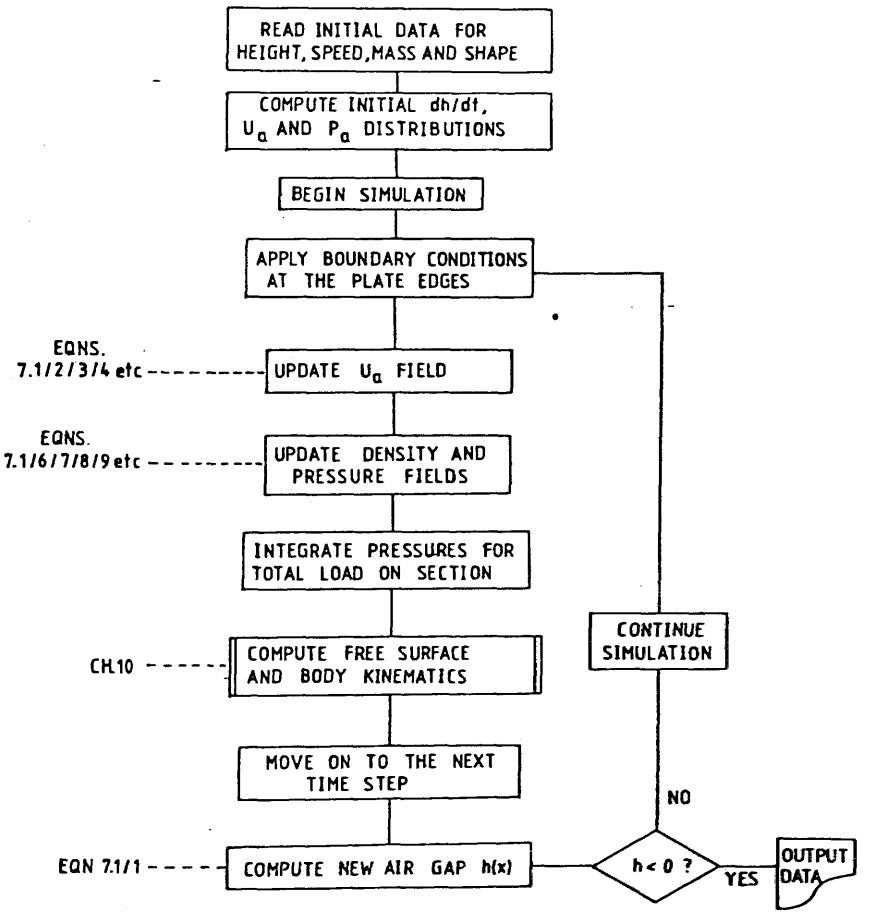

Figure 7-2

$$U_{aj}^{n} = U_{aj}^{n-1} - \frac{\Delta t}{2\Delta x} U_{aj}^{n-1}\left(U_{aj+1}^{n-1} - U_{aj-1}^{n-1}\right) - \frac{\Delta t}{\Delta x \bar{\rho}_{aj}^{n-1}}\left(P_{aj}^{n-1} - P_{aj-1}^{n-1}\right)$$

where $\bar{\rho}_{aj}$ is a mean density at node j 7.1/2

An upwinded formulation for the convection terms resulted in two equations for u_a, ie:-

$$U_{aj}^{n} = U_{aj}^{n-1} - \frac{\Delta t}{\Delta x} U_{aj}^{n-1}\left(U_{aj}^{n-1} - U_{aj-1}^{n-1}\right) - \frac{\Delta t}{\Delta x \rho_{aj}^{n-1}}\left(P_{aj}^{n-1} - P_{aj-1}^{n-1}\right)$$

$$U_{aj} > 0 \qquad \text{---} 7.1/3a$$

$$U_{aj}^{n} = U_{aj}^{n-1} - \frac{\Delta t}{\Delta x} U_{aj}^{n-1}\left(U_{aj+1}^{n-1} - U_{aj}^{n-1}\right) - \frac{\Delta t}{\Delta x \rho_{aj}^{n-1}}\left(P_{aj}^{n-1} - P_{aj-1}^{n-1}\right)$$

$$U_{aj} < 0 \qquad \text{---} 7.1/3b$$

It was also possible to combine a leapfrog time marching method with either of the central or upwind convection schemes. For example:-

$$U_{a}^{n} = U_{a}^{n-1} - \frac{\Delta t U_{aj}^{n-1}}{\Delta x}\left(U_{aj+1}^{n-1} - U_{aj-1}^{n-1}\right) - \frac{2\Delta t}{\Delta x \rho_{aj}^{n-1}}\left(P_{aj}^{n-1} - P_{aj-1}^{n-1}\right) \qquad \text{---} 7.1/4$$

represents a leapfrog/central difference formulation.

It will be noted that the explicit schemes shown above use data on the right hand side from t = (n-1)Δt. This can be explained by examining the role of the air entrapment calculation within the full computational routine. The air pressures and flow velocities are always calculated on a domain of known shape. Therefore, as this can only arise after the free surface has been moved, the updating procedure needs to be retrospective, as opposed to the predictive character of the Navier Stokes solvers.

Having calculated the new velocity field, the fluid densities and pressures were updated. Equation 3.8/2 was re-written in the form

$$h\frac{\partial \rho_a}{\partial t} + \rho_a \frac{\partial h}{\partial t} = -\rho_a u_a \frac{\partial h}{\partial x} - h u_a \frac{\partial \rho_a}{\partial x} - h \rho_a \frac{\partial u_a}{\partial x} \qquad \text{---7.1/5}$$

A backward time step, central difference discretisation of this equation results in a fully explicit marching formula in ρ_a, ie:-

$$\frac{\rho_{aj}^{n} - \rho_{aj}^{n-1}}{\Delta t} = -\frac{\rho_{aj}^{n-1}}{h_j^{n-1}}\left[\frac{\delta h}{\delta t}_j^{n-1} + \frac{\bar{u}_{aj}^{n-1}}{2\Delta x}\left(h_{j+1}^{n-1} - h_{j-1}^{n-1}\right)\right] - \frac{\bar{u}_{aj}^{n-1}}{2\Delta x}\left(\rho_{aj+1}^{n-1} \; \rho_{aj-1}^{n-1}\right) - \frac{\rho_{aj}^{n-1}}{\Delta x}\left(u_{aj+1}^{n-1} - u_{aj}^{n-1}\right) \qquad \text{---7.1/6}$$

where $\bar{u}_{aj}$ is an average value caculated using data from cell sides (see figure 7-1).

The density may therefore, be updated using:-

$$\rho_{aj}^{n} = \rho_{aj}^{n-1}\left[1 - \frac{\Delta t}{h_j^{n-1}}\left(\frac{\delta h}{\delta t}_j^{n-1} + \frac{u_{aj}^{n-1}}{2\Delta x}\left(h_{j+1}^{n-1} - h_{j-1}^{n-1}\right)\right)\right] - \frac{\bar{u}_{aj}^{n-1}\Delta t}{2\Delta x}\left(\rho_{aj+1}^{n-1} - \rho_{aj+1}^{n-1}\right) - \frac{\rho_{aj}^{n-1}\Delta t}{\Delta x}\left(u_{aj+1}^{n-1} - u_{aj}^{n-1}\right) \qquad \text{---7.1/7}$$

Three alternative formulations were also used. The first applied upwinding to the central derivatives in h and ρ_a (though not to u_a). This results in the following explicit formulae for updating the density field:-

$$\rho_{aj}^{n} = \rho_{aj}^{n-1}\left[1 - \frac{\Delta t}{h_j^{n-1}}\left(\frac{\delta h}{\delta t}_j^{n-1} + \frac{u_{aj}^{n-1}}{\Delta x}\left(h_j^{n-1} - h_{j-1}^{n-1}\right)\right)\right] - \frac{u_{aj}^{n-1}\Delta t}{\Delta x}\left(\rho_{aj}^{n-1} - \rho_{aj-1}^{n-1}\right) - \frac{\rho_{aj}^{n-1}\Delta t}{\Delta x}\left(u_{aj+1}^{n-1} - u_{aj}^{n-1}\right)$$

$$u_{aj} > 0 \qquad \text{---7.1/8a}$$

$$\rho_{aj}^{n} = \rho_{aj}^{n-1}\left[1 - \frac{\Delta t}{h_j^{n-1}}\left(\frac{\delta h}{\delta t}^{n-1} + \frac{\bar{u}_{aj}^{n-1}}{\Delta x}\left(h_{j+1}^{n-1} - h_j^{n-1}\right)\right)\right]$$

$$- \frac{\bar{u}_{aj}^{n-1}\Delta t}{\Delta x}\left(\rho_{aj+1}^{n-1} - \rho_{aj}^{n-1}\right) - \frac{\rho_{aj}^{n-1}\Delta t}{\Delta x}\left(u_{aj+1}^{n-1} - u_{aj}^{n-1}\right)$$

$$u_{aj} < 0 \qquad \text{---} 7.1/8$$

The second possible formulation was to apply central time differencing and central space differencing resulting in:-

$$\rho_{aj}^{n} = \rho_{aj}^{n-2} - \frac{\rho_{aj}^{n-1}\Delta t}{h_j^{n-1}}\left[\frac{\delta h}{\delta t}_j^{n-1} - \frac{\bar{u}_{aj}^{n-1}}{\Delta x}\left(h_{j+1}^{n-1} - h_{j-1}^{n-1}\right)\right]$$

$$- \frac{\bar{u}_{aj}^{n-1}\Delta t}{\Delta x}\left(\rho_{aj+1}^{n-1} - \rho_{aj-1}^{n-1}\right) - \frac{\rho_{aj}^{n-1}\Delta t}{\Delta x}\left(u_{aj+1}^{n-1} - u_{aj}^{n-1}\right)$$

--- 7.1/9

The combination of central time differencing and upwinded first derivatives may also be made. It was also decided to test implicit/explicit schemes, in order to ascertain whether their greater convergence rate when solving steady state problems would lead to improvements in accuracy.

The pressure field was then directly calculated using the identity:-

$$\frac{p_{aj}^{n}}{\rho_{aj}^{n}} = \frac{p_0}{\rho_0} = C_a^2$$

where p_0 , ρ_0 are the initial conditions on pressure and density, atmospheric values being applied in practice.

The pressure value p_a could then be used as a boundary condition in the Poisson pressure solver at section 4.8. In fact, this

value forms part of the dynamic pressure field. However, it proved more convenient to superimpose these boundary conditions on to the steady pressure solver.

A flow chart for this computation is shown in figure 7-2. The initial conditions for the simulation were as follows. The density was set to its atmospheric value, indicating incompressible flow in the air between body and free surface. The velocity distribution was found by consideration of continuity in the air layer. The free surface was consid red horizontal.

Boundary conditions at the edges were easily applied. The flow beyond the chines was considered to be represented by a divergent jet (49) wherein the density was assumed constant. The velocity field in this region was found by application of continuity alone.

Numerical stability in compressible flow simulations governed by the formulations used herein is ensured if the time step is restricted by the Courant-Friedrichs-Lewy criterion based on acoustic wave speed, ie:-

$$C_{FL} = \frac{(|U_a| + C_a)}{\Delta x} \leqslant 1 \qquad \text{---7.1/10}$$

(See references 99,127,130).

In fact, this poses a severe restriction on the overall simulation. Fortunately, this part of the computation was only carried out until the instant of first contact between the body and free surface. This first contact may occur at the centre of the section, as in the case of some wedge shaped bodies, or at the edges resulting in the formation of a trapped air bubble.

The air entrapment program was, at first, considered as a method of supplying initial conditions to the main water entry simulation. At the first time step after initial contact, the air layer would be 'removed' and the air pressure considered as a boundary condition applied upon the body contour. In order to vindicate this model, some measure of the thickness of the air layer at initial contact was required.

Chapter 10 presents the results of some preliminary studies made in order to quantify aspects of the above problem. A potential flow model of fluid behaviour was used because of its simplicity and the ability to perform a full three dimensional simulation of the air entrapment problem within a reasonable computing time.

As reviewed in section 3.8/2, the inclusion of energy conservation in the air entrapment model required the generalised form of the momentum transport equation (3.8/7) and a new equation in energy transport to be discretised. Figure 7-3 shows details of the principle variables and node arrangement for this new model. The one dimensional finite difference 'cell' shown has the velocity nodes placed at cell sides and all other variables, pressure (p_a), density (ρ_a), internal energy (e), total energy (E_s), temperature (T) and acoustic sound speed (C_a) positioned at the cell centre.

Equation 3.8/7 may be re-written in the following form in order to aid the discretisation process.:-

$$\frac{\partial u_a}{\partial t} = -\frac{u_a}{\rho_a}\frac{\partial \rho_a}{\partial t} - \frac{1}{\rho_a}\frac{\partial p_a}{\partial x} - \frac{u_a^2}{\rho_a}\frac{\partial \rho_a}{\partial x} - \frac{\partial (u_a)^2}{\partial x} \qquad \text{---7.2/1}$$

The simplest time marching method used a backward time step, central difference scheme as follows:-

$$\frac{u_{aj}^{n} - u_{aj}^{n-1}}{\Delta t} = -\frac{u_{aj}^{n-1}}{\rho_{aj}^{n-1}}\frac{\Delta \bar{\rho}_{aj}^{n-1}}{\Delta t} - \frac{1}{\bar{\rho}_{aj}^{n-1}}\frac{p_{aj+1}^{n-1} - p_{aj}^{n-1}}{\Delta x} - \frac{(u_{aj}^{n-1})^2}{\bar{\rho}_{aj}^{n}}\frac{\rho_{aj+1}^{n-1} - \rho_{aj}^{n-1}}{\Delta x} - \frac{(u_{aj+1}^{n-1})^2 - (u_{aj-1}^{n-1})^2}{\Delta x} \qquad \text{---7.2/2}$$

where $\bar{\rho}_{aj}$ represents the density at velocity node j as a mean of the densities at nodes $j+\frac{1}{2}$ and $j-\frac{1}{2}$

$\Delta\bar{\rho}_{aj}$ represents the change in mean density at node j from the previous time step.

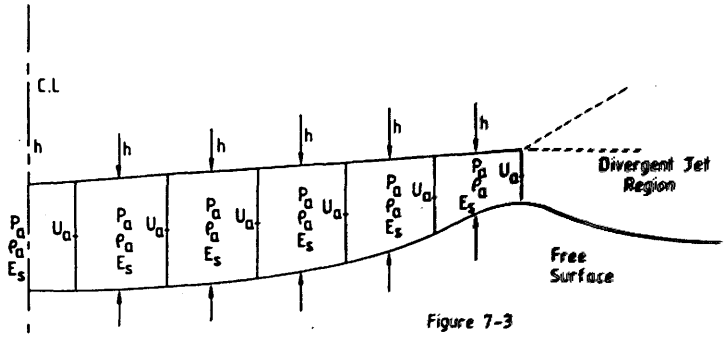

Figure 7-3

Figure 7-4

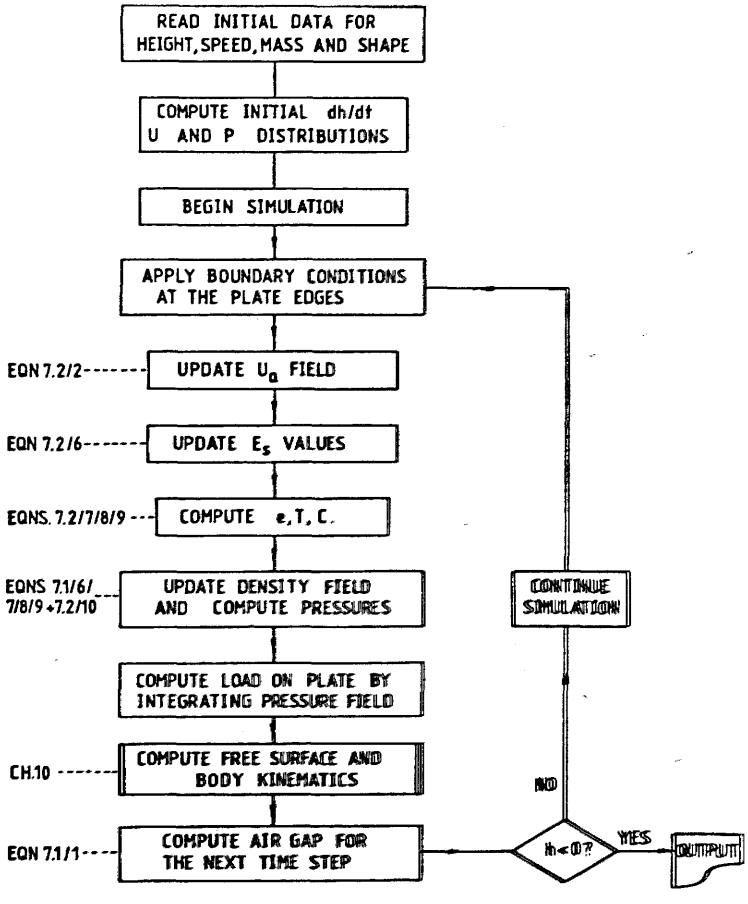

A fully upwinded scheme may be employed by replacing the central difference expression for the velocity gradient, given by the last term in equation 7.2/2 by:-

$$\frac{\partial (u_a)^2}{\partial x} \qquad \frac{(u_{aj})^2 - (u_{aj-1})^2}{\Delta x}$$

$$u_{aj} > 0 \qquad \text{---7.2/3}$$

$$\frac{\partial (u_a)^2}{\partial x} \qquad \frac{(u_{aj+1})^2 - (u_{aj})^2}{\Delta x}$$

$$u_{aj} < 0 \qquad \text{---7.2/4}$$

It is clear that a leapfrog time marching scheme or an implicit/explicit formulation is also possible for these equations.

The energy transport equation was similarly split up into the following form prior to discretisation:-

$$\frac{\partial E_s}{\partial t} = -\frac{E_s}{\rho_a}\frac{\partial \rho_a}{\partial t} - \frac{u_a}{\rho_a}\frac{\partial}{\partial x}(\rho_a E_s) - E_s\frac{\partial u_a}{\partial x} - \frac{p_a}{\rho_a}\frac{\partial u_a}{\partial x} - \frac{u_a}{\rho_a}\frac{\partial p_a}{\partial x}$$

---7.2/5

Variables are grouped together as they appear on the finite difference mesh in order to simplify the finite difference approximations and reduce the need for averaging.

As with the momentum transport equation, a simple backward time step, central difference approximation may be formulated as:-

$$\frac{E_{sj}^{n} - E_{sj}^{n-1}}{\Delta t} = -\frac{E_{sj}^{n-1}}{\rho_{aj}^{n-1}}\frac{\Delta \rho_{aj}^{n-1}}{\Delta t} - \frac{u_{aj}^{n-1}}{\rho_{aj}^{n-1}}\cdot\frac{\rho_{aj+1}^{n-1}E_{sj+1}^{n-1} - \rho_{aj-1}^{n-1}E_{sj-1}^{n-1}}{2\Delta x}$$

$$-\left(E_{sj}^{*} + \frac{p_{aj}^{*}}{\rho_{aj}^{n-1}}\right)\frac{u_{aj+1}^{n-1} - u_{aj}^{n-1}}{\Delta x}$$

$$-\frac{u_{aj}^{n-1}}{\rho_{aj}^{n-1}}\frac{p_{aj+1} - p_{aj-1}}{2\Delta x} \qquad \text{---7.2/6}$$

where

$$E^{*}_{sj} = E^{n-1}_{sj} - E^{o}_{sj}$$

$$p^{*}_{aj} = p^{n-1}_{aj} - p^{o}_{aj}$$

$$E^{o}_{sj} = e^{o}_{j} + -(u^{o}_{a})^{2}_{j}$$

u_a^o p_a^o are derived from the initial incompressible flow conditions.

Again, upwind or leapfrog schemes may be applied without difficulty and were a subject of study to be reviewed in chapter 10.

The time marching solution method is detailed in the flow chart shown in figure 7-4 and can be seen to be similar to the previous constant acoustic speed model, except that the updating of the variable E_s occurs after the velocity field is calculated. Once this new value of E_s is known on each node, the state variables of internal energy e, temperature T and acoustic speed C_a may be derived. Equation 3.8/12 is re-arranged to give:-

$$e_j \quad E_{sj} - \frac{1}{2}(u_{aj})^2 \qquad \text{---7.2/7}$$

The air temperature is then found using equation 3.8/8, ie:-

$$T^{n}_{j} = \frac{e^{n}_{j}}{C_v} \qquad \text{---7.2/8}$$

Finally the acoustic sound speed is calculated by applying:-

$$C^{n}_{aj} = (\gamma R (T^{n}_{j} - T^{o}))^{1/2} \qquad \text{---7.2/9}$$

where T^o is the initial air temperature.

Once the discrete density field has been updated, again by using either of equations 7.1/7 to 7.1/9, the pressuress may be evaluated. The pressure is now also a function of internal energy hence equation 3.8/11 is applied to give:-

$$p_{aj} = (\gamma - 1)\, e_j \rho_{aj} \qquad \text{---} 7.2/10$$

The time step for this computation was again derived using the Courant-Friedrichs-Lewy condition given in equation 7.1/11.

As noted in chapter 2, the three dimensional nature of the flow induced in a realistic ship slamming situation is cited as a reason for the lack of correlation between previous computations and the full scale trial results. Experience with simulations of the two dimensional flow set up by the air entrapment problem lead to confidence that a three dimensional model could be attempted. The two dimensional model of the air layer which results is described using the equations defined in section 3.8. The time marching scheme was identical to that used in the one dimensional model.

The finite difference mesh used to represent the air layer in this latter problem was somewhat different to that applied to the one dimensional model. Consideration of the way in which the boundary conditions were applied at the edges of the plate led to the arrangement shown in figure 7-5. The velocity nodes were placed at cell corners, with pressure/density nodes placed at cell centres. An example of the effect upon the discretisation of equations 3.8/7, 3.8/8 and 3.8/9, is given below. The example used is based on the simple backward time step, central difference philosophy, though again, use of various combinations of the operators given in section 4.4 is possible.

The terms of equation 3.8/7 may be expanded for convenience to give the following formula:-

$$\frac{\partial \rho_a}{\partial t} = -\frac{\rho_a}{h}\left(\frac{\partial h}{\partial t} + U_a\frac{\partial h}{\partial x} + V_a\frac{\partial h}{\partial y}\right) - \rho_a\left(\frac{\partial U_a}{\partial x} + \frac{\partial V_a}{\partial y}\right) - U_a\frac{\partial \rho_a}{\partial x} - V_a\frac{\partial \rho_a}{\partial y}$$

---7.3/1

The free surface height and air gap are specified at cell

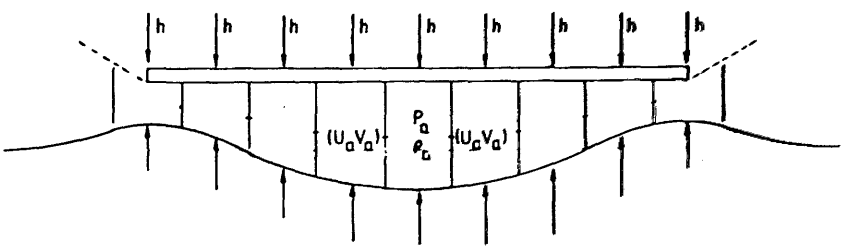

Figure 7-5 Arrangement Of Nodes And Principal Variables For 3-D Air Entrapment Simulation

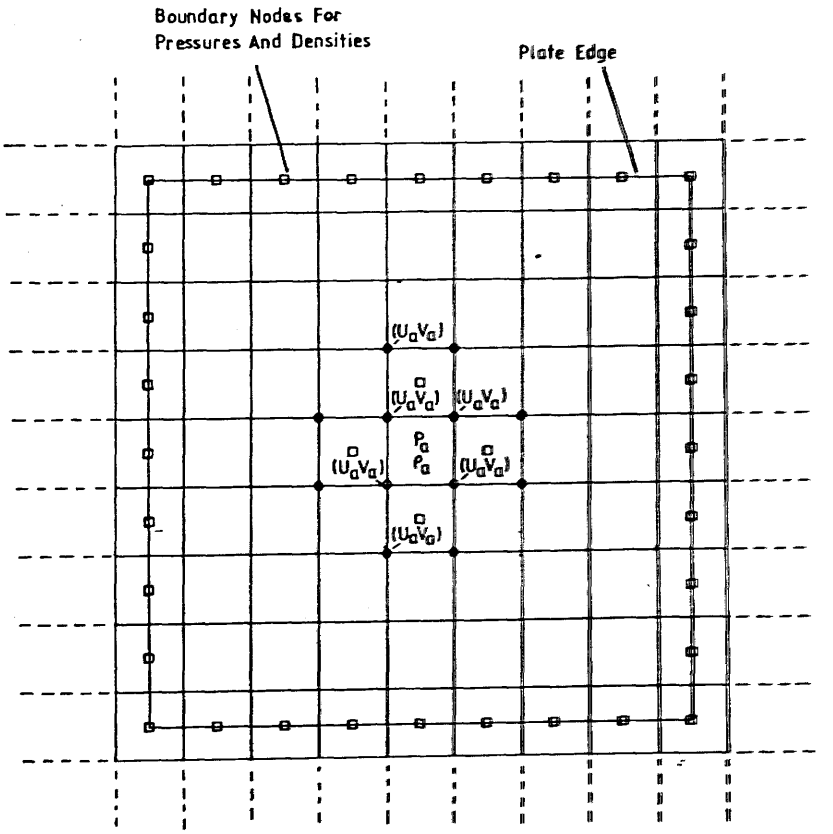

centres. The value of $\partial h/\partial t$ was found using equation 7.1/1. The following formulae were used for the individual terms in equation 7.3/1:-

$$\frac{\partial \rho_a}{\partial t} = \frac{\rho_{aij}^{n} - \rho_{aij}^{n-1}}{\Delta t} \qquad \text{---} 7.3/2$$

$$U_a \frac{\partial h}{\partial x} = \bar{U}_a \frac{h_{ij+1} - h_{ij-1}}{\Delta x} \qquad \text{---} 7.3/3$$

where $$\bar{U}_a \quad \frac{U_{aij} + U_{aij+1} + U_{aj+1j} + U_{aj+1j+1}}{4}$$

$$V_a \frac{\partial h}{\partial y} = \bar{V}_a \frac{h_{i+1j} - h_{i-1j}}{\Delta y} \qquad \text{---} 7.3/4$$

where $$\bar{V}_a \quad \frac{V_{aij} + V_{aij+1} + V_{ai+1j+1} + V_{ai+1j}}{4}$$

$$\frac{\partial U_a}{\partial x} = \frac{U_{aij+1} + U_{ai+1j-1} - U_{aij} - U_{ai+1j}}{\Delta x} \qquad \text{---} 7.3/5$$

$$\frac{\partial V_a}{\partial y} = \frac{V_{ai+1j} + V_{ai+1j-1} - V_{aij} - V_{aij+1}}{\Delta y} \qquad \text{---} 7.3/6$$

$$U_a \frac{\partial \rho_a}{\partial x} = \bar{U}_a \frac{\rho_{aij+1} - \rho_{aij-1}}{\Delta x} \qquad \text{---} 7.3/7$$

$$\frac{\partial \rho}{\partial y} = \bar{V}_a \frac{\rho_{aj+1} - \rho_{aj-1}}{\Delta y} \qquad \text{---} 7.3/8$$

Using central difference formulae for the convection terms in equations 3.8/8 and 3.8/9 allows the following relationships to be derived for the updating of the velocity components:-

$$U^{n}_{a_{ij}} = U^{n-1}_{a_{ij}} - \frac{\Delta t}{2\Delta x} U^{n-1}_{a_{ij}} (U^{n-1}_{a_{ij+1}} - U^{n-1}_{a_{ij-1}}) -$$

$$V^{n-1}_{a_{ij}} \frac{\Delta t}{2\Delta y} (U^{n-1}_{a_{i+1j}} - U^{n-1}_{a_{i-1j}}) - \frac{\Delta t}{\Delta x \bar{\rho}^{n-1}_{a}} (\bar{p}^{n-1}_{a_{ij}} - \bar{p}^{n-1}_{a_{ij-1}}) \quad \text{---7.3/9}$$

where:

$$\bar{\rho}_a = (\rho_{a_{ij}} + \rho_{a_{i-1j}} + \rho_{a_{ij-1}} + \rho_{a_{i-1j-1}}) / 4$$

$$\bar{p}_{a_{ij}} = (p_{a_{ij}} + p_{a_{i-1j}}) / 2$$

$$\bar{p}_{a_{ij-1}} = (p_{a_{ij-1}} + p_{a_{i-1j-1}}) / 2$$

$$V^{n}_{a_{ij}} = V^{n-1}_{a_{ij}} - \frac{\Delta t}{2\Delta y} V^{n-1}_{a_{ij}} (V^{n-1}_{a_{i+1}} - V^{n-1}_{a_{i-1}}) -$$

$$- U^{n-1}_{a_{ij}} \frac{\Delta t}{2\Delta x} (V^{n-1}_{a_{ij+1}} - V^{n-1}_{a_{ij-1}}) - \frac{\Delta t}{\Delta y \bar{\rho}^{n-1}_{a}} (\bar{p}^{n-1}_{a_{ij}} - \bar{p}^{n-1}_{a_{i-1}}) \quad \text{---7.3/10}$$

where $\bar{\rho}_a$ is as above

$$\bar{p}_{a_{ij}} = (p_{a_{ij}} + p_{a_{ij-1}}) / 2$$

$$\bar{p}_{a_{i-1j}} = (p_{a_{i-1j}} + p_{a_{i-1j-1}}) / 2$$

CHAPTER 8

EXPERIMENTS IN THE NUMERICAL MODELLING OF FLOWS

CHAPTER 8

EXPERIMENTS IN THE NUMERICAL MODELLING OF FLOWS

1. INTRODUCTION

During the development of the ideas put forward in the previous chapter, hydrodynamic problems other than those involved in the water entry simulation were investigated. Two basic routines were programmed, one to examine a steady two dimensional free surface flow, the other to study wave generation. A number of particular aspects of the numerical models described in chapter 4 could be tested in isolation. The programs also offered the opportunity to refine the book keeping procedures of chapter 5.

In this chapter, these routines and the flow problems they model will be briefly described. Further information may be found in referencees (137) and (141).

2. FLOW88

2.1. Description of the Flow Model

The program FlOW88 was used to model two dimensional flow bounded by a free surface. The computational domain was similar to that shown in figure 4-3, given in chapter 4. An inlet boundary condition was used upstream as described in sections 3 and 4. The bottom boundary was considered as a rigid floor as described in section 3.5. The aspects of flow modelling to be investigated with this simulation were:-

a. Free surface height convection via the fluxing routines described in 5.1.

b. The properties of the discretised Sommerfeld radiation condition.

c. The use of steady source/sink distributions to represent flow past curved boundaries.

d. The resolution of laminar boundary layers.

e. Factors affecting the accuracy and convergence rate of the iterative solution schemes in general.

A number of simple flow situations were examined, though three particular domain geometries were studied in greatest detail. The first, shown in figure (8-1), illustrates flow past a simple source/sink distribution placed just below the free surface. It was intended to study the ability of this technique to model two dimensional, free slip boundaries such as that common to a circular cylinder. In this case the flow was completely inviscid.

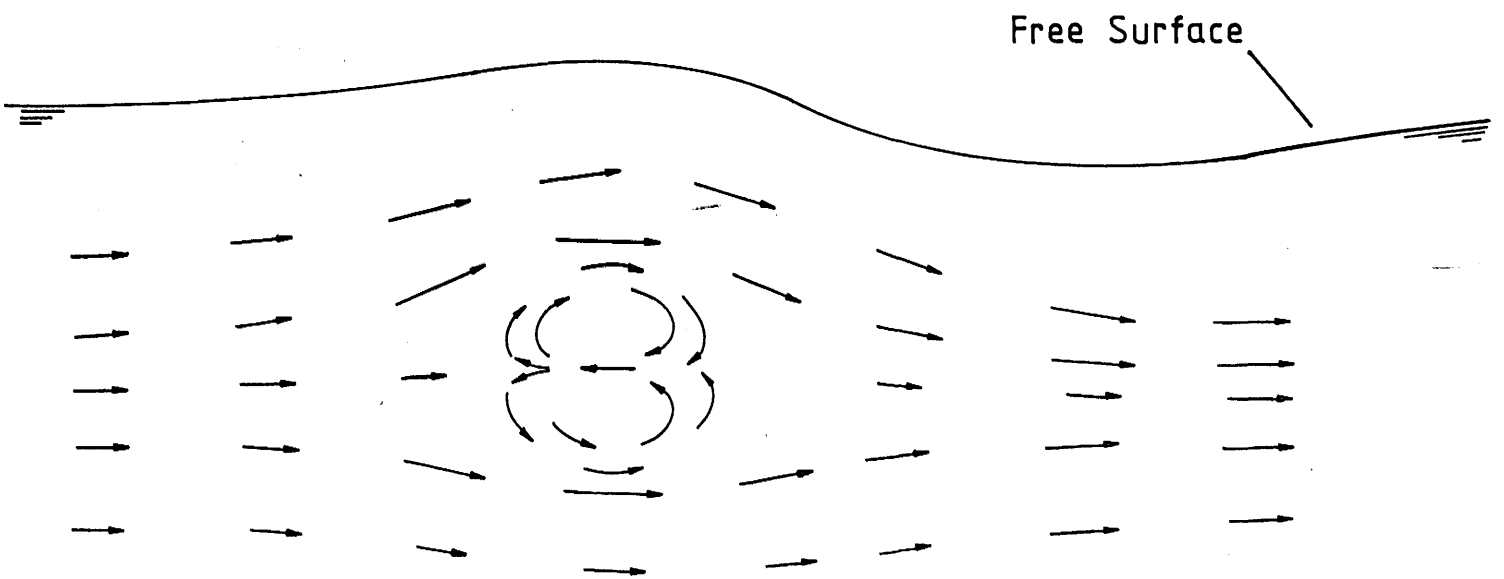

Figure 8-1 Schematic View Of Inviscid Flow Past A Source/Sink Combination, To Be Modelled By Program FLOW88

The second case, figure (8-2), studied the flow about a rectangular body placed just below the free surface. The boundaries coincided with the T3 mesh geometry. The flow was considered to be either viscous or fully inviscid. As a special case, the source/sink distribution method was combined with this model. It was hoped that the sources and sinks could be distributed on the upstream side of the rectangular body so as to create a 'bulbous' forward end.

The third case studied the flow past a rectangular wall, rising from the bottom boundary. The flow was considered fully viscous. This proved to be a good test case by which to study eddy formation in relation to the mesh size.

2.2. The Numerical Procedure

A flow chart for the program FLOW88 is shown in figure (8-3). Initial conditions for all the computations were the same. The flow velocity over the whole domain was set at the upstream boundary value. The pressure field was also set to zero over the whole domain.

Boundary conditions at the upstream, bed, downstream and free surface extremities of the computational mesh, were as described in section 3.5 and 4.7. When required, a constant source or sink strength (Q_{ij} , eqn 4.9/15) could be applied to a finite number of cells within the fluid domain.

Once the initial conditions and source strengths had been set, the computational loop was entered. The first stage was to apply velocity boundary conditions to dummy nodes outside the free surface

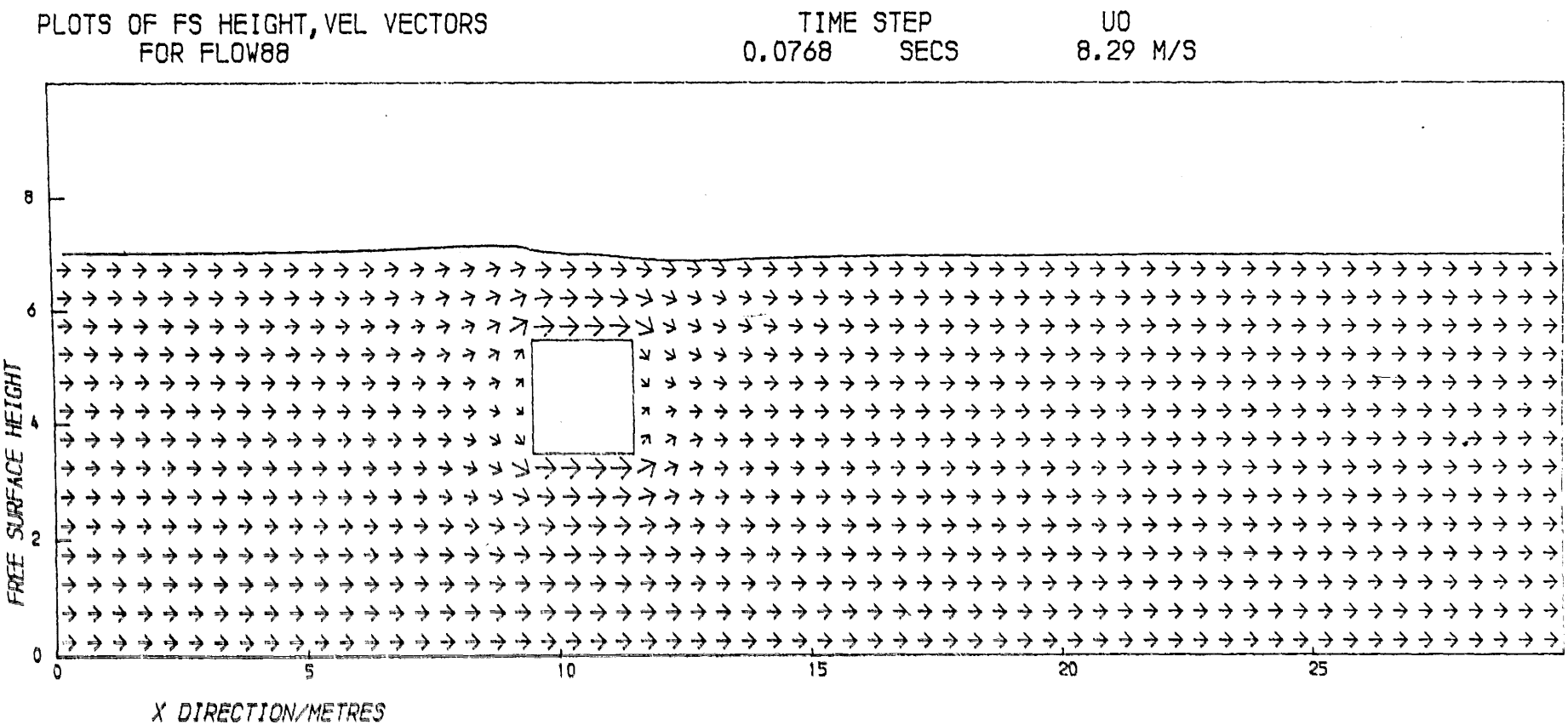

Figure 8-2 Flow Past A Rectangular Block

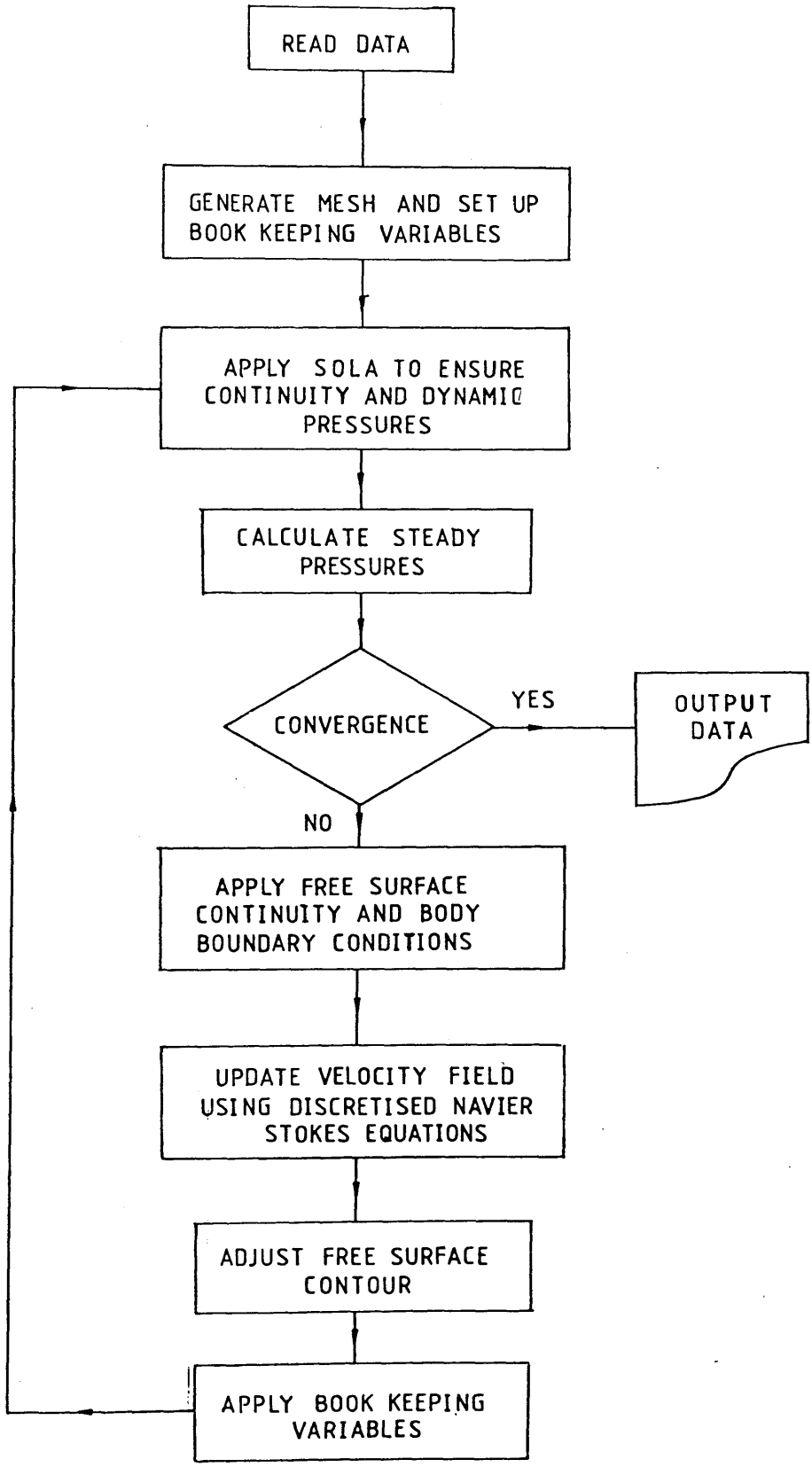

Figure 8-3 Flow Chart For FLOW88

via the techniques outlined in 4.7. The next task was to update the velocity field within the fluid domain via the explicit formulae given in section 4.5. In particular, the forward time step central difference (4.5/1), forward time step upwind difference, leapfrog central 4.5/5 and leapfrog upwinded schemes were applied. Since the flow was known to reach some steady state, the implicit/explicit schemes, and fully implicit schemes were also experimented with.

At this stage, the updated velocity field did not satisfy continuity. This was remedied by the application of the SOLA algorithm. As there were no moving solid boundaries within the flow, the divergence from the first time marching step could be wholly accounted for by the incompatability between initial conditions and domain geometry. The 'dynamic' pressure field thus calculated via SOLA was totally unphysical in nature, but its inclusion as an input to the next time marching phase was found to speed up convergence. In later time steps, the moving free surface also served to alter the dynamic pressures. As the final solution was approached, a decreasing level of computational effort was expended on the SOLA routine, until the only source of divergence was the (small) truncation errors caused by the updating schemes.

Having satisfied continuity and resolved the dynamic pressure field, the steady pressure components were calculated as described in section 4.8. At this stage, the steady pressure gradients were balanced by convection but the equilibrium state had not yet been reached. The difference between the fluid variables at this stage and their final values resulted in an imbalance in the free surface geometry and lead to a non-zero dynamic pressure field. Thus the next operation was to move the free surface and perform the resulting book

keeping processes as described in chapter 5.

Having changed the fluid domain geometry, the velocity field was again updated, the whole iteration procedure being repeated as shown in figure (8-3). Upon reaching the steady state, it was found that convection and diffusion terms in the Navier Stokes equations were balanced by steady pressure gradients. The hydrostatic pressure field was balanced by gravity and the dynamic pressure field was zero.

2.3. Properties of the Fluid Fluxing Scheme

In these types of fluid problems, the flows are predominantly one dimensional in character. Bodies or source distributions placed within the flow produce local perturbations, resulting in variations in vertical velocity component, but these tend to die out downstream. With this in mind it can be seen that the fluid fluxing routine is required to mimic the characteristics of the free surface kinematic condition given by equation 5.1/1. Equation 5.1/7 is therefore sufficient to describe the increments in fluid fractional volume.

It was thus possible to examine the effect of the different fractional volume averaging methods given in section 5.1 on the evolution of the free surface shape. Figures 8-4 to 8-7 show the results of using the relationships given by 5.1/13, 5.1/15, 5.1/17 and 5.1/19 respectively.

Figure (8-4) uses the simple averaging scheme and, as might be expected considering the equivalent central difference scheme for the convection of the free surface height, some irregularity is observed. The same can be said of the 'higher order' scheme given by

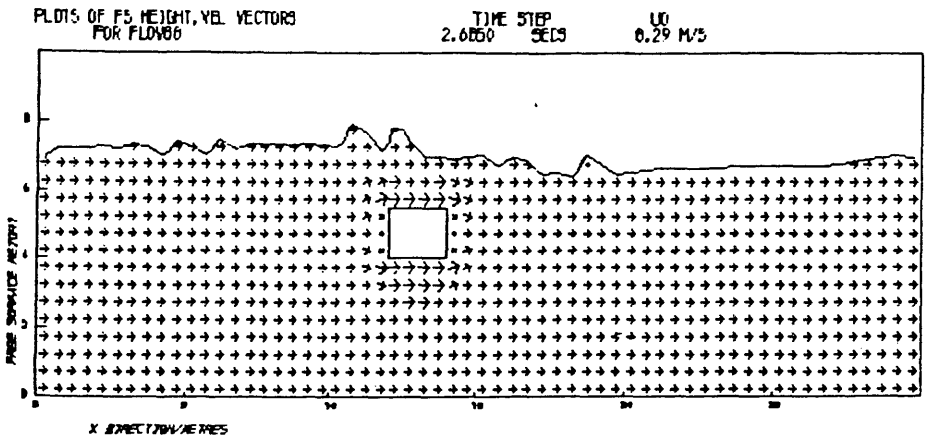

Figure 8-4

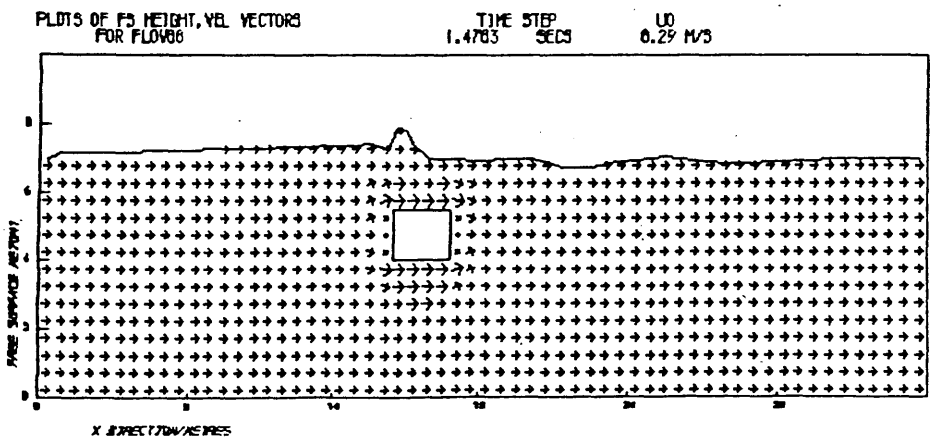

Figure 8-5

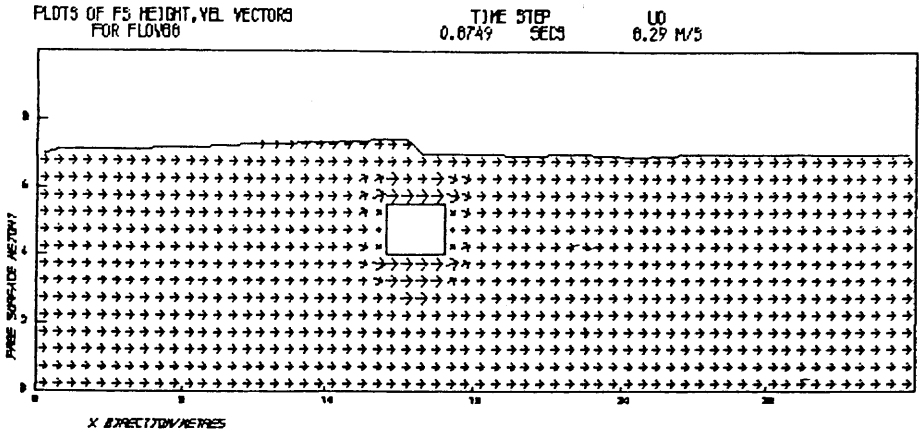

Figure 8-6

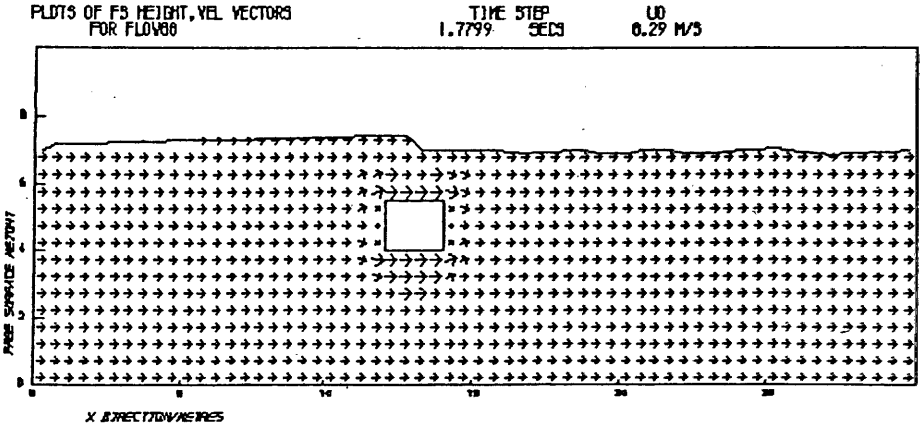

Figure 8-7

5.1/15 and illustrated in figure (8-5). No improvement in free surface resolution is evident despite a theoretical increase in accuracy.

Figure (8-6) shows the result of using the donor/acceptor cell method given by equations 5.1/17. The resulting profile has none of the spurious inaccuracies of the previous central difference schemes. However, the resolution is still considered poor. The jump in free surface height is a typical result of using upwind schemes for the convection of a scalar quantity. Figure (8-7), shows the use of 'Simpson's first rule' averaging given by equations 5.1/19. The same, flat, stepped solution is obtained, despite the lower level of numerical damping inherent in this formulation. The most striking difference between the centrally differenced and upwinded schemes can be seen to be the speed of convergence. Figures (8-4) and (8-5) imply that these computations have some way to go before a final solution is reached. However, figures (8-6) and (8-7) show rapid convergence of the free-surface shape. This type of result is typical of schemes which use upwinding, being subject to heavy artificial damping.

It should also be noted that the coarse mesh used was a barrier to an accurate resolution. In later work using the program NWAV90, reported in section 8.3, the number of full cells between the crests and troughs of free surface waves was found to be critical to an accurate representation of the free surface shape. Refining the mesh in the vertical direction was found to have a beneficial effect in this respect, a conclusion also borne out by later experience during the investigation of viscous flow, on a much finer mesh, to be reported further on in this section.

2.4. The Properties of the Discretised Downstream Radiation Condition

Owing to the limitations imposed by mesh geometry, spatial discretisation was restricted to upwind formulations. However, it was possible to vary the type of time marching scheme, the choice being to use either a forward or a leapfrog time step. Neither of these two formulations resulted in numerical instability or the production of spurious reflections from the downstream boundary. It should be noted however that such problems could still be inherent in the use of these schemes, but rigorous conservation of mass, as supplied by the use of the SOLA code, may disguise these effects.

2.5. The Use of Source/Sink Distributions to Simulate Curved Boundaries

The purpose of this study was twofold. Primarily, confirmation of the assumptions made in applying the modified SOLA routine and its ability to calculate dynamic pressures was required. Further, an investigation of the type of source/sink distributions needed to produce particular shapes of curved boundary was to be carried out.

Figure (8-8) shows the flow resulting from the solution of the continuity equation given by 4.9/15, applied at the first time step only. The fluid domain contains a single source and sink placed parallel with the flow. The result is a small inner recirculating region superimposed upon the main, near unidirectional, flow. An approximation to the classical hydrodynamic Rankine oval/doublet representation of the flow about an ellipse or circle is therefore made. Upon application of the time marching routine, the free surface

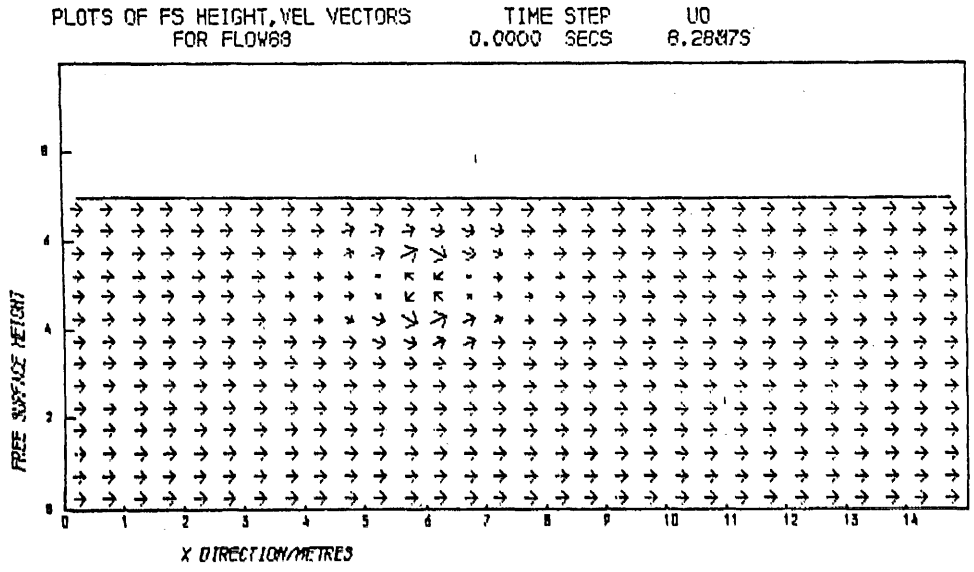

FIG 8-8
Effect of doublet
on a uniform flow

changes in shape directly above the source/sink pair. Eventually, a steady state is reached. The main disadvantage of such a representation is that it is difficult to be sure of where the 'imaginary' free slip boundary is. The single source/sink pair combination does not provide an accurate enough approximation on such a coarse mesh. However, this numerical experiment did confirm the authenticity of the modified SOLA code as a continuity and pressure solving routine.

The second geometry to which this source/sink concept was applied was that of the flow past a rectangular cylinder. Sources and sinks covered the leading edge of the rectangle. The fixed distribution is shown in figure (8-9). After the first time step, the flow past the rectangle is seen to be modified, as if a bulbous forward end had been fitted.

These experiments proved highly informative confirming the link between the recently developed techniques of computational fluid dynamics, in particular the SOLA code, and the methods of classical hydrodynamic theory.

2.6 The Modelling of Viscous Flow

The two flow examples used in these experiments were those of flow past a rectangular box, and flow past a vertical wall. The critical factor to be studied was the relationships between mesh size, eddy structure and Reynolds number.

The domain length was taken as three metres, with a mesh spacing in the x direction of 0.05m. For a flow speed of 10 metres per

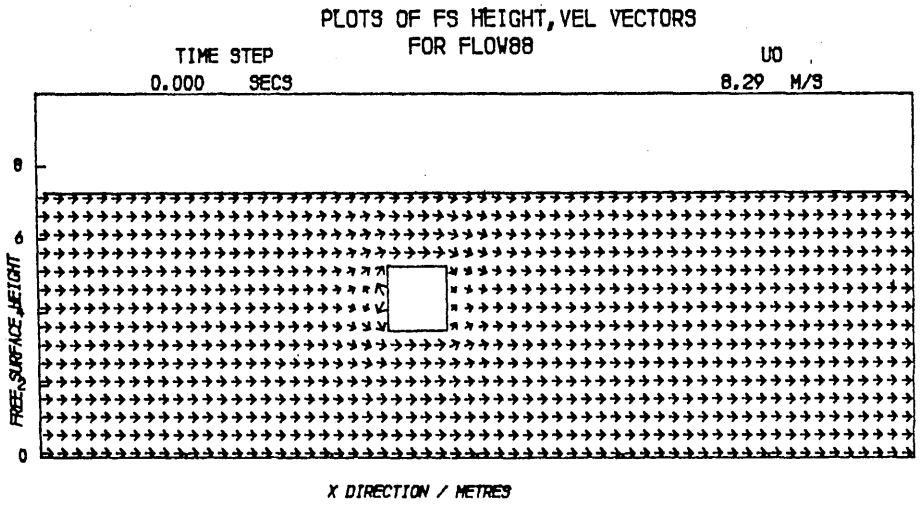

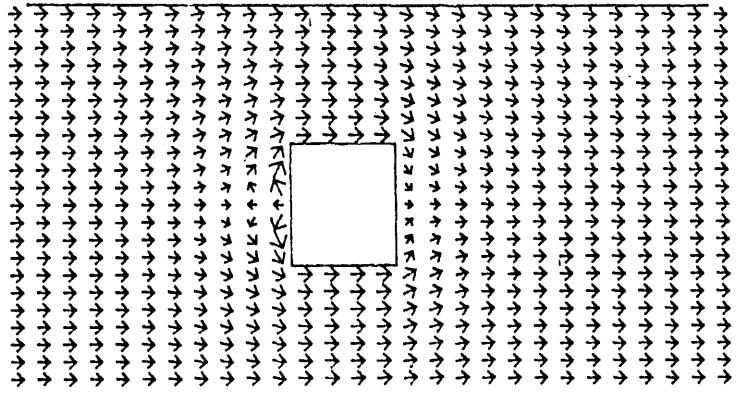

Figure 8-9
Effect Of Source Distribution
Placed Over The Leading Edge
Of A Rectangular Box

second, the Reynolds number based on the dimensions of the rectangle would have been approximately 3.0×10^6. Such a flow would have undoubtedly had some turbulent regions and, whilst modelling such a flow would have proved interesting, it would not have been a cost effective exercise. Regard for the order of magnitude of the viscous terms in the Navier Stokes equations and their effect upon the time marching process, revealed that the mesh spacing would need to be of order of 10^{-3} metres. Indeed, regard for the boundary layer thickness at such Reynolds numbers indicated that even this level of discretisation would provide a fairly coarse resolution of the velocity distribution close to the no-slip boundary.

Whilst it was theoretically possible to perform computations at these Reynolds numbers, the number of finite difference cells required (of the order 10^6), and the degree of sophistication needed to deal with turbulence modellng, indicated that such a program would be uneconomic. For the purposes of numerical experimentation, flows at Reynolds numbers in the 100 - 1000 range proved adequate. This was achieved by increasing the kinematic viscosity of the fluid to between 10^{-3} - 10^{-2}. At this level, the viscous terms in the Navier Stokes equations were of near the same order as the convection terms. Similarly, the normal pressure gradients caused by shear stresses at no-slip boundaries were of order 10^{-1} - 1.0, enabling the pressure terms calculated via equation 3.5/8 to have an early discernable effect upon the flow.

The results of two such numerical experiments are shown in figures (8-10) and (8-11). In the first, flow past a rectangular box beneath the free surface, the laminar boundary layer can easily be seen. No separation takes place however at this particular Reynolds

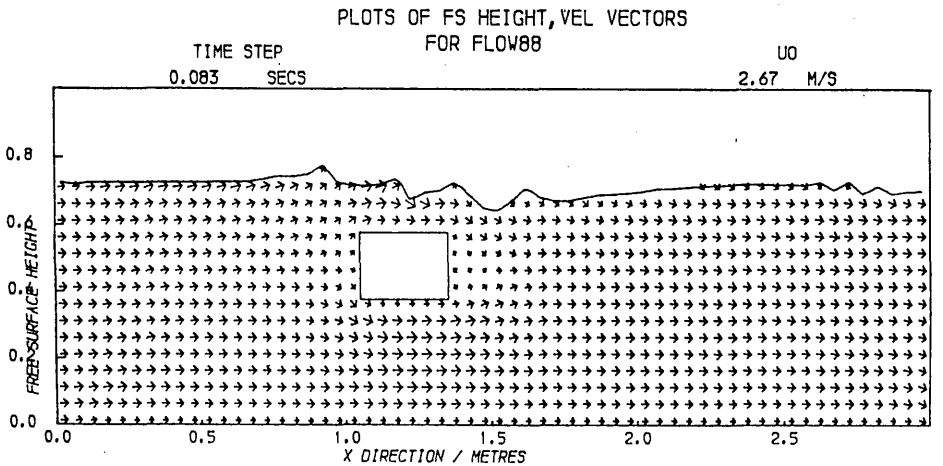

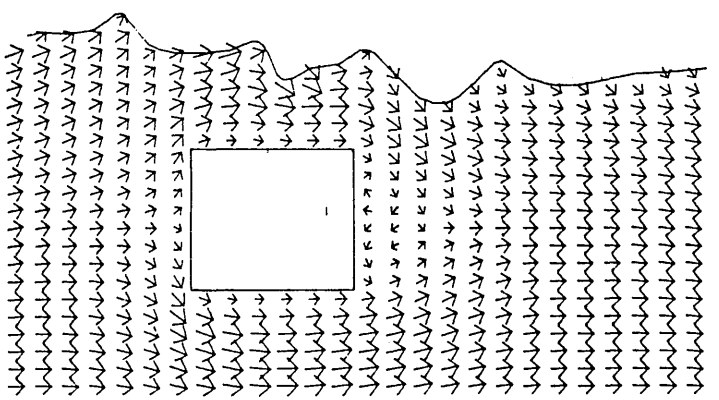

Figure 8-10
Viscous Flow Past A
Rectangular Box

Reynold's No = 801

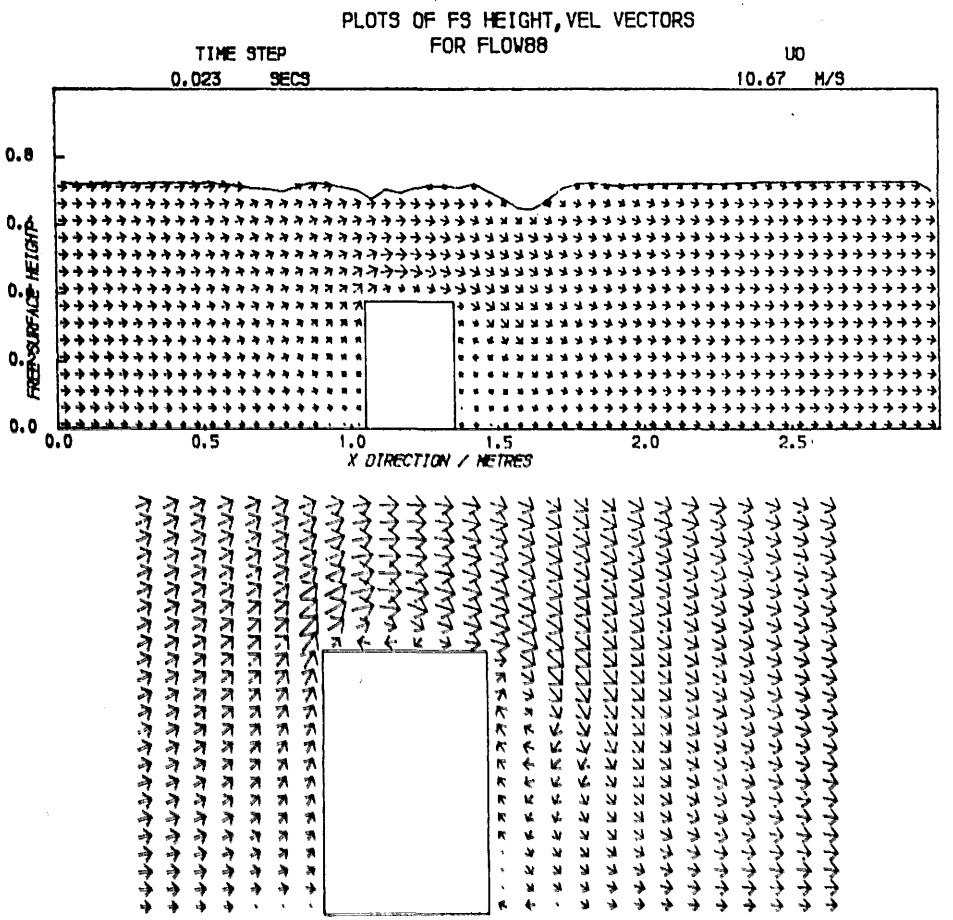

FIG 8-11
Developing viscous flow past a submerged wall.

$R_e = 320$

number. One cannot be certain with the mesh size used whether this is the correct state of affairs, since the level of discretisation is coarse in comparison with the size of the rectangle. The second example shows both separation and the formation of an eddy to the rear of a rectangular wall placed within the flow. Again, the mesh spacing is coarse but the result is of the correct form.

2.7. Factors Affecting Accuracy and Convergence

The chief problem in producing an accurate solution was found to be the efficient solution of the continuity equation. The shape of the free surface was highly sensitive to the degree of mass conservation. Thus the computation of changes in fractional volume needed careful attention to accuracy. It was noted that some tolerence level had to be applied to the fractional fluid volume per finite difference cell in order for the book-keeping processes to progress smoothly. In particular, choosing whether the fractional volume was exactly one or zero needed a 'rounding process'. It was found that the tolerence levels given by:-

$$F_{ij} < 10^{-6} \quad \text{PTYPE = 'EMTY'}$$

$$F_{ij} > 1.0 - 10^{-6} \quad \text{PTYPE = 'FULL'}$$

provided the required level of accuracy in free surface shape over the complete computational cycle. It can be shown that, from the definitions of change in fractional volume per time step, the above tolerence levels were equivalent to a fluid divergence level given by:-

$$\nabla.\bar{U}_{ij}\Delta t = \Delta F_{ij}$$

The time step Δt was chosen using the Courant-Friedrichs-Lewy

criterion (4.6/6) applied locally using the largest resultant fluid velocity. However, it can be seen that the greatest levels of accuracy are required when Δt is large. The greatest value of Δt possible is that found from the CFL condition based on the free stream flow velocity. For example, a free stream velocity of 5 m/s with a mesh spacing of 0.05m produces a time step requirement of:-

$$\Delta t < 0.05/5 = 0.01 \text{ seconds}$$

Thus for a tolerence on F_{ij} of 10^{-6}, the continuity equation must be solved down to a divergence level of 10^{-4}. In practice such a level of convergence took many iterations to achieve. Often for the purposes of development, the tolerence on F_{ij} was relaxed in order to speed up computing time.

The choice of relaxation factor for the solution of steady pressures was at first made by reference to the numerical experiments detailed in appendix 1. However, in most of the computations made, the mesh spacing in the x and y directions was unequal and, in particular the ratio:-

$$\frac{\Delta x}{\Delta y} = 2$$

was used. In theory, this reduces the optimum relaxation parameter (ω_b) by a factor of 5/8. Therefore, the optimum value of ω, found in appendix 1 to be between 1.7 and 1.8 for a square mesh, was reduced to the range 1.06 - 1.125, which was confirmed in practice.

Initial computations were performed usng a forward time step centrally differenced discretisation scheme for the Navier Stokes equations. Highly rigorous application of continuity was required however, since the method was very sensitive to non-linear

instabilities or 'wiggles'. A more robust method was supplied by forward time step fully upwinded differencing schemes. This was at the expense of accuracy however, owing to the introduction of numerical viscosity. For the problems requiring a viscous solution, the mesh size chosen was $\Delta x = 0.025m$, $\Delta y = 0.05m$. Updating the horizontal velocity component u, induced two 'extra' viscous terms, derived from the error in the convection operators. These terms introduced the positive numerical damping values:-

$$U_{ij} \frac{\Delta x}{2} \frac{\partial^2 U}{\partial x^2} + V_{ij} \frac{\Delta y}{2} \frac{\partial^2 U}{\partial y^2}$$

to the right hand side of equation 4 which on the mesh used amounted to:-

$$0{\cdot}0125\, U_{ij} \frac{\partial^2 U}{\partial x^2} + 0{\cdot}025\, V_{ij} \frac{\partial^2 U}{\partial y^2}$$

with similar terms applied to the updating of the v component. Such terms stabilise the numerical procedure, but decrease the effective cell Reynolds number to a constant level of 80 in the x direction and 40 with regard to the y axis. If the physical viscosity of the flow is high enough, this effect may not be too serious. However, in the case of hydrodynamic flows, this type of scheme proves problematical.

It was found that the increase in accuracy achieved by use of the leapfrog time marching schemes benefitted the computational procedure on two levels. Primarily, the improved estimations of updated velocity fields reduced the risks of instabilities. Secondly, this greater level of accuracy reduced the fluid divergence resulting after any given time step. This allowed a higher level of mass conservation to be achieved during the SOLA routine for the same

computational effort as that expended during the forward time step algorithms. Both central and upwind convection schemes were applied, but the increased accuracy of the leapfrog method reduced the tendency for 'wiggles' to appear and, therefore, the use of upwinding proved unnecessary.

The implicit/explicit schemes were only ever used in association with leapfrog time marching methods and hence their effect upon stability was dificult to assess. However, figure (8-12) shows a plot of convergence of the solution. The measure used to define convergence was the sum of the squares of the changes in free surface height per time step, ie:-

$$\sum_{1}^{jx} (\eta_j^{n+1} - \eta_j^{n})^2$$

It can bee seen from figure 8-12, that the implicit/explicit schemes converged more rapidly in all cases. This is a common result in solutions of steady flow problems by time marching simulation (92).

The fully implicit scheme was also experimented with, applied primarily to the flow past a rigid wall problem. A matrix assembly routine was written for equations 4.5/20 and applied at first to some coarse mesh approximations. An 'in house' NAG routine was used to invert the appropriate matrices and perform the matrix multiplications. At first the technique proved very promising on the coarse meshes, though flow resolution was poor. Decreasing the mesh size radically increased the storage requirement for the matrices. The need for double precision accuracy for the main variables also added to these problems, revealing a limit on the total number of fluid nodes of about 250, (ie a 10 x 25 two dimensional mesh).

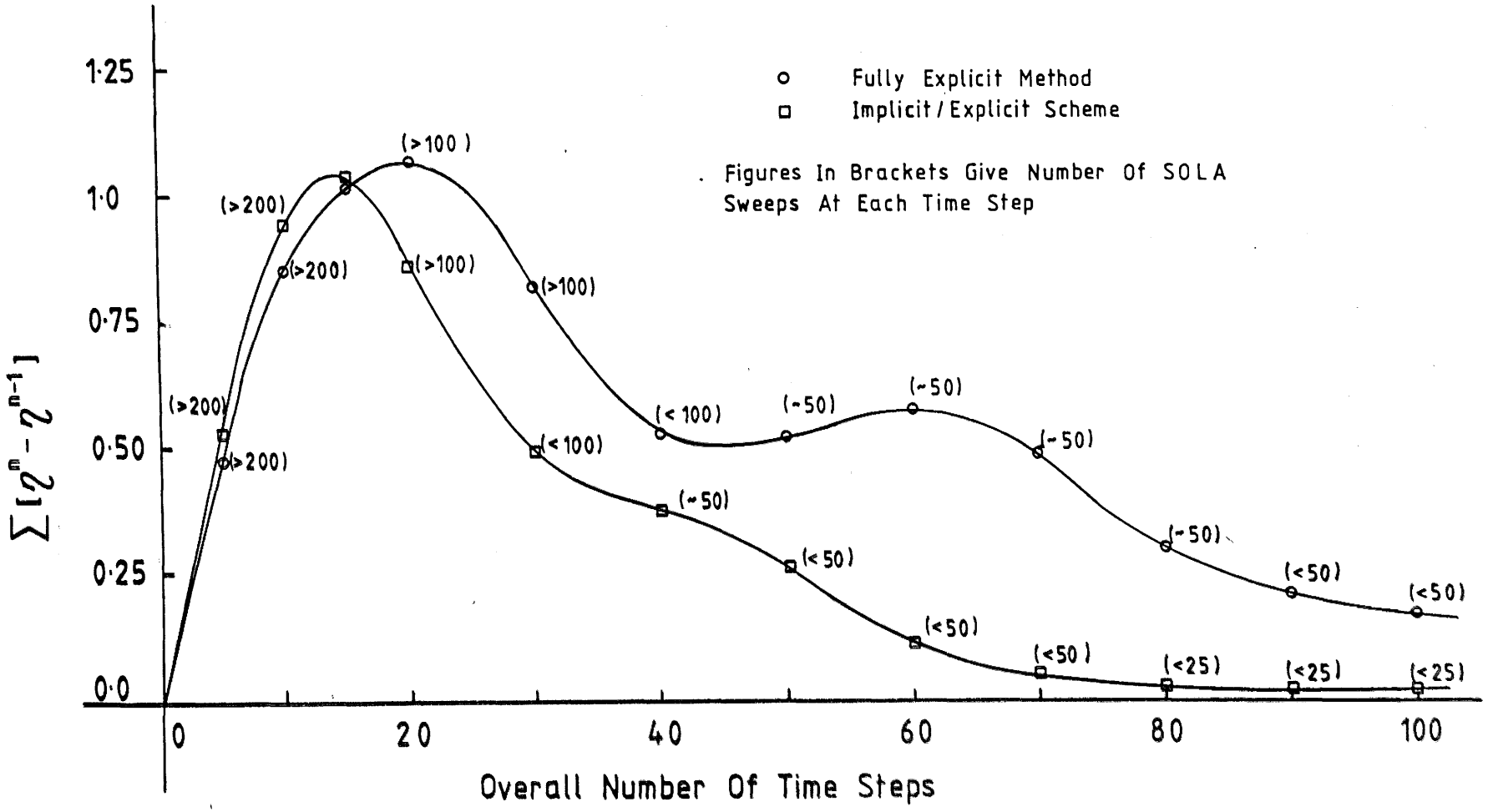
1·25
1·0
0·75
0·50
0·25
0·0
$\sum |\eta^n - \eta^{n-1}|$
0
20
40
60
80
100
Overall Number Of Time Steps
Fully Explicit Method
Implicit / Explicit Scheme
. Figures In Brackets Give Number Of SOLA Sweeps At Each Time Step
(>100)
(>200)
(>200)
(>200)
(>200)
(>100)
(>100)
(<100)
(~50)
(~50)
(~50)
(~50)
(<100)
(~50)
(<50)
(<50)
(<50)
(<50)
(<50)
(<25)
(<25)
(<25)

Figure 8-12

This level of discretisation was too coarse for the purposes of slam simulations and hence the technique had to be abandoned

2.8. General Conclusions on FLOW88

The main objectives of the program FLOW88 were to experiment with and learn about the numerical methods proposed for slam simulations. To these ends, the exercise proved very successful. The limitations of the individual discretisation schemes were well defined and the ability to combat reported shortcomings (ie instabilities) via rigorous application of the continuity criterion proved encouraging.

The development of FLOW88 will be continued. In particular, improvments in the iterative procedure associated with the continuity and pressure solvers may be made by use of 'Multigrid' (101) techniques. The resulting increase in accurcy should allow more realistic flow problems to be solved without resort to excessive computing times.

3. NWAV90

Two dimensional free surface flow was again the subject of study for NWAV90. However, in this case the program was to study the generation and development of free surface waves. It is worth noting that the chief difference between NWAV90 and FLOW88 was that the former aimed to produce a real time dynamic simulation, whereas the latter attempted only to find a steady state solution.

Figure 4-4, given in chapter 4, shows the computational domain set up with a time varying source distribution on the left hand boundary. The right hand side boundary could be considered as either a solid wall or a radiation boundary. For the latter case, the finite fluid depth fixed the wave phase speed to the value:-

$$C_x = (g\,d)^{1/2}$$

where d is the fluid depth. This value could be applied directly to the discretised Sommerfeld radiation condition such that the horizontal velocity component on the boundary could be derived from:-

$$U^{n-1}_{ijx} = U^{n-1}_{ijx} = \frac{\Delta t (g.d)^{1/2}}{\Delta x} \left(\frac{U^{n+1}_{ijx} - U^{n-1}_{ijx}}{2} - U^{n}_{ijx-1} \right)$$

A single source was placed in each cell adjacent to the left hand boundary. The strengths of these sources varied linearly with depth and were weighted by the fractional volume of the cell. This latter precaution allowed the free surface height at the boundary to vary as if a wave were entering the domain through the boundary.

Owing to the coarseness of the mesh spacing ($\Delta x = 0.5m$, $\Delta y = 0.25m$), only inviscid flow was considered. The major parts of the

computational routine were therefore, the SOLA continuity solver, successive over relaxation applied to the 'steady' pressure Poisson equation, and the overall time marching routine. A flow chart for the computation is shown in figure (8-13). It can be seen that the scheme is similar to those described in earlier parts of this thesis. A special point to note however, is the double application of the continuity/pressure solving routine during each cycle. The first eliminates the effects of time marching truncation error and is applied using the source strengths from the previous time step. The source strengths are then updated and the routine applied again. In this second iterative sweep, the only cause of divergence is that owing to the change in source strength. Thus the dynamic pressures may be calculated as shown in section 4.9.

Figures (8-14) shows a series of stages in the simulation of a free surface wave moving through the domain. The source strength/time history is of the form:-

$$Q_{ij} = Q_0 \cos \omega t$$

The frequency was chosen to allow two full wavelengths to exist within the domain at any one time. The speed of the wave was fixed by the depth of the fluid. It was found that the wave phase speed was the decisive factor in choosing the time step. The analogy between the pressure/divergence relationship used in the continuity solver and the wave equation dictated that:-

$$C_p = C_w = \sqrt{gd}$$

Thus for a shallow water wave the time step is given by:-

$$\Delta t = \left(\frac{1}{2.g.d\left(1/(\Delta x)^2 + 1/(\Delta y)^2\right)} \right)^{1/2}$$

Figure 8-13 Flow Chart For NWAV 90

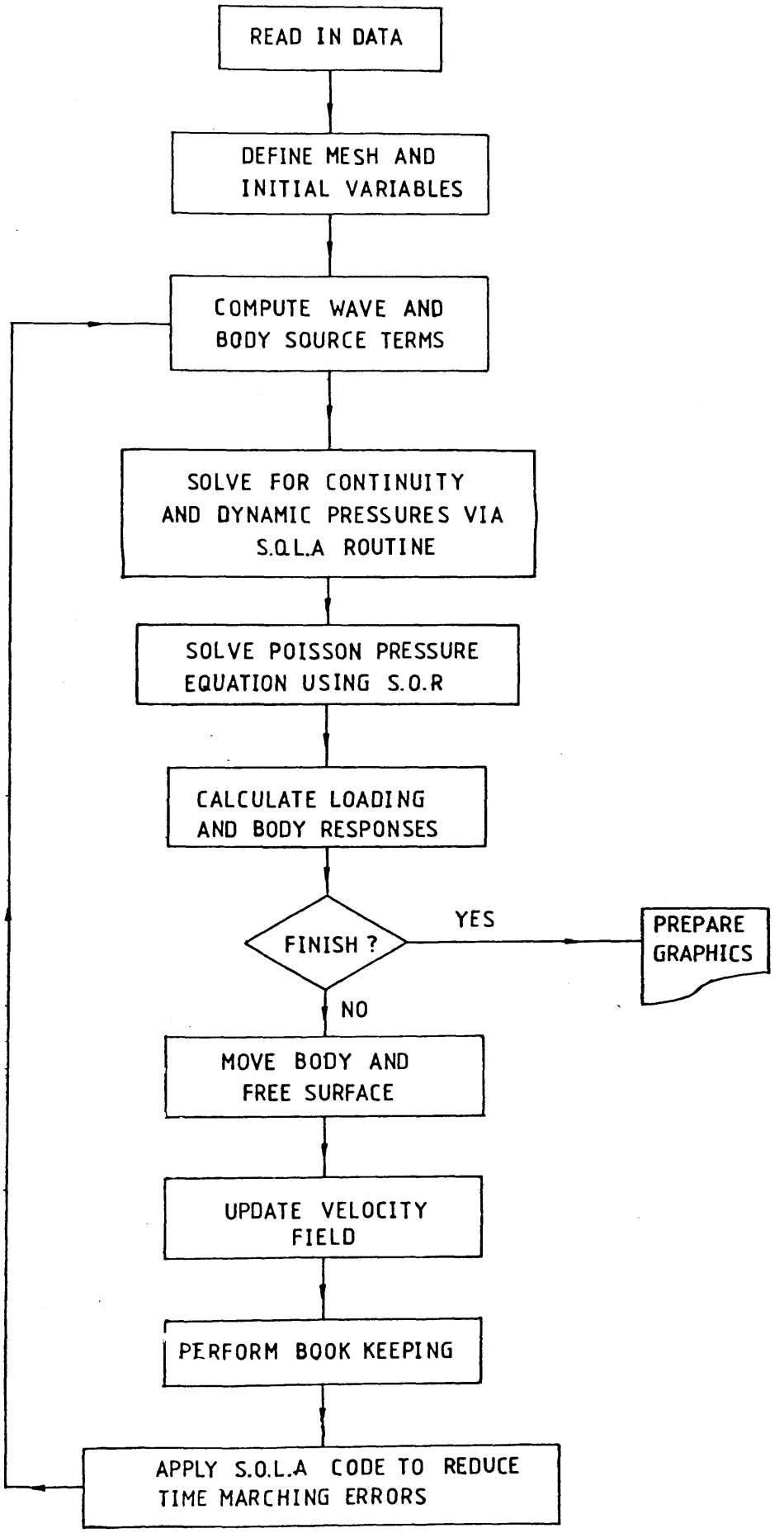

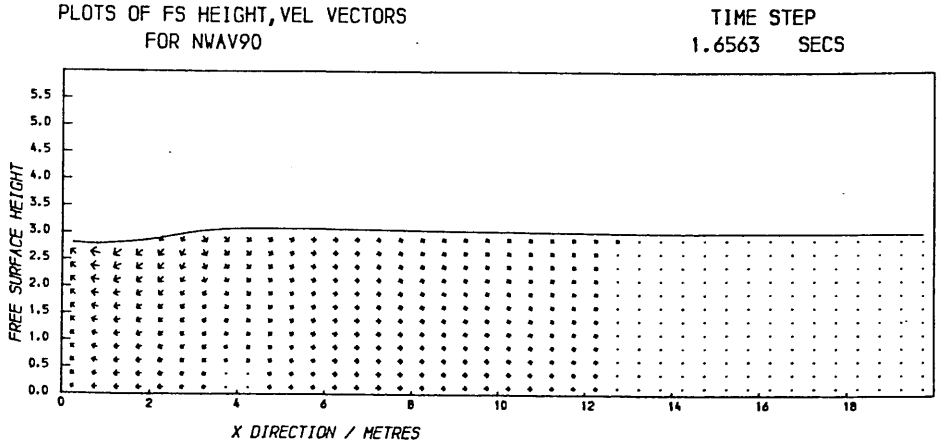
PLOTS OF FS HEIGHT, VEL VECTORS
FOR NWAV90
TIME STEP
1.6563 SECS
FREE SURFACE HEIGHT
X DIRECTION / METRES

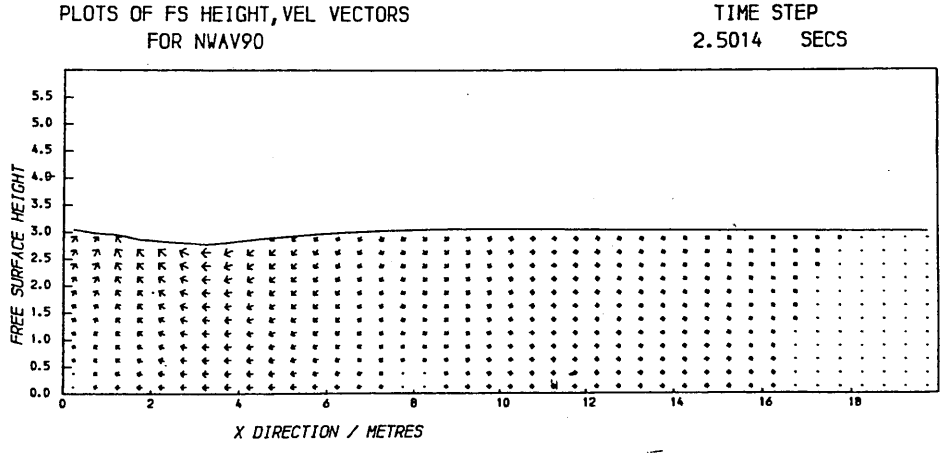
PLOTS OF FS HEIGHT, VEL VECTORS
FOR NWAV90
TIME STEP
2.5014 SECS
FREE SURFACE HEIGHT
X DIRECTION / METRES

Figure 8-14 a

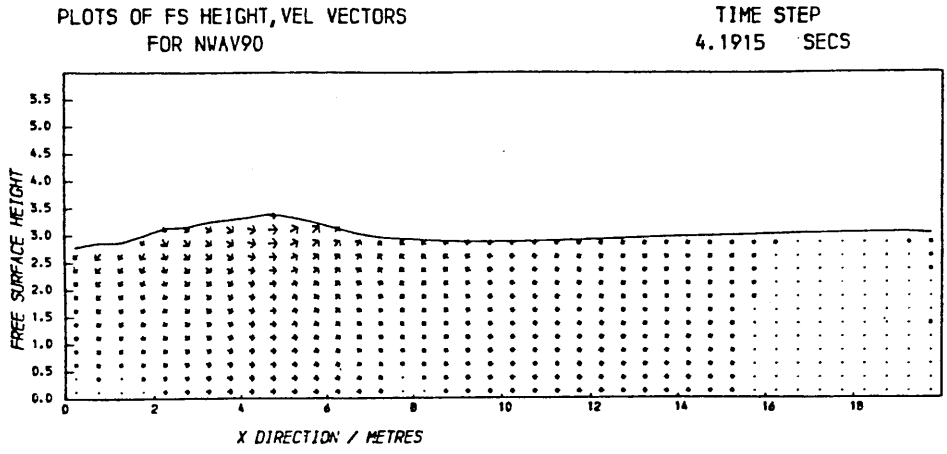
PLOTS OF FS HEIGHT, VEL VECTORS
FOR NWAV90
TIME STEP
4.1915 SECS
FREE SURFACE HEIGHT
X DIRECTION / METRES

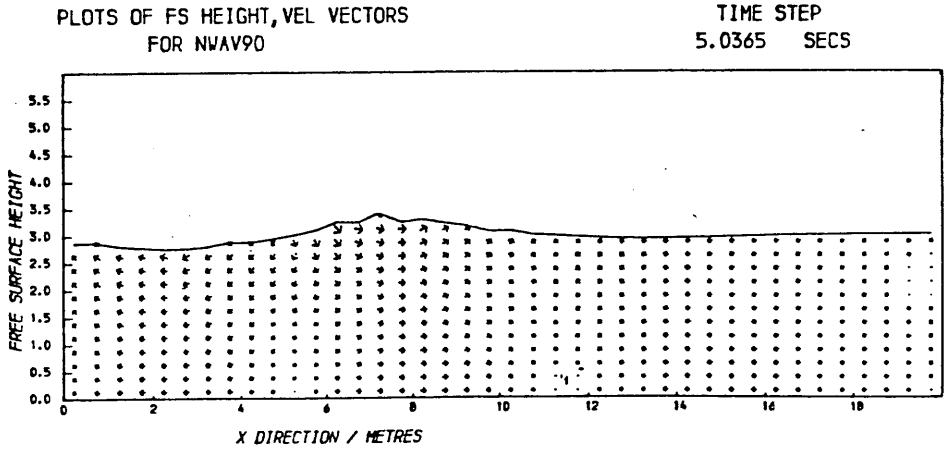
PLOTS OF FS HEIGHT, VEL VECTORS
FOR NWAV90
TIME STEP
5.0365 SECS
FREE SURFACE HEIGHT
X DIRECTION / METRES

Figure 8-14 b

The values Δx and Δy were set primarily by consideration of accuracy in defining the free surface shape. It was found necessary to have at least eight full cells between crest and trough, since continuity is guaranteed only in full cells. Numerical experiment showed it to be vital that the fluid equations of motion were solved in this crest to trough region. Without this constraint, the wave rapidly 'died' as it travelled along the domain.

The same tolerences were applied to the continuity solver in these numerical experiments as was used in FLOW88. It was found that the simple averaging techniques for cell fractional volumes were sufficient to guarantee the evolution of a smooth free surface during the fluid fluxing routines. This was in spite of the coarse mesh used and the evidence from FLOW88 that such approximations could prove unsatisfactory. The success of the resulting central difference approach for the free surface kinematics was thought to be the consequence of the lack of strong convection in the flow. Unlike the flows modelled in FLOW88, which were highly unidirectional and therefore, convection dominated, the fluid accelerations calculated in NWAV90 were heavily dependent upon the dynamic pressure gradients. It was thought likely that the flows set up during the water entry simulation would be likewise dominated by dynamic pressures, allowing the simplest fractional volume averaging techniques to be used.

The use of source distributions to represent the dynamic boundaries was further tested with a series of numerical experiments on wave loading and the motions of idealised floating vessels. Further details are given in reference (142). A full description is beyond the scope of this thesis. However, the figures listed below demonstrate the capabilities of the program.

Figure (8-15) Plots of forced heaving of an idealised semi-submersible model.

Figure (8-16) Plots of forced rolling of an idealised semi-submersible model.

Figure (8-17) Simulation of wave run-up against a rectangular cylinder.

It should be noted that the amplitudes of motion were restricted to excursions no greater than the mesh spacing. This was not due to any assumptions concerning the mathematics of the problems, but rather the lack of any book keeping routines to track the body position.

In conclusion, the development and implementation of the program NWAV90 furnished valuable information concerning the simulation of flows dominated by dynamic pressure terms. It was found that the principles of mass conservation were most important in order to guarantee a successful computation.

n

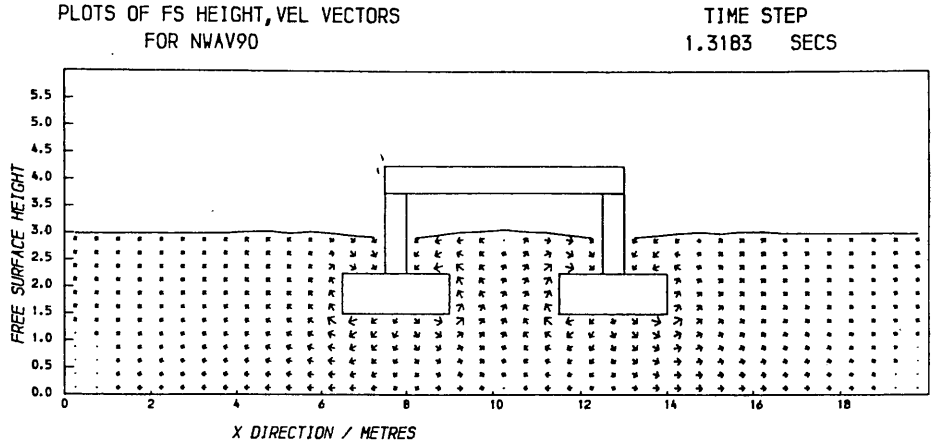
PLOTS OF FS HEIGHT, VEL VECTORS
FOR NWAV90
TIME STEP
1.3183 SECS
FREE SURFACE HEIGHT
5.5
5.0
4.5
4.0
3.5
3.0
2.5
2.0
1.5
1.0
0.5
0.0
0
2
4
6
8
10
12
14
16
18
X DIRECTION / METRES

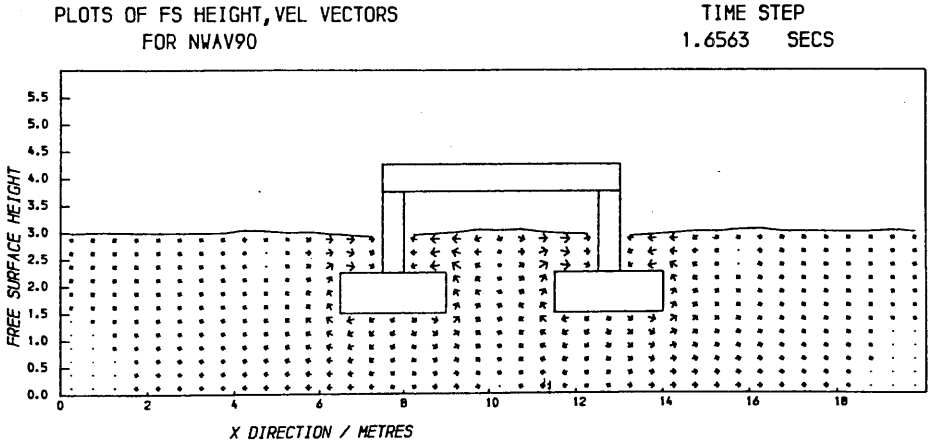
PLOTS OF FS HEIGHT, VEL VECTORS
FOR NWAV90
TIME STEP
1.6563 SECS
FREE SURFACE HEIGHT
5.5
5.0
4.5
4.0
3.5
3.0
2.5
2.0
1.5
1.0
0.5
0.0
0
2
4
6
8
10
12
14
16
18
X DIRECTION / METRES

Figure 8-15

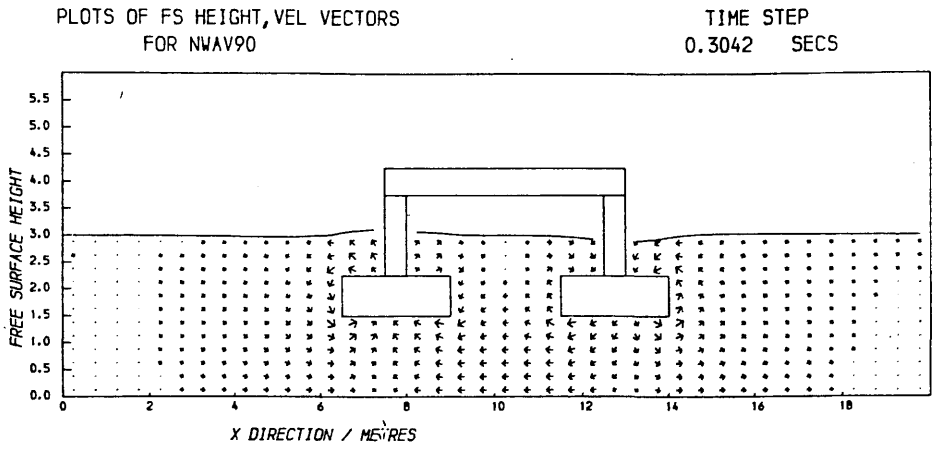
PLOTS OF FS HEIGHT, VEL VECTORS
FOR NWAV90
TIME STEP
0.3042 SECS
FREE SURFACE HEIGHT
X DIRECTION / METRES

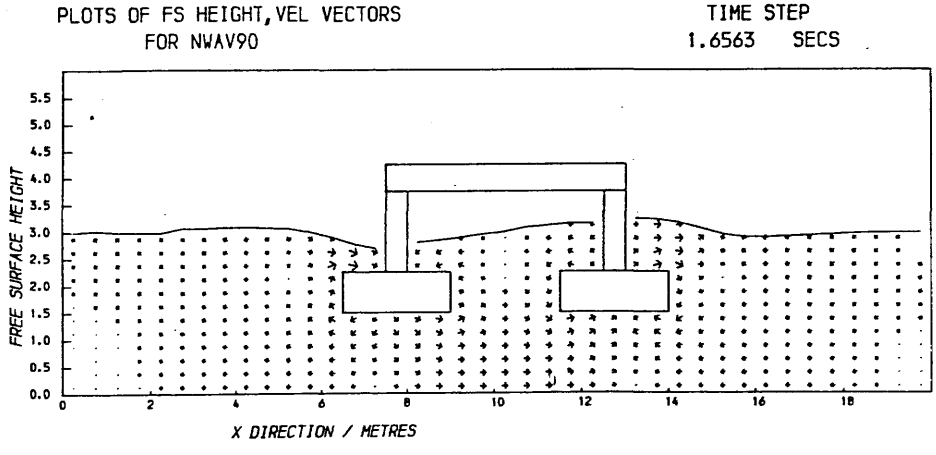
PLOTS OF FS HEIGHT, VEL VECTORS
FOR NWAV90
TIME STEP
1.6563 SECS
FREE SURFACE HEIGHT
X DIRECTION / METRES

Figure 8-16

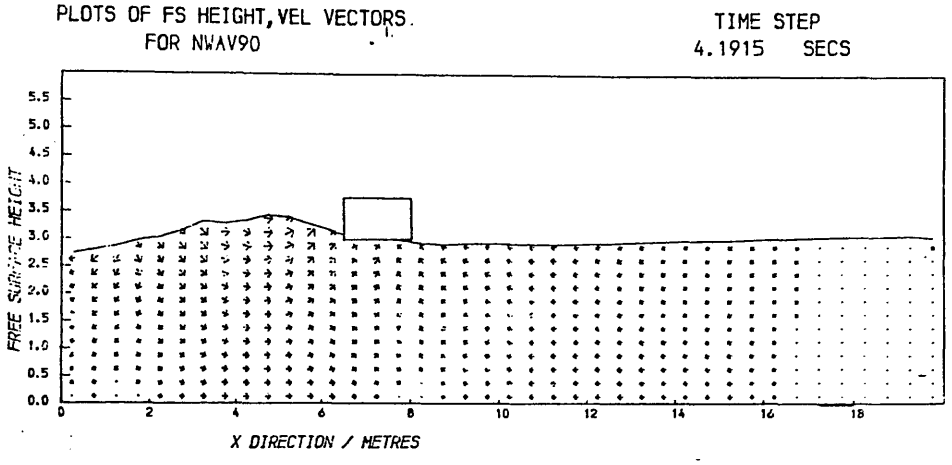
PLOTS OF FS HEIGHT, VEL VECTORS.
FOR NWAV90
TIME STEP
4.1915 SECS
FREE SURFACE HEIGHT
X DIRECTION / METRES

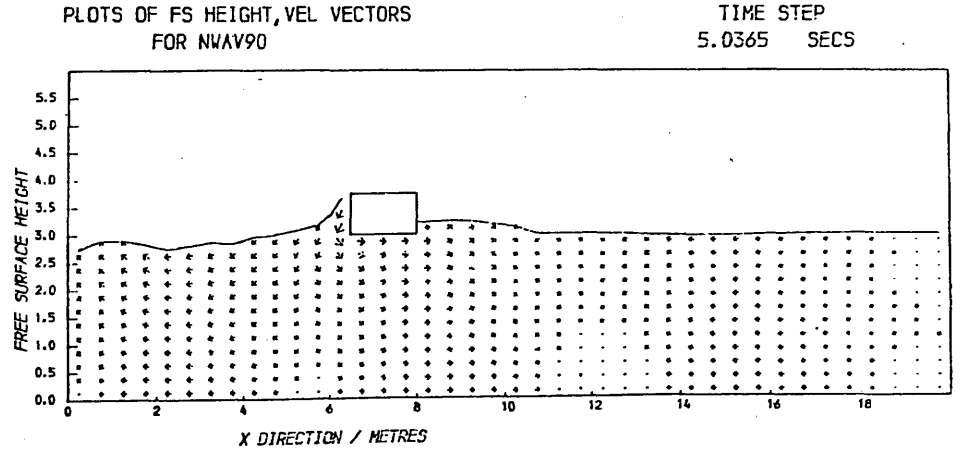
PLOTS OF FS HEIGHT, VEL VECTORS
FOR NWAV90
TIME STEP
5.0365 SECS
FREE SURFACE HEIGHT
X DIRECTION / METRES

Figure 8-17

CHAPTER 9

PROGRAM SLAM, SIMULATION OF HYDRODYNAMIC IMPACT

CHAPTER 9

PROGRAM SLAM, SIMULATION OF HYDRODYNAMIC IMPACT

1. INTRODUCTION

The flow modelling described in the previous chapter laid the foundations for the successful development of SLAM, a computer simulation of hydrodynamic impact. However, SLAt represented a requirement for a much higher level of computational achievement than either FLOW88 or NWAV90. The precise demands put upon SLAM were laid down in the problem statement at the beginning of chapter 3. The numerical tools required to fulfil these specifications had, in part, been tested in programs FLOW88 and NWAV90. To re-cap, these building-blocks may be listed as:-

a. various time marching discretisations of the Navier Stokes equations, suitable for the simulation of unsteady flows.

b. an algorithm to ensure continuity within the flow.

c. a free surface tracking scheme to define the extent of the fluid domain.

d. a link between the continuity solver and dynamic pressures via the fluid wave equation.

e. the use of steady source/sink distributions common to classical hydrodynamics, within the framework of a computational fluid dynamics algorithm.

f. the use of pulsating source distributions to initiate wave motion and represent low amplitude oscillations of floating bodies.

g. a well tried, steady pressure solver based on the successive over relaxation method applied to the Poisson pressure equation.

h. a discrete radiation boundary condition capable of convecting fluid variables out of the computational domain without causing numerical instability.

Further development of these techniques and the introduction of new routines specific to the demands of the water entry problem was required. The following algorithms were needed to supplement those already tested.

a. a method to represent solid boundaries moving freely within the mesh.

b. a development of the static source distribution method to a steady or accelerating source model.

c. the introduction of the variational method described in chapter 6.

d. the use of the algorithm designed to model the 'slightly' compressible flow described in chapters 3 and 4.

This chapter deals with the final stages of development of the four algorithms mentioned above, their inclusion in SLAM, and the results obtained from running the program. Section 9.2 details the final choice of method for representing the shape and dynamics of the body. Section 9.3 describes a series of tests carried out to examine

accuracy and rate of convergence

A study of the parameters affecting time step and mesh size is made in section 9.4.

At this point, all the data required to run SLAM purely to simulate hydrodynamic impact existed. However, some method of generating hull section offsets as input data, and an algorithm to produce slam load data independently for the purpose of comparison with SLAM was needed. Section 9.5 deals with the way in which this information was produced.

The finite size of the model fluid domain lead to the conclusion that for the greater part of the simulation, shallow water effects were of importance. Section 9.6 deals with the calibration of the slamming model such that realistic comparisons may be made with the data produced by the methods described in section 9.5.

Four examples of hydrodynamic impact simulations for varying ship sections are presented, along with discussion of the results, in section 9.7.

Section 9.8 deals with a particular application of the slightly compressible fluid model, making special note of the way in which the real physical conditions required may be modelled using the present technique.

Finally, section 9.9 concludes this chapter with comments on the applicability of the finite difference technique.

2. REPRESENTATION OF MOVING BOUNDARIES WITHIN THE MESH

Three techniques for the representation of the body contour and computation of source strengths were detailed in chapter 5. Experience gained during the development of SLAM eventually lead to a compromise technique based on the combination of marker particles to represent source positions, and a time marching computation of body fractional volumes.

Up to 360 marker particles were used to delineate the contour of the section. The x and y co-ordinates of each particle were updated every time step using a constant acceleration approximation based upon the kinetics of the body.

At any instant, the total source strength within any finite differene cell could be found by:-

a. counting the number of marker particles (nc) within the confines of the cell (I,J).

b. summing up the discrete source strengths Q_{ij}, thus

$$Q_{ij} = \sum_{n=1}^{nc} Q_{p_n} \qquad \text{---} \ 9.2/1$$

The particle source strengths were found by using equation 5.3/4, repeated below for clarity:-

$$Q_p = U_b h \text{SIN}\,\theta + V_b h \text{COS}\,\theta \qquad \text{---} \ 9.2/2$$

This equation may be simplified by assuming h, the arc length, to be given by:-

$$h^2 = [(XC_{n+1} - XC_{n-1})^2 + (YC_{n+1} - YC_{n-1})^2] / 2 \qquad \text{---} \ 9.2/3$$

where XC, YC are the co-ordinates of the two adjacent marker particles. Further simplification allows the rearrangement of 9.2/2 as:-

$$Q_p = [\, U_b(XC_{n+1} - XC_{n+1}) + V_b(YC_{n+1} - YC_{n-1}) \,]/2 \qquad \text{---} 9.2/4$$

In practice, approximately 10 to 20 particles per cell were required in order that a reasonably smooth rise in source strength could be achieved within each control volume.

This steady variation in cell source strength was essential to the realisation of a smooth pressure time history via the modified SOLA code.

A secondary role for the marker particle source strength distribution was to provide a technique for the convection of body fractional volume throughout the mesh. Thus, in any one cell, the time rate of change of body fractional volume was assumed to be:-

$$\frac{\Delta FB_{ij}}{\Delta t} = \frac{Q_{ij}}{VL_{ij}} \qquad \text{---} 9.2/5$$

where FB_{ij} : cell fractional volume

Q_{ij} : cell source strength

VL_{ij} : cell volume (area)

The cell volume VL_{ij} was defined as:-

$$VL_{ij} = (1 - FB_{ij})\ \Delta x\, \Delta y \qquad \text{---} 9.2/6$$

Thus, as more of the cell volume was taken up by the encroaching body contour, the rate of change of FB was increased. This

tied in with the concept of a modified control volume analysis for the SOLA code such that, as the cell volume was decreased, the rate of change of divergence could be increased.

As with the free surface fluxing method, cell side heights had to be defined for the modified control volumes lying along the body contour. The following simple mean value was used as a first approximation.

$$HY_{ij} = (VL_{ij} + VL_{ij-1}) / 2\Delta x \qquad \text{---} 9.2/7$$

where HY_{ij} : cell side height applied to u node ij

VL_{ij}, VL_{ij-1} : modified cell volumes either side of u node ij

With VL_{ij}, VL_{ij-1} being functions of the body fractional volumes FB_{ij}, FB_{ij-1} via equation 9.2/6, it can be seen that equation 9.2/7 results in a view of the convection of the body shape through the mesh similar to the fluid fluxing routine.

To summarise, the body shape was represented by a series of marker particles which also acted as groups of sources. The body fractional volume was computed on a time marching basis as a function of the total source strength in any particular cell. Finite difference cells which coincided with the body contour were modified by consideration of their variable volume (a function of body volume) and changing fluxing heights (a function of local body geometry).

3. TESTS ON ACCURACY AND CONVERGENCE

In chapter 8 it was seen that the particular techniques of computational fluid dynamics developed in this thesis were capable, even on very coarse meshes, of providing good flow visualisations. Some measure of the accuracy to be expected from these methods, and comparison with existing knowledge, was required. One critical measure of program accuracy was thought to be the ability to calculate added mass coefficients for various sections and obtain agreement with previously published results.

There is relatively little data available for such comparitive studies. However, a suitable set of values for the added mass of a rectangular barge in shallow water have been calculated by Flagg and Neuman (142) and confirmed by Bai (143). The barge geometry was well suited to analysis by the finite difference method since it was possible to generate a body fitted mesh for which the application of boundary conditions was trivial. This concept had been well tested in the programs NWAV90 and FLOW88.

In order to ensure that the computer program would not require too much time to run, an essential feature if a broad parametric study is to be carried out, the following assumptions were made:-

a. the fluid velocity at any point could be expressed as:-

$$\tilde{U}(x,y,t) = \tilde{U}_0(x,y)\, e^{i\omega t} \qquad \text{--- } 9.3/1$$

where $\tilde{U}$ represents the vector (u, v)

this is similar to assumptions made prior to computations

of the complex fluid potential for an oscillating body. Consequently, the solution is obtained in the frequency domain, leaving a single boundary value problem for continuity to be solved by the SOLA algorithm.

b. without a formal application of free surface boundary conditions, such as is common to the potential flow formulation (via the linear free surface kinematic condition and Bernoulli's equation) it was impossible to complete a full, frequency domain computation. Thus, by using the SOLA code, a zero pressure gradient boundary condition was implied giving the zero frequency added mass solution.

The outcome of these assumptions was that, for the geometry shown in figure 9-1, with the correct velocity boundary conditions applied at the body/mesh interface (ie source strengths), the first application of the SOLA code would solve the continuity equation, and hence provide the correct flow field. The added mass could then be computed by evaluating the total kinetic energy in the fluid and applying the relationship:-

$$2T = M_a V_b^2 \qquad \text{--- 9.3/2}$$

where T : total fluid kinetic energy

$$T = \sum_{i=1}^{ix} \sum_{j=1}^{jx} \frac{1}{2} \rho (u_{ij}^2 + v_{ij}^2) \Delta x \Delta y \qquad \text{--- 9 3/3}$$

V_b : body vel osity.

The total load upon the body was also computed by integration of the pressure field about the body contour. This provided a check on

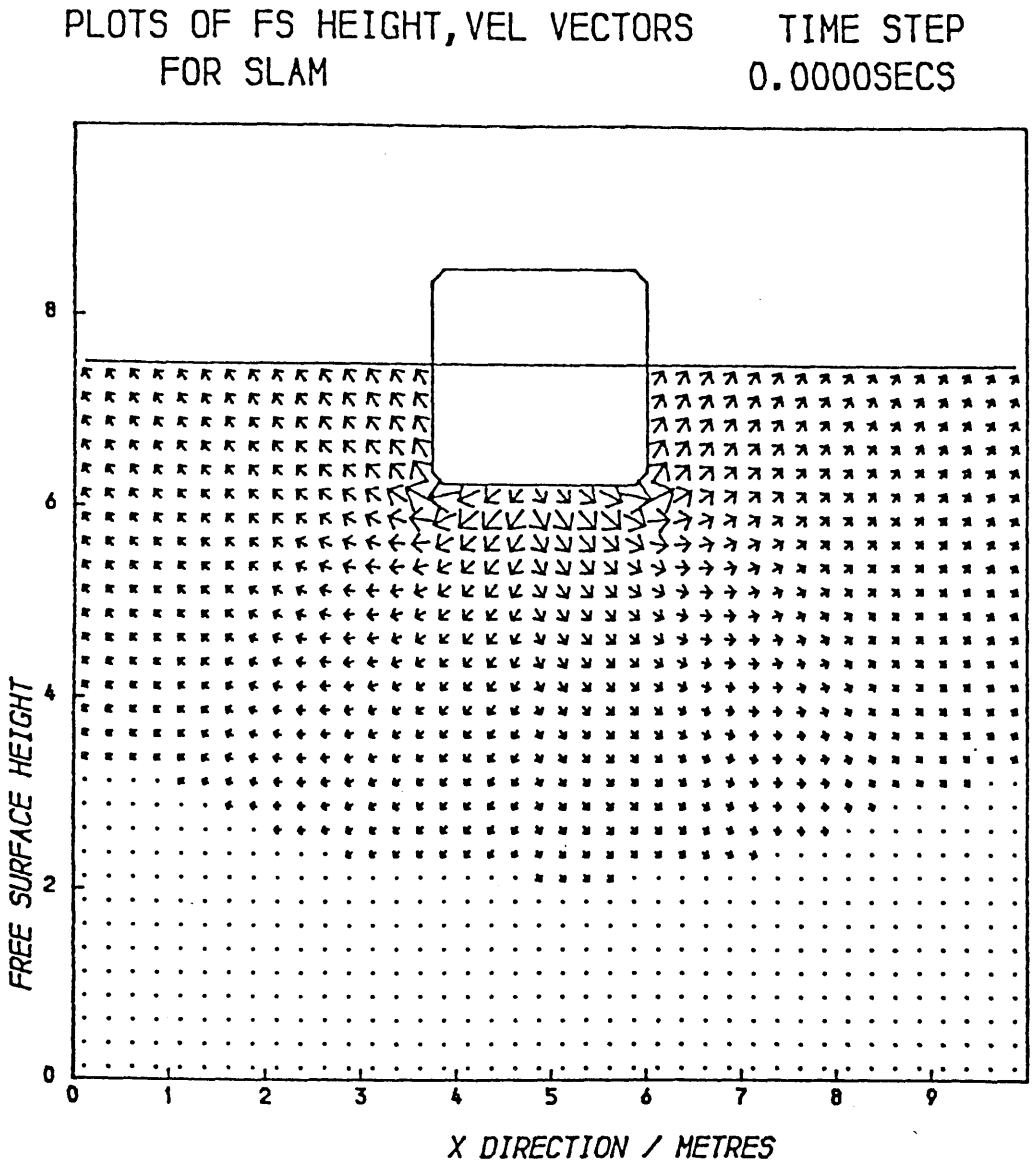

Figure 9-1
Heave Of Rectangular Barge
Flow Field After Single Application Of SOLA Code

Fluid Depth = h Beam = 2b Draught = d

the formulation described above.

The heave added mass of the barge in shallow water was chosen to be the subject of the following study. The beam, draught and depth of water were varied and the added mass computed for each. Each calculation was performed with various divergence based tolerence levels on the SOLA code. Consequently it was possible to compare convergence rates for this problem with those found during study of the programs NWAV90 and FLOW88. Valuable information was compiled for the prediction of the required tolerence levels and computing times for SLAM.

Figure 9-1 shows the geometry of the problem and the flow field which resulted. A unit body velocity was used at first such that the total source strength in each cell adjacent to the body contour became:-

$$Q = V_b \Delta x + U_b \Delta y \qquad \text{--- 9.3/4}$$

where, for heave only $V_b = \pm 1.0 ms^{-1}$

$U_b = 0.0$

and for sway, $V_b = 0.0$

$U_b = \pm 1.0 ms^{-1}$

The area shown in figure 9-1 represents one third (the central portion), of the total domain. The mesh extends for a further 10m either side of the boundaries shown but is excluded for the sake of clarity. The width of the domain was never less than 8 times the total beam of the body, such that the ratio of draught to fluid depth provided the major variation in added mass coefficient.

A total of twelve variations were made, three in draught to depth and four in half beam to draught ratio. Table 9-A details some of this data, and includes for some cases, the number of SOLA sweeps required to reach given levels of tolerence. The difference between added masses computed with these levels of tolerence and the final values can be seen to be within ten percent of each other.

Finally, figure 9-2 shows curves of added mass coefficient versus draught to depth ratio for various beam to draught ratios plotted using data from references 142 and 143. Values calculated using the present method are superimposed upon these curves. It can be seen that the level of agreement is very good for a tolerence level on the residual $\nabla.\bar{u}$ of 10^{-3}. Even with the convergence criterion relaxed by an order of magnitude, the added masses calculated were within 10% of those computed by Flagg and Neuman.

The tests described above used a unit body velocity. A further examination was carried out with this model in order to study the effect of higher values of V_b on the accuracy of the solution. As V_b was increased, the total source strength and subsequently the level of initial fluid divergence, grew accordingly. This resulted in an increase in the number of iterations required by the SOLA code to produce convergence. The finite domain width also began to play a part as V_b was increased since the total kinetic energy within the fluid became greater. The total spread of kinetic energy was therefore constricted by the far boundaries. In a time marching simulation, this energy could have been removed from the domain by the radiation boundary condition. However, for the purposes of this computation a limit to the heave velocity had to be set based on the finite computational resources available.

TABLE 9A

DIMENSIONS OF KINETIC ENERGY IN Kgm^2/s^2

Added Mass Coefficients for a Rectangular Barge in Shallow Water

Mesh Size x = 0.25, y = 0.25

Width of Domain = 8.0 x beam

b = half beam (m)

h = depth of fluid (m)

d = draught of barge (m)

Run No	b/d	d/h	Fluid K.E	C_A	SOLA TOL
1	0.2	0.133	1239.7	4.9	10^{-3}
2	0.5	0.133	1391.5	2.2	10^{-3}
3	0.5	0.133	1265.0	2.0	10^{-2}
4	1.0	0.133	1481.4	1.1	10^{-3}
5	1.0	0.133	1397.1	1.04	10^{-2}
6	2.0	0.133	1879.5	0.75	10^{-3}
7	0.2	0.266	1290.3	5.10	10^{-3}
8	0.5	0.266	1518.0	2.40	10^{-3}
9	1.0	0.266	1771.0	1.40	10^{-3}
10	2.0	0.266	2150.5	0.85	10^{-3}
11	0.2	0.50	1290.1	5.10	10^{-3}
12	0.5	0.50	1929.1	3.05	10^{-3}
13	1.0	0.50	2530.0	2.0	10^{-3}
14	1.0	0.50	2277.0	1.80	10^{-2}
15	2.0	0.50	3668.5	1.45	10^{-3}

Figure 9-2 Comparison Of Added Mass Coefficients As Deduced By:

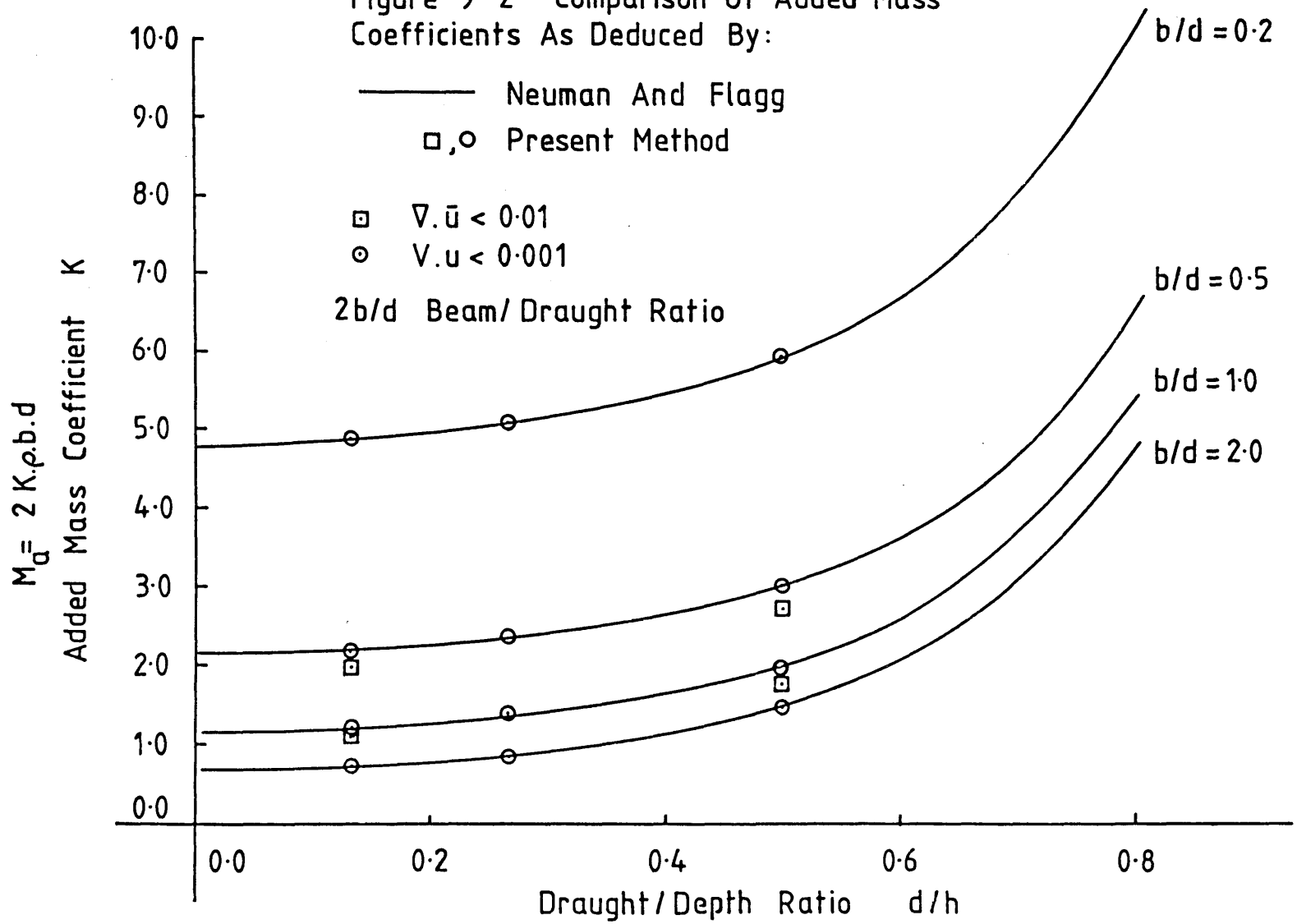

Figure 9-3 shows a combined plot of the number of iterations required to reach convergence (normalised using the number required at unit heave velocity) versus body velocity, and the added mass coefficient as computed using equation 9.3/4 versus heave velocity. It can be seen that, up to a value of V_b of 5.0m/s there is little change in the added massc coefficient for this geometry. However, at a value of V_b equal to 10m/s the added mass coefficient has increased by 23%. A cautious approach was adopted when using high impact velocities in program SLAM as a result of these observations. However, it was found that the problem was less acute for the drop test type simulation. In this case the body velocity was reduced by the applied fluid loading before a sufficient level of immersion arose to cause this 'blockage' type phenomenon. Unfortunately, these considerations did not apply to the forced impact scenario.

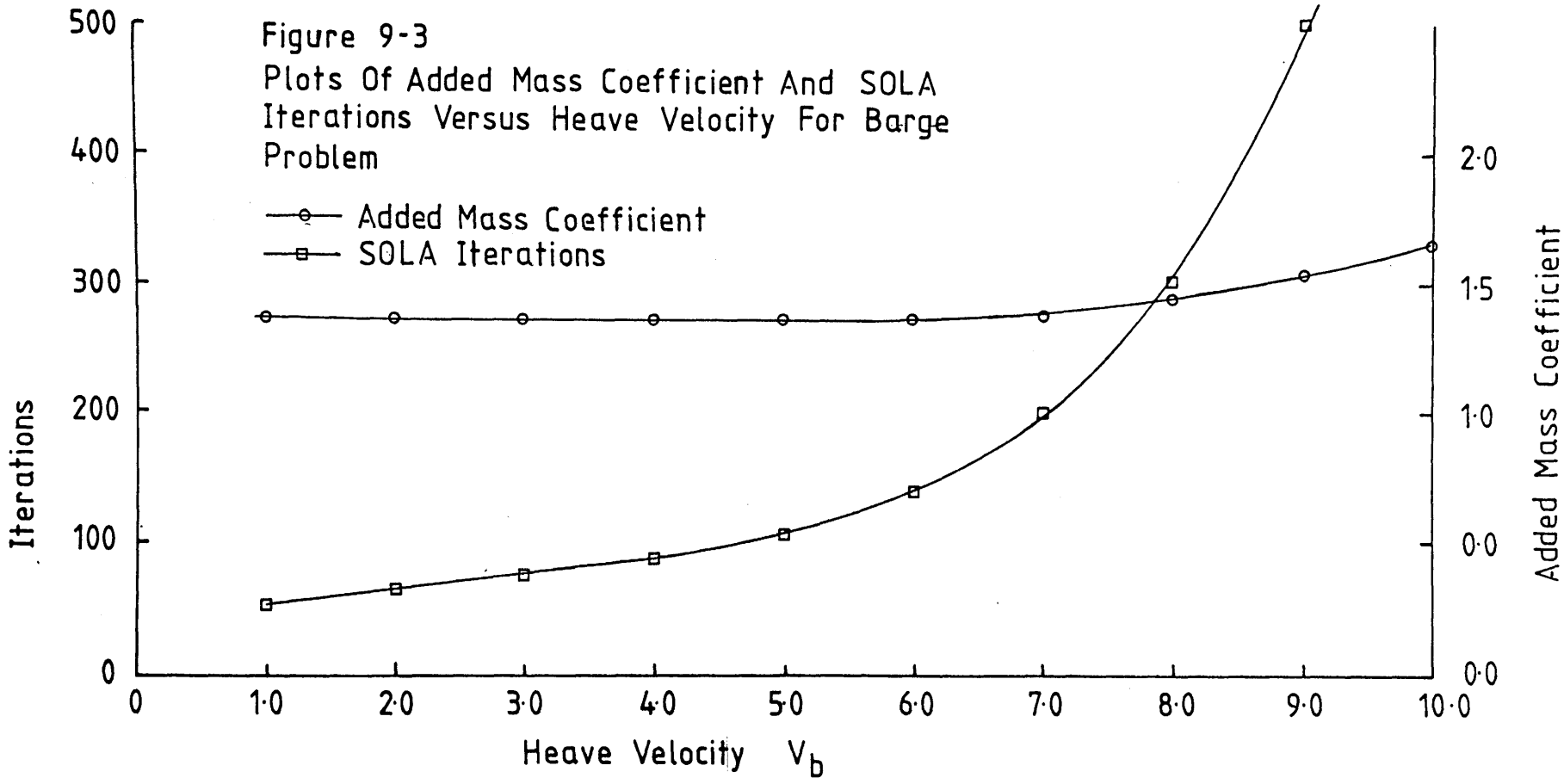
Figure 9-3
Plots Of Added Mass Coefficient And SOLA Iterations Versus Heave Velocity For Barge Problem
Added Mass Coefficient
SOLA Iterations
Iterations
Added Mass Coefficient
Heave Velocity V_b
0
100
200
300
400
500
0·0
0·0
1·0
1·5
2·0
0
1·0
2·0
3·0
4·0
5·0
6·0
7·0
8·0
9·0
10·0

It was seen in chapter 4, section 9 that the development of the SOLA algorithm was based on the introduction of the rate of change of divergence into the right hand side of the Poisson equation for pressure. In this thesis, the SOLA code was modified such that the divergence could be matched to the source strengths representing moving boundaries and that, via analogy with the wave equation, the dynamic pressures could be calculated. This latter property resulted in the following time step criterion:-

$$\Delta t = \left(\frac{1}{2C^2\left(1/(\Delta x)^2 + 1/(\Delta y)^2 \right)} \right) \qquad \text{---} 9.4/1$$

where C is some physical wave speed.

For the slamming models used herein, there were two choices of wave speed.:-

a. the shallow water wave speed:-

$$C = \sqrt{g.d}$$

where d is the fluid depth.

b. the fluid acoustic wave speed:-

$$C = 1410 \text{ m/s}$$

Figure 9-4 shows a plot of time step in milliseconds versus mesh spacing. The main feature of these plots is the very small size of time step required even for this hydrodynamic model. Furthermore, the time step would seem to be invariant with body velocity. In fact, this is not so, owing to the practical consideration that the book keeping routines responsible for tracking the motions of the body

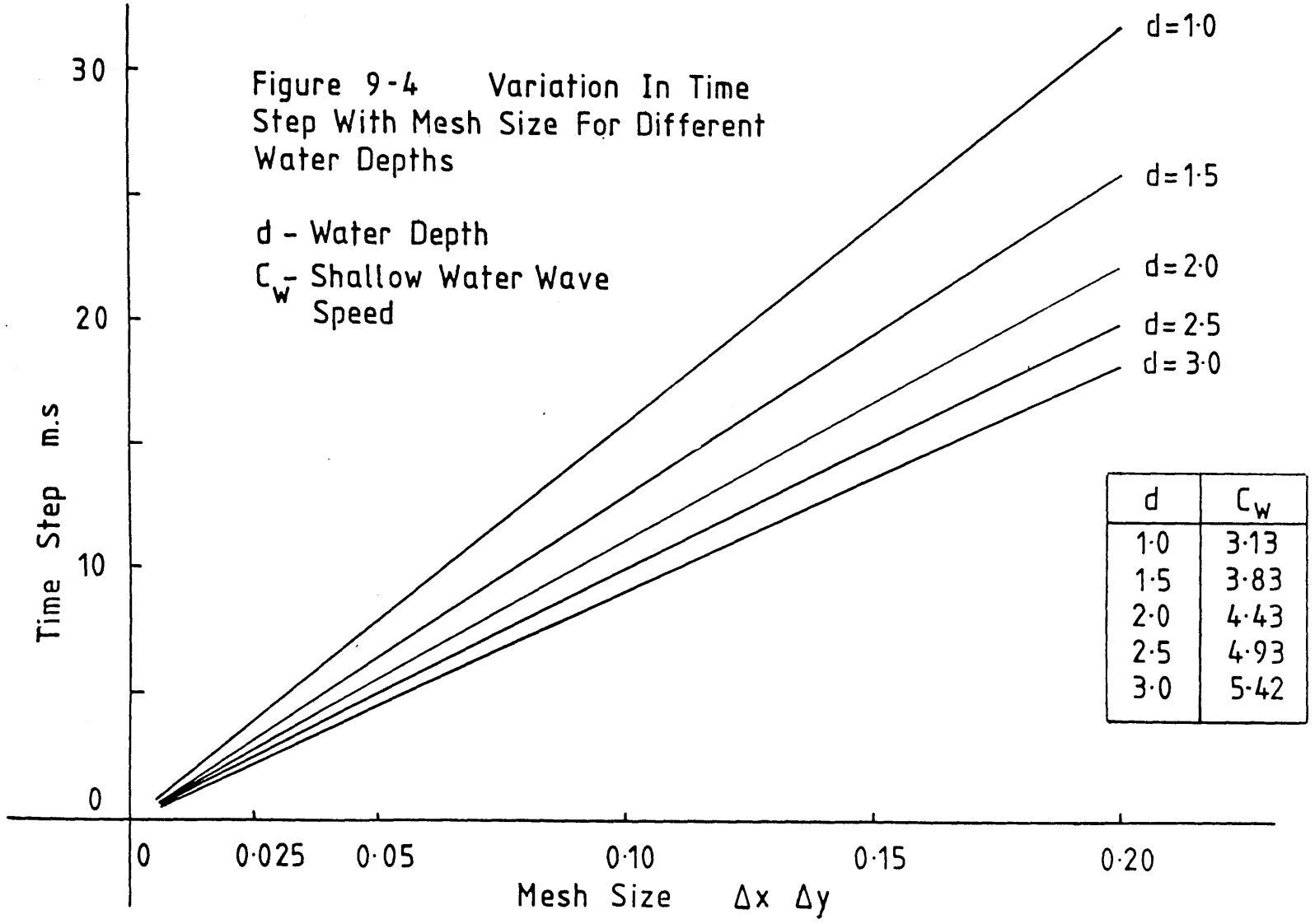
Figure 9-4 Variation In Time Step With Mesh Size For Different Water Depths
d - Water Depth
C_w - Shallow Water Wave Speed
d=1·0
d=1·5
d=2·0
d=2·5
d=3·0
Time Step m.s
30
20
10
0
0
0·025
0·05
0·10
0·15
0·20
Mesh Size Δx Δy
d | C_w
1·0 | 3·13
1·5 | 3·83
2·0 | 4·43
2·5 | 4·93
3·0 | 5·42

would break down if the C.F.L condition given by:-

$$\frac{V_b \Delta t}{\Delta x} \leq 1 \qquad \text{---} 9.4/2$$

were to be violated.

The choice of time step for the hydrodynamic impacts was made by balancing the following considerations in order of importance:-

a. depth of water

b. mesh size

c. beam of section

d. speed of body.

The depth of the fluid fixed the wave speed, thus allowing the time step to be deduced from figure 9-4 for any mesh size. The number of fluid nodes in the vertical direction could then be calculated. Similarly, the number of nodes allowed to cover the beam of the section, and the total number required to discretise the full width of the fluid domain could be deduced. A check on the body C.F.L condition given by 9.4/2 was the made. If the total number of fluid nodes were too high, or the time step too small, an excessive computing time would result. However, experience of running the impact simulation routines soon led to the ability to weigh up the criteria listed above to produce a reasonable compromise between good flow resolution and overall computing time.

Table 9-B below gives the time step size computed using the acoustic wave speed for water, for various mesh spacings.

Mesh Size (m) $\Delta x = \Delta y$	Time Step Δt m.s
0.025	8.86
0.050	17.72
0.10	35.44
0.15	53.16
0.20	70.88

Table 9-B

The linear behaviour is the result of keeping the mesh ratio equal to one. The major feature is the very small time step required when acoustic fluid behaviour needs to be studied. However, these considerations are essential when examining the slam behaviour of a section at the instant of contact. Some slam theories allow for infinite pressures to be generated when the body first touches the fluid. The consideration of fluid compressibility would remove this unphysical behaviour replacing it by a finite pressure rise time. Campbell and Wellicombe have reported load rise times of the order of 20μs (90,91,92) which even the smallest time step given in table 9-B would have difficulty resolving.

Finally, the decision to retain a square mesh for the fluid domain was based on the need to produce a fast Poisson pressure solver. The successive over relaxation scheme used for this part of their simulation was found to be less efficient when the mesh ratio was not equal to one. Whilst the change of relaxation parameter (ω) mentioned in chapter 8 went some way to assisting with this problem, the more complicated expressions required to form the desired recursive relationships played the major role in increasing the total computing time. It was not found that the constraint of unit mesh

ratio caused any extra problems. Indeed, most steps in the simulation benefitted from this constraint.

5. DATA PREPARATION FOR IMPACT TESTS

In order to run the computer simulation, data was required in two areas:-

a. definitions of modelling parameters, for example, fluid density, viscosity, depth, mesh spacing, body position (co-ordinates of centre of gravity) and initial impact velocity.

b. definition of body shape, ie the co-ordinates of the marker particles used to delineate the section contour.

The parameters listed in subsection (a) above may be assigned values by use of a Fortran DATA statement in the main program. The definition of marker particle co-ordinates was a somewhat more complex task. A program to generate a ship section was written in which the transverse hull form was represented by a series of three curves. These were:-

a. a straight line (denoted curve A) of formula:-

$$y = MX + C$$

where M : deadrise gradient based upon rise and width of floor.

C : position of the keel below the x axis, ie the initial draught.

over a small portion of the bottom defined by the width of floor. Alternatively, a second order polynomial could be defined to cover this part of the section.

b. a third order polynomial (denoted curve B) whose four coefficients were derived by a curve fitting routine. This second curve determined the hull form between the edge of the bottom section, as defined above and an arbitrary point upon the ship side. The data for the curve fit was provided by the co-ordinates of its two end points, the deadrise gradient M, and a slope defined at, for example, the turn of the bilge.

c. a third order polynomial (denoted curve C), which ran from the end point of curve B up to the sheer line. The data for the curve fit was provided by the co-ordinates and gradient at the end of curve B, and the co-ordinates and gradient (ie flare angle) at the sheer line.

Figure 9-5 illustrates these three curves and the data points to be input to the form generation program. A closed contour was required, hence a straight line was fitted between the centreline and the deck edge. Half of the marker particles were then distributed between these four curves, starting at the centre of the deck and moving around to the keel. The co-ordinates for the remaining marker particles were found by reflection.

Having computed the two dimensional hull form and defined the marker particle positions, the following computations were made at various draughts:-

a. the sectional area.

b. the added mass coefficient.

Both of these quantities were found by numerical approximation (Simpson's rules). The sectional area provided the

Figure 9-5
Data Required For Hull Form Generation

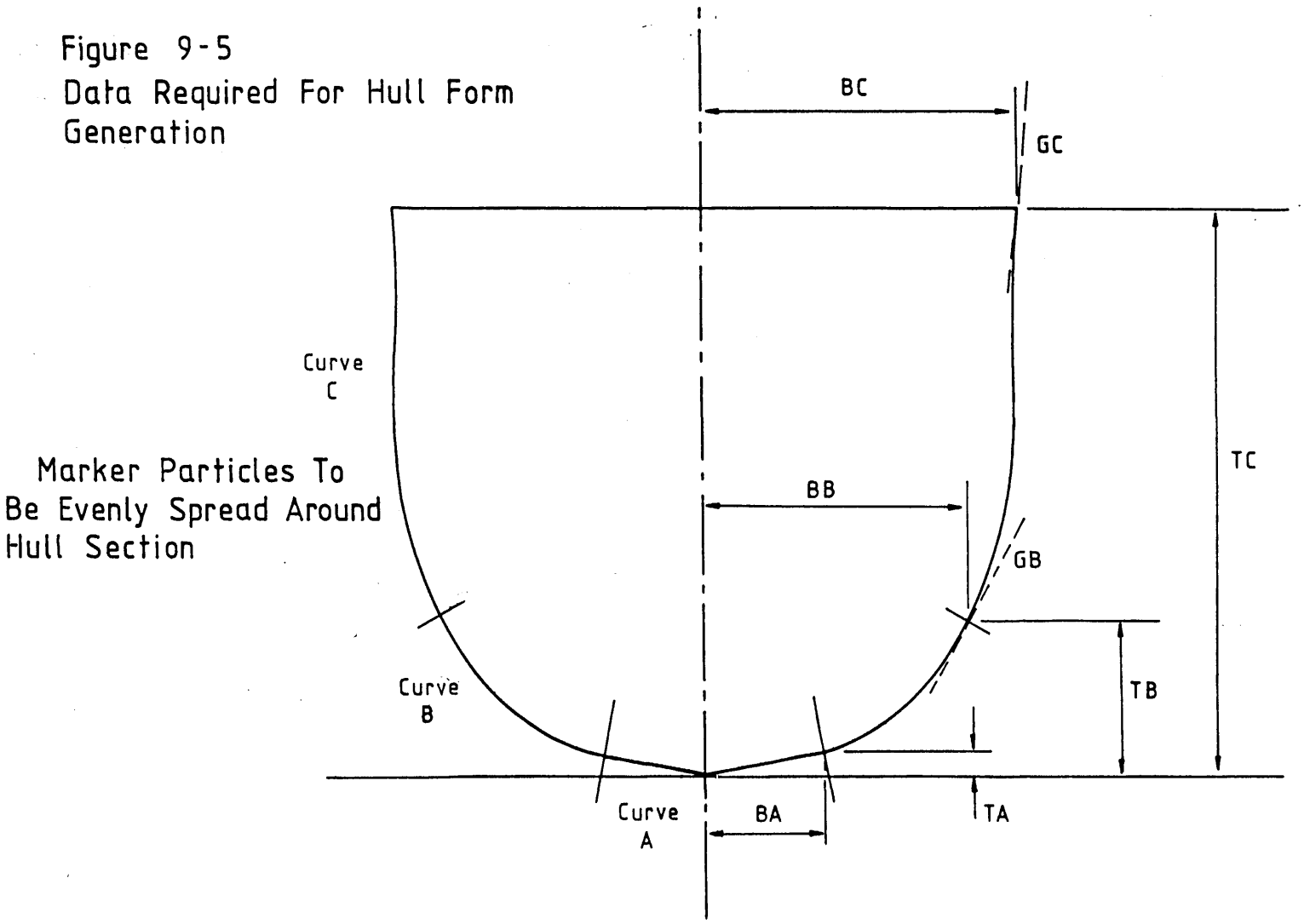

buoyancy force per unit length at various draughts. The added mass coefficient at each draught was found using a Lewis three parameter mapping technique. The required values of beam to draught ratio, sectional area coefficient and second moment of area coefficient were easily deduced using the aforementioned numerical approximations. Consequently, the computation of the rate of change of added mass with draught (via a finite difference approximation to dM /dz) allowed a comparitive measure of slam loading to be defined for each section. Furthermore, the Lewis form coefficients (a_1, a_3, a_5) at one tenth of the draught were used to compute Ochi's slam coefficient as given by equation 2.4/29.

Figure 9-6 shows a sample plot of the data produced by the routines described above.

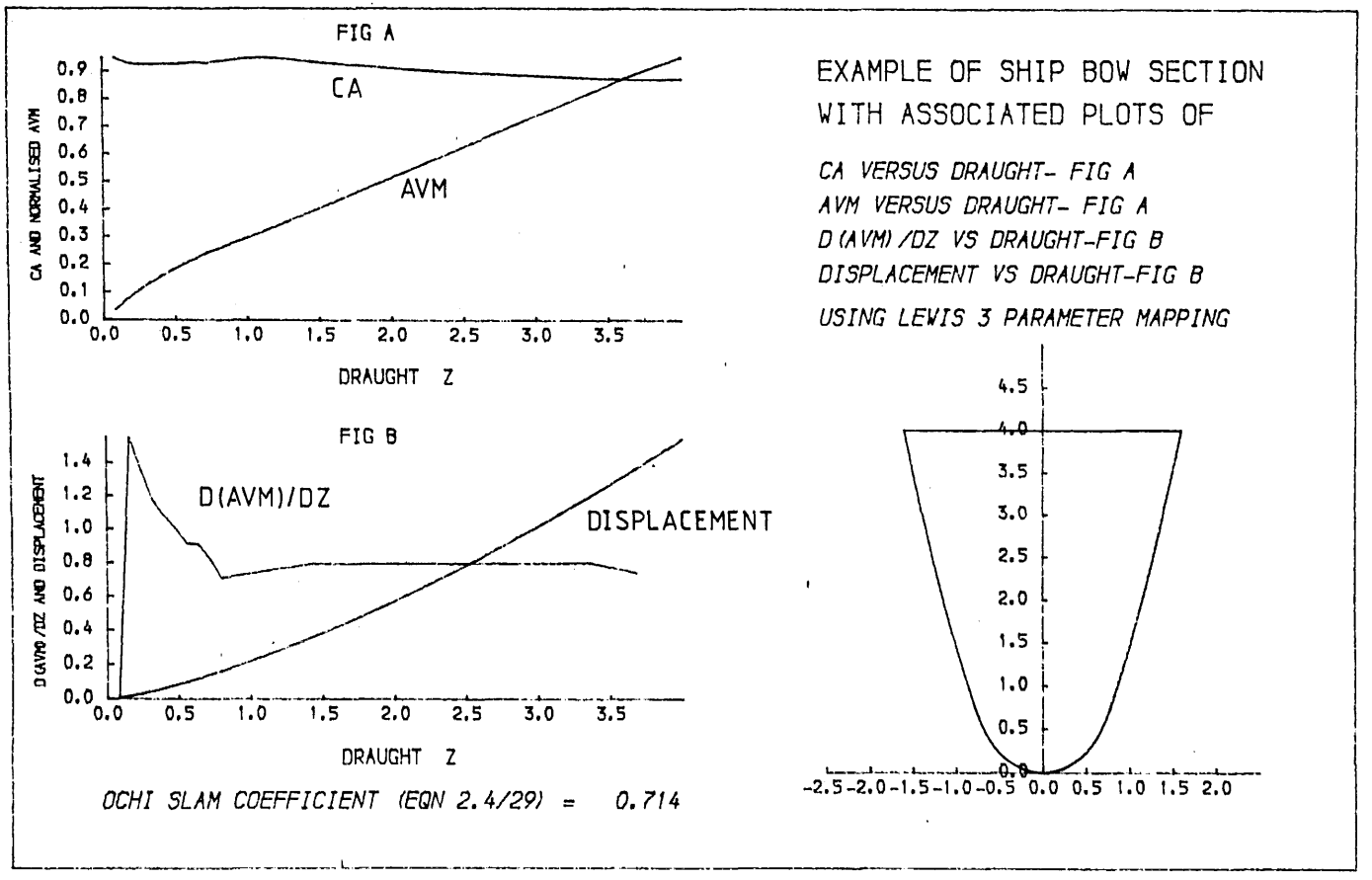
FIG A
CA
AVM
CA AND NORMALISED AVM
DRAUGHT Z
FIG B
D(AVM)/DZ
DISPLACEMENT
D(AVM)/DZ AND DISPLACEMENT
DRAUGHT Z
OCHI SLAM COEFFICIENT (EQN 2.4/29) = 0.714
EXAMPLE OF SHIP BOW SECTION
WITH ASSOCIATED PLOTS OF
CA VERSUS DRAUGHT- FIG A
AVM VERSUS DRAUGHT- FIG A
D(AVM)/DZ VS DRAUGHT-FIG B
DISPLACEMENT VS DRAUGHT-FIG B
USING LEWIS 3 PARAMETER MAPPING

Figure 9-6

6. CALIBRATION OF THE MODEL FOR SHALLOW WATER

As noted in the introduction to this chapter, the limited size of the finite difference domain suggested that shallow water effects may influence the slam loading experienced by the ship section. In order to quantify these effects, the following calibration method was applied.

The algorithm used in section 9.3 to test accuracy and convergence was repeated, but applied to ship sections. The hull lines were generated by the method described in the previous section. The fluid domain and finite difference mesh used in this calibration process was identical to that to be utilised for the impact simulations. The added mass was computed for a number of draughts, with the free surface remaining static. These values were then compared to those calculated using the Lewis three parameter mapping method.

Figure 9-7 shows a series of flow visualisations at various draughts resulting from the single step computation. It is interesting to note that this representation is similar to that originally envisaged by Von-Karman. Figure 9-8 shows the resulting plot of added mass coefficient versus draught. The Lewis form added mass coefficient is plotted on the same scale as a basis for comparison.

The rate of change of added mass with draught for each of the two computational techniques is plotted in figure 9-9. The considerable differences between the two curves widen as the draught of the section is increased. The effect of the finite depth of the fluid domain was considered responsible for this variation.

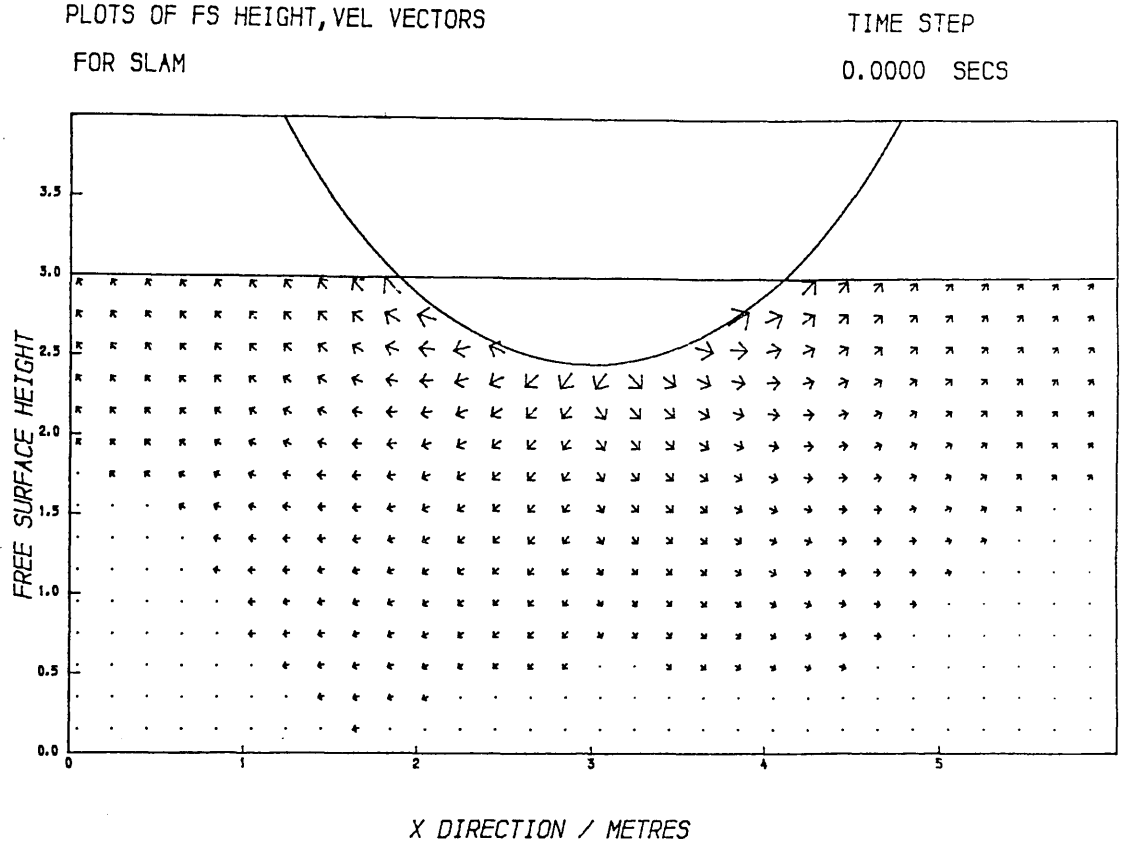

Figure 9-7

Flow Visualisation For Single Step A.V.M Computation

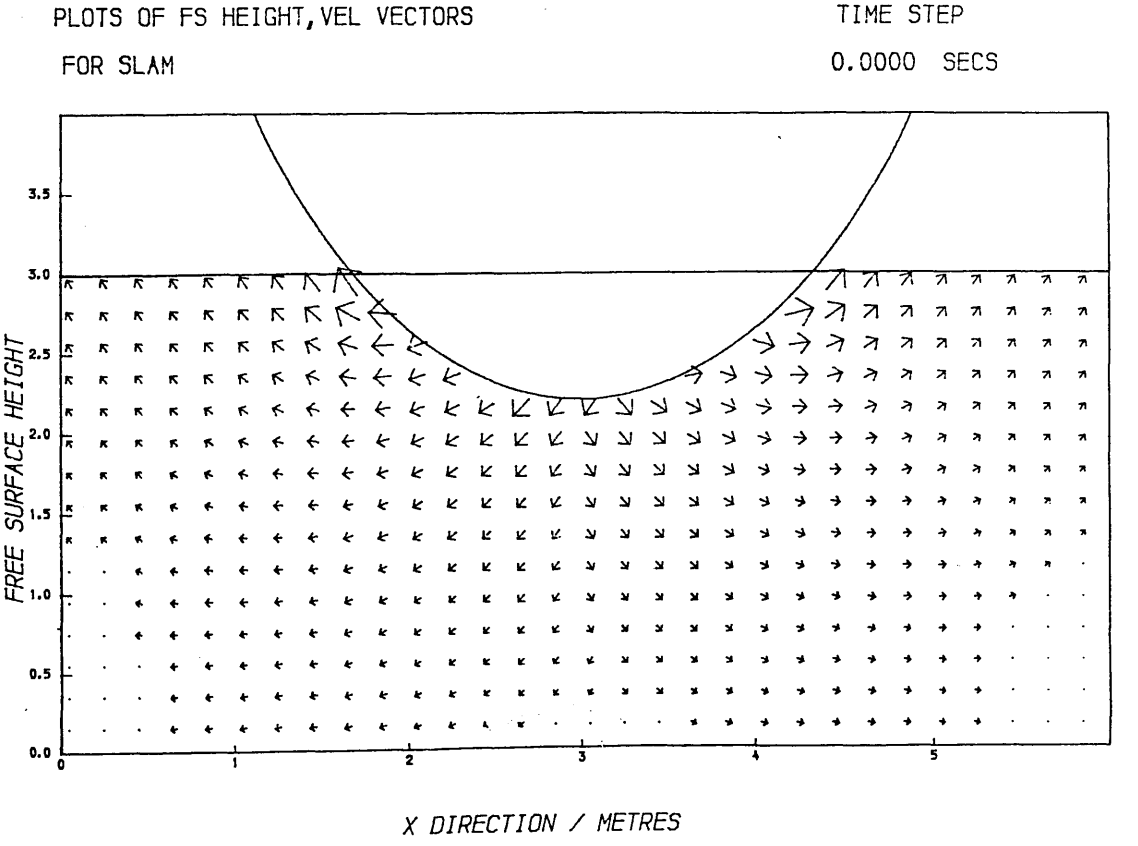

Figure 9-8
Comparison Of Section Added Mass
As Computed Using-

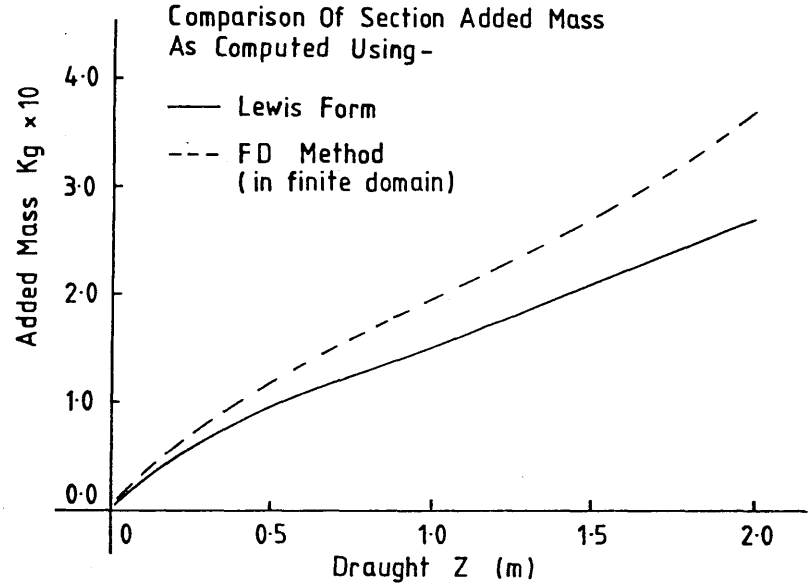

Figure 9-9
Comparison Of D(AVM)/DZ
Using

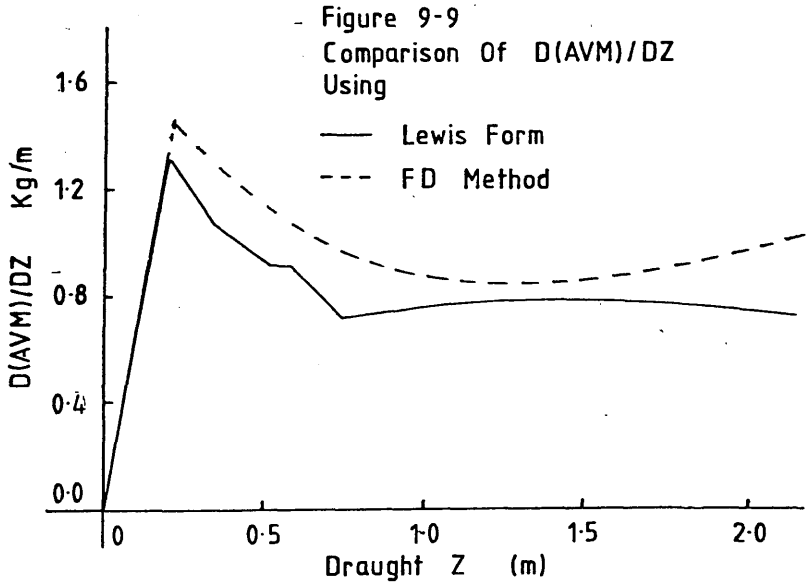

Fortunately, the largest difference was confined to section draughts which would only be reached after the initial peak in the load time history.

These observations lead to the definition of calibration factors for both the added mass and rate of change of added mass with draught. The two factors were derived by taking the ratio of M and dM /dz, calculated using the present method, to values computed using the Lewis three parameter technique. The variation of these calibration factors k_a, k_s with draught are plotted in figure 9-10.

It should be noted that, for shallow draughts, the present method was liable to be less precise since the mesh resolution of the body shape was poorer than that achieved when more of the body was immersed. Some computations of added mass were performed using a finer mesh at these shallow draughts and better agreement with the Lewis form values was achieved. The original calibration factors were retained however, but consideration of the source of these values was extended to include numerical errors in the finite difference discretisation.

Figure 9-10
Example Calibration Factors K_a, K_s

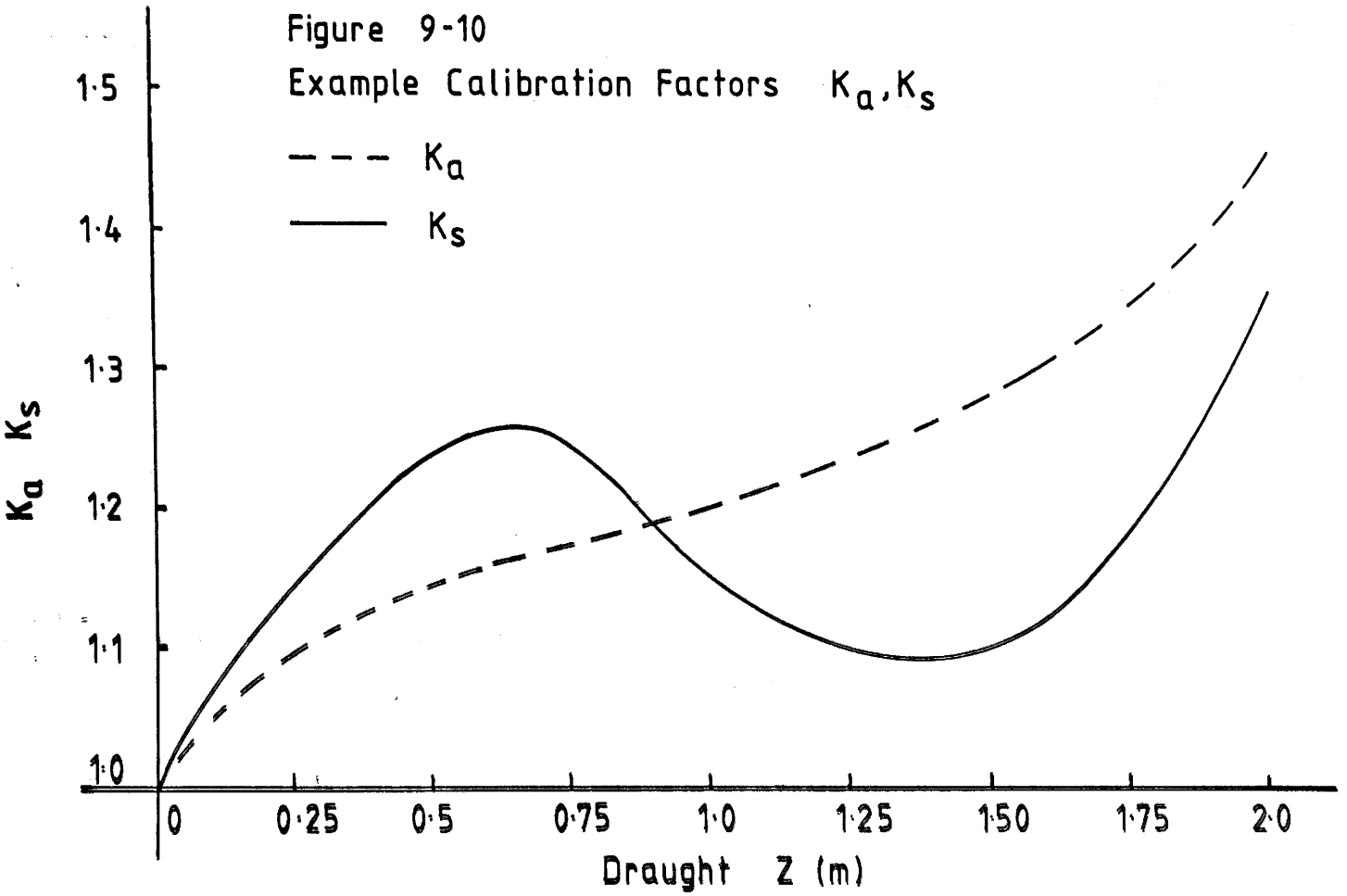

7. EXAMPLES OF HYDRODYNAMIC IMPACT

7.1. Introduction

This section details the simulation of drop tests performed with four different body shapes. Initially, the impact of a circular cylinder upon a still free surface was studied. The results from these computations are given in section 9.7.2 along with a comparative study with other author's work.

A further three ship shaped sections were also tested. The hull forms were generated using the data preparation routine described in section 9.4. Thus comparative data was available, supplied by the Lewis form, rate of change of added virtual mass approach.

Various initial impact velocities were used in each of the tests, with load and pressure time histories being the major items of output. Correlations between loads calculated by pressure integration and rate of change of added mass approaches were used as a test of the accuracy of the numerical method.

Figure 9-11 shows the initial geometry and flow conditions for a typical impact simulation. The body contour is just touching the free surface and is moving with velocity V_b. The time marching simulation begins with the free surface being penetrated by a small amount ΔS over the first time step. The subsequent dynamic simulation has already been described in chapter 4, section 10. At each time step the following items of data were output by the program:-

a. draught below still water level (d_s).

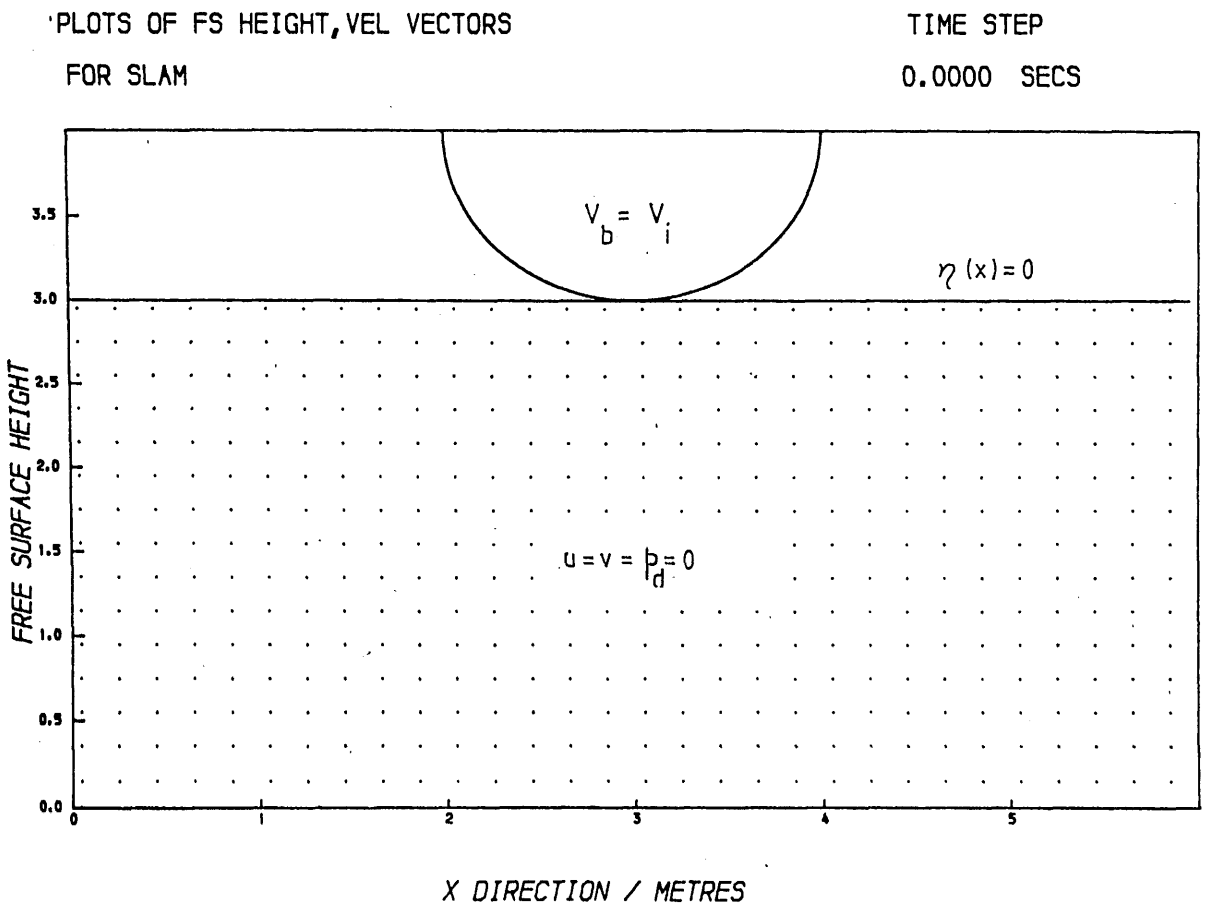
'PLOTS OF FS HEIGHT, VEL VECTORS
FOR SLAM
TIME STEP
0.0000 SECS
$V_b = V_i$
$\eta(x) = 0$
$u = v = p_d = 0$
FREE SURFACE HEIGHT
3.5
3.0
2.5
2.0
1.5
1.0
0.5
0.0
0
1
2
3
4
5
X DIRECTION / METRES

Figure 9-11

b. beam at still water level (b_s).

c. total draught, ie including height of spray root (d_r).

d. total wetted beam (b_r).

e. total load as computed by pressure integration.

f. pressure distribution over the wetted surface.

g. velocity and acceleration of the body.

h. kinetic and potential energy of the fluid.

i. kinetic and potential energy of the fluid.

In addition to the items of numerical output listed above, a standard computer graphics package (GHOST) was used to produce flow visualisation records of the type already seen in chapter 8. Unfortunately, it was possible to produce only a few such pictures during each run owing to the quantity of computer storage space required to hold the necessary data.

7.2. Impact of a Circular Cylinder

Both drop tests and forced impact simulations were carried out with a circular cylinder of 1.0 metres radius. Various drop heights or initial impact velocities were applied.

Comparative data was obtained from a number of sources. Primarily, Kaplan's approach (86) using the rate of change of added mass with draught of a circular arc (given in chapter 2, equation 2.8/2), and the experimental results of Campbell et al (90,91,92) were used.

Figure 9-12 shows the plots of slam force with draught for both in terms of the variation of slam coefficient C_s. It should be noted at this point, that the evaluation of equation 2.8/2 as given by Kaplan did not produce satisfactory agreement with a finite difference computation of the gradients $d(C_a)/dz$ based on the original expression for added mass given by J Lockwood-Taylor (87). Re-analysis of equation 2.8/1 gave the following expression:-

$$\frac{\partial M_a}{\partial Z} = \frac{\rho R}{2\,SIN\theta}\left[\frac{2\pi^3(1-COS\theta)}{3(2\pi-\theta)^3}\left(2SIN\theta + \frac{3(1-COS\theta)}{2\pi-\theta}\right)\right.$$

$$\left. + \frac{\pi}{3}SIN\theta + COS\theta - 1\right] \qquad \text{---9.7/1}$$

Comparison with equation 2.8/2 reveals a considerable discrepancy. In terms of the slam coefficient used in this work equation 9.7/1 may be re-arranged to give:-

$$C_s = \frac{1}{4R.SIN\theta}\left[\frac{2(1-COS\theta)}{3(2\pi-\theta)^3}\left(2SIN\theta + \frac{3(1-COS\theta)}{2\pi-\theta}\right)\right.$$

$$\left. + \frac{\pi}{3}SIN\theta + COS\theta - 1\right] \qquad \text{---9.7/2}$$

where C_s : slam coefficient $= F_s / 0{\cdot}5\rho D^2 V_i^2$

F_s : slam force

D : cylinder diameter

V_i : impact velocity

Figure 9-12 also shows an estimation of the effect of the spray root on the rate of change of added mass (modified via the rate of change of the half vertex angle θ). The 'wetted surface

Figure 9-12

Time Dependence Of Slam Coefficient (C_s)
Based Upon Fractional Immersion Rate

Δ Campell & Wellicombe (90,91,92)
o Kaplan & Silbert (86)
□ As Above With Spray Root Effect

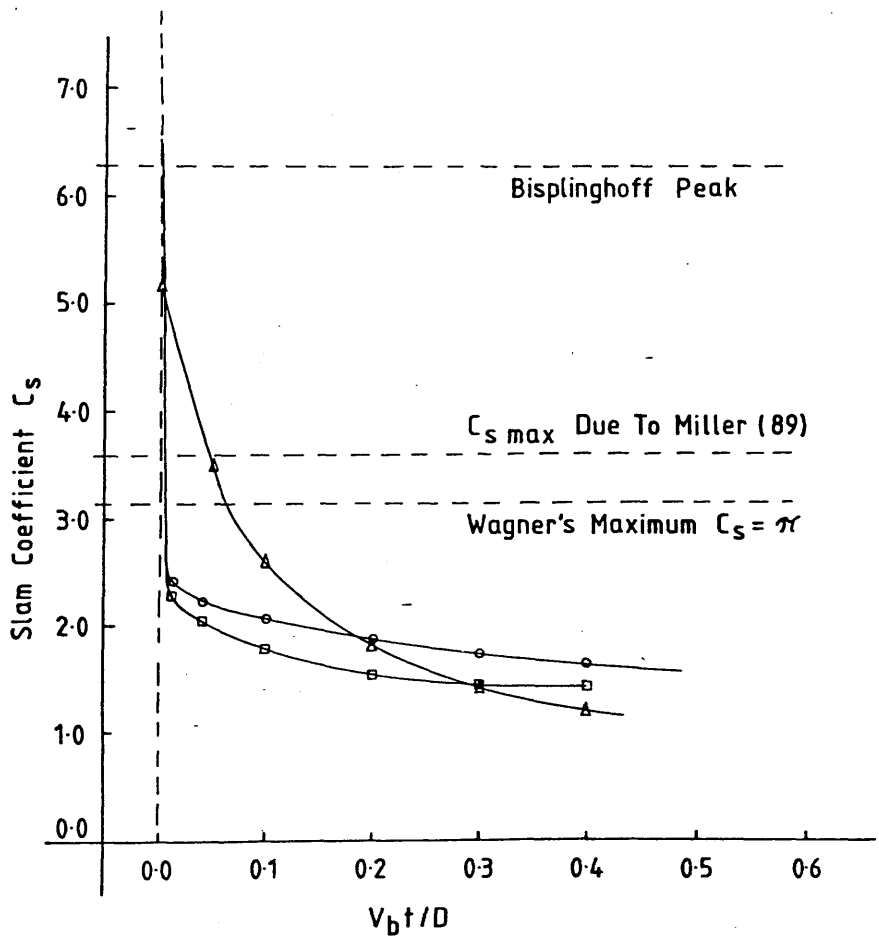

correction' was derived by following Wagner (26) and Chuang's (39) methods, substituting the rate of change of wetted arc for the rate of change of beam. The result is a steeper drop in load after the initial peak.

The application of the spray root enhanced rate of change of wetted beam concept to equation 9.7/2 revealed a paradox generated by the two, fundamentally different approaches to the water entry problem. The expanding flat plate model of Wagner, Chuang etc, ignores the pressure irregularity generated at the instant of contact. In such an approach, the inclusion of the spray root increases the total load at any given instant by consideration of the enhanced wetted beam. The rate of change of added virtual mass concept assumes the load to be infinite at the instant of contact. Hence the effect of the increased rate of change of wetted beam is to reduce the total load at any given time after first contact. Fortunately, the present computational technique was able to resolve this problem as will be shown later in this section.

The maximum slam coefficients according to Von-Karman (25) of $C_s = \pi$, Fabula (28), with $C_s = 2\pi$, and the experimental value of $C_s = 3.6$ given by Miller (89) are also included on figure 9-12.

Tests were carried out at first for the forced or constant velocity impact case. It was decided that the elimination of cylinder dynamics would aid the initial analysis of the data produced by SLAM. As an introduction to the presentation of the results, the following plots were prepared for a typical impact scenario:-

a. Flow visualisations produced by computer graphics for the impact of a circular cylinder at 1.0 m/s - figure 9-13.

b. Load time histories for the above impact produce by both pressure integration and rate of change of added mass considerations - figure 9-14.

c. Kinetic, potential and total fluid energy with respect to time - figure 9-15.

d. A series of transverse pressure distributions calculated at particular time instants - figure 9-16.

The computer generated flow visualisations give a reasonably realistic view of the impact of a circular cylinder. The inability to produce such pictures at each time step (owing to restrictions on the amount of processed graphical data that could be stored) was one frustrating element of this work. In many cases, the development of interesting features in the flow could not be followed closely. However, the flow visualisations that were produced were of great use in the development of the numerical models.

The load time histories shown in figure 9-14 show good agreement with each other, again indicating the numerical approach used. The total pressure on the surface of the body was computed using the least squares surface fit method described in chapter 4, section 7. The change in total energy of the fluid over each time step was used as a measure of the work done, from which the comparative measure of impact force was deducted. Plots of the kinetic and potential energies of the fluid are shown in figure 9-15.

Finally, the transverse pressure distributions are shown in figure 9-16. These plots ignore the buoyancy or hydrostatic pressure contribution in order to clarify the fluid dynamic pressure components

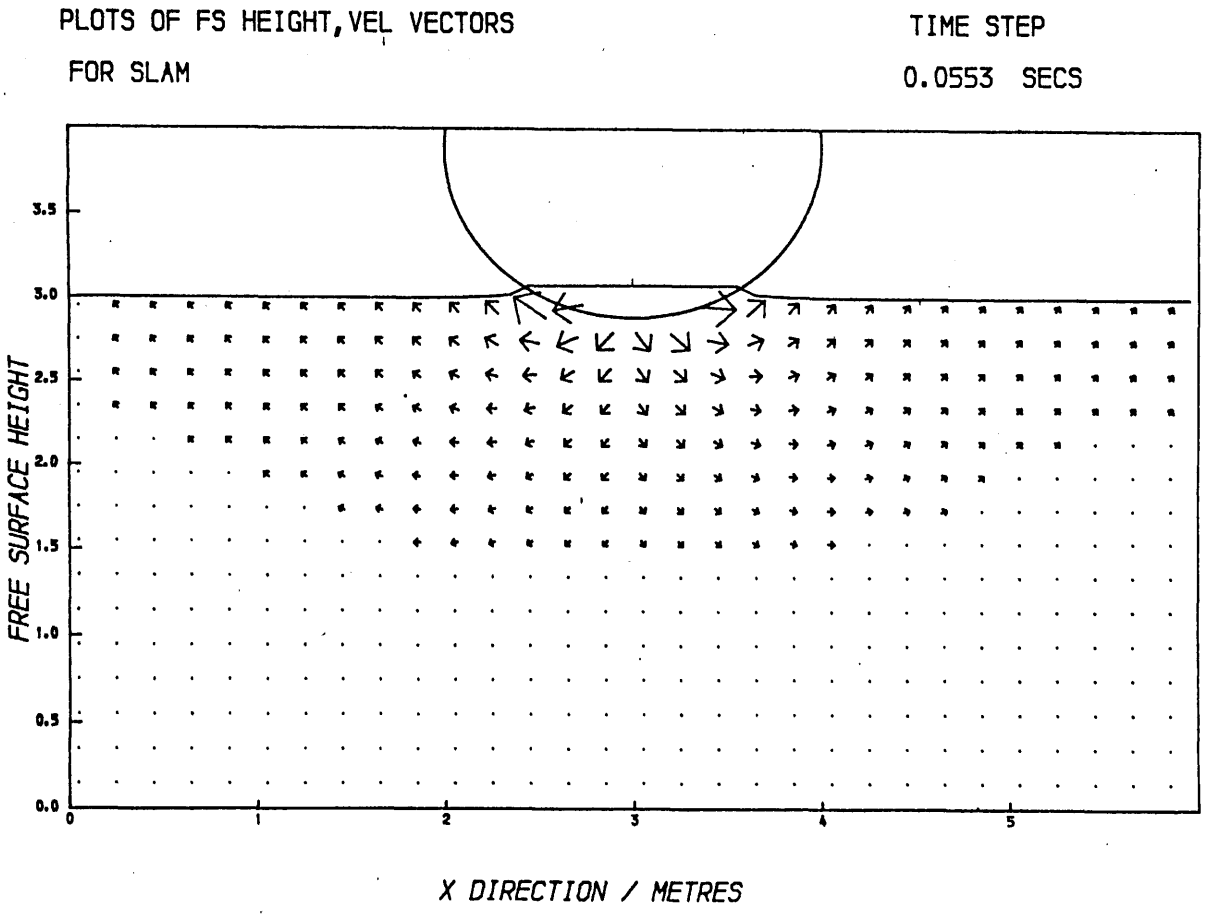
PLOTS OF FS HEIGHT, VEL VECTORS
FOR SLAM
TIME STEP
0.0553 SECS
FREE SURFACE HEIGHT
3.5
3.0
2.5
2.0
1.5
1.0
0.5
0.0
0
1
2
3
4
5
X DIRECTION / METRES

Figure 9-13a

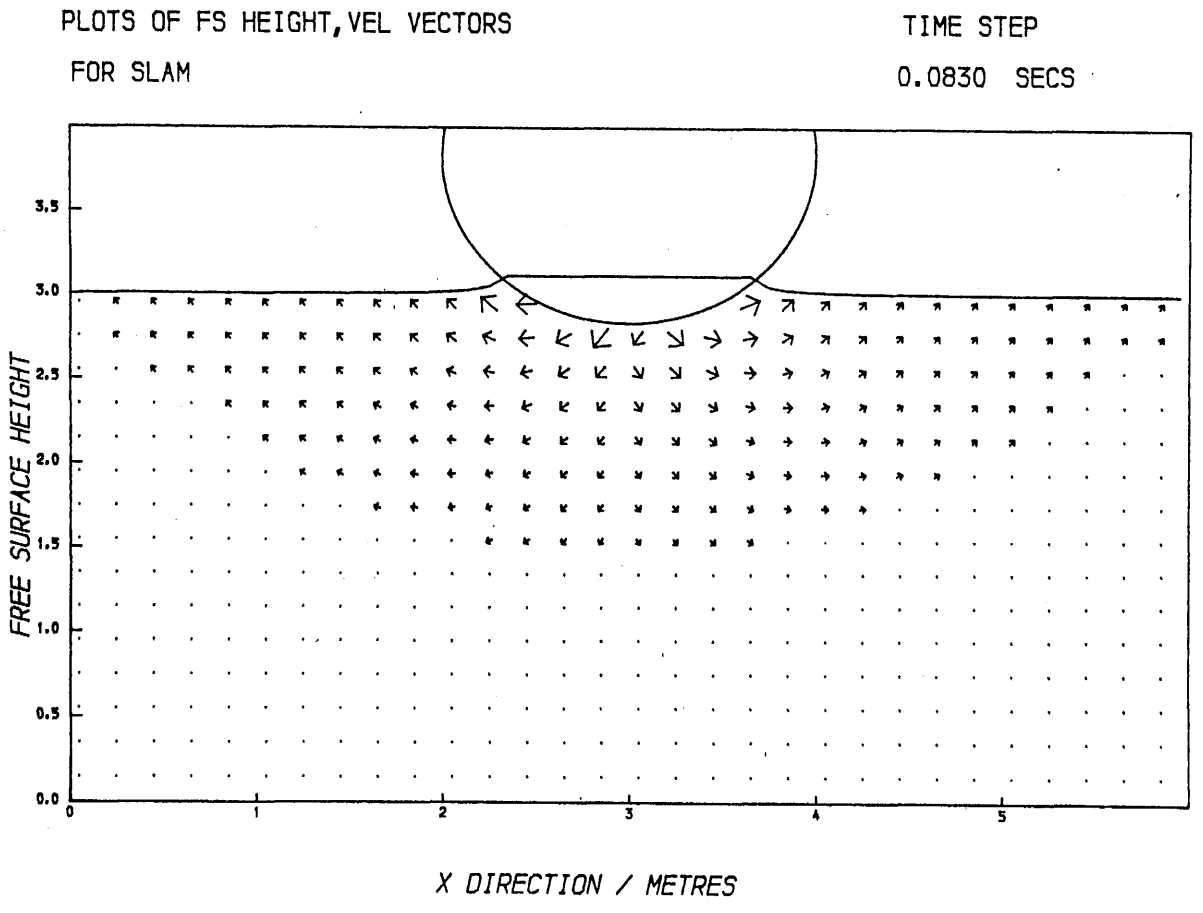
PLOTS OF FS HEIGHT, VEL VECTORS
FOR SLAM
TIME STEP
0.0830 SECS
FREE SURFACE HEIGHT
3.5
3.0
2.5
2.0
1.5
1.0
0.5
0.0
0
1
2
3
4
5
X DIRECTION / METRES

Figure 9-13 b

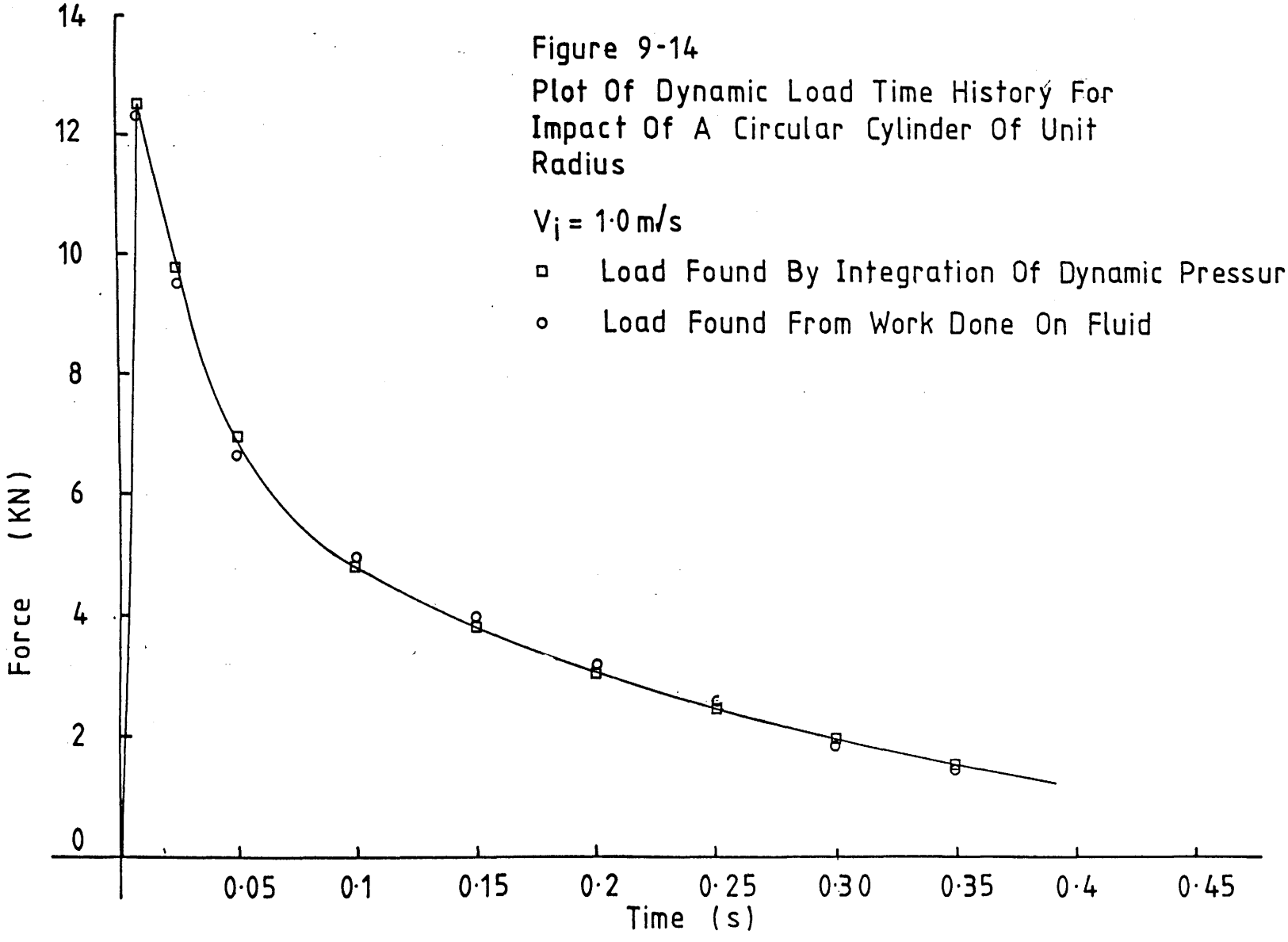

Figure 9-14

Plot Of Dynamic Load Time History For Impact Of A Circular Cylinder Of Unit Radius

$V_i = 1{\cdot}0$ m/s

▫ Load Found By Integration Of Dynamic Pressures

○ Load Found From Work Done On Fluid

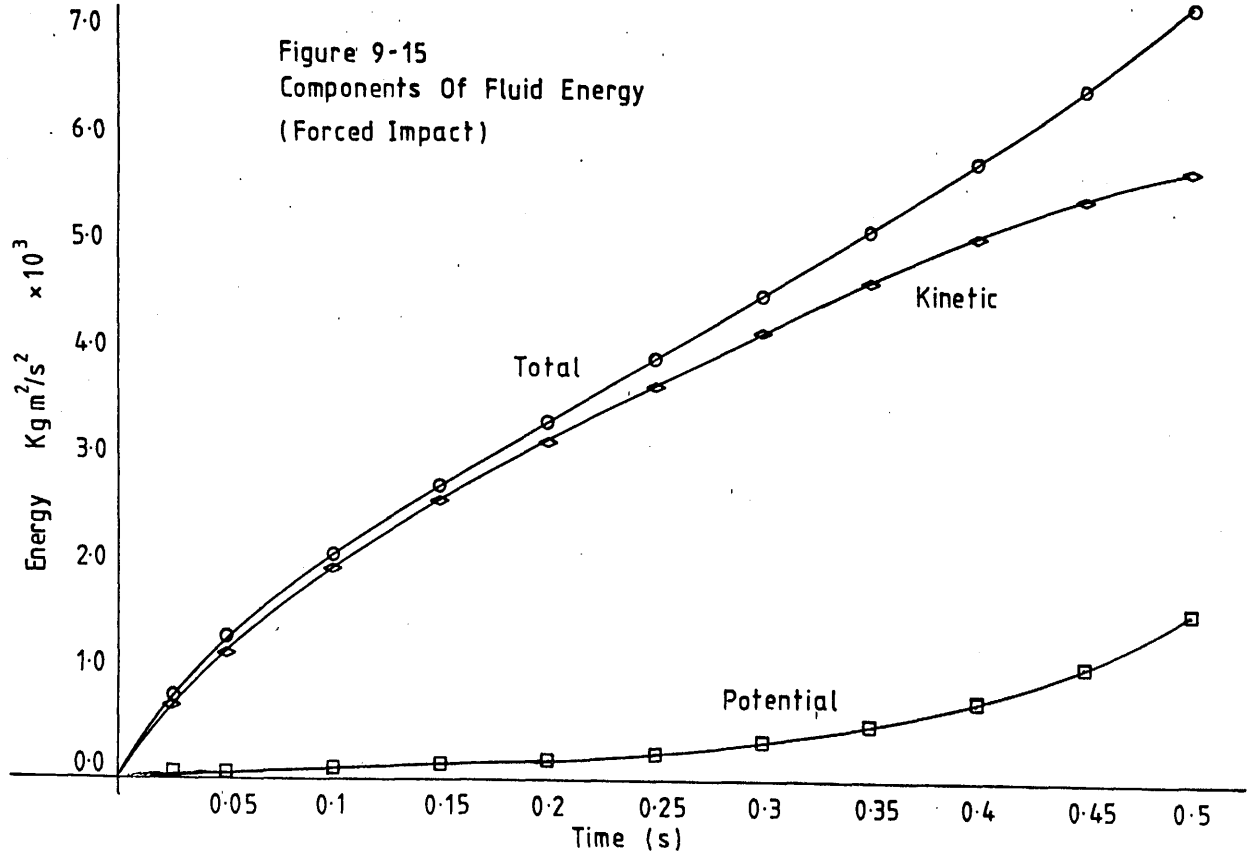
Figure 9-15
Components Of Fluid Energy
(Forced Impact)
Energy Kg m²/s² x10³
7·0
6·0
5·0
4·0
3·0
2·0
1·0
0·0
Total
Kinetic
Potential
0·05
0·1
0·15
0·2
0·25
0·3
0·35
0·4
0·45
0·5
Time (s)

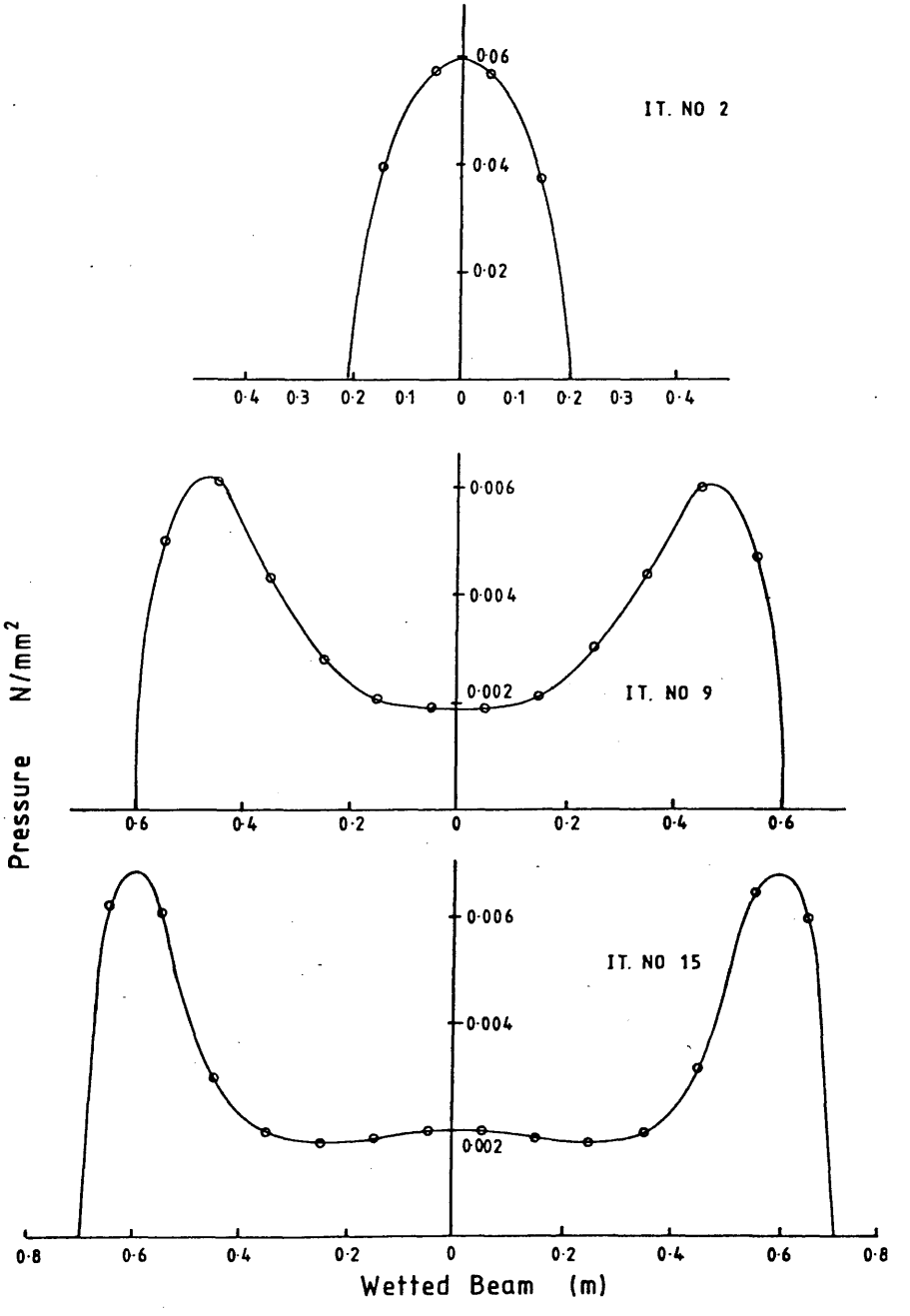

Figure 9-16 Pressure Distributions For Circular Cylinder Impact

(computed in the SOLA and SOR routines). However, the buoyancy was, of course, included in the computation of total load.

Before comparison of these results with the works of other authors, some remarks concerning the performance of the computation over the first few time steps are necessary. Of the two pressure components assumed responsible for the slam loading, ie the dynamic and stagnation components, only the dynamic pressure was directly affected by the time step restrictions laid down in section 9.4. Figure 9-17 shows the effect of this property on the load time history and illustrates the dominant feature of this type of slamming model. The loads due to dynamic and stagnation pressures are plotted against the non dimensional paramater:-

$$\text{Fractional immersion} = \frac{V_j\, t}{D}$$

where t : total time into simulation.

D : diameter of the cylinder.

V_j : impact velocity of 1.0 m/s.

for various values of the discrete time step. Consistency between time step, mesh size and shallow water wave speed was maintained throughout this survey by use of equation 9.4/1.

The first feature of figure 9-17 to be noted is the way in which the load due to the stagnation pressure remained consistent with the varying time step over the full range of fractional immersion. A fairly steep rise was followed by a smooth peak and the beginning of a steady decline. This load component was dominated by the rate of change of beam, and the transverse distribution of the steady pressure. Examination of the changes in the load history due to dynamic pressures as a result of varying the time step showed that,

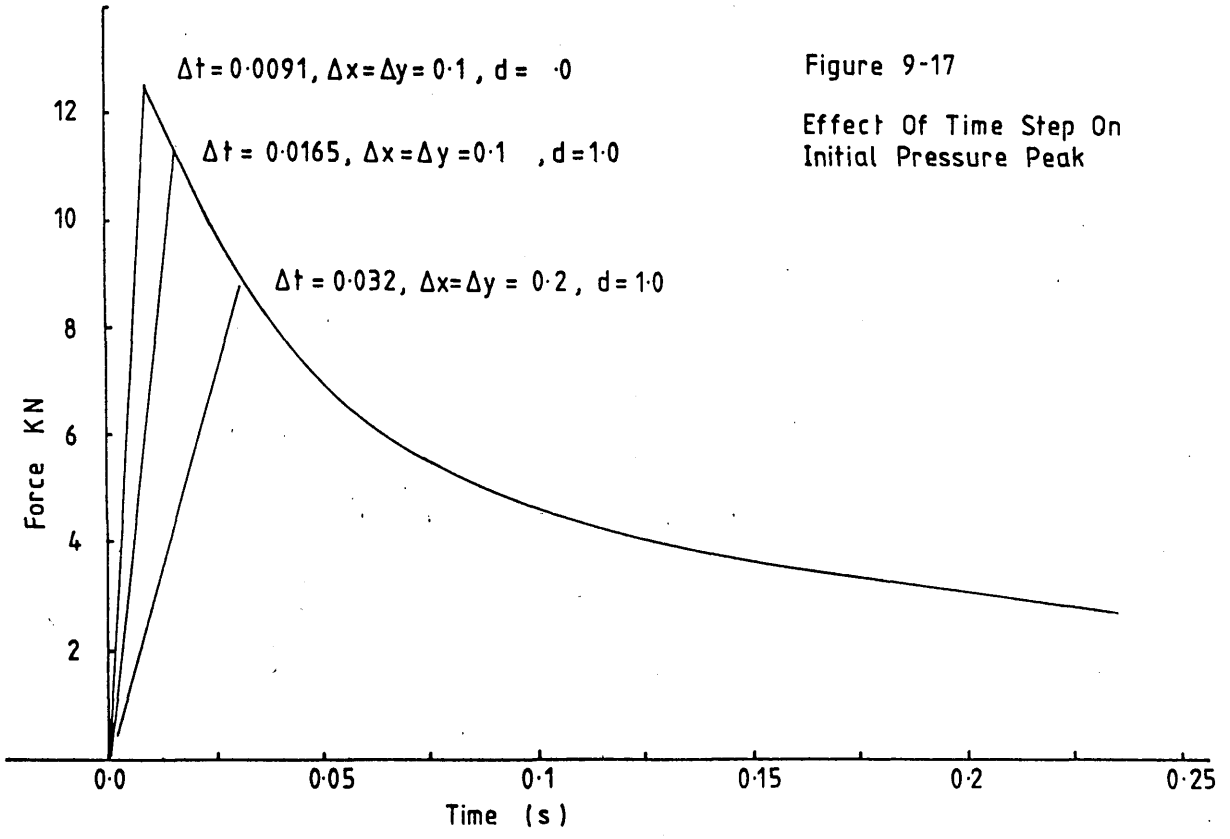

Figure 9-17

Effect Of Time Step On
Initial Pressure Peak

whilst the modified SOLA code produced the correct dynamic pressure field for any given instant of time or immersion, a reduction in time step increased the peak load. Indeed, in the limit for zero time step, the technique would produce infinite pressures at the instant of contact.

By way of an analogy, the results presented in figure 9-17 were similar to those that would be expected from varying the response characteristics of a pressure transducer used to measure slam pressures by experiment. A slow response would produce pressure time histories consistent with those calculated by the present method using a low time step. Decreasing the response time of the transducer would increase the peak pressure measured.

The first realistic lower bound upon the time step was given by the value computed by use of the fluid acoustic speed. Consideration of physically realistic effects such as air entrapment, spray and irregularities on the surface of the section, further reduced the possibility of the type of singular behaviour predicted by 'ideal' water entry models.

These observations lead this author to the conclusion that the best method to ensure consistent results from this finite difference model of the water entry problem would be for the time step at the first instant to be given its acoustic value, and to assume full compressibility of the fluid if the rate of change of wetted beam were to exceed the speed of sound in water. If this criterion were not met, then the time step would revert to its hydrodynamic value. The time step would be governed by the mesh size, which was chosen to allow the wetted beam to cover one cell width per step.

This refined numerical model was subsequently used in a series of tests to determine the value of the peak impact load coefficient for a circular cylinder by a series of computations at constant velocity. Figure 9-18 shows a plot of peak load versus the square of the impact velocity. A linear relationship was seen to exist with the gradient giving a slam coefficient C_s of 6.12. This value was higher than that found by experiment, but lower than the ideal flow value deduced by Fabula to be 6.28 (2π).

Figure 9-19 shows a plot of the non-dimensional load time history for these impact tests as a comparison with figure 9-12. The finite rise time was much greater for the present numerical model than the values suggested by Cambell and Weynberg (92). Furthermore, the peak loading was higher. The drop in pressure was similar in form however, suggesting that the lack of agreement over the initial time step is due to the particular properties of the numerical method. Thus as the flow becomes fully developed, the accuracy of the numerical model was improved.

It should also be noted that the present computer simulation does not take into account the effect of air entrapment. The programs developed in chapter 10 revealed that for curved bodies, a movement of the free surface prior to contact would certainly occur for the type of impact test carried out by Cambell and Wellicombe. The lower slam coefficient may arise because the relative velocity between free surface and body at the instant of contact is not equal to the velocity of the cylinder, owing to the effects of the air layer. This phenomenon was also observed in the correlation of the results from the air entrapment computations reported in chapter 10 with drop test

Figure 9-18
Peak Impact Load Versus Square Of Impact Velocity For Circular Cylinder

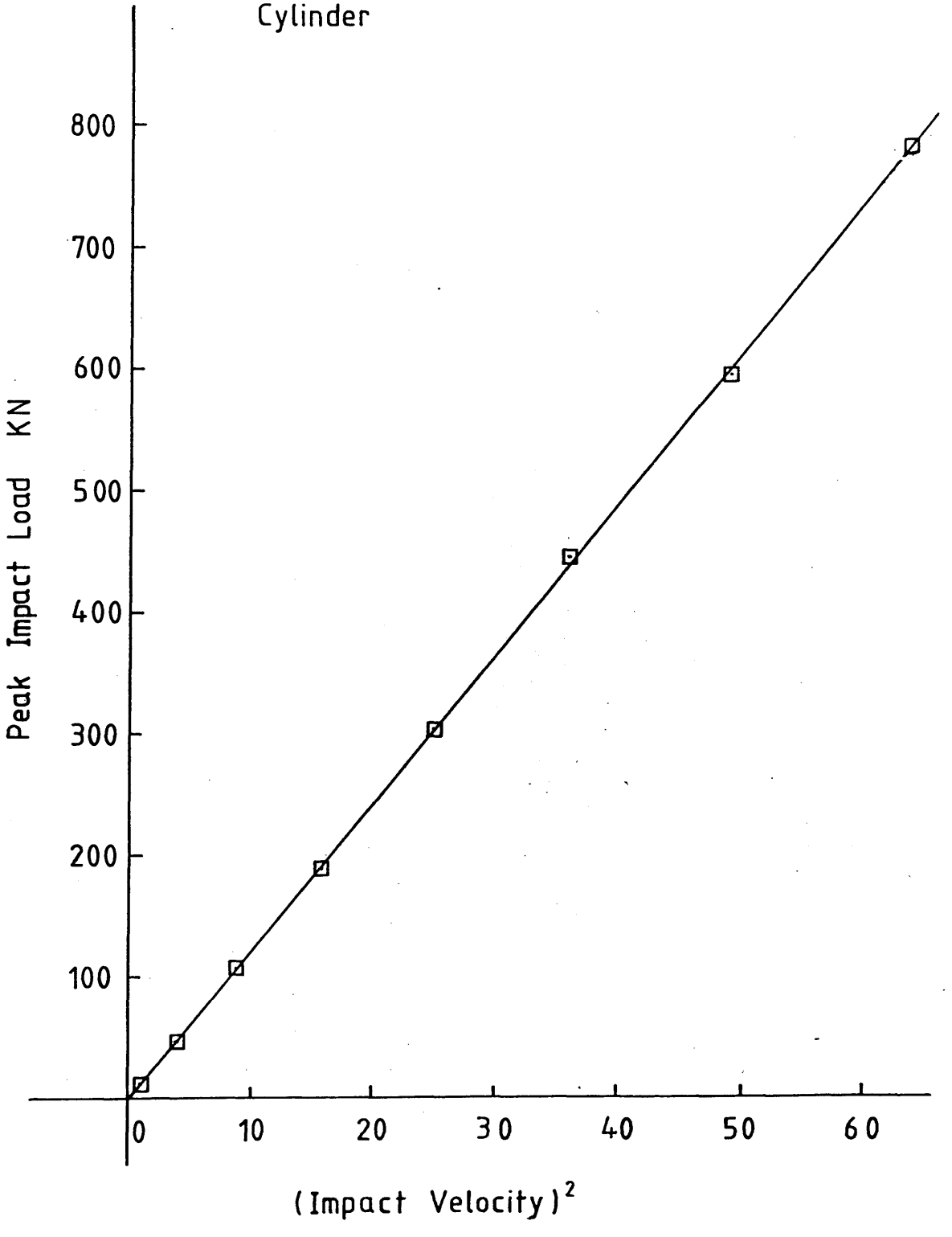

Figure 9-19

Comparison Of Slam Coefficient Time History Computed Using Present Method (□) And Data From Figure 9-12

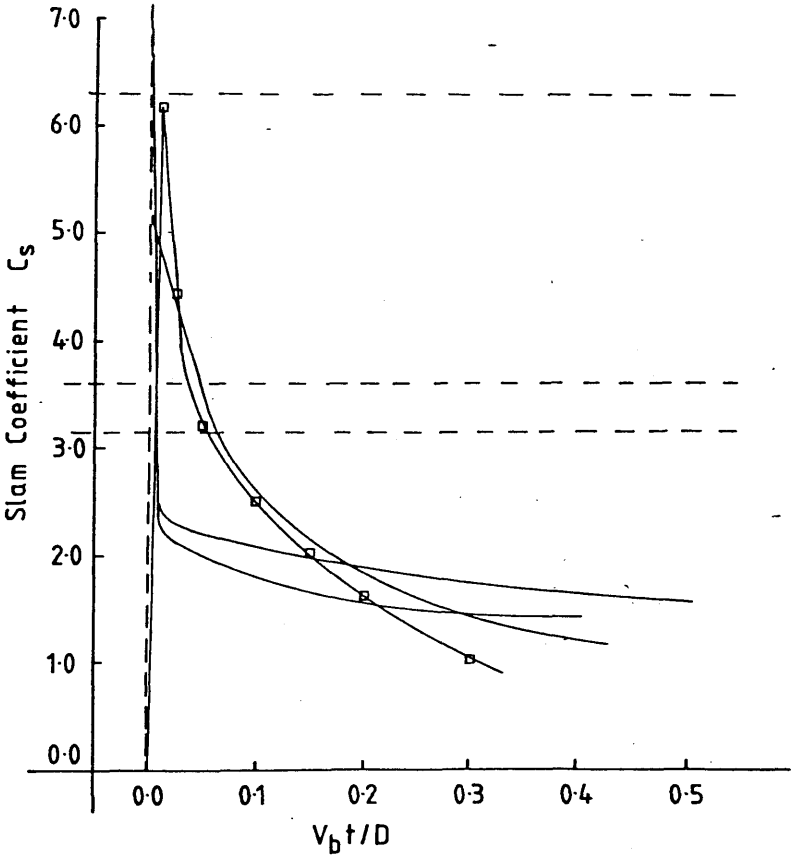

data provided by Chuang (34).

It was considered that, despite the limitations set by the interpretation of the instant of initial contact for this numerical model, the results were good and that the program SLAM could represent many of the major features of the water entry problem with sufficient accuracy.

The final step in the analysis of the impact of the cylinder was to simulate the drop test problem. The body was assigned a series of mass values. The simulation thus became fully interactive, with the acceleration of the body being computed as:-

$$\dot{V}_b = -g + F_T / M_b \qquad \text{---9.7/3}$$

where g :-9.81 m/s^2 is the acceleration due to gravity.

F_T : total force applied to the cylinder by the fluid found by integrating pressures.

Figure 9-20 shows a plot of a body velocity and deceleration records for three typical mass values of 1.57, 3.14 and 6.28 tonnes (per unit length). These mass values will be recognised as those required to give the cylinder a draught of 1.0m, neutral buoyancy and a negative buoyancy of twice its displacement, respectively.

Although the resulting simulations were not numerically unstable, some oscillations were evident in the body velocity records. These inaccuracies resulted in the development of the variational algorithm described in chapter 6. Figure 9-21 shows a plot of the kinetic and potential energy of the fluid, along with the kinetic and potential energy of the body. Also shown is a plot of the total energy

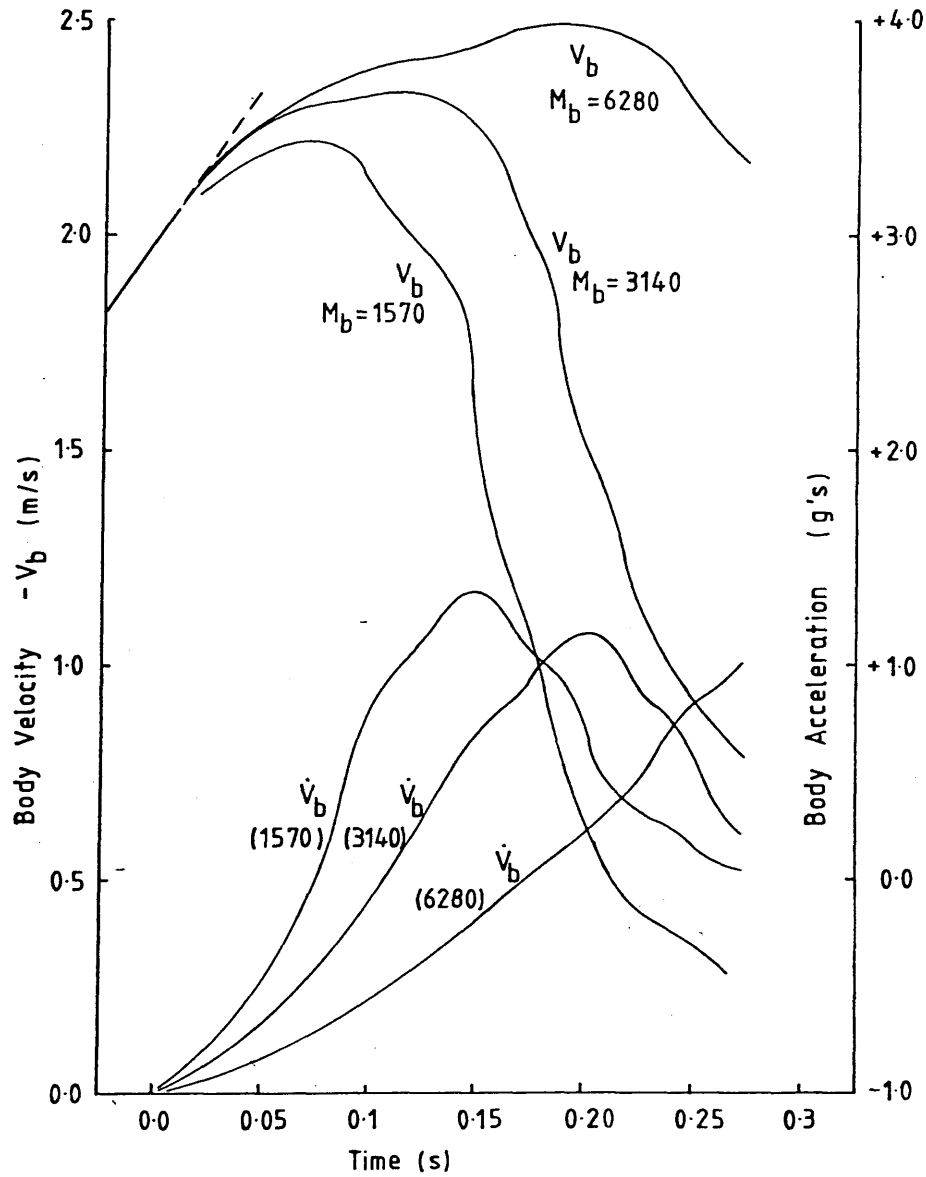

Figure 9-20 Time Histories Of Body Velocity And Acceleration For Circular Cylinder Drop Test Simulation

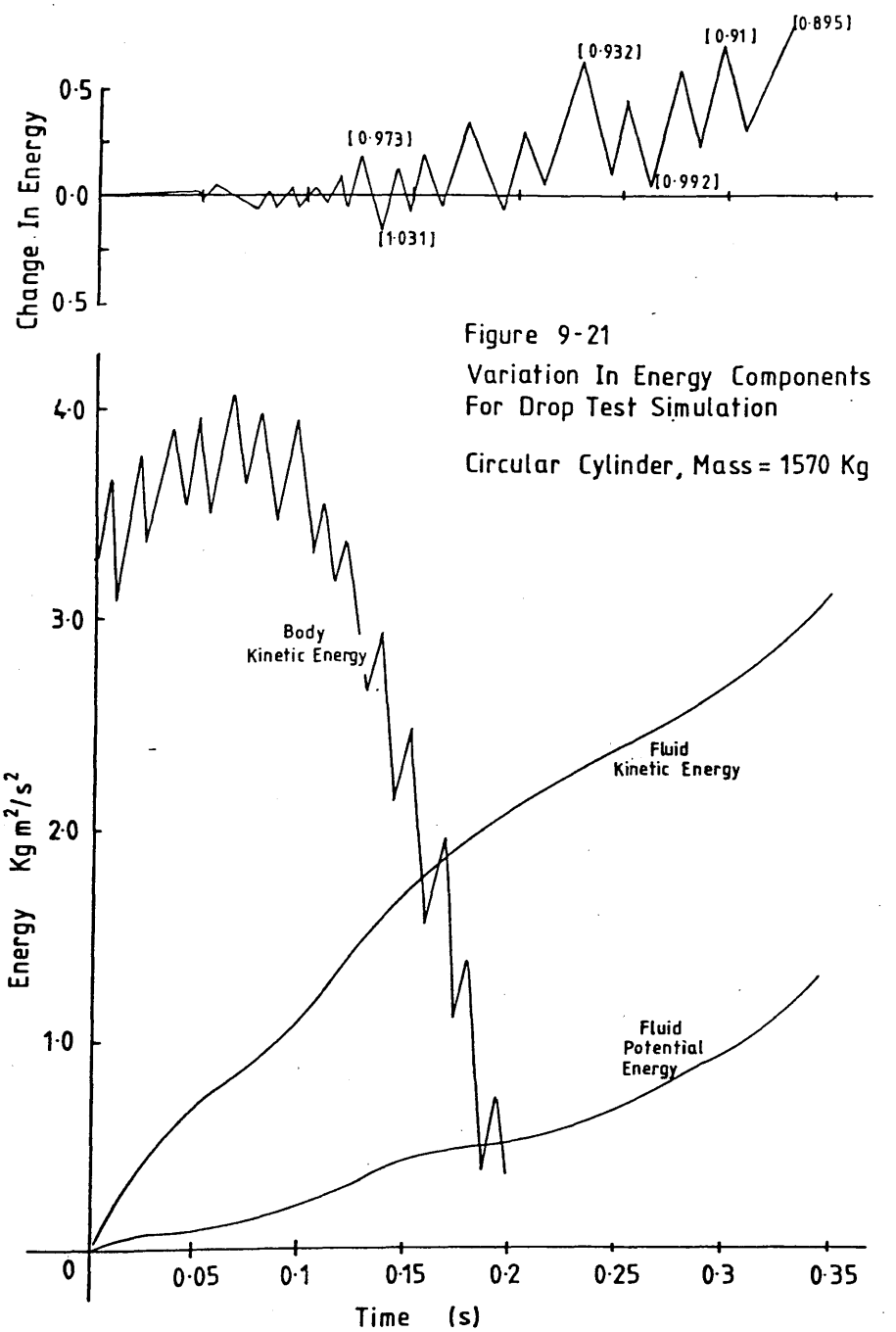

Figure 9-21

Variation In Energy Components For Drop Test Simulation

Circular Cylinder, Mass = 1570 Kg

of the system minus the work done by gravity upon the falling body.

The time histories of these energy components showed some considerable oscillations about their mean values. More serious however, was the consistent rise in the total energy of the system. Over the short period of the simulation, this did not cause total numerical instabiliuty, but it did give rise to inaccurate results, and would eventually lead to a breakdown of the computation. The figures in brackets beside the plot of fluid kinetic energy give the fractional adjustment rate (X) that would be required at each stage to assure energy conservation. These values also showed an oscillatory behaviour and a steadily increasing trend.

The application of the variational algorithm had two effects. Primarily, it halted the trend towards instability by keeping the total energy of the system constant to within 2.5%. Secondly, the oscillations which had appeared in the energy time histories were deduced. Thus, this particular aspect of the numerical modelling proved highly successful. Furthermore, as discussed in chapter 6, the number of iterations required for the SOLA algorithm to produce convergence were also reduced, allowing a much longer real time simulation to be carried out. Figure 9-22 shows the number of SOLA iterations (N_S) needed to reach a tolerence level on divergence of:-

$$\nabla.\bar{u} \quad < \quad 10^{-3}$$

both with and without the addition of the variational method. Again two features are evident. Firstly, although the number of iterations required before the addition of the energy method are generally higher than those needed without this technique, there are a number of occasions when the value of (N_S) drops well below the mean. The

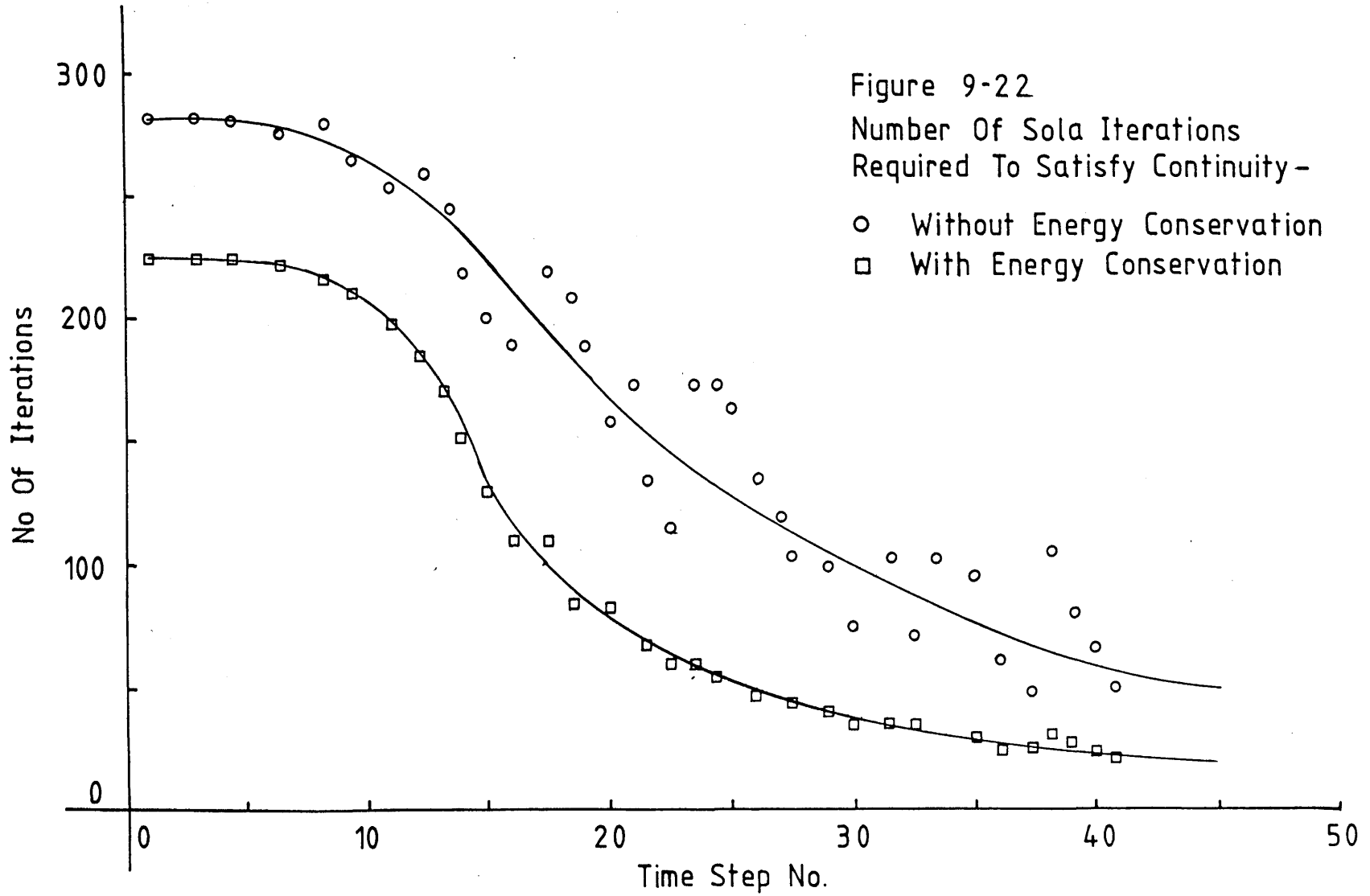

Figure 9-22
Number Of Sola Iterations
Required To Satisfy Continuity -

○ Without Energy Conservation
□ With Energy Conservation

convergence characteristics of the relaxation type solution (which SOLA mimics), often shows an oscillatory character (99) though the lower divergence levels achieved during these transients do not indicate that the final solution has been achieved. This type of behaviour is not evident in the plot of N_s resulting from the use of the variational method.

Secondly, the seemingly random fluctuations in N_s were removed when energy conservation was rigidly enforced. Thus it can be seen that the effect of the variational method on the SOLA algorithm is to smooth its convergence characteristics. This greatly aided the decision making processes needed during the running of the computer program.

Finally, figure 9-23 shows the effect of body dynamics upon the impact load time history. Whilst the peak dynamic pressures were consistent with the forced impact case, the deceleration of the cylinder can be seen to cause a progressivly steeper drop in pressure with decreasing body mass. For the most part this was the type of behaviour that would be expected, with the buoyancy and 'steady' hydrodynamic pressure components being of greater importance than the very short slam pressure loading.

7.3. Impact of Ship Shaped Sections

In this section, the results from forced impact tests upon three typical ship shaped bodies are presented.

The marker particle co-ordinates were defined as described in section 9.5. Comparative data was furnished by the Lewis form, three

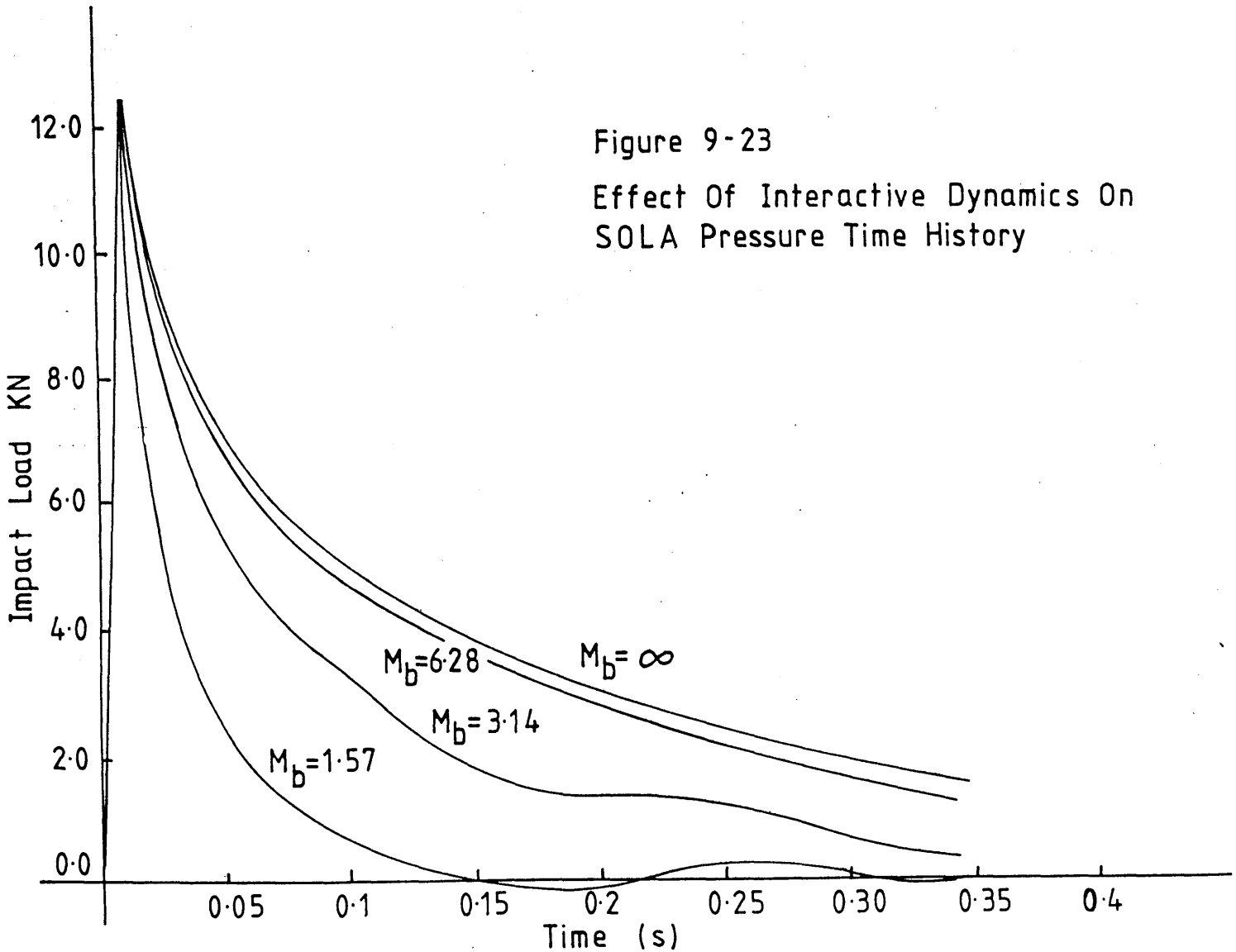

Figure 9-23

Effect Of Interactive Dynamics On SOLA Pressure Time History

parameter mapping computations of added mass and slam load. Figures 9-24, 9-25 and 9-26 show plots of added mass coefficient, sectional area, buoyancy force and slam load against the draught of the section, as deduced from the Lewis form method. The Ochi slam coefficient is also given. The three sections are denoted A, B and C and are illustrated in figures 9-24, 9-25 and 9-26, respectively.

As noted in section 9.6, calibration of the added mass coefficients to counter the effects of finite fluid depth was required. The zero frequency added mass coefficients were computed using the modified SOLA code for a number of draughts and compared with the Lewis form values. Figures 9-27, 9-28 and 9-29 shows these comparative plots for sections A, B and C, respectively. Figure 9-30 shows plots of the added mass calibration factors K_a for each section.

The rate of change of added virtual mass with draught was deduced from the above curves for each section and again was plotted along with the Lewis form values as a basis for comparison. Figures 9-31, 9-32 and 9-33 show these results. Figure 9-34 shows a plot of the calibration factor K_s derived from these curves.

The lessons learned during evaluation of the cylinder impact trests were applied to these simulations. The mesh spacing was chosen so that, for each impact velocity, one full cell width would be covered by the expanding beam of the section. This geometrical property could only be maintained over the first few time steps owing to the combination of the effects of changing section shape and piled up water. However, this was sufficient.

The variational method was included in the algorithm by

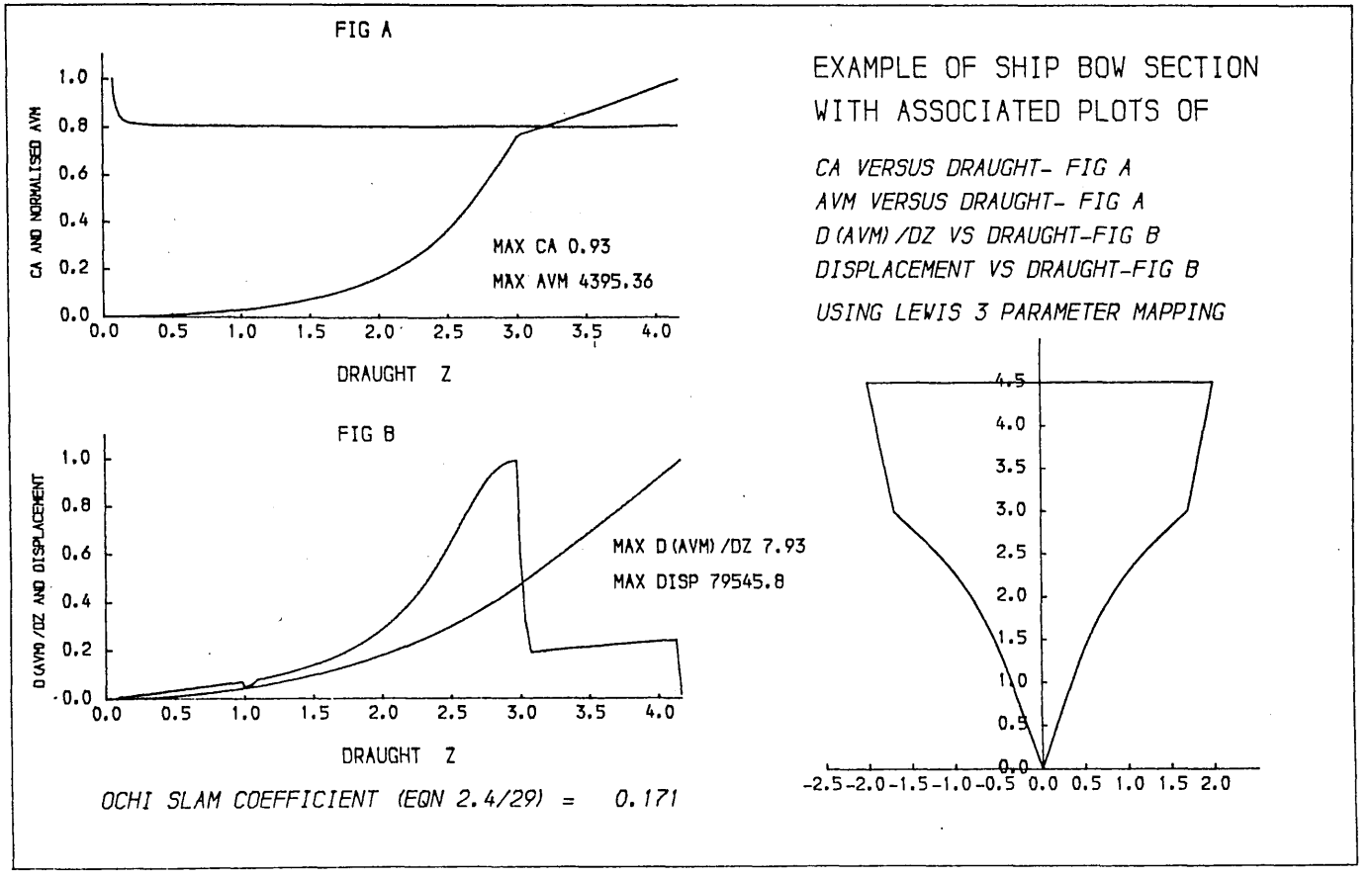

Figure 9-24 Section A

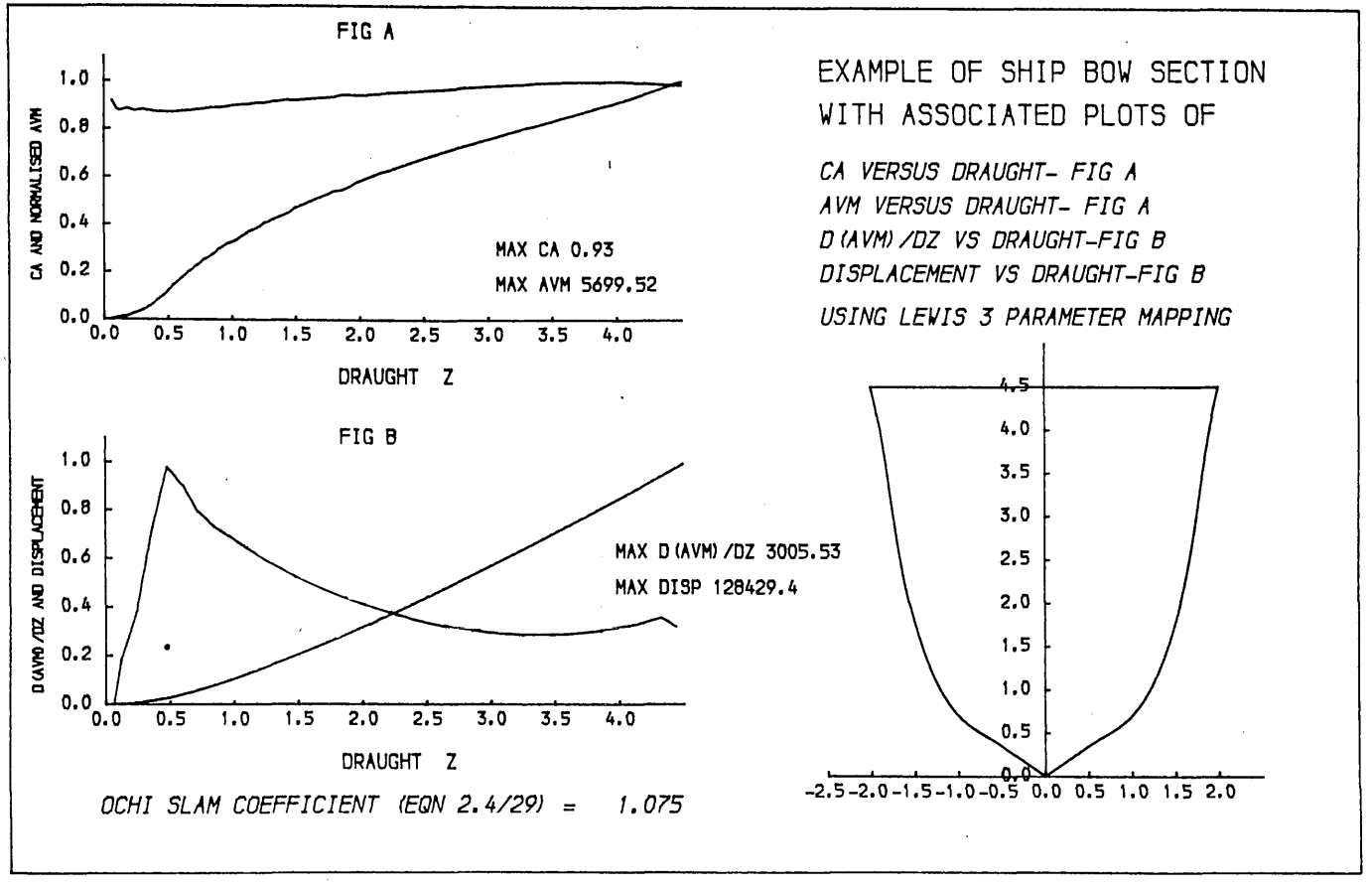

Figure 9-25 Section B

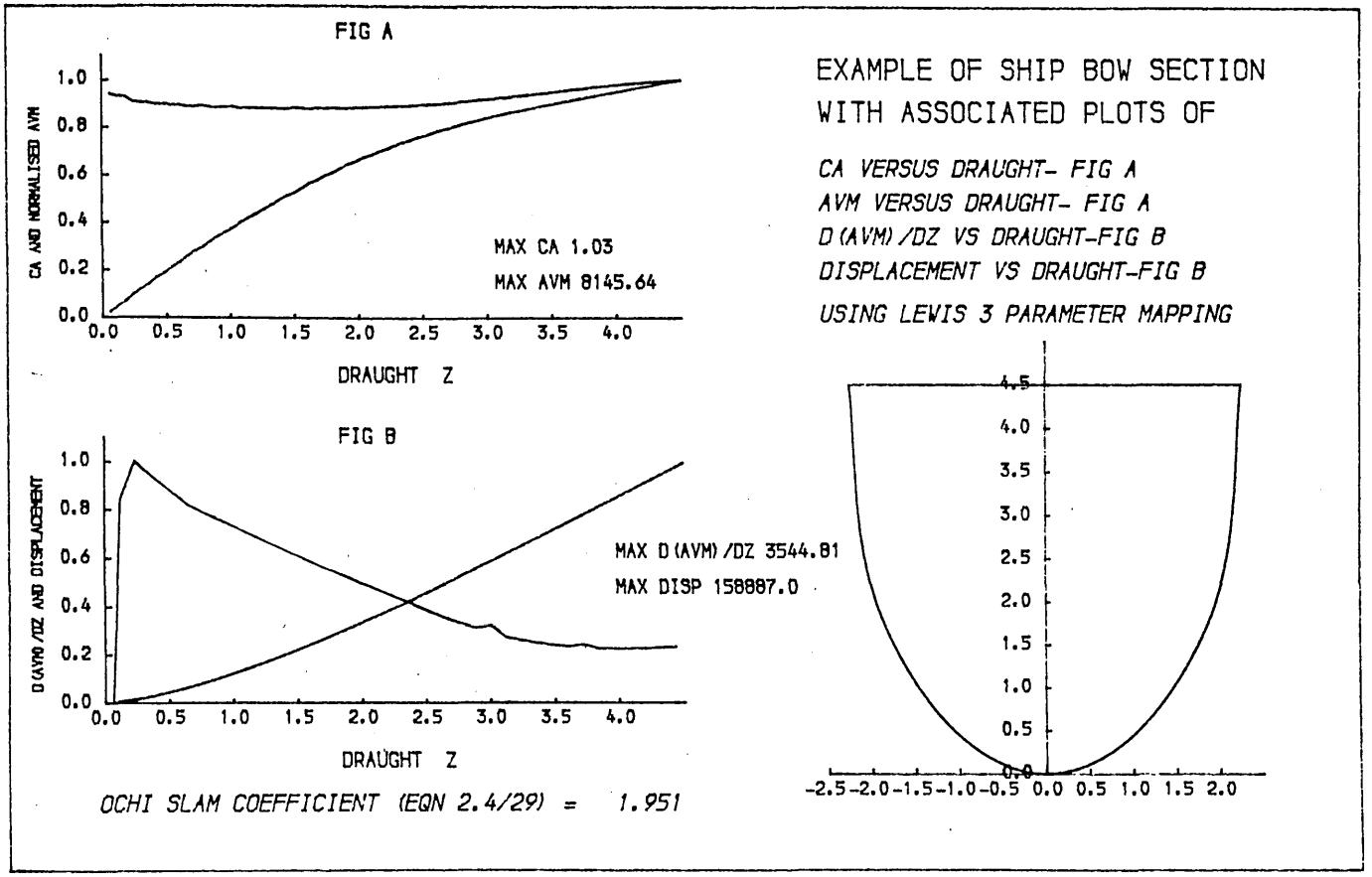

Figure 9-26 Section C

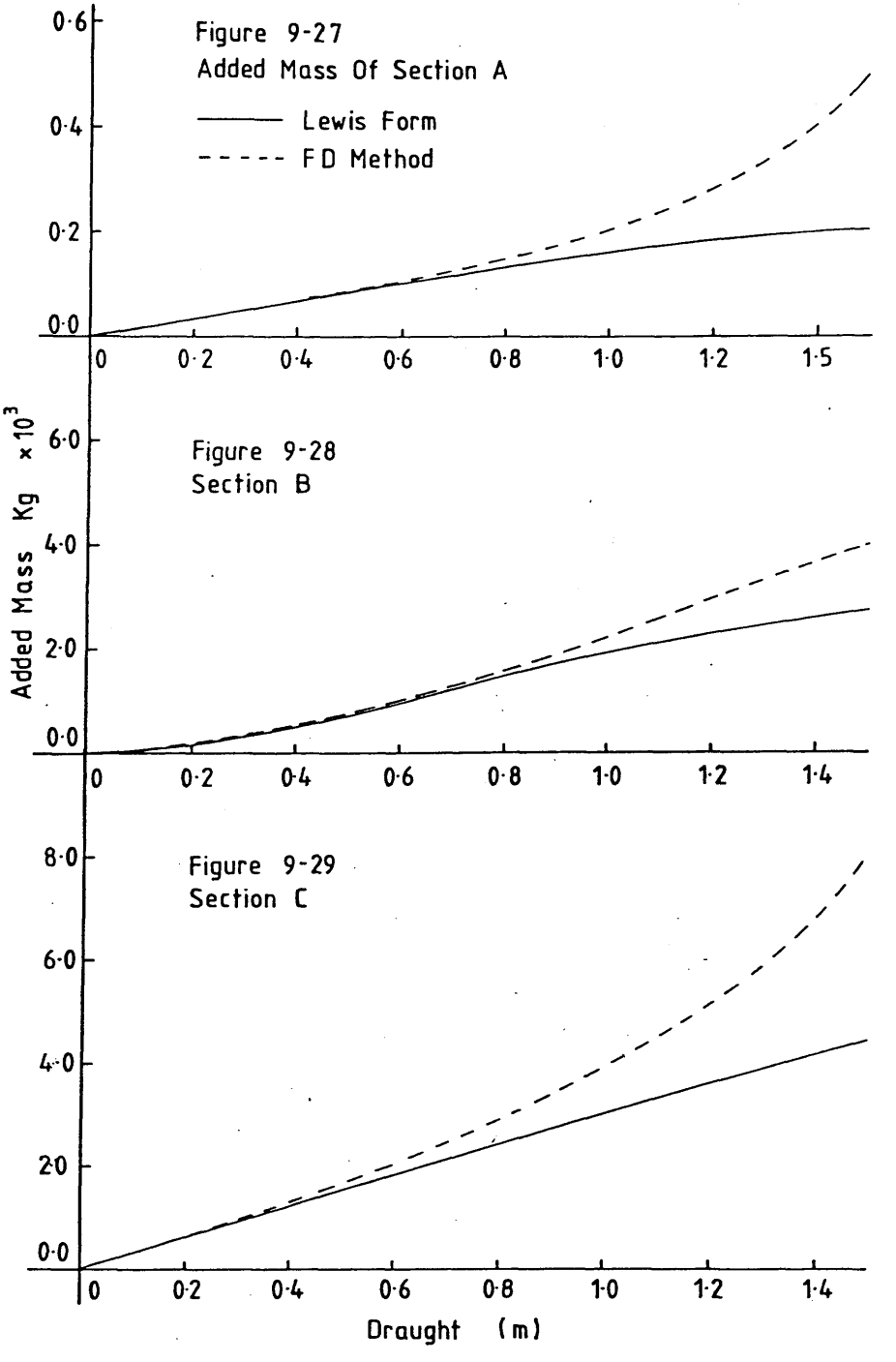
Figure 9-27
Added Mass Of Section A
Lewis Form
FD Method
0·6
0·4
0·2
0·0
0
0·2
0·4
0·6
0·8
1·0
1·2
1·5
Figure 9-28
Section B
Added Mass Kg x 10³
6·0
4·0
2·0
0·0
0
0·2
0·4
0·6
0·8
1·0
1·2
1·4
Figure 9-29
Section C
8·0
6·0
4·0
2·0
0·0
0
0·2
0·4
0·6
0·8
1·0
1·2
1·4
Draught (m)

Figure 9-30

Calibration Factor K_a For Added Mass, Sections A,B,C

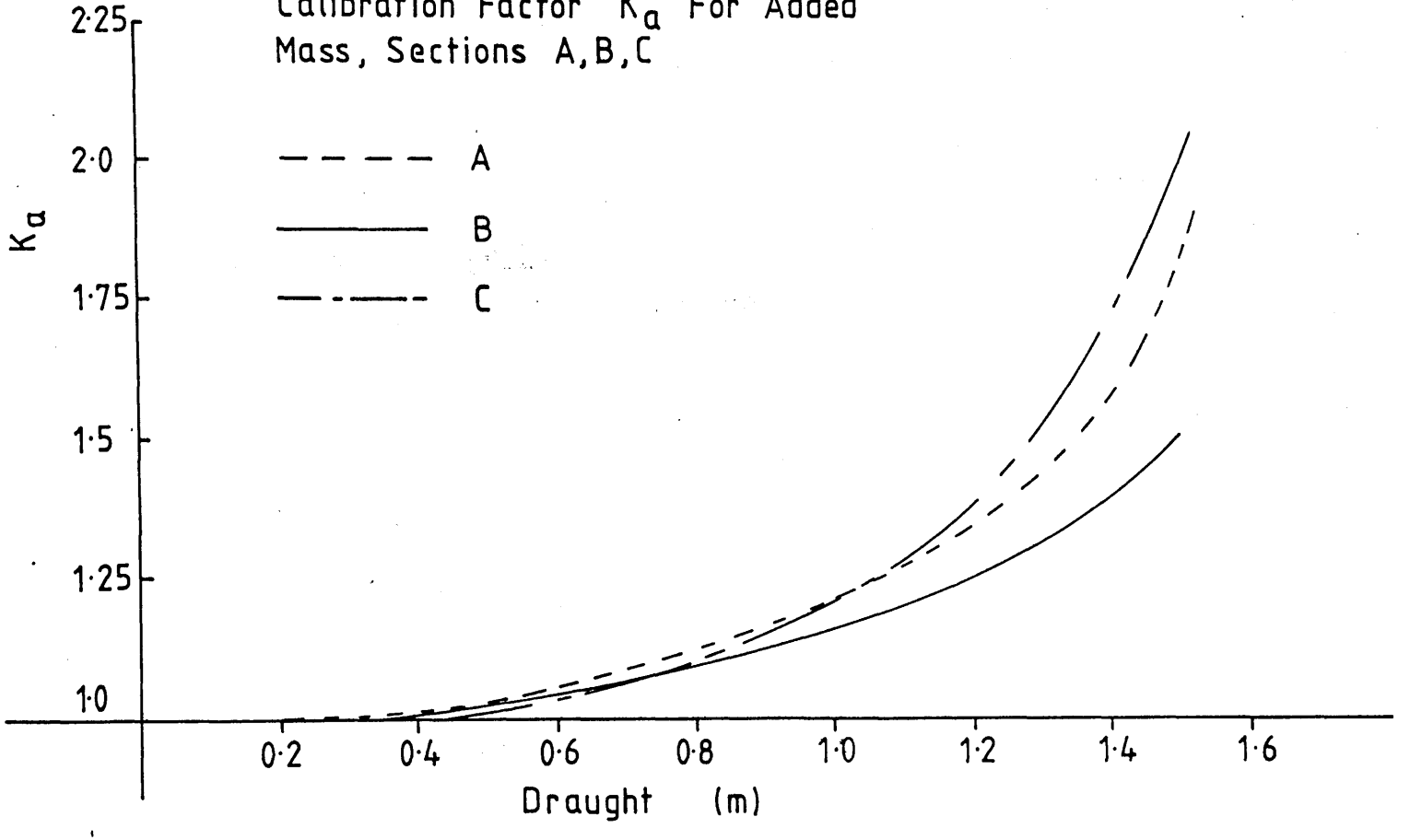

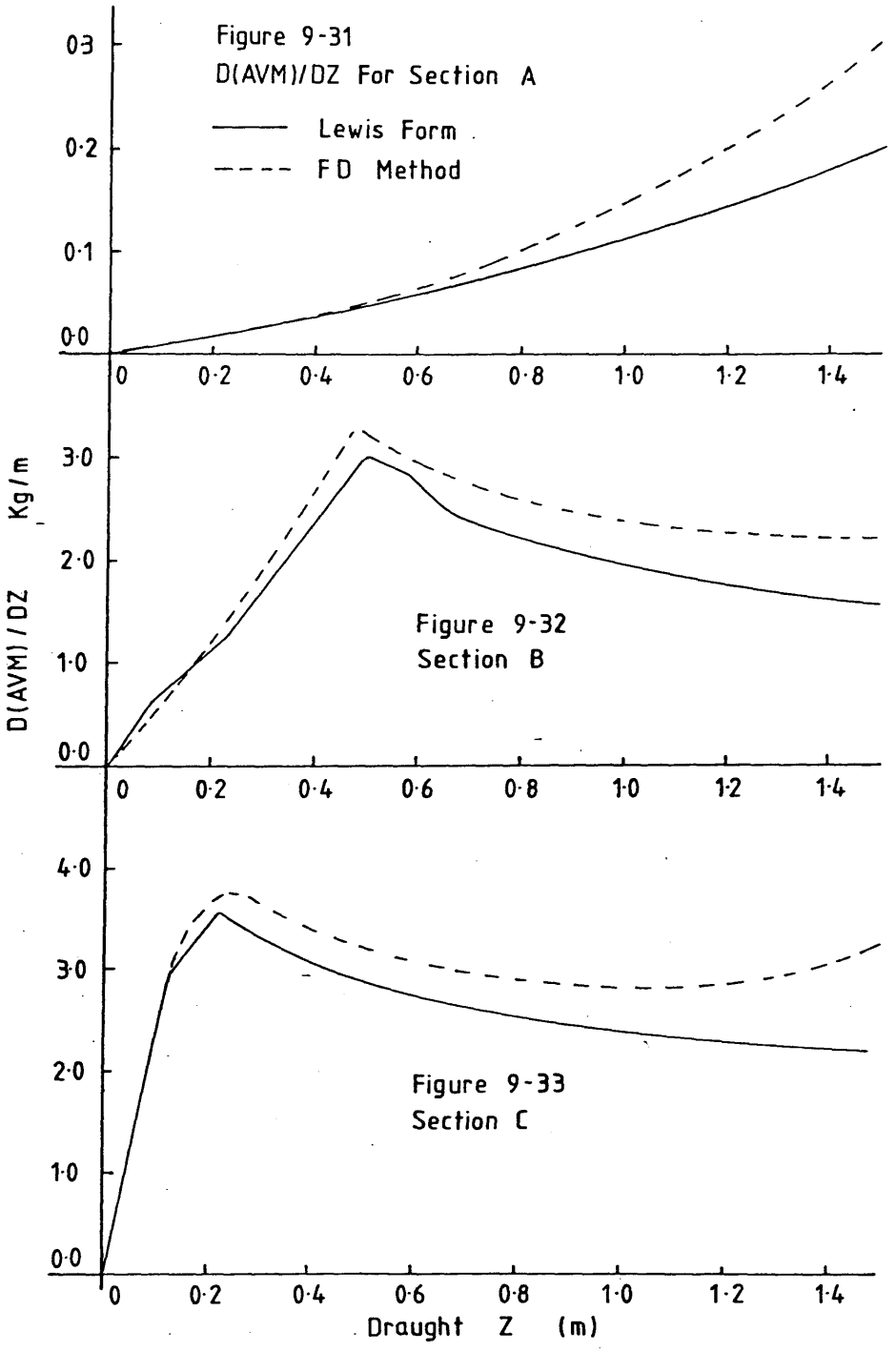
Figure 9-31
D(AVM)/DZ For Section A
Lewis Form
FD Method
0·3
0·2
0·1
0·0
0
0·2
0·4
0·6
0·8
1·0
1·2
1·4
D(AVM) / DZ Kg / m
3·0
2·0
1·0
0·0
Figure 9-32
Section B
4·0
3·0
2·0
1·0
0·0
Figure 9-33
Section C
Draught Z (m)

Figure 9-34

Calibration Factor K_s For D(AVM)/DZ, Sections A,B,C

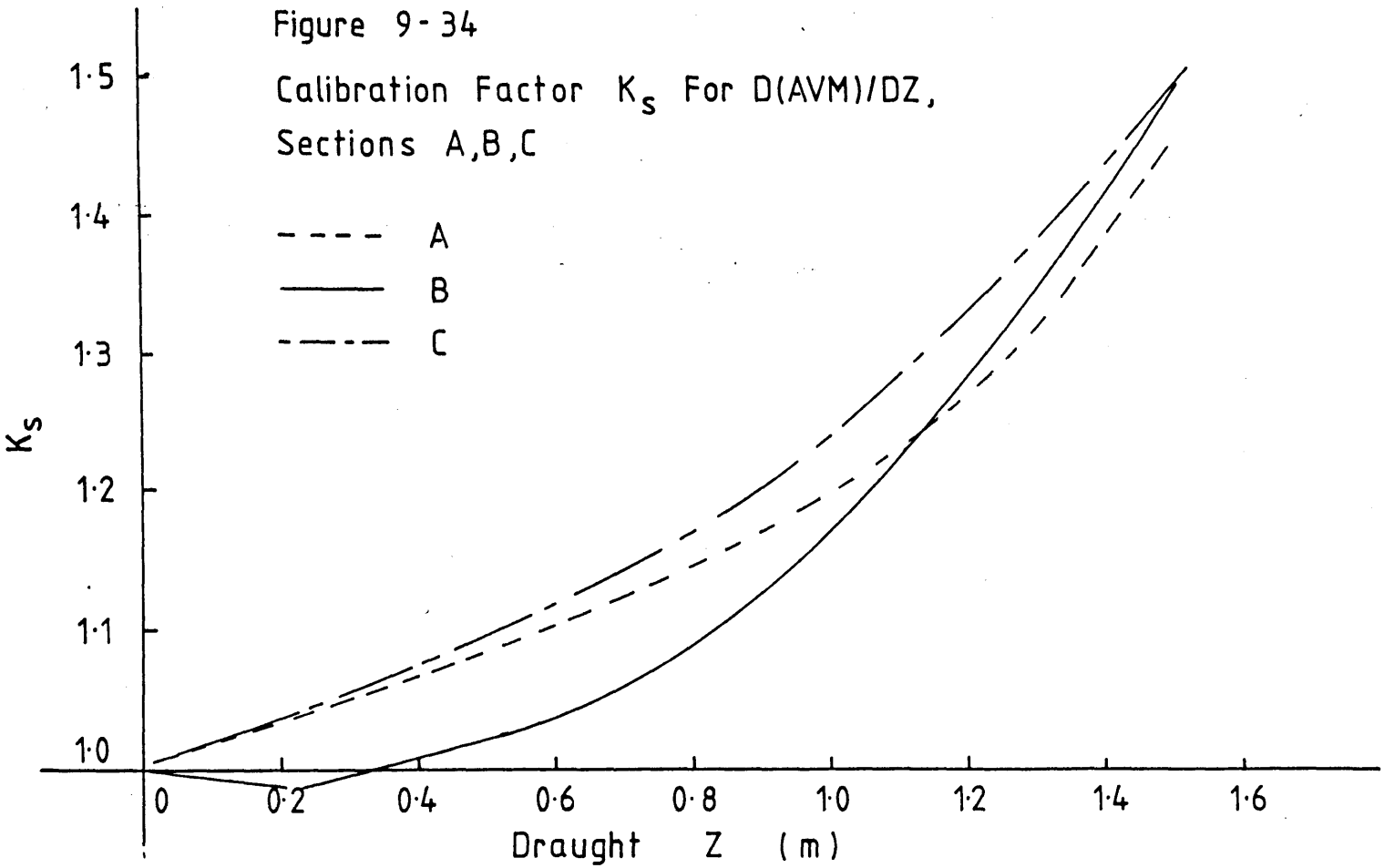

employing the developing load time history to compute the work done on the fluid at each time step. The total fluid kinetic energy at any instant was taken to be equal to the total work done minus the fluid potential energy.

The following plots were prepared for each impact simulation:-

a. Computer generated graphical output of the flow visualisations resulting from each slam.

b. Load time histories for each section. These time histories were divided up into loads due to buoyancy, and those resulting from hydrodynamic considerations.

c. A series of transverse pressure distributions for each section at given instants during the simulation.

Figures 9-35, 9-36 and 9-37 show the flow visualisation data for each section at a series of times during impact. Velocity vectors are shown only at alternate mesh points in order to avoid a confused picture. The interesting feature of all these plots is the way in which the volume of fluid fluxing method was able to cope with the modelling of the 'piled up water' at the spray roots. It may also be seen that the radiation boundaries allowed some mass flux to pass out of the domain without causing spurious oscillations.

Figures 9-38, 9-39 and 9-40 show the load time histories for each of the sections for an impact velocity of 2.0 m/s. It is interesting to note the differences in the curves as a result of the varying section shape. The sharp wedge shape of curve A resulted in a comparatively low slam induced loading, as one might expect. Section

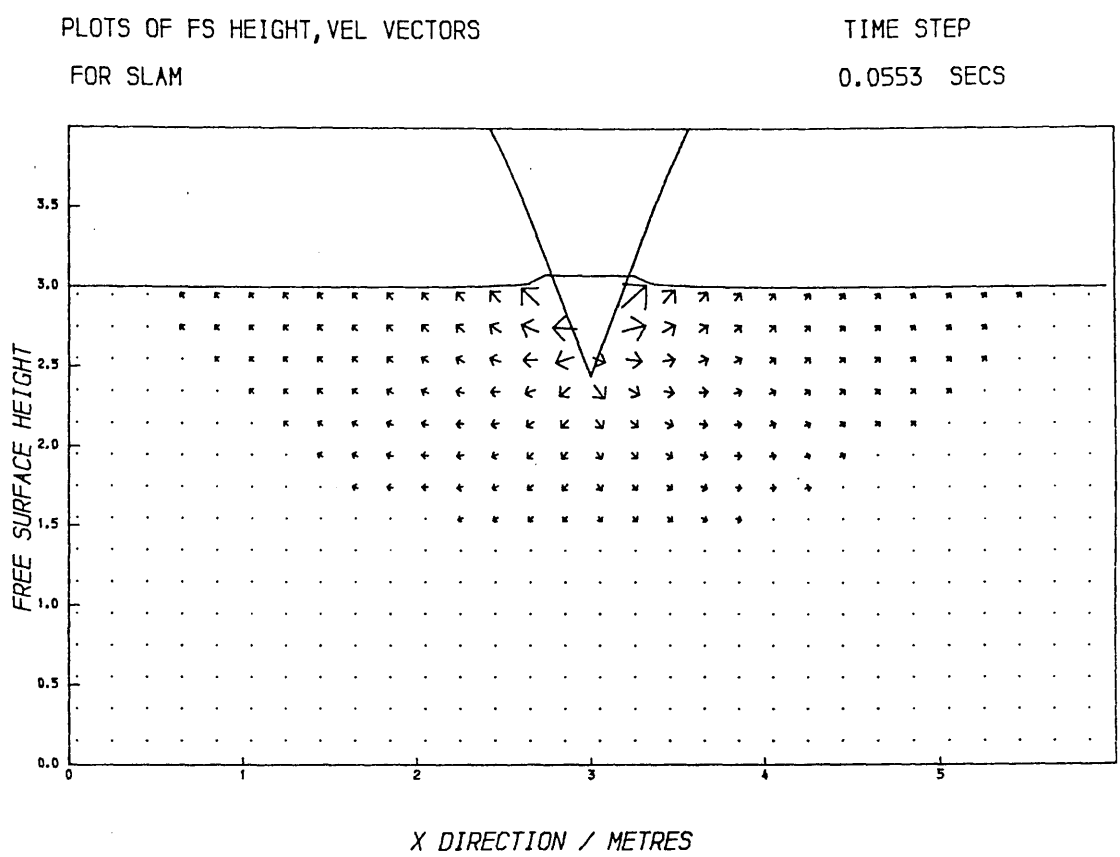

Figure 9-35
Impact Of Section A

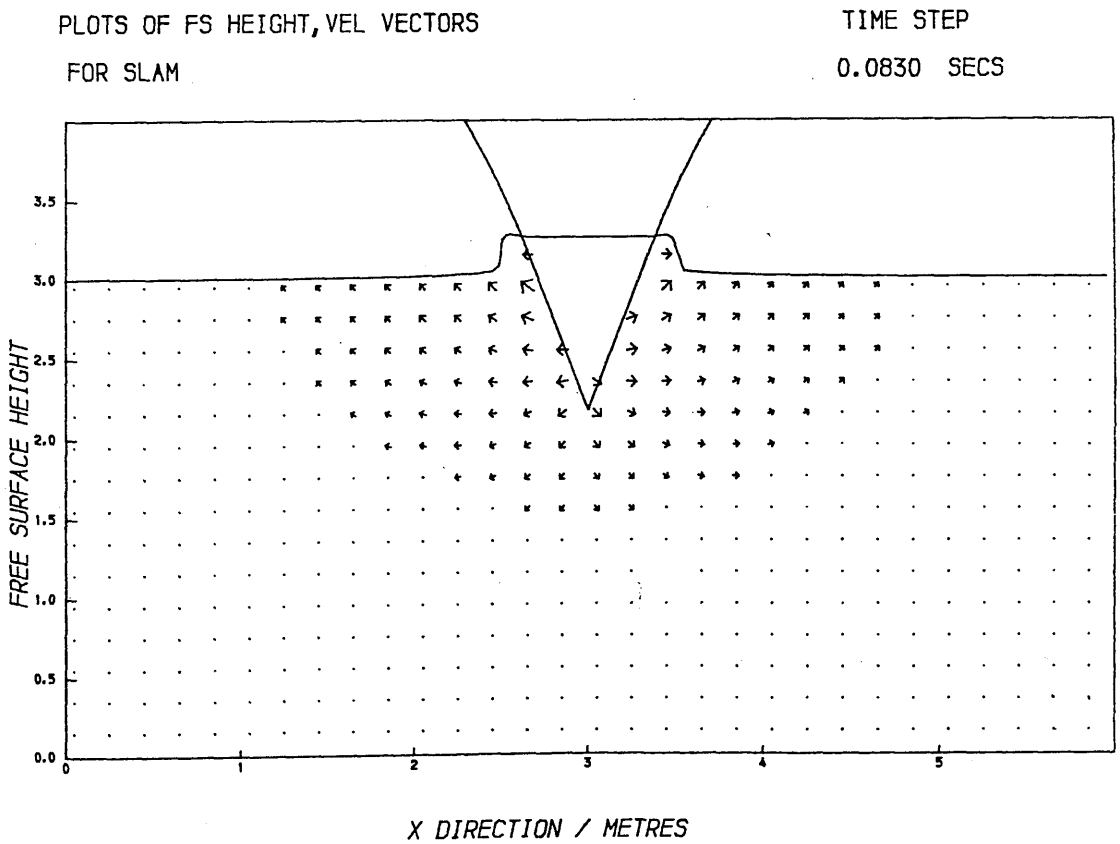

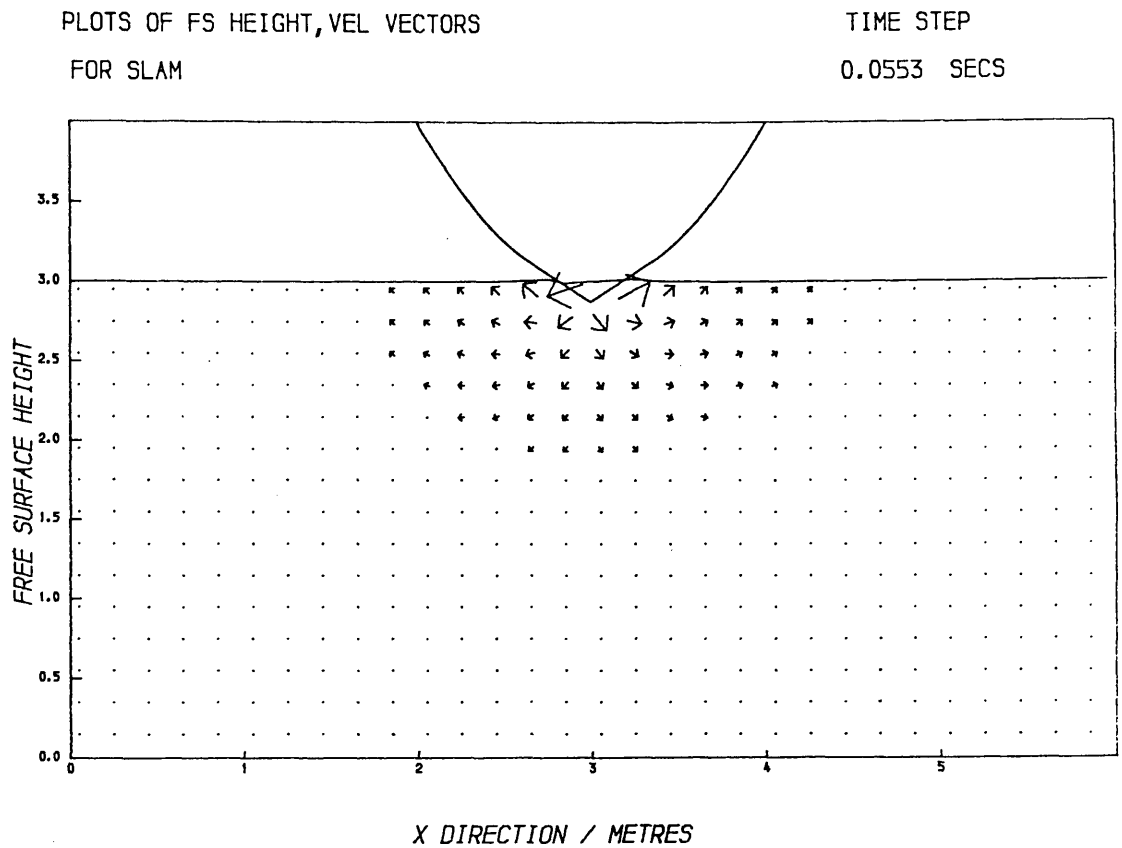

Figure 9-36
Impact Of Section B

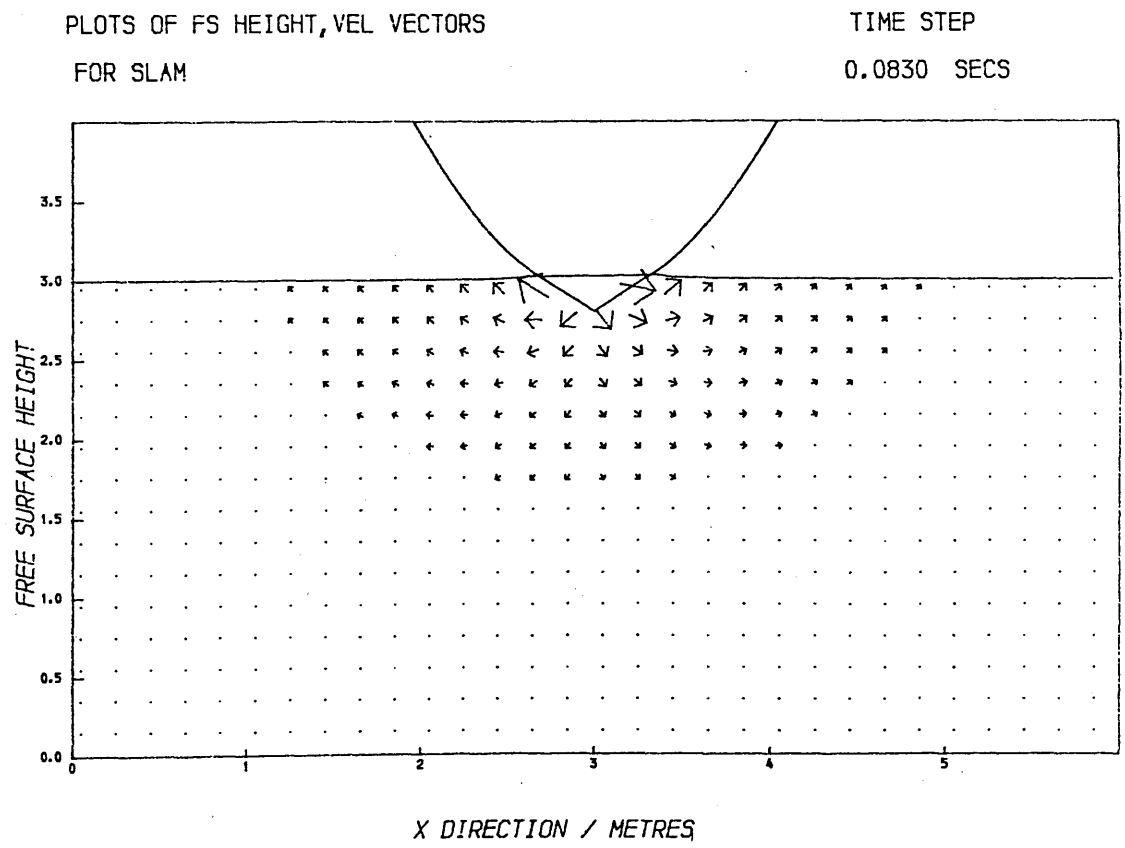

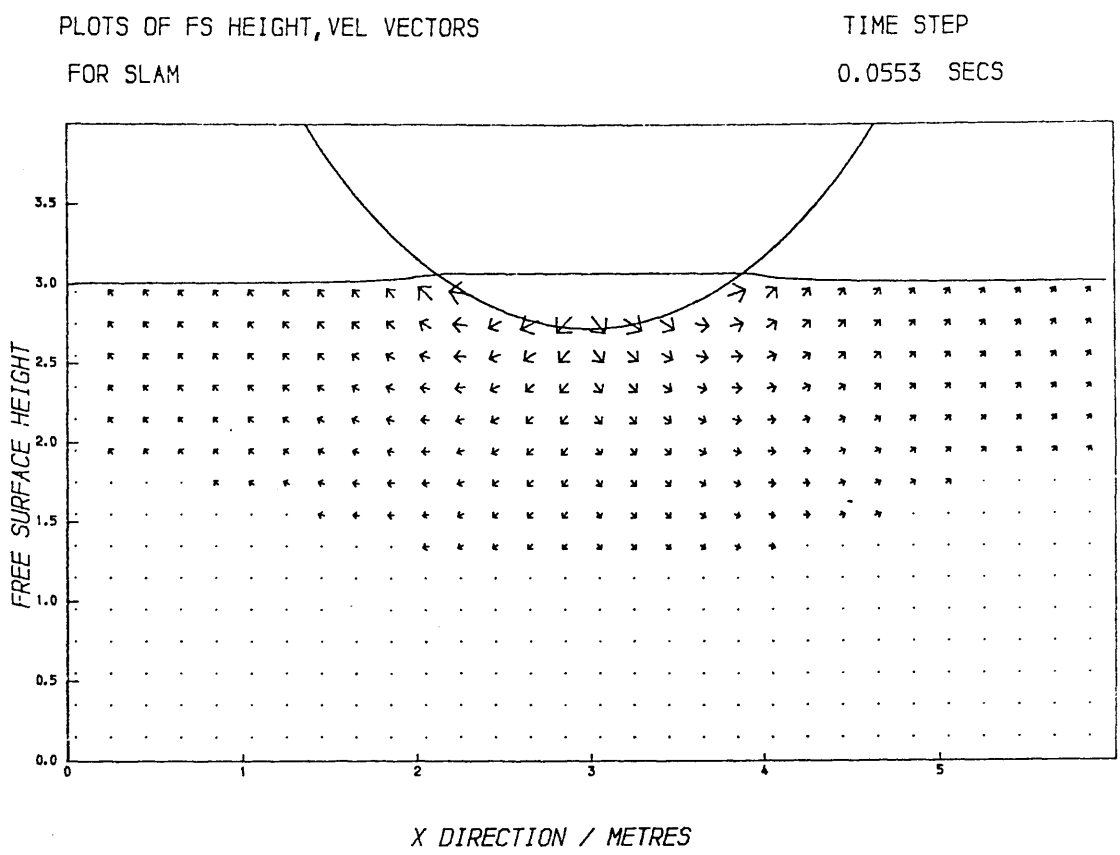

Figure 9-37
Impact Of Section C

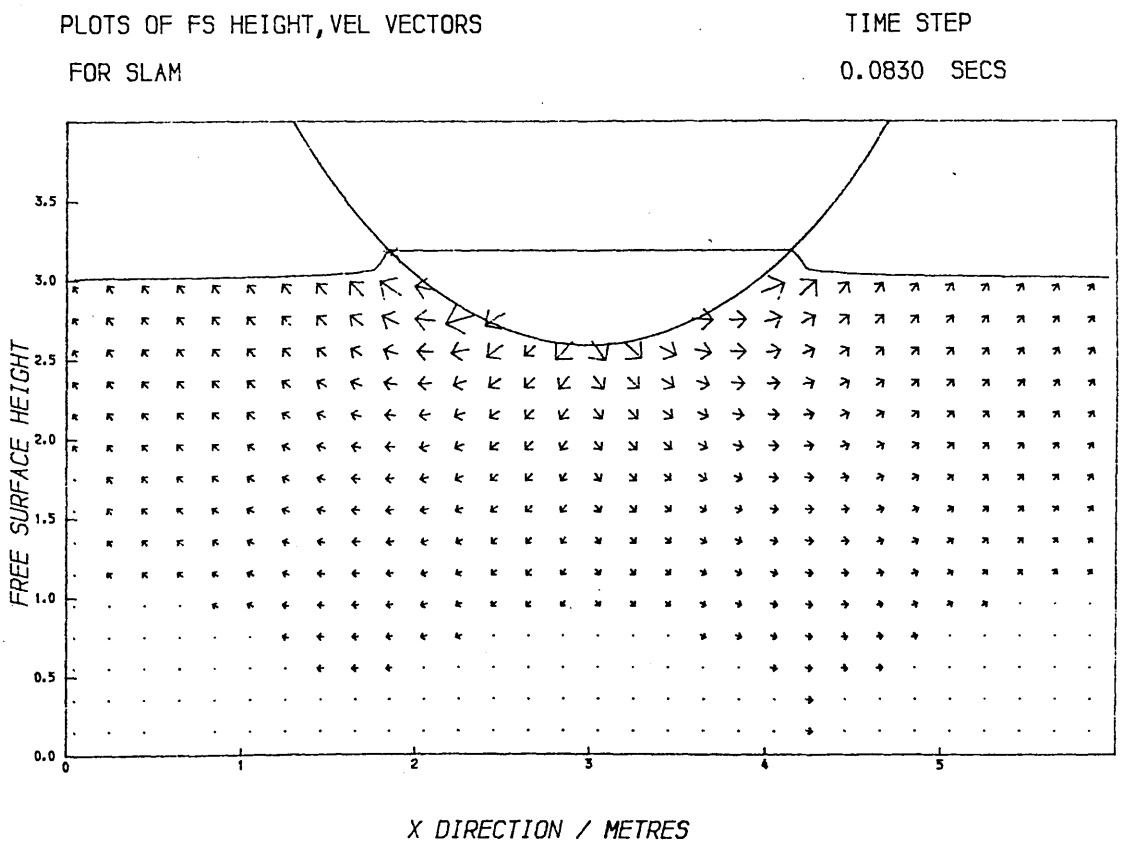

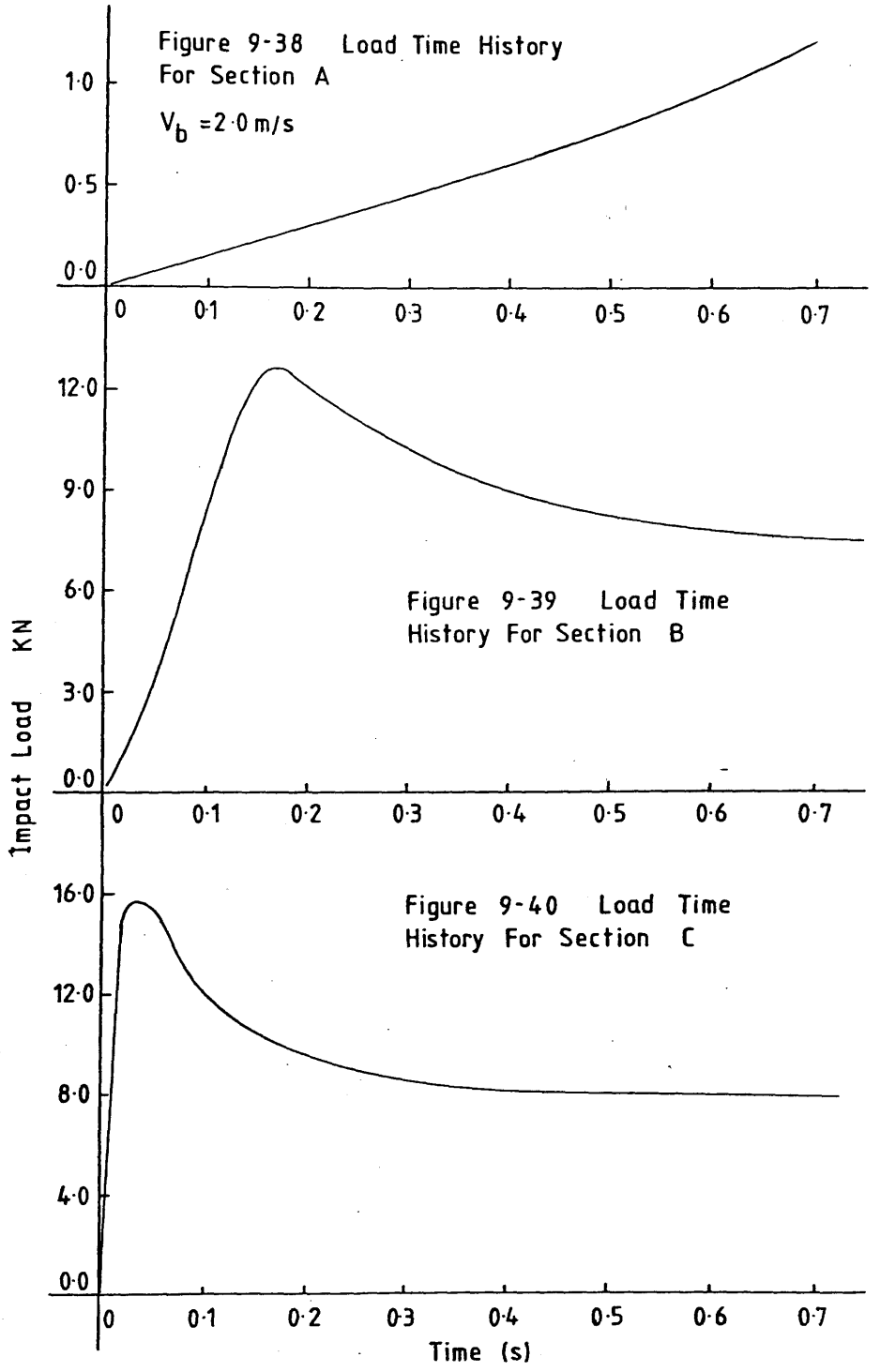
Figure 9-38 Load Time History For Section A
V_b =2·0 m/s
1·0
0·5
0·0
0
0·1
0·2
0·3
0·4
0·5
0·6
0·7
12·0
9·0
6·0
3·0
0·0
Figure 9-39 Load Time History For Section B
Impact Load KN
16·0
12·0
8·0
4·0
0·0
Figure 9-40 Load Time History For Section C
Time (s)

B, with its initial 35 degree deadrise angle produced a gradual rise in hydrodynamic load, with a gentle peak at 12.7 KN. Section C produced a rapid change in impact load over the first few time steps, with a peak at 15.9 KN. The drop in loading was rapid at first, but levelled out beyond a draught of 0.75m.

It was not possible to continue these simulations for long enough to provide full immersion of the section owing to the amount of computing time that would have been required. Thus the load time history for section A did not include the peak predicted by the Lewis form computation caused by the immersion of the chines.

Figures 9-41, 9-42 and 9-43 show the load time histories plotted against the fractional immersion given by:-

$$\frac{V_b\, t}{Z}$$

where z was chosen to be 1.5m. The slam loads given by the 'static' computations of rate of change of added virtual mass with draught, as derived from figures 9-31, 9-32 and 9-33, are also shown as a basis for comparison. The slam loads computed by the present method are seen to have a slightly different character. The main differences were:-

a. the peak loads for sections B and C occur earlier in the finite difference computation.

b. the loads over this initial portion of the time history are higher.

c. after the pressure peak (for section B and C), the pressure decay is more rapid when computed using the present method.

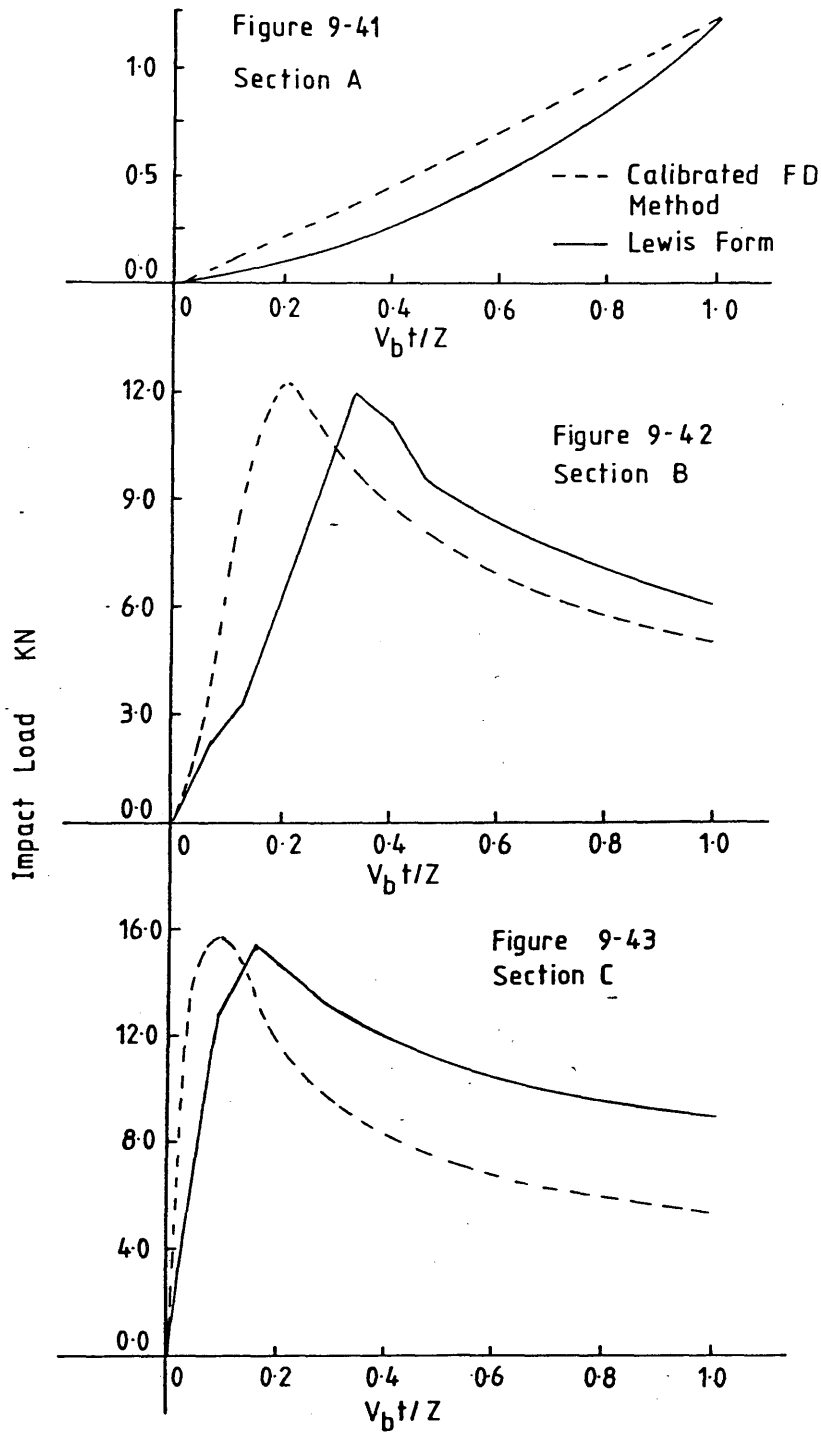
Figure 9-41
Section A
1·0
0·5
0·0
0
0·2
0·4
0·6
0·8
1·0
$V_b t/Z$
--- Calibrated FD Method
—— Lewis Form
Impact Load KN
12·0
9·0
6·0
3·0
0·0
Figure 9-42
Section B
16·0
12·0
8·0
4·0
0·0
Figure 9-43
Section C

The slam load history for section A never reached a peak when either method was used, though loads were slightly higher for the finite difference method when compared with the momentum slam approach.

A comparison of the results from the two approaches over the range of sections used indicated that the greatest variations occurred when the mean deadrise angle was low. It was concluded that the piled up water or spray root formation was responsible for these differences.

Finally, figures 9-44, 9-45 and 9-46 show transverse pressure distributions for sections A, B and C, respectively, at various instants during the simulation. It can be seen that the wedge type section A produced a sharp pressure peak adjacent to the furthest extent of the wetted beam for all time instants. Curve B, with its wedge type shape over the lower portion produced similar distributions at first, though the edge peaks died away as the curved portions of the hull became immersed. Section C was parabolic in shape over the portion under examination. No sharp peaks in the pressure distribution were noticed at any time during the simulation. It was concluded that positive curvature in the hull section results in a more even pressure distribution. The development and shape of the spray root may also play some role in this phenomenon, but how this interaction occurs could not be deduced from these computations.

Tests were carried out over a range of impact velocities from 1.0 to 7.0 m/s. A square law relationship for peak slam load coefficient was evident enabling table 9-C to be compiled. The slam

Figure 9-44
Transverse Pressure
Distribution For Section A

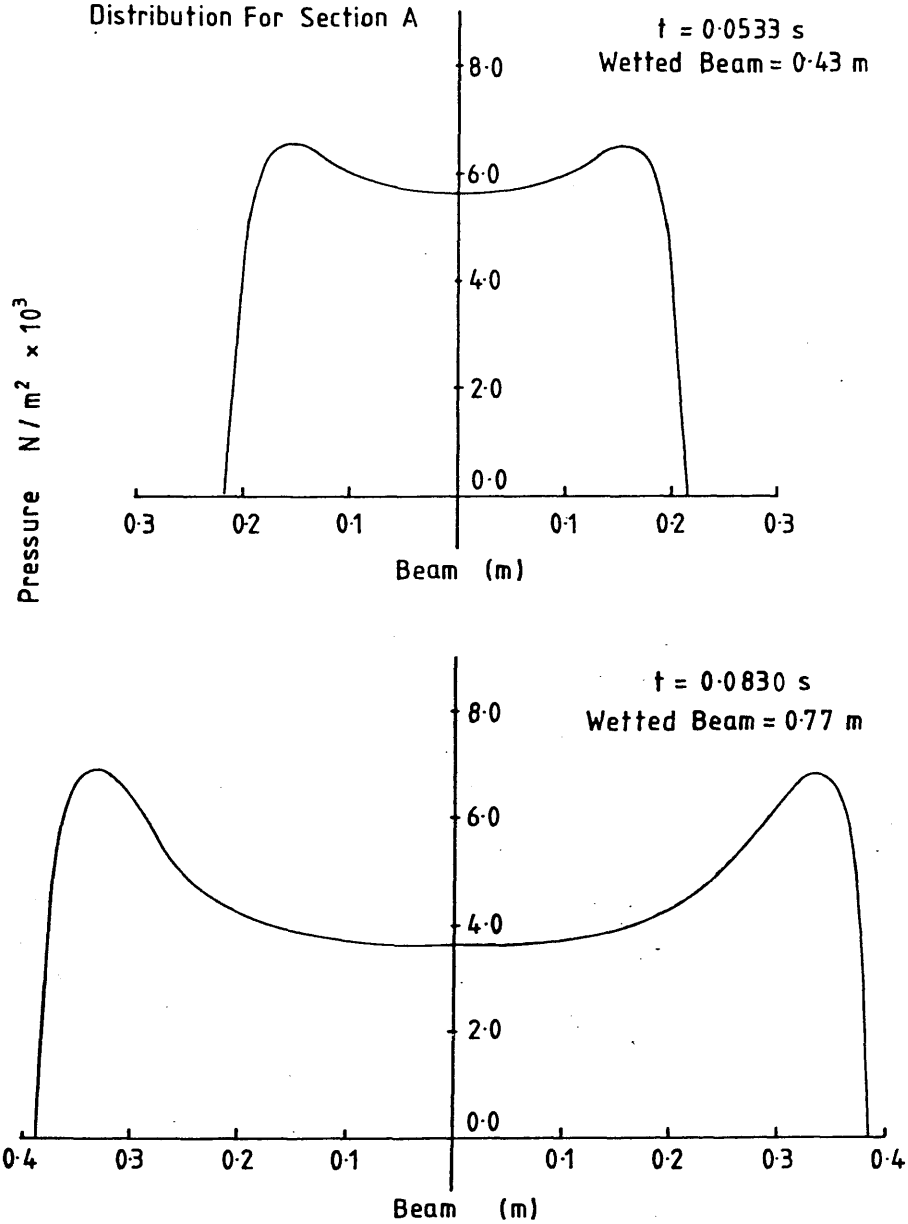

Figure 9-45

Transverse Pressure Distribution For Section B

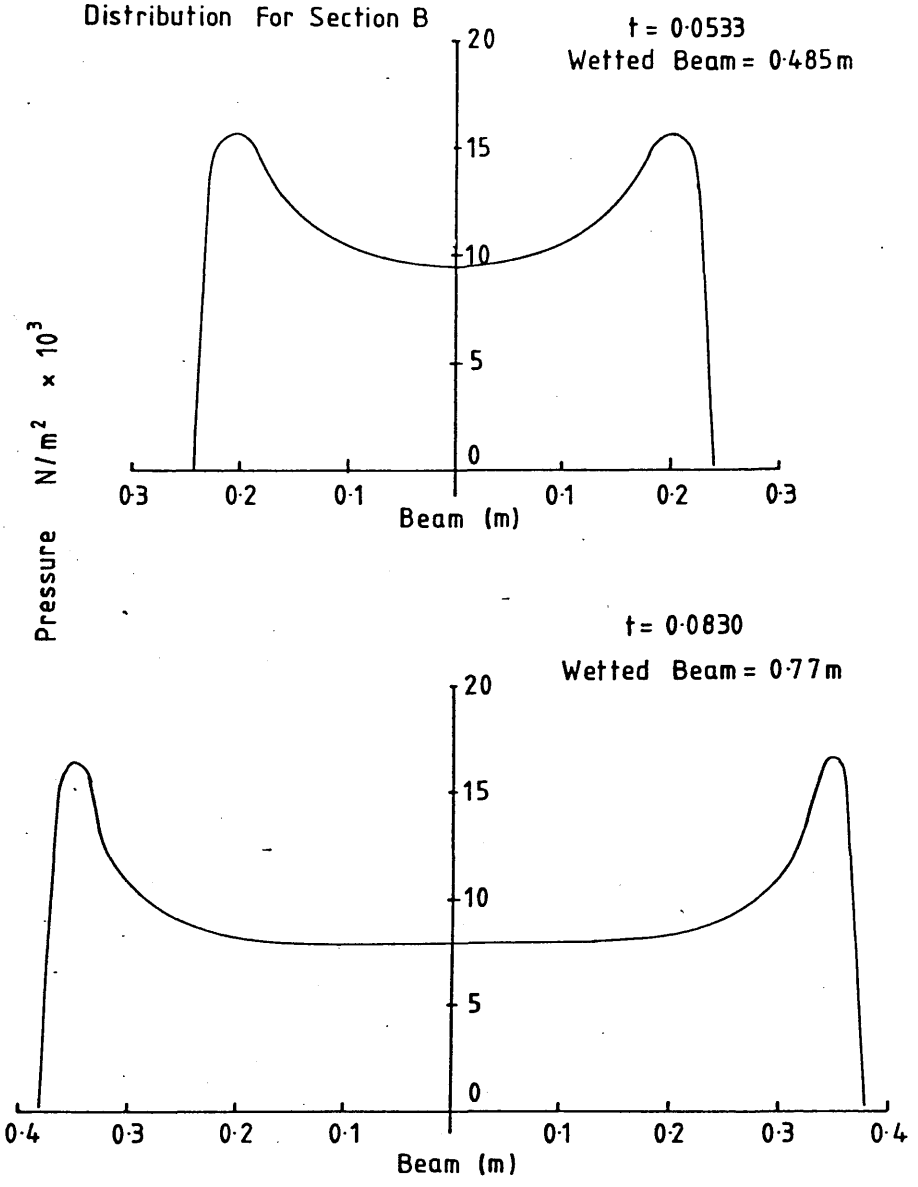

Figure 9-46
Transverse Pressure
Distribution For Section C

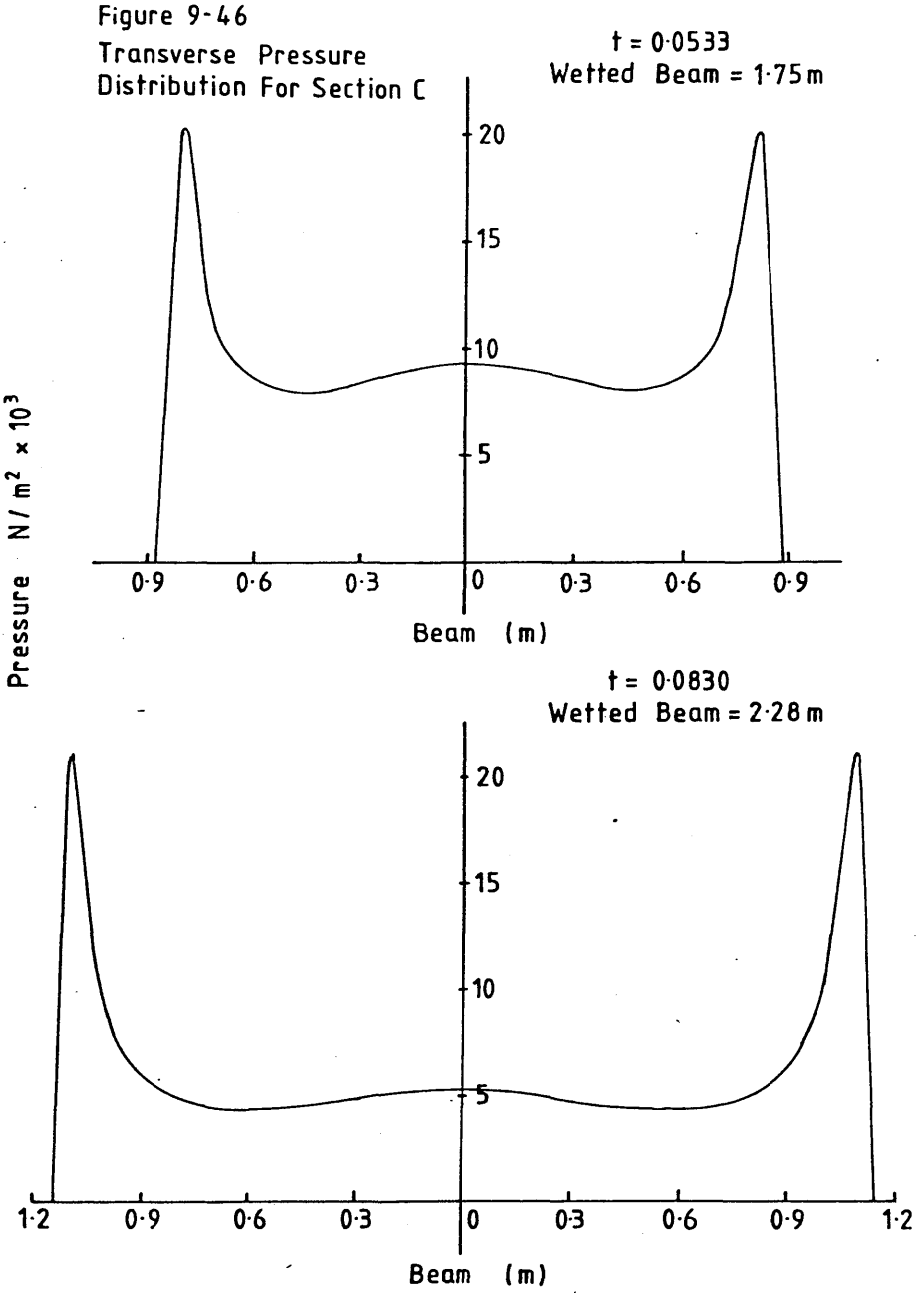

load coefficient for each section was divided by the load calibration factor in order to allow for the previously mentioned shallow water effects. The slam coefficient was calculated via the following formula:-

$$C_s = F_s / 0{\cdot}5 \rho V_b^2 b_t^2$$

where b_t : the beam at one tenth of the total draught of the section.

Thus table 9-C shows a comparison of Ochi's slam coefficient with the present method. It is evident that Ochi's coefficients are considerably lower than those predicted herein. These differences may be attributable to:-

a. Non-linearities in the scaling problem

b. A lack of three-dimensionality in the present method.

c. Air entrapment, especially for section C.

Section	F.D. Method	Ochi
A	—	0·171
B	4·05	1·075
C	2·31	1·951

Table 9c

8. THE SLIGHTLY COMPRESSIBLE FLOW MODEL

As already noted, the time step and mesh spacing were closely linked to the dynamic pressure computation (SOLA). Equation 3.7/2 relating to the rate of change of density to the divergence is restated below as:-

$$\frac{\partial \rho}{\partial t} = - \rho \nabla . \bar{u} \qquad 9.8/1$$

It can be seen that this too may be re-formulated in terms of the SOLA code by setting the fluid wave speed equal to the acoustic value of 1410 m/s. In order to produce the compressible flow model, the time step was deduced using this acoustic value for C in equation 9.4/1. Since the flow was to be considered compressible, it was not necessary to apply the continuity solving routines during this phase of the impact. In fact the major source of divergence in equation 9.8/1 was the encroachment of the body into the finite difference cells. Thus 9.8/1 could be re-arranged to give, in finite difference form:-

$$\frac{\Delta \rho}{\Delta t} = - \rho_{ij} \left(\frac{U_{ij+1} - U_{ij}}{\Delta x} + \frac{V_{i+1j} - V_{ij}}{\Delta y} - \frac{Q_{ij}}{\Delta x \Delta y} \right) \qquad 9.8/2$$

where Q_{ij} is the source strength in each cell.

The simulation was very much the same as for the incompressible flow case, with equations 3.7/4 and 3.7/5 being used to update the velocity field.

Two problems arose in the use of this flow model:-

a. the time steps were too small to produce a long enough simulation.

b. the effective deadrise angle required was so small, (0.041 V_b degrees), that air entrapment would most certainly have occurred in practice for this geometry of impact.

In chapter 10 it will be shown that this full acoustic impact type of behaviour may well occur in the slamming of curved sections where air cushioning effects allow the free surface to take up the shape of the body prior to contact. However, this is a highly complicated impact scenario which is too difficult to model at this stage. A compromise was reached therefore in order to evaluate the present numerical model. A deadrise angle of 0.50 degrees was chosen, with an impact velocity of 6.0 m/s. At this value of β, a lower relative impact angle exists at contact due to the air cushioning effects. Furthermore, the sound speed was reduced to 350 m/s in order to increase the time step and allow some acoustic modelling to be carried out.

With this geometry, the rate of change of beam is equal to 687 m/s at an impact velocity of 6.0 m/s. The time step for a 0.1m mesh spacing was 0.143ms, with the half beam equal to 0.5m, five time steps were required for full immersion of the wetted beam. Similarly, ten time steps were required for the acoustic wave to travel the same distance. The total rise time was therefore to be 1.43 ms.

After ten time steps had elapsed hydrodynamic flow was invoked by:-

a. changing the time step back to its shallow water hydrodynamic value.

b. taking the total change of fluid density in each cell and converting it to an equivalent source strength to be included in the next time step.

c. adding the total stored strain energy to the fluid kinetic energy via the variational described in chapter 6.

Figure 9-47 shows the centreline pressure time history for this wedge impact. It can be seen that the peak pressure reaches its acoustic value given by:-

$$p_m = \rho_w C V_b = 2{\cdot}10 \text{ N/mm}^2$$

after 9 time steps. Upon the introduction of hydrodynamic flow after the tenth time step the pressure dropped dramatically and followed the usual pattern of behaviour thereafter.

It was not considered that this was a particularly realistic simulation. Whilst the influence of air cushioning may provide the correct conditions for this type of flow model to be of use, the extra problem of modelling any trapped bubble layers would require a higher level of sophistication than that presented herein.

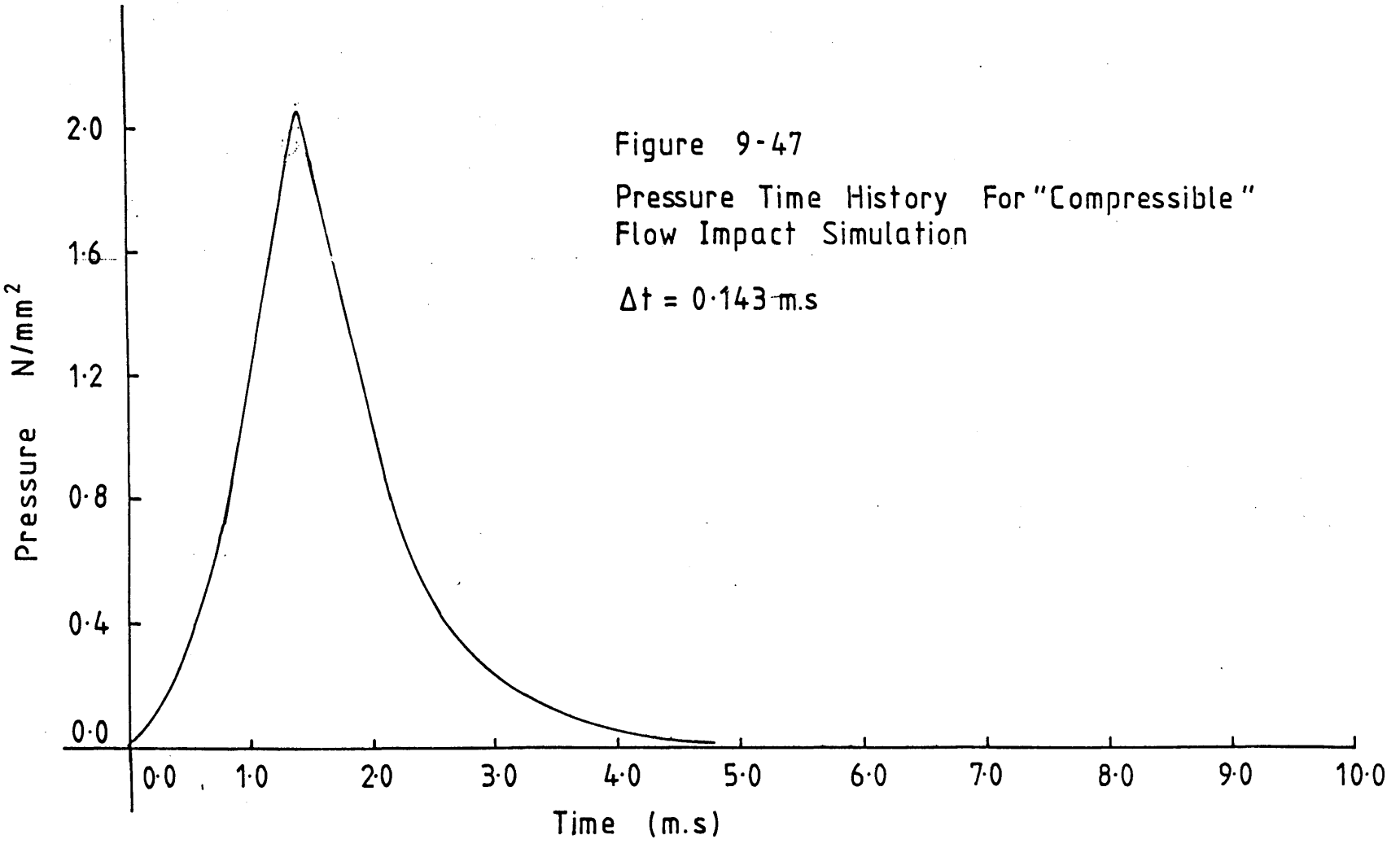

Figure 9-47

Pressure Time History For "Compressible" Flow Impact Simulation

$\Delta t = 0{\cdot}143$ m.s

9. SUMMARY AND CONCLUSIONS

This chapter has concerned the use of computational fluid dynamics and, in particular, the finite difference time marching method to provide a model of the water entry problem for an arbitrarily shaped body.

At first it was shown that the computational methods developed in chapter 8 to model steady state and dynamic flows with a free surface could be developed to accurately calculate the hydrodynamic coefficients of regular shaped bodies in shallow water. The link between the solution of the continuity equation and the dynamic pressure solver (SOLA) was confirmed practically by the use of a discrete source distribution to represent dynamic boundaries.

The next stage was the final development and testing of the modified control volume analysis required to model the dynamics of arbitrarily shaped bodies on a regular finite difference mesh. This feature, believed to be unique in the field of hydrodynamics at the present time, enabled the evaluation of the water entry problem to go ahead.

The impact problem was at first simulated for a circular cylinder of radius 1.0m. Initial analysis showed the interpretation of the first contact between body and free surface to be critical to the peak pressures calculated. Both peak pressures and post contact load time histories agreed well with contemporary theory. The infinite peak loads predicted to occur at the instant of contact could not, of course, be reproduced. Physical reasoning dictated that such considerations were in any case impossible and that other phenomenon

such as compressibility and air entrapment would be required to explain the behaviour of the load time history at first contact with the free surface.

The variational energy algorithm was shown to provide a much needed stabilizing influence on the dynamically interactive drop tests simulations.

These methods were extended to deal with the forced impact of ship shaped sections for which calibration of the model to account for the effects of a finite depth of water was required. It was seen that as the mean deadrise angle was decreased, the effect of the spray root formation was to shorten the initial load rise time, increase the peak load, and cause a more rapid decrease in loading. It was also concluded that section curvature had the effect of smoothing out the transverse pressure distribution, thus avoiding the high local edge pressures common to wedge shaped bodies.

The introduction of fluid compressibility was hampered by the extremely short time steps required to perform the simulation. A 'compromise' hest was performed in which this model of compressible behaviour was shown to be able to produce authentic heavy slam like behaviour. It was considered that the physical conditions required to initiate this type of behaviour would, in practice, need to be associated with air entrapment in order for the free surface and section shape to aquire the necessary geometry.

CHAPTER 10

STUDIES ON AIR ENTRAPMENT

CHAPTER 10

STUDIES ON AIR ENTRAPMENT

1. INTRODUCTION

This investigation was carried out in order that the solution procedure for the equations of conservation of mass and momentum in the trapped air layer could be studied in isolation. At first it was thought that this could be achieved by simulating the build up of air pressure between a falling flat plate and an horizontal, rigid surface. This had been the procedure carried out by Johnson for which some success had been claimed. However, this numerical model was found to become unstable after a few tens of time steps, no matter what type of discretisation technique was used for equations 3.8/2 and 3.8/3. It was concluded that the deformation of the free surface was an essential feature in producing a stable and accurate model of this type of impact.

Therefore, to test the numerical schemes used for the air layer model prior to inclusion into the water entry simulation, a program was written in which the free surface motions were represented by a potential flow. A linear free surface kinematic boundary condition was used to calculate the rate of change of free surface height, whilst a simplified Bernoulli condition coupled air layer and fluid dynamic pressures. The governing Laplace equation was solved by the use of a finite difference technique.

The resulting computer program coupled the developing

pressure field to the free surface motions to produce a simple but accurate picture of air entrapment or air cushioning. This initial success led first to a survey of numerical schemes for the discretisation of the air layer. Similarly, the effect of varying boundary conditions for velocity, ie throttling at the plate edge, was studied. The effect of differing initial conditions for , and h on the development of the pressure field was also examined.

Once satisfied that a consistent numerical model had been developed for the isothermal gas flow equations, a parametric study was undertaken to produce pressure and load time histories for bodies with varying geometry. The following parameters were systematically varied for each computer run:-

a. deadrise angle

b. curvature

c. mesh spacing

For each of the above, a series of different impact velocities and mass loadings were applied. Approximately 180 computer runs were required in order to complete this survey. With each run requiring approximately 7500 cpu seconds to be completed, a considerable amount of time and effort was needed. Sections 10.6 to 10.9 present the results of this work.

Further studies were carried out concerning the physical modelling of the flow. The influence of one dimensional energy transport within the air layer and the effect of the three dimensional flow model outlined in section 3.8.3 are reported in sections 10.10 and 10.12, respectively.

2. POTENTIAL FLOW MODEL OF FREE SURFACE BEHAVIOUR

With regard to figure 10-1, the two dimensional fluid domain is shown bounded by a free surface above and rigid walls on the other three sides. The fluid is considered inviscid, incompressible and irrotational and is thus governed by potential flow represented by the Laplace equation:-

$$\nabla^2\phi = 0 \qquad \text{---10·2/1}$$

where ϕ is the fluid potential.

The velocity components (u, v) are given by:-

$$u = \frac{\partial\phi}{\partial x} \qquad v = \frac{\partial\phi}{\partial y} \qquad \text{---10.2/2}$$

At the free surface, the fluid potential is governed by the Bernoulli relationship:-

$$\frac{\partial\phi}{\partial t} + g\eta + \frac{p_a}{\rho} = 0 \qquad \text{---10.2/3}$$

where η = free surface height

p_a = air pressure

ρ = density of water.

The free surface height is found via the linearised free surface kinematic condition:-

$$\frac{\partial\eta}{\partial t} = v = \frac{\partial\phi}{\partial y} \qquad \text{---10.2/4}$$

The rigid wall boundaries are represented by the free slip, zero normal flux condition given by:-

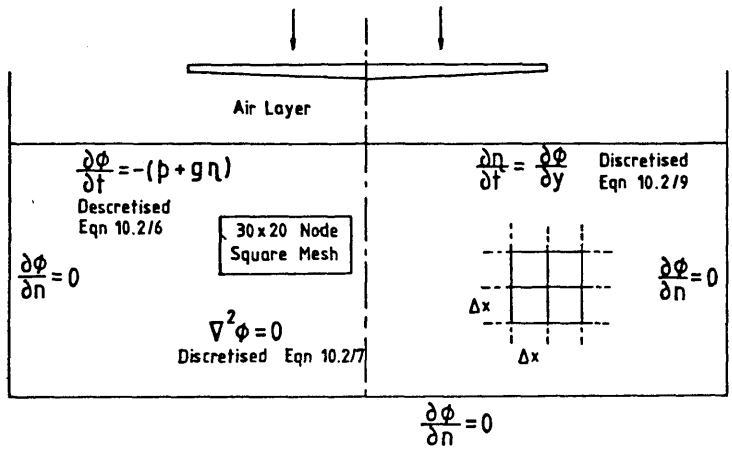

Figure 10-1 Fluid Domain For Air Entrapment Problem

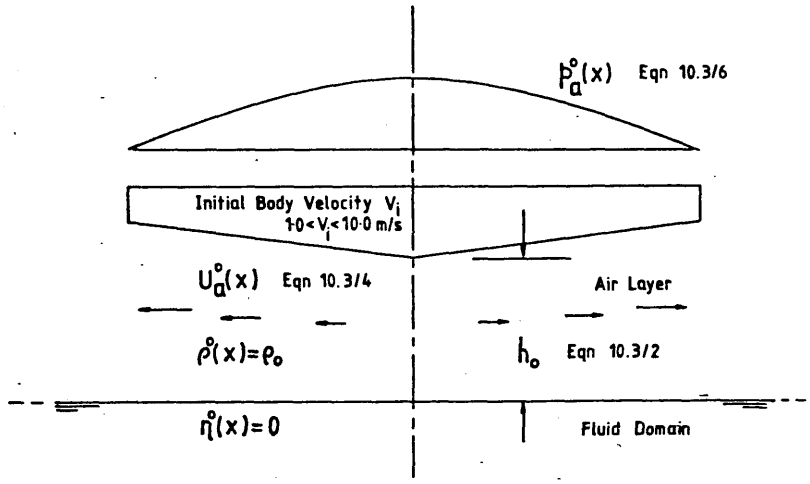

Figure 10-2 Initial Conditions For Air Entrapment Problem

$$\frac{\partial \phi}{\partial n} = 0 \qquad \text{---10.2/5}$$

The above equations are introduced into the time marching simulation of air entrapment via the following discretisation procedure. Equation 10.2/3 provides the value of the fluid potential on the free surface via the relationship:-

$$\phi_{ix,j}^{n+1} = \phi_{ix,j}^{n} - \Delta t \left(g\eta^{n} + \frac{p_a^{n}}{\rho} \right) \qquad \text{---10.2/6}$$

This value of ϕ applies to a mean free surface level only. Thus the computational domain is represented by the rectangle as shown in figure 10-1. The domain is split into a regular finite difference mesh over which equation 10.2/1 may be discretised using the fourth order accurate central difference operators given by 4.4/17. This leads to a successive over relaxation solution procedure similar to that used for the Poisson pressure equation. The resulting recursive relationship for the velocity potential at each node within the fluid is:-

$$\phi_{ij}^{k+1} = (1-\omega)\,\phi_{ij}^{k} - \frac{\omega}{2(1+\beta^2)} \left(\phi_{ij+1}^{k} \;\; \phi_{ij-1}^{k+1} \;\; \beta^2 (\phi_{i+1j}^{k} \;\; \phi_{i-1j}^{k+1}) \right) \qquad \text{---10.2/7}$$

applied to

$$1 < i < ix-1$$
$$1 < j < jx$$

where ix and jx represent the maximum extent of the discretised domain. The free surface nodes are excluded from this part of the routine as they provide the known 'forcing' terms via equation 10.2/6. It can be seen that, directly beneath the falling body, the pressure applied to the free surface is non-zero, thus producing a finite rate of change of fluid potential. After this boundary condition has been introduced into equation 10.2/7, the fluid potential gradient at the free surface gives rise to a change in free surface height which may

be found from equation 10.2/4 as:-

$$\eta_j^{n+1} = \eta_j^n + \Delta t \left(\phi_{ix,j}^n - \phi_{ix-1,j}^n \right) / \Delta y \qquad \text{---10.2/8}$$

and

$$\frac{\Delta \eta}{\Delta t}^n = \left(\phi_{ix,j}^n - \phi_{ix-1,j}^n \right) / \Delta y \qquad \text{---10.2/8}$$

which may be used directly in equation 7.1/1 in order to find the rate of change of air gap thickness during the air entrapment routine.

3. INITIAL CONDITION AND FULL SIMULATION PROCEDURE

The major dimensions and initial conditions are illustrated in figure 10-2. It had been noted in initial numerical experiments that the rise in air pressure due to compressibility effects did not begin until the plate was a few centimeters above the free surface. Similar computational schemes described in reference (35) assumed the initial air gap to be based on a fraction of the width, ie:-

$$h(0) = 0{\cdot}05\ b \qquad 10{\cdot}3/1$$

where b is the beam of the section.

This author found that the initial velocity of the body, V_i , was also a deciding factor. If the initial air gap was too small, the time history for the pressure field and total load contained spurious oscillations as shown in figure 10-3. However, the computation would take up too much time, and output data files would be too large if an excessive initial drop height were chosen.

Experience with the computation showed that, whilst the time step varied in size with flow speed, a mean value of 1.25×10^{-4} s could be used in an estimate of the total time taken for a simulation based on a one hundred time step cycle. This set the initial air gap (in meteres) at:-

$$h(0) = 0{\cdot}0125\ V_i \qquad ---10.3/2$$

It had to be assumed that the velocity of the body was unaffected by the air flow around it up until this initial value of h was reached.

The initial air velocities u_a were found by assuming

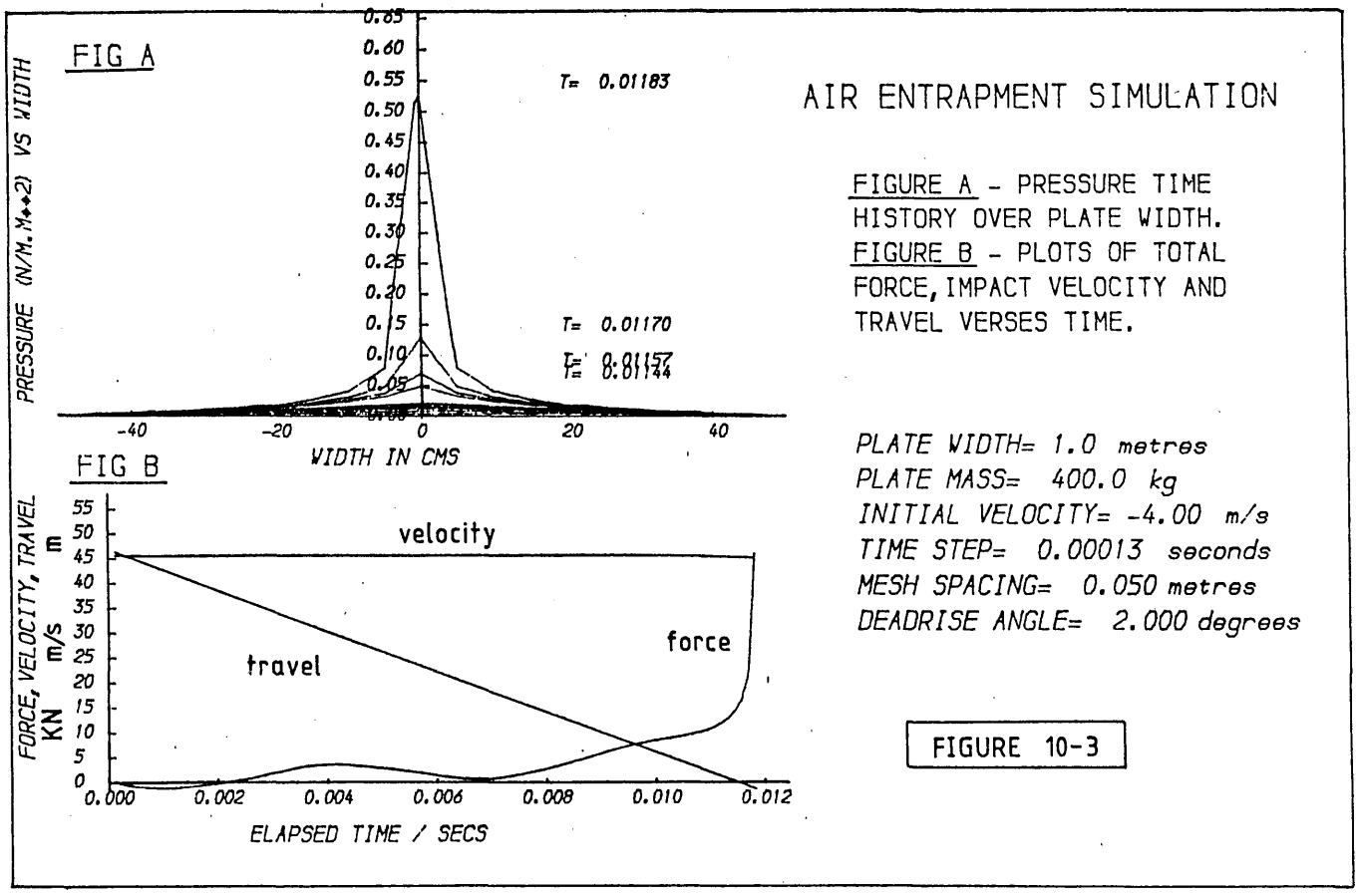

AIR ENTRAPMENT SIMULATION

FIGURE A - PRESSURE TIME HISTORY OVER PLATE WIDTH.
FIGURE B - PLOTS OF TOTAL FORCE, IMPACT VELOCITY AND TRAVEL VERSES TIME.

PLATE WIDTH= 1.0 metres
PLATE MASS= 400.0 kg
INITIAL VELOCITY= -4.00 m/s
TIME STEP= 0.00013 seconds
MESH SPACING= 0.050 metres
DEADRISE ANGLE= 2.000 degrees

FIGURE 10-3

incompressibility and hence applying continuity using a modified form of equation 3.8/2:-

$$\frac{\partial h}{\partial t} = - h \frac{\partial u_a}{\partial x} \qquad \text{---10.3/3}$$

which, upon consideration that:-

$$u_a(x) \; : \; x = 0 \; , \quad u_a(0) = 0$$

and

$$\frac{\partial h}{\partial t} = V_i$$

gave

$$u_a^o(x) = - V_i x / h \qquad \text{---10.3/4}$$

Similarly the initial pressure distribution was obtained by substitution of equation 10.3/4 into 3.8/3. The resulting differential expression was integrated with respect to x with the following boundary conditions on air pressure applied at the plate boundaries:-

$$p_a(-b/2) = p_a(b/2) = p_o = 1{\cdot}02 \times 10^5 \; N/m^2 \qquad \text{---10.3/5}$$

This gave a formula for the initial pressure distribution as:-

$$p_a(x) = p_{a_o} + \rho_a \left(\frac{b^2}{4} - x^2 \right) \left(V_i^2 - \frac{h}{2} \dot{V}_i \right) \Big/ h_0^2 \qquad \text{---10.3 6}$$

If required, the initial conditions for the energy transport model were derived as follows. The fluid state variables γ, C_p, C_v, R and T_o were taken as:-

$\gamma = 1.4$

$C_p = 1015.35 \; m^2 \, s^{-2} \, {}^\circ k^{-1}$

$C_v = 725.25 \; m^2 \, s^{-2} \, {}^\circ k^{-1}$

$R = 290.10 \; m^2 \, s^{-2} \, {}^\circ k^{-1}$

$T_o = 293.00^\circ k$

$C_a = 344.9 \; ms^{-1}$

This gave the initial internal energy, e(x) as:-

$$e(X) = \frac{C_v}{T_0} \qquad \text{---10.3/7}$$

With the initial air velocity and pressure distributions found using equations 10.3/4 and 10.3/6, the energy distribution $E_s(x)$ was found by applying equation 3.8/12, ie:-

$$E_s(X) = e(X) + \frac{1}{2}(U_a(X))^2 \qquad \text{---10.3/8}$$

Figure 10-4 shows a flow chart for the complete computation. The simulation procedure for the air layer is contained in a single step, as a condensed form of figures 7-2 or 7-4. The inclusion of the moving free surface computation required that equation 10.2/6 was used to calculate the free surface potential as a boundary condition for the relaxation method given by 10.2/7. For the over relaxation scheme used, it was found that the residual of the Laplace equation given by:-

$$R(\phi) = (\phi_{ij+1} + \phi_{ij-1} + \phi_{i+1j} + \phi_{i-1j} - 4\phi_{ij})/(\Delta x)^2 \qquad \text{---10.3/9}$$

could be reduced to a value of order 10^{-8} within one thousand iterations. A regular 30 x 20 mesh was used to discretise the domain as shown in figure 10-1. Each simulation ran until first 'contact' between the plate and free surface.

The definition of when contact occured was dependent upon the type of impact scenario. Section 10.6 describes the categories of impact more fully. Suffice it to say that, at the instant of contact, the zero thickness of air layer required infinite pressures to exist within the numerical model for some types of impact. Not only was this an unacceptable, non-physical idealisation, but also a practical impossibility. Consideration of a realistic environment beneath a ship

Figure 10-4
Flow Chart For Air Entrapment Simulation

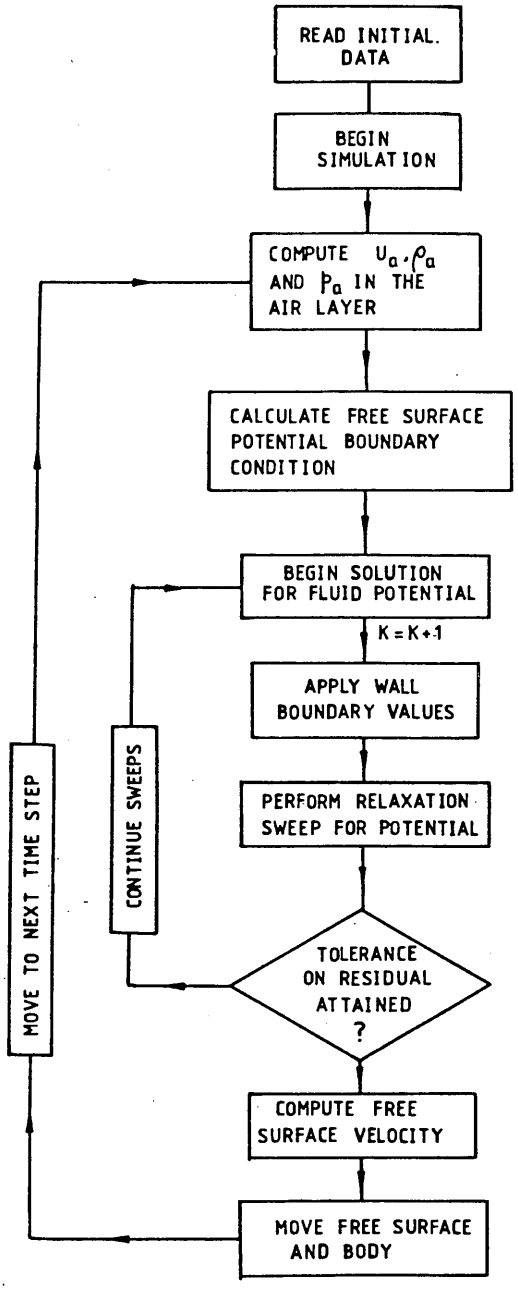

hull about to slam must include the effects of spray, hull wetness and marine growths. Thus allied with information concerning the type and geometry of impact, a reference distance above the free surface was chosen as an 'effective contact point'. Whilst above this point, data produced by the simulation was considered reliable. However, the simulations were often allowed to run past this effective contact point, but the data produced by the numerical model was then viewed with much greater suspicion.

Some impact scenarios did not produce such problems. However, in those which did, the effective contact point was used as a datum by which to compare individual impacts.

4. THE EFFECT OF DIFFERING NUMERICAL SCHEMES

4.1. Introduction

During the early stages in development of the adiabatic model of air layer behaviour, the backward time step, upwind scheme was used. There were two reasons for this decision. Firstly, previous reports concerning such flow modelling (35,49) used this type of scheme exclusively, and hence the method was known to be successful. Secondly, any numerical instabilities occurring during program development would have prevented 'de-bugging' and obscured the effects of variations in the formulation of boundary conditions. As expected, the resulting numerical simulation proceeded smoothly, producing results similar to those given by previous authors. Comparisons between the results of these calculations and those of known experimental and computational work are presented in section 10.13. The following examination of various numerical schemes uses the backward time step, upwind scheme as a basis for comparison. Figure 10-5 shows a typical result for a flat plate impact using the basic scheme.

4.2. Backward Time-Step Central Difference Scheme

Figure 10-6 shows the result for the build up of pressure beneath a flat plate with an initial velocity of 6m/s and a mass of 200kg. The numerical scheme employed a backward time step and central difference formulation. Comparison with the basic scheme shown in figure 10-5 shows the pressure distribution and time history to be of the same form. There is a slight discrepancy in the final peak

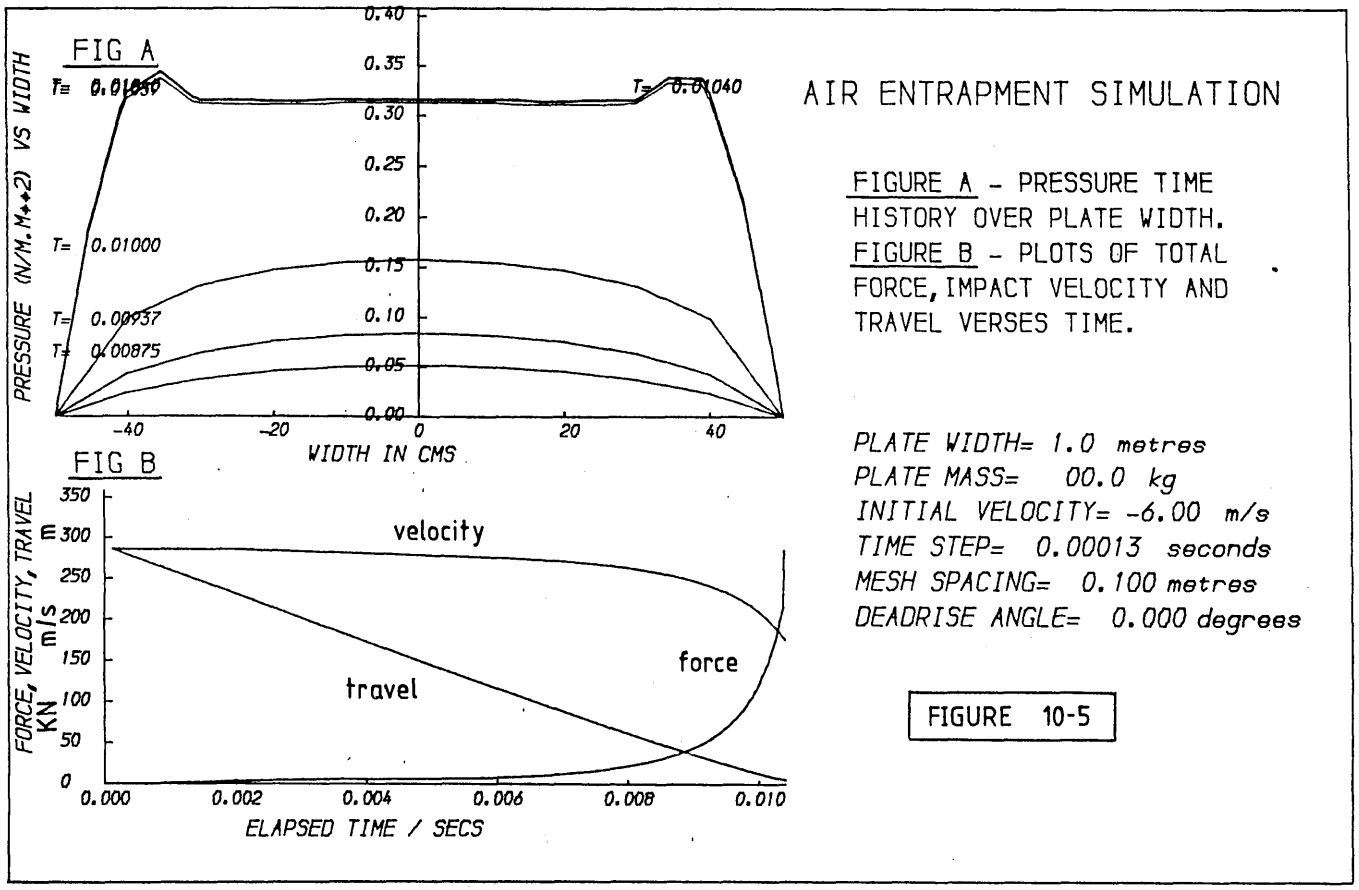

AIR ENTRAPMENT SIMULATION

FIGURE A - PRESSURE TIME HISTORY OVER PLATE WIDTH.
FIGURE B - PLOTS OF TOTAL FORCE, IMPACT VELOCITY AND TRAVEL VERSES TIME.

PLATE WIDTH= 1.0 metres
PLATE MASS= 00.0 kg
INITIAL VELOCITY= -6.00 m/s
TIME STEP= 0.00013 seconds
MESH SPACING= 0.100 metres
DEADRISE ANGLE= 0.000 degrees

FIGURE 10-5

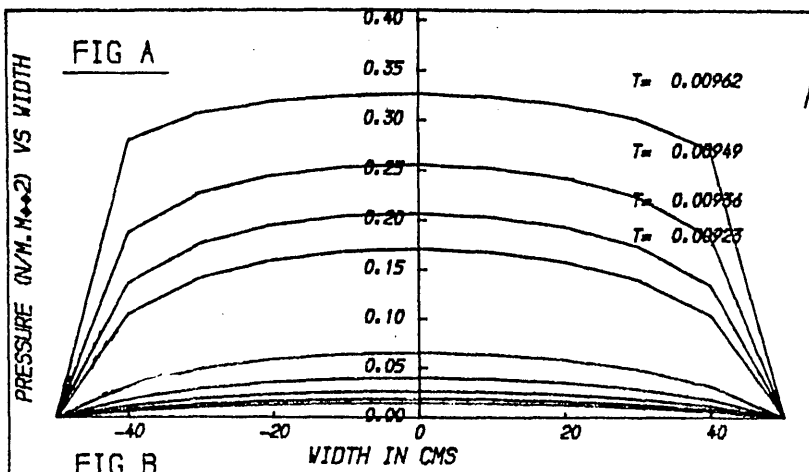

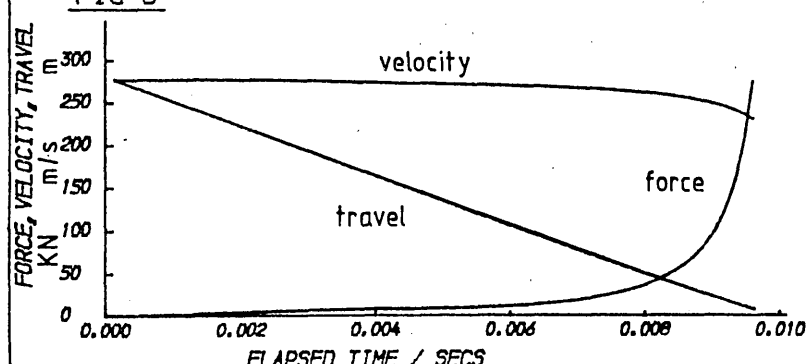

AIR ENTRAPMENT SIMULATION

FIGURE A - PRESSURE TIME HISTORY OVER PLATE WIDTH.
FIGURE B - PLOTS OF TOTAL FORCE, IMPACT VELOCITY AND TRAVEL VERSES TIME.

PLATE WIDTH= 1.0 metres
PLATE MASS= 200.0 kg
INITIAL VELOCITY= -6.00 m/s
TIME STEP= 0.00013 seconds
MESH SPACING= 0.100 metres
DEADRISE ANGLE= 0.000 degrees

FIGURE 10-6

pressure caused by the two simulations being stopped at different positions above the effective contact point referred to in section 10.3. Suitable extrapolation of the pressure/load time history to a single datum point, chosen as 2×10^{-4}m above the free surface, showed much better agreement.

The slight lack of symmetry in the pressure distribution given in figure 10-6 was caused by small errors in the free surface solution. These errors were removed by increasing the number of iterations required to solve the potential flow problem.

Thus it can be seen that the use of central differences in the convection scheme caused none of the 'wiggles' or non-linear instabilities that were mentioned by other investigators of the air entrapment problem (35,49). This may have been due to the dominance of the pressure gradient terms over convection in the overall scheme, but it is also important to note that the air flow beneath the body is smooth and shock free. Thus the central difference convection scheme was adopted in favour of upwinding and its associated, and undesirable, numerical viscosity.

4.3. Central Time-Step, Upwinded Convection Scheme

This type of scheme is best represented by the formulation given in equation 7.1/4. Surprisingly, it was found very difficult to ensure stability for this method. When applying Von-Neuman's analysis to centrally differenced time marching schemes in section 4.6 it was noted that, if the amplification factor at the previous time step was less than unity, the domain of stability in the complex plane was increased. Numerical experiments showed however, that far from curing

instabilities, this scheme actually worsened the problem. Thus if G from equation 4.6/8 was allowed to be greater than unity at any time step, the domain of stability at the next step would be reduced. In fact, equation 4.6/8 requires rigid adherence to the C.F.L stability criterion. The presence of rounding errors in the use of digital computers made this type of scheme less than reliable. Whilst it was possible to perform complete simulations quite satisfactorily, the scheme was apt to fail occasionally. Furthermore, there were no detectable differences between the pressure/load time histories computed using the central time step, upwinded convection operators and those found using the backward time step methods.

4.4. Central Time Step, Central Difference Convection Scheme

As with the previous scheme, it was difficult to ensure numerical stability for the central time step, central difference method. The use of the central difference convection scheme seemed to cause no extra problems and was thus used exclusively in subsequent computations. The central time step was considered the main cause of failure, and was therefore abandoned.

5. EFFECT OF VARIATIONS IN BOUNDARY CONDITIONS MESH SPACING AND TIME STEP

5.1. Introduction

A small series of numerical experiments were undertaken in order to study the effect of variations in the following three parameters:-

a. θ, the angle of divergence of the free jet at the plate edge.

b. Δx, the mesh spacing in the air layer

c. Δt, the time step and its equivalent parameter, the Courant number C_{fl}.

5.2. Boundary Conditions

The pressures and densities at the plate edge were dictated by physical considerations, hence only variations in the velocity gradient at ends of the domain were possible. With the mesh geometry used in these calculations, the assignment of values to $U_{a\,j=jx}$ and $U_{a\,j=1}$ at the boundaries became a function of θ, the angle of divergence of the free jet at the plate edge.

For upwinded convection schemes, the boundary values on U_a had no effect upon the calculation, as can be seen by inspection of equations 7.1/3a and 7.1/3b. However, a central difference scheme was applied for most of the computer runs and hence values of beyond the plate edge influenced the development of the air layer. Values for U_a within the divergent jet were found by consideration of continuity. As the angle θ was increased, the boundary values $U_{a\,1}, U_{a\,jx}$ were

reduced. For the case of a flat or near flat plate (β < 0.25 degrees) the high pressure gradient at the plate ends became an increasingly dominant term in equation 7.1/2 as θ was allowed to rise. Figure 10-7 shows how the velocity gradient was affected at the plate edge by these considerations. If θ was increased sufficiently, the velocity gradient became negative. The result was that the speed of the air flow at the edges increased rapidly and caused numerical instability. In order to avoid this problem, the angle θ was kept below 30 degrees as recommended in previous studies (35,49).

For higher deadrise angles (β > 0.5 degrees), the behaviour of the divergent jet had little influence since the highest pressures and pressure gradients occurred along the centreline of the body. This type of pressure distribution resulted in a near linear velocity field at the plate edges, as can be seen from figure 10-8. The subsequent smooth transition in flow conditions across the boundary suggested that the free jet like behaviour began beneath the body as a result of the free surface/body geometry.

5.3. The Effect of Mesh Spacing

In general, the solutions to flow problems found using the techniques of computational fluid dynamics are improved as the mesh spacing is progressively reduced. Therefore, an attempt was made to study the effect of mesh refinement upon the accuracy of the finite difference model of air entrapment. The number of (p_a, U_a, ρ_a) nodes in the air layer was doubled, thus halving the mesh spacing. However, the degree of discretisation in the fluid domain was unchanged, since a reduction of the mesh spacing in this region would have unduly increased the computational effort. An interpolation method was

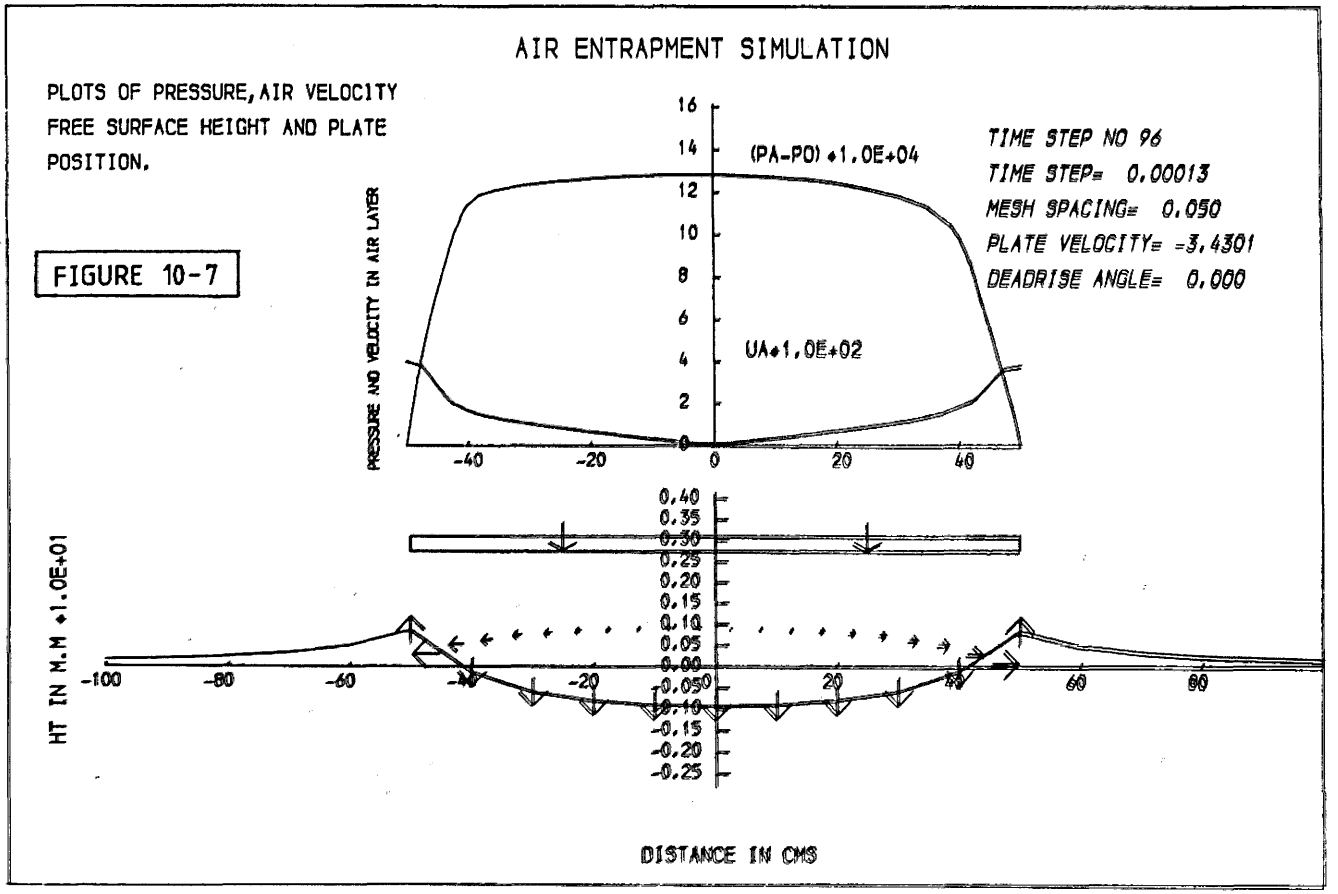
AIR ENTRAPMENT SIMULATION
PLOTS OF PRESSURE, AIR VELOCITY FREE SURFACE HEIGHT AND PLATE POSITION.
FIGURE 10-7
(PA-PO) *1.0E+04
UA*1.0E+02
PRESSURE AND VELOCITY IN AIR LAYER
TIME STEP NO 96
TIME STEP= 0.00013
MESH SPACING= 0.050
PLATE VELOCITY= -3.4301
DEADRISE ANGLE= 0.000
HT IN M.M *1.0E+01
DISTANCE IN CMS

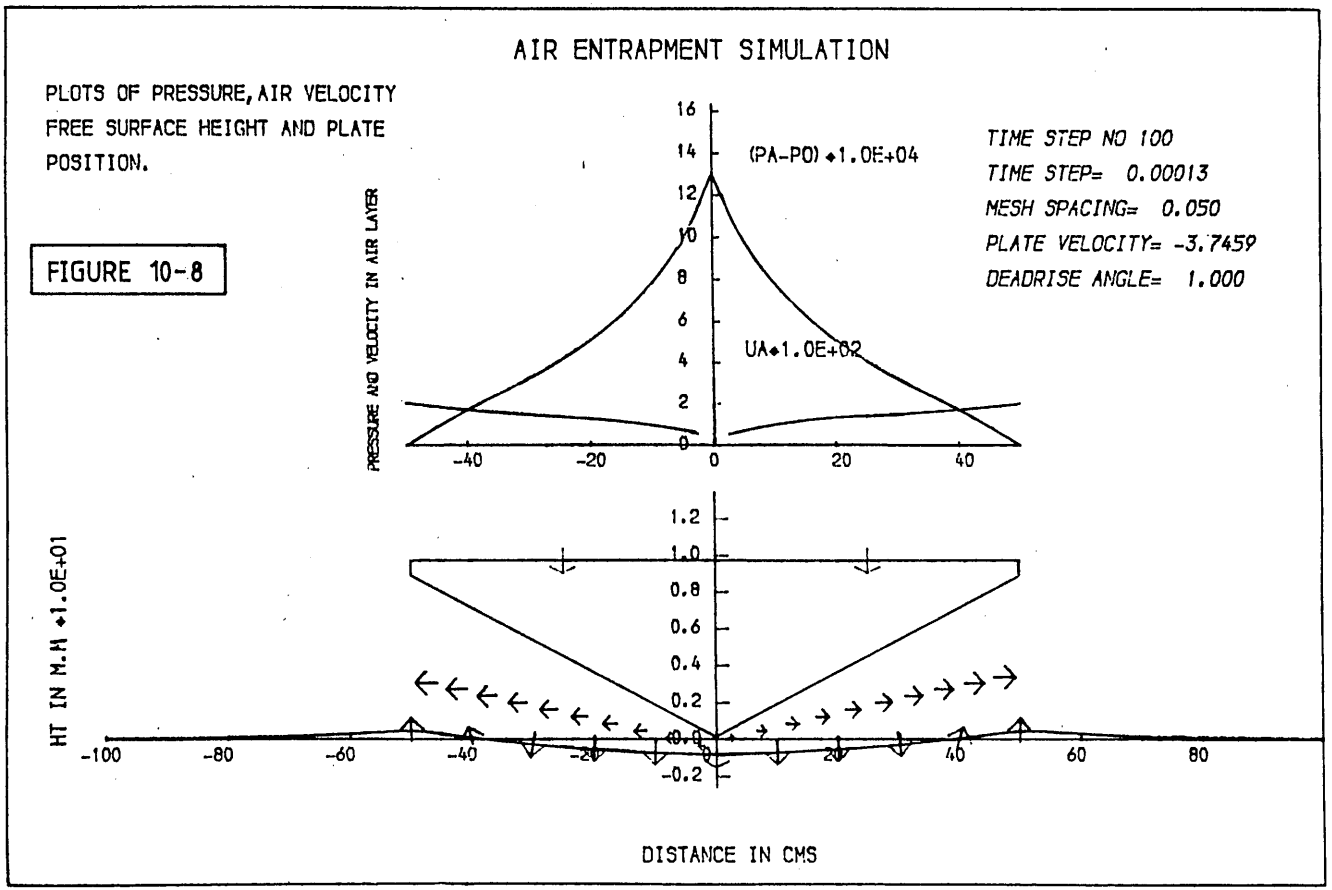
AIR ENTRAPMENT SIMULATION
PLOTS OF PRESSURE, AIR VELOCITY FREE SURFACE HEIGHT AND PLATE POSITION.
FIGURE 10-8
TIME STEP NO 100
TIME STEP= 0.00013
MESH SPACING= 0.050
PLATE VELOCITY= -3.7459
DEADRISE ANGLE= 1.000
(PA-PO)*1.0E+04
UA*1.0E+02
PRESSURE AND VELOCITY IN AIR LAYER
HT IN M.H *1.0E+01
DISTANCE IN CMS

employed to calculate the free surface height and velocity at nodes in the air layer which did not coincide with fluid nodes.

Tests were conducted with a mesh spacing of $\Delta x = 0.1m$ and 0.05m for a range of deadrise angles. For low deadrise angles, ie $0 < \beta < 0.25$ degrees, there was little difference between the solutions obtained on the two meshes. The flat, plateau like pressure distributions common to these geometries was responsible for this. The only contribution made by the mesh refinement being to introduce a slightly steeper pressure gradient at the edges.

For deadrise angles $\beta > 0.5$ degrees, the reduced mesh spacing improved the accuracy of the total load calculation by reducing the width of the central pressure peak characteristic of these impact geometries. Figures 10-9 and 10-10 show pressure distributions and force time histories for the impact of a 400kg plate, with an initial velocity of 6m/s and a deadrise angle of 1.0 degree. The four types of impact category are described in a later section. This particular impact scenario consisted of air cushioning only, followed by hydrodynamic impact. Therefore, the simulation continued just up to the instant of contact. It can be seen from the two figures that, whilst the peak pressure values are identical at 1.6 N/mm^2, the coarser mesh refinement in figure 10-9 lead to a higher peak loading of 275KN as compared with 215KN for the refined mesh. A finer mesh spacing would reduce the peak loading further. However, problems were encountered when attempting to continue the mesh refinement process.

Inaccuracies, brought about by the interpolation technique used to match the coarse mesh in the fluid domain to the refined mesh in the air layer finally resulted in numerical instability. This

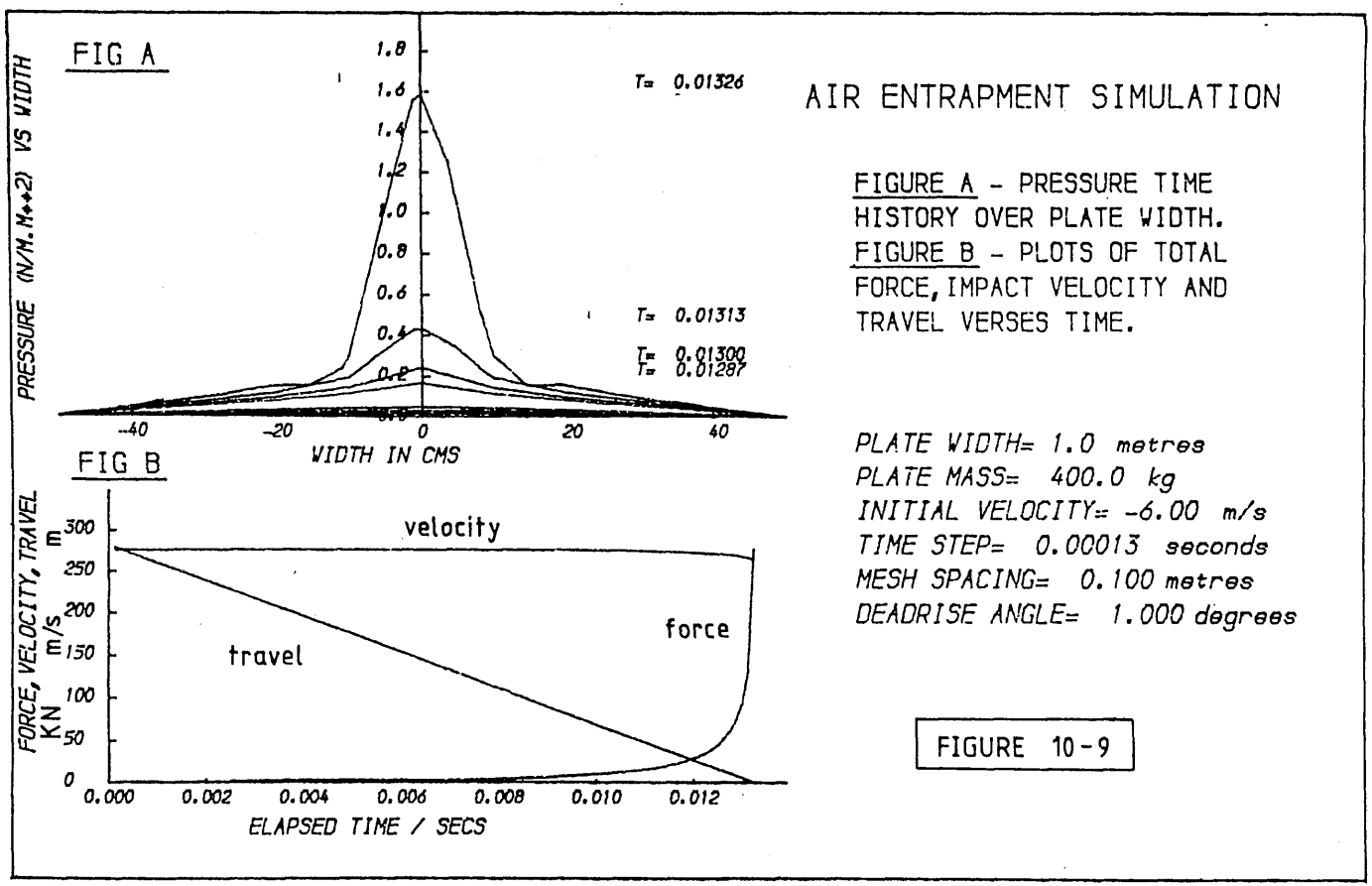

AIR ENTRAPMENT SIMULATION

FIGURE A - PRESSURE TIME HISTORY OVER PLATE WIDTH.
FIGURE B - PLOTS OF TOTAL FORCE, IMPACT VELOCITY AND TRAVEL VERSES TIME.

PLATE WIDTH= 1.0 metres
PLATE MASS= 400.0 kg
INITIAL VELOCITY= -6.00 m/s
TIME STEP= 0.00013 seconds
MESH SPACING= 0.100 metres
DEADRISE ANGLE= 1.000 degrees

FIGURE 10-9

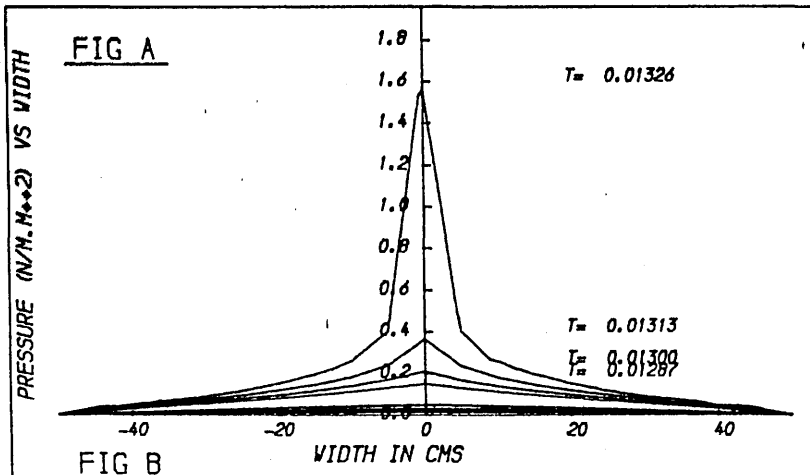

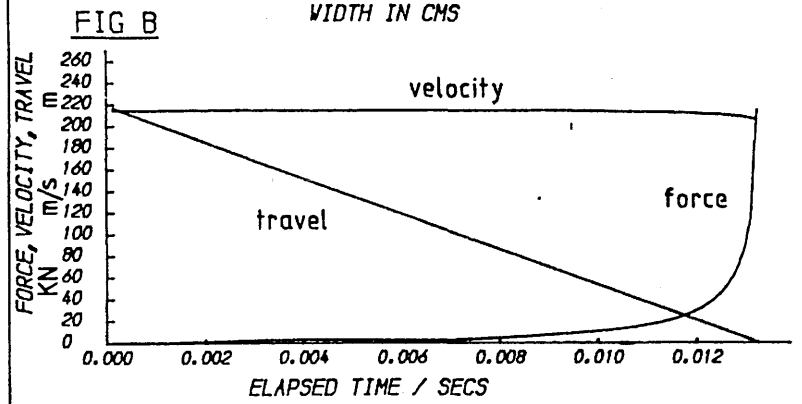

AIR ENTRAPMENT SIMULATION

FIGURE A - PRESSURE TIME HISTORY OVER PLATE WIDTH.
FIGURE B - PLOTS OF TOTAL FORCE, IMPACT VELOCITY AND TRAVEL VERSES TIME.

PLATE WIDTH= 1.0 metres
PLATE MASS= 400.0 kg
INITIAL VELOCITY= -6.00 m/s
TIME STEP= 0.00013 seconds
MESH SPACING= 0.050 metres
DEADRISE ANGLE= 1.000 degrees

FIGURE 10 -10

phenomenon had been noted even with the 2:1 mesh ratio used in the above example, but had been cured by increasing the number of iterations used to solve the fluid potential problem. Thus to improve the solution any further would require the mesh spacing in the fluid domain to be further reduced and hence suffer from an over expensive computer simulation.

A suitable approximation solution to this problem was found by noting that, from a position 0.1m out from the centreline, the pressure distributions were very similar. Therefore, during the total load computation (via pressure integration), a third order polynomial curve fit was used between the centreline and the first node either side. The values used to define the four polynomial coefficients were the two pressures at the centreline and its adjacent node, the pressure gradient at the adjacent node, and an assumed infinite pressure gradient at the centreline. For practical purposes, this last parameter assumed a value of 10^6. The resulting analytical pressure integration produced a load calculation much less susceptable to variations in mesh spacing.

5.4. Variations in Time Step

In order to retain numerical stability in any of the formulations used for these problems, the previously quoted Courant-Friedrichs-Lewy criterion ie:-

$$\Delta t \leq (|U_a| + C_a)/\Delta x \qquad \text{---} 10.5/1$$

was used to compute the time step.

It was found that the adiabatic model was insensitive to

variations in the Courant number and remained numerically stable whatever the time step.

However, the simulation which used the additional energy transport model for an ideal gas required strict adherence to a unit Courant number such that:-

$$\Delta t \equiv (|U_a|_{max} + C_{a\,max}) / \Delta x \qquad \text{---10.5/2}$$

where both U_a and C_a are variables.

Figure 10-11 illustrates the consequences of using a constant time step for this type of computation. The changing sound speed combined with constant time step varies the characteristic for these non-linear hyperbolic equations resulting in a stepped pressure-time history. If the artifice of steady motion were used to set the axes in the moving air layer, this behaviour would result in standing shock waves. However, they are non physical in nature, being the result of a lack of matching between the numerical model and the original conservation equations.

Thus the adiabatic model was more versatile when a variable time step was required in order to perform some of the studies to be described later in this chapter. Indeed, the time step restriction on the ideal gas flow model was to prove a major factor in the decision to use the adiabatic air flow model for most of the computations.

FIG A

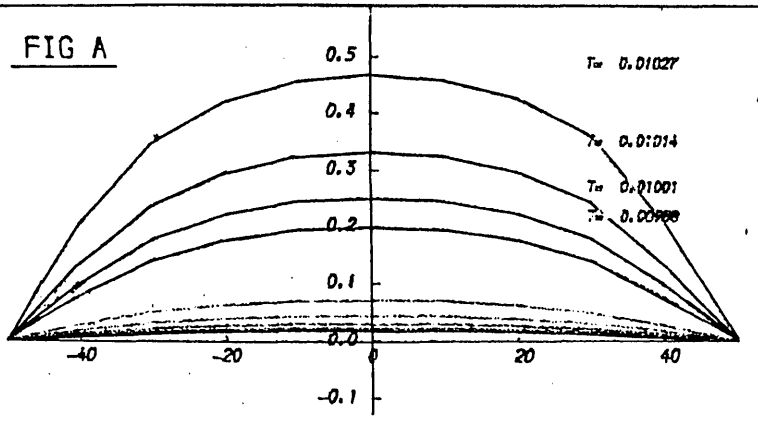

FIG B

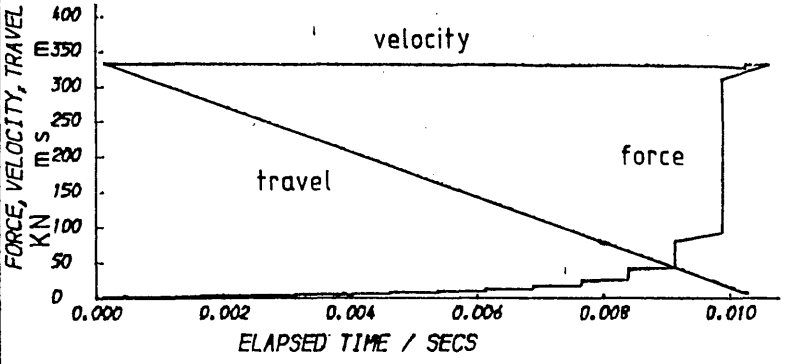

AIR ENTRAPMENT SIMULATION

FIGURE A - PRESSURE TIME HISTORY OVER PLATE WIDTH.
FIGURE B - PLOTS OF TOTAL FORCE, IMPACT VELOCITY AND TRAVEL VERSES TIME.

PLATE WIDTH= 1.0 metres
PLATE MASS= 1000.0 kg
INITIAL VELOCITY= -10.00 m/s
TIME STEP= 0.00013 seconds
MESH SPACING= 0.100 metres
DEADRISE ANGLE= 0.000 degrees

FIGURE 10-11

6. CATEGORISATION OF IMPACT TYPES

Having run the computer simulation for a number of different deadrise angles, initial impact velocities and mass loadings, it was realised that there was not one single impact scenario but four. The interaction between the free surface and body dynamics was quite complex and dependent upon section shape, initial impact velocity and mass loading. The four domains of behaviour are shown in figure 10-12 which uses the following categories to describe the final stages of impact:-

a. Full air entrapment with pressure peak before contact.

b. Full air entrapment, pressure peak after impact.

c. Air cushioning only, pressure peak before impact.

d. Air cushioning only, pressure peak after impact

The first of these categories (a) is illustrated by the computer plots of load/time history and pressure distributions in figure 10-13, along with the plots of free surface shape and body position shown in figure 10-14. The peak in the load time history occurred before contact with the free surface and, interestingly, whilst the thickness of the air gap was still decreasing. The relative velocity between the body and free surface became zero at some point after the peak in air pressure had occurred, but in many cases, a further hydrodynamic impact also took place.

The second type of impact (b), is that normally considered as the main candidate for air entrapment in ship slamming. Figures 10-15 and 10-16, illustrate this case for a flat plate impact. No pressure peak occurred before contact with the free surface. The edges of the

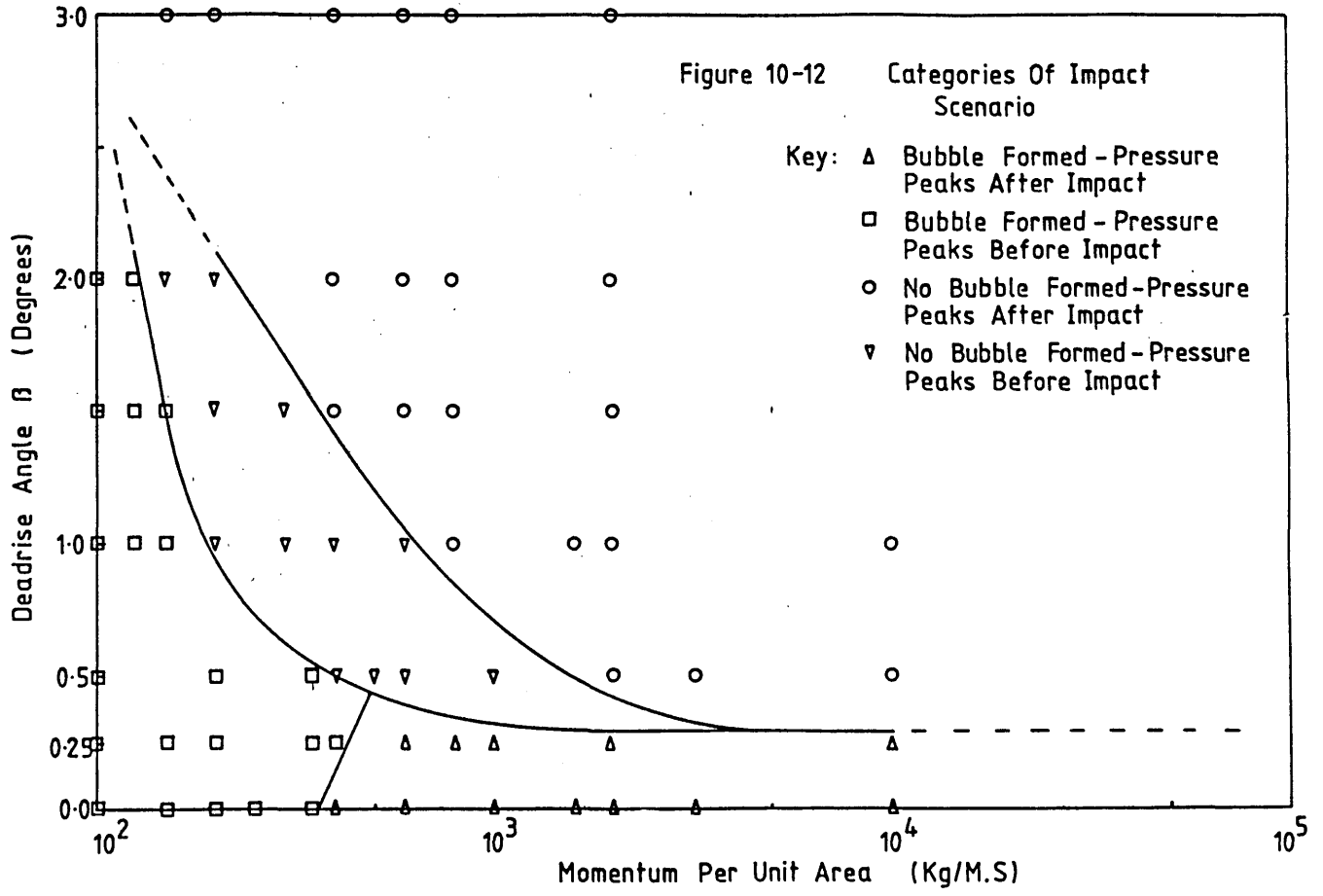

Figure 10-12 Categories Of Impact Scenario

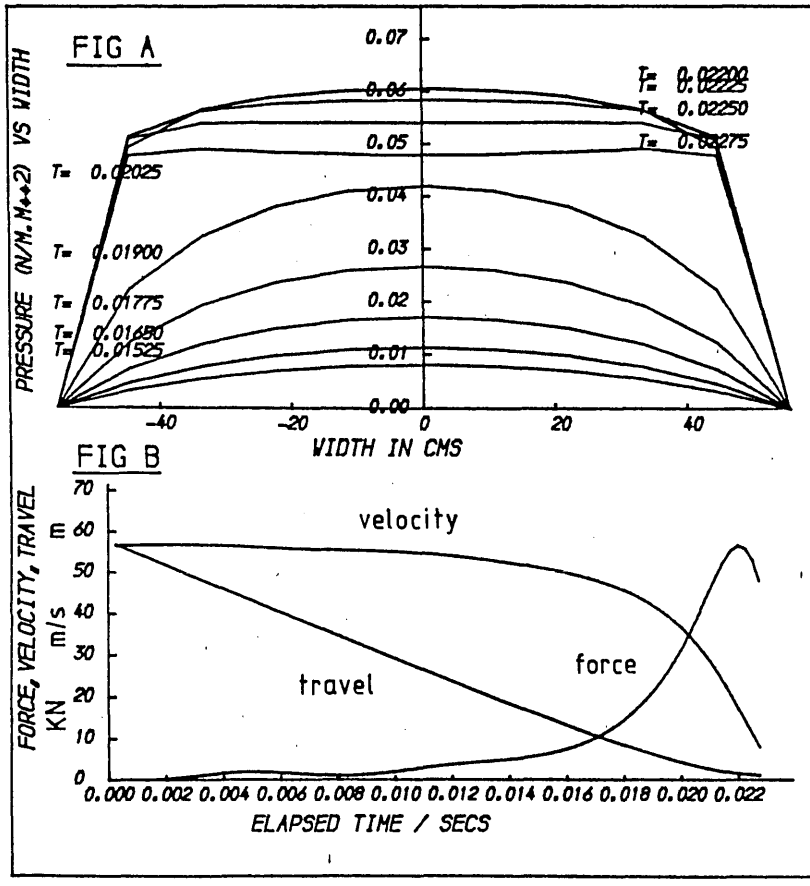

AIR ENTRAPMENT SIMULATION

FIGURE A - PRESSURE TIME HISTORY OVER PLATE WIDTH.
FIGURE B - PLOTS OF TOTAL FORCE, IMPACT VELOCITY AND TRAVEL VERSES TIME.

PLATE WIDTH= 1.0 metres
PLATE MASS= 50.0 kg
INITIAL VELOCITY= -5.00 m/s
TIME STEP= 0.00025 seconds
MESH SPACING= 0.111 metres

FIGURE 10-13

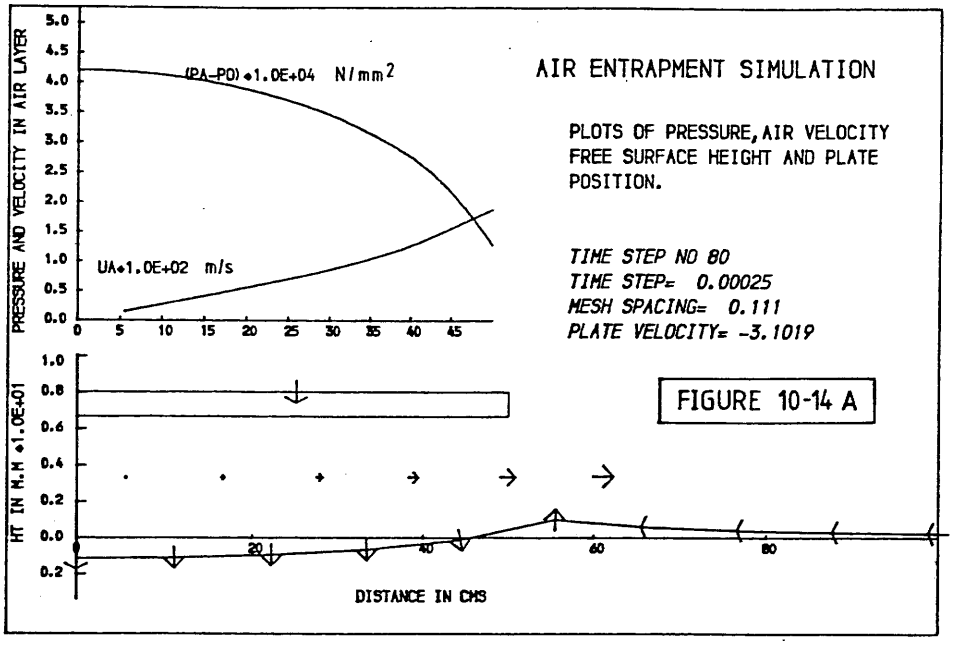

FIGURE 10-14 A

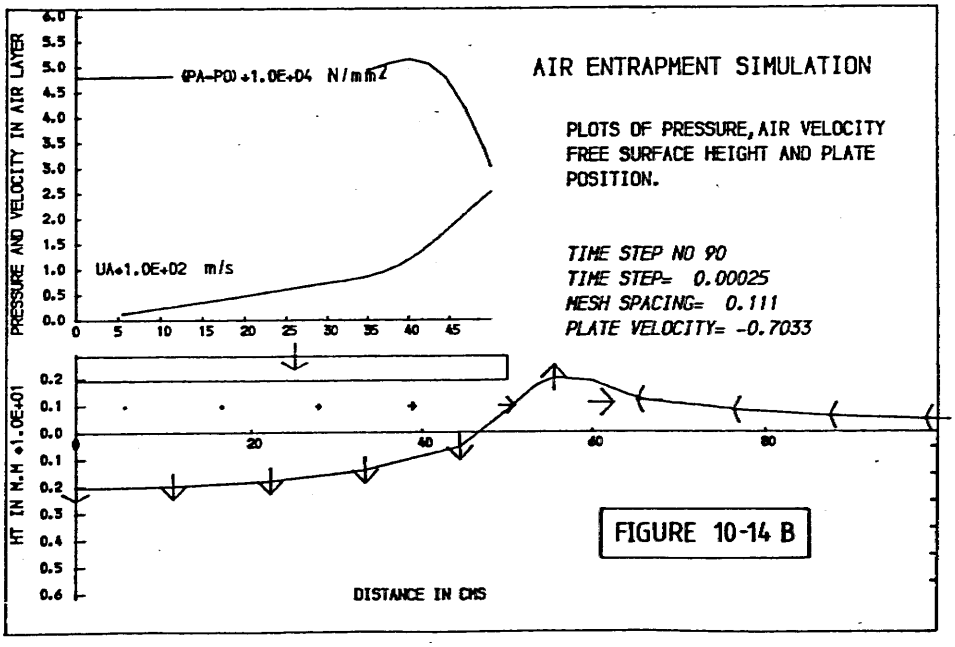

FIGURE 10-14 B

FIG A

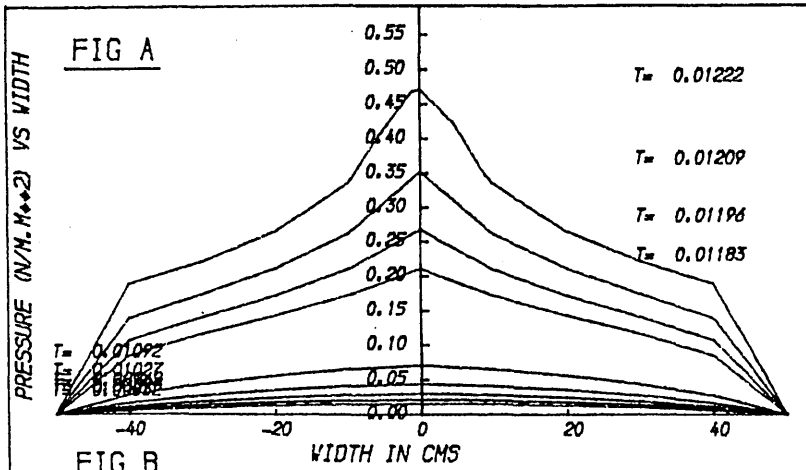

FIG B

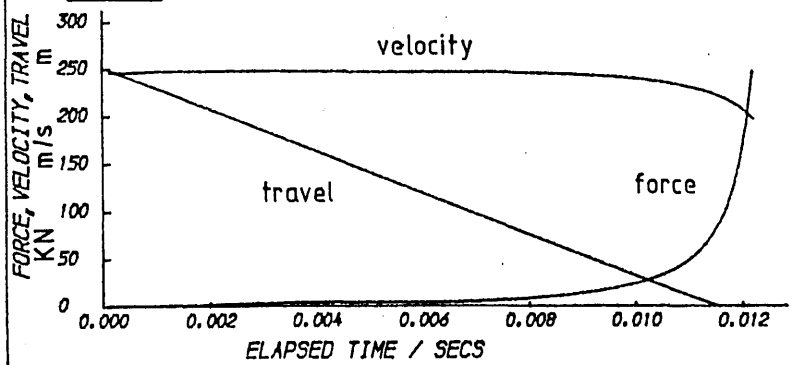

AIR ENTRAPMENT SIMULATION

FIGURE A - PRESSURE TIME HISTORY OVER PLATE WIDTH.
FIGURE B - PLOTS OF TOTAL FORCE, IMPACT VELOCITY AND TRAVEL VERSES TIME.

PLATE WIDTH= 1.0 metres
PLATE MASS= 400.0 kg
INITIAL VELOCITY= -2.00 m/s
TIME STEP= 0.00013 seconds
MESH SPACING= 0.100 metres
DEADRISE ANGLE= 0.250 degrees

FIGURE 10-15

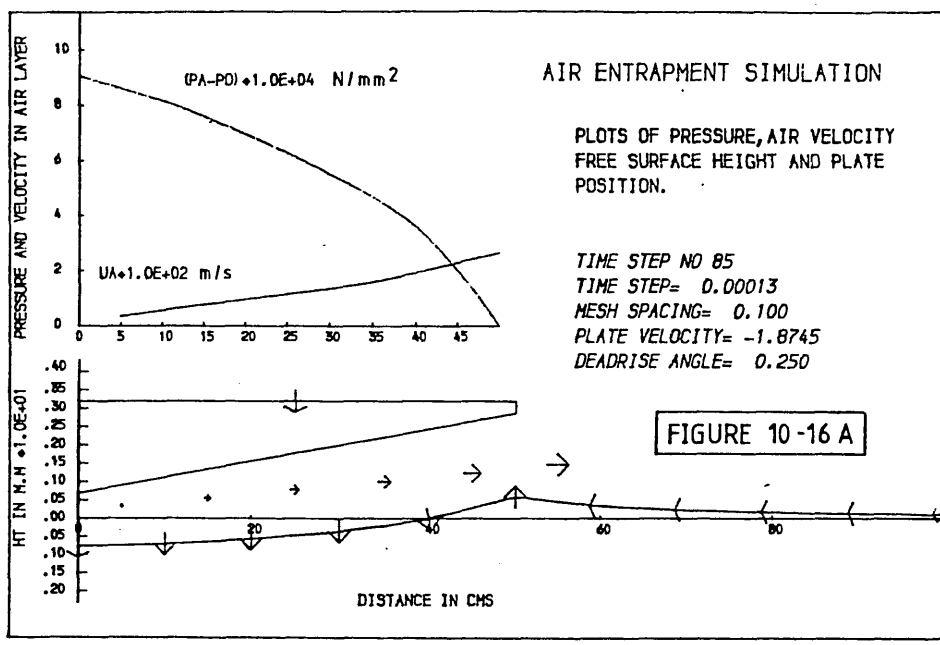

FIGURE 10-16 A

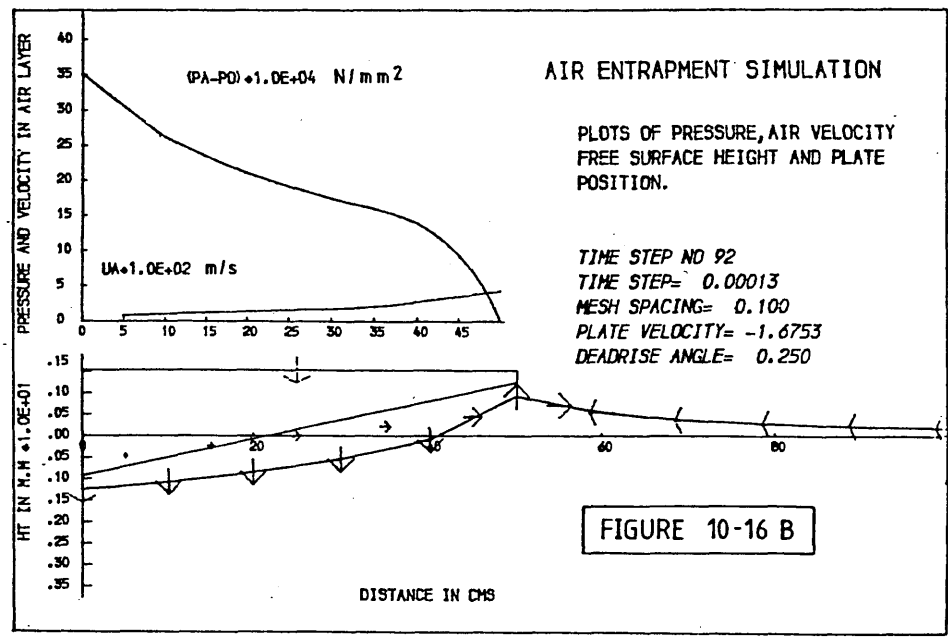

FIGURE 10-16 B

flat plate touched first, trapping and continuing to compress the resulting air bubble. The air layer model as described so far in this thesis was unsuitable for the anlysis after the initial contact had been made. An approximate method to deal with the post impact behaviour is described in section 10.11.

The third and fourth categories, (c) and (d), illustrate the case of air cushioning, wherein the shape of the section was such that initial contact with the free surface occurred along the centreline only. No air bubble was trapped, though the build up of air pressure prior to impact did cause the free surface to accelerate away from the falling body along the centreline, thus reducing the effective impact velocity. In case (c), the pressure peak occurred before impact and, as with case (a), before the relative velocity between body and free surface was reduced to zero. Case (c) was confined to deadrise angles greater than 0.5 degrees and to low momentum impacts. Figures 10-17 and 10-18, show just such an impact time history.

Finally, figures 10-19 and 10-20 show the development of an air cushioned impact in which no pressure peak occurred in the air layer prior to first contact with the free surface. Ideally, the air pressure at the centreline would tend to infinity as the air gap was reduced to zero since the equation to calculate the rate of change of density (equation 3.8/2) reduces to:-

$$\frac{\partial \rho_a}{\partial t} = -\frac{\rho_a}{h}\frac{\partial h}{\partial t} \qquad \text{---10.4/1}$$

This problem was resolved by realising that in the ideal case, this pressure acts over zero width of section. However, the numerical model had a finite mesh size resulting in large pressures acting upon the body when the node arrangement shown in figure 7-1 was

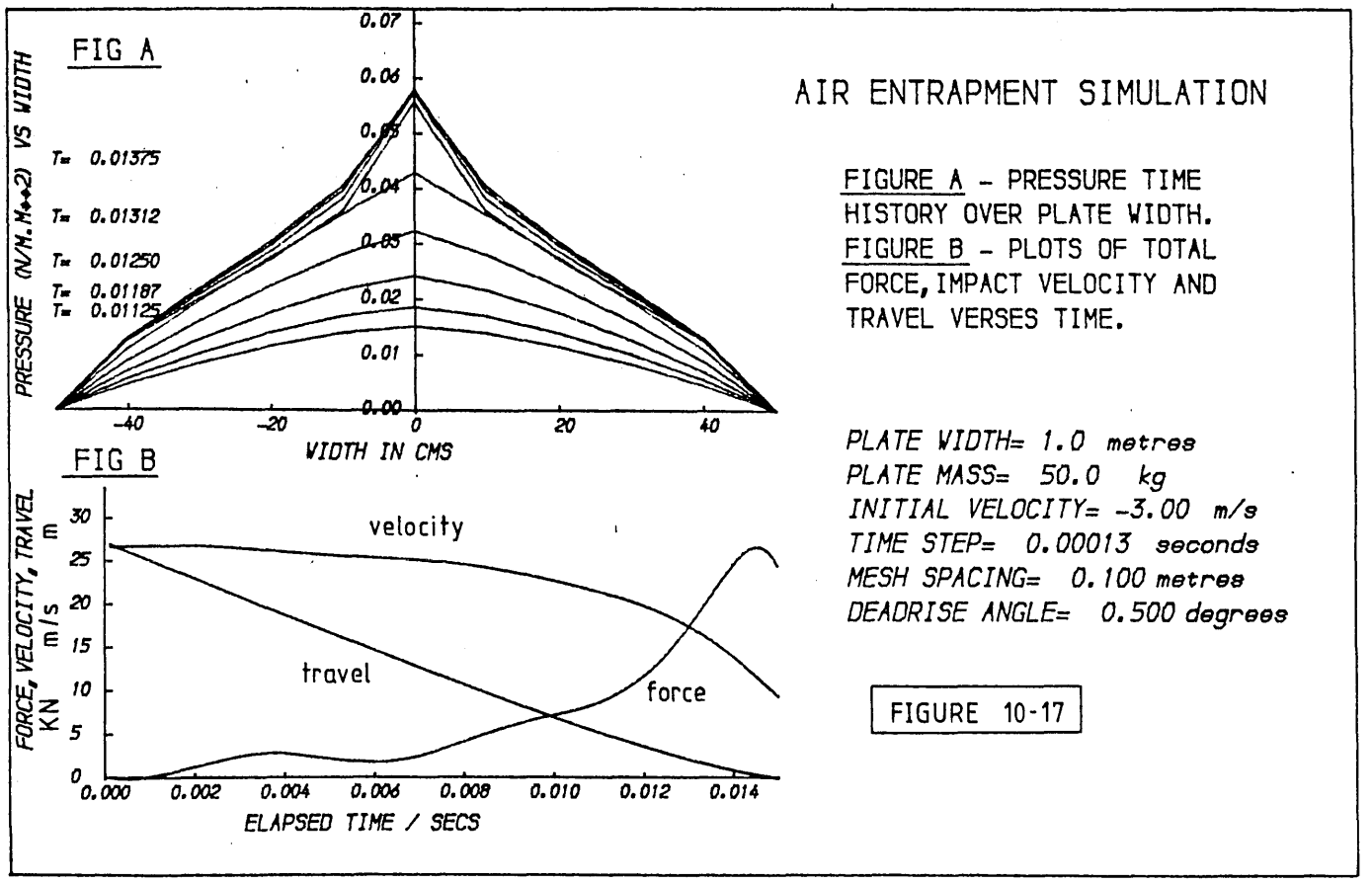

AIR ENTRAPMENT SIMULATION

FIGURE A - PRESSURE TIME HISTORY OVER PLATE WIDTH.
FIGURE B - PLOTS OF TOTAL FORCE, IMPACT VELOCITY AND TRAVEL VERSES TIME.

PLATE WIDTH= 1.0 metres
PLATE MASS= 50.0 kg
INITIAL VELOCITY= -3.00 m/s
TIME STEP= 0.00013 seconds
MESH SPACING= 0.100 metres
DEADRISE ANGLE= 0.500 degrees

FIGURE 10-17

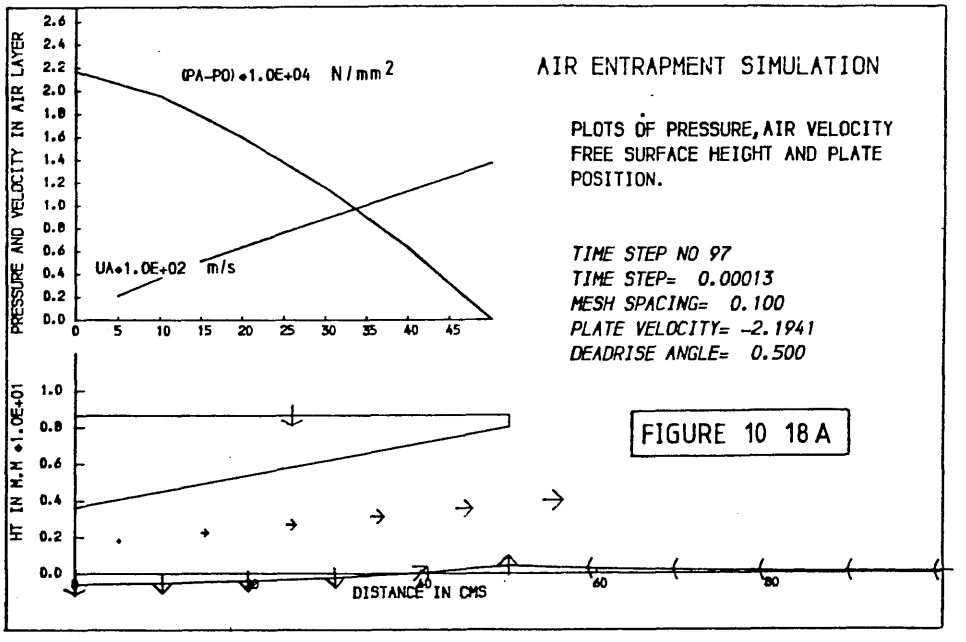
PRESSURE AND VELOCITY IN AIR LAYER
(PA-PO)*1.0E+04 N/mm2
UA*1.0E+02 m/s
HT IN M.M *1.0E+01
DISTANCE IN CMS
AIR ENTRAPMENT SIMULATION
PLOTS OF PRESSURE, AIR VELOCITY FREE SURFACE HEIGHT AND PLATE POSITION.
TIME STEP NO 97
TIME STEP= 0.00013
MESH SPACING= 0.100
PLATE VELOCITY= -2.1941
DEADRISE ANGLE= 0.500
FIGURE 10 18 A

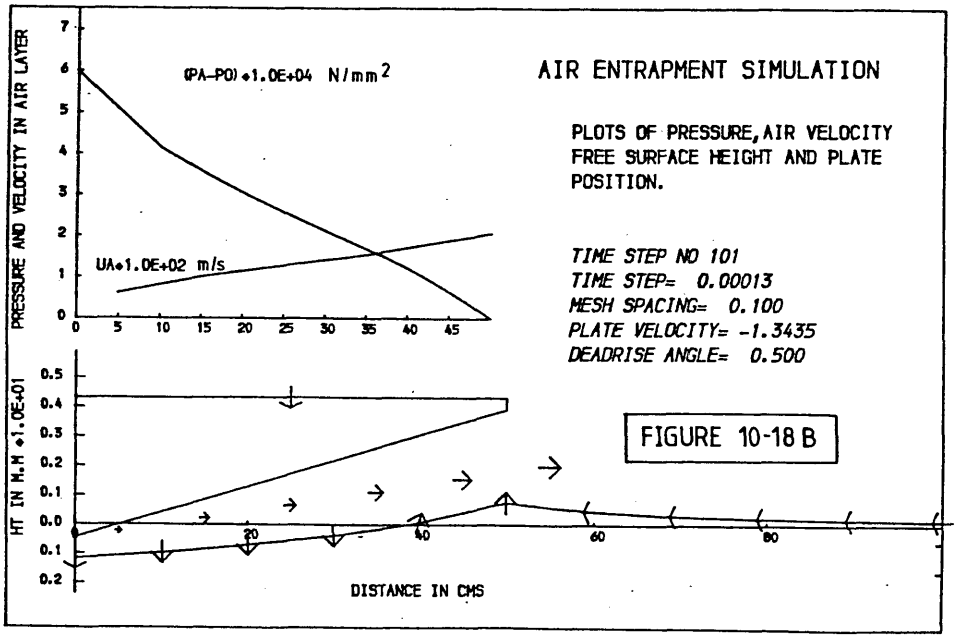
PRESSURE AND VELOCITY IN AIR LAYER
(PA-PO)*1.0E+04 N/mm2
UA*1.0E+02 m/s
HT IN M.M *1.0E+01
DISTANCE IN CMS
AIR ENTRAPMENT SIMULATION
PLOTS OF PRESSURE, AIR VELOCITY FREE SURFACE HEIGHT AND PLATE POSITION.
TIME STEP NO 101
TIME STEP= 0.00013
MESH SPACING= 0.100
PLATE VELOCITY= -1.3435
DEADRISE ANGLE= 0.500
FIGURE 10-18 B

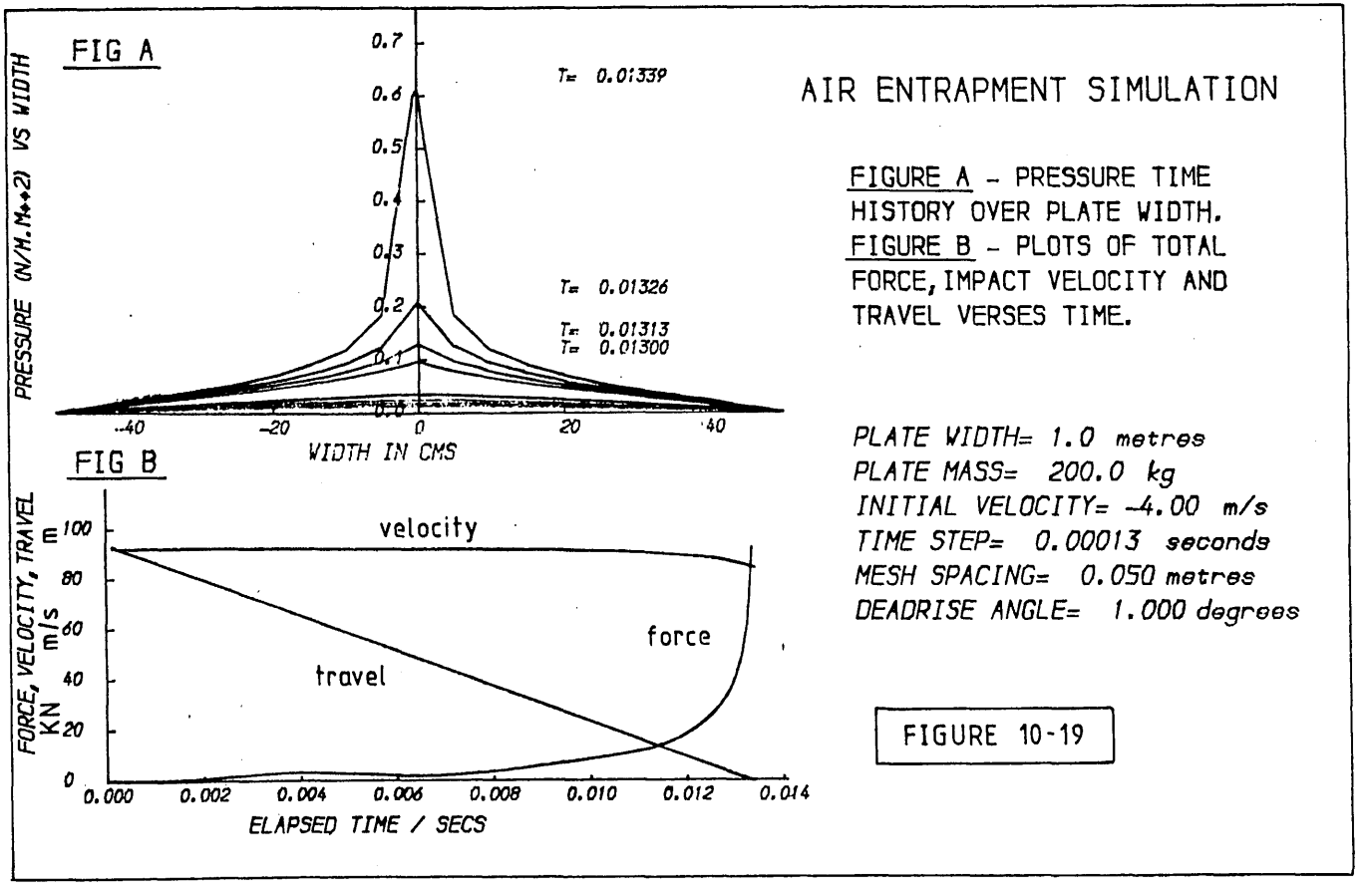

AIR ENTRAPMENT SIMULATION

FIGURE A - PRESSURE TIME HISTORY OVER PLATE WIDTH.
FIGURE B - PLOTS OF TOTAL FORCE, IMPACT VELOCITY AND TRAVEL VERSES TIME.

PLATE WIDTH= 1.0 metres
PLATE MASS= 200.0 kg
INITIAL VELOCITY= -4.00 m/s
TIME STEP= 0.00013 seconds
MESH SPACING= 0.050 metres
DEADRISE ANGLE= 1.000 degrees

FIGURE 10-19

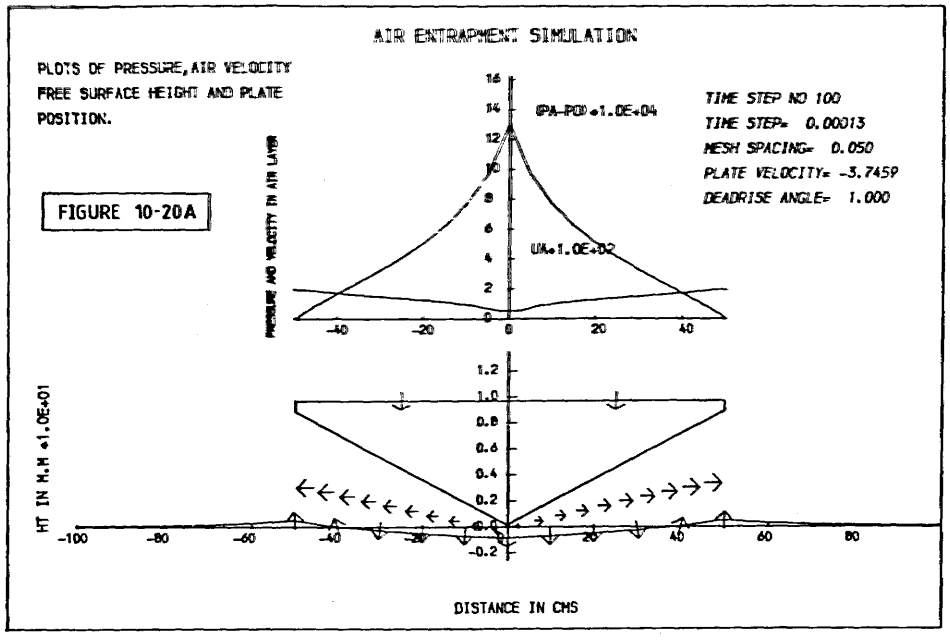
AIR ENTRAPMENT SIMULATION
PLOTS OF PRESSURE, AIR VELOCITY
FREE SURFACE HEIGHT AND PLATE
POSITION.
FIGURE 10-20A
(PA-PO) *1.0E+04
UA*1.0E+02
PRESSURE AND VELOCITY IN AIR LAYER
TIME STEP NO 100
TIME STEP= 0.00013
MESH SPACING= 0.050
PLATE VELOCITY= -3.7459
DEADRISE ANGLE= 1.000
HT IN M.H *1.0E+01
DISTANCE IN CMS

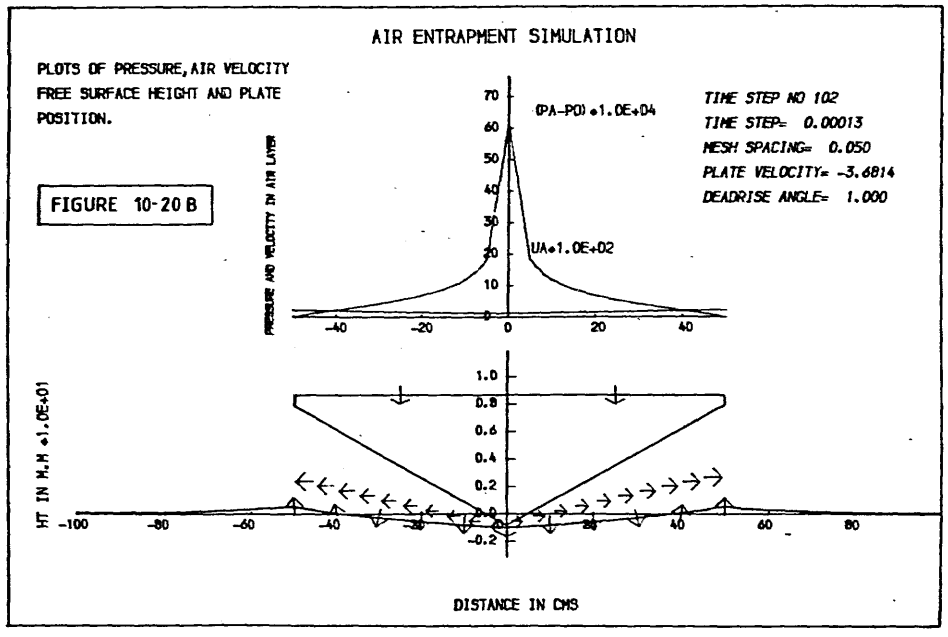
AIR ENTRAPMENT SIMULATION
PLOTS OF PRESSURE, AIR VELOCITY
FREE SURFACE HEIGHT AND PLATE
POSITION.
FIGURE 10-20 B
(PA-PO) *1.0E+04
UA*1.0E+02
PRESSURE AND VELOCITY IN AIR LAYER
TIME STEP NO 102
TIME STEP= 0.00013
MESH SPACING= 0.050
PLATE VELOCITY= -3.6814
DEADRISE ANGLE= 1.000
HT IN M.H *1.0E+01
DISTANCE IN CMS

used. This problem was overcome by shifting the mesh arrangement so as to have a single velocity node on the centreline and two pressure nodes a distance $\Delta x/2$ either side.

In case (d) therefore, no pressure peak occurred due to the air layer. The peak loading would be due to the hydrodynamic impact, though at a reduced imppact velocity.

Owing to this problem of slam categorisation, great care was needed when evaluating data output by the program. Since the simulation was incapable of calculating the hydrodynamic loads after first contact, case (d) above required special consideration. In fact, the only useful data to come out of this routine was the reduced impact velocity, since the load time history was incomplete.

Other types of variation in section shape also required consideration. In particular, the radius of curvature of the section relative to the curvature of the free surface at the instant of contact could be such that the conditions for an acoustic type impact as described in section 3.7, would prevail.

Furter tests were required in order to confirm that the four types of impact could be regarded in isolation. In particular, those with pressure peaks forming before first contact had to be separated from those whose peak loading occurred after. Also, for deadrise angles greater than zero, it was necessary to decide whether or not any bubble could form and, allied to this, whether the relative velocity between the free surface and the body could become zero at some point.

A constant time step prohibited investigation of the above factors and hence the discovery of the extent of each of the four impact types for various momentum loadings and deadrise angles. A specific algorithm was formulated in order to test for the different behavioural regimes. The simulation was run using the adiabatic air layer model and a constant time step, until the instant before first contact with the free surface. The time step was then halved so as to delay, in computational time, the instant of impact. The simulation continued in this way, with the time step being halved each time the body threatened to contact the free surface.

It was hypothesised that, if a pressure peak were likely to occur within the air layer prior to contact, this algorithm would allow it to do so.If no pressure peak were possible, the time step would continue to be halved with no perceptable change in the pressure distribution or velocity field - the simulation would effectively be 'frozen'.

This 'Achillies and Tortoise' type scenario proved very effective in providing data concerning impact type. A considerable number of tests with varying mass, impact velocity and deadrise angle were carried out in order to complete figure 10-12. However, the numerical model already contained a considerable number of idealisations. The real physical conditions beneath a ship hull may cause the zones of behaviour to be shifted. In particular, surface roughness and imperfections would have a large effect on air bubble formation and the position of the initial contact point.

7. EFFECT OF VARYING INITIAL IMPACT VELOCITY

The relationship between peak pressures or loads and the impact velocity for a given shape of section is perhaps the most useful piece of data to result from a study of slamming. It has already been noted that four different types of air entrapment model are possible; a fact which complicates the interpretation of data and inhibits the discovery of a single constant relating peak load and impact velocity.

For the purpose of analysis, classes (a) and (c) were grouped together. The common feature of peak pressures occurring before impact indicated that both these classes were dominated by the aerodynamics of the air layer. With reference to figure 10-12, it can be seen that these two types of impact were restricted to 'light' or low 'momentum per unit area' slams. Thus any relationships derived were applicable to low speed impacts on the ship scale, or small scale model experiments only.

Figures 10-21 and 10-22 show plots of peak loading and peak pressure versus the square of the initial impact velocity. The dashed lines indicate where 'borderline' data is being employed, ie data extrapolated from the results of a different class of impact. The linearity of the plots is very marked, enabling the following formulations for peak load and pressures to be made:-

$$F_{max} = K_1 \rho V_i^2 \qquad \text{---10.7/1}$$

$$p_{max} = K_p \rho V_i^2 \qquad \text{---10.7/2}$$

where ρ is the density of water (not air layer).

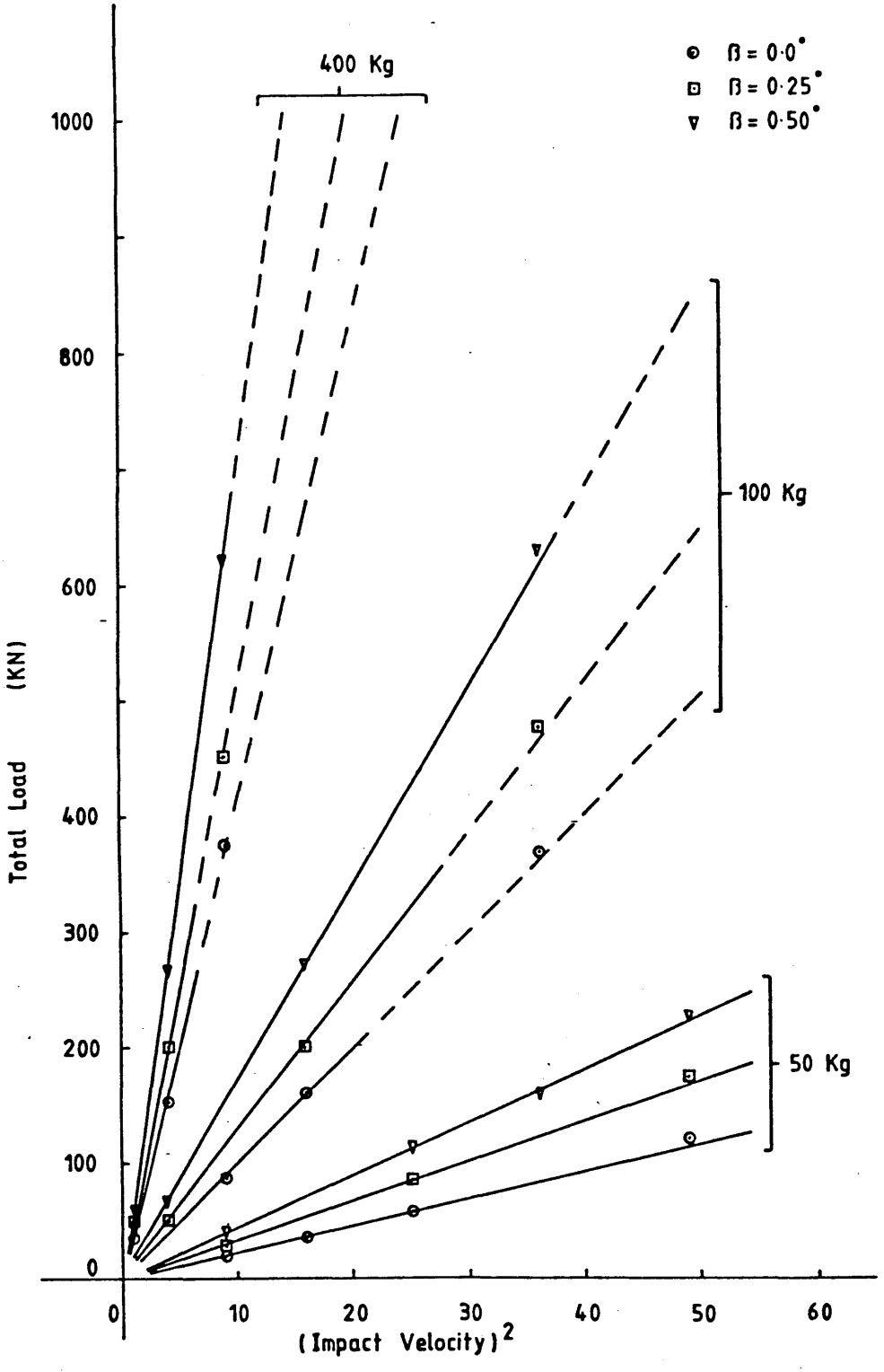

Figure 10-21 Plots Of Total Load Versus Impact Velocity Squared

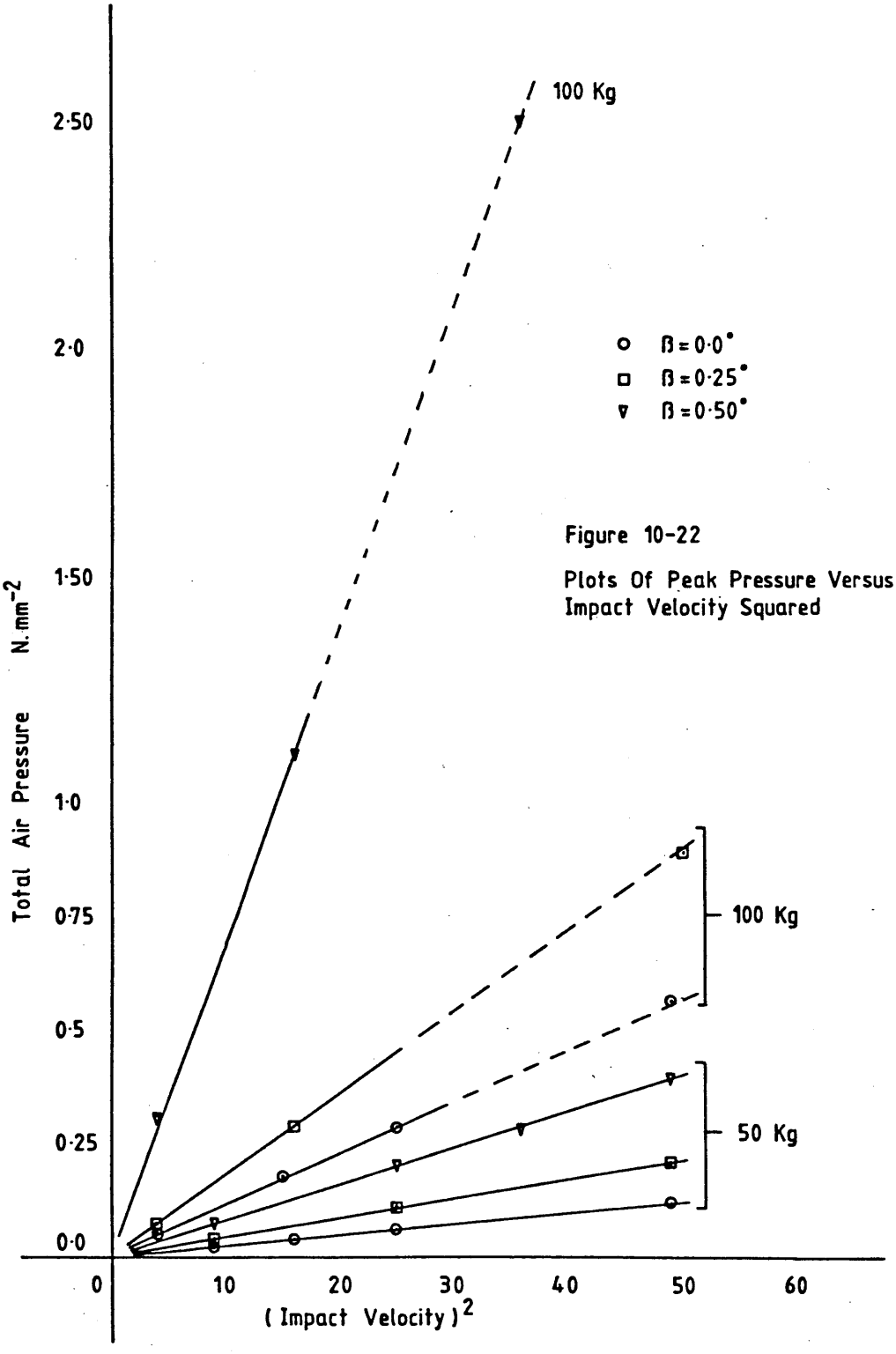

Figure 10-22

Plots Of Peak Pressure Versus Impact Velocity Squared

Values for K_l and K_p are given in tables 10-A and 10-B. Values in brackets indicate where only one or two items of data were available to calculate the coefficients. This occurred occasionally when the plate mass or deadrise angle were so high as to require low impact velocities in order to fit into the correct class of slam scenario.

Where enough data points were available, an estimate of the error in the values K_l and K_p, in terms of a standard deviation, has been quoted. This type of analysis is perhaps not completely appropriate, since the slight variations in slam coefficient are the result of an accumulation of truncation errors. The total error is therefore a deterministic factor, dependent upon time step and mesh size. As these discretisation parameters are reduced, the differences between values of K_l, K_p as computed at different initial impact velocities should tend to zero.

Furthermore, the relationship between the impact velocity and the error in the calculation of the K_l, K_p coefficients may be non-linear, such that, even the simple mean value used is also inappropriate. An alternative may be to attempt to calculate the accumulated error during the computation, by comparing the results from the algorithm used with those resulting from a higher order finite difference technique. In practice, this is very difficult to achieve, since not all high order schemes exhibit the desired stability requirements, as seen in section 10-4 during the analysis of central difference time marching methods.

TABLE 10A

SLAM LOAD COEFFICIENTS K_L

MASS β^o	0.0	0.25	0.50	1.0	2.0	3.0
50Kg	2.31 (3.1%)	3.37 (5.6%)	4.54 (6.3%)	9.02 (6.2%)	26.30 (-)	21.20 (-)
100Kg	10.05 (4.3%)	14.83 (3.1%)	17.04 (3.45%)	36.70 (-)	91.60 (-)	60.0 (-)
400Kg	41.20 (-)	51.32 (-)	69.40 (-)			

TABLE 10B

PEAK PRESSURE COEFFICIENTS K_p

MASS β^o	0.0	0.25	0.50	1.0	2.0	3.0
50Kg	2.39 (5.1%)	4.13 (5.5%)	7.93 (5.8%)	18.75 (-)	57.0 (-)	48.0 (-)
100Kg	11.25 (0.1%)	16.73 (4.4%)	36.0 (5.3%)	105.5 (-)	194.5 (-)	143.0 (-)

Therefore, the use of a statistical measure of error should not be construed as an attempt to explain inaccuracies in the computation as if they were subject to the randomness associated with experimental methods. It was thought however, that the standard deviations quoted would give some estimate of the accuracy of the overall computational technique.

It has already been noted that the air entrapment model as used so far was incapable of computing the peak pressures associated with impact class (b). The numerical model became unrealistic after first contact between the body and the free surface, thus the load time history was incomplete.

As a result, a modified view of the flat plate impact was formulated wherein, after contact with the free surface, the plate and air bubble were considered to move together through the fluid. The treatment of the air layer during this phase is dealt with in section 10-11. Observation of the fluid behaviour prior to impact revealed an interesting phenomenon however. Figure 10-23 shows a plot of total kinetic energy in the fluid domain versus impact velocity for a 1000kg flat plate. At higher initial impact velocities, the dynamics of the flat plate are virtually unaffected by the pressure rise beneath the section. Accordingly, the total fluid kinetic energy shows asymptotic behaviour when plotted against initial impact velocity.

The presence of the fluid kinetic energy may be regarded in terms of a finite added mass associated with the plate. The added mass may be computed via the relationship:-

$$M_a = \frac{2\,T_e}{V_r^2} \qquad \text{---10.7/3}$$

where T_e is the kinetic energy of the fluid at the instant of contact.

V_r is the representative velocity.

The choice of value for V_r is difficult. It was found that at both the free surface velocity along the centreline at the instant of impact and the velocity of the body at contact showed asymptotic behaviour similar to the kinetic energy. Substitution of these two measures of V_r into 10.7/3 produced two near constant measures of M_a. Which of the two, if either, could be considered the correct value to use was unresolved. The concept showed however, that it might be possible to achieve a level of kinetic energy in the fluid such that, at contact with the free surface, the body experiences no impulsive

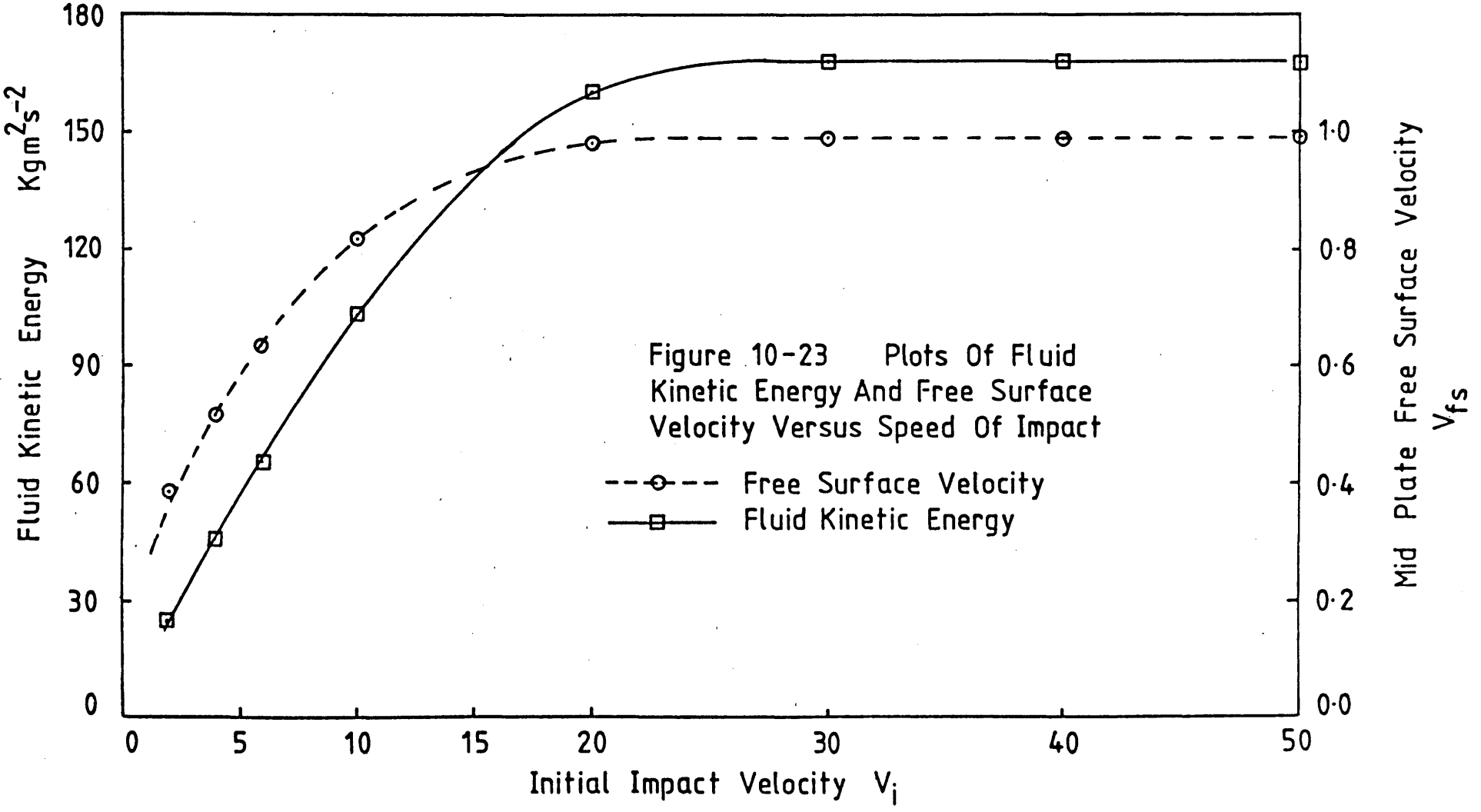

Figure 10-23 Plots Of Fluid Kinetic Energy And Free Surface Velocity Versus Speed Of Impact

load due to changes in added virtual mass. Some reduction in the initial rate of change of added mass at least is possible. This concept is discussed more fully in section 10.11.

The final part of this section examines results from impact class (d). Again, the air entrapment program was unsuitable for computing peak pressures since these were hydrodynamic in origin, occurring along the centreline of the section.

Thus the effect of the trapped air layer was to cause the free surface to accelerate away from the body prior to impact and so reduce the effective impact velocity. Figure 10-24 shows the percentage decrease in impact velocity for various mass loadings at 0.5, 1.0 and 2.0 degrees of deadrise, respectively. A number of features are worth comment. As the initial impact velocity was increased, the percentage reduction in impact velocity was reduced but showed asymptotic behaviour. The general form of the curves for β = 0.5 degrees suggests that, at low impact velocities, the reduction in the speed of the body was responsible for the decrease in relative velocity. There was a middle range in which both the accelerating free surface and the decelerating body had an appreciable effect. Finally, at high initial impact velocities, the momentum of the body was reduced only slightly during the slam leaving the moving free surface as sole contributor to the decrease in relative impact velocity. The effect of mass and deadrise angle will be discussed in following sections. It seems logical to assume that there will be a finite reduction in the effective impact velocity whatever the mass or momentum of the section. However, this class of impact does not predict the possibility that the free surface can manage to match the speed of the oncoming section, thus removing the possibility of a slam ever occurring.

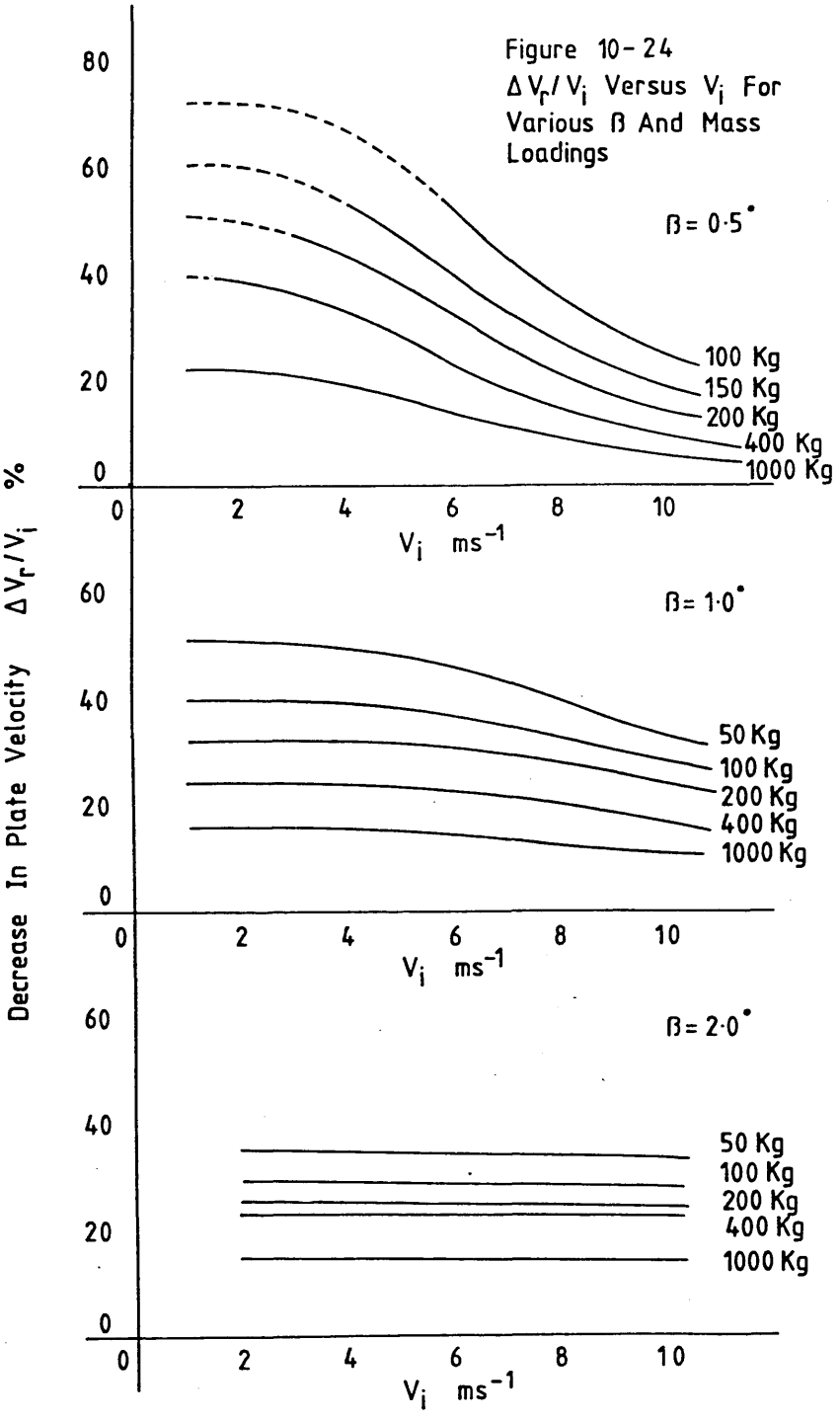
Figure 10-24
$\Delta V_r / V_i$ Versus V_i For Various β And Mass Loadings
Decrease In Plate Velocity $\Delta V_r / V_i$ %
β= 0·5°
100 Kg
150 Kg
200 Kg
400 Kg
1000 Kg
β= 1·0°
50 Kg
100 Kg
200 Kg
400 Kg
1000 Kg
β= 2·0°
50 Kg
100 Kg
200 Kg
400 Kg
1000 Kg
V_i ms^{-1}

8. EFFECT OF VARYING SECTION SHAPE

8.1. Results From Wedge Impact Tests

As with the previous section, classes (a) and (c) were grouped together, with impact types (b) and (d) regarded separately.

Firstly, slam coefficients from tables 10-A and 10-B were plotted to a base of deadrise angle for the case of a wedge impact of type (a) or (c). The results are shown in figures 10-25 and 10-26. Whilst the range of mass loading values are small for both figures, the general trend may be discerned. The main feature of both figures is a definite peak in load coefficient occurring at around 2 degrees of deadrise. It was unfortunate that classes (a) and (c) could not provide further data at both larger values of and mass loading. However, the simulations run within these ranges did provide valuable insight into the behaviour of the air layer for comparison with light drop test experiments. These comparisons are discussed in section 10-13.

The effect of deadrise angle on class (b) impacts seemed negligible. Both flat plates and wedges with $\beta < 0.25$ degrees seemed always to trap an air bubble. The post impact behaviour of the bubble may be a function of deadrise angle, but neither the initial air entrapment calculations, or the simple post contact models discussed in section 10-11 were suitable to analyse such problems.

With regard to the reduced impact velocities illustrated by figure 10-24, the deadrise angle had some appreciable effects. As the value of was increased, the range of reductions in impact velocity

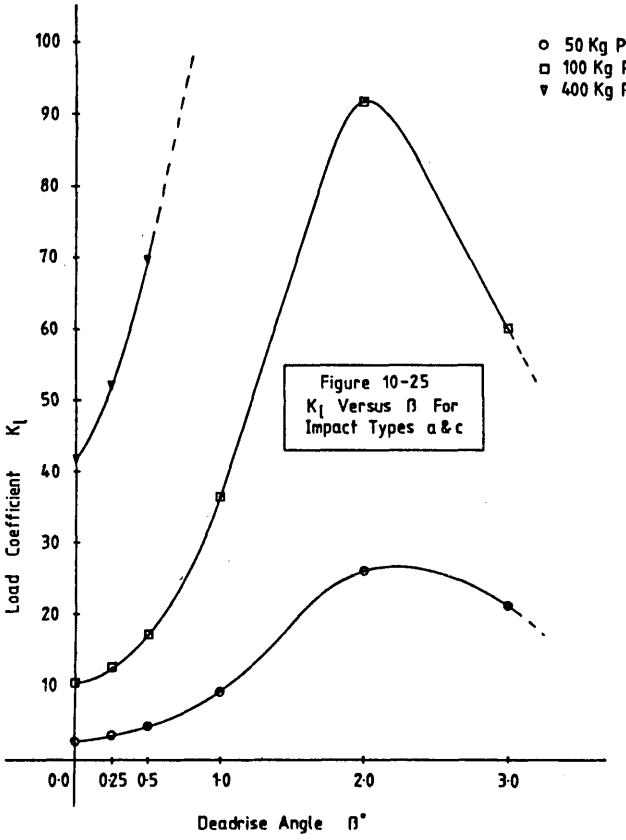

Figure 10-25
K_l Versus β For
Impact Types a & c

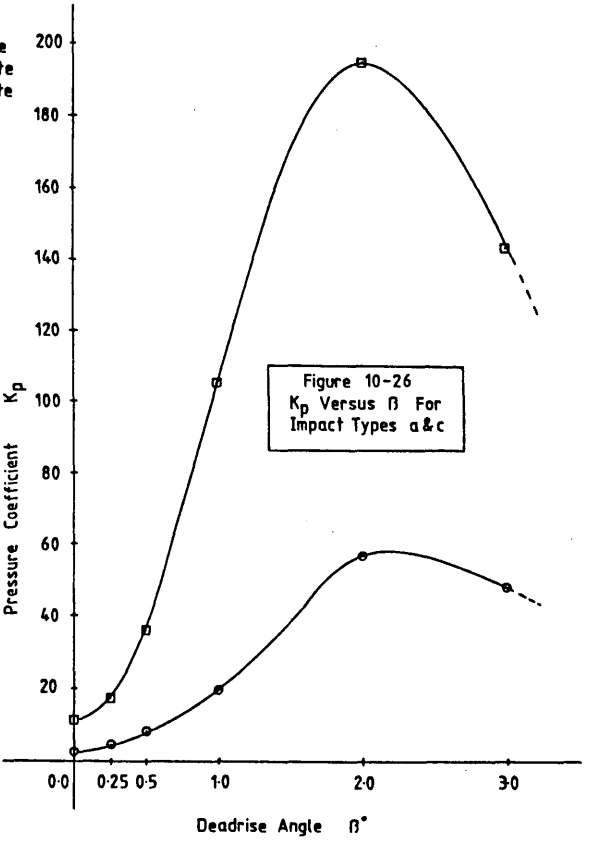

Figure 10-26
K_p Versus β For
Impact Types a & c

was greatly decreased, such that at 2 degrees, there was little change in $\Delta V_r / V_i$ over the range of velocities used for any given mass loading. This phenomenon is more clearly illustrated by figure 10-32, from section 10-9. The greater linearity of $\Delta V_r / V_i$ at β = 2 degrees was the result of the kinematics of the body remaining unaffected by the aerodynamics of the air layer. The reduction in effective impact velocity was therefore influenced more by the kinetics of the free surface as the deadrise angle was increased.

It should also be noted that it was possible for the value $\Delta V_r / V_i$ to be higher at a deadrise angle of 2 degrees than at β = 0.5 degrees, as the initial impact velocity was increased. This was due to the high pressures generated along the centreline of the more sharply vee'd sections. This further illustrates the non-linear aspects of air entrapment. Not only were there a number of different impact scenarios, but local effects within the air layer had a large part to play in the outcome of the simulation.

8.2. Effect of Curvature

The effect of sectional curvature was briefly studied by simulating the air flow beneath a circular cylinder about to impact upon an initially level free surface.

Two factors arose which were unique to this impact geometry:-

a. Without a distinct edge to the plate, the application of boundary conditions became dificult.

b. the ratio of mesh size to sectional radius of curvature was critical to the accurate resolution of the free surface.

The first of these problems was resolved by setting the plate edges to coincide with the position where the section deadrise angle reached 15 degrees. The velocity boundary conditions were subsequently applied as if the flow consisted of an incompressible free jet beyond the edge of the plate, with a divergence angle of 15 degrees.

Unlike the flat or wedge section problem, the above solution to problem (a) allowed variations in total plate width with radius of curvature. Therefore, for each value of curvature, all other dimensions in the computation were normalised with respect to the effective beam. This had the effect of solving problem (b), since the ratio of the plate beam to cylinder diameter was constant owing to the choice of computational domain made to overcome problem (a).

Figures 10-27 and 10-28 show load time histories, pressure distributions and the evolution of the free surface shape for the impact of a circular cylinder, radius 10 metres with an initial velocity of 6 m/s and a mass loading of 150kg/m . The free surface shape just prior to impact suggested that this is a type (d) slam. Unfortunately, time did not permit as rigorous a study as that applied to wedge impact. However, one important observation may be made.

The relative curvature between the body and free surface just before contact suggests a very low effective deadrise angle. This could lead to one of two possible types of behaviour:-

a. an acoustic type impact in which the rate of change of wetted beam upon water entry would be greater than the speed of sound in water.

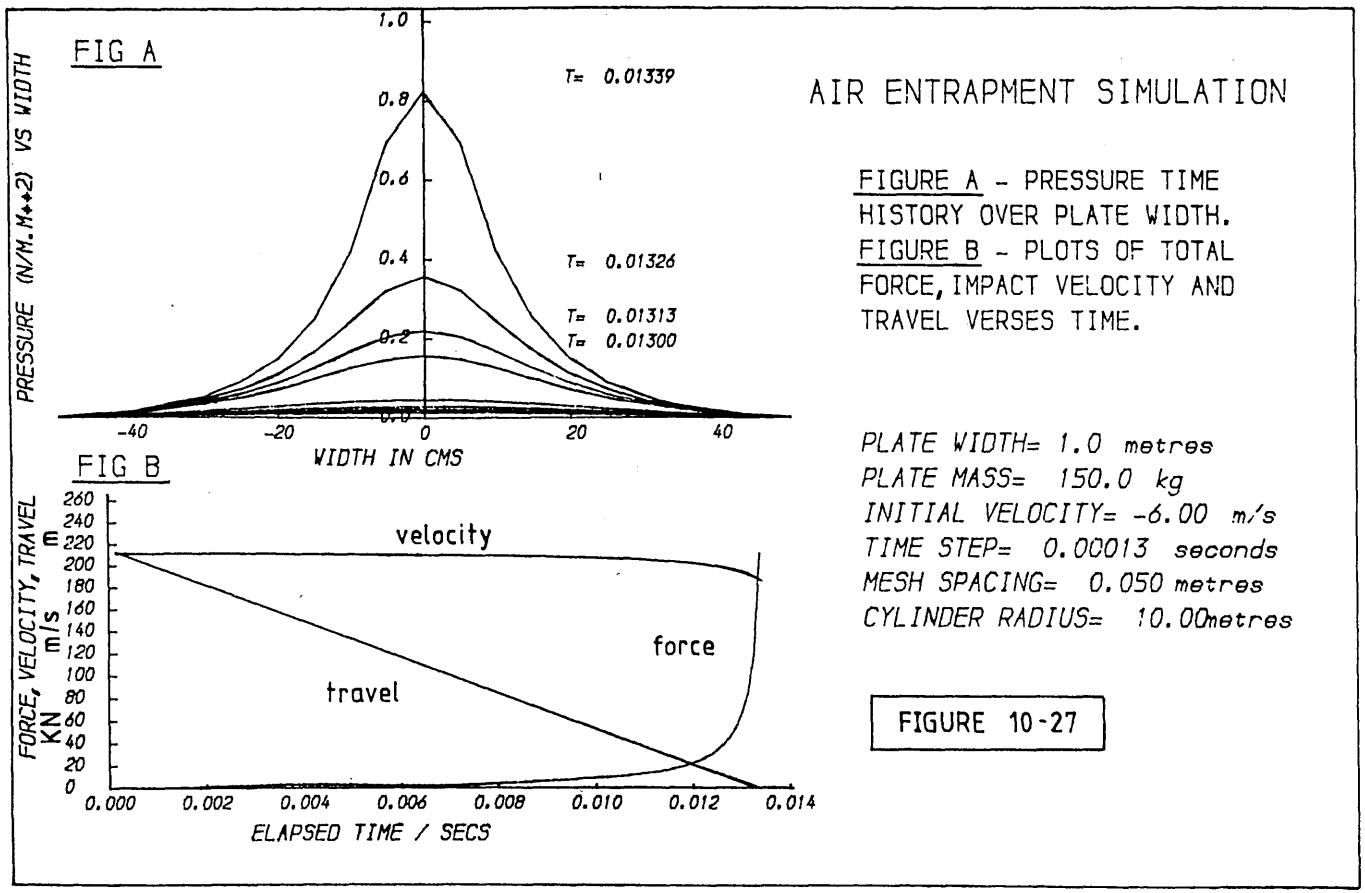

AIR ENTRAPMENT SIMULATION

FIGURE A - PRESSURE TIME HISTORY OVER PLATE WIDTH.
FIGURE B - PLOTS OF TOTAL FORCE, IMPACT VELOCITY AND TRAVEL VERSES TIME.

PLATE WIDTH= 1.0 metres
PLATE MASS= 150.0 kg
INITIAL VELOCITY= -6.00 m/s
TIME STEP= 0.00013 seconds
MESH SPACING= 0.050 metres
CYLINDER RADIUS= 10.00metres

FIGURE 10-27

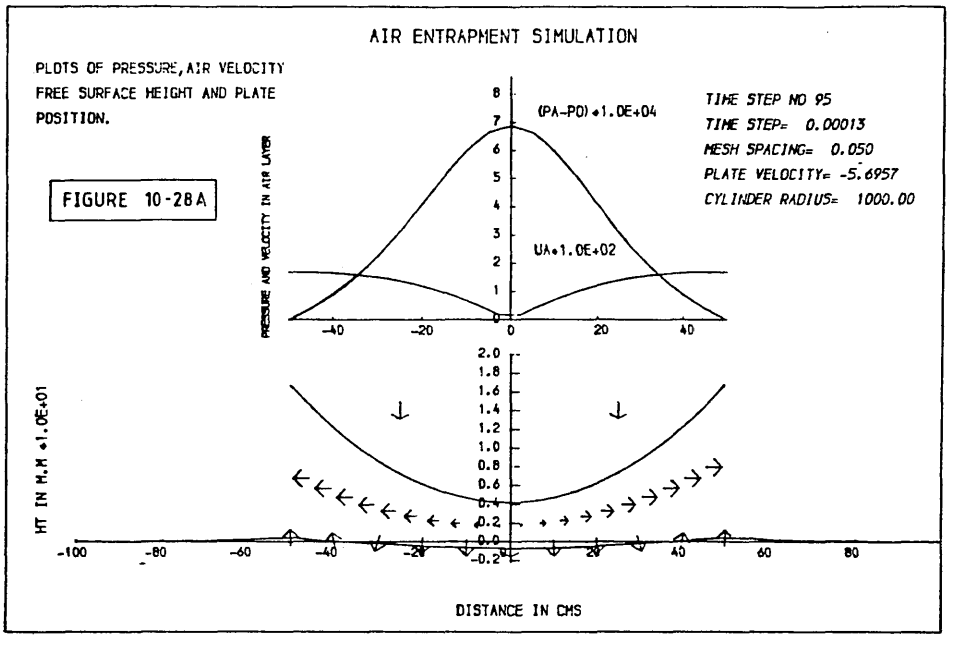
AIR ENTRAPMENT SIMULATION
PLOTS OF PRESSURE, AIR VELOCITY FREE SURFACE HEIGHT AND PLATE POSITION.
FIGURE 10-28A
(PA-PO)*1.0E+04
UA*1.0E+02
PRESSURE AND VELOCITY IN AIR LAYER
HT IN M.M *1.0E+01
DISTANCE IN CMS
TIME STEP NO 95
TIME STEP= 0.00013
MESH SPACING= 0.050
PLATE VELOCITY= -5.6957
CYLINDER RADIUS= 1000.00

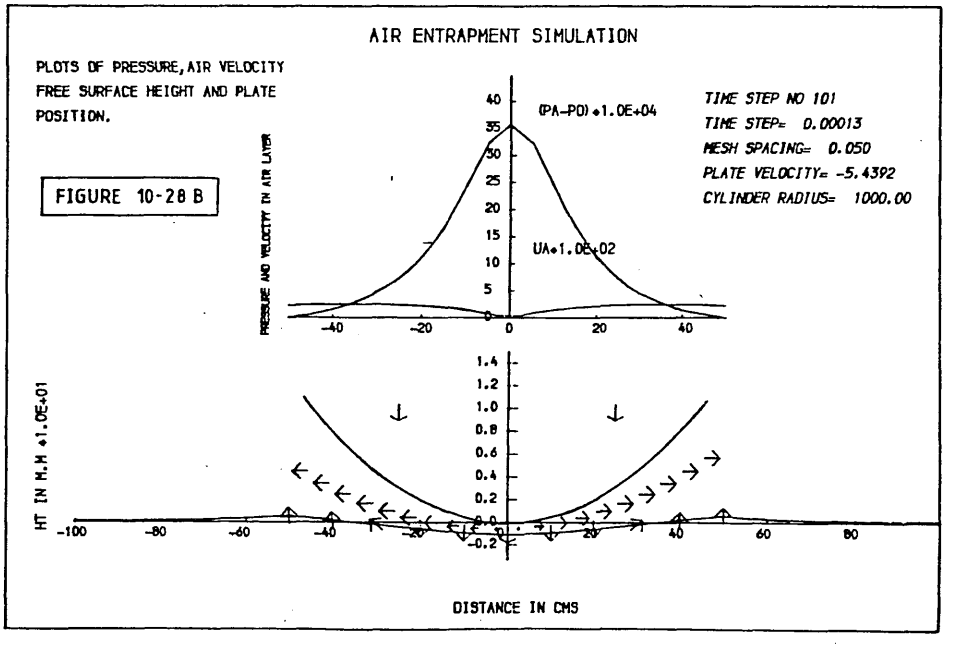
AIR ENTRAPMENT SIMULATION
PLOTS OF PRESSURE, AIR VELOCITY FREE SURFACE HEIGHT AND PLATE POSITION.
FIGURE 10-28 B
(PA-PO)*1.0E+04
UA*1.0E+02
PRESSURE AND VELOCITY IN AIR LAYER
HT IN M.M *1.0E+01
DISTANCE IN CMS
TIME STEP NO 101
TIME STEP= 0.00013
MESH SPACING= 0.050
PLATE VELOCITY= -5.4392
CYLINDER RADIUS= 1000.00

b. the formation of a secondary bubble over the last few time steps which would prevent the acoustic impact.

The non-dimensionalisation of this problem suggests that scenario (b) is more likely. However, more study with a finer mesh spacing and shorter time steps is required. Unfortunately, this would be beyond the computational resources available to the author. Furthermore, it is likely that consideration of surface roughness and other features common to a realistic environment at sea would increase the chances of bubble formation.

8.3. Surface Irregularities

Figures 10-29 and 10-30 show plots of load time histories, pressure distributions and the evolution of the free surface shape for a 'W' shaped section of deadrise angle 1 degree. It was hoped that the results given by this type of geometry could suggest ways in which local surface irregularities in hull shape would affect the total load.

For most of the time history prior to contact, the air flow was similar to that expected from a flat plate. However, for the last six time steps the 'W' shaped section generated pressure peaks local to the two contact points either side of the central cavity. The pressure in this central section was equal to that generated by a flat plate with the same mass loading and initial velocity. The volume of air entrapped was greater however.

This computation stretched the air entrapment model to its limits. In order to produce this order of resolution, the level of discretisation in the air layer was twice that used in the fluid

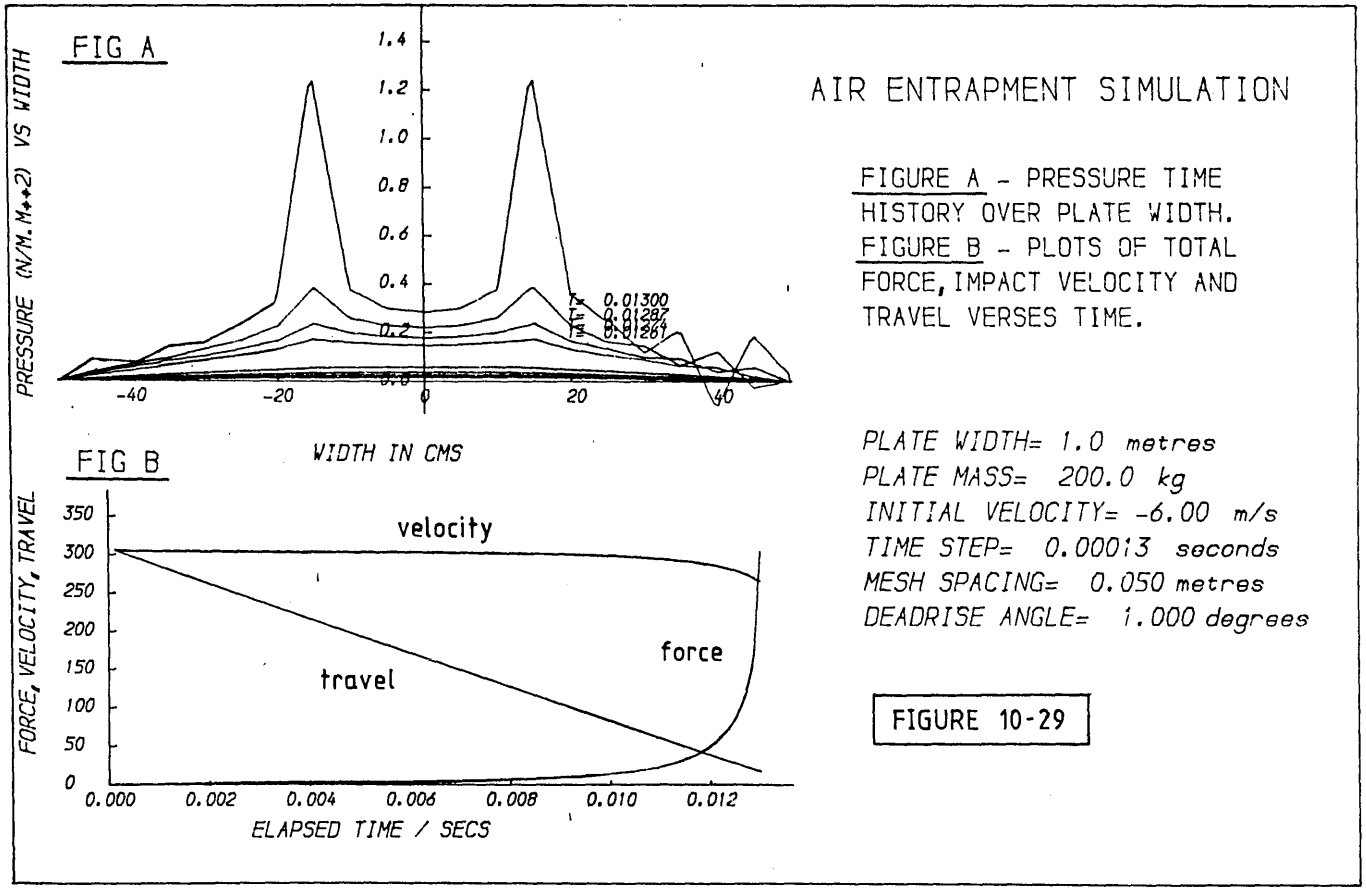

AIR ENTRAPMENT SIMULATION

FIGURE A - PRESSURE TIME HISTORY OVER PLATE WIDTH.
FIGURE B - PLOTS OF TOTAL FORCE, IMPACT VELOCITY AND TRAVEL VERSES TIME.

PLATE WIDTH= 1.0 metres
PLATE MASS= 200.0 kg
INITIAL VELOCITY= -6.00 m/s
TIME STEP= 0.00013 seconds
MESH SPACING= 0.050 metres
DEADRISE ANGLE= 1.000 degrees

FIGURE 10-29

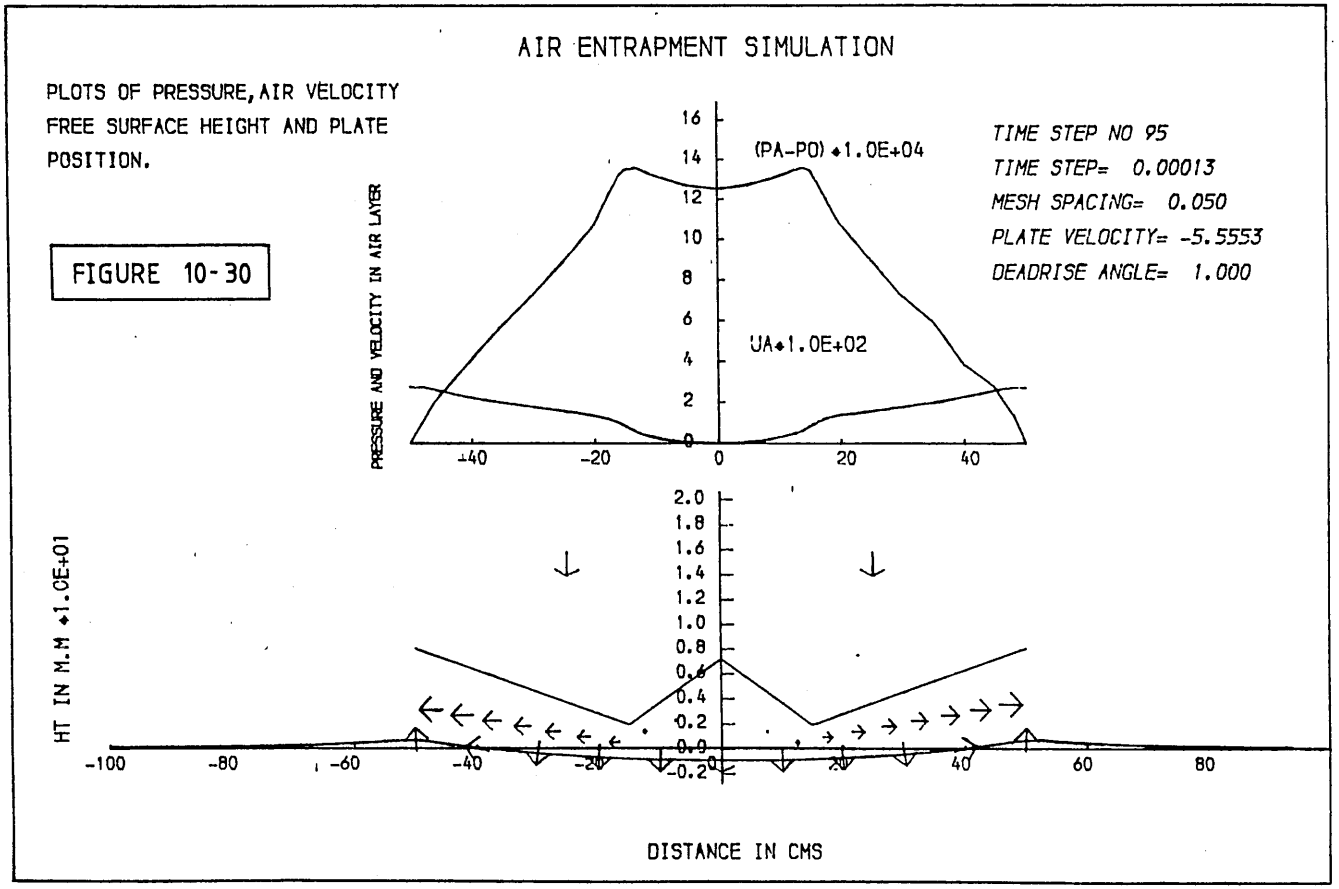
AIR ENTRAPMENT SIMULATION
PLOTS OF PRESSURE, AIR VELOCITY FREE SURFACE HEIGHT AND PLATE POSITION.
FIGURE 10-30
(PA-PO) ♦1.0E+04
UA♦1.0E+02
PRESSURE AND VELOCITY IN AIR LAYER
TIME STEP NO 95
TIME STEP= 0.00013
MESH SPACING= 0.050
PLATE VELOCITY= -5.5553
DEADRISE ANGLE= 1.000
HT IN M.M ♦1.0E+01
DISTANCE IN CMS

domain. As a result, the inaccuracies mentioned in section 10.5.3 arose towards the end of the computation as can be seen in figure 10-29. The cure for this problem would be to match fluid and air layer mesh sizes exactly. This would need a large increase in computational time. It was estimated that four times the number of air layer and fluid nodes presently used could provide the required accuracy. Consequently some 40,000 (cpu) seconds on the ICL 2988 computer would be needed for one simulation. Whilst it was feasible to run such a program a few times, a full study, such as carried out for the wedges, was beyond the scope of this study.

It is tentatively concluded from the few tests that were run, that surface imperfections will only be of significance where the free surface geometry allows a near flat impact. The pressure time history would then be similar to that of a flat plate though the total load may well be higher owing to the characteristic pressure distribution shown in figures 10-29 and 10-30. The total volume of air trapped would of course be greater than for a perfectly flat section. This would greatly affect the post impact behaviour.

9. EFFECT OF VARYING MASS LOADING

Some insight into the effect of body mass upon impact parameters has already been gained from figure 10-12. As the mass of the body was progressively increased, the response of the free surface became increasingly important to the aerodynamic problem. For low mass loadings, it was possible for rising pressures in the air layer to reduce the velocity of the body quite substantially. This phenomenon was a major factor in bringing about the pressure peaks in impact classes (a) and (c). Figure 10-31 shows the effect of increasing body mass upon the load coefficient. Unfortunately, there was not enough data to provide an equivalent set of curves for the variation of pressure coefficient. The data used for figure 10-31, is also rather sparce. It may well be that a straight line fit to the curves would have been more in accord with the amount of data available. However, the information gained at the lower end of the mass loading scale was considered the most reliable and hence care was taken to ensure that these points were properly fitted. Furthermore, physical reasoning dictated that the curves should be asymptotic as mass loading in increased.

The effect of mass loading on class (b) impacts, ie those with full air entrapment and pressure peaks after first contact with the free surface is analysed in section 10-11.

Figure 10-32 plots the percentage reduction in relative impact velocity versus mass loading for three deadrise angles from data provided by the class (d) air entrapment simulations. The main feature of each set of curves is their asymptotic nature. Thus, as the body mass was increased, the free surface dynamics dominated the air

Figure 10-31 Load Coefficient Versus Mass Loading

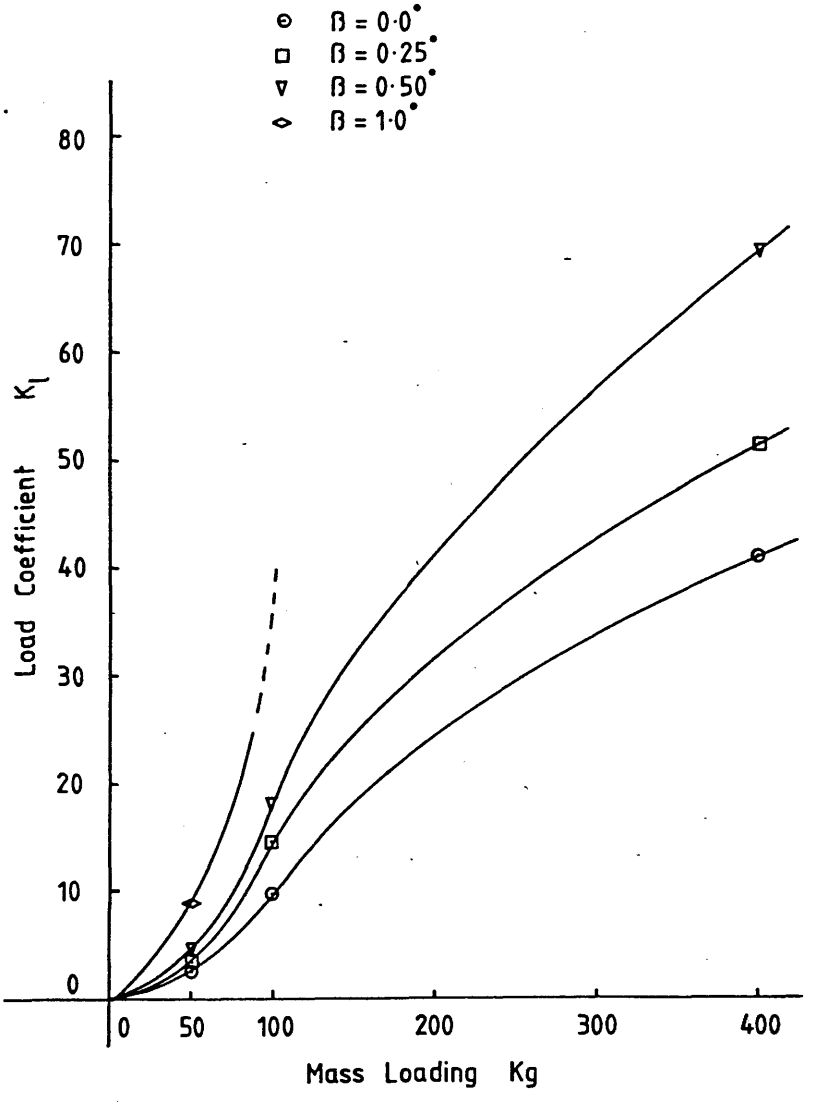

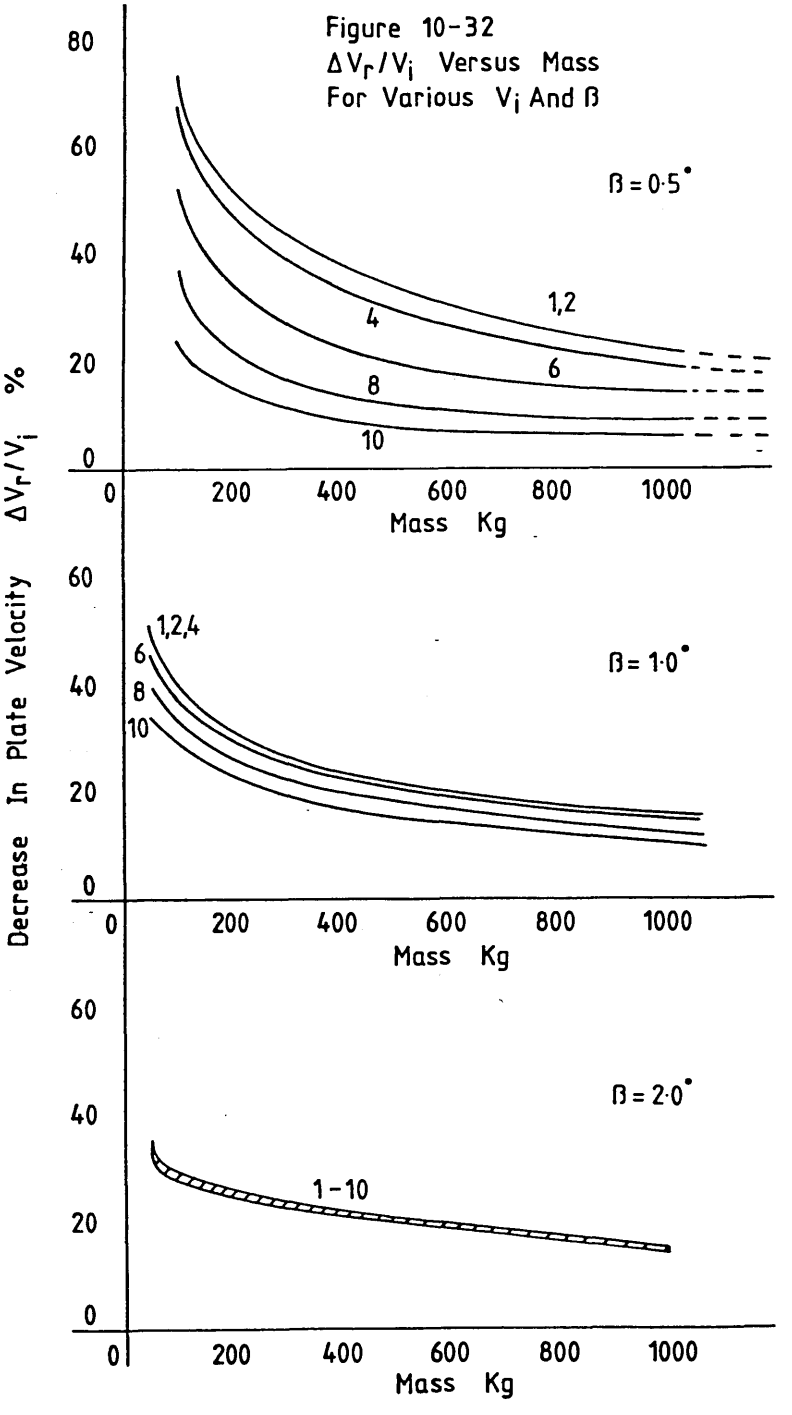
Figure 10-32
$\Delta V_r / V_i$ Versus Mass
For Various V_i And ß
Decrease In Plate Velocity $\Delta V_r / V_i$ %
ß = 0·5°
1,2
4
6
8
10
ß = 1·0°
1,2,4
6
8
10
ß = 2·0°
1-10
0
20
40
60
80
200
400
600
800
1000
Mass Kg

cushioning phenomenon. It seems likely that such behaviour is common to bottom slamming of ships, where the orientation of the free surface permits, since the decrease of relative impact velocity will be invarient with the inertia of the ship section.

Computations of hydrodynamic pressure or impact loads during slamming for low deadrise sections should take account of the reduced velocity of the body relative to the free surface. There is a strong possibility that this phenomenon alone can explain the behaviour of curves of impact coefficient versus deadrise angle at the lower end of the scale.

10. THE ENERGY TRANSPORT MODEL

A small study was carried out into the effect of using the ideal gas flow, energy transport model, on the total load and pressure time history. The modified equations decribed in section 3 and discretised in section 4, were used to simulate the air entrapment phase only, no post impact model was applied. The extra state variables of temperature (T) and sound speed (C) were monitored throughout the computation.

Figures 10-33 and 10-34 show plots of pressure distributions, with load, velocity and travel time histories for two similar drop test simulations. The results given by figure 10-33 are for the adiabatic model whilst figure 10-34 shows values obtained whilst using the energy transport simulation. Unfortunately, the results published are of two different (though close) initial impact velocities of 7.0 and 8.0m/s, respectively. This was as a result of the quality of plot for the adiabatic case at 8.0m/s not being of good enough quality to put into the thesis. However, it can be seen that the results were similar, despite this problem, indicating that the effects of energy transport, as modelled in section 4, were negligible. This conclusion is supported by plots shown in figures 10-35 and 10-36 of distributions and time histories for sound speed and temperature of the air for the ideal gas flow model. Considering figure 10-35, it can be seen that there was a slight rise in both sound speed and temperature towards the centreline of the plate, but that this increase never exceeded 4% of the original values. Both T and C_a are set by the boundary conditions to their adiabatic flow values at the edges of the plate. The time histories of temperature and sound speed

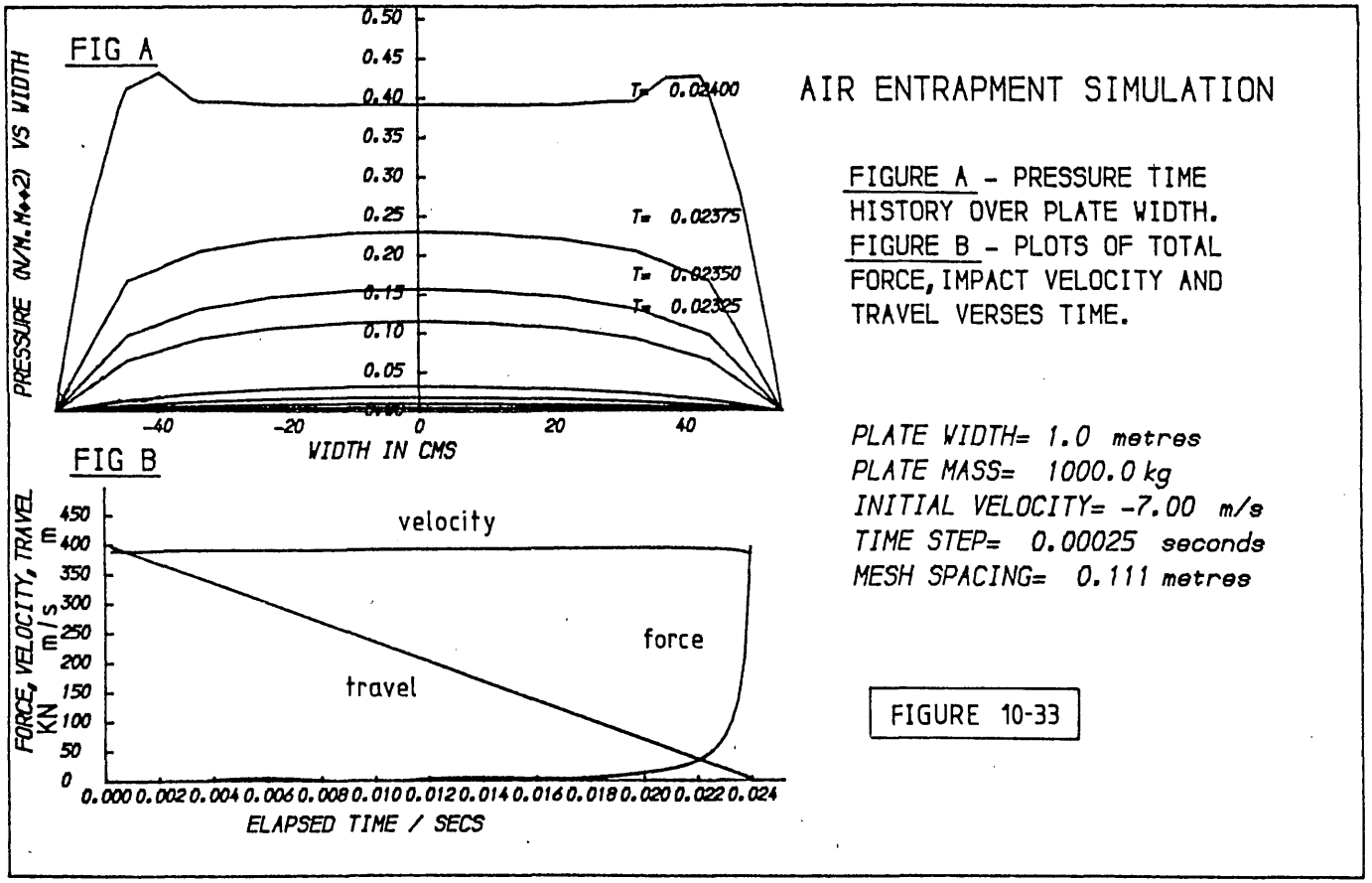

AIR ENTRAPMENT SIMULATION

FIGURE A - PRESSURE TIME HISTORY OVER PLATE WIDTH.
FIGURE B - PLOTS OF TOTAL FORCE, IMPACT VELOCITY AND TRAVEL VERSES TIME.

PLATE WIDTH= 1.0 metres
PLATE MASS= 1000.0 kg
INITIAL VELOCITY= -7.00 m/s
TIME STEP= 0.00025 seconds
MESH SPACING= 0.111 metres

FIGURE 10-33

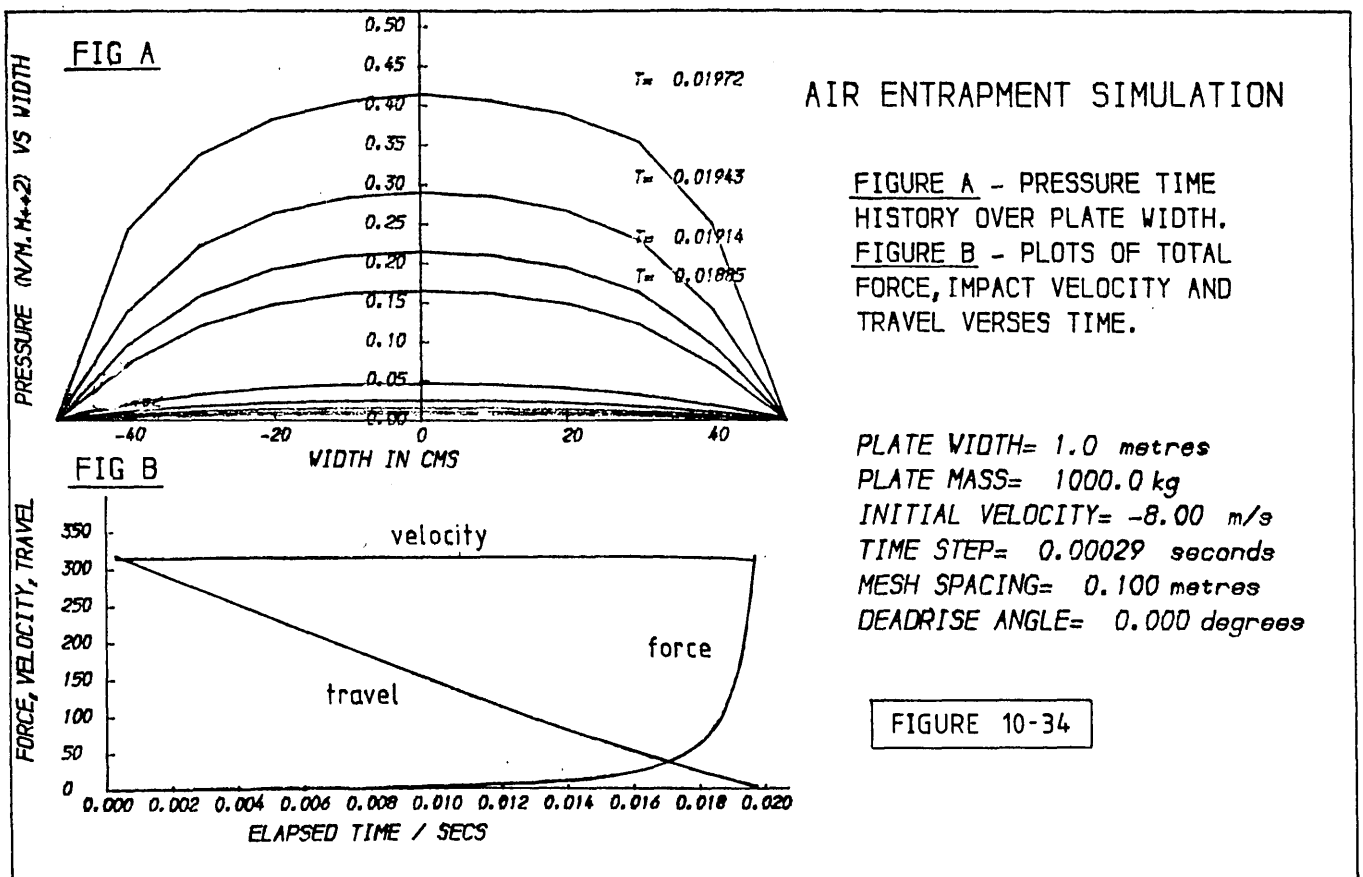

AIR ENTRAPMENT SIMULATION

FIGURE A - PRESSURE TIME HISTORY OVER PLATE WIDTH.
FIGURE B - PLOTS OF TOTAL FORCE, IMPACT VELOCITY AND TRAVEL VERSES TIME.

PLATE WIDTH= 1.0 metres
PLATE MASS= 1000.0 kg
INITIAL VELOCITY= -8.00 m/s
TIME STEP= 0.00029 seconds
MESH SPACING= 0.100 metres
DEADRISE ANGLE= 0.000 degrees

FIGURE 10-34

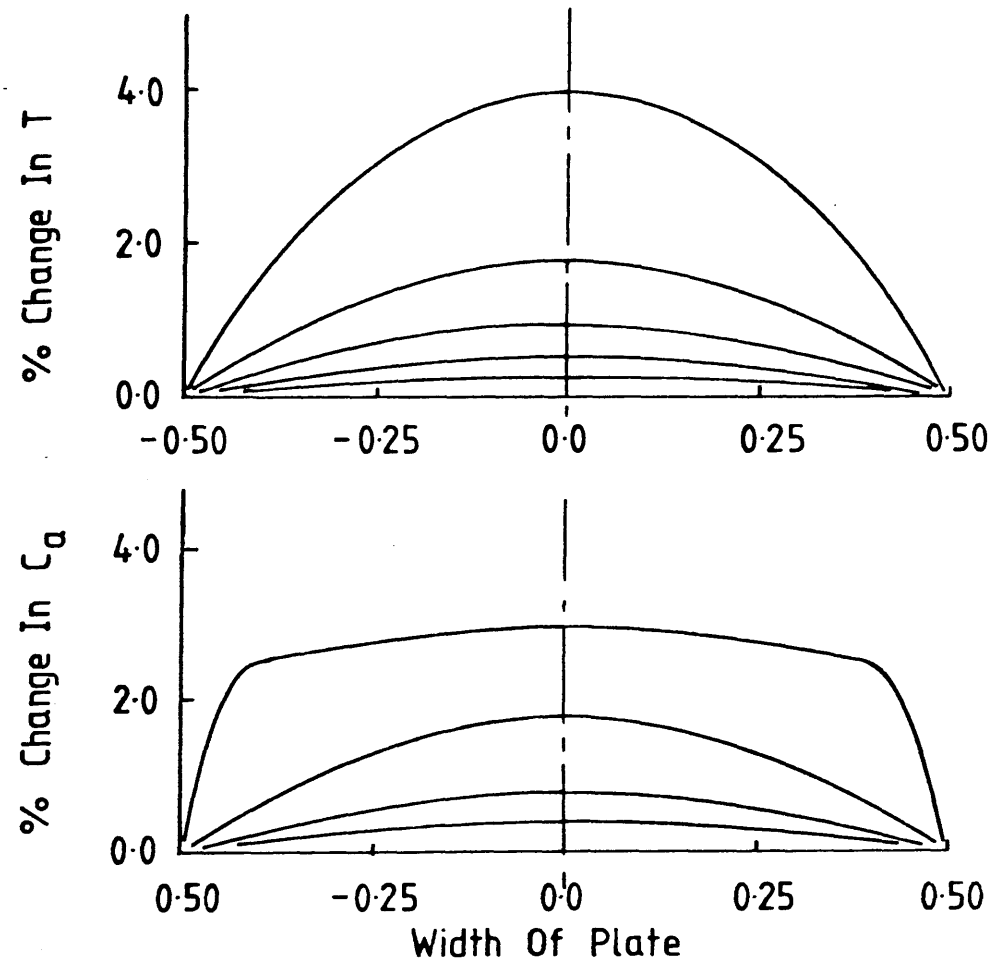

Figure 10-35 (above) Percentage Change In State Variables Over Plate Width

Figure 10-36 (below) Time History Of Change In State Variables

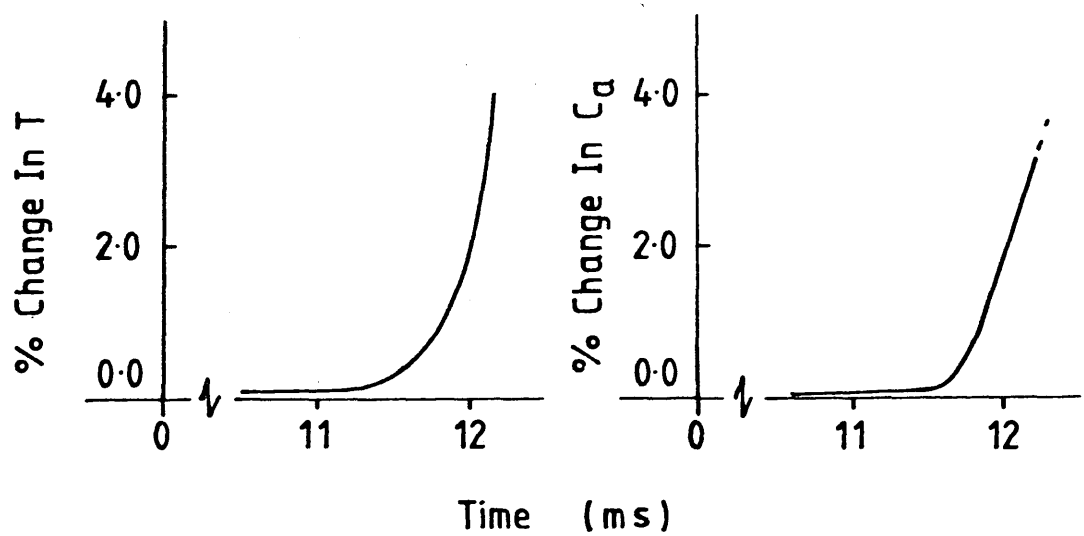

along the centreline showed the largest rates of increase towards the end of the simulation, in a manner similar to the pressure and load records.

In the light of these observations, the energy transport equations were re-examined. The inviscid flow models applied had no energy dissipation mechanisms, such as would be the result of viscous effects in laminar flow, or factors owing to turbulence. For the form of the conservation equations and the simulation procedure applied in this model, it was concluded that the momentum and energy transport models should have been synonymous. The small rises in temperature and sound speed were therefore, regarded as functions of the errors in the time marching method.

Other, more practical considerations, such as the need for a constant time step, lead to the decision to disregard the gas ideal flow model for the purposes of this study. A more precise two or three dimensional model of the air layer including viscous and turbulent loss effects would be required before such a level of realism could be seriously considered.

11. POST IMPACT BEHAVIOUR OF FLAT PLATES

This section discusses the post impact behaviour of the air layer trapped beneath plates with deadrise angles $\beta < 0.25$ degrees, and of high 'momentum per unit area' loading. As noted in a previous section, the trapped bubble was considered to move with the body such that a simple gas-spring analogy could be used to compute the pressures within it. In common with other approaches to the problem (33,35), the fluid dynamics were represented by a single added mass. This, in association with the mass of the body led to the following expression for the second derivative, with respect to time, of the mean air gap thickness:-

$$\frac{\partial^2 h}{\partial t^2} = \frac{\bar{p}_a\, b}{(M_b + M_a)} \qquad \text{---10.11/1}$$

where M_a mass of the body

M_b added mass of fluid

b plate width

$\bar{p}_a$ mean pressure in the air layer

Thus the rate of change of the thickness of the air gap was deduced by using the following finite difference formula:-

$$\frac{\partial h}{\partial t}^{n+1} = \frac{\partial h}{\partial t}^{n} + \frac{\bar{p}_a\, b\, \Delta t}{(M_a + M_b)} \qquad \text{---10.11/2}$$

The rate of change of density was computed as:-

$$\frac{\partial \rho_a}{\partial t} = -\frac{\rho_a}{h}\frac{\partial h}{\partial t} \qquad \text{---10.11/3}$$

from which the following finite difference representation was obtained:-

$$\rho_a^{n+1} = \rho_a^n - \Delta t \frac{\rho_a^n}{h^n} \frac{\partial h^n}{\partial t} \qquad \text{---10.11/4}$$

The total pressure was then found using:-

$$p_a^{n+1} = c_a^2 \rho_a^{n+1} \qquad \text{---10.11/5}$$

where C_a is the speed of sound in air.

Equations 10.11/1 to 10.11/5 were used to produce a time marching scheme in mean density, pressure, air gap thickness and rate of compression. Initial values were derived from the final time step of the flat plate simulation routine. A number of different values of M_b, body mass and initial impact velocities were chosen. It was hoped that the peak pressure could be achieved during the running of this routine.

Unfortunately, this model was suitable for low values of body mass only. The load time histories were dominated by the interaction between body and free surface dynamics. Pressure peaks were generated, coinciding with a change from bubble compression, to expansion. It was noted that the compression of the air bubble alone could not generate a sufficient load on the plate for mass loadings greater than 50kg to allow this reversal to take place. The result was that the mean air gap thickness could become negative, ie the body passed through the bubble, for high plate mass loadings. This was not considered reasonable behaviour for this simple model. Furthermore, the use of half the flat plate added mass to represent the fluid dynamics was also considered unrealistic, since the fluid kinetic energy upon contact was too low to warrant such a treatment.

A second model was developed in which the hydrodynamic loading on the edges of the plate could be included. The effect was to prevent the premature collapse of the bubble by reduction of the plate velocity. The resulting algorithm required the following assumptions:-

a. The bubble could be represented by a half ellipse with major axis b and minor axis h, the air gap thickness.

b. During compression, the ratio b/h remained constant.

c. The total added mass for the plate was given by:-

$$M_a = \rho \pi (B - b)^2$$

where B = half breadth of plate = 0.5m.

d. The resulting hydrodynamic load was generated by the rate of change of added mass concept wherein the reduction in b caused by bubble compression, resulted in an increase of wetted beam and hence added mass given by:-

$$\frac{\partial M_a}{\partial t} = -2\rho\pi(B - b)\frac{\partial b}{\partial t} \qquad \text{---10.11/6}$$

e. The total load on the body consisted of the hydrodynamic load:-

$$F_h \quad \frac{\partial M_a}{\partial t} V_b \qquad \text{--10.11/7}$$

and the load generated by compression of the air bubble.

$$F_a = 2 p_a b \qquad \text{---10.11/8}$$

For this model, the pressure in the air layer was computed using the rate of decrease in bubble volume, hence equation 10.11/4 became:-

$$\rho_a^{n+1} = \rho_a^n \left(1 - \Delta t \left(\frac{dA}{dt} \right)^n / A^n \right) \qquad \text{---10.11/9}$$

where A is the cross sectional area of the bubble and is given by:-

$$A^n = \pi b^n h^n / 2 \qquad \text{---10.11/10}$$

The pressure was again found using equation 10.11/5. The rate of change of area may be deduced by differentiating equation 10.11/10 thus:-

$$\frac{dA}{dt} = \frac{\pi}{2} \left(b \frac{\partial h}{\partial t} + h \frac{\partial b}{\partial t} \right) \qquad \text{---10.11/11}$$

since b/h is a constant, it can be shown that:-

$$\frac{\partial b}{\partial t} = \frac{b}{h} \frac{\partial h}{\partial t} \qquad \text{---10.11/12}$$

hence equation 10.11/11 became:-

$$\frac{dA}{dt} = \pi b \frac{\partial h}{\partial t}$$

The expression for the density is therefore:-

$$\rho_a^{n+1} = \rho_a^n \left(1 - 2 \Delta t \frac{\partial h}{\partial t}^n / h^n \right) \qquad \text{---10.11/13}$$

The computational routine was similar to the previous method except that the body and bubble dynamics were treated separately. The whole system was represented by two freely moving bodies connected by a spring. One body represented the plate and its asociated added virtual mass. The second represented the fluid added virtual mass alone. The compression of the bubble provided the required non-linear, spring stiffness via equation 10.11/13. The dynamics of the two masses

were treated separately. First, the deceleration of the body was found using the combined loading resulting from bubble pressure, and rate of change of added virtual mass, ie:-

$$\frac{\partial V_b}{\partial t} = (F_h + F_a) / (M_b + M_a) \qquad \text{---10.11/14}$$

The acceleration of the free surface was found using:-

$$\frac{\partial^2 \eta}{\partial t^2} = F_a / M_a \qquad \text{---10.11/15}$$

Equations 10.11/14 and 10.11/15 were used to update the body and free surface velocities from which the rate of change of air gap thickness was deduced as:-

$$\frac{\partial h}{\partial t} = V_b - \frac{\partial \eta}{\partial t} \qquad \text{---10.11/16}$$

As before, the computational method consisted of a simple time marching routine in density, pressure, air gap thickness, added virtual mass, plate velocity etc, with initial data obtained from the last time step of the air entrapment calculations.

Figures 10-37 and 10-38 show the results of combining the two time histories given by the initial air entrapment routine and the post impact routine for two typical drop test simulations. The smooth curves of pressure, and pressure induced loading are typical of the air entrapment problem and agree well with experimental results quoted by other authors (33,35,36). When plotted on the same time base, the curve of hydrodynamic loading was seen to have a peak just after contact with the free surface. The peak in the loading coincided with the highest rate of change of wetted beam (as controlled by bubble collapse), and a high plate velocity. The time history of plate velocity exhibited its maximum deceleration at this point. Since the

Figure 10-37

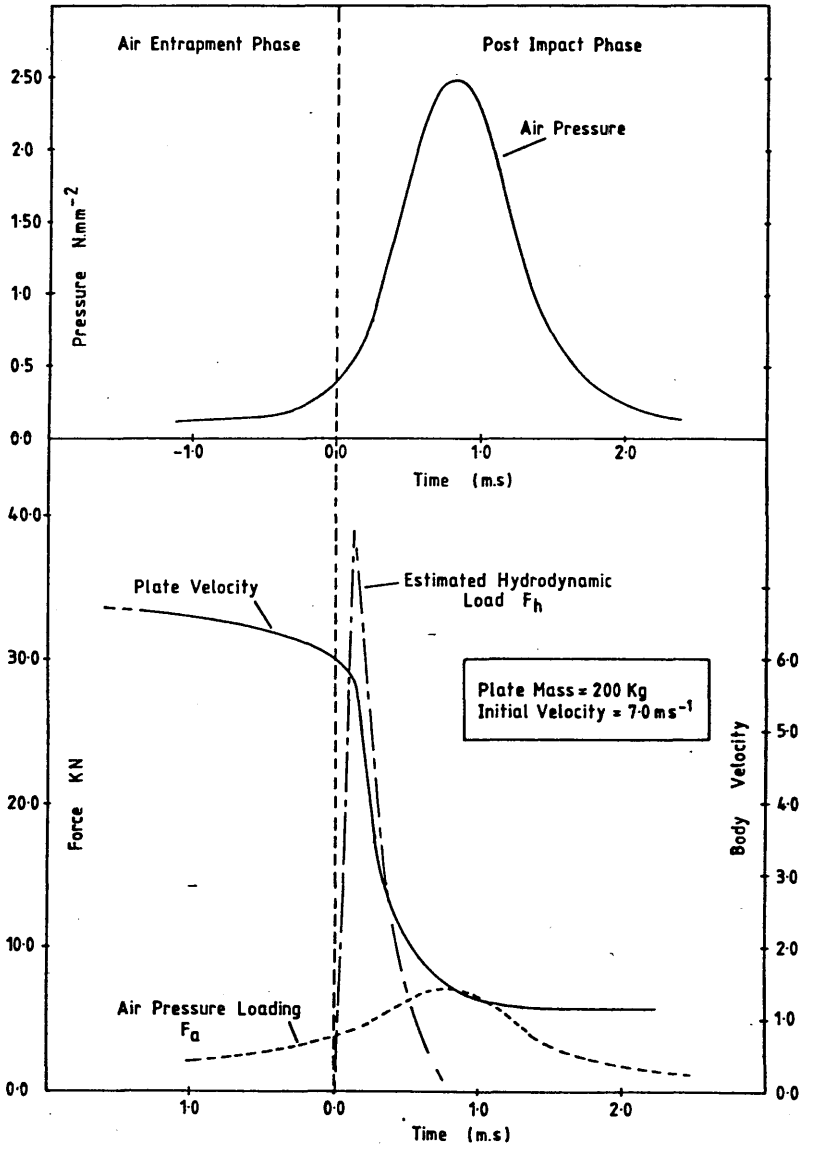
Air Entrapment Phase
Post Impact Phase
Air Pressure
Pressure N.mm⁻²
2·50
2·0
1·50
1·0
0·5
0·0
-1·0
0·0
1·0
2·0
Time (m.s)
40·0
30·0
20·0
10·0
0·0
Plate Velocity
Estimated Hydrodynamic Load F_h
Plate Mass = 200 Kg
Initial Velocity = 7·0 m s⁻¹
Force KN
Body Velocity
6·0
5·0
4·0
3·0
2·0
1·0
0·0
Air Pressure Loading F_a
1·0
0·0
1·0
2·0
Time (m.s)

Figure 10-38

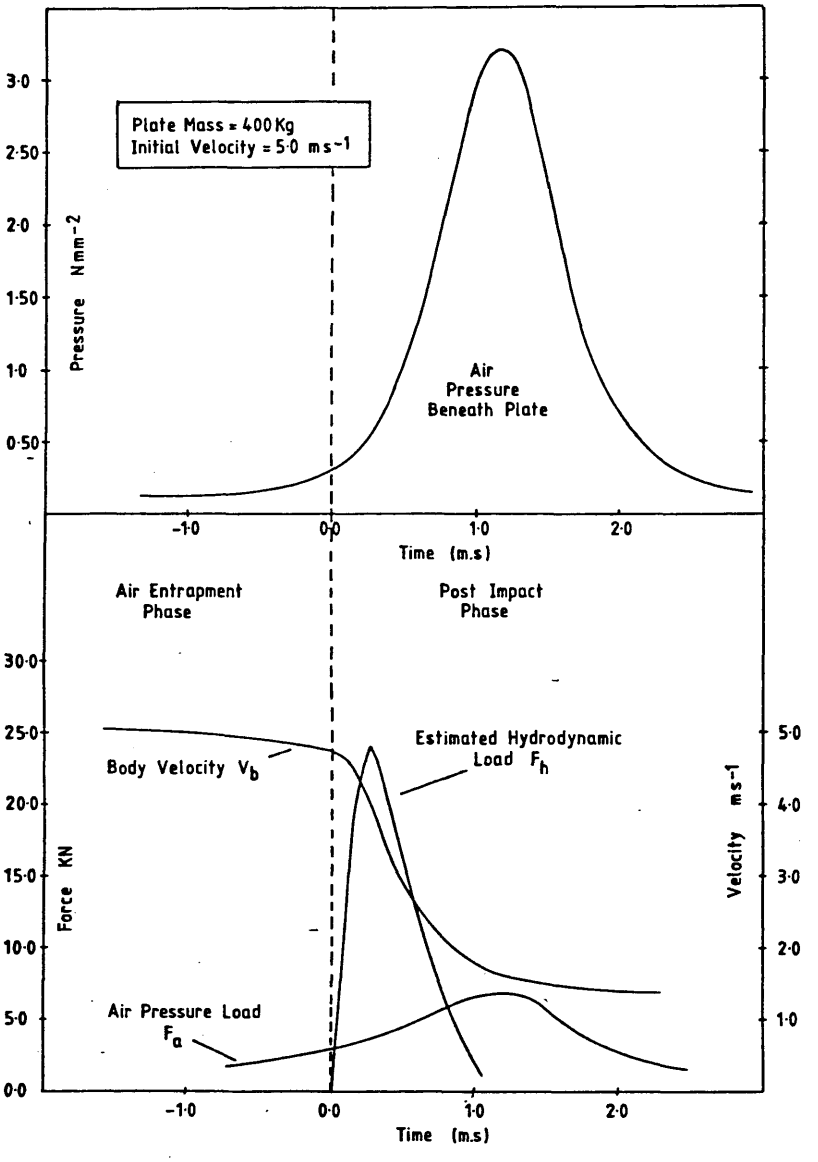
Plate Mass = 400 Kg
Initial Velocity = 5·0 m s⁻¹
Pressure N mm⁻²
3·0
2·50
2·0
1·50
1·0
0·50
Air
Pressure
Beneath Plate
-1·0
0·0
1·0
2·0
Time (m.s)
Air Entrapment
Phase
Post Impact
Phase
30·0
25·0
20·0
15·0
10·0
5·0
0·0
Force KN
Body Velocity V_b
Estimated Hydrodynamic
Load F_h
Air Pressure Load
F_a
Velocity m s⁻¹
5·0
4·0
3·0
2·0
1·0
-1·0
0·0
1·0
2·0
Time (m.s)

maximum air pressure loading was nearly an order of magnitude lower than that due to the fluid, and was out of phase with the peak body deceleration, it was clear that the force produced by the compression of the air layer was of secondary importance for this class of impact. However, it should be noted that, if the air bubble were not present, an infinite rate of deceleration would exist.

The role of air bubble formation in the slamming problem can thus be seen as:-

a. Prevention of unreasonable high acoustic impact pressures upon first contact by distortion of the free surface such that hydrodynamic loads are confined to the edges of the plate.

b. Control of the rate of change of wetted beam and hence rate of change of added mass after first contact.

The method of estimating hydrodynamic loads in this simulation was very crude. A much more sophisticated technique is required to study bubble dynamics beneath the hull section of a ship. The effect of marine growth and discontinuities in section shape may be to prevent (or accelerate) bubble contraction. The interaction between bubble dynamics and hydrodynamic loading is a highly complex problem. However, it is considered that the model described herein provided a good 'first guess' at the major features of this type of slam.

12. RESULTS FROM THREE DIMENSIONAL MODELLING

Running the three dimensional air layer model proved highly problematical owing to the large amount of computing time required. It was found that the 30 x 30 x 20 node mesh used to discretise the fluid domain required proportionally more iterative sweeps to solve the potential flow model than an equivalent two dimensional simulation. A reduction in the total number of time steps used during the simulation, combined with a lower initial drop height, resulted in a program which was much more difficult to run. Each simulation required approximately 60,000 cpu on the University of Glasgow ICL 2988 mainframe computer.

Consequently, only a few 'strategic' tests were possible, all with a simple flat plate. Four tests were carried out at a low mass loading of 50kg/m using a square plate, 1m x 1m in size. Initial impact velocities of 2,3,4 and 6 m/s were used.

A further four tests were performed with a high mass loading and various plate aspect ratios. It was hoped that the effect of three dimensionality on the quantity of air entrapped, and the pressure distribution at the instant of contact could be ascertained.

Figure 10-39 shows the free surface elevation beneath the 50Kg plate at the instant loading. The plot is sectioned along the centreline of the plate for clarity. The maximum free surface height at the edge of the plate is approximately 0.5mm. The depth of the bubble is 1.4mm. The vertical axes have been distorted by the GHOST routine used to perform the plots.

PLOT OF FREE SURFACE HEIGHT FOR
3-D AIR ENTRAPMENT PROBLEM.

INSTANT OF PEAK LOAD

PLATE WIDTH = 1.0 METRES
ASPECT RATIO = 1.0
DEADRISE ANGLE = 0.0 DEGS
PLATE MASS = 50.0 KG
PLATE VELOCITY = 4.0 M/S

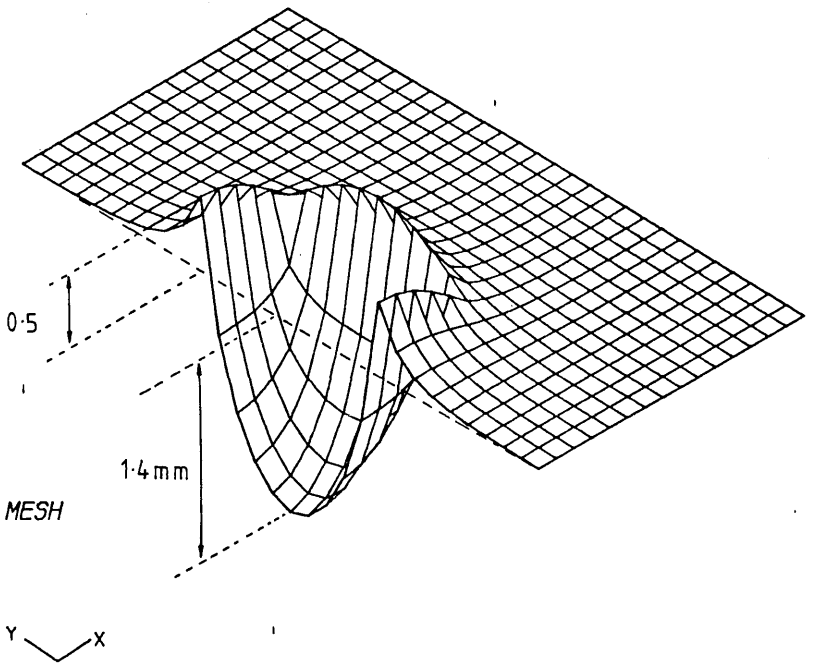

FIGURE 10-39

MESH SPACING = 0.1 METRES
DISCRETISED BY 30 BY 30 BY 20 MESH

Figure 10.40 shows the corresponding pressure distribution. A similar type of plateau-like pressure field is generated, though the peak pressures occur at the plate corners. The peak centreline pressure for this case was 0.1138N/mm^2. The total load time history for this impact is shown in figure 10-41 along with that from the equivalent two dimensional case. Apart from a few spurious oscillations in the record from the 3.0 test, caused by the low dropt height required to reduce the computing time, the general form of the curves is the same. However, the peak load is some 32% lower for the three dimensional impact.

As with the one dimensional air layer model, the peak pressures and loads were proportional to the square of the impact velocity. The pressure and load coefficients were 1.67 and 1.57, respectively.

The variations in aspect ratios were achieved by adjusting the mesh spacing in the x and y directions, ie by altering the horizontal mesh size ratio. The area of the plate was however held constant at 1.0 m . The resulting effect of varying the aspect ratio upon the pressure distribution may be deduced from figure 10-42 which shows a plot of pressures and loads at the instant of contact versus aspect ratio. An initial impact velocity of 4 m/s was used for each test. Figure 10-42 shows that both pressures and loads were reduced as the aspect ratio was increased as expected. However, it was also noted that the loading decreased more rapidly, suggesting that the pressure distribution no longer retained its plateau-like shape.

These two brief studies illustrated the importance of horizontal, two dimensional effects in the air layer. Such behaviour

PLOT OF PRESSURE DISTRIBUTION FOR
3-D AIR ENTRAPMENT PROBLEM

INSTANT OF PEAK LOAD

PLATE WIDTH = 1.0 METRE
ASPECT RATIO = 1.0
DEADRISE ANGLE = 0.0 DEGS
PLATE MASS = 50.0 KG
IMPACT VELOCITY = 4.0 M/S

Figure 10-40

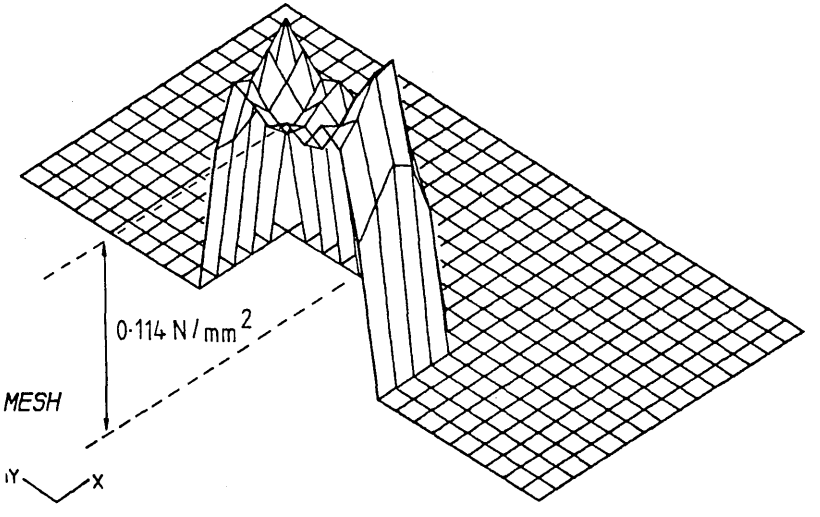

MESH SPACING = 0.1 METRES
DISCRETISED BY 30 BY 30 BY 20 MESH

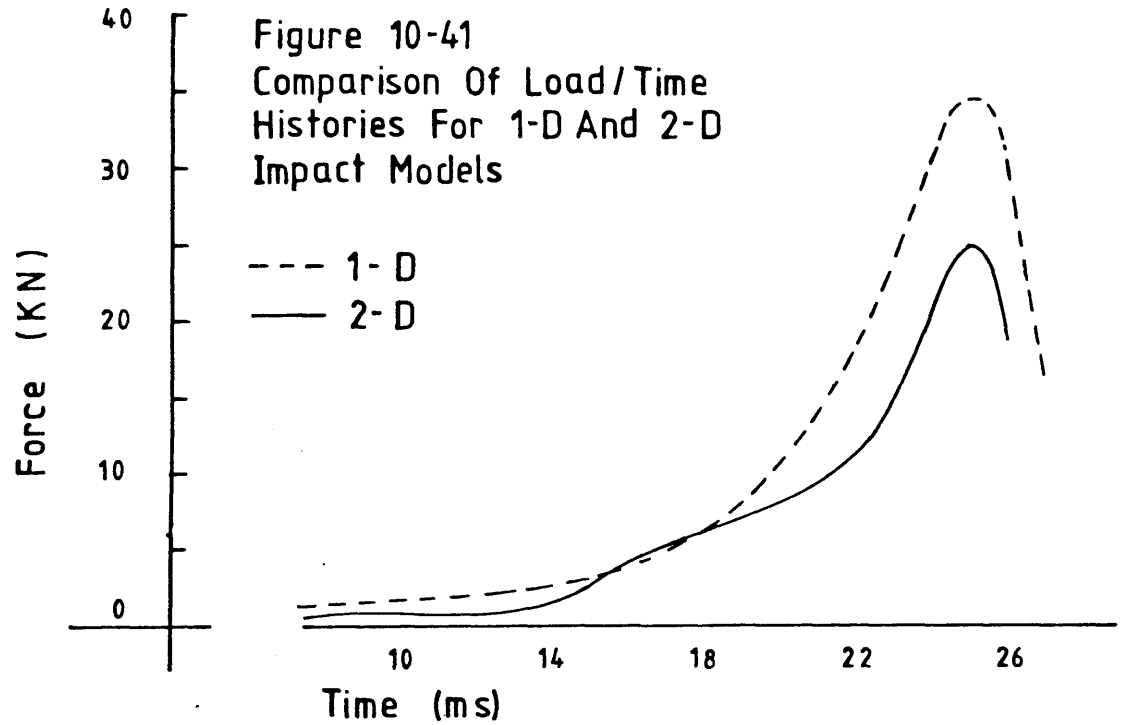

Figure 10-41
Comparison Of Load/Time Histories For 1-D And 2-D Impact Models

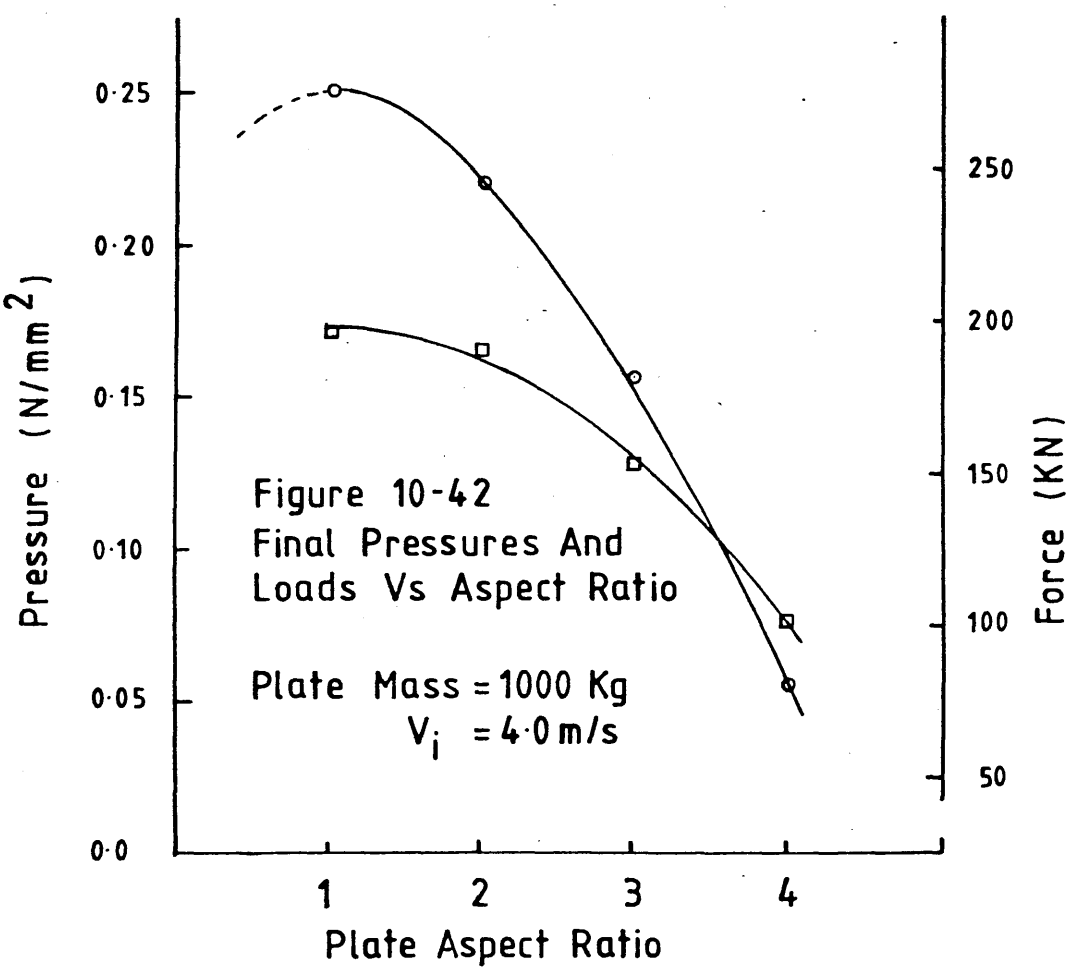

Figure 10-42
Final Pressures And Loads Vs Aspect Ratio

was to be expected considering the relatively greater outflow area at the plate edge for the three dimensional impact model. The square plate had the highest loads applied to it. However, these studies were carried out prior to contact with the free surface so that general conclusions concerning the variation of the complete force/time history could not be drawn.

13. COMPARISONS WITH EXISTING COMPUTATIONAL AND EXPERIMENTAL RESULTS

Research by various authors in the field of air entrapment effects in slamming has been briefly reviewed in chapter 2. This section will examine more closely the results detailed in these publications and this author's own work. This review will be carried out, for convenience, in chronological order. Table 10-C gives details of the range of experiments and computations carried out as published in the open literature and thus available to this author.

The series of experiments on flat plates and wedges carried out by Chuang and reported in references 33 and 34 are the first to be examined. As seen from table 10-C, the mass loading and range of impact velocities used places these tests firmly in categories (a) and (c). Chuang's results showed the peak pressure to be linearly proportional to the impact velocity for flat plates, with a rising index for V at higher deadrise angles. This disagreed with the results presented in section 10-7, in which it was shown to be possible to define peak pressure and loading coefficients using a square law relationship for this class of impact.

It was also assumed by Chuang that the peak impact pressure occurred at or before the instant of first contact. Whilst true for this particular class of slam, it has been shown that for higher mass loadings, this is not the case. Chuang's assumptions led to a post impact model in which the total momentum gained by the fluid and, hence, the impulse applied to the body, was taken to be the same whether air had been trapped or not. Whilst convenient, this model had two faults. Firstly, it ignored the interaction between air pressure

Table 10-C

Authors, year & Ref No	Mass Loading Kg/m	Max Drop ht Max Impact V	Present Class-ification	Comments
Chuang, 1966 Ref 33	340.0	0.19m $1.93ms^{-1}$	(a)	Flat plate $\beta=0$. Duration of Time History 2.5-3m s. Pressure $\propto V_i$
Chuang, 1967 Ref 34	340.0	0.19m $1.93ms^{-1}$	(a) & (c)	$0 < \beta < 15$. Pressure $\propto V^n$ given in Table 2A. Air entrapment only up to $\beta=1^\circ$.
Verhagen, 1967 ref 35	50	0.5m $3.13ms^{-1}$	(a)	Flat plate $\beta=0$. Low M_b V_b, $P \propto V_i^2$. Expts performed in small shallow tank.
Lewison & Maclean, 1968 ref 36	Up to 2366.0 but most quoted at 1338.0	1.52m $5.46ms^{-1}$	(b)	Flat plate $\beta=0$. Duration of time history -10ms $P \propto V_i^2$
Koehler & Kettleborough 1977, Ref 48	Up to 2366.0	1.52m $5.4ms^{-1}$	(b) (d)	Flat Plate $\beta=0$. Attempt to verify Lewison & Maclean's results by computation. Overestimated Pressures. Also treat $\beta=0.25^\circ$ and 0.5°. Air entrapment for $0^\circ < \beta < 0.25^\circ$

and hydrodynamic loading essential for post impact behaviour. Secondly, it assumed the added mass 'achieved' by the flow at the instant of contact to be equal to that of the immersed section.

Whilst computing the rise in kinetic energy in the fluid for this author's method, it was noted that, for flat plates, the total amount achieved showed asymptotic behaviour when plotted against the initial impact velocity. However, the use of the body velocity to compute the effective added mass produced results well below those required to confirm Chuang's hypothesis. As a result, the post impact model described in section 10-11 was developed and showed that the maximum pressure in the air layer was reached sometime after first contact and that the resulting peak load was the result of hydrodynamic considerations.

Chuang's results for varying deadrise angles showed that the peak pressures were proportional to V_i , with n ranging between 1.0 for a flat plate, and 2.0 for $\beta > 6$ degrees. It has already been seen from section 10-7, that the actual relative velocity between body and free surface was reduced prior to impact by the action of air cushioning. It is proposed that the results quoted by Chuang were affected by this phenomenon.

Figure 10-43 shows a plot of V_r^2 , as deduced from the last time step of the air cushioning simulations used in this thesis, against V_i raised to the power 1.4, the value given by Chuang for the 1 degree deadrise wedge. The data was taken from figure 10-24, within the range of velocities used by Chuang, and supplemented by a series of specific computations at these lower values of V_i . The data was interpolated using a mass loading of 340Kg/m .

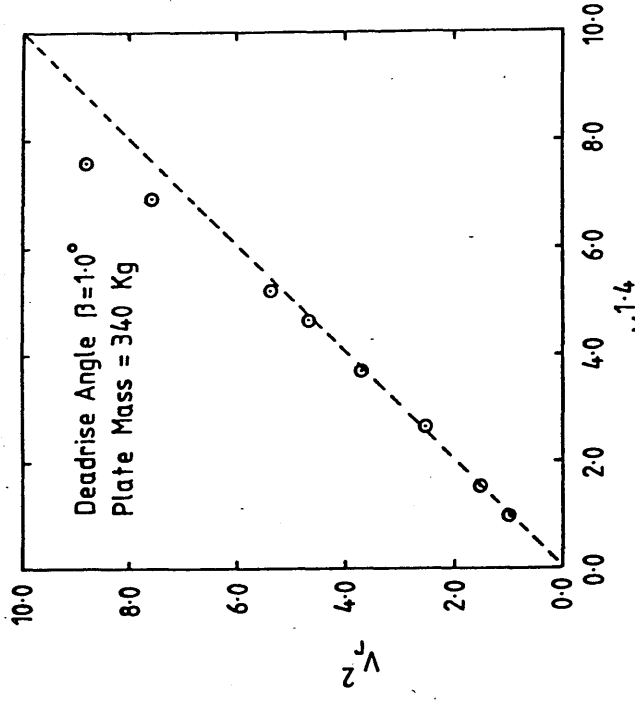

Figure 10-43 Comparison Of Initial And Final Impact Velocities Via Chuang's V^n Law

The agreement at these low velocities was good, with the gradient of a least squares fit through the points found by numerical method being within 5% of the mean line found from experiment. The agreement deteriorated at higher impact velicities however. It was thought that, for higher drop heights, and mass loadings, the V_i^n laws developed by Chuang would be less precise.

Verhagen's results for flat plate impacts indicated that, at low impact velocities, the pressure was directly proportional to V_i, whereas, with increasing V_i, the familiar square law prevailed. A greater range of impact velocities was used, the peak value being $3.13ms^{-1}$. The plate was light however, with an equivalent mass loading at $50Kg/m^2$. It should also be noted that the tank used for the experiments was very small, such that problems with 'imaging' or shallow water effects may have had some influence upon Verhagen's conclusions. In general, the results from the present computational method predicted pressures lower than those found by Verhagen. However, comparison of the results was difficult since some of the drop heights used in these experiments, air cushioning effects may have been prevalent as soon as the body was released. Thus the effective impact velocity became dificult to assess.

Unlike Chuang and Verhagen, Lewison and Maclean used a large scale drop testing facility and a heavy mass loading of up to $2366Kg/m^2$. All tests were conducted with zero deadrise angle, using high impact velocities of up to 5.46m/s . In all cases, the maximum impact pressure was stated to be proportional to the square of the impact velocity.

These drop tests fall into category (b) as outlined in

section 10-6. Thus the post impact behaviour model used in section 10-11 is of importance. The impact pressure coefficients derived from Lewison and Maclean's drop tests are slightly lower than those computed herein, whereas, with the higher mass loading of the model, higher values would have been expected. In reference 36, some pressure time histories are presented from which a number of conclusions may be drawn.

a. The maximum impact pressures were generally found to be proportional to the square of the impact velocity. However, two time histories were given for drop tests using models ballasted to within 2.5Kg of each other. The peak pressure coefficients derived using an impact velocity squared rule were $k_p = 41.1$ (for $V_i = 3.47$m/s) and $k_p = 24.1$ (for $V_i = 5.36$m/s). Clearly, these two figures should have been identical.

b. The pressure peak at the edges occurred before the peak along the centreline for a number of drop tests indicating that the slam followed the simulation set out in section 10-11.

c. The time scale for Lewison and Maclean's results was similar to that obtained using the method set out in section 10-11.

Lewison and Maclean gave plots of acceleration velocity and travel for one of their impacts as figure 8 of reference 36. Unfortunately, this figure could not be reproduced in this thesis. However, these plots compare favourably with figures 10-37 and 10-38 from the numerical methods herein, though absolute magnitudes differ owing to the different geometries tested.

It would perhaps have been prudent to have attempted modelling the exact geometries and mass loadings used by Lewison and Maclean. However, there were problems in setting up such a simulation. The chief difficulty was that, in order to have comparable accuracy with the present method, the mesh spacing for the computational routine would need to be retained. For the size of model tested this would have required a three or fourfold increase in the number of fluid nodes and a correspondingly large increase in computing time.

A second problem arises when modelling a drop test and subsequently attempting to correlate numerical computations. If the initial drop height required of the computer simulation is too high, an excessive amount of time will be spent upon the computation. If the drop height is too low, the relative velocity between the body and free surface at the instant of contact may not be correctly evaluated. This problem worsens as the beam of the section to be modelled is increased. It has already been shown, when examining Chuang's results, that defining the effective impact velocity is difficult.

Koehler and Kettleborough's attempts at modelling air layer behaviour were very similar to the present method. Unfortunately, the model did not include post impact behaviour and so when attempting to compare their technique with Lewison and Maclean's experiments, poor correlation was achieved. However, in common with the present method, air bubble formation was limited to deadrise angles less than 0.5 degrees. Comparison of pressure, velocity and travel time histories prior to impact between Koehler and Kettleborough's work and results obtained with the present method were good. Spatial pressure distributions also agreed well. However, Koehler and Kettleborough did not run a large series of tests and did not produce pressure or load

coefficients at low plate mass and impact velocities, where it would have been possible to simulate the pressure peaks encountered by slam categories (a) and (c).

Finally, figure 2-10, reproduced from reference 48 and reviewed in chapter 2 shows, amongst others, a curve of impact coefficient versus impact angle for a series of wedge tests. These tests were carried out at the David Taylor Naval Ship Research and Development Centre by Chuang whose work has been discussed previously. Upon presentation in this form, these test results show good agreement with the curves given in figures 10-25 and 10-26, for the range $0 < \beta < 3$ degrees. Reservations concerning absolute values of the slam coefficient should be considered owing to the mass loadings and model geometry used for these tests, and the interpretation of impact velocity employed.

14. CONCLUSIONS

14.1. Numerical Schemes for Air Layer Computations

The most reliable and numerically stable models of the escaping air layer were based on the backward time stepping discretisation of the one dimensional mass and momentum conservation equations. The assumption of adiabatic behaviour was also found to be sufficient. Either central or upwind finite difference operators could be used for the convection terms, though the former was preferred as it promised greater accuracy.

Whilst the relaxation solution to the potential flow problem in the fluid domain required the majority of the computing effort, the technique was considered stable, accurate and well suited to the overall simulation scheme.

14.2. General Conclusions Drawn From Impact Model

It has been shown that there are four distinct ways in which the air layer may affect the impact scenario. The deadrise angle (or relative impact angle) and momentum loading per unit area are the two major parameters influencing slam behavior.

At low values of momentum loading ($M_b.V_i$ < 600kg . m/s depending upon deadrise angle), the peak in the air pressure may be reached prior to contact with the free surface. Furthermore, the fluid vslocity may match that of the body itself, thus preventing a high slam loading. This type of behaviour is typical of the light drop tests performed by various researchers (33,34,35) though it is

considered by this author to be totally unrepresentative of the general ship slamming problem. Reasonable agreement was obtained between results obtained using the models described in this thesis and those quoted in the references cited above. However, the lack of a common view concerning the types of impact scenario prevented a closer, quantitative comparison.

It was concluded that the air layer would affect ship slamming in the following two cases:-

a. Where the relative impact angle was less than 0.5 degrees, an air bubble would form. Unlike previous researchers, it was not assumed by this author that the air pressure would reach its peak at the instant of contact. In fact, the air layer continues to be compressed for some time after impact. In this way the bubble acts both as a 'cushion' and as a controlling factor for the hydrodynamic loading.

b. Where the relative impact angle is greater than 0.5 degrees, but less than 3 degrees, the build up of air pressure beneath the section serves to accelerate the free surface reducing the effective impact velocity quite substantially. First contact for this impact geometry, occurs along the centreline. Some slam loading is therefore bound to occur.

It was difficult to ascertain from this study whether curvature of the section would allow bubble formation or not. For the ideal case of a perfectly smooth, dry circular cylinder impacting upon a totally still free surface, it was concluded that bubble formation was likely to occur just prior to impact.

A small study on the effect of discontinuities in the body shape showed that the air trapped in the small pockets caused by these surface imperfections would have a mean pressure equal to that attained under flat plate impact conditions, though it was possible for the overall loading to be greater.

The three dimensional impact geometry showed that the air pressures developed beneath a flat plate would be at least some 30% lower at peak than for the two dimensional case. Since only plates with low momentum loadings per unit area exhibited the phenomenon of pressure peaks prior to impact, few conclusions were possible concerning effects on the full ship scale.

14.3. On The Combination of Hydrodynamic and Air Entrapment Simulation Routines

Whilst a great deal of analysis has been carried out using the air entrapment/potential flow model, the primary aim of this study was to produce a combined air entrapment/SOLA based slam simulation.

It has been shown that only two of the four possible slam scenarios are important to ship slamming. In both of these cases, the peak loading is reached after first contact with the free surface. It was decided that the best way to combine the air entrapment and hydrodynamic impact simulations was via the following assumptions:-

a. That the two remaining impact types, ie the air cushioning and bubble formation at high momentum loadings, should be treated separately.

b. In both cases, data produced by the air entrapment

simulation should be used only as initial conditions for the hydrodynamic simulation.

c. For the case of air entrapment, the model of bubble collapse used in section 10.11 should be retained. The added sophistication of the finite difference time simulation of the fluid flow at the plate edges would replace the 'rate of change of added mass' computation used previously.

d. For the air cushioning scenario, the problem to be solved is that of a wedge entering an already moving free surface. The post impact behaviour of the bisected air layer requires closer examination. An emperical model of the decay in air pressure above the fluid would need to be developed so as to promote computational efficiency.

e. The thickness of the air layer at the instant of contact (less than 5 millimetres) was sufficiently small for ts effect upon the shape of the section to be ignored. Furthermore, the mesh size in the hydrodynamic computation would not be low enough to provide good resolution of the bubble behaviour.

Unfortunately, the combination of the hydrodynamic and air entrapment simulation routines requires further study and was considered beyond the scope of this thesis.

CHAPTER 11

CONCLUSIONS AND FUTURE WORK

CHAPTER 11

CONCLUSIONS AND FUTURE WORK

1. SUMMARY AND CONCLUSIONS

This thesis has concerned the development of the discipline of computational fluid dynamics to model slamming of ships and offshore stuctures. It had been concluded from the initial literature survey that uncertainty concerning the quantitative physics behind the impact loadings had resulted in naval architects and offshore engineers being unable to include slamming in their design formulations on anything other than an empirical basis. It was hoped that the versatility in flow modelling offered by computational fluid dynamics would allow the development of a load prediction program which could take into account all physical uncertainties.

General free surface flow programs were developed using a finite difference time marching solution of the continuity coupled Navier Stokes equations. Both free surface wave generation and steady viscous two dimensional flow simulations were developed. It was concluded that simple explicit time marching formulae were sufficient to accurately model these flows. The solution of continuity was of prime concern and, to that end, it was concluded that the Los Alamos SOLA algorithm could be developed successfully. A link between the continuity solver and the dynamic pressure equation was exploited by the introduction of source distributions to represent dynamic free boundaries.

A study of free surface tracking methods concluded that analogy between simple volume fluxing techniques and the free surface non-linear kinematic boundary conditions could be used as the basis of a simple 'book-keeping' method to define the extent of the computational domain. Discrete formulations for the radiation boundary condition were also tested successfully.

A study on viscous flow development using the program FLOW88 concluded that with the computational facilities available, only low Reynolds number flows could be modelled accurately. This restriction was due to limits on the mesh size imposed both by storage requirements and speed of computation.

In Chapter 9 it was shown that these methods could be used to accurately calculate the hydrodynamic coefficients for a rectangular barge in shallow water. It was concluded that the theoretical link between the source strength representation of the moving boundary and the dynamic pressure computation was proved to exist for the numerical model as well. With the introduction of the modified control volume analysis into the existing continuity solver (SOLA), the numerical tools required to fulfil the requirements laid down at the beginning of Chapter 3 were in existence.

An examination of time step and mesh spacing revealed that the peak dynamic pressure rise time was limited by the time step of the numerical model. However, it was considered that this phenomenon, whilst of importance to theoretical considerations, would be outweighed by other modelling uncertainties such as air entrapment and fluid compressibility.

Program SLAM was first applied to the forced and free hydrodynamic impact of a circular cylinder. Good agreement between theory and experiment was found. It was confirmed that, for the numerical model, peak loads were proportional to the square of the impact velocity, with a slam coefficient of $C = 6.12$ being defined for this type of idealised impact. The main advantages of using the present method over existing techniques was thought to be:-

a. Accurate modelling of the piled up water phenomenon.

b. The ability to include vehicle dynamics in an interactive simulatiion.

c. The ability to included local fluid compressibility if permitted by computational resources.

d. The ability to include viscous effects, again, if computational power were to permit.

The program was also used to simulate the water entry of ship shaped sections. The results for load time histories were considered better than those achieved by use of the rate of change of virtual mass approach owing to the inclusion of the spray roots in the computational domain. Previous techniques for computing the effect of piled up water had been restricted to idealised shapes such as wedges and ellipsoids. It is believed that the program SLAM is unique in its ability to deal with any shape of ship section. A comparison of slam coefficients computed using the present method and those deduced by Ochi concluded that the results from the experiments performed in reference (43) underestimated slam loading, perhaps as a result of scaling problems.

It was concluded that the major aim of this work, to develop a versatile hydrodynamic impact simulation routine for an arbitrary shaped body, had been achieved. The choice of the finite difference method guaranteed the ability to extend the program to deal with viscous and/or three dimensional flows when computational facilities permit.

It had been noted that the behaviour of the free surface prior to impact could be affected by the dynamics of the air layer. It was considered desirable for this type of phenomenon to be included in the dynamic simulation of impacts. Chapter 10 dealt with the preliminary evaluation of the effect of air layer dynamics upon the state of the free surface.

Four types of impact scenario were identified dependent upon the mass, velocity and shape of the section. Low momentum loadings applied to the body allowed pressure peaks to occur in the air layer prior to contact with the free surface. It was concluded that this type of behaviour would be confined to experimental drop test type situations only. The two most important cases for ship slamming both exhibited pressure peaks after first contact. For deadrise angles less than 0.5 degrees, an air bubble was formed, otherwise the air layer was responsible for a cushioning type behaviour which served to reduce the effective impact velocity.

In all cases, the peak loading was found to be proportional to the square of the effective impact velocity. However, for the case of air entrapment on the ship scale, it was concluded that the hydrodynamic load was mainly reponsible for the deceleration of the body.

A study on the effect of section curvature left some doubt as to the type of impact which would result from the behaviour of the air layer. It was seen that it was possible for the free surface to assume a shape locally matching the curvature of the section very closely.

This indicated that an acoustic type impact could well occur. However, the pressure of the air layer may also have resulted in bubble formation. Furthermore, it was shown that, as with wedge impacts, the final relative velocity between body and free surface was not equal to the original impact velocity due to the presence of the air layer. This would affect both empirical measurements made by previous researchers (90,91,92) and the realism of the impact simulation used in program SLAM.

It was decided that bubble formation was less likely from a theoretical basis, since the rise of water at the edges of a flat plate was a function of the free jet boundary conditions. No such conditions could be imposed arbitrarily beneath the curved section, so that in the limit, the maximum curvature of the free surface would match that of the body. However, surface discontinuities have a major role to play in the entrapment of air as illustrated by the drop tests performed with the 'w' shaped section. The effect of marine growth and the wetted condition of the section could also affect the free surface flow conditions at the instant of initial contact.

A study of the development of a two dimensional representation of the three dimensional air layer showed reduced peak load and pressure time histories. It was considered of paramount importance to include these aspects of three dimensional flow in any future work.

2. FUTURE WORK

The programs developed so far have shown that the numerical tools furnished by computational fluid dynamics are capable of modelling many of the physical phenomena associated with slamming. However, the techniques are restricted by the computing power available. Hence, a primary aim for future work is to introduce multi-level adaptive fast solvers (multigrid) for the solution of the boundary value problems set up both in SLAM and the air entrapment computations.

With this higher computational efficiency it will be possible to model the flows either with finer grids, allowing the study of viscous effects, or with three dimensional domains.

The combination of the air entrapment and hydrodynamic impact programs should also be given a high priority. Much of the initial research has already been completed towards this end.

The extension of program NWAV90 should allow the study of impact between ship sections and waves, initially in two dimensional flow but finally in a three dimensional domain. It is hoped that a full simulation of ship bow re-entry may be carried out in the near future.

Whilst the application of computational fluid dynamics to ship hydrodynamic problems is still at a very early stage, the techniques developed in this thesis show great promise for the study of flows caused by extreme conditions in ship motions, which traditional linearised potential flow methods can never deal with. It

is felt by this author that simulation techniques typified by SLAM have a considerable contribution to make to our understanding of non linear problems in ship hydrodynamics.

APPENDIX 1

NUMERICAL EXPERIMENTS WITH SUCCESSIVE OVER RELAXATION

APPENDIX 1

NUMERICAL EXPERIMENTS WITH SUCCESSIVE OVER RELAXATION

The successive over relaxation method was used to solve the following Poisson equation for steady pressures:-

$$-\nabla p = \left(\frac{\partial u}{\partial x}\right)^2 + 2\frac{\partial u}{\partial y}\frac{\partial v}{\partial x} + \left(\frac{\partial v}{\partial y}\right)^2 = s \qquad \text{---A.1/1}$$

A recursive finite difference formulation for the solution of this equation was given in Chapter 4 as (equation 4.8/14):-

$$p_{ij}^{k+1} = (1-\omega)p_{ij}^{k} + \frac{\omega}{2(1-\beta^2)}\left(p_{ij+1}^{k} + p_{ij-1}^{k+1} + \beta^2\left(p_{i+1j}^{k} + p_{i-1j}^{k+1}\right) + (\Delta x)^2 S_{ij}\right) \qquad \text{---A.1/2}$$

where β is the mesh ratio $\Delta x/\Delta y$

ω is the relaxation factor

Numerical experiments were carried out in order to define the optimum value of the over-relaxation parameter . The simple example of irrotational flow about a circular cylinder was chosen for the test. A regular finite difference mesh was laid down over the computational domain which consisted of the flow region local to a circular cylinder in an infinite fluid. The stream function is given by:-

$$\psi = -Uy\left(r - \frac{a^2}{r}\right)\text{SIN}\,\theta \qquad \text{---A.1/3}$$

which in cartesian co-ordinates becomes:-

$$\psi = -Uy + \frac{Ua^2y}{(x^2+y^2)} \qquad \text{---A.1/4}$$

The u and v velocity components may be found by differentiation. These components were then evaluated at each nodal point on the mesh, enabling the term S on the right hand side of equation A.1/2 to be evaluated using the finite difference formulae described in Chapter 4.

A square mesh was chosen ($\beta = 1$) such that equation A.1/2 becomes:-

$$p_{ij}^{k+1} = (1-\omega)\,p_{ij}^{k} + \frac{\omega}{4}\left(p_{ij+1}^{k} + p_{ij-1}^{k+1} + p_{i+1j}^{k} + p_{i-1j}^{k+1}\right) + \frac{\omega(\Delta x)^2}{4} S_{ij} \qquad \text{---A.1/5}$$

A series of computations were carried out using this formula for various mesh sizes (Δx). Boundary conditions were of the Dirichelet type supplied by the Bernoulli equation.

The number of sweeps required to reach convergence for various values of the relaxation factor were computed. Convergence was defined by the residual given by:-

$$R_{ij} = S_{ij} - \frac{p_{ij+1} + p_{ij-1} + p_{i+1j} + p_{i-1j} - 4p_{ij}}{(\Delta x)^2} \qquad \text{---A.1/6}$$

Sufficient accuracy was assumed to have been reached when:-

$$\text{Max}\,|R_{ij}| < 10^{6} \qquad \text{---A.1/7}$$

Figure A-1 shows a plot of the number of sweeps to convergence against relaxation factor , for four mesh spacings. It can be seen that the optimum relaxation factor is dependent upon mesh size but may be taken to be between 1.7 and 1.8 for practical purposes.

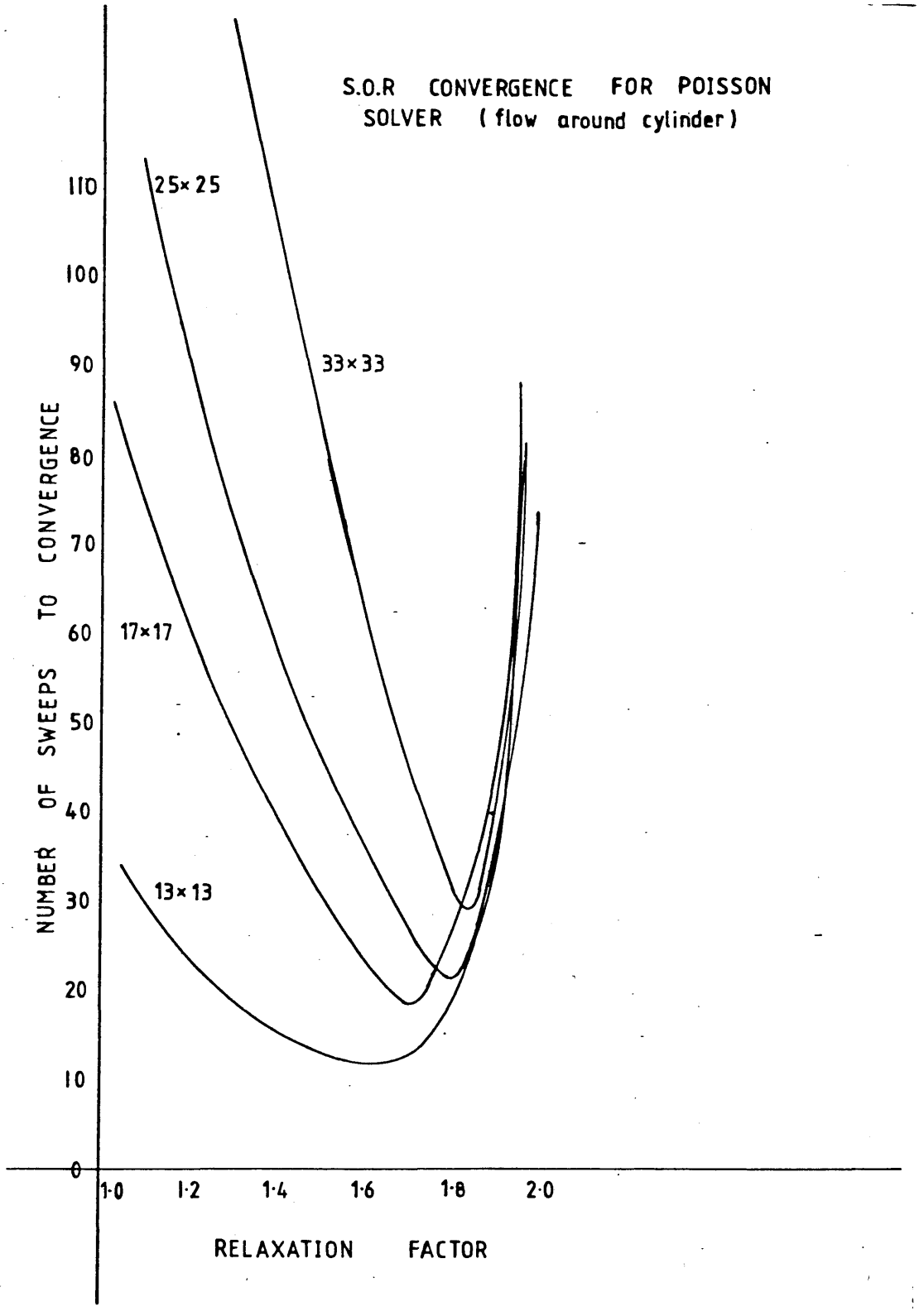
S.O.R CONVERGENCE FOR POISSON SOLVER (flow around cylinder)
25×25
33×33
17×17
13×13
NUMBER OF SWEEPS TO CONVERGENCE
110
100
90
80
70
60
50
40
30
20
10
0
1·0
1·2
1·4
1·6
1·8
2·0
RELAXATION FACTOR

It is also interesting to note how a decrease in mesh size causes the number of sweeps to convergence to increase regardless of relaxation factor. However, this increase is greatly reduced if the optimum value of ω is used for the computation.

REFERENCES

1 **GREENSPON, J.E.; JASPER, N.H; BIRMINGHAM, J.T:**

Sea Tests on the U.S.C.G.C. Unimak, Part 3, Pressures Strains and Deflections on the Bottom Plating Incident to Slamming.
Int. Shipbuilding Progress Vol.3, No.25, September 1956.

2 **JASPER, N.H.; BIRMINGHAM, J.T:**

Strains and Motions of the U.S.S. Essex (CVA9), During Storms near Cape Horn.
D.T.M.B. Report 1216, August 1958.

3 **JASPER, N.H.; ANDREWS, J.N.**

Preliminary Report of Strains and Motions of U.S.S. Ranger (CVA 61) During a Voyage around Cape Horn.
D.T.M.B. Report 1289, January 1959.

4 **AERTSSEN, G.**

Service Performance and Seakeeping Trials of M.V. Lukuga.
TRANSACTIONS R.I.N.A. Spring Meetings 1963.

5 **AERTSSEN, G.**

Service Performance and Seakeeping Trials of M.V. Jordaens.
R.I.N.A. Quarterly Transactions. Volume 108, No.4, October 1966.

6 **AERTSSEN, G.**

Service Performance and Seakeeping Trials on a Large Containership.
TRANSACTIONS R.I.N.A. Spring Meetings, 1972.

7 **AERTSSEN, G.**

An Estimate of Whipping Vibration Stress Based on Data from Four Ships.
Int. Shipbuilding Progress No.26, 1979.

8 **AERTSSEN, G; DELEMBRE, I:**

A Survey of Vibration Damping Factors Found from Slamming Experiments on Four Ships.
Trans North East Coast Engineers & Shipbuilders, Volume 87 No.3, 1981.

9 **WHEATON, J.W.; KANO, C.H.; DIAMANT, P.T.; BAILEY, F.C.:**

Analysis of Slamming Data from S.S. Wolverine State.
Ship Structures Committee Report, SSC 210, 1970.

10 **MACLEAN, W; LEWIS, E.V:**

Analysis of Slamming Stresses on S.S. Wolverine State.
Marine Technology Volume 10, January 1973.

11 **WHEATON, J.W.**

Further Analysis of Slamming Data from S.S. Wolverine State.
Ship Structures Committee Report, SSC 255, 1976.

12 **ANDREWS, R.N.; LLOYD, A.J.R.M:**

Full Scale Measurements of the Behaviour of Two Frigates in Severe Head Seas.
TRANSACTIONS R.I.N.A., No. 123, 1981.

13 **CLARKE, J.D.**

Measurement of Hull Stresses in Two Frigates during a Severe Weather Trial.
TRANSACTIONS R.I.N.A. No. 124, 1982.

14 **SAVITSKY,D.**

On the Seakeeping of Planing Hulls.
Marine Technology Volume 5, April 1968.

15 **RAMA WAHAB; CLARK PRITCHETT; LAWRENCE C. RUTH:**

On the Behaviour of the A.S.R. Catamaran in Waves.
Marine Technology, Volume 8, 1971.

16 **AKITA, Y; OCHI, K:**

Model Experiments on the Strength of Ships Moving in Waves.
TRANSACTIONS S.N.A.M.E., Vol. 63, 1955.

17 **OCHI, K.M.**

Model Experiments on Ship Strength and Slamming in Regular Waves.
TRANSACTIONS S.N.A.M.E., Volume 66, 1958.

18 **OCHI, K.M.**

Model Experiments on the Effect of a Bulbous Bow on Ship Slamming.
D.T.M.B. Report, 1360, 1960.

19 **BLEDSOE, M.D.; SCHWARTZ, F.M.:**

Experiments in Rotational Impact.
D.T.M.B. Report, 1145, October 1961.

20 **TODD, M.A.**

Slamming due to Pure Pitching Motion.
D.T.M.B. Report, 883, January 1955.

21 **OCHI, K.M.**

Experiments on the Effect of Bow Form on Ship Slamming.
D.T.M.B. Report, 1400, January 1962.

22 OCHI, K.M.

Extreme Behaviour of a Ship in Rough Seas, Slamming and the Shipping of Green Water.
SNAME New York Met., Nov 12-13, 1964.

23 **LEWISON, G.R.G.**

On the Reduction of Slamming Pressures.
TRANSACTIONS R.I.N.A., 1969

24 **CHUANG, S.L; BIRMINGHAM, J.T; FURIO, A.J.:**

Experimental Investigation of Catameran Cross-Structure Slamming.
NSRDC Report 4653, Sept. 1975.

25 **VON-KARMAN**

The impact of Seaplane Floats During Landing.
NACA TN321, Ocotober 1929

26 **WAGNER, H.**

Uber Stoss-Und Gleitvorgange Und der Oberflache von Flussigkeiten.
ZAMM, band 12, heft 4, 1932 pp.193-215

27 **SZEBEHELY, V.G.**

"Hydrodynamic Impact"
Applied Mechanics Reviews, Volume 12, 1959 pp.297-300

28 **FABULA, A.G.**

Ellipse Fitting Approximation of Two Dimensional Normal Symmetric Impact of Rigid Bodies in Water
5th Midwestern Conference on Fluid Mechanics, Ann Arbor, Michigan, 1957.

29 **BISIPLINGHOFF, R.L; DOHERTY, C.S:**

Some Studies of the Impact of Vee Wedges on A Water Surface
Journal of the Franklin Institute, Volume 253 pp 547-561, 1952

30 **CHU, WEN-HWA; ABRAMSON, M.N.:**

Hydrodynamic Theories of Ship Slamming, Review and Extension.
Journal of Ship Research, March 1961.

31 **OGILVIE, F.T.**

Compressibility Effects in Ship Slamming.
Shiffstechnik, Bd 10, 1963, Heft 53.

32 FERDINANDE, V.

Theoretical Considerations of the Penetration of a Wedge into the Water.
International Shipbuilding Progress, Volume 13, April 1966.

33 CHUANG, S.L.

Experiments on Flat Bottomed Slamming.
Journal of the Ship Research, March 1966.

34 CHUANG, S.L.

Experiments on Slamming of Wedge Shaped Bodies.
Journal of Ship Research, September 1967.

35 VERHAGEN, J.H.

The Impact of a Flat Plate on a Water Surface
Journal of Ship Research, December 1967.

36 LEWISON, G; MACLEAN, W.M.:

On the Cushioning of Water Impact by Entrapped Air.
Journal of Ship Research, Volume 12, No.2 June 1968.

37 JOHNSON, R.S.

The Effect of Air Compressibility on the Impact of a Flat Body upon a free surface.
College of Eng. Report, NA 66-8, University of California, Berkley 1966.

38 JOHNSON, R.S.

The Effect of Air Compressibility in a First Appromination to the Ship Slamming Problem.
Journal of Ship Research, March 1968.

39 CHUANG, S.L.

Theoretical Investigations on Slamming of Cone Shaped Bodies.
Journal of Ship Research. December 1969.

40 CHUANG, S.L; MILNE, DAVID T.

Drop Tests of Cones to Investigate the Three Dimensional Effects of Slamming.
N.S.R.D.C. Report 3543, April 1971.

41 CHUANG, S.L.

Impact Pressure Distributions on Wedge-shaped Hull Bottom of High Speed Craft.
N.S.R.D.C. Report 2953, August 1969.

42 JONES, R.R; ALLEN, R.G.

A Semi-empirical Computerised Method for Predicting Three Dimensional Slamming.
N.S.R.D.C. Report 4005, December 1972.

43 OCHI, K.M; MOTTER, L.E:

A Method to Estimate Slamming Characteristics for Ship Design.
Marine Technology Volume 8, No.2, April 1971.

44 CHUANG, S.L.

Slamming Tests of Three Dimensional Models in Calm Water and Waves.
N.S.R.D.C. Report 4095, September 1973.

45 CHUANG, S.L; BIRMINGHAM, J.T; FURIO, A.J:

Experimental Investigation of Catamaran Cross-structure Slamming in Waves.
N.S.R.D.C. Report 4653, September 1975.

46 WHITMAN, A.M; PACIONE, M.C.:

A Similitude Relationship for Flat Plate Hydrodynamic Impact.
Journal of Ship Research, No.17, 1973.

47 GALLAGHER, P.

Slamming - Some Ideas on the Origins of Wave Induced Impact Loads on Ships at Sea.
Final Year Project Report, University of Glasgow, 1980.

48 STAVOVY, ALEX B; CHUANG,S.L:

Analytical Determination of Slamming Pressures for High Speed Vehicles in Waves.
Journal of Ship Research, Volume 20, No.4, December 1976.

49 KOEHLER; KELLEBOROUGH:

Hydrodynamic Impact of a Falling Body on a Viscous Incompressible Fluid.
Journal of Ship Research, Volume 23, No.3, 1977.

50 GEERS, THOMAS L.

Boundary Element Method for Slamming Analysis.
Journal of Ship Research, Volume 26, No.2,, 1982.

51 GREENSPON, J.E.

Stresses and Deflections in Flat Rectangular Plates Under Dynamic Lateral Loads Based on Dynamic Theory.
International Shipbuilding Progress, Volume 3, No.18, 1955.

52 NAGAI, T.

Permanent Set of a Bottom Shell Plate due to Slamming Loading.
University of California at Berkeley, Inst. Of Eng. Research,
Series 186, Issue 2, 1962.

53 NAGAI, T.

Large Permanent Set of Ship Bottom Plating due to Slam Loads.
University of California at Berkeley, Inst. of Eng. Research,
Series 186, Issue 5, 1962.

54 LEIBOWITZ, R.C.; GREENSPON, J.E.:

A Method for Predicting the Plate Hull Girder Response of a Ship
Incident to Slam.
D.T.M.B. Report 1706, 1964.

55 CHUANG, S.L.

Experimental Investigation of Dynamic Interaction Between
Rectangular Elastic Plate and Fluid During Flat Bottomed Slamming.
N.S.R.D.C. Report 2411, June 1967.

56 CHUANG, S.L.

Design Criteria for Hydrofoil Hull Bottom Plating (A Practical
Application of Research on Slamming).
N.S.R.D.C. Report 3509, June 1971.

57 SELLARS, F.H.

The Influence of Structural Characteristics on Slamming Impact
Pressures.
Journal Of Ship Research, March 197 .

58 SELLARS, F.H.

Water Impact Loads.
Marine Technology, Volume 13, No.1, June 1976.

59 JONES, NORMAN.

Slamming Damage.
Journal of Ship Research, June 1973.

60 YUHARA

Fundamental Study of Wave Impact Loads on Ship Bow
Journal of Society of Naval Architects of Japan, Volume 137, 1974

61 BORG, S.F.

The Analysis of Ship Structures Subject to Slamming Loads.
Journal of Ship Research, December 1960.

62 LEIBOWITZ, R.C.

Comparison of Theory and Experiment for Slamming of a Dutch Destroyer.
D.I.M.B. Report 1511, June 1962.

63 **LEIBOWITZ, R.C.**

A Method for Predicting Slamming Forces on and Responses of a Ship Hull.
D.T.M.B. Reports 1691, September 1963.

64 **KAPLAN, P; SARGENT, T.P:**

Further Studies of Computer Simulation of Slamming and Other Wave Induced Vibratory Structural Loadings on Ships in Waves.
Ship Structures Committee Report, SSC-231, 1972.

65 **MANSOUR,A; d'OLIVEIRA, J.M.:**

Hull Bending Moment due to Ship Bottom Slamming in Regular Waves.
Journal of Ship Research, Volume 19, No.2, June 1975.

66 **GRAN, S; OLSEN,H; TELLSGARD F:**

Hull Response to Hydrodynamic Responses on Bow Flare.
Norwegian Maritime Research, No.3, Volume 4, 1976.

67 **NAGAI, T.**

Review of Structural Response Aspects of Slamming.
Journal of Ship Research, Volume 21, No.3, September 1973.

68 **KAWAKAMI; MICHIMOTO; KOBAYASHI:**

Prediction of Long Term Whipping Vibration Stress due to Slamming of a Large Full Ship in Rough Seas.
International Shipbuilding Progress, Volume 24, 1977.

69 **TAMAMOTO, Y; FUJIN, M; FUKASAWA, T:**

Motion and Longitudinal Strength of a Ship in Head Sea and the Effects of Non-Linearities.
Journal Soc. Naval Archs. of Japan, Volume 143, June 1978, Volume 144 December 1978, Volume 145, June 1979.

70 **BISHOP, R.E.D; PRICE, W.G; TAM, P.K.Y:**

On the Dynamics of Slamming.
Transactions R.I.N.A, Spring 1978.

71 **BISHOP, R.E.D; CLARKE, J.D; PRICE, W.G:**

Comparison of Full Scale and Predicted Responses of Two Frigates in a Severe Weather Trial.
Transaction R.I.N.A, 1983.

72 BISHOP, R.E.D; EATOCK-TAYLOR; JACKSON, K.L:

On the Structural Dynamics of Ships Hulls in Waves.
Transactions R.I.N.A., 1973.

73 **BISHOP, R.E.D; PRICE, W.G; TAM, P.K.Y:.**

Wave Induced Response of a Flexible Ship.
International Shipbuilding Progress, No. 24, 1977.

74 **BISHOP, R.E.D.; PRICE, W.G; TAM,P.K.Y:**

A Unified Dynamic Analysis of Ship Response to Waves.
Transaction R.I.N.A., 1977.

75 **BELIK, O; PRICE, W.G:**

Comparison of Slamming Theories in the Time Simulation of Ship Responses in Irregular Waves.
International Shipbuilding Progress, No.28, 1981.

76 **TICK, L.J.**

Certain Probalities Associated with Bow Submergence and Ship Slamming in Irregular Seas.
Journal of Ship Research, No. 2, 1958-59.

77 **FERDINANDE, V.**

Analysis of Slamming Phenomena on a Model of a Cargo Ship in Irregular Waves.
International Shipbuilding Progress, Volume 15, 1968.

78 **OCHI, M.K; MOTTER, L.E:**

Prediction of Extreme Values of Impact Pressure Associated with Ship Slamming.
Journal of Ship Research, June 1969.

79 **OCHI, M.K; MOTTER, L.E:**

Prediction of Slamming Characteristics and Hull Responses for Ship Design.
S.N.A.M.E. Annual Meeting N.Y. Section, Nov. 15-17, 1973.

80 **PSARAFTIS, H.N.**

Some New Aspects of Slamming Probability Theory.
Journal of Ship Research, Volume 22, No. 3,September 1975.

81 **OCHI, M.K.**

Extreme Values of Waves and Ship Responses Subject to the Markov Chain Condition.
TRANSACTIONS S.N.A.M.E., 1981.

82 CHEN, YUN-HSIANG.

Ship Vibration in Random Seas.
Journal of Ship Research, Volume 24, No.3, September 1980.

83 **MANSOUR, A.E; LOZOW, J:**

Statistical Theory of the Slamming Response of Marine Vehicles in Random Seas.
Journal of Ship Research, Volume 26 No. 4, 1982.

84 **RICE**

Mathematical Analysis of Random Noise
Bell System Technical Journal, Volume 23, 1944

85 **FERRO, G.**

Statistical Models for Low-frequency Springing and Impact Loads on Ships.
Ship Vibration Symposium; May 22-29, Geneva, July 1984.

√ 86 **KAPLAN, P; SILBERT, M.N:**

Impact Forces on Platform Horizontal Members in the Splash Zone.
Offshore Technology Conf. Paper, OTC 2498, 1976.

87 **LOCKWOOD-TAYLOR, J**

Some Hydrodynamic Inertia Coefficients
Philosophical Magazine, Series 7, Volume 9, 1930

88 **DALTON, C; NASH, J.M:**

Wave Slam on Horizontal Members of an Offshore Platform.
Offshore Technology Conf. Paper, OTC 2500, 1974.

89 **MILLER, B.L.**

Wave Slamming Loads on Horizontal Circular Elements of Offshore Structures.
Transactions R.I.N.A, April, 1977.

90 **CAMPBELL, I.M.C; WELLICOMBE, J.F; WEYNBERG, P:**

An Investigation into Wave Slamming Loads on Cylinders (Osflag 2A) Final Report.
Wolfson Marine Craft Unit, Report No. 317, March 1977.

91 **CAMPBELL, I.M.C; WEYNBERG, P:**

Slam Load Histories on Cylinders.
Wolfson Marine Craft Unit, Report No. 416, August 1979.

92 CAMPBELL, I.M.C; WEYNBERG, P:

Measurement of Parameters affecting Slamming, Final Report.
Wolfson Marine Craft Unit, Report No. 440, February 1980.

93 OCHI, M.K; TASAI, C.H:

Prediction of Impact Pressure Induced by Breaking Waves on Vertical Cylinders in Random Seas.
Applied Ocean Research, Volume 6, No.3, 1984.

94 LEWIS, E.V; HOFFMAN, D; MACLEAN, W.M; HOFF, R.V; ZUBALY, R.B:

Load Criteria for Ship Structural Design
Ship Structures Committee Report, SCC 240, 1973

95 OCHI, M.K (Chairman) et AL

Report of the ISSC Committee on Slamming and Dynamic Loads
ISSC Transactions, 1976

96 LAMB, H.

Hydrodynamics (6th Edition)
Dover Publications, New York

97 SCHLICHTING, H.
Boundary Layer Theory
McGraw-Hill, New York, 1968

98 BATCHELOR, G.K.

An Introduction to Fluid Dynamics
Cambridge University Press, Bently House, London. 1967.

99 ROACHE, P.J.

Computational Fluid Dynamics.
Hermosa Publishers, Albuquerque, New Mexico

100 FREIDMAN, A.

Partial Differential Equations
Holt, Rinehart Wilson, 1969.

101 BRANDT, A.

Multi-level Adaptive Solutions to Boundary Value Problems
Mathematics of Computational, Volume 31, No. 138 pp 333-390
April, 1977

102 ORLANSKI, I.

A Simple Boundary Condition for Unbounded Hyperbolic Flows
Journal of Computation Physics, No. 21 pp 251-264, 1976

103 HANDSON AND PETSCHEK

A Boundary Condition for Significantly Reducing Boundary Reflections with a Langrangian Mesh.
Journal of Computational Physics, No.21 , 1976

104 **NEWMAN, J.N.**

Marine Hydrodynamics
MIT Press, Cambridge Massachusettes, 1977

105 **SALVESEN, N.**

Five Years of Numerical Naval Ship Hydrodynamics at D.T.N.S.R.D.C.
Journal of Ship Research Volume 25, No. 4, December 1981

106 **HIRT, C.W; SHANNON, J.P:**

Free-Surface Stress Conditions for Incompressible Flow Calculations
Journal of Computational Physics, No. 2 pp 403-411, 1968

107 **NICHOLS, B.D; HIRT, C.W:**

Improved Free-Surface Boundary Conditions for Numerical Incompressible Flow Calculations
Journal of Computational Physics, No.8 pp 434-448, 1971

108 **MASSEY, B.S.**

Mechanics of Fluids (3rd Edition)
Van Nostrand Reinhold, 1978

109 **TAYLOR, C; HINTON; OWEN:**

Finite Element Programming of the Navier Stokes Equations
Pergammon Press, 1981

110 **BAKER, A.J:**

Finite Element Computational Fluid Dynamics
McGraw-Hill, New York, 1983

111 **CHEUNG; YEO**

A Practical Introduction to Finite Element Analysis
Pitman, 1980

112 **JENNINGS, A.**

Matrix Computation for Engineers and Scientists
Wiley, 1977

113 **HARLOW, F.H; WELCH, J.E:**

The M.A.C. Method: A Computing Technique for Solving Viscous Incompressible, Transient Fluid Flow Problems Involving Free Surfaces
The Physics of Fluids, No.8 pp 21-82, 1965

114 **CHAN, R.K.C; STREET, R.L:**

A Computer Study of Finite Amplitude Water Waves
Journal of Computational Physics, No. 6 pp 68-94, 1970

115 **GRAY, W.G**

An Efficient Finite Element Scheme for Two Dimensional Surface Water Waves.
Proc 1st. International Conference on Finite Elements in Water Resources. Pentech Press, London 1977.

116 **OLSEN, M.V; IRANI, M.B:**

Finite Element Analysis of Viscous Flow-Solid Body Interaction.
3rd. International Conference on Numerical Methods in Laminar and Turbulent Flow, 1983.

117 **RICHTMYER, R.D.**

Difference Methods for Initial Value Problems.
Interscience Publishers Inc., 1957.

118 **AMES, W.F.**

Numerical Methods for Partial Differential Equations.
Barnes & Noble Inc., 1969.

119 **MITCHELL, A.R.**

Computational Methods in Partial Differential Equations.
J. Wiley & Sons Ltd., 1969.

120 **MITCHELL, A.R.**

The Finite Difference Method in Partial Differential Equations.
J. Wiley & Sons Ltd., 1980.

121 **ROACHE, P.J.**

On Artificial Viscosity.
Journal of Computational Physics, Volume 10, No.2, October, 1972.

122 **GRESHO, P.M; LEE, R.L:**

Don't Suppress the Wiggles - They're Telling You Something.
Journal of Computational Fluids, Volume 9, 1981.

123 LEONARD, B.P.

A Stable and Accurate Convective Modelling Procedure Based on Quadratic Upstream Interpolation.
Computer Methods in Applied Mechanics and Engineering, Volume 9, June, 1979.

124 GENTRY, R.A; MARTIN, R.E; DALY, B.J:

An Eulerian Differencing Method for Unsteady Compressible Flow Problems.
Journal of Computational Physics, Volume 1 pp 87-118, 1966.

125 PEACEMAN, D.W; RACHFORD,H.H:

The Numerical Solution of Parabolic and Elliptic Differential Equations.
Journal of the Society of Industrial Applications of Mathematics No. 3 pp 28-41, 1955.

126 HIRT, C.W.

Heuristic Stability Theory for Finite Difference Equations.
Journal of Computational Physics, No.2 pp 339-355, 1968.

127 COURANT, R; FRIEDRICHS, K; LEWY H:

On the Partial Differential Equations of Mathematical Physics.
IBM Journal, pp 215-234, March, 1967.

128 LEONARD, B.P.

A Survey of Finite Differences of Opinion on Numerical Muddling of the Incomprehensible Defective Confusion Equation.
Applied Mathematical Modelling, Volume 4, 1980.

129 MacCORMACK, R.W; VIVIAND, H:

Computational Efficiency Achieved by Time Splitting of Finite Difference Operators.
A.I.A.A. Journal, January, 1972.

130 PEYRET, R; VIVIAND H:

Computation of Viscous Compressible Flows Based on the Navier Stokes Equations.
AGARDograph No. 212.

131 HACKBUSH

Introduction to the Multigrid Method for the Numerical Solution of Boundary Value Problems.
V.K.I. Lecture Series in Computational Fluid Dynamics, No. 5, 1981.

132 FRANKEL, S.P.

Convergence Rates of Iterative Treatments of Partial Differential Equations.
Math Tables and Other Aids to Computation, Volume 4, 1950.

133 YOUNG, D.

Iterative Methods for Solving Partial Differential Equations of the Elliptic Type.
Trans. Americal Mathematical Society, Volume 7, 1954.

134 GALLAGHER, P.

SPLASH - A Description of a Finite Difference Simulation Program.
University of Glasgow, Department of Naval Architecture and Ocean Engineering Report NAOE-82-14, 1982.

135 HIRT, C.W; NICHOLS, B.D; ROMERO, N.C:

S.O.L.A. A Numerical Solution Algorithm for Transient Fluid Flows.
Los Alamos Scientific Laboratory Report LA5852, 1975.

136 NICHOLS, B.D; HIRT, C.W:

Volume of Fluid Method (V.O.F.) for Dynamic Free Boundaries.
Journal of Computational Physics, No. 39, 1981.

137 GALLAGHER, P.

Flow 88 - A Program to Resolve Inviscid and Laminar Flow Around Rectangular Bodies and Source Distributions Beneath a Free Surface.
University of Glasgow, Marine Technology Centre Report, NAOE-84-51, 1984.

138 SASAKI, Y.K.

Variational Design of Finite Difference Schemes for Initial Value Problems with an Integral Invariant.
Journal of Computational Physics, No. 21 pp 270-278, 1976.

139 GALLAGHER, P.

A Finite Difference Time Marching Solution of the Slamming Problem (Water Entry Problem).
Proceedings of the 3rd. International Conference on Numerical Methods in Laminar and Turbulent Flows.
Pineridge Press, 1983.

140 HACKBUSH, W; TROTTENBERG, P:

Multigrid Methods.
Proceedings - Koln-Portz Conference on Multigrid Methods, 1981.

141 GALLAGHER, P.

NWAV90 - A Program to Simulate Free Surface Waves and Wave Loading on Fixed and Free Floating Structures.
University of Glasgow, Marine Technology Centre Report, NAOE-84-50, 1984.

142 FLAGG, C.N; NEWMANN, J.N:

Sway Added Mass Coefficients For Rectangular Profiles in Shallow Water.
Journal of Ship Research, Volume 15, pp 257 - 265, 1971.

143 BAI, K.J.

The Added Mass of 2-Dimensional Cylinders Heaving in Water of Finite Depth.
Journal of Fluid Mechanics, Volume 81, pp 85-105, 1977.